

**The Design, Construction, Simulation and Testing of  
a Novel Prototype Two-Stroke Opposed-Piston  
Engine**

By

**Samuel Frederick Furze**

(UEA Registration Number 100090123)

For

**The degree of Doctor of Philosophy**

at

**The University of East Anglia**

**The School of Engineering, Mathematics and Physics**

**2025**

This copy of the thesis has been supplied on condition that anyone who consults it is understood to recognise that its copyright rests with the author and that use of any information derived therefrom must be in accordance with current UK Copyright Law. In addition, any quotation or extract must include full attribution.

## Abstract

Climate change is of increasing concern globally, and there are extensive efforts to curb greenhouse gas emissions rates from many sectors of society, including transportation. Low-carbon fuels like biomethane are an important option in this respect, and using them more efficiently could help maximise their positive impact. Opposed-piston two-stroke engines might offer this opportunity. They are increasingly well-proven in compression ignition form, benefitting from thermodynamic advantages like a higher stroke-to-bore ratio, uniflow scavenging, and reduced heat loss to coolant. However, biomethane and similar fuels are very well-suited to spark ignition: contemporary examples of spark ignition opposed piston engines, which face challenges such as a large flame propagation distance and lack of tumble, are rare. In this project therefore, a new and novel design of spark ignition opposed piston engine, dedicated to the task of engine research, was proposed. The engine design was based on key identified requirements. These included that it be self-scavenging, with this process de-coupled from piston motion, and feature a separated oil-system and computer-controlled direct fuel injection. Critically, it required the ability to incorporate a cylinder-pressure transducer for future data acquisition. Numerous parts were designed in-house and machined both at the University of East Anglia and an external supplier, and these were coupled with select off-the-shelf parts to reduce manufacturing effort. The resulting engine is compact at less than 120 cm<sup>3</sup> swept volume, with a maximum engine case dimension of less than 450 mm. Computational fluid dynamics simulations were also performed of the air side cylinder surfaces, generating a fuelling map that was used to program the engine control unit for testing. Useful indicators for real engine behaviour were gained in addition: for example, in a fuelled simulation case at 5000 rpm and 150 kPa scavenge pressure the required fuel was more than 40 % over-estimated. This suggested that scavenging performance decreases markedly at higher engine speeds and lower scavenge pressures. Conversely, at 1500 rpm and 120/150/180 kPa, and 3000 rpm and 150/180 kPa, results suggested the motored simulations were able to predict the required fuel within 2%. Furthermore, three-dimensional visual results indicated the swirling intake port geometry may be able to improve combustion rates, by distorting the flame front around the combustion chamber rather than letting it progress radially. The most significant results however were gained when the design and simulation work were tested by trying to fire the engine for the first time. Despite a persistent over-fuelling issue, the engine started and ran smoothly, proving the initial success of the design. It therefore represents a significant research contribution and opportunity for further engine research, however additional work is required before it can be fully commissioned. This includes resolving the over-fuelling issue, as well as remedial modification to the timing system to prevent timing belt failure. Following this, sustained running under a load whilst using the cylinder pressure transducer could provide vital information over how well the design works under different conditions.

## **Access Condition and Agreement**

Each deposit in UEA Digital Repository is protected by copyright and other intellectual property rights, and duplication or sale of all or part of any of the Data Collections is not permitted, except that material may be duplicated by you for your research use or for educational purposes in electronic or print form. You must obtain permission from the copyright holder, usually the author, for any other use. Exceptions only apply where a deposit may be explicitly provided under a stated licence, such as a Creative Commons licence or Open Government licence.

Electronic or print copies may not be offered, whether for sale or otherwise to anyone, unless explicitly stated under a Creative Commons or Open Government license. Unauthorised reproduction, editing or reformatting for resale purposes is explicitly prohibited (except where approved by the copyright holder themselves) and UEA reserves the right to take immediate 'take down' action on behalf of the copyright and/or rights holder if this Access condition of the UEA Digital Repository is breached. Any material in this database has been supplied on the understanding that it is copyright material and that no quotation from the material may be published without proper acknowledgement.

## Acknowledgements

Convergent Science provided CONVERGE licenses and technical support for this work.

Special thanks to the Faculty of Science, University of East Anglia, for offering a scholarship (Reference: 100090123) that aided the carrying out of this work. I'd additionally like to thank the School of Engineering, Mathematics and Physics and Professor Chris Atkin, for bailing me out and investing in getting this prototype completed. I really am grateful, particularly as I had no idea if it would actually work. I should probably also acknowledge myself for the donation of small things like heat shrink and such; my parents for things I needed at very short notice from the online market-place that cannot be named, and any small donations from people that I have since forgotten about!

I could not have done this without the support of my parents, to whom I am eternally grateful for your love, the roof over my head, food, and much red wine supplied for 'therapy'! Also, my wonderful (and crazy) dalmatian Teddie (short for Theodora), you are my best friend in the whole world. Even if you do keep chewing my cuddly toys. Thanks of course go to some of my oldest friends, Alexander Baker, Daniel Tompson and Mark Rainsford – who I have known now for what seems like forever. Thanks also to Jim Rijks, for many drinks and kind words, and the same to Dr. 'terrible influence' Keith Alcock, and Dr. 'even worse influence' Michael O'Brien. My advisers have been the best: Dr. Sonia Melendi-Espina, who has got me through this and on extremely rare occasion even offered praise, and Dr. Dianzi Liu, who has helped me not go around in circles when trying to run CFD simulations. Special mention goes to Professor Lawrence Coates – I am proud to consider myself 'a product of the Lawrence years' of Engineering at UEA; also to Dr. Kathryn Coventry, who has been the kindest 'kind ear' I have ever met, and my therapist Shirley De Marco, who has been utterly wonderful. Many thanks to Scott Cordy for his CNC machining prowess, and Steven Barraclough – engineer, mentor, unofficial proof-reader and machinist extraordinaire – for your help throughout this project. I couldn't have done it without you, or your engineering works – thanks also then to Expansion Engines Limited. My gratitude to the support team at Life Racing Limited, who helped me through configuring and programming the ECU, to the HPC team at UEA for invaluable assistance in the use of the high-performance computing resources, and to Dr. Daniel Netherwood and Dr. Jack Panter for their assistance in writing section 6.4.

Finally, I'd like to remember Gareth – brilliant machinist and engineer, who helped me with my undergraduate project and who I really had hoped would see this new prototype run. It wouldn't have worked without your efforts, because the tensioner on the front belt that drives the blower is the one you made for me, way back when.

## Table of Contents

<b>Abstract</b> .....	<b>ii</b>
<b>Acknowledgements</b> .....	<b>iii</b>
<b>List of Figures</b> .....	<b>viii</b>
<b>List of Tables</b> .....	<b>xiv</b>
<b>Abbreviations and Nomenclature</b> .....	<b>xv</b>
<b>1. Introduction</b> .....	<b>1</b>
1.1 The Role of Emissions Legislation .....	1
1.1.1 Criteria Pollutants .....	1
1.1.2 Tailpipe GHG Emissions.....	2
1.2 Pressures on Internal Combustion Engine Technology.....	2
1.2.1 A Complex Problem.....	3
1.3 Using the Opposed Piston Engine to Help Reduce CO <sub>2</sub> Emissions.....	4
<b>2. Research Project Aims and Objectives</b> .....	<b>6</b>
<b>3. Literature Review Part 1: Background and Orientation</b> .....	<b>8</b>
3.1 Historical Context .....	8
3.1.1 Understanding the Four-Stroke Engine.....	13
3.1.2 Compression Ignition.....	15
3.2 Two-Stroke Engines .....	16
3.3 Opposed-Piston Engines .....	19
3.3.1 OP2S Operating Principle.....	20
3.3.2 Examples of OP2S Engines .....	21
3.4 Thermodynamic Advantages of Opposed-Piston Engines .....	26
3.4.1 High Stroke-to-Bore Ratio .....	27
3.4.2 De-coupled, Uniflow Scavenging.....	27
3.4.3 Two-Stroke Operation.....	29
3.5 Oil Short-Circuiting in Piston-Ported Engines.....	30
3.6 The Modern Engine .....	30
3.6.1 The Importance of Digital Engine Control .....	31

3.6.2	Recent Commercial Developments.....	32
3.7	Alternative Fuels.....	35
3.8	Alternative Combustion Strategies .....	36
3.8.1	Combustion in SI and CI Engines.....	37
3.8.2	HCCI Combustion and Related Strategies.....	38
3.9	Novel Engine Architectures .....	40
3.9.1	Reducing Oil Consumption in Piston-Ported Two-Stroke Engines .....	40
3.9.2	Renewed Interest in Two-Stroke Architectures.....	41
3.10	Contemporary Opposed-Piston Engine Research .....	42
3.10.1	Unconventional OP2S Mechanics.....	43
3.10.2	Computational Fluid Dynamics Studies.....	46
3.11	Summary.....	48
<b>4.</b>	<b>Literature Review Part 2: Spark Ignition in OP2S Engines .....</b>	<b>49</b>
4.1	Scavenging and Port Geometry.....	49
4.1.1	Flow Through Cylinder Ports.....	50
4.1.2	Useful Scavenging Parameters.....	52
4.1.3	Variations in Two-Stroke Scavenging Performance with Speed and Load.....	54
4.2	Measuring and Modelling Real Engine Flows.....	56
4.2.1	Early Scavenging Models .....	57
4.3	Challenges of SI Operation in OP2S Engines.....	58
4.3.1	Lack of Tumble .....	59
4.3.2	Mixture Preparation and Combustion .....	60
4.4	Summary Comments and an Opportunity for a Significant Research Contribution.....	63
<b>5.</b>	<b>Engine Design and Construction .....</b>	<b>64</b>
5.1	Starting Point .....	64
5.1.1	Basic Engine Parameters.....	64
5.1.2	Engine Synchronisation .....	67
5.2	Pistons, Cylinder Block and Cylinder Liner .....	69
5.2.1	Liner Porting .....	73

5.2.2	Injector, Spark Plug and Cylinder Pressure Transducer.....	75
5.3	Main Engine Cases .....	79
5.4	Engine Lubrication.....	84
5.4.1	Oil Sump .....	88
5.5	Front Shaft Housing and Output Shaft.....	89
5.6	Scavenging Arrangement .....	91
5.6.1	Engine Governor.....	95
5.7	Exterior Engine Components and Assembly.....	96
5.8	Summary Comments on Engine Design .....	101
<b>6.</b>	<b>Engine Simulation.....</b>	<b>103</b>
6.1	Structural Geometry.....	103
6.1.1	Intake and Exhaust Porting .....	103
6.1.2	Injector and Spark Plug.....	105
6.1.3	Complete Geometry .....	106
6.2	Boundary Conditions .....	106
6.3	Flow-Control, Initial Conditions, and Simulation Duration .....	108
6.4	RANS Equations.....	109
6.5	Volume Mesh and Timestep.....	111
6.5.1	Mesh Dependency Analysis .....	111
6.6	Motored Simulation Results.....	114
6.7	Fuelled Simulations .....	119
6.7.1	Configuration .....	119
6.7.2	Mesh Dependency Analysis .....	123
6.7.3	Fuelled Simulation Results .....	126
6.7.3.1	Cylinder Pressure Graphs.....	132
6.7.3.2	Air Motion During Scavenging.....	135
6.8	Summary Comments on Engine Simulation Work .....	145
<b>7.</b>	<b>Test Firing the Engine.....</b>	<b>147</b>
7.1	Engine Control Unit, Wiring Harness .....	147

7.1.1	Revised Wiring System.....	149
7.1.2	Running Stand.....	151
7.2	Timing the Engine and Programming the ECU.....	153
7.2.1	ECU Parameters and Fuelling Configuration.....	154
7.2.2	Dry Cranking.....	155
7.3	First Firing of the Engine.....	157
7.3.1	Scope and Results.....	157
7.3.2	Final Comments on Testing.....	160
<b>8.</b>	<b>Conclusions and Further Work.....</b>	<b>161</b>
8.1	Significant Research Contribution.....	161
8.2	Future Works.....	163
	<b>References:.....</b>	<b>164</b>
	<b>Bibliography:.....</b>	<b>178</b>
	<b>Appendix A: Engineering Drawings.....</b>	<b>179</b>
	<b>Appendix B: Additional Engine/Component Photographs, Machining and Assembly Processes.....</b>	<b>248</b>
	<b>Appendix C: Published Paper.....</b>	<b>261</b>

## List of Figures

Figure 1 - Felsted Belle, a 1916 Garrett Steam Traction Engine, Exhibited at the 2022 Strumpshaw Steam Engine Rally, Norfolk, England (Owned by S. Barraclough).....	9
Figure 2 - 1946 Lister D Engine Driving a Lister H2 Water Pump, Exhibited at the 2022 Strumpshaw Steam Engine Rally, Norfolk, England (Owned by A. Howlett).....	11
Figure 3 - Gardner 1F Hot Tube Engine Exhibited at the 2022 Strumpshaw Steam Engine Rally, Norfolk, England (Owned by R. Sadd).....	12
Figure 4 - Amanco Engine with Mechanical Spark Ignitor - Exhibited at the 2022 Strumpshaw Steam Engine Rally (Exhibitor not Known).....	12
Figure 5 - A Lucas Chain-Driven Magneto and LODGE Spark Plug .....	13
Figure 6 - The Four Stroke Cycle: A - Intake, B - Compression, C - Combustion/Expansion, D – Exhaust .....	14
Figure 7 - Petter Tank Cooled 2 Stroke Engine Lighting some Incandescent Bulbs, exhibited at the 2022 Strumpshaw Steam Engine Rally, Norfolk, England (Exhibitor not Known) .....	16
Figure 8 – Cross-Flow Scavenging (Left), Schnürle Loop Scavenging (Right).....	17
Figure 9 - MAN Loop Scavenging (Left), Valved Uniflow Scavenging (Middle), OP2S Uniflow Scavenging (Right) .....	18
Figure 10 – Simplified Valved Uniflow Blower-Scavenged Diesel Two-Stroke Cycle: A – Compression, B – Combustion/Expansion, C – Scavenging .....	19
Figure 11 - OP2S Operating Cycle .....	20
Figure 12 - Junkers OP2S Layout - B = Blower, IP = Intake Piston, EP = Exhaust Piston.....	21
Figure 13 - Napier Culverin Engine [57].....	22
Figure 14 - Napier Deltic CT18-42K [58] .....	23
Figure 15 - Part-Sectioned Three-Quarter Front View of Rootes TS3 Engine [60] .....	24
Figure 16 - Rootes TS3 With Rocker Cover Removed.....	24
Figure 17 - Different Configurations of OP2S Engine .....	26
Figure 18 - Annotated Example PV Diagram of an OP2S Engine .....	28
Figure 19 – Comparison Between SI and SI-CAI Heat Release Curves .....	39
Figure 20 - Example of Swirl-Inducing Intake Ports.....	49
Figure 21 - Cylinder Port Geometry and Port Types .....	50
Figure 22 - Perfect Mixing vs. Perfect Scavenging .....	54
Figure 23 - Trapping Efficiency vs. Delivery Ratio for a Loop-Scavenged GDI Two-Stroke Engine at Different Engine Speeds [88].....	55
Figure 24 - Benson 3-Stage Scavenging Model.....	58

Figure 25 - Illustrative Example of Tumbling Motion in OP2S Cylinder (Left) and Pent-Roof Four-Stroke Engine (Right) .....	59
Figure 26 - Comparison of Spark Plug Location on OP2S Cylinder (Left) and Four-Stroke Cylinder (Right).....	61
Figure 27 – A: Squish in Wedge-Head Engine; B: OP2S Engine with Centralised Piston-Bowl; C: OP2S Engine with Piston-Bowl at Edge; D: OP2S Engine with Offset Piston Bowl; E: OP2S Engine with Raised Piston Crown.....	62
Figure 28 - Prototype Engine from Undergraduate Project; Engine Width approximately 423 mm....	65
Figure 29 - One of the Crankshafts for the Engine .....	66
Figure 30 – Mock-up of the Belt Profile.....	67
Figure 31 - Details of the Flywheel Body.....	68
Figure 32 - Completed Pistons for the New Prototype .....	69
Figure 33 - Cylinder Block and Liner.....	70
Figure 34 - Cylinder Block and Liner Cutaway with Component Locations; IN = Intake, EX = Exhaust, SP = Spark Plug, SN = Sensor, INJ = Injector.....	71
Figure 35 - Cylinder Block Drawing View.....	71
Figure 36 - Simple Example of Worst-Case Scenario Tolerance Stack Up.....	72
Figure 37 – Simple Example of Corner Radius Tolerances.....	73
Figure 38 - Inlet Port Pattern .....	74
Figure 39 - Intake and Exhaust Port Profiles, Projected Along Port Central Axes; Dimensions in mm .....	75
Figure 40 - Bosch Fuel Injector .....	76
Figure 41 - Kistler 6054 Pressure Transducer .....	76
Figure 42 - Cross Section at Central Upstand of Cylinder Block and Cylinder Liner Assembly; Dimensions in degrees and mm .....	77
Figure 43 - View into the Cylinder Liner from the Intake End; Inner Diameter of Liner 39 mm .....	79
Figure 44 - Pressure Transducer in Position .....	79
Figure 45 – Inside Rear Engine Case – 1: Air Reservoir; 2: Cooling Jacket; 3: Oil Side; Black Arrows: Oil Drainage Channels; Red and White Arrows: Bearing Locations.....	80
Figure 46 - Front and Rear Engine Cases with Piston .....	81
Figure 47 - Drawing View of Rear Engine Case; Dimensions in mm .....	82
Figure 48 - Oil Pump Parts in Recess in Rear Engine Case.....	84
Figure 49 - Oil Pump Housing and Associated Parts.....	84
Figure 50 – Extract of Pump Housing Drawing; Dimensions in mm .....	85
Figure 51 - Oil Pickup Tube Position .....	86
Figure 52 - Oil Pump in the Rear Engine Case.....	86
Figure 53 - Oil Distribution Block and Crankcase Breather in Position on the Front Shaft Housing ..	87

Figure 54 - Oil Feed Jets.....	87
Figure 55 - The Oil Sump and Associated Components.....	88
Figure 56 – Extract of Oil Sump Drawing; Dimensions in mm .....	89
Figure 57 - Front Shaft Housing Details.....	90
Figure 58 - GDI Pump Plunger and Steel Pad .....	90
Figure 59 - Engine Output Shaft Drawing .....	91
Figure 60 - Ogura TX02 Roots Type Supercharger.....	92
Figure 61 - Performance Map for the TX02 Supercharger [147] .....	92
Figure 62 - OP2S Scavenging System .....	93
Figure 63 - Bypass Valve Assembly in Position on the Engine .....	94
Figure 64 – Simplified Bypass Valve Housing Drawing; Dimensions in mm .....	94
Figure 65 - Mechanical Governor Components.....	95
Figure 66 - The Engine During a Test Assembly .....	96
Figure 67 - Front View of the Engine During Further Assembly .....	97
Figure 68 - Top View of the Engine when Close to Completion.....	99
Figure 69 - General Overview of the Front of the Engine when close to Completion .....	100
Figure 70 - Rear View of the Engine on a Running Stand.....	100
Figure 71 - View of the Completed Engine on the Running Stand. ....	101
Figure 72 - Cross Section Showing Cylinder (purple), Intake Gallery (green) and Exhaust Gallery (orange).....	104
Figure 73 – Left: View of Intake Gallery from Cylinder End; Right: View of Exhaust Gallery from Cylinder End.....	104
Figure 74 - Isolated View of Central Part of Cylinder (purple), with Injector Tip (yellow) and Spark Plug Tip (brown).....	105
Figure 75 - Simulation Geometry; Cylinder (Purple, cutaway), Intake Gallery (Green, cutaway), Exhaust Gallery (Orange, cutaway), Intake Piston (Blue), Exhaust Piston (Pink), Injector Tip (Yellow) and Spark Plug Tip (Brown).....	106
Figure 76 - Trapped Mass Variation with Mesh Size, and Default Configuration .....	112
Figure 77 - Cell-Count Variation with Mesh Size, and Default Configuration .....	113
Figure 78 - Runtime Variation with Mesh Size, and Default Configuration .....	113
Figure 79 - In Cylinder Trapped Mass of all Species, 1st Engine Cycle .....	114
Figure 80 - In Cylinder Trapped Mass of all Species, 2nd Engine Cycle.....	115
Figure 81 - In Cylinder Trapped Mass of all Species, 3rd Engine Cycle .....	115
Figure 82 - 1st Cycle Initial Cylinder Mixture Remaining.....	116
Figure 83 - 2nd Cycle Initial Cylinder Mixture Remaining.....	116
Figure 84 - 3rd Cycle Initial Cylinder Mixture Remaining .....	117

Figure 85 - Isolated View of Central Part of Cylinder (purple), with Injector Tip (yellow) and Spark Plug Tip (brown) and Injector Gas Inlet (1) and Injector Tube (2).....	120
Figure 86 - Equivalence Ratio Variation with Base Mesh Cell Size, and Default Configuration .....	123
Figure 87 - Cell Count Variation with Base Mesh Cell Size, and Default Configuration .....	124
Figure 88 - Runtime Variation with Base Mesh Cell Size, and Default Configuration.....	124
Figure 89 - Cylinder Pressure vs. Crank Angle for 3rd Engine Cycle with Variation in Base Mesh Cell Size, and Default Configuration.....	125
Figure 90 - Cylinder Pressure vs. Volume for 3rd Engine Cycle with Variation in Base Mesh Cell Size, and Default Configuration .....	125
Figure 91 - Equivalence Ratio in the Centre of the Cylinder, 618 CAD to 693 CAD.....	128
Figure 92 - Temperature Contour Slices at Z=0 (left), X=0 (middle), Y=0 (right) for 3rd Cycle Combustion Event, 693 CAD to 703 CAD.....	129
Figure 93 - Temperature Contour Slices at Z=0 (left), X=0 (middle), Y=0 (right) for 3rd Cycle Combustion Event, 708 CAD to 718 CAD.....	130
Figure 94 - Temperature Contour Slices at Z=0 (left), X=0 (middle), Y=0 (right) for 3rd Cycle Combustion Event, 723 CAD and 728 CAD.....	131
Figure 95 - In-Cylinder Pressure Tracing for Motored Case (Black Line) and Fuelled Case (Red Line) .....	132
Figure 96 - Pressure Volume Graph for the Motored Case (Black Line) and Fuelled Case (Red Line) .....	133
Figure 97 - Cylinder Pressure vs. Volume for 1500 rpm, 120/150/180 kPa Fuelled Cases, 3rd Engine Cycle.....	134
Figure 98 - Cylinder Pressure vs. Volume for 3000 rpm, 120/150/180 kPa Fuelled Cases, 3rd Engine Cycle.....	134
Figure 99 - Cylinder Pressure vs. Volume for 5000 rpm, 120/150/180 kPa Fuelled Cases, 3rd Engine Cycle.....	135
Figure 100 - Velocity Magnitude in the X Plane (Left) and Y Plane (Right) of the Cylinder, 463 CAD to 523 CAD.....	136
Figure 101 - Velocity Magnitude in the X Plane (Left) and Y Plane (Right) of the Cylinder, 543 CAD to 603 CAD.....	137
Figure 102 - Velocity Profile Through Intake Ports (Z Slice), 463 to 603 CAD.....	138
Figure 103 - Turbulent Velocity (m/s) through the Intake Ports, 463 to 603 CAD.....	140
Figure 104 - TKE Through the Intake Ports, 463 to 603 CAD.....	141
Figure 105 - TKE in the X Plane (Left) and Y Plane (Right) of the Cylinder, 463 CAD to 523 CAD .....	142
Figure 106 - TKE in the X Plane (Left) and Y Plane (Right) of the Cylinder, 543 CAD to 603 CAD .....	143

Figure 107 - H2O Mass Fraction in the X Plane (Left) and Y Plane (Right), 483 CAD to 523 CAD	144
Figure 108 - H2O Mass Fraction in the X Plane (Left) and Y Plane (Right), 583 CAD to 603 CAD	145
Figure 109 - The Handheld Control Pendant	149
Figure 110 - Main Power Circuit: ES1 = Emergency Stop Switch; KS1 = Key Switch; MI1 = Manual Isolator; NC = Normally Closed	150
Figure 111 - Inside the Wiring Box	151
Figure 112 - Completed Test Stand with Engine ready for Testing	152
Figure 113 - Test Stand Wiring	153
Figure 114 - Adding Timing Marks to the Crankshaft Pulleys	153
Figure 115 – Front View of Engine Turning during Dry-Cranking	155
Figure 116 - Rear View of Engine Turning during Dry-Cranking	156
Figure 117 - Oil Light off Indicating Oil Pump Function	156
Figure 118 - First Engine Start Video Still 1	158
Figure 119 - First Engine Start Video Still 2	158
Figure 120 - First Engine Start Video Still 3	158
Figure 121 - Engine Run Video Still Belt Motion 1	159
Figure 122 - Engine Run Video Still Belt Motion 2	159
Figure 123 - Fuel Injector Located in its Seat after that has just been Machined; Overall Cylinder Block Length 203 mm	248
Figure 124 - Spark Plug in Position in the Middle of the Intake and Exhaust Galleries; Overall Cylinder Block Length 203 mm	248
Figure 125 - Positioning of the Milling Machine Quill to Machine the Pressure Sensor Seat	249
Figure 126 - Completed Cylinder Block and Liner Assembly, With Spark Plug, Injector and Pressure Transducer Seats, Ready for Installation; Overall Length of Cylinder Block 203 mm	249
Figure 127 - Front (top) and Rear (bottom) Engine Cases - Interior View	250
Figure 128 - Front (top) and Rear (bottom) Engine Cases - Exterior View	251
Figure 129 - Crank Slider Mechanisms and Cylinder Block and Liner Before Assembly	252
Figure 130 - Inserting the Cylinder Block and Crank Sliders into the Rear Engine Case	252
Figure 131 - Output Shaft Assembly	253
Figure 132 - Rear Engine Case on top of the Oil Sump	253
Figure 133 - Flywheel Pulley during Machining	254
Figure 134 - The Flywheel Assembly	254
Figure 135 - Rear of the Engine During a Test Fit of the Timing Apparatus	255
Figure 136 – RINGFEDER® Locking Assembly	255
Figure 137 - Detail of Blower Mounting	256
Figure 138 - Bypass Valve Open; Bore Diameter Approximately 27 mm	257
Figure 139 - Bypass Valve Closed; Bore Diameter Approximately 27 mm	257

Figure 140 - Governor Drive Gear and Fly-Weight Governor .....	258
Figure 141 - The Governor Shaft and its Drive Gear in Position .....	259
Figure 142 - Yellow Metal Insert for GDI Pump Plunger .....	259
Figure 143 - The Coolant Outlet Hose and Temperature Sensor .....	260

## List of Tables

Table 1 - Engine Bore and Piston Stroke.....	66
Table 2 - Specifications of RINGFEDER® RfN 7004 Locking Assembly, 19 mm x 47 mm .....	68
Table 3 - Kistler 6054C Sensor Specifications .....	78
Table 4 – NTK Lambda Sensor Specification .....	98
Table 5 - Details of Engine Sensors.....	98
Table 6 - Geometry Boundary Conditions. Note that 'Direction' represents the normal direction of the piston crowns, and 'Phase' the difference between crankshaft position.....	108
Table 7 - Initial Conditions for Regions at -272 CAD.....	109
Table 8 - Mesh Dependency Simulation Cases .....	112
Table 9 – Fuel Table: In-Cylinder Air Mass as a Percentage of Full Speed and Load.....	118
Table 10 - Fuel Gas Mass Flow Rate for 3000 rpm 150 kPa Fuelled Simulation .....	120
Table 11 - Ignition Energy Sources .....	122
Table 12 - Equivalence Ratio and Error Per Cycle.....	126
Table 13 - Injected Fuel Mass (kg) and Error Per Cycle .....	126
Table 14 - Life Racing ECU Specifications.....	147
Table 15 - Example ECU Pin Configuration .....	148
Table 16 - ECU Parameter Configuration for Engine Testing.....	154
Table 17 - Injection Base Timing for ECU.....	155

## Abbreviations and Nomenclature

1D: One-Dimensional	IPO: Intake Port Open
2D: Two-Dimensional	kg/CAD: kilograms-per-crank-angle-degree
3D: Three-Dimensional	kg/s: kilograms-per-second
AMR: Adaptive Mesh Refinement	m/s: metres-per-second
BEV: Battery Electric Vehicle	MPPR: Maximum Pressure Rise Rate
BSFC: Brake Specific Fuel Consumption	N <sub>2</sub> : Nitrogen
BTE: Brake Thermal Efficiency	NMOG: Non-Methane Organic Gases
CAD: Crank Angle Degrees	NO <sub>x</sub> : Oxides of Nitrogen
CARB: California Air Resources Board	O <sub>2</sub> : Oxygen
CFD: Computational Fluid Dynamics	OP2S: Opposed-Piston Two-Stroke
CH <sub>4</sub> : Methane	PCCI: Premixed-Charge Compression-Ignition
CI: Compression-Ignition	PCV: Positive Crankcase Ventilation
CNC: Computer Numerical Control	PFP: Peak Firing Pressure
CNG: Compressed Natural Gas	ppm: parts-per-million
CO: Carbon Monoxide	PV: Pressure/Volume
CO <sub>2</sub> : Carbon Dioxide	RANS: Reynolds-Averaged Navier-Stokes
DI2S: Direct-Injection Two-Stroke	RDE: Real Driving Emissions
ECU: Engine Control Unit	rpm: revolutions-per-minute
E-Fuels: Electro-Fuels	SCR: Selective Catalytic Reduction
EGR: Exhaust Gas Recirculation	SI: Spark-Ignition
EPO: Exhaust Port Open	SO <sub>2</sub> : Sulphur Dioxide
Eq.: Equation	SOC: Start of Combustion
FPE: Free-Piston Engine	SVR: Surface Area to Volume Ratio
FPLG: Free-Piston Linear-Generator	TDC: Top Dead Centre
GDI: Gasoline Direct Injection	
GHG: Greenhouse Gases	
GWP: Global Warming Potential	
H <sub>2</sub> O: Water	
HCCI: Homogenised Charge Compression Ignition	
HEV: Hybrid Electric Vehicle	
HGV: Heavy Goods Vehicle	
IDC: Inner Dead Centre	
IMEP: Indicated Mean Effective Pressure	

## 1. Introduction

The internal combustion engine is among the most important machines to the modern world [1]. It is well known for powering the overwhelming majority of global land and sea-based transportation, but it finds use in other sectors too, like in stationary power generation, and in industrialised agriculture, where the European Agricultural Machinery Association notes it is, and will remain, essential [2], [3], [4]. The success and wide field of application of internal combustion engine technology has largely been possible thanks to an abundance of energy dense fuels, sourced mostly from petroleum (oil and gas) [5]. It is noted that in 2022 more than 80% of global primary energy consumption originated from fossil fuels, including petroleum and coal [2], [6]. However, the extensive usage of these fuels can cause pollution and environmental degradation, and the greenhouse gas ('GHG') emissions from their combustion are a major driver of anthropogenic climate change. The seemingly logical reaction to this has been to try and reduce fossil fuel use, with significant political pressure in this direction.

### 1.1 The Role of Emissions Legislation

The desire to control emissions from the exhaust stream of an internal combustion engine needs little justification: understanding of these exhaust emissions and their role in air-pollution has grown over time, as has the knowledge on the damage that they can cause. For example, in addition to the aforementioned climate forcing effect of GHG emissions, air pollution in general is known to cause increased rates of mortality and affect numerous body systems – not just respiratory and cardiovascular [7]. As a result, over the last few decades legislation has been enacted globally which aims to limit the emissions not only of carbon dioxide ('CO<sub>2</sub>'), but also criteria pollutants [8].

#### 1.1.1 Criteria Pollutants

Criteria pollutants are those with air-pollution impacts, including particulate matter, and harmful gases like oxides of nitrogen ('NO<sub>x</sub>'), non-methane organic gases ('NMOG') and carbon monoxide ('CO') [8]. Conway *et-al.* note that the emissions limits for these are tightening globally but vary in their approach. In the USA for example it is expected that a 2025 model vehicle will in effect require a reduction in the total mass of particulate emissions of approximately 99% in comparison to a 2000 model vehicle, and a reduction of NO<sub>x</sub> and NMOG emissions of approximately 90% - among the tightest in the world for the latter. Consequently, a trend has been to adopt sophisticated aftertreatment systems to reduce these gaseous emissions [8]. In Europe on the other hand, a particle number method is used for particulate matter, and real driving emissions ('RDE') testing is required. As a result, particulate filters are now a routine exhaust aftertreatment method in both spark ignition ('SI') and compression-ignition ('CI') automotive engines to ensure compliance [8].

### 1.1.2 Tailpipe GHG Emissions

Conway et-al. also described how tailpipe CO<sub>2</sub> emissions are tightening globally. It was expected that European emissions limits would be less than 59 g/km by 2030 – a reduction of some 37.5% from the 2020 level [8]. There is a degree of uncertainty at present given that the European commission has revised an intermediary target for 2025 that gives more time for manufacturers to meet it [9]. This is pertinent given that recently fleetwide CO<sub>2</sub> emissions in the European automotive sector have not continued to fall as expected – it was suggested by Conway et-al. that a growing preference for larger, heavier vehicles is partly to blame for this. However, standards are likely to continue tightening and the pressure on engine technologies continues to grow [8].

## 1.2 Pressures on Internal Combustion Engine Technology

In addition to emissions standards, technologies that burn fossil fuels have increasingly become political targets, including the internal combustion engine – despite the significant progress in reducing emissions to date [1]. For example, some western countries including the United Kingdom have committed to being ‘net zero’ greenhouse gas emitters by the middle of the century, with eye-catching policies such as banning the sale of new petrol and diesel vehicles in favour of ‘zero emission’ battery electric vehicles (‘BEV’s) by a certain date. Whilst some of these policies might please environmental-pressure groups, it is becoming increasingly clear that many are unlikely to be successful in achieving meaningful real world CO<sub>2</sub> reductions [2], [8].

BEVs are a case in point. For example, averaging of emissions from electricity generation to determine their GHG emissions rates may indicate significant advantages, but as Burton *et-al.* note, this will result in values significantly different to the real-world emissions rates. Instead, in proposing a more accurate method for the United States grid, Burton *et-al.* found that BEVs do not in fact result in uniformly lower emissions rates than hybrid electric vehicles (‘HEV’s), and in some cases actually have higher emissions [10]. Furthermore, the impact that the additional weight of BEV powertrains has on both emissions and infrastructure must also be considered. Emissions Analytics, a U.K.-based company investigating the emissions of various pollutants mainly from road vehicles, has joined others in voicing concerns over vehicle weight. Private vehicles have become heavier over time, and this is markedly worse with large BEVs. The resulting increased wear on tyres and brakes can cause non-exhaust emissions rates that are orders of magnitude greater than the regulated emissions from a vehicle exhaust [11]. Hence, whilst BEVs may have no tail-pipe they are certainly not ‘zero emissions vehicles’; notably the U.K. Advertising Standards Authority has recently clamped down on the use of the term [12].

This is not to say that BEVs are not part of the future: on the contrary, as Senecal *et-al.* note they may help improve local air quality, but it is important to consider the impact of a transport system over its lifetime, and not just ‘at the tailpipe’. They argue that a diverse portfolio of technologies, including electrification *and* improved combustion engines, is more likely to successfully reduce GHG emissions from the transport sector overall than any ‘prescribed technology strategy’ [1].

It is also important to consider other impacts beyond air pollution and GHG emissions. For example, Kalghatgi notes the significant human toxicity potential of BEVs that is associated with the mining of the minerals required for their batteries [2]. Concerns exist for alternative fuels too; first generation biofuels in particular face the arguably legitimate criticism around ‘food vs. fuel’ – i.e. using crops to produce fuel that could otherwise be used to produce food. It is noted that this is not true for all biofuels - some (like biomethane) mainly rely on feedstock that would otherwise be considered waste [13]. Similarly, hydrogen could be produced using renewable electricity via electrolysis; the HYBRIT collaboration for example employs this process to reduce emissions from steel production by replacing coking coal with hydrogen [14]. There may even exist the further possibility to take advantage of heat from nuclear power plants to support high-temperature steam electrolysis [15]. Presently though, the procurement of hydrogen relies overwhelmingly on fossil fuels, in particular coal and natural gas [16]. Kalghatgi also argues that whilst not quite as bad for hydrogen itself, the making of electro-fuels (‘E-Fuels’) from renewable electricity is not an energy efficient process, although they might offer an additional way of supporting intermittent sources such as wind and solar (as an alternative means of storage). More importantly however, he notes the comparative lack of energy density of alternatives to petroleum; in the case of batteries for example, this poses very serious limitations on long distance and heavy-duty applications [2].

### **1.2.1 A Complex Problem**

The above should serve to highlight that global decarbonisation is an inherently complex problem and that there is no single solution to it. Furthermore, Professor Sir Dieter Helm presents particularly sobering assessments that throw many of the current aspirations of reaching net zero global CO<sub>2</sub> emissions by the middle of the century into significant doubt. He raises very serious questions about the assumptions and arguments behind net zero targets, as well as noting the importance of not equating renewable electricity generation solely with its marginal costs [17]. Worse still, he notes that UK CO<sub>2</sub> emissions are not being measured correctly in the first place: UK net zero targets are based on territorial emissions or ‘carbon production’, so incentivising the exporting of CO<sub>2</sub> emissions overseas. He contends that CO<sub>2</sub> emissions should be measured in terms of carbon consumption instead of domestic carbon production - particularly considering the fact that the emissions from Drax power station are not even included in the latter [18]. Whilst noting the reduction in global GHG emission rates is essential,

he also argues that it is important to be realistic about the costs involved, and the fact that presently, the 1.5-degree Celsius warming target is highly unlikely to be achieved [17].

In addition to being complex, the scale of problem is vast: in the transport sector alone *billions* of litres of fuel are consumed daily [2]. It is also expected that a significant proportion (possibly the majority) of transport energy will still come from petroleum in the coming decades. In light of these realities, it is essential that the internal combustion engine continue to be improved [3]. Were it not to be, and alternative technologies do not perform as well as hoped, in the years that pass a potentially significant GHG reduction opportunity will have been wasted.

### **1.3 Using the Opposed Piston Engine to Help Reduce CO<sub>2</sub> Emissions**

Exploring alternative and more thermally efficient engine architectures, like opposed-piston two-stroke ('OP2S') engines, is one of the possible ways of approaching this task. OP2S engines benefit from fundamental thermodynamic advantages over conventional four-stroke engines, such as a very high stroke to bore ratio without the need for a correspondingly high piston speed, because there are two pistons per cylinder. A high stroke-to-bore ratio is advantageous since it reduces the available surface area for heat transfer whilst also increasing the volume for a given cylinder diameter, so each cylinder can produce more power. The second piston also can operate at higher surface temperatures in comparison to a cylinder head (which OP2S engines do not have), further reducing heat loss. They couple these benefits with two-stroke operation resulting increased power density, and uniflow-scavenging driven by a separate scavenging system that lowers pumping losses in comparison to a conventional poppet-valve engine [19], [20], [21], [22].

Indeed, CI OP2S engines have in recent years become a focus of development, with real examples routinely demonstrating that the thermal advantages the OP2S architecture offers are not just theoretical [3]. It is noted however that whilst it exists, contemporary literature on the subject of SI OP2S engines is much less prevalent than it is for CI OP2S engines, particularly in regards to real, working engines. This is surprising given that SI engines in general can offer a relatively simple way of igniting fuels that may not be as well suited to a CI system on their own: Gaseous fuels are a good example of this, where a pilot fuel is sometimes employed in a CI engine to ignite the main fuel charge [23].

SI operation does bring with it a penalty to thermal efficiency, mainly due to the lower compression ratios used, but utilising an OP2S architecture and leveraging its inherent thermodynamic advantages might present a way of more efficiently using fuels better suited to SI operation, which might include hydrogen, natural-gas, or ethanol, for example [5]. There may also exist the possibility of exploiting ultra-lean combustion strategies with some fuels - hydrogen is noted as a very good example of this

given the difficulty of using it in a CI system on its own [24], [25]. The aim of this research project therefore is to design and demonstrate a new and novel, proof-of-concept SI OP2S engine prototype, that is of a similar architecture to its modern CI counterparts that are becoming increasingly well proven [26], [27]. In doing so, it could help to validate the possibility of more efficiently utilising fuels like those discussed above. It could thereby enable future research towards another option in the vital quest to reduce the rate of anthropogenic GHG emissions and avoid the worst effects of climate change.

This thesis is organised into chapters. Chapter 2 defines the aim of the research project and delineates it into three key objectives, and a two-part literature review begins in chapter 3, covering the wider internal combustion field including opposed piston engines and the state of the art. The second part of the literature review, chapter 4, addresses spark ignition in opposed piston engines in much more detail. Chapter 5 represents the first of the objectives identified in chapter 2, presenting the design and construction of the prototype engine. Similarly, chapter 6 represents the second objective and covers the computational fluid dynamics simulations that were undertaken of the engine cylinder. Likewise, chapter 7 addresses the third objective, and discusses the integration of the work of chapters 4 and 5 into a preliminary engine firing (that ultimately proved successful). Chapter 8 concludes the thesis and reflects on the significant findings of the research, as well as future work directions that the next researcher could undertake, such as loaded engine testing. References and bibliography follow, succeeded by appendices. These include numerous figures such as engineering drawings and photographs, many of which are referred to in chapter 5, as well as a published paper covering much of the work in chapter 6.

## 2. Research Project Aims and Objectives

The overall aim of the research project is to provide a real, blower scavenged SI OP2S engine prototype as a platform for future research. Opposed piston engines are relatively unique in their layout and operation, so modifying commercially available four-stroke, or indeed two-stroke engines into a prototype OP2S engine was deemed likely to bring unacceptable limitations, particularly in regard to physical layout. As such, the most appropriate course of action identified was to design a one-off prototype, as a suitable platform to enable future engine research. Because of the magnitude of such a task, several key objectives were defined, and the project split into manageable work packages which are described by the three key objectives listed below.

**Objective one:** Design and construct an OP2S engine prototype. The following engine characteristics were identified as important:

- The engine must be blower-scavenged to retain decoupled pumping work, and ‘self-sustaining’ such that it does not require external mechanical or electrical power to function beyond the typical 12-volt apparatus such as ignition coil and water pump.
- The oil side of the engine needs to be separate from the combustion side, and the fuel needs to be injected directly into the cylinder of the engine to minimise fuel short-circuiting.
- The engine needs to be of a suitable size and design so as to be reasonably manufacturable and transportable, as well as easy to disassemble and maintain by trained personnel.
- It also needs to be able to feature data acquisition apparatus such as a cylinder pressure sensor, and couple up to a load for testing.

**Objective two:** Generate a base fuelling map for the engine control unit (‘ECU’) such that it can look-up the required value for the relevant operating conditions. Given the lack of any empirical test data for the engine, computational fluid dynamics could be used to do this by modelling the proposed cylinder geometry and provide an approximation of the trapped mass of air in the cylinder under different conditions. It could also provide a useful evaluation on:

- The bulk in-cylinder flow regimes.
- How well the scavenging process is achieved.
- Whether a high degree of swirl is established (to aid mixing of the fuel and flame propagation).

**Objective three:** Proof test the engine to demonstrate its successful functioning. Since the design of the prototype itself carries with it a risk of failure because of its novelty, it was important to minimise

risk elsewhere. Therefore, petroleum spirit (i.e. petrol/gasoline) was deemed the most appropriate fuel choice for the initial testing. This is because petroleum spirit is a fuel for which the safe handling thereof is well understood, many inexpensive and commercially produced components already exist that are designed to work with it, and it is a widely accepted fuel for analysing engine performance. Before engine testing could commence however, an engine running stand suitable for the task needed to be commissioned. This running stand needed the following components/characteristics:

- A fully stand alone, integrated wiring system to support the engine functions and controls.
- A means of starting, running and stopping the engine.
- The means to manage the ancillary needs of the engine such as fuel delivery and cooling water.
- Be portable so that the engine and test stand can be transported to suitable testing facilities.
- Feature the required safety apparatus such as belt guards.

The final part of commissioning the running stand was to conduct a 'dry-cranking' test. Dry-cranking is where the engine is cranked over using the starter motor but is not fuelled, so it cannot start. This vital step helped to ensure basic functions like ECU synchronisation, oil circulation, sensor functioning, and so on, in a low-risk way (due to the engine being unable to start). Once this was completed, only then could a first firing attempt of the engine be undertaken. It is important to remember that the primary research objective was to deliver the OP2S engine as a research platform for testing the architecture using alternative fuels and spark ignition, given the novelty of such a machine. Therefore, the most important aspect of fuelled testing was to provide evidence that it was able to function, and so meet that objective. If so, it could then also provide insight to the following:

- How easily (or otherwise) did the engine start?
- Were there any problems with it, or undesirable characteristics that it displayed?
- What future works would be required to surmount any of the above problems?

With these questions answered satisfactorily, then the research project could be deemed to have delivered its overall objective.

### **3. Literature Review Part 1: Background and Orientation**

This literature review is split into two parts. In part 1, the historical context and importance of internal combustion engine technology is explored. Taking advantage of small agricultural engines as useful examples, the development of both spark and compression ignition systems is documented. Two-stroke engines are discussed, including different scavenging arrangements, before OP2S engines are introduced. The operation, various configurations, and thermodynamic benefits of OP2S engines are described in detail, using historic examples. This is followed by the problem of excessive lubricating oil consumption in piston-ported engines, a characteristic which OP2S engines were known to exhibit. The current dominance of four-stroke engines is noted, highlighting the advanced technical state of contemporary commercial architectures. A short review of some state-of-the-art engine development efforts is presented, including key focus areas such as alternative fuels, different injection and combustion strategies, and novel engine architectures. The renewed interest in two-stroke engines (and in particular OP2S engines) is also addressed.

In part 2, spark ignition in OP2S engines is addressed in much more detail, using the context of the essential processes (i.e. scavenging, mixture preparation, and combustion) that occur in the engine cylinder. Particularly important OP2S architecture, such as cylinder porting arrangements, in-cylinder flow regimes during scavenging, and the different analysis techniques available to understand them form an essential grounding. Challenges to SI operation are identified and discussed, and consequently an opening for a significant research contribution is identified.

Special attention is given to the work of J. B. Heywood [5], which is amongst the most authoritative and thorough texts on the subject of internal combustion engines in general and is cited extensively throughout this review. The works of R. Van Basshuysen and F. Schäfer [28], and V. Smil [29], are also invaluable sources, and particularly that of E. Sher in the context of scavenging two-stroke engines [30].

#### **3.1 Historical Context**

The internal combustion engine is often said to have superseded steam power, though it is noted that in some applications steam remains firmly in place, especially in electricity generation in the form of large steam turbines. Indeed, the importance of steam technology in the development of modern civilisation cannot be overstated (the particularly detailed works of T. Tredgold comprise a useful record of steam engine development [31]), and even in those areas where steam has mostly now disappeared, it was by no means a consistent process. In the rail sector for example, the proliferation of diesel and electric locomotives varied across the world. Steam locomotives had become increasingly powerful, and railways had been built to support them with coal bunkers, water supplies etc. that ensured the viability

of steam power well into the 20th Century in many locales. In the United States for example, during WWII the Union Pacific Railroad commissioned the so called ‘Big-Boy’ steam locomotives - massive machines of several thousand horsepower and capable of pulling enormous freight trains over long distances [32]. Even in the 21st Century in China, JS-282 steam locomotives were employed in commercial service at the Sandaoling coal mine right up until 2022, pulling large trains of coal [33].

In the present-day steam power is no-where near as visible as it once was, but there exists a prominent movement dedicated to acknowledging and preserving western (and indeed global) industrial heritage, including all manner of steam engines. Rail locomotives once again provide a case in point: Though they may be almost non-existent in commercial service, and many have sadly been scrapped, some decommissioned steam locomotives have been rescued and continue to run on small, independent railways. This is clearly visible in the UK, where following Beeching’s Report in 1963 numerous railway lines, many of which were smaller branch lines, were decommissioned. Some of these were later purchased by preservation societies and now exist as their own entities, such as The Poppy Line in North Norfolk [34], [35]. Similarly, a significant number of agricultural and road-going steam engines are also now in preservation and can often be seen at ‘steam rallies’ across the world. Felsted Belle, a preserved example of a Garrett traction engine from 1916, is shown in Figure 1:



*Figure 1 - Felsted Belle, a 1916 Garrett Steam Traction Engine, Exhibited at the 2022 Strumpshaw Steam Engine Rally, Norfolk, England (Owned by S. Barraclough)*

Engines like this, themselves developed over many years, offered much more power than could a draught horse, and often drove large farm machinery like a threshing machine – in other words, they

began to allow mechanisation of agriculture, reducing the requirement for manual labour. Larger so-called ‘ploughing engines’ often operated in pairs, and (using a cable system) could pull a plough up and down a field, with an operator on board the plough for steering [36].

The earliest internal combustion engines developed from stationary steam engines, the mechanics of which are very similar to that of Felsted Belle in that they feature the same crank-slider arrangement and often a double acting cylinder. They owe their roots to numerous pioneers of the 19th Century, one of whom - Jean Joseph Etienne Lenoir - patenting his such ‘non-compression’ engine in 1860: This is widely regarded as the first commercially successful internal combustion engine [5], [28].

In Lenoir’s non-compression engine, the piston ‘draws’ fuel and air into the cylinder for the first part of the downstroke. The mixture is then ignited, and the remaining piston stroke used to harness the expanding gases. These spent gases are exhausted as the piston returns to the top of the cylinder, whereupon the cycle repeats. However, whilst Lenoir’s engines were relatively simple, they were only capable of around 5% thermal efficiency; Heywood notes though that the later Otto and Langen engine was more successful and about twice as efficient [5]. This also ignited a fuel/air charge using a non-compression stroke, but the ignition was used to propel a free piston along a cylinder, the resulting motion of which creates a pressure lower than atmospheric at the end of its stroke due to the momentum of the moving assembly. Then, via a one-way roller clutch, atmospheric pressure pushes the piston back down again [5]. This engine was physically very large, indeed Smil notes that the cylinder was nearly 4 metres tall [29]; more practical internal combustion engines were only made possible later by the realisation that compressing the fuel/air charge would increase engine efficiency and power [5]. As Van Basshuysen and Schaefer note, this only became feasible itself following the invention of the one-piece self-tensioning piston ring by John Ramsbottom in 1854 [28].

Whilst the four-stroke cycle featuring compression was patented by Alphonse Beau de Rochas in 1862, it took until 1876 for Nicolas August Otto to patent his engine that used compression [5], [28]. Despite earlier efforts at harnessing compression from the likes of Brayton with his ‘Ready Motor’ [37], [38], it was Otto’s engine that proved to be revolutionary. Not only was it more powerful, but it was also much smaller and lighter in weight, and markedly more efficient than both Lenoir’s engine and the intermediary Otto and Langen atmospheric engine [5], [29]. Otto’s early engines were physically large, but Smil notes that later, Gottlieb Daimler (who had left Otto’s subsequent company in 1882) had, with Wilhelm Maybach, successfully developed a smaller, higher-speed engine, and mounted a version of it on wooden coach by 1886. Also, Karl Benz had independently developed his own engine and mounted it on a 3-wheeled carriage in the same year [29]. Van Basshuysen and Schaefer also highlight the significance of Maybach’s ‘Nozzle Carburettor’, since it atomised the fuel for the engine. Previously, ‘carburettors’ had relied on evaporation of only the most volatile elements of petroleum spirit [28].

The development of the modern engine took many years, but like steam engines, the early internal combustion engine quickly proved its value in agricultural applications, beginning initially with stationary engines. These could be used for a variety of tasks, such as pumping water or grinding animal feed, and Meyer argues that one of the reasons for their success was the comparative speed with which they could be started, and stopped, in comparison to steam engines [39]. Furthermore, whilst earlier examples were not always reliable, Meyer also suggests that great significance lies in the training these engines gave to American farmers, enabling them to become competent mechanics. As time progressed, this resulting expertise went on to influence the success of automobiles [39]. Figure 2 shows a Lister D, a hugely successful British stationary engine that had a production run of around 38 years, driving a load like that which it may have done originally [40]:

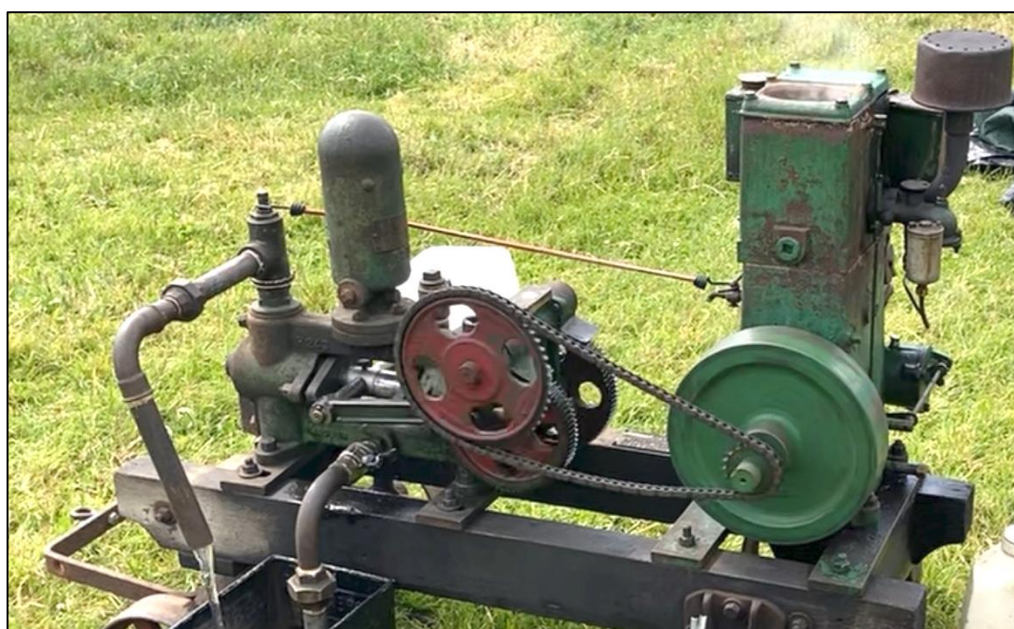


*Figure 2 - 1946 Lister D Engine Driving a Lister H2 Water Pump, Exhibited at the 2022 Strumpshaw Steam Engine Rally, Norfolk, England (Owned by A. Howlett)*

In addition to their importance towards industrialising agriculture, these early engines also present an interesting record of various types of ignition system; though Lenoir had in fact used a spark ignition system himself [5], flame-ignition and hot tube ignition systems (not to be confused with hot-bulb engines) were among the first systems to be used commercially. In hot tube engines however, the air/fuel charge is compressed into a heated tube and then ignites spontaneously under increasing temperature and pressure [28]. Figure 3 shows a hot tube ignited stationary engine:



*Figure 3 - Gardner 1F Hot Tube Engine Exhibited at the 2022 Strumpshaw Steam Engine Rally, Norfolk, England (Owned by R. Sadd)*

The obvious disadvantage of this system is the general lack of control of ignition timing - something which the spark ignition system largely mitigates. One form of early spark ignition system is the mechanical ignitor, where a spark is generated across two contacts as they open inside the cylinder [28]. Figure 4 shows an AMANCO stationary engine which uses a mechanical ignitor:



*Figure 4 - Amanco Engine with Mechanical Spark Ignitor - Exhibited at the 2022 Strumpshaw Steam Engine Rally (Exhibitor not Known)*

However, this system was largely superseded by the high-voltage spark plug. This humble device, on which most modern SI systems still rely, does not have any moving parts in and of itself, and instead

relies on a higher voltage discharge across an electrode gap to initiate combustion. The spark is generated externally with the majority of systems using some form of high voltage inductive ignition coil; many agricultural engines like the Lister D engine shown in Figure 2 use a magneto to generate this spark. A magneto is a mechanically driven inductive ignition system that does not require an external electrical power source [41]. Figure 5 shows a chain-driven Lucas magneto as fitted to a Lister D type engine:

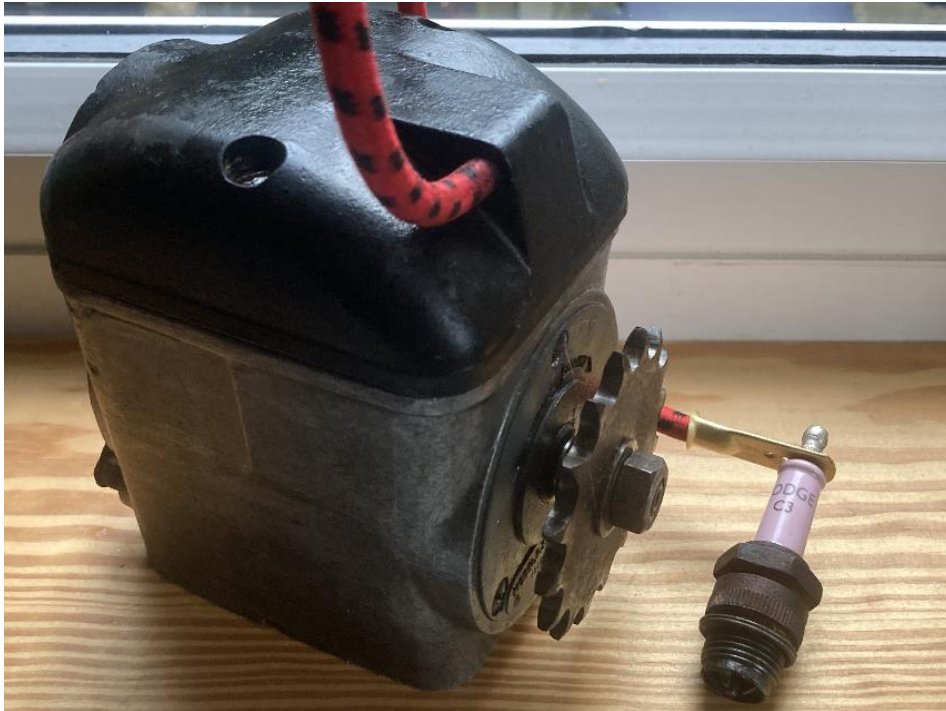


*Figure 5 - A Lucas Chain-Driven Magneto and LODGE Spark Plug*

### **3.1.1 Understanding the Four-Stroke Engine**

As transformational as it was, the four-stroke cycle is relatively simple, making use of the fact that the piston acts both as an energy harvesting device, as well as a pump. Combined with appropriate valving, a four-stroke engine can therefore scavenge itself, all whilst lubrication is (in theory) kept separate from the combustion side. Figure 6 below shows a simplified representation of the four-stroke cycle:

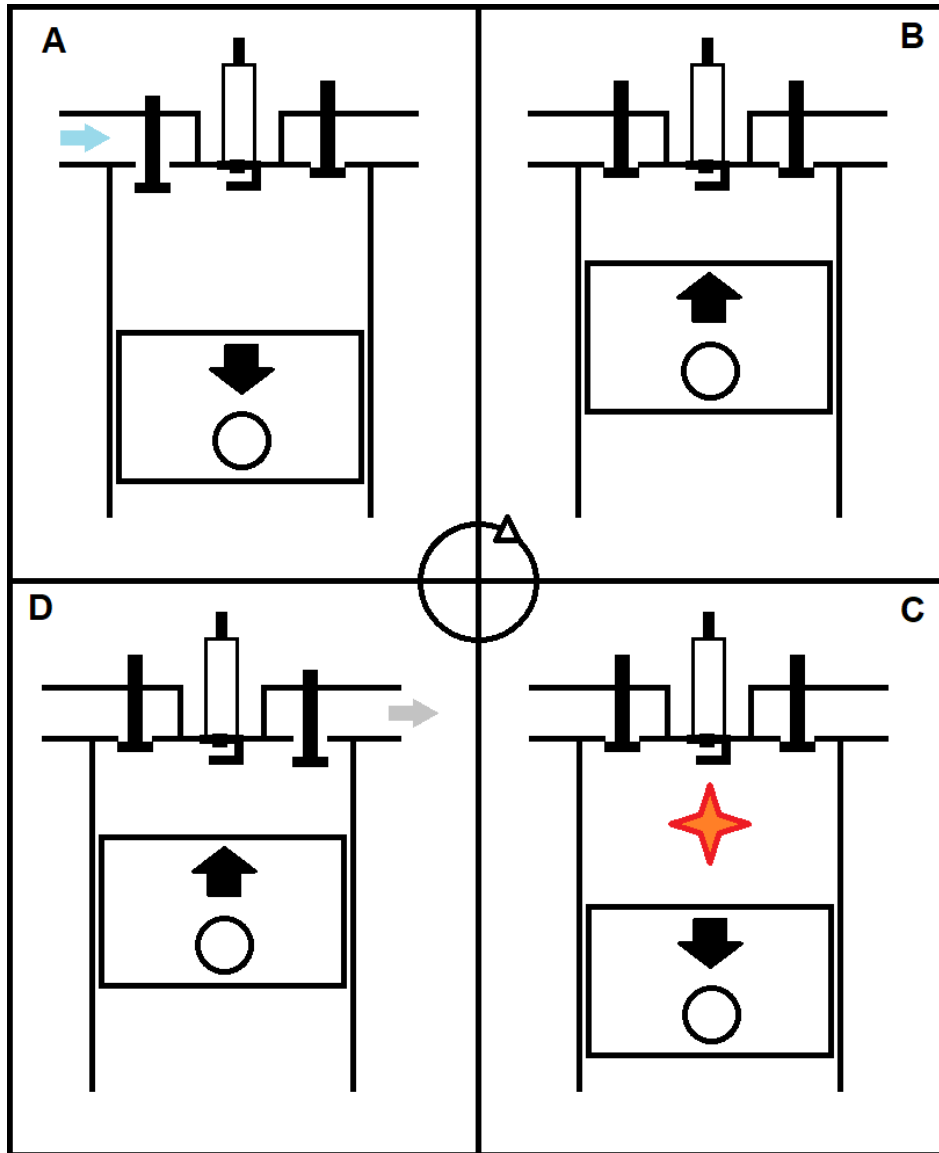


Figure 6 - The Four Stroke Cycle: A - Intake, B - Compression, C - Combustion/Expansion, D - Exhaust

Beginning with 'A' in the above, the engine is in the intake phase. The intake valve (in this case a poppet-valve – by far the most popular) is open, and the descending piston causes the pressure in the cylinder to drop. Atmospheric pressure pushes a fresh air/fuel charge into the cylinder, until the piston reaches BDC and the intake valve closes. From here, the compression phase ('B' in Figure 6) begins where the piston compresses the trapped mixture as it ascends the cylinder, until a spark ignites the compressed mixture. At this point, the combustion/expansion stroke has begun ('C' in Figure 6) whereupon the descending piston harvests some of the energy from the expanding, enflamed mixture, until around BDC again the exhaust valve opens. The piston, once again rising in part 'D' of Figure 6, completes the exhaust stroke by pushing the spent gases out of the cylinder to the atmosphere. And so, the cycle repeats – sometimes thousands of times per minute [5], [28].

### 3.1.2 Compression Ignition

Herbert Akroyd-Stuart pioneered the first truly successful example of an engine featuring no internal ignition system with his ‘oil engine’. Legend has it that he was inspired by an accident where he knocked over an oil lamp that spilled fuel into a bowl of molten tin, which when vaporised rose into a lamp flame and ignited [42]. This type of engine (often referred to as a ‘hot-bulb’ engine) works by externally preheating a ‘bulb’ that is connected to the combustion chamber by a small passage. As Wrangham describes, the fuel injected into this bulb (potentially much earlier than in a ‘diesel’ engine) cannot burn fully due to lack of sufficient oxygen, instead vaporising. Then during compression, cylinder pressure forces more air into the bulb and the resulting mixture ignites spontaneously, causing a high-pressure jet to rush back into the cylinder through the narrow tube, where the combustion process is completed [43]. Once the engine is running the heat of combustion is usually enough to keep the bulb hot enough such that the external heat can be removed (Wrangham notes that ignition timing advances with increasing bulb temperature), although under low loads the temperature can drop to the extent that external heat must be maintained. Under very high loads the bulb can get so hot the advance in ignition timing becomes too great, with the mitigating strategy being to drip water into the air intake to cool the charge [43].

As Smil notes, Akroyd-Stuart (with Charles Binney) patented his engine in 1890 on behalf of Richard Hornsby and Sons – i.e. before Rudolf Diesel patented his engine cycle - and by 1892 Hornsby and Sons were manufacturing it commercially [29]. The ‘hot-bulb’ engine proved to be a major success: In fact, it took several decades and a lot more development before the CI diesel engine fully superseded the hot-bulb engine, and much of this occurred only after Diesel’s untimely death in 1913. Somerscales suggests it’s probably better to refer to them as ‘compression ignition’ engines and not as ‘diesel engines’ since in practise, modern CI engines operate differently to how Diesel had initially envisaged when he patented his engine cycle; indeed, Smil similarly notes that Diesel’s patented ‘isothermal combustion’ was entirely unpracticable [29], [37].

It is often said that in his later years, Akroyd-Stuart was quite upset over the lack of recognition for his work on CI engines. This is not surprising given the similarities between hot-bulb and modern CI engines and the fact that Diesel is often credited as the inventor of the CI engine, when in fact as Smil suggests, it is questionable that he was entirely unaware of Akroyd Stuart’s patents (despite his claims to the contrary) [29], [42]. This is further complicated by the fact that, as Wrangham describes, so-called ‘semi-diesel’ engines evolved as a later development of the hot-bulb engine, using much higher compression ratios [43]. Because of this, the pre-heated surface in these engines was much smaller than in the original hot-bulb engines and the fuel injection needed to occur at the end of the compression

stroke - Akroyd-Stuart was a key enabler of this with his atomiser [43]. However, the key difference in a CI ‘diesel’ engine is that the injected fuel ignites spontaneously as it diffuses into the heated and high-pressure atmosphere alone, without the need for any external heat or ignition system. It does this because the CI engine utilises much higher compression ratios than a hot-bulb, ‘semi-diesel’ or ‘Otto’ engine, and as a result ‘diesels’ quickly proved to be markedly more efficient than both. In time, whilst Akroyd-Stuart’s earlier hot-bulb engine was indeed a success, Diesel’s engine would prove to be transformational, something which continued long after his death. In various cylinder configurations, CI engines became major drivers of the heavy industry, transportation, and global trade upon which the modern world is built, and they remain vital in these same roles to the present day [29].

### 3.2 Two-Stroke Engines

The four-stroke engine in both SI and CI form gradually grew to dominate the world of internal combustion engines by the late 20th Century. But, for many years, the two-stroke engine has co-existed with it. Two-stroke engines work in much the same way as four-stroke engines, but they accomplish exhaust, scavenging, compression, combustion, and expansion using only two ‘strokes’ of the piston. They are typically mechanically simpler and more power dense, so it is understandable that great development effort has been dedicated to them over time [5]. Indeed, early agricultural engines also existed in two-stroke form such as those manufactured by Petters of Yeovil [44]; an example of a 2-stroke Petter engine is shown in Figure 7:



*Figure 7 - Petter Tank Cooled 2 Stroke Engine Lighting some Incandescent Bulbs, exhibited at the 2022 Strumpshaw Steam Engine Rally, Norfolk, England (Exhibitor not Known)*

Nearly all SI two-stroke engines use the crankcase for scavenging, where the underside of the piston serves as a scavenge pump – a configuration invented by Joseph Day in 1891 [45]. The main

disadvantage of this configuration though is the typical use of a total-loss oiling system, which can contribute to excessive emissions, and as Blair notes it is almost inevitable that some of the fresh fuel/air charge will ‘short-circuit’ into the exhaust from the transfer ports. Mitigating strategies were developed, such as resonance chambers in the exhaust and in particular Schnürle porting [45]. Loosely reflecting Sher [30], Figure 8 shows a simplified comparison between cross-flow scavenging and Schnürle porting:

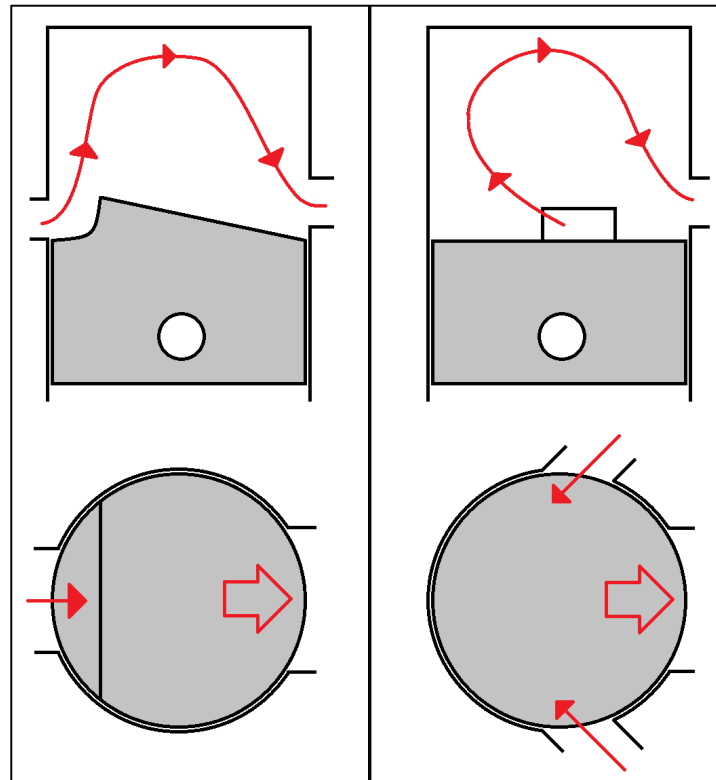
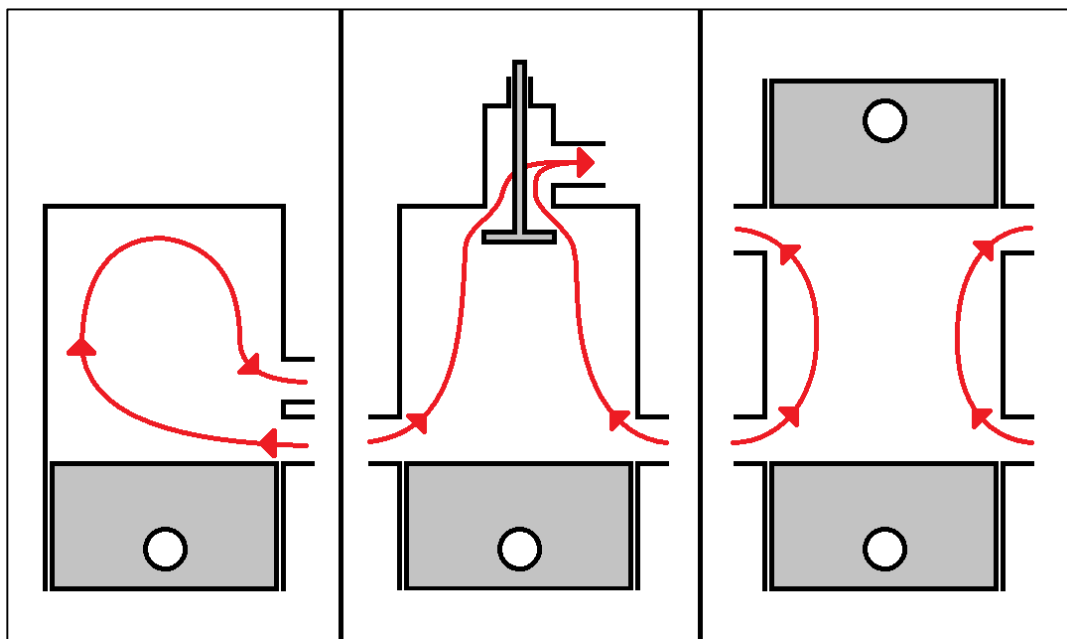


Figure 8 – Cross-Flow Scavenging (Left), Schnürle Loop Scavenging (Right)

As is visible in Figure 8, in the cross-flow engine there is often a deflector fitted to the piston crown to direct the incoming fuel/air mixture upwards; this is a simple approximation based on Heywood [5]. The deflector is intended to reduce the amount of fresh charge that is simply ejected out of the exhaust [30]. The Schnürle ported engine does not require the deflector, but as Sher notes, even this arrangement will almost inevitably still have fuel short-circuiting issues [30]. Despite this, in smaller applications the mechanical simplicity, high power density and light weight of the crankcase-scavenged engine are compelling [5]. As a result, SI two-stroke engines have found use in motorcycles, large chainsaws, or ultralight aircraft for example. Nevertheless, whilst some automotive examples were developed, they have long since been discontinued [28], [45]. It is noted that more modern versions consume significantly less oil than older designs and produce much more power, but their utilisation is still comparatively limited [45].

Early CI engines also existed in a similar two-stroke form using the crankcase for scavenging; two-stroke ‘semi-diesel’ engines found use in Marshall tractors, for example [46]. However, it has historically always been easier to separate the scavenging process from the crankcase in two-stroke CI engines, so separating the oil circuit, because the fuel is not pre-mixed with air like it usually is in an SI engine (though it is possible to inject the fuel directly into the cylinder to mitigate this [45]). There have been numerous approaches employed including impressive loop-scavenged marine engines like the MAN K SZ engine and its later descendants [23], with others using a ‘uniflow’ process, where gases flow in one direction along the cylinder. Figure 9, also loosely reflecting Sher [30], shows a comparison between the MAN loop-scavenged, valved uniflow, and OP2S uniflow scavenging approaches.



*Figure 9 - MAN Loop Scavenging (Left), Valved Uniflow Scavenging (Middle), OP2S Uniflow Scavenging (Right)*

Notable examples that used valved uniflow scavenging include the road-going Detroit Diesel ® engines in the USA and the architecturally similar Foden FD series engines in the UK [45], [47], [48]. The Detroit engines are very well known (and were highly successful in their time), but the lesser known Foden engines were developed in-house by their own engineers to respond to a lack of Gardner engines available to Foden’s in the mid-20th century. In this type of engine, scavenging is driven by an external air blower that pushes air through ports arranged radially around the bottom of each cylinder. The incoming air displaces exhaust gases out of the poppet valves in the cylinder head, and the oil is kept in a separate circuit in much the same way as it is in a four-stroke engine [48]. Figure 10 shows a simplified representation of the valved-uniflow two-stroke CI operating cycle. Note that the scavenging chest typically extends around the cylinder [5].

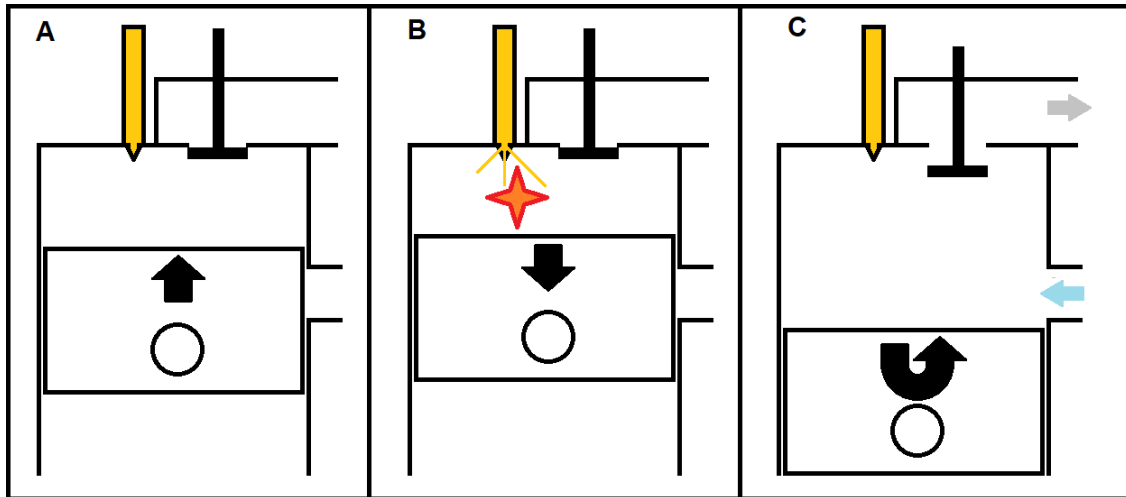


Figure 10 – Simplified Valved Uniflow Blower-Scavenged Diesel Two-Stroke Cycle: A – Compression, B – Combustion/Expansion, C – Scavenging

Lighter in weight and more powerful than the comparable Gardner engines of the time, the Foden engines proved initially very successful. But as one of the engineers behind the development of the Foden two-stroke notes, in road-going engines there was an unfortunate tendency of cracking to occur between the two exhaust valve seats in each ‘unit’ cylinder head. This proved to be impossible to resolve at the time (even though marine spec engines were largely immune to this problem), and ultimately contributed to the demise of the Foden two-stroke. The engineers suspected that the ‘unit’ cylinder heads were causing this, but these were themselves a replacement for earlier multi-cylinder heads, which had suffered from premature gasket failure [48]. Notably though, large contemporary marine engines often use a two-stroke cycle like that shown in Figure 10, though as Heywood notes due to their enormous size, they typically feature cross-heads to absorb the side forces that would otherwise be exerted on the cylinder walls [5], [23].

### 3.3 Opposed-Piston Engines

A more unusual form of two-stroke engine is the opposed-piston engine. Four-stroke opposed piston engines do exist in research [49], [50], and indeed the Atkinson Differential Engine was one of the first examples of an internal combustion engine to use opposed-pistons, using a four-stroke cycle. It did not use the Otto Cycle however, since owing to the unique (and more complex) crank-slider mechanism, the expansion and exhaust strokes were longer than the intake and compression strokes. James Atkinson’s original design of 1886 saw little commercial use, although later the Atkinson Cycle would find use in automotive engines as discussed later [5], [51], [52]. However, the two-stroke opposed-piston engine has (and continues to be) much more successful than its four-stroke variants. For this reason, hereafter the term ‘opposed piston engine’ is used exclusively to refer to OP2S examples.

### 3.3.1 OP2S Operating Principle

Instead of using poppet valves in a cylinder head for the exhaust, an OP2S engine has another piston to uncover an additional set of ports at the other end of the cylinder. Figure 11 shows a simple representation of an OP2S operating cycle, beginning and ending during the scavenging process. The two piston strokes are split into three parts each: the first is from points A through C, and the second from points D through F, progressing anticlockwise around Figure 11. Starting at point A, the exhaust piston (red) and intake piston (blue) are moving towards one another. The exhaust piston leads the intake, and there exists a pressure gradient across the engine cylinder from the intake to the exhaust port, provided by a scavenge pump (not shown). Scavenge air (light blue) flows into the cylinder, pushing residual exhaust gases (light grey) out of the exhaust port. As the engine rotates, at point B the exhaust port has closed off, the pressurised intake air now driving a moderate supercharging process. A small amount of residual exhaust is still present due to an imperfect scavenging characteristic (this is discussed in subsequent sections). At point C the intake port is also closed off, the trapped fractions being compressed as the two pistons approach one-another. At point D, the combustion process is initiated and expansion commences, the two pistons now moving apart from one another. At point E, the exhaust port has opened, causing exhaust blowdown – this is sometimes referred to as ‘free exhaust’ [53], [54]. At point F, the intake port has opened, and pressurised intake air begins to scavenge the cylinder. As the pistons reverse their direction at the end of their travel, the cycle restarts at point A.

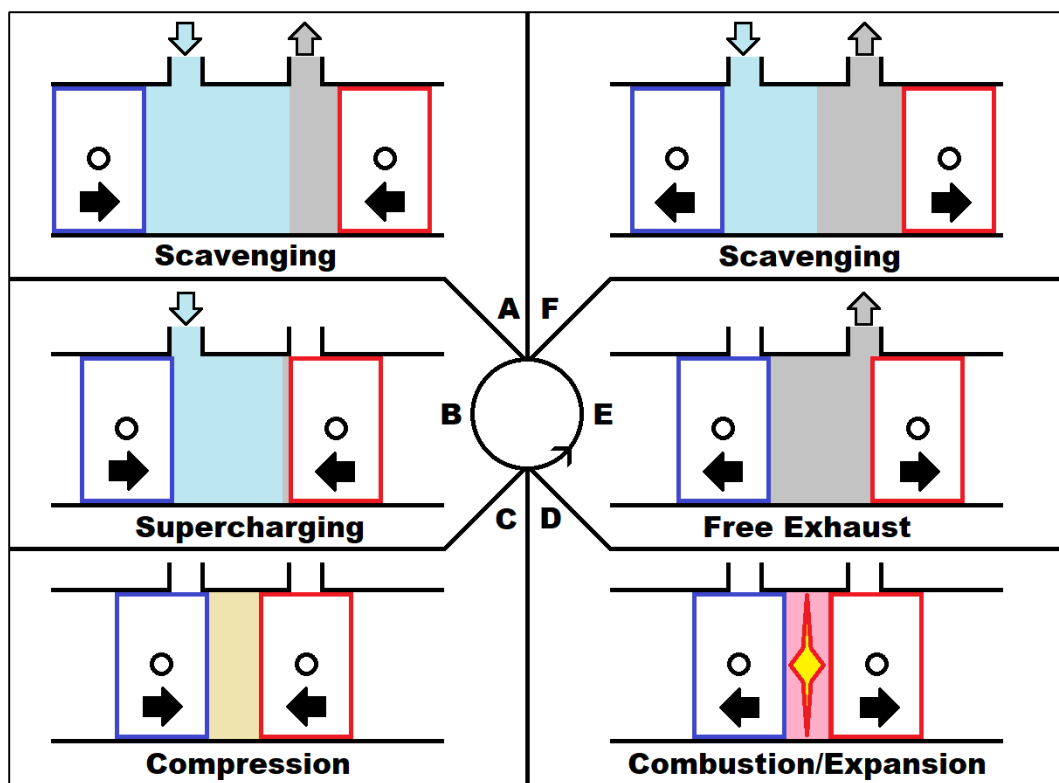


Figure 11 - OP2S Operating Cycle

Note that in Figure 11 no mixing of the burned/unburned fractions is assumed for the sake of visual clarity, and the combustion process could be spark or compression ignition (or other novel method), though CI has generally been more popular as discussed below with examples of the architecture.

### 3.3.2 Examples of OP2S Engines

The earliest OP2S engines were low-speed examples and date from the late 19th Century, but the most significant developments occurred during the early-to-mid 20th Century, with designs varying from aircraft applications all the way up to those propelling massive ships [23], [55], [56]. Doxford engines are well known for the latter [23], but it was Hugo Junkers who developed some of the first higher speed, multi-cylinder engines, called ‘Jumo’ engines (which as Pirault and Flint note is a name based on his engine manufacturing division, Junkers Motorenwerke AG [56]). The Jumo 204, 205 and 207 engines used two crankshafts – one each for the intake and exhaust pistons – and a centrifugal blower for scavenging; the 207 was a development of the 205 that also featured turbocharging, among other differences [56]. Figure 12 shows a simple schematic of an OP2S engine using the ‘Junkers’ configuration:

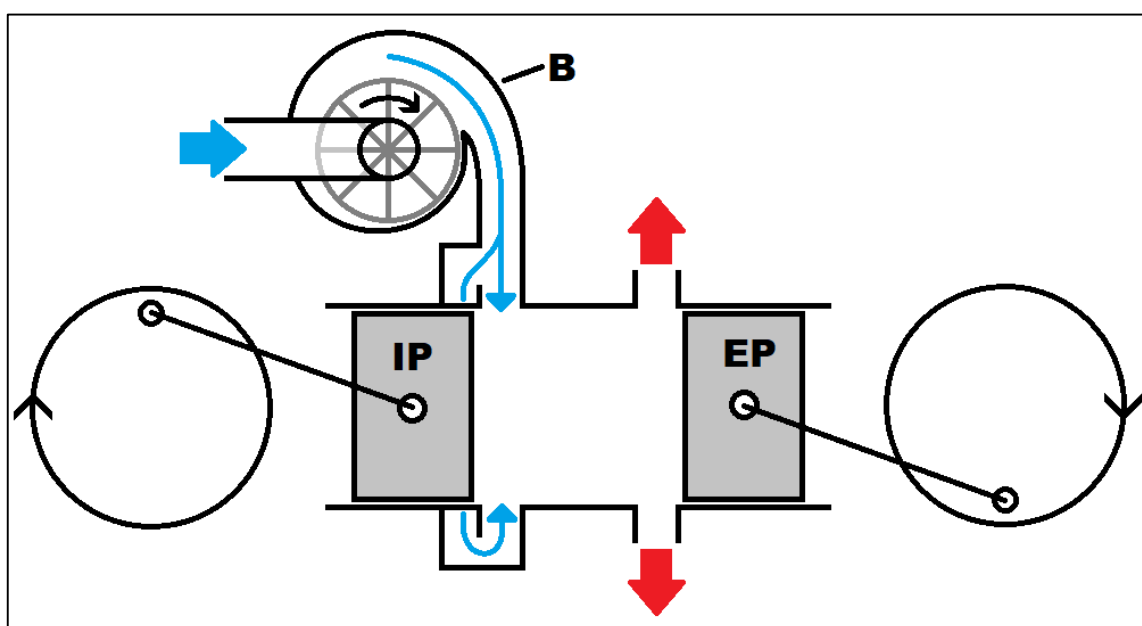
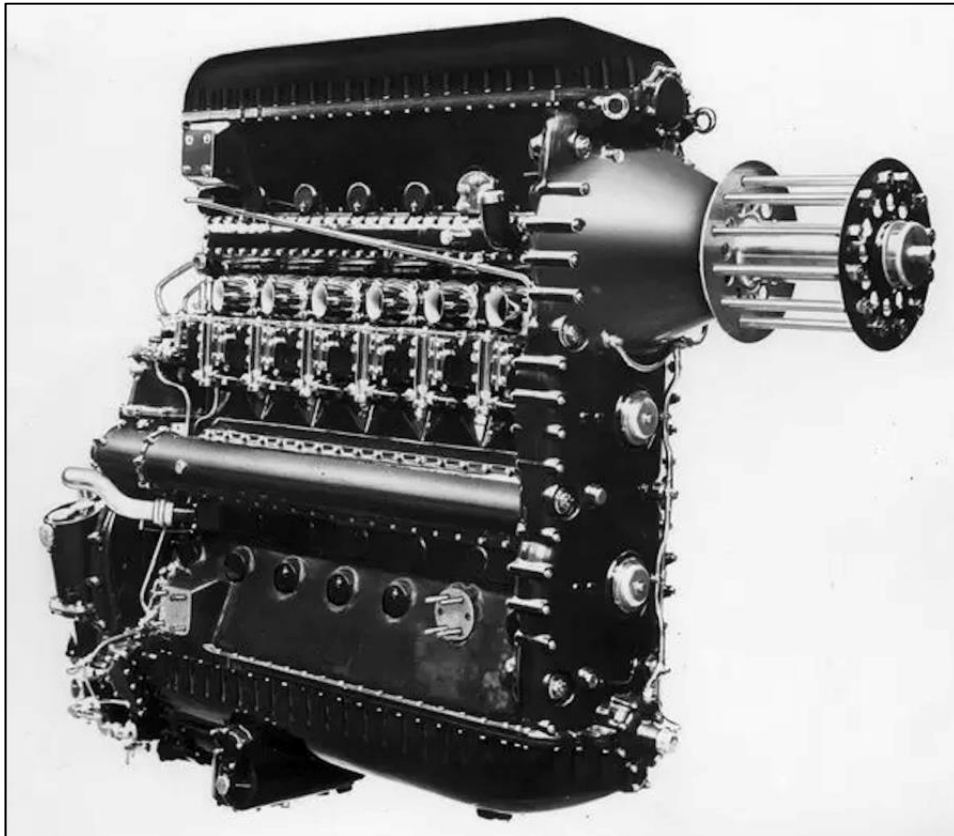


Figure 12 - Junkers OP2S Layout - B = Blower, IP = Intake Piston, EP = Exhaust Piston

In Figure 12, the blower is of the centrifugal type with the impeller wheel shown in grey. The atmospheric intake tube is above the impeller wheel feeding its centre, and the blue ‘streamlines’ indicate the path of the scavenging air from the blower to the liner ports. The large red arrows indicate exhaust outlets; piston phasing is not considered. Some Jumo engines saw use in German WWII aircraft,

but it should be noted that due to not aligning with the terrible politics of the time in Germany, Hugo Junkers had been confined largely to his house in 1934, and died in 1935 [55], [56]. Despite their unfortunate associations, the Jumo engines proved extremely capable, and helped lay the foundations for other OP2S engine architectures, both contemporary and future alike. For example, D. Napier and Son acquired licenses to produce the Jumo 204 engines in 1933, as the Napier Culverin. Figure 13 shows a photo of a Napier Culverin viewed from the output end [57]:



*Figure 13 - Napier Culverin Engine [57]*

Like the Jumo engine on which it is based, the Culverin is an inline six-cylinder CI engine. The intake ports are at the bottom and the exhaust ports at the top; the two crankshafts and output drive are connected via gears inside a housing at the front of the engine. Following WW2 Napier was selected by the British Admiralty to develop a power unit for motor torpedo boats. The ‘Deltic’ concept was then developed, featuring either 9 or 18 cylinders [56].

The Deltic uses 3 crankshafts: one at each corner of an inverted triangle that resembles the Greek letter Delta, hence the name of the engine. The crankshafts are connected together via a phasing gear housing, which also links them to the output shaft. Timing (specifically piston phasing) of the Deltic was aided when an admiralty engineer suggested that one of the three crankshafts should rotate in the opposite

direction to the other two. This allowed the correct phasing between the intake and exhaust pistons in all three banks of the engine: in a Deltic, the bottom crankshaft rotates in the opposite direction to the other two crankshafts at the top of the ‘delta’ [56]. Figure 14 below shows a Napier Deltic 18-cylinder engine, featuring turbocharging; the turbocharger (in addition to the scavenge blower) is on the right-hand side of the engine [58]:

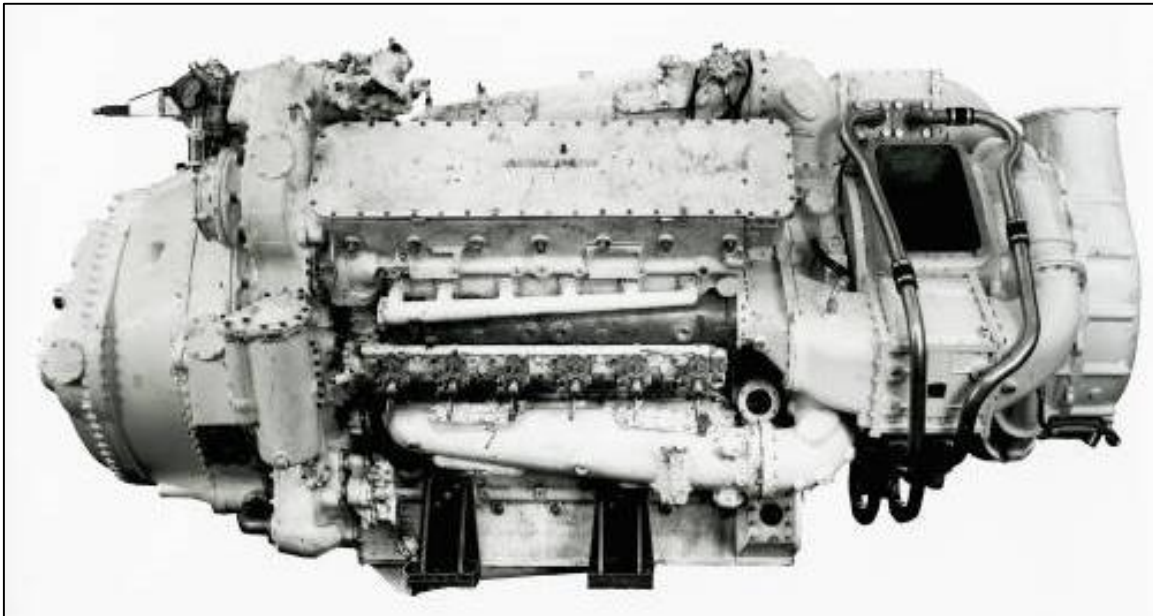


*Figure 14 - Napier Deltic CT18-42K [58]*

An extremely powerful design in a (relatively) compact and lightweight structure, Pirault and Flint note that Napier even produced experimental Deltics with an 8-stage axial compressor, located in the centre of the Delta – such engines were capable of 5600 bhp [56]. But notwithstanding its vastly different outside appearance, as noted the Deltic still used two crankshafts for each cylinder bank like the Jumo engines. However, the commercially very successful and much smaller TS3 - a road-going engine developed and put into production in the mid-20th Century by the UK Rootes Group – used an altogether different approach. It relied on a single ‘folded crank’ mechanism, with large rocker arms to connect both the intake and exhaust pistons to a common crankshaft running underneath the cylinders. This folded crank design benefitted from negligible piston side-loading thanks to the rocker arrangement, yet it still had a combined stroke of more than 200 mm in an incredibly compact frame. The TS3 became renowned as an economical, power-dense, and reliable engine: the final versions of the engine (approximately 3.5 litres) were capable of nearly 30 kW/litre of displacement, and a torque of 476 Nm. In addition to powering industrial equipment, it saw use powering Commer lorries [56], [59].

Figure 15 shows a sectioned view of a Roots TS3; the blower is visible at the front of the engine on the right of the image [60]:

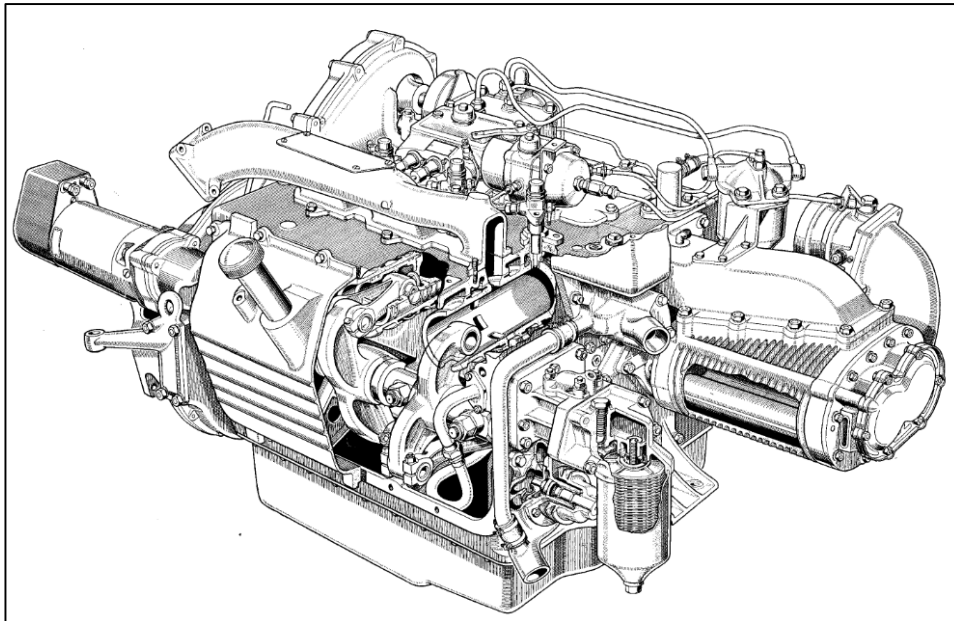


*Figure 15 - Part-Sectioned Three-Quarter Front View of Roots TS3 Engine [60]*

Here, the horizontal orientation of the cylinders is visible, with the rocker arms at either end of them. Figure 16 shows a de-commissioned Roots TS3 engine with rocker covers removed, in which the arrangement can be seen more clearly.



*Figure 16 - Roots TS3 With Rocker Cover Removed*

The three cylinders are visible at the top; the crankshaft is at the bottom and mostly obscured by the intake rocker levers in the foreground. The middle cylinder has had its pistons removed and consequently the top of the exhaust rocker lever for this cylinder is visible through it. The large nuts

retain the rocker assembly; the blower is missing on this example. Because of its success the TS3 was further developed into the 4-cylinder TS4, however the UK Rootes Group was taken over by Chrysler, who cancelled the project. Only a few examples of the TS4 prototypes survived [56], [59].

It is notable that the majority of commercially successful OP2S engines have been compression ignition, but historic examples of SI OP2S engines also exist. For example, Junkers and Oechelhaeuser had developed a large gas-fuelled OP2S engine in 1892, and Junker's gasoline Fo2 saw service towards the end of WW1 [56]. At the opposite end of the scale, Simpson's balanced two-stroke was a crankcase-scavenged engine from the early 20th Century, that used a 'folded crank' mechanism [61]. Later developments include the Vincent Airborne Liferaft Engine, which used a central cylinder as a scavenge pump to push a fresh charge into the two cylinders on either side of it. Notable too is the Africar engine, which was a carburetted, blower scavenged engine that ran but was not tested. For more information on OP2S engine history however, the reader is referred to the excellent work of Pirault and Flint [56].

Given the variety of crank-slider arrangements that can be employed in OP2S engines, Figure 17 shows a simplified comparison between them. This includes the folded crank mechanism as used in the Rootes TS3, the crosshead mechanism with an extended set of 'pulling rods' as used in Doxford engines, the double crank (Junkers/Napier Culverin), and the Napier Deltic:

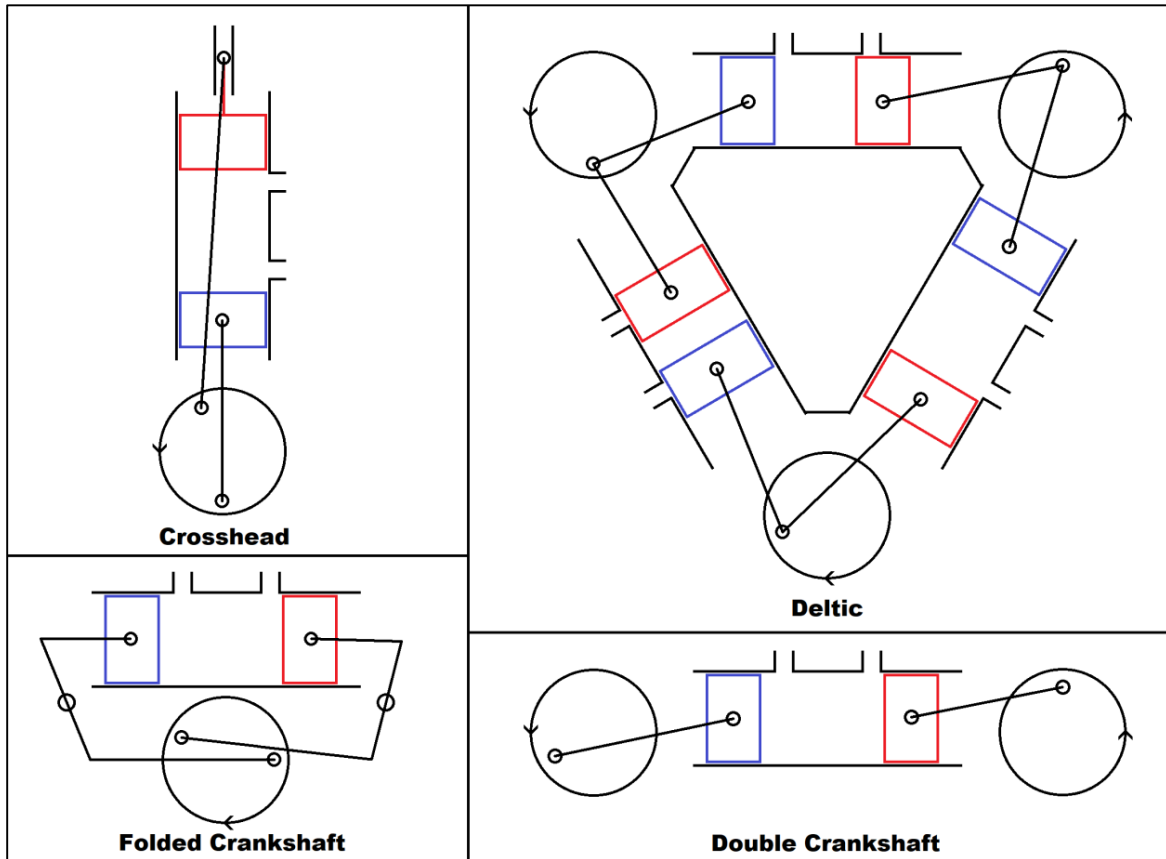


Figure 17 - Different Configurations of OP2S Engine

Note that the timings between pistons are not an exact representation, but the exhaust piston leads the intake piston in all cases. It is also obvious in Figure 17 that if the bottom crank of the Deltic rotated in the same direction as the upper two crankshafts, the intake piston of the left cylinder bank would be moving away from inner dead centre ('IDC') as the exhaust piston approaches IDC. Similarly, the intake piston of the right bank would be moving away from outer dead centre ('ODC') as the exhaust piston approaches ODC. With it (correctly) rotating in the opposite direction, the exhaust piston always leads the intake piston as required, and in this case the right bank leads the left, which in turn leads the upper cylinder bank [56], [62].

### 3.4 Thermodynamic Advantages of Opposed-Piston Engines

The successes of OP2S engines are in part because they possess inherent thermodynamic advantages thanks to their architecture. Particularly important among these are a high stroke-to-bore ratio, uniflow scavenging that is de-coupled from piston motion, and two-stroke operation – each of these advantages is discussed separately below.

### 3.4.1 High Stroke-to-Bore Ratio

It is well understood that a high stroke-to-bore ratio is advantageous in terms of engine thermal efficiency. This is because a cylinder with a higher stroke to bore ratio has less surface area available for heat loss to coolant. OP2S engines share compression/expansion between two pistons, and because of this, it is possible to have effectively double the stroke-to-bore ratio without the engine speed limitations that are traditionally imposed by increasing piston speeds. This is somewhat offset by the intake and exhaust ports which occupy a portion of the cylinder length, but OP2S engines can have stroke-to-bore ratios well in excess of 2:1 - far higher than most conventional engines [21], [63]. Furthermore, for a given bore diameter, an OP2S engine cylinder can displace a greater volume and so deliver more power. Therefore, fewer cylinders are required for a given power output, further reducing heat loss to coolant [21].

### 3.4.2 De-coupled, Uniflow Scavenging

The unique arrangement of an OP2S engine means that they employ uniflow-scavenging that is de-coupled from piston motion. To illustrate what this can mean thermodynamically, Figure 18 shows an example pressure/volume ('PV') plot of an OP2S engine cylinder, annotated to show the rough timing of key events of the operating cycle. These are 1: exhaust port open ('EPO'), 2: intake port open ('IPO'), 3: exhaust port close ('EPC'), 4: intake port close ('IPC'), and 5: start of combustion ('SOC'). Note that this plot was generated from 3D computational fluid dynamics ('CFD') simulations of an SI OP2S engine, which are discussed later in chapter 6.

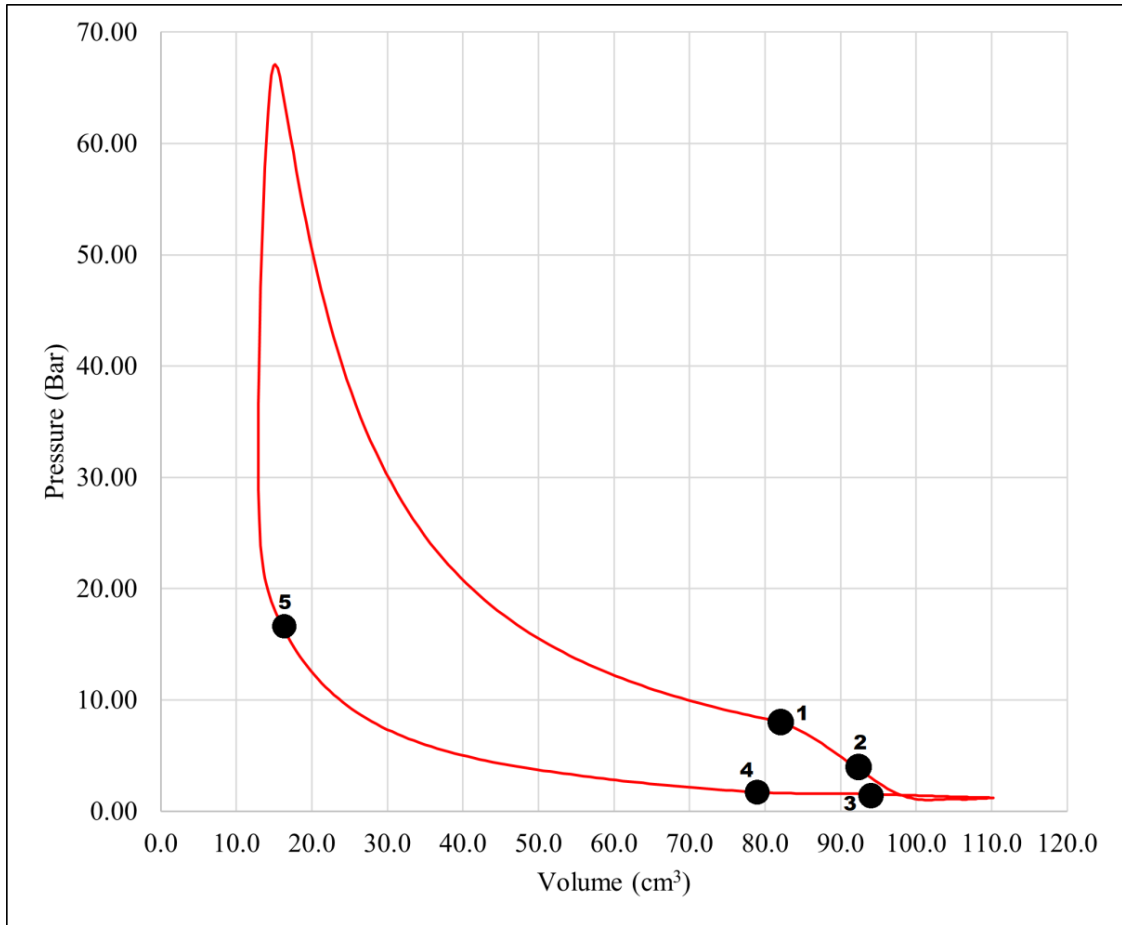


Figure 18 - Annotated Example PV Diagram of an OP2S Engine

The part of the PV line to the right of points 1 and 4 in Figure 18 indicate the part of the engine cycle during which scavenging occurs. This shows one of the fundamental thermodynamic advantages of decoupled scavenging: unlike in a typical four-stroke engine, there is no separate pumping loop underneath; see [5] for example four-stroke PV diagrams. This is because in the OP2S engine, there is no dedicated exhaust/inlet stroke, these are instead replaced with an external scavenging system used to provide pressure to the intake chest [64]. Therefore, pumping work in an OP2S engine is largely external to the cylinder and (aside from port timing) is mostly independent of piston motion: scavenging is governed by the pressure ratio between the cylinder and exhaust ports [65].

Salvi *et-al.* note that because of this, there exists the possibility for an extra degree of control over pumping load: instead of fully scavenging the cylinder, it is possible to control the scavenge pressure such that the cylinder is only partially scavenged, particularly at low loads or idle conditions, reducing the required work. This achieves a similar effect to exhaust gas recirculation ('EGR') by retaining a significant proportion of the residual fraction in the cylinder [65]. Conversely, because there is a dedicated exhaust and intake stroke in a traditional four-stroke engine, the cylinder is effectively fully evacuated of exhaust gases by the piston motion before the intake stroke begins, hence the exhaust gases

must be re-circulated back to the intake. Regner *et-al.* note however that at higher loads external EGR is still required for emissions compliance in modern OP2S engines [20].

The uniflow scavenging characteristic also presents two additional advantages in the case of OP2S engines. Firstly, in an OP2S cylinder each piston controls one set of ports located at the outer extremity of its motion. Therefore, there is an increased available porting area on the cylinder wall for the intake and exhaust ports in comparison to other piston-ported arrangements, so increasing the available area through which gases can flow. This is effectively unique to the OP2S architecture and is not reproduced either in valved (single piston) uniflow or loop scavenged engines, or traditional four-stroke engines [22].

Secondly, an OP2S engine has no cylinder head or valvetrain. Aside from its complexity, a cylinder head is a significant source of heat loss in conventional engines, since it is positioned at the top of the cylinder and comprises (effectively) half of the combustion chamber. It must therefore withstand high temperatures and pressures, but it must also seal against the mating face of the engine block. For this reason, it cannot operate with surface temperatures as high as can a piston: thermally-induced deformation of the (typically large and flat) sealing surface could result in head gasket failure. As Regner *et-al.* note, replacing the cylinder head with another piston crown at a higher surface temperature means that less heat will be lost from the combustion chamber [21].

### 3.4.3 Two-Stroke Operation

Two-stroke engines have a power stroke once per crankshaft revolution instead of once every other revolution as in a four-stroke engine. Regner *et-al.* note that whilst this can be exploited to produce an engine with higher power density to a comparable four-stroke engine, because of the increased firing frequency it is possible for a two-stroke engine to operate with lower BMEP. This is advantageous because of the decrease in peak temperatures and pressures, which results in a reduction in NOx generation (although as will become clear OP2S engines have historically faced challenges in the context of emissions compliance) [21].

Another benefit results from the same double firing frequency. This can be (simplistically) understood recalling the equation for ideal engine efficiency using a constant volume cycle [5], in this case converted to a percentage:

$$\eta (\%) = \left(1 - \frac{1}{r_c^{\gamma-1}}\right) * 100 \quad \text{Eq. 1}$$

Where  $\eta$  is the engine thermal efficiency in percent,  $r_c$  is the compression ratio, and  $\gamma$  is the ratio of specific heat capacities of the working fluid. It is noted that this is an ideal equation, relying on assumptions that in practical engines are not realistic (for example combustion is finite, compression/expansion is not adiabatic...) [27]. However, due its simplicity it does serve as a useful tool for comparison: assuming the compression ratio is the same, increasing the ratio of specific heat capacities will result in a more efficient engine – this however requires a leaner combustion condition [63]. To maintain the same power output as a comparable four-stroke engine, in an OP2S engine the amount of fuel injected per firing event can be roughly halved (because of the doubled firing frequency). Therefore an OP2S engine can theoretically operate at leaner conditions for the same power output as a comparable four-stroke engine, thus resulting in an improvement in the ratio of specific heat capacities of the working fluid in the cylinder and, consequently, engine efficiency [63].

### **3.5 Oil Short-Circuiting in Piston-Ported Engines**

That the OP2S architecture possesses such fundamental thermodynamic advantages over four-stroke engines and even has advantages in terms of emissions compliance in the case of NO<sub>x</sub>, raises the question as to why it fell out of favour in the way that it did. This is particularly so given the success of commercially produced opposed piston engines like the Napier Deltic, and especially the Rootes TS3 that at first glance appears only to have been ended by an unfortunate corporate takeover.

There is likely no single reason that can provide an adequate answer to this, but one contributory factor might be found in the oil circuit of an OP2S engine which shares many similarities with other piston-ported two-stroke engines that similarly faded from view, for example the venerable Detroit engines. The lubrication systems in these engines are virtually identical in design and operation to those in four-stroke engines – the oil is a separate system and is not pre-mixed with fuel. However, the cylinder walls of a piston-ported engine differ in that they feature the necessary openings for scavenging. Whilst this is not necessarily a problem in itself, traditionally a fine cross-hatch pattern is ground into the surfaces of engine cylinders, and these serve to retain oil on the surface. The resulting ‘honing marks’ can form a leakage path, allowing oil to wick into the liner port holes and thence into the air-side of the engine, causing elevated emissions [66]. With the advent of modern emissions standards in the latter half of the 20th Century, this presented a problem that at the time could not be solved economically. In four-stroke engines, that do not feature piston-porting, this oil leakage path is not present, and so emissions compliance was much less challenging [21].

### **3.6 The Modern Engine**

There are a number of reasons why four-stroke poppet valve engines have come to currently dominate the world of (reciprocating) internal combustion engines. As previously discussed, the introduction and progressive tightening of emissions legislation – and the comparative ease with which four-stroke engines have been able to meet it – is a primary factor [21]. Another is the fact that by the 1960's the four-stroke engine was so entrenched in many manufacturers that there was little room for other architectures to evolve. They are also convenient: a four-stroke engine uses its piston to accomplish all of the necessary processes required to complete an operating cycle, like that shown in Figure 6 – it doesn't *need* any external pumping component. With appropriate valving and timing mechanisms, the piston scavenges the cylinder, compresses the air charge (which may be mixed with fuel) and extracts useful work, whilst simultaneously keeping lubrication oil and products of combustion separated with only minor oil consumption relative to the consumption of fuel [28].

Four-stroke engines are also incredibly durable: they are able to produce enormous amounts of power with the addition of turbo- and/or super-charging, and last for many thousands of hours before needing overhaul; diesel engines used in road haulage frequently last well in excess of 1,000,000 miles [28].

### **3.6.1 The Importance of Digital Engine Control**

Increasing fuel efficiency and reducing emissions from internal combustion engines are presently major focus areas for engine development, whilst preserving the required performance for the intended application of the engine [5]. Though in principle similar to the engines of more than 100 years ago, modern architectures are now much more reliable, more powerful and more fuel efficient, all whilst emitting far fewer harmful pollutants. The automotive/road transport sector has been one of the biggest drivers behind the extraordinary level of engine development in recent decades, and the improvement in computer, simulation and sensor technologies has allowed major engine operating parameters to become increasingly computer controlled [28]. Variable valve timing is an example of such a computer-controlled system, and Akal *et-al.* discuss the advantages it offers, as well as different configurations of the valve systems in modern four-stroke engines [67]. In a traditional cam-driven valve system, the duration and lift of both the intake and exhaust valves are fixed, and at higher engine speeds the volumetric efficiency of the engine can drop. One way to mitigate against this has been to increase the number of valves per cylinder rather than increase the size of the valves themselves. This makes better use of the limited available space and helps preserve optimum spark plug location. However variable valve timing offers further benefits by allowing flexibility in valve timing and lift, so that even at higher engine speeds good volumetric efficiency can be maintained [67]. To show this, the authors reviewed the Audi 'Valvelift' system, the BMW 'Valvetronic' system, the Porsche 'Variocam' system, the Toyota 'VVTL-I' system, and the Fiat 'MultiAir' system, highlighting some of the various approaches utilised commercially by different manufactures. These valve systems – many of which were developed more

than a decade ago - all allow for variability in the valve train, but not all operate in the same way [67]. For example, the Audi and Toyota systems both have two different cam profiles and a mechanism for switching between them. But the specific mechanics of each differ somewhat, with the Toyota system using a two-piece rocker arm and the Audi system using actuators to slide cams back and forth. The Porsche system works in an altogether different way however, since it alters the angular position of the camshaft to either advance or retard valve timing. The BMW and Fiat systems are arguably even more sophisticated, since they are able to vary the amount of air admitted to the engine using their valvetrain alone such that they do not require a throttle valve. The Fiat system makes use of an electrohydraulic device that varies the lift and duration of the intake valves individually, whilst the BMW system uses an intermediate arm between the intake rocker arm and camshaft, whose position can be altered by means of an additional eccentric shaft [67].

Another important technology employed in modern SI engines has been ‘multipoint’ electronic fuel injection coupled with closed loop control, where Heywood notes that moving the site of injection closer to the cylinder improves the engine response to transient load conditions [5]. A further trend in recent years has been to inject the fuel directly into the cylinder, rather than (or in addition to) the ports. Whilst detailed analyses of fuel sprays and injectors are not the focus of this research, they do serve as a reminder of the advanced state of modern engine technology and understanding. Duronio *et-al.* showed this in their works [68], [69], where they discuss not only the evolution of fuel jets, but also the myriad of different spray measurement techniques used in fuel spray research. Most measurement approaches utilise a visual method to evaluate the evolving jet, with ‘windows’ typically featuring on specially designed test vessels. Example techniques include mie scattering, shadowgraphy and schlieren photography, laser-induced fluorescence, phase Doppler particle anemometry, X-ray phase-contrast imaging and plenoptic imaging [68], [69].

### 3.6.2 Recent Commercial Developments

Internal combustion engine development is not stationary, and neither variable valve timing nor multipoint fuel injection can be considered ‘state-of-the-art’ anymore, even in the case of (relatively) ‘conventional’ designs. Leach *et-al.* comprised a wealth of information on current engine architectures, identifying the factors that affect engine efficiency and exhaust emissions, and investigating their scope for further improvement [50].

With SI engines it was noted that whilst the use of leaner air/fuel mixtures could theoretically improve engine efficiency, this is typically counterbalanced by slower combustion rates, increased cycle-to-cycle variation, and higher fractions of partially burned fuel in the exhaust, which all decrease efficiency. Lean operation can also increase nitrogen oxide (‘NOx’) emissions due to the higher combustion

temperatures, since there is less in the way of evaporative cooling [50]. Consequently, the vast majority of modern production SI engines still operate close to stoichiometry, but different trends were identified in such engines. One is to use a larger naturally aspirated engine and operate it with an over-expansion type Atkinson/Miller Cycle. Here, the expansion ratio is larger than the (effective) compression ratio, and this is typically achieved through valve timing to reduce the volume inducted into the cylinder by closing the intake valve either early or late. The reduction in pumped volume significantly reduces throttling losses, far outweighing the losses due to the reduced compression ratio. Toyota is noted for employing this strategy with their 2.5 litre engine that is capable of 40% Break Thermal Efficiency ('BTE') peak, and it was noted that the engine uses a long stroke to reduce the surface area to volume ('SVR') ratio and therefore thermal losses. A long stroke does increase frictional losses, so Toyota employs countermeasures such as variable displacement oil pump, reciprocating component lightweighting, and very low viscosity oil [50].

Another option discussed is a down-sized and boosted (here meaning turbocharged) engine with a lower geometric compression ratio. By lowering the geometric compression ratio, the turbocharger, which captures energy from the moving exhaust gases to increase engine scavenging efficiency, can be used over a wider operating range, since the risk of pre-ignition is reduced. The current 1.5 litre Honda engine was identified as a good example. This also features a long-stroke and variable valve timing, and at lower torque levels it has an efficiency higher than the Toyota engine. At higher torque levels and low/moderate engine speeds however, it is less efficient than the Toyota, but it was noted that an obvious third approach is to combine both strategies such as in the VW EA211 or Audi TFSI engines, which combine Atkinson/Miller operation with turbocharging. Indeed, the fuel efficiency of the Audi engines is significantly higher than that of a previous generation turbocharged engine of smaller displacement [50].

However, the potential of ultra-lean SI engines was noted, particularly in the light of the efficiency benefits associated with it, even though lean-burn approaches have conventionally required more expensive NO<sub>x</sub> after treatment strategies. An economical alternative has been to employ EGR dilution which reduces pumping losses and the risk of knock, but does not require expensive aftertreatment.

However, Mazda appear to have found a clever solution to ultra-lean combustion in the form of 'Spark Controlled Compression Ignition' (this is very like SI-CAI, which is discussed in section 3.8.2). The spark plug is used regardless of whether the engine is using 'spark ignition' or 'compression ignition', and crucially, the architecture does not require more complex NO<sub>x</sub> aftertreatment. Mazda achieved this by using a very lean fuel charge, a very high compression ratio (for a gasoline engine) of more than 16:1 and geometry that promotes a large amount of swirl. The engine works by using the spark plug to ignite a small flame front, resulting in a corresponding increase in pressure and temperature of the

remaining fuel charge that causes it to auto-ignite. Using this strategy at low loads, it was described that as load increases the engine adds EGR to help control peak combustion temperatures, pressure rise rates and NO<sub>x</sub> emissions, and at very high loads, the engine reverts to (stoichiometric) SI operation with several strategies, including significant EGR, to control 'knock'. It is worth identifying that in ultra-lean mixtures the reduction in evaporative cooling is less significant, because if the fuel charge is lean enough then the combustion temperatures do not get high enough to form NO<sub>x</sub> – in other words there is not a NO<sub>x</sub> penalty like there is in 'lean' combustion in the traditional sense of the word; these mixtures are not easy to ignite in an SI engine however [50].

Further examples of recent developments, including from other very large industry players, were discussed in another particularly useful review of present and future engine technologies by Conway *et-al.* [8]. This included a 3-cylinder, 1.1 litre SI engine by General Motors, that uses two cylinders for firing, whilst the third cylinder is utilised for secondary expansion of the engine exhaust. Although not mass production ready, this engine employs a very lean combustion strategy and a relatively high compression ratio of 13.5:1. It was noted that very-lean, dilute (hence lower temperature) combustion appears to be a growing development trend, citing encouraging results from Sandia National Laboratory, as well as Nissan who announced their new E-Power system. The dedicated-hybrid engine in this system demonstrated 46% BTE using an ultra-lean strategy, and 50% BTE when employing exhaust gas energy recovery, and whilst the difficulty of igniting ultra-lean mixtures was again discussed, mitigating strategies under consideration were put forward. These include pre-chambers, low temperature plasma and even lasers [8].

Conway *et-al.* also highlighted the significant amount of engine development in the heavy duty on-road sector (i.e. CI engines), which has produced a range of very efficient engines: some capable of in excess of 50% peak BTE. For example, Mack have incorporated a turbo-compounding system linked to the (13-litre, MP8HA) engine crankshaft to recover energy from the exhaust, whilst another manufacturer announced a similarly rated engine that was the first high-speed diesel engine capable of in excess of 50% BTE. Such efficiency was previously found only in the very largest of marine diesel engines, and Weichei – the Chinese company that achieved it – are said to have done so through the increase of peak firing pressure, the optimisation of fuel/air mixing and air flow, exhaust energy recovery and friction reduction, as well as careful control of the engine [8]. It was further noted that Volvo, PACCAR and Cummins have themselves demonstrated in excess of 50% BTE, but that at the time of publication, mass production of those engines had not yet started [8].

### 3.7 Alternative Fuels

Alternative fuels are those which do not rely on petroleum as their primary feedstock, thus are an active research area in reducing GHG emissions from internal combustion engines. In particular E-Fuels, of which hydrogen is the simplest, are a significant and growing area of research. Hydrogen as a fuel for internal combustion engines has itself recently become a significant area of interest with research occurring globally, with some studies suggesting that hydrogen internal combustion engines may achieve fuel-cell levels of efficiency [70]. Hydrogen does have some desirable combustion characteristics, such as a very high laminar flame speed, a rapid diffusion rate, and a very wide flammability range [25], [71]. Indeed, in SI engines, Stępień noted that whilst some studies note that the NO<sub>x</sub> emissions from stoichiometric hydrogen mixtures are higher than in a stoichiometric gasoline fuelled engine, it is possible to exploit the wide flammability range of hydrogen and use an ultra-lean strategy. In doing so, the lower combustion temperatures reduce the production of NO<sub>x</sub> emissions, whilst also reducing heat rejection, making the engine more efficient [25]. A noteworthy hydrogen engine development occurred in late 2023 when Bosch introduced their hydrogen direct injector at Agritechnica: Even though hydrogen has effectively zero lubricity, Bosch were able to overcome this to the extent that the injector survived more than 1 billion cycles without the need for any additional lubrication [72].

Ammonia – a more energy dense way of storing hydrogen – is also being explored as a fuel for internal combustion engines, both in the marine sector in CI engines, but also elsewhere. For example, Lhuillier *et-al.* quantified an experimental database for an ammonia-hydrogen dual fuel, modern SI engine of typical automotive size. Hydrogen enrichment of between 0% and 60% by volume was evaluated, and it was found that low and moderate hydrogen addition achieved the best indicated mean effective pressure ('IMEP') and thermal efficiency values, with slightly fuel rich and fuel lean mixtures respectively [73]. The possibility of using *in-situ* ammonia cracking to produce hydrogen using a catalyst and waste heat was also discussed. Indeed, this was previously demonstrated by Comotti *et-al.*, who developed a hydrogen generation system based upon a commercial ruthenium-based catalyst called ACTA 10010. This was made feasible because the cracking of ammonia into nitrogen and hydrogen gas is an endothermic process, and the ruthenium catalyst used was able to function at temperatures within the range of the exhaust temperature of a spark-ignition engine, with full conversion possible at temperatures of 450 Celsius. The system was coupled to a small industrial gasoline engine converted to run on an ammonia-hydrogen blend, taking advantage of the exhaust heat to produce the hydrogen. The researchers found it was possible to produce more than sufficient amounts of hydrogen gas to achieve stable combustion utilising only the exhaust heat of the engine to drive the reaction when the engine was warm at lambda 1. To address cold-start problems, electrical heating elements were added. The significance of the successful testing of this system lies in the fact that it means an ammonia-hydrogen

fuelled reciprocating internal combustion engines do not necessarily need to carry a separate hydrogen storage system and can instead rely solely on ammonia storage [74]. Comotti *et-al.* further noted that a threshold sensor set at 100 parts per million ('ppm') was used to detect any ammonia slip through the engine. Since it did not register any, it was concluded that ammonia concentrations were likely to be below 100 ppm. However, NO<sub>x</sub> emissions were a problem with additional hydrogen injection resulting in higher levels of emissions due to higher in-cylinder temperatures. It was suggested that the operation of a selective catalytic reduction ('SCR') system, used to convert NO<sub>x</sub> emissions to water and nitrogen, is however potentially aided by the fact that the ammonia required is already on-board [74].

In addition to hydrogen and ammonia, there are a plethora of other alternative fuels of varying maturity and origin, in particular 'biofuels'. For example, Duarte Souza Alvarenga Santos *et-al.* suggest that biofuels will be essential for future mobility in their work, identifying different generations of biofuels and the myriad of different types that have been, and are being developed. Earlier generations of biofuels often faced criticism in that they often rely on the same feedstocks as food for human consumption, but newer generations of biofuels can use various waste streams as feedstock. For example, alcohols, in particular ethanol\*, have proven particularly controversial due to their use of corn and sugarcane as feedstock, so more recent research has explored the use of lignocellulosic methods [13]. However, biogas was presented as an example of a fuel that can use various waste feedstocks, including animal manure, food waste and even human waste. Whilst the requirement to upgrade biogas into biomethane for use as a fuel (in particular the need to remove CO<sub>2</sub> and sulphur dioxide ('SO<sub>2</sub>') from the raw biogas) was noted, it was argued that by avoiding the release of methane directly into the atmosphere there is an additional advantage. Methane has a much higher global warming potential ('GWP') than CO<sub>2</sub> [13]. Indeed, bio-methane sourced from waste materials such as food-waste is a popular fuel for some heavy goods vehicle ('HGV') fleets. In the U.K. CNG Fuels operate a growing number of compressed natural gas ('CNG') refuelling stations [75].

\*Ethanol is commonly mixed with gasoline in a number of countries [76].

### **3.8 Alternative Combustion Strategies**

A corollary to alternative fuels, combustion strategies that differ from the conventional SI and CI systems are subjects of intensive research efforts that have in notable cases led to real world application. Arguably no better example of this exists than Mazda's SPCCI discussed earlier in section 3.6.2, but there are other approaches. It is therefore useful at this point to form a descriptive overview of the SI and CI processes as a grounding for the alternative strategies that aim to replace them.

### 3.8.1 Combustion in SI and CI Engines

Much detail on the combustion processes in internal combustion engines is included in Heywood, on which the following descriptions of SI and CI combustion rely heavily [5]. In a spark ignition engine, air and fuel is premixed and ignited via an electrical discharge. This adds enough energy to the local volume of gases around the spark plug such that combustion is initiated. The flame resulting from this is a laminar flame; the flame front separates unburned gaseous mixtures ahead of it and burned gaseous mixtures behind it. The flame front propagates locally through the unburned mixture at its laminar flame speed, which is typically less than 1 m/s; conduction of thermal energy released from combustion, along with the transport of reactive species, allow this to happen. Flames that have higher temperature gradients from un-burned to burned mixtures propagate faster i.e. laminar flame speed scales with the temperature gradient: in a fuel-lean condition it would propagate more slowly because leaner fuel mixtures typically have lower flame temperatures [5]. However, whilst locally (i.e. on a very small scale) the flame front propagates at the laminar flame speed, turbulence distorts the laminar flame front such that its surface area is dramatically increased and it becomes a turbulent flame, with a characteristic turbulent flame speed [5]. Turbulent flame-speeds are typically much higher than laminar flame speeds, and it is for this reason that SI internal combustion engines are able to work, because as the in-cylinder turbulence increases with piston speed, so does the rate of the turbulent flame front. Were this not the case engines would not be able to run at high speeds since combustion would occur much too slowly [5].

In a typical compression ignition engine however, fuel is injected at high-pressures into the heated and high-pressure atmosphere inside the engine cylinder at close to maximum engine compression. There is a characteristic delay before SOC since the fuel jets must first spread outward from the injector into the combustion chamber, eventually coalescing into small droplets. Heywood notes that only upon evaporation of these droplets and subsequent mixing with air in the combustion chamber, does the mixture auto-ignite [5]. It is through the continuous preparation of more mixed air and fuel vapour that combustion progresses, hence the CI combustion process is effectively mixing-controlled and the associated flames often called 'diffusion flames'. Furthermore, much of the combustion process occurs in a thin 'reaction sheet' located where fuel/air mixtures are close to stoichiometry, and that the turbulence in the engine cylinder similarly distorts the flame front into a turbulent diffusion flame. Because of this, there are clear boundaries between the fuel plume(s) emanating from an injector and surrounding air: the high temperatures can cause soot formation in the fuel-rich area behind the flame, and NO<sub>x</sub> formation in the fuel-lean area ahead of it [5], [77].

### 3.8.2 HCCI Combustion and Related Strategies

Homogenised Charge Compression Ignition or simply ‘HCCI’ is effectively a combination of SI and CI strategies; it is compression ignition but of a pre-mixed charge of air and fuel like that used in spark ignition [77]. It has been widely explored as alternatives to *both* SI and CI, and one of the reasons for this is the apparent thermodynamic benefits associated with it since it is very close to constant volume combustion. As Reitz and Duraisamy note in a particularly useful review, it is also a potential method of reducing NO<sub>x</sub> and particulate emissions generation in CI engines [78]. However, there are several challenges associated with HCCI combustion. Yao *et-al.* note that the main challenge with HCCI is controllability, since there is no way of directly controlling when combustion occurs – it is reliant on the auto-ignition properties of the air-fuel mixture. These properties are in turn influenced by a variety of factors, for example the degree of mixture homogeneity, fuel latent heat of vaporisation, residual rate, and several other factors [77]. Thus, the largely spontaneous nature of HCCI can result in high cycle-to-cycle variation, and very rapid heat release and pressure rise rates: these are challenging for the crank-slider mechanics of an engine. Compounding this are challenges such as cold-starting, HCCI operation range, mixture preparation, and high levels of unburnt hydrocarbon and carbon monoxide emissions [77], [78].

Therefore, a variety of other approaches have been/are being explored in literature, and all discussed in following paragraphs attempt to introduce some degree of control over SOC: PCCI, which stands for ‘Premixed Charge Compression Ignition’ is one such example. Reitz and Duraisamy state that many research efforts have gravitated towards this combustion process instead of HCCI as a replacement for traditional CI. As in HCCI, the objective of PCCI in this case is that by ensuring the fuel is pre-mixed, there is a reduced NO<sub>x</sub> and soot formation rate in comparison to CI, but unlike HCCI it aims to preserve the link between the mixing of fuel and air and SOC that is present in CI combustion [78]. To achieve this, the strategy employed is to inject the fuel charge much earlier in the compression stroke in comparison to a CI engine. Reitz and Duraisamy noted that whilst PCCI can still suffer from high UHC and CO emissions, several researchers have demonstrated that PCCI (and HCCI) can operate at near 100% combustion efficiency when boosted by high intake pressures, and using piston bowl designs with minimum crevice volumes [78]; see [79] and [80] for the noted PCCI and HCCI studies respectively.

Reactivity-Controlled Compression-Ignition or ‘RCCI’ is a different approach, which Reitz and Duraisamy describe as a ‘dual fuel’ strategy. In RCCI, a fuel of low reactivity (i.e. more resistant to autoignition e.g. ethanol) is injected early on and consequently forms a well-mixed atmosphere as in SI operation. Then, a fuel of high reactivity (i.e. less resistant to autoignition e.g. diesel fuel) is injected directly into the combustion chamber before SOC, as in CI operation, igniting the main charge [78].

The authors reviewed an extensive number of works in RCCI, including for example different fuel configurations and injection strategies, application to both heavy- and light-duty diesel engines, and computational and experimental approaches. It was duly noted that RCCI appears promising in terms of meeting emissions standards without relying on extensive NOx/soot aftertreatment, whilst also demonstrating very high thermal efficiencies [78].

Whilst PCCI and RCCI are largely focused on traditionally CI engines (although the latter often employs traditionally SI fuels [78]), SI-CAI, short for Spark Ignition – Controlled Auto Ignition is focused more on traditionally SI engines. SI-CAI is a form of ‘hybrid combustion’ strategy that blends the controllability of SI with HCCI (the latter of which is sometimes referred to as CAI) [81]. In SI-CAI, sometimes also called SACI (Spark Assisted Compression Ignition), the combustion process occurs in three stages. As described by Wang *et-al.*, SI-CAI begins with an SI stage that progresses to a flame-propagation stage much like a conventional SI engine. However, the resulting increase in temperature and pressure in the remaining un-burned mixture drive it into auto-ignition. A characteristic of SI-CAI is it is a distinctly two-stage heat release process, Figure 19 shows a visual representation of the difference in heat release rates, based on Wang *et-al.* [82]:

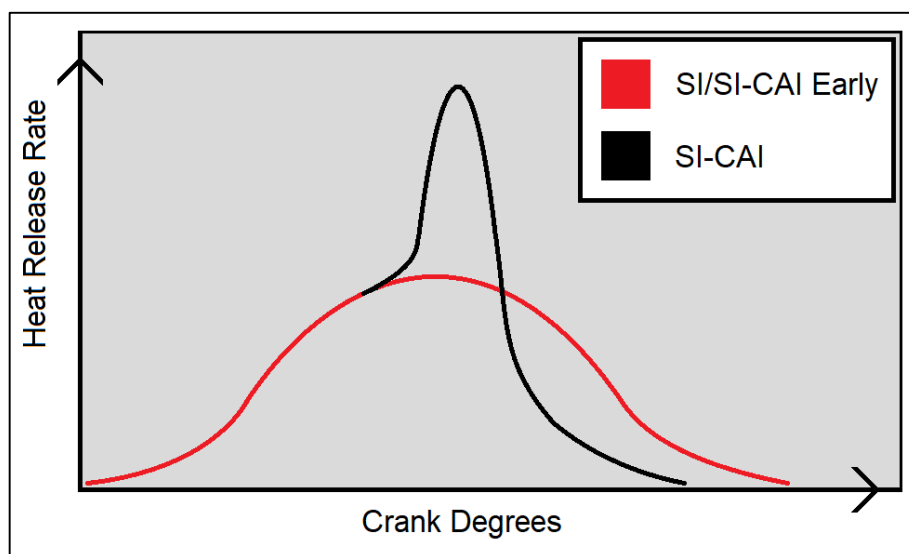


Figure 19 – Comparison Between SI and SI-CAI Heat Release Curves

The red curve is SI combustion and early SI-CAI combustion, the black curve is SI-CAI combustion after autoignition; the point of separation is determined as the location of autoignition timing. It is also apparent that SI-CAI presents a thermodynamic advantage due to the shortened combustion duration in comparison to traditional SI [82].

### **3.9 Novel Engine Architectures**

A majority engine development efforts are still four-stroke engines. However, alternative engine architectures are increasingly being investigated. Many of these appear to take inspiration from earlier works, and rotary engines are a case in point: perhaps the most well-known ‘unconventional’ engine architecture is the Wankel rotary engine. Instead of using pistons travelling the length of the cylinders in which they are situated, the Wankel rotary engine uses a rotor shaped like a flattened Reuleaux triangle rotating within an epitrochoid housing, but still operates using a four-stroke cycle [83]. It has notable advantages, such as being extremely compact and has far fewer moving parts than a reciprocating piston engine; there has even been a project investigating a ‘Micro Rotary Engine Power System’ at the University of California, at Berkeley [83], [84].

Commercially, Mazda Renesis engines are a notable automotive example, and Fichtel and Sachs of Germany also produced small industrial engines which used the Wankel architecture, such as the KM 48 [5], [85]. However, despite its success and its advantages, the Wankel engine has some notable downsides. One of the most serious issues is that of oil consumption, since a Wankel Engine generally relies on a small amount of oil injected into the engine to lubricate the rotor(s) and the apex and side seals that are essential for the engine to run. This oil is subsequently burnt, in a total-loss system [83]. Furthermore, as Heywood notes, the Wankel engine has an inherently high amount of heat transfer and is well known for suffering problems with gas sealing [5]. Nevertheless, the power-density of Wankel engines and their capability of reaching very high engine speeds has proven compelling enough that renewed interest in ‘rotary engines’ exists. For example, a U.S. – based company called ‘LiquidPiston’ is developing such an engine where the rotor is ovoid in shape and operates in a housing with three combustion chambers. The external appearance of one of their engines is rather like a triangle, but the engine operates differently to the traditional Wankel engine, and it is claimed to have several advantages. These include better sealing; indeed, the geometry used has been described as an ‘inverted Wankel’ [86], [87].

#### **3.9.1 Reducing Oil Consumption in Piston-Ported Two-Stroke Engines**

Two-stroke architectures have recently become the subjects of new development efforts. However, the oil short-circuiting problem in piston-ported engines (which nearly all two-stroke engines are) was a subject that required extensive development to resolve satisfactorily. Achates Power are a very good example of how it has been solved in the case of OP2S engines. Based in the United States of America and formed in 2004, Achates Power have extensively re-developed the OP2S architecture, dedicating significant resources to reducing the oil consumption of their engines to levels that are comparable to, or even less than contemporary four-stroke engines. How this was achieved is partially detailed in a

publication discussing aspects of their A48-1 single cylinder engine, where Achates Power noted the importance of the liner surface preparation. For example, the application of modern industry standard practices such as a laser ablation method developed by Gehring is discussed, which allows much more precise control over liner surface design, as well as liner cooling strategies to reduce cylinder bore distortion at temperature [66]. Test results from the A48-1 indicated that fuel specific oil consumption (measured with a sulphur-tracing system) has been reduced to 0.04% fuel on a weighted drive-cycle average basis, and 0.052% at rated load, and it was highlighted that with increasing run-time, the oil-consumption of the test engine seemed to decrease further. It is believed this is due to the liner and ring pack ‘wearing in’ as the engine runs [66].

In addition to the liner itself, Achates Power has undertaken significant analyses on other aspects of the cylinder, including the piston pins, ring packs, skirts, and crowns (including the crown geometry to aid mixing of the fuel and air) [66]. For example, improvements to the piston pin were pursued extensively because of the decreased oscillatory loading to the small end bearing experienced in two-stroke engines. In four-stroke engines, the inertia of the piston causes an oscillating load condition as the piston changes direction, which helps oil to migrate all the way around the small-end bearing. This is possible between the exhaust and intake strokes, where there is effectively no positive pressure on top of the piston. However, in two-stroke engines, the pressure on the piston crown is effectively always positive at top dead centre (‘TDC’), or indeed IDC in an OP2S engine. Because of this, the pressure can overcome the inertia of the piston, preventing (or significantly reducing) the oscillating load condition at the piston pin, and so prevent adequate lubrication. The solution to this problem adopted by Achates Power was to use a compounded bearing surface, much like in larger, two-stroke locomotive engines. Each surface is periodically loaded and unloaded as the assembly rotates, allowing sufficient lubrication to reach the entire bearing and significantly reducing the rates of wear and premature failure [63].

### **3.9.2 Renewed Interest in Two-Stroke Architectures**

Though prominent, Achates Power are by no means alone in OP2S research, and the wider two-stroke engine field has recently become more active in general. For example, Borghi *et-al.* are one of a number of groups focused on two-stroke engines specifically designed as range extenders for electrified vehicles. In their work, the authors detail a two-stroke gasoline direct injection engine with a target output of 30 kW, finding that it could have lower weight, thermal and mechanical loads and lower heat rejected versus a similar four-stroke engine the authors proposed. A number of one-dimensional (‘1D’) and three-dimensional (‘3D’) CFD studies were performed, and the engine used an external scavenging pump in a loop-scavenging configuration, instead of crankcase scavenging [88]. The proposed engine was developed from an earlier design, with a key change being to use an electrically driven supercharger as a scavenge pump, which the authors highlighted would be ideal in a range-extender application since

there would be sufficient battery capacity to drive it. Some areas where results were suggested to be less optimal included less efficient operation of a 3-way catalyst for exhaust emissions mitigation, a complex configuration process for the injection parameters that requires support from 3D CFD simulations, and the possible need for a particulate filter, among others [88].

Many notable works were presented at the 2022 Direct-Injection Two-Stroke ('DI2S') conference. These included a uniflow, blower-scavenged two-stroke SI engine with separated oil system, and Libertine who discussed testing a free-piston engine ('FPE') design on hydrous ethanol (90% ethanol, 10% water). The free piston nature of the engine enabled the use of a variable compression ratio that, when increased for starting, reduced engine misfire [89]. Indeed, there is much interest in the possibility of FPEs being used as range extenders, and Rathore *et-al.* present a useful review on free-piston engines [90]. Whether of single piston and combustion chamber, dual piston and combustion chamber or opposed piston design, a free-piston linear-generator ('FPLG') employs a linear alternator to facilitate the generation of electricity directly from the reciprocating motion of the piston(s), instead of using a crank-slider mechanism [90]. The alternator may be of a flat or tubular type and is used both for starting the engine and controlling the reciprocating motion of the piston(s) [90]. However, misfiring due to the lack of a flywheel to maintain consistent motion can occur, although it was suggested that the reduced number of components reduces frictional losses and so contributes to potentially higher efficiency. It is also argued that because the motion of the piston is controlled by the linear alternator, and not a crankshaft, that the engine can adapt to different alternative fuels by varying the compression ratio [90].

### **3.10 Contemporary Opposed-Piston Engine Research**

Given its inherent thermodynamic advantages (see section 3.4), it is unsurprising that of all the alternative engine architectures available, many researchers are focusing on opposed-piston engines, including some of those discussed above. As noted, Achates Power is by far the most prominent in the field and their work extends beyond that of resolving excessive oil consumption. For example, they have also resolved many of the other mechanical issues that have historically made piston-ported architectures less popular, including the difficulties associated with gearing together the two separate crankshafts that their OP2S engines utilise [65]. These efforts have proven worthwhile: test results from several of their multi-cylinder engines show very low pollutant formation as well as high thermal efficiencies across a wide range of operating conditions. One Achates Power architecture recently demonstrated best in class fuel efficiency and emissions in heavy duty fleet service trials, and another engine (engineered in partnership with Cummins) has been selected as a powerplant for a US Army combat vehicle due to its high efficiency, high power output and physical compactness [91], [92]. It is a 1000hp four-cylinder unit that is more compact, more efficient and lighter in weight than the V8 four-stroke engine it could replace. Their research, some of which has been awarded funding from bodies

such as the California Air Resources Board ('CARB') and major organisations like ARAMCO, also extends to gasoline compression ignition engines, and simulation of hydrogen OP2S engines. In fact, in 2022 they formed the 'Hydrogen Opposed Piston Engine Working Group', which is a consortium of parties with an interest in hydrogen-fuelled OP2S engines, citing the increased interest in hydrogen combustion in general [93]. Then, in 2023 and in partnership Argonne National Laboratory, Achates Power also succeeded in initial testing of a single-cylinder, purely hydrogen CI OP2S engine. The authors explored strategies of non-premixed CI as well as 'partial pre-mixed charge compression ignition' (partial 'PCCI'), though they noted that the compression ignition of solely hydrogen fuel is very challenging to exploit outside of a narrow operating range, due to its resistance to autoignition [24].

Another impressive CI OP2S engine is the relatively small displacement single-cylinder example developed by Baker Engineering in the U.S., which is designed as a power generation unit, featuring two generators for power output. Interestingly, the crankshafts of the engine appear to be timed together by a toothed belt [94].

An interesting approach was employed in 2021 by Ma *et-al.*, who managed to experimentally characterise the combustion behaviour of gasoline in an OP2S gasoline direct injection ('GDI') engine made largely from two 125cc motorcycle engines [95]. A toothed belt system was utilised to time the intake and exhaust crankshafts together, whilst also using a separate scavenge pump, but this was driven separately via an electric motor and not by the engine itself. The authors used two fixed scavenging pressures of 110 kPa and 120 kPa and utilised a cylinder pressure sensor to gather data. It was found that the heat release characteristics of the engine broadly reflects that of a traditional engine, but that the exhaust tended to have quite a high amount of energy, which could be a target for improvement. Helpfully though, it was found that a crankshaft phase difference of approximately 15 CAD offered improved scavenging performance [95].

### **3.10.1 Unconventional OP2S Mechanics**

A common trend among other works in the OP2S field are investigations into replacing the well-proven crank slider mechanism with something else. SI OP2S engines of any type appear comparatively rare, but several examples of SI cam-plate engines (that in some respects are mechanically related to the venerable 'Dyncam' four-stroke engines) have been found; the unfortunate controversies surrounding the Dyncam engine are duly noted on its own website [96]. In a cam-plate arrangement, there is no crankshaft, where instead the cylinders typically run axially aligned to the power shaft, connected to it by means of rollers (or other form of follower) that follow the profile of the cam-plate to create the reciprocating motion. The mechanism is well proven in applications such as an air conditioning pump

- see for example Toyota Industries Corporation [97]. However, it is noted that there is an inherent risk in employing this mechanism in an internal combustion engine, since the forces it has to endure are likely many times more severe than those it may traditionally see.

Even so, physical prototypes exist. For example, Devize Motors, based in the United States, have developed an engine design which is an opposed-piston engine with four cylinders, using two cam-plates to move the intake and exhaust pistons. It is a GDI engine and utilises an external scavenging pump, operating on a two-stroke cycle in each cylinder. The engine was first started in 2023, has a total displacement of 2141 cc, and the technology is intended for various applications including on-road vehicles, military vehicles, marine applications, unmanned aerial vehicles and power generation. The company is also developing an axial four-stroke engine too [98].

INNEngine's designs also fit into the cam-plate engine category. Based in Spain [99], their prototypes include a GDI opposed-piston version which they claim is more compact and lightweight than a comparable crank-slider engine. Called the 'e-REX', it is a four-cylinder, spark ignition 'barrel-shaped' engine that is intended to be used as a range-extender for an electric vehicle. It uses two cam-plates – one for the intake pistons and one for the exhaust pistons - and has the means to vary the phase angle between them (so varying the difference between intake and exhaust port timing as well as the compression ratio). It is claimed that the engine is mechanically simpler and more lightweight than a traditional engine, that it has multi-fuel capabilities, and has run successfully for hundreds of hours. Interestingly, INNEngine call the e-REX a 'one stroke engine', citing the fact that because the four pistons are grouped into two pairs of two, there are two combustion events per revolution. The motivation appears to be to distance the design from the traditional association of the term 'two-stroke engine' with requiring a mixture of fuel and oil [100], [101]. On a cylinder-by-cylinder basis however, it is clear that the engine operates on an externally scavenged, two-stroke cycle [101]. INNEngine is also developing a smaller, single piston (per cylinder) engine called the 'REX-B', which they also call a 'one-stroke' engine (again on a cylinder-by-cylinder basis, it is a two-stroke engine). In this case, the underside of each piston is used for scavenging, so the engine uses mixed fuel, much like a conventional crankcase-scavenged two-stroke engine. Nevertheless, the naturally aspirated 125cc engine is capable of in excess of 21.5 HP, and is intended as an ultralight, high-power output generator for unmanned aerial vehicles [99], [100].

Outside of cam-plate engines, Pattakos *et-al.* have produced several interesting prototypes of very unusual engine designs including OP2S engines, some of which they have patented [102], [103]. Their website indicates a prolific exploration of various fields not all of which relate directly to internal combustion engines, but those that do include a 'connecting rod valve', as well as the so-called 'PatOP' engine [104]. The connecting rod valve is used in the scavenging apparatus of an engine, and forms part

of a 'valve in piston' approach to connect a 'scavenging cylinder' to a 'combustion cylinder'. Note here the careful choice of words. This is to reflect the fact that there are several different variations of the 'connecting rod valve' of varying complexity. In one example, the valve is incorporated into the inside of the piston-skirt in a crankcase-scavenged two-stroke engine, and the valve controls the passage of fluid through the piston skirt to an additional transfer port in the side of the cylinder. Another part of the piston skirt is also used as a conventional piston-slide valve. In this case, the 'scavenging cylinder' is the crankcase alone [102], [104].

In another configuration, the valves are located in the crowns of two 'double-ended pistons' of an OP2S engine. One crown of each piston is the 'combustion side', sharing a common combustion cylinder, whereas the other crowns are part of two pumping circuits, and feature the connecting rod valves. The crankshafts are positioned in the middle of each double-ended piston, and port holes in the skirt of each controls the flow of fuel and air mixture into the two 'crankcases', similar to in a conventional crankcase-scavenged 2-stroke engine [102], [104]. However, as the connecting rod valves open and close, the spaces between the underside and topside of each of the pumping-crowns is connected and disconnected, thereby connecting and disconnecting flow from each crankcase to the top of each pumping crown. The fresh charge is then delivered to the (combined) power cylinder by means of transfer ports, using the 'closed' connecting rod valves in the pumping crowns to build pressure. Here therefore, each 'scavenging cylinder' is composed not only of each crankcase but also, periodically, the pumping side of each double-ended piston, and each double ended piston itself also acts as a slide valve [102], [104].

The 'PatOP' engine also uses a double-ended piston (though with no valve in the crown), with the crankshaft sitting in the middle of a large slot that also encompasses its connecting rods. It is a CI engine and uses the crankshaft to drive a diesel injection pump for an injector that delivers fuel directly between the two piston crowns [104]. It uses one 'end' of the double-ended piston as the intake piston in the OP2S layout, controlling the flow of gases into the power cylinder using the piston as a slide valve. However, instead of using the underside of the piston and crankcase like a conventional two-stroke engine, the air is instead pushed through to the power cylinder via ports that connect to the other end of the piston, which serves as a scavenging pump [103], [104]. In this way, the oil system is kept separated like in a four-stroke engine. The connecting rods for the exhaust piston extend outside the cylinder to a cross-head like mechanism that, via large 'pulling-rods' that run parallel to the cylinder, moves the other piston. Mechanically, this is rather like the piston configuration in a Doxford engine [23].

### 3.10.2 Computational Fluid Dynamics Studies

CFD models have become increasingly important to engine design since they allow the engineer to investigate hypotheses in a less risky and more time- and cost-effective manner, as compared to making an (or modifying an existing) engine. Numerous works in the OP2S field rely extensively on simulation, in addition to those highlighted previously. For example, Yang *et-al.* generated a 3-dimensional CFD model of a diesel OP2S engine, which they physically validated through a steady-flow test bench. This particularly impressive work established what the authors described as a ‘scavenging curve’ method. This was described using a graph with axes set as the cylinder residual ratio (y) against the exhaust residual ratio (x). The graph began with cylinder/exhaust residual ratios of 1 and 1 – i.e. fully burned mixtures, and finishes at 0, 0 – i.e. all of the burned gases are cleared from the cylinder and exhaust regions. On the same graph were two theoretical lines – one assuming perfect scavenging, and one assuming perfect mixing. The perfect scavenging line assumed that there is no mixing of the burned and unburned mass fractions, whereas the perfect mixing line assumed the burned and unburned mass fractions combine entirely such that there exists a uniform mixture in the cylinder. The real scavenging curve then fell somewhere between these two lines [105].

One of the motivations for the work was the fact that in an opposed-piston engine, the intake and exhaust ports are open at the same time, so there is likely to be considerable mixing of the burned and unburned mass fractions. Because of this, to evaluate the scavenging process (so to be able to improve it, for example) a large number of carefully selected parameters were traditionally required, and that the scavenging curve method significantly simplifies matters [105]. Using this method to evaluate their 3D geometry, Yang *et-al.* defined a ‘preferred zone’ where the scavenge curves should lie, itself located inside a wider envelope defined by the scavenge lines featuring the maximum and minimum port heights that were tested. The preferred zone was described as existing between port-height-to-stroke-ratios of between 0.11 and 0.15. The authors varied the intake and exhaust port heights to see the effects on the scavenge curves. It was found that whilst increasing both the intake and exhaust port heights helped the scavenging curve to move closer to the perfect scavenging line, increasing the exhaust port height is more conducive to speeding up the movement of the scavenging interface than increasing the intake port height. It was also suggested that increasing the exhaust port height was generally better at reducing the backflow of gases [105].

Another study is of a unique ‘rotary opposed-piston engine’, investigated by Jingbing Gao *et-al.* [106]. Note this is not a two-stroke engine. The scavenging characteristics of this architecture were studied using Ansys FLUENT and subsequently the power output, brake specific fuel consumption (‘BSFC’) and thermal efficiency using Ricardo WAVE software [106]. The engine features a displacement of approximately 547cc, 4 ‘cylinders’ and uses gasoline. After considerable evaluation of the methods and

assumptions employed to simulate the engine, the authors detail the results of their simulations which indicated a minimum BSFC of 245g/kWh and a peak brake thermal efficiency of approximately 33%, as well as lower NOx emissions due to lower in-cylinder temperatures [106].

Wang *et-al.* also made use of 3D CFD simulations to investigate the effects of swirl-spray impact on the performance of OP2S engines. The authors used a prototype test bench to validate the simulation model by comparing cylinder pressure tracings, and concluded that a 4.5 mm mesh size was sufficiently accurate [54]. The geometry investigated was notable in that the intake ports of the cylinder were split in half: the first half of the ports was designed to be conducive to establishing swirl, and opened first as the intake piston approaches ODC. The second half, which opens afterwards, was designed to control the axial motion of the gases through the cylinder, so as to improve the overall scavenging performance. It was suggested that by using split scavenge ports in this way, scavenging could be optimised by varying the pressures in each part of the port, for example it would be possible to increase swirl largely independent of the delivery ratio, such that the pumping loads do not become excessive [54]. Various injection patterns were subsequently evaluated, and it was concluded that a reverse swirl-spray impact (when the majority of the fuel spray from the injector is against the direction of the swirling regime) was, generally, more beneficial than forward swirl-spray impact (when the majority of the fuel spray is with the direction of the swirling regime). This is because it was found that not only does reverse swirl-spray impact improve spray distribution and atomisation (as does forward), it also helped to improve the scavenging process: by using the reverse impact to degrade the in-cylinder swirl ratio during each cycle, the buildup of exhaust gases close to the cylinder wall was reduced [54].

Tulwin *et-al.* investigated the diversity of fuel sprays in a diesel opposed piston engine using CFD, focusing on how fuel delivery methods affect the heat release coefficient [107]. They also considered the fuel combustion rate and cylinder pressure as a function of the crank angle, with the exhaust piston leading the intake piston by 14 crank angle degrees ('CAD'), as well as evaluating the heat exchange process between the cylinder volume and the cylinder walls as well as the thermal efficiency. Different injector designs in both single and diametrically opposed configuration were investigated, and detail was provided for the mesh that was used for the 'combustion chamber', which is effectively formed by the two piston crowns. It was shown that two injectors corresponded to a significantly higher heat release rate due to better mixing of fuel and air. In a single injector configuration, a 4-hole injector performed better than 8-hole injectors since it exhibited greater rates of heat release during injection [107].

Mattarelli *et-al.* used CFD simulations in a virtual development process of a hydrogen opposed-piston engine, rated at 27 kW. Interestingly, in computer-aided-design renditions of the fluid side of the engine, the actual injection points are two sets of three 'ducts', with each set of ducts being fed by a low-

pressure injector. The ducts are located just downstream of the intake liner ports. The authors envisage that the manufacturing costs of the engine should be comparable with four-stroke engines, due to the mechanical simplicity of the architecture. It was estimated that the mass of the engine in the configuration detailed would be approximately 30 kg [108].

### **3.11 Summary**

In part 1 of this literature review, the development of internal combustion engine technology including both SI, CI, four-stroke and two-stroke engines has been charted, and the OP2S engine revealed as one of the most thermally efficient architectures ever developed. The thermodynamic benefits of OP2S engines, such as uniflow-scavenging, two-stroke operation and high stroke-to-bore ratio, were noted as significant advantages over conventional engine architectures. Nevertheless, the challenges of complying with emissions legislation likely led to its demise in the latter parts of the 20th Century, whilst conventional engines became ever more sophisticated. The contemporary dominance of the modern four-stroke engine was acknowledged, including the importance of digital engine controls, as well as the significant research and development into improving it further, such as through using alternative fuels and combustion strategies, and different engine operating cycles. However, it was also found that research into alternative engine architectures continues, with research active in both rotary- and piston-type designs; notably the OP2S engine enjoys renewed attention. The extensive work of Achates Power in this field was identified as significant, having helped to resolve the challenges posed by emissions standards through successfully reducing oil consumption and improving mechanical integrity. Their focus on CI engines co-exists along with an increasing array of other novel, CI OP2S architectures by other researchers. SI OP2S engines were also identified, including those from the earliest days of OP2S engine design. However, they are not as common as their CI counterparts and several more modern examples use highly unusual engine mechanics. Part 2 of this literature review discusses SI in OP2S engines in more detail, and identifies some of the challenges it may face.

#### 4. Literature Review Part 2: Spark Ignition in OP2S Engines

In this chapter, SI in OP2S engines is discussed in much more detail. The porting and scavenging of an OP2S engine, which generates an in-cylinder motion that differs substantially in some of its global characteristics from that in a conventional poppet-valve engine, is used as a starting point, expanding to two-cycle engines in general to present useful parameters and equations. Variations in scavenging performance, and methods to measure and model the process are noted, followed by some of the challenges SI can face in OP2S engines. An opportunity for a significant research opportunity is subsequently identified.

##### 4.1 Scavenging and Port Geometry

As described in section 3.3.1, an OP2S engine does not use its pistons for pumping work, instead relying on a pressure gradient between the intake and exhaust ports positioned at the extreme ends of the cylinder. During uniflow scavenging, the flow moves along the cylinder from intake to exhaust and typically (though not universally) incorporates swirl. Swirl is defined as a rotational motion around the central (longitudinal) axis of the cylinder [5]. The uniflow method is advantageous in important aspects such as available port-open area, but in some cases it can leave a central core of the cylinder largely unscavenged [22], [30]. If swirl is used, this is typically achieved through intake port geometry. An example of a swirl inducing geometry is shown in Figure 20:

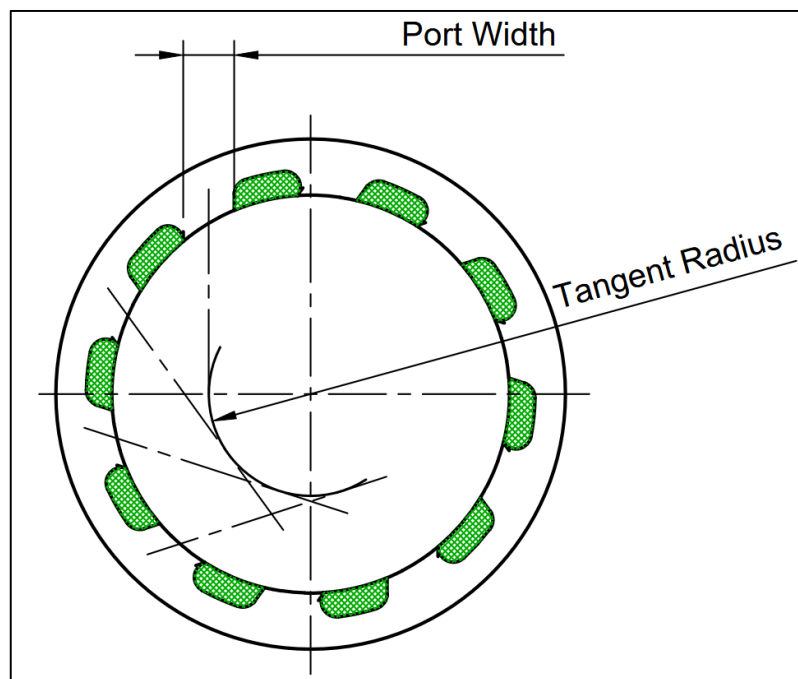


Figure 20 - Example of Swirl-Inducing Intake Ports

Here, the green shaded portions represent the bridges between the ports (i.e. cylinder liner material). The swirl is achieved in this case by offsetting the central port axes from the axial centreline of the cylinder by the ‘tangent radius’. There is no convergence of the ports in this case. Sher notes a more detailed geometric description of ports [30], a version of which is shown in Figure 21:

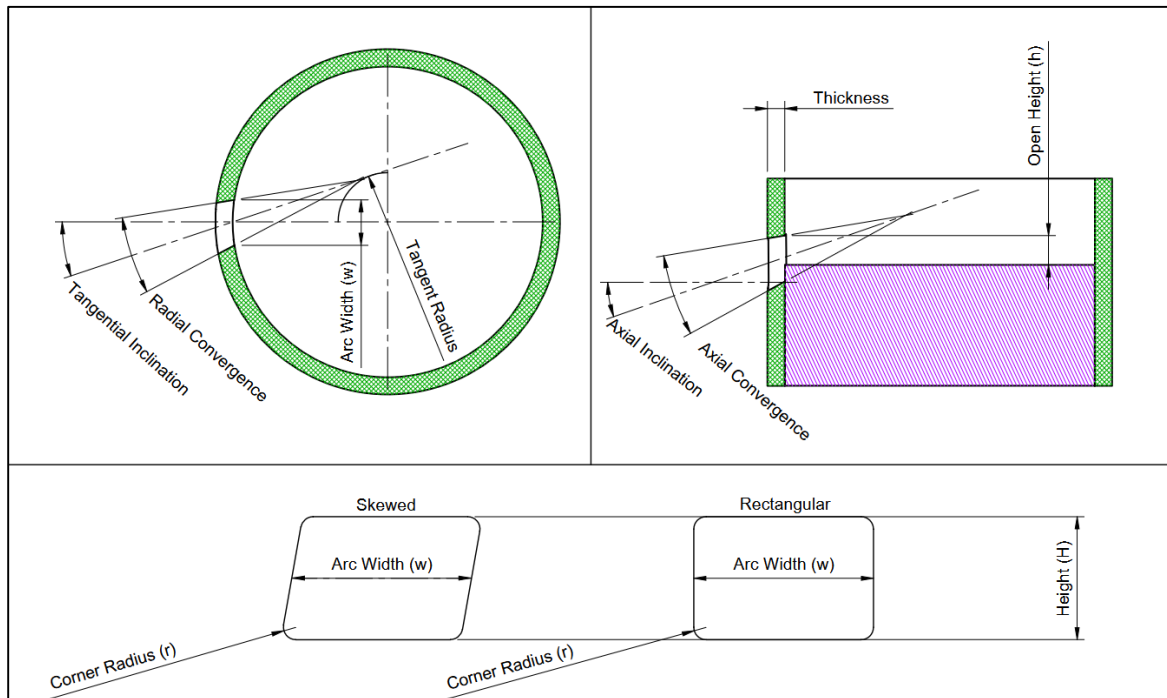


Figure 21 - Cylinder Port Geometry and Port Types

The green hashed parts indicate the liner, and purple hashed parts indicate the piston. The two port designs at the bottom are those noted as making the best use of the available space on the liner. Several variables are identified in Figure 21, including corner radius ‘r’, arc width ‘w’, port height ‘H’, and open height ‘h’ [30].

#### 4.1.1 Flow Through Cylinder Ports

The discharge jet direction and discharge coefficient of a cylinder port is affected not just by the port geometry itself, but also by the influence of the piston geometry at times when the port is not fully open [30]. The discharge coefficient, or ‘Cd’, is a measure of how the actual discharge through a constriction (like a port) compares to what the discharge would be through an ideal, frictionless port given the same upstream and downstream conditions, in other words [5]:

$$C_d = \frac{\text{Actual Mass Flow}}{\text{Ideal Mass Flow}} \quad \text{Eq. 2}$$

A real port will always present a restriction to flow that results in an irrecoverable pressure drop from one side to the other, whereas an ideal port does not. Conveniently,  $C_d$  can also be expressed in terms of area, such that [5]:

$$C_d = \frac{A_{eff}}{A_{ref}} \quad Eq. 3$$

Where  $A_{eff}$  is the effective area of the ideal, frictionless port that would pass the mass flow that is measured (during a blow-rig test, say), and  $A_{ref}$  is the appropriate reference area usually defined as the minimum cross-sectional area of the real port [5]. Note the minimum area is often called the ‘throat’ in cases such as a convergent/divergent nozzle; for consistency in the following equations however the subscript ‘ref’ is used instead of ‘t’ on the assumption that  $A_{ref}$  exclusively represents the smallest area of a port, thus is equivalent to throat area ‘ $A_t$ ’. For the geometries illustrated in Figure 21, there are two different appropriate values for  $A_{ref}$  for evaluating the discharge coefficient, and which one is used depends on the extent of port opening as defined by ‘ $h$ ’ (the open height); as in Sher [30]:

For  $r < h < (H - r)$ ,  $A_{ref}$  is:

$$A_{ref} = wh - 0.43r^2 \quad Eq. 4$$

And for  $h = H$ ,  $A_{ref}$  is:

$$A_{ref} = wH - 0.86r^2 \quad Eq. 5$$

Then, the mass flow rate through a linear port can be described with the one-dimensional equation for compressible flow through a restriction at sub-critical (i.e. not choked) conditions [5]:

$$\dot{m} = \frac{C_d * A_{ref} * p_0}{\sqrt{R * T_0}} * \left(\frac{p_{ref}}{p_0}\right)^{\frac{1}{\gamma}} * \left\{ \frac{2\gamma}{\gamma - 1} \left[ 1 - \left(\frac{p_{ref}}{p_0}\right)^{\frac{\gamma-1}{\gamma}} \right] \right\}^{\frac{1}{2}} \quad Eq. 6$$

Where  $C_d$  is the discharge coefficient,  $p_{ref}$  is pressure at  $A_{ref}$ ,  $p_0$  is stagnation pressure,  $T_0$  is stagnation temperature,  $R$  is a gas constant, and  $\gamma$  the ratio of specific heats of the fluid [5],

$$\gamma = \frac{C_p}{C_v} \quad Eq. 7$$

For given values of stagnation pressure and temperature, the maximum mass flow occurs when the fluid velocity at the throat (i.e.  $A_{ref}$ ) is equal to the speed of sound, and this is called choked flow. Choked flow occurs at the critical pressure ratio [5]:

$$\frac{P_{ref}}{P_0} = \left( \frac{2}{\gamma + 1} \right)^{\frac{\gamma}{\gamma - 1}} \quad Eq. 8$$

And the mass flow rate for choked flow is [5]:

$$\dot{m} = \frac{C_d * A_{ref} * p_0}{\sqrt{R * T_0}} * \gamma^{\frac{1}{2}} * \left( \frac{2}{\gamma + 1} \right)^{\frac{\gamma + 1}{2 * (\gamma - 1)}} \quad Eq. 9$$

Broadly therefore, a reduction in the discharge coefficient will result in a reduction in the mass flow rate at a given condition. Heywood notes that  $C_d$  tends to increase with an increasing pressure ratio across the port but will tend to decrease as the tangential inclination of the port increases, and the geometry of scavenging ports has the greatest influence on  $C_d$  at the lower and upper ends of port open-height (i.e. when  $h$  is closer to 0 or  $H$ ). Also, ports with rounded entries indicate better discharge coefficients as the open-fraction approaches  $H$ , and a rounded entry coupled with a tapering convergence helps to prevent flow detachment within the ports themselves [5]. In the case of exhaust ports, the pressure ratio (from cylinder to exhaust chest) has a particularly significant effect on  $C_d$ , and in thicker cylinder walls, an outward taper is commonly incorporated to encourage flow diffusion. In thinner cylinder walls, the angle between the exuding jet and the longitudinal cylinder axis increases rapidly with piston position, from approximately 50 degrees at port open to 80 degrees at roughly 20% open height [5].

#### 4.1.2 Useful Scavenging Parameters

It is helpful at this point to define some important variables in scavenging two-stroke engines in general, which are affected by several factors including port  $C_d$ . For example:

The charging efficiency  $\eta_c$  [30]:

$$\eta_c = \frac{m_a}{m_0} \quad Eq. 10$$

Compares the mass of air delivered that has been trapped in the cylinder after port closure ( $m_a$ ), with the ambient swept volume mass of air ( $m_0$ ) i.e. the mass of air that would occupy the swept volume of the cylinder\*. It indicates how completely the cylinder has been filled with a fresh charge. Note that the swept volume mass is equal to the mass of air that would be required in the case of perfect displacement scavenging at ambient conditions (discussed shortly) [5].

The scavenging efficiency  $\eta_s$ :

$$\eta_s = \frac{m_a}{m_a + m_b} \quad \text{Eq. 11}$$

Compares the mass of delivered air trapped after port closure ( $m_a$ ), with the mass of the overall cylinder mixture (i.e. delivered air ( $m_a$ ) *and* any burnt mixture ( $m_b$ )) trapped after port closure, thus it indicates how well the residual species in the cylinder have been displaced with air [5].

The delivery ratio  $\lambda$ :

$$\lambda = \frac{m_i}{m_0} \quad \text{Eq. 12}$$

Compares the mass of delivered air per cycle ( $m_i$ ), with the ambient swept volume mass of air, so indicating how over- or under-supplied (with fresh air or mixture) the cylinder is [5], [30]. Then, the trapping efficiency can be defined as the ratio between the charging efficiency and the delivery ratio. Sher states that for a naturally aspirated engine, the ideal situation would be one where  $\eta_c=1$  such that the mass of delivered air trapped in the cylinder is exactly equal to that of the ambient swept (or trapped) volume mass of air;  $\eta_s=1$  such that the trapped mass of pumped air is exactly equal to that of the trapped cylinder mass in total (i.e. the only trapped fraction is air); and  $\lambda=1$  such that the amount of air delivered per cycle is exactly equal to that of the equivalent swept (or trapped) volume of ambient air. In a supercharged engine, the ideal scavenging efficiency would still be  $\eta_s=1$ , but the charging efficiency would be  $\eta_c>1$ , and similarly the delivery ratio would be  $\lambda>1$  [30].

In reality such conditions are highly unlikely to occur. Firstly, they require a ‘perfect displacement’ scavenging condition, where the incoming fresh charge pushes the residuals out like a ‘fluid piston’ without any mixing between the two fractions. Some form mixing between the fresh and residual fractions during the scavenging process is virtually inevitable, so an amount of fresh charge will likely be wasted through the exhaust ports [5]. The corollary to perfect displacement is perfect mixing, where a given mass of air entering the cylinder mixes completely with the entire volume of the gases in the cylinder; at the same time an equal mass of the mixture leaves the cylinder. It is possible to plot these two processes on a graph with respect to the delivery ratio; Figure 22 shows an approximate representation of what this would look like, based on Heywood [5]:

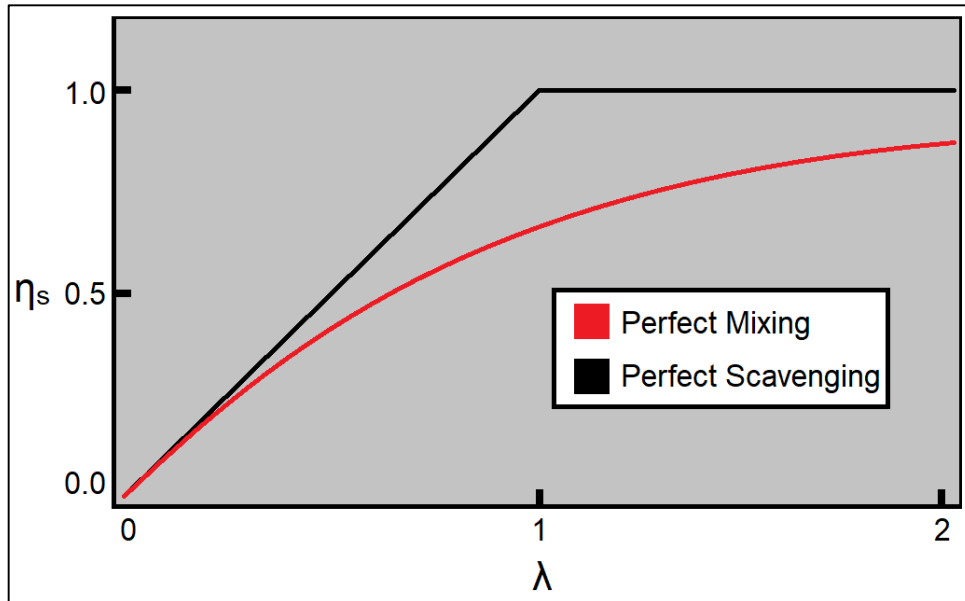


Figure 22 - Perfect Mixing vs. Perfect Scavenging

In other words, a much higher delivery ratio is required to fully scavenge a cylinder of residual fractions in the perfect mixing process than in the perfect scavenging process, thus resulting in significant additional pumping work to supply the extra air (or mixture) required. A plot of a reasonable real scavenging process would likely lie somewhere in the middle of the two, given that some mixing will occur [5], although it is possible in an extreme case that a significant proportion of fresh charge could short circuit and be lost through the exhaust without mixing at all [30]. Such a plot on Figure 22 could be expected to lie below that of even the perfect mixing line. However, the short circuiting of fresh charge through the exhaust ports is only of great concern if it is an air/fuel mixture due to the high unburnt HC emissions that will result. If it is just air then it is less concerning [5], though this does not consider any possible influence on the requirements of the exhaust aftertreatment system.

#### 4.1.3 Variations in Two-Stroke Scavenging Performance with Speed and Load

The scavenging performance of a two-stroke engine will naturally vary with different engine loading and engine speeds. For example, many crankcase-scavenged two-stroke engines are designed to operate in a specific ‘power band’, representing optimal engine speeds and loads. Outside of these conditions, engine performance may fall precipitously [5]. A detailed analysis on why this is the case, and the changes in scavenging performance of all the various types of two-stroke engine at different engine speeds and loads, is beyond the scope of this work. However, to highlight the relationship between scavenging and engine performance, some examples are given below.

The first two examples are discussed by Sher [109]. In one case a small, crankcase-scavenged engine was operated at low engine speeds of approximately 2000-3000 rpm and high loads of between 2 and 6 hp. With these conditions, it was found that as much as 30% of the fresh charge entering the cylinder was lost through the exhaust port (short-circuiting). However, the same engine operating at the same load of between 2 and 6 hp, but at higher speeds of approximately 5000-6000 rpm, exhibited short-circuiting losses between 1/2 and 1/3 of this [109]. In another instance, a 175 cm<sup>3</sup> engine rated at 4.9 kW at 5000 rpm was tested at WOT and an exhaust gas analysis performed across a series of load points, from which the trapping efficiency of the engine could be determined (in addition to pollutant information). It was found that the trapping efficiency of the engine increased modestly with rpm. However, by modifying the engine and introducing either an additional piston-valve to control the exhaust port, or air blast (direct) fuel injection, the trapping efficiency increased significantly. With additional data from HC emissions, it was concluded that fuel short-circuiting was a problem with the base engine. Similarly, an increasing rate of CO emissions at higher rpm was suggestive of poor mixing that resulted in highly diluted pockets of un-flammable mixture [109].

The third example, from Borghi *et-al.*, shows a plot of trapping efficiency vs. delivery ratio for the scavenging system of a loop-scavenged two-stroke engine, as calculated using 3D-CFD simulations, with perfect displacement and perfect mixing lines included for reference [88]:

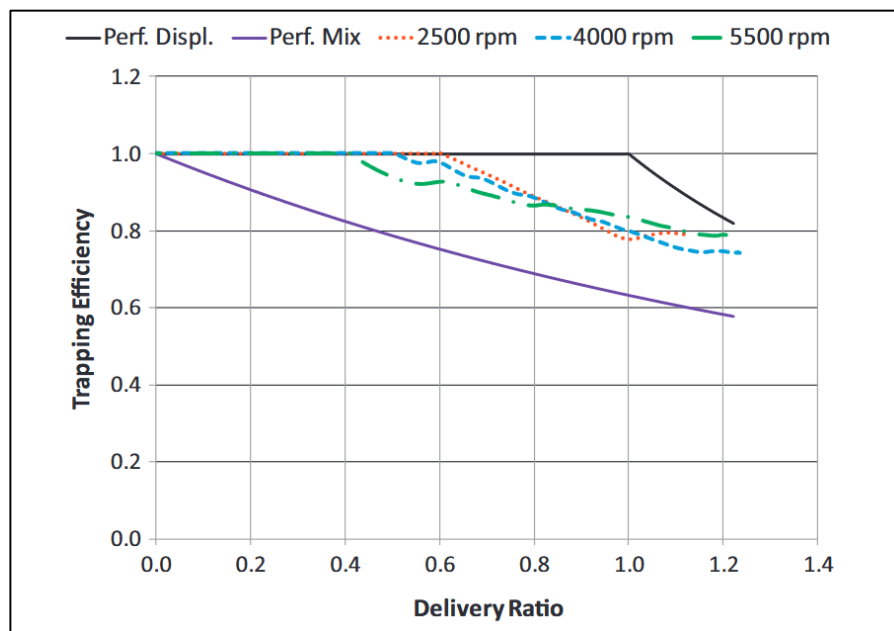


Figure 23 - Trapping Efficiency vs. Delivery Ratio for a Loop-Scavenged GDI Two-Stroke Engine at Different Engine Speeds [88]

This is the same work that was discussed in section 3.9.2, which is geared towards a range-extender application where an engine can be optimised to run at a specific speed. In Figure 23 it can be seen that

all plots fall in between perfect displacement and perfect mixing, and notably the trapping efficiency remains in the region of 80% at all engine speeds even at a delivery ratio of 1.0. Also, short circuiting does not begin to occur until the cylinder is roughly 40% to 60% scavenged (based on where the trapping efficiency departs the ideal line), though appears to occur earlier as rpm increases [88].

## 4.2 Measuring and Modelling Real Engine Flows

The loop-scavenged engine study discussed above highlights the power of simulation to model engine processes. Models of engine processes necessarily rely on assumptions, often based on empirical data. But as noted by Sher [30], to measure the *real* scavenging performance of an engine is challenging, although the author detailed numerous approaches that have been used to estimate it. These broadly fall into three categories: static model tests, dynamic model tests, and fired engine tests [30].

In a static model test, air is blown through a test-cylinder, but the piston(s) is not moved and instead locked at BDC (ODC in an OP2S engine). The primary objective of these experiments is usually to determine the path of scavenge air flow and how effectively that could be expected to scavenge the engine, and they have been used extensively in loop-scavenged engine research [30]. For example, Sher describes the Jante method of measuring the air currents in a two-stroke engine at the cylinder head interface (with the cylinder head removed) removed and then plotting them on a cross-sectional map. The ideal map suggested by Jante was one where the air currents rise sharply upward along the cylinder wall opposite to the exhaust ports, whilst remaining essentially stationary in the middle region between the intake and exhaust ports [30], [110]. Sher follows that Blair et-al., and Ishihara et-al. have subsequently improved the method: the former removing much of the laborious work involved through improvements to data recording, process and analysis, and the latter by extending it to consider all three vector components of the gas velocity at the cylinder head interface [30], [111], [112], [113], [114]. Another, particularly relevant result was noted by Heywood. Flow tests of a uniflow two-stroke diesel engine (with a poppet exhaust valve) were conducted, and the angle of the intake ports (and resulting air 'jets') was varied to give a range of swirling conditions. It was found that intake air jets directed towards a tangent radius of roughly half the cylinder diameter gave the best scavenging front profile over a variety of conditions [5]. Though the engine was not OP2S, the same challenges of ensuring adequate scavenging without excessive mixing of the fresh air and residual fractions exist in both OP2S and poppet-valve uniflow engines.

Dynamic model tests are similar in principle to static model tests, except that the influence of piston motion is included by way of driving the engine with external power such as an electric motor. Sher discusses that Sammons used a method of this type to investigate the scavenging process in loop-scavenged engines [30], [115]. Tests were performed at atmospheric temperature, and the conditions in

the cylinder and exhaust regions were simulated using an array of different gases at suitable pressures, to accurately represent the respective mixture densities. Then, the scavenging efficiency could be determined by measuring the specific density of the in-cylinder mixture after the engine was motored and thus scavenged [30], [115]. Sammons also used a transparent cylinder and light powder entrained in the air stream to visualise the in-cylinder motion, and concluded that increasing the air density and exhaust back-pressure resulted in better scavenging for the same volumetric scavenging rate [30], [115].

Fired engine tests are even more useful in that they help to facilitate the understanding of how different scavenging arrangements etc. impact the overall performance of *real* engine, and they do this by measuring the scavenging efficiency either directly or in-directly [30]. Sher uses the method proposed by Hori as an example of directly measuring the scavenging efficiency, wherein a sample is taken of the working fluid in the cylinder both before and after scavenging as the engine is running. Then, chemical analysis could be performed on the two mixtures to establish their CO<sub>2</sub> content. It was noted though that in taking the first sample, the in-cylinder conditions are altered sufficiently that it would be necessary to allow several following cycles to elapse before taking the post scavenging sample, to allow any adverse effects to dissipate [30], [116]. Another approach that Sher describes is the tracer gas method, as proposed by Schweitzer and Deluca in 1942 and which has subsequently been employed extensively in various studies [30], [117]. In the tracer gas method, a small quantity of a gas that does not readily react during scavenging conditions, but will subsequently react during combustion such that it is effectively consumed, is fed continuously into the scavenge air. It is then possible to evaluate the trapping efficiency of the engine by measuring the amount of tracer gas in the exhaust ports using chemical analysis [30], [117]. Schweitzer and Deluca used monomethylamine (CH<sub>3</sub>NH<sub>2</sub>) as the tracer gas, but others have subsequently used other gases including n-butane (C<sub>4</sub>H<sub>10</sub>) and carbon-monoxide (CO) [30].

#### 4.2.1 Early Scavenging Models

Measuring of real engine flows using methods such as those above has led to useful models for the scavenging process, as well as the much more complex engine simulations like those discussed in section 3.10. The simplest of these are the perfect mixing and perfect displacement models that were discussed earlier; Sher refers to these as ‘One-Phase Models’ and they rarely, if ever, reflect actual scavenging processes. Multi-zone models however are more accurate, since they aim to better reflect real processes typically by dividing the cylinder volume into (generally) two or three zones. In two-zone models such as that of Maekawa, the cylinder is divided into a fresh-charge zone and a mixing zone, whereas in three-zone models such as that of Benson the cylinder is divided into a fresh-charge zone, a mixing zone, and an exhaust zone [30], [118].

Benson’s model is particularly useful in loop and cross-scavenged engines. Heywood notes its intrinsic value lies in the fact that scavenging occurs in three distinct stages: first the fresh air pushes burnt gas out of the exhaust port. The incoming air jets begin to mix with the burnt gas at the boundaries between the two, creating a third ‘mixing’ zone. Then, a short-circuiting stage occurs where exclusively fresh charge is ejected through the exhaust, as the mixing zone grows. Finally, the mixing zone is sufficiently large that a mixture, of varying composition in time, is expelled through the exhaust. Based on Sher and Heywood, Figure 24 shows a diagram of the Benson 3-stage scavenging model [5], [30], [118]:

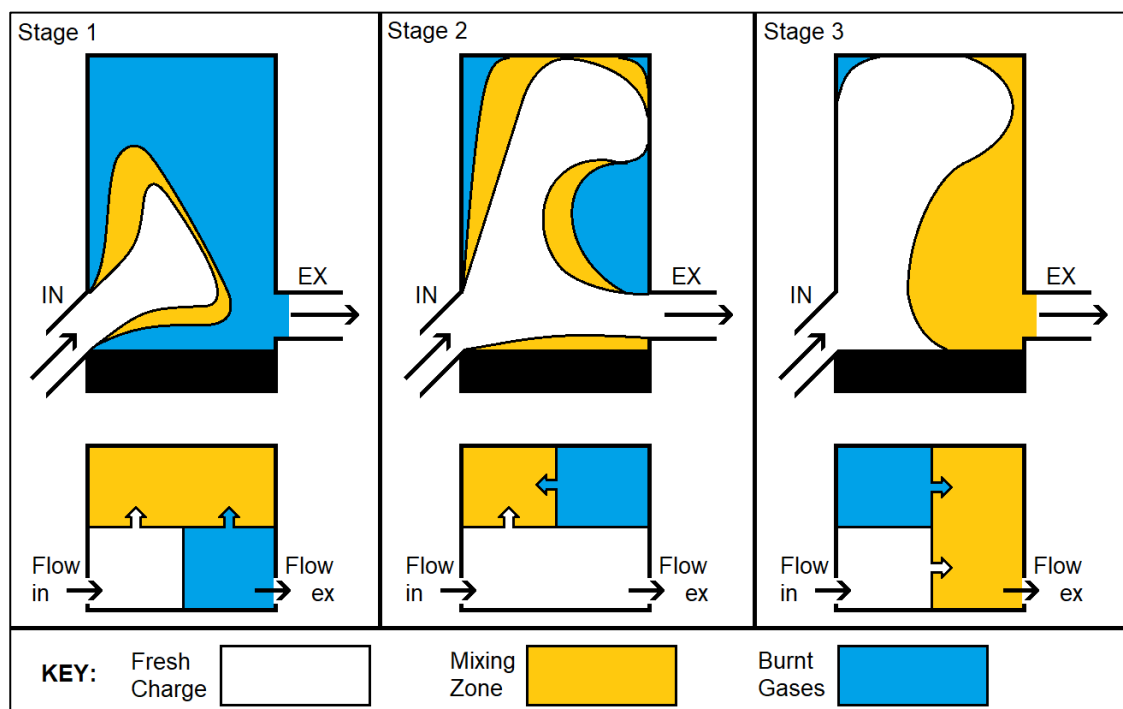


Figure 24 - Benson 3-Stage Scavenging Model

The piston is shown as a solid black rectangle at the base of the cylinder; the crown is in-line with the scavenge port. The square boxes underneath the cylinder and piston schematics indicate the flows across respective zone boundaries, scavenge flow (‘Flow in’) and exhaust flow (‘Flow ex’). The zones are coloured according to the key at the bottom of Figure 24.

### 4.3 Challenges of SI Operation in OP2S Engines

Despite limitations such as significant short-circuiting losses and elevated HC emissions (see section 4.1.3 for example) two-stroke SI engines have clearly proven very successful, and a great deal of understanding on their characteristics has been gained over time. This is largely limited to loop-scavenged examples however, and OP2S engines generally use uniflow scavenging, which can present difficulties to achieving stable SI combustion.

### 4.3.1 Lack of Tumble

The SI combustion process involves a turbulent, premixed flame which propagates through the combustion chamber of the engine [5]. For this to occur, the fuel and air charge must be adequately mixed, and there must be sufficient turbulent kinetic energy to enable rapid flame propagation; in most SI engines, specific in-cylinder flow motions have been long established as suitable for generating these conditions [5]. Tumble is one of the most important and is defined as a rotating motion about an axis orthogonal to that of the main cylinder axis (in other words, the rotation of tumble is orthogonal to that of swirl). Loop-scavenging a two-stroke SI engine is therefore a kind of ‘tumbling’ process, since the loop is usually orthogonal to the main cylinder axis. Heywood notes that in a pent-roof four-stroke engine, a tumbling motion is typically generated by the intake port geometry, aided by the piston which gradually ‘pulls’ the regime down the cylinder [5]. As the piston subsequently ascends and squashes the tumbling regime during compression, it becomes unstable and breaks up into smaller vortices, generating turbulent kinetic energy. This will significantly aid early flame development and combustion rates [5]. However, Figure 25 shows why a tumbling motion is unsuitable for an OP2S engine, in addition to an illustrative example of tumble in a four-stroke engine cylinder (reflecting Heywood [5]):

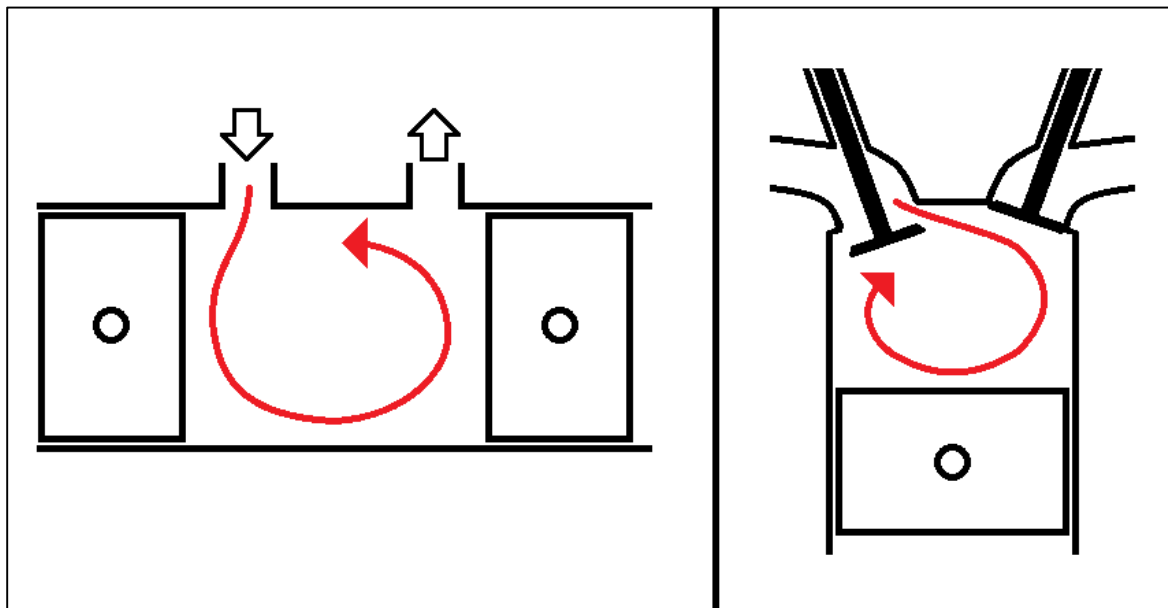


*Figure 25 - Illustrative Example of Tumbling Motion in OP2S Cylinder (Left) and Pent-Roof Four-Stroke Engine (Right)*

Because of the port locations at the extreme ends of the cylinder, the tumbling motion in an OP2S cylinder (SI or CI) would encourage mixing of the fresh and residual fractions during scavenging, significantly impacting the scavenging efficiency of the engine, hence why swirl is preferred [54]. Swirl can be advantageous in some cases: many CI engines employ it to aid early spray breakup (often coupled

with a bowl-in-piston), to improve early combustion rates [5]. In a CI OP2S engine, it is even possible to exploit the extra degree of freedom that two piston-crowns offer vs. a cylinder head, tailoring their geometry to optimise early combustion conditions. This is because the fuel is injected only slightly before SOC in a CI engine, and so can be directed in-between the two crowns, where combustion then begins; see for example [119].

### 4.3.2 Mixture Preparation and Combustion

The location of the fuel injector(s) in an OP2S engine is generally in the axial centre of the cylinder. In the CI OP2S engine, this location serves the need to inject the fuel between the two piston crowns around IDC. In an SI OP2S engine it is to prevent fuel-short circuiting; given that some short circuiting of fresh charge during scavenging will occur, port fuel injection would be inherently risky. However, the location of the injector in the cylinder wall increases the risk of spray impingement on the opposite side of the cylinder; Pirault and Flint note that this should not be a problem with modern injector systems [56], but at smaller cylinder diameters it may be significant [120]. Diametrically opposed injectors might help reduce this effect but considering the need for one (or two) spark plugs in addition, this may worsen packaging. Additionally, the uniflow-scavenging characteristic of the OP2S engine means that there is less time for fuel droplets to break up, disperse, evaporate and mix with the surrounding air: Heywood notes that in many production four-stroke GDI engines, fuel can be injected during the intake stroke, giving more time for mixing and thus producing an essentially homogenous mixture. Such strategies are often used at full-load operation. Alternatively, the fuel may be injected later during compression, to create a locally rich mixture around the spark plug but a lean condition overall. This will improve engine efficiency and is called stratified operation, and is typically used at part load [5].

Conversely in the SI OP2S engine, injecting fuel only after *both* EPC and IPC is the approach that most reduces the risk of fuel short-circuiting to the exhaust, or back-flowing into the intake. Fuel-mixture back-flow into the intake gallery of an OP2S engine is undesirable because it creates an opportunity for fuel short-circuiting to occur during subsequent engine scavenging cycles. Furthermore, with injection occurring only after IPC, the charge-cooling effect of the evaporating fuel droplets in an SI OP2S engine occurs only after air induction is completed, limiting the benefits of increasing charge density; this is not the case in four-stroke engines where fuel can be injected during the intake stroke [5].

Therefore, the mixture preparation process in a (gasoline) SI OP2S engine is clearly distinct from that in conventional GDI engines, since it must occur in a shorter timeframe (crank angle wise), features limitations in terms of injector location, and there is less tumbling motion to aid fuel mixing and early flame propagation - but potentially significant swirl. It could be argued that in the case of a small cylinder diameter and only one injector, it might be similar to an air/wall-guided process used in four-

stroke engines, so it is likely that the resulting mixture will be stratified and not homogenous, and there may be excessive cylinder wall wetting from spray impingement [5].

The combustion of the prepared mixture is then initiated via the spark plug, the location of which is also constrained to the outer edge of the combustion chamber in the axial centre of the cylinder (i.e. the cylinder wall). SOC therefore occurs at an extremity, and not between the two piston crowns like in a CI engine, and this results in a much a greater distance through which combustion must propagate than in a typical combustion chamber. To illustrate this, Figure 26 shows two hypothetical thin-cylindrical combustion chambers of equal height  $h$  and radius  $r$ . On the left is the chamber in an SI OP2S engine (formed between two flat piston crowns), and on the right is the chamber in a four-stroke engine (formed between the piston crown and cylinder head). The spark plug location is illustrated in both with a red silhouette.

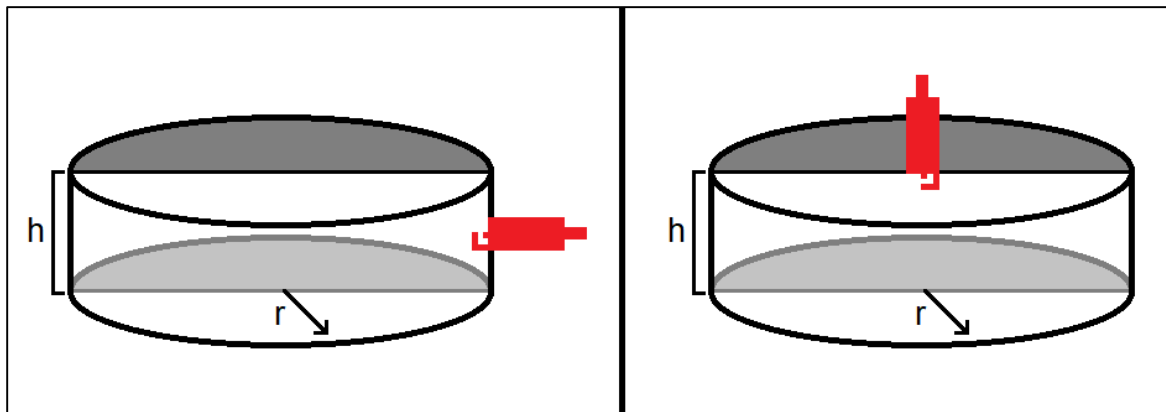


*Figure 26 - Comparison of Spark Plug Location on OP2S Cylinder (Left) and Four-Stroke Cylinder (Right)*

Following SOC, the flame front resulting from the spark plug in the OP2S combustion chamber in Figure 26 has to travel a distance of  $2*r$  to the other side, whereas it only has to travel approximately half of that in the four-stroke engine. In this instance a high degree of swirl may be useful, since it could be used to distort the flame front from its usual spherical shape such that it ‘wraps around’ the combustion chamber instead of progressing radially across it [5]. Another mitigating strategy would be to use two diametrically opposed spark plugs such that two separate flame fronts are initiated to speed up the combustion process. But as with dual injectors, the additional degree of complexity and packaging considerations associated with the additional spark plug would need to be considered.

This is not the only challenge posed by the SI OP2S combustion chamber. ‘Squish’ is another important engine characteristic, and it describes the radial motion of in-cylinder gases that are displaced by the geometry of the combustion chamber. During compression this is from a more confined to a more open region of the chamber [5]. Many four-stroke SI engines (including the pent-roof example) exploit this

characteristic to concentrate the flammable mixture in a region close to the spark plug, as well as the complex interactions between swirl, tumble, and squish to generate turbulent kinetic energy and thereby speed up early combustion rates [5]. In an SI OP2S cylinder this is more challenging to achieve, since due to a combination of the spark-plug location and the fact that the engine is piston-ported, it is difficult to ‘direct’ the mixture outwards towards the spark plug(s) before SOC. To illustrate this, Figure 27 shows a comparison between a wedge-shape SI engine combustion chamber (based on Heywood [5]), and four hypothetical variations of an SI OP2S combustion chamber. Three use a bowl-in-piston approach to squish, one uses a raised piston crown. In the OP2S examples, it is assumed that the clearance between the two piston crowns at IDC is of the same order as the clearance between the piston crown and cylinder head in the wedge-shaped combustion chamber. Note that injector position is not considered in these examples.

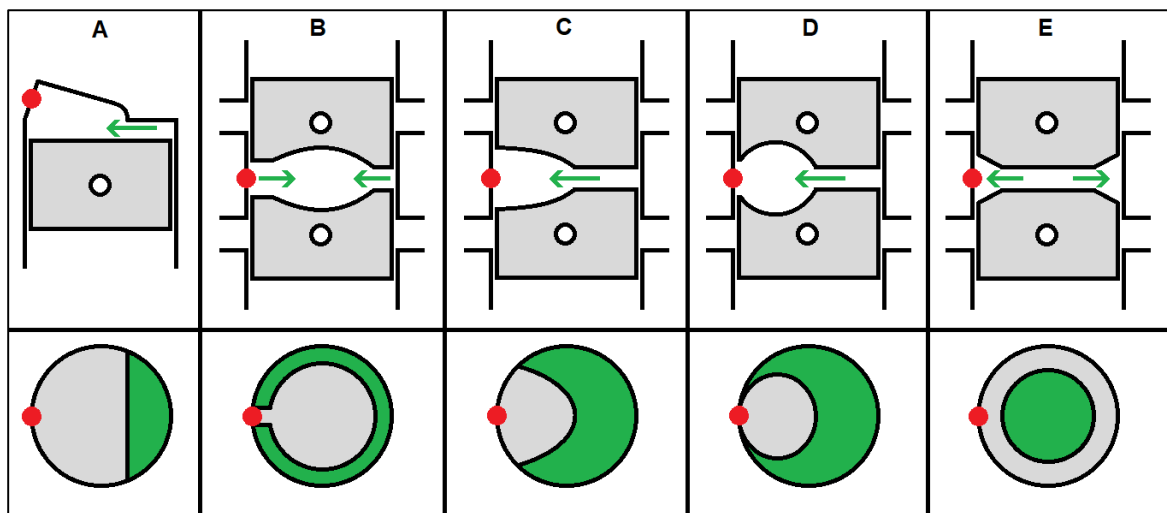


*Figure 27 – A: Squish in Wedge-Head Engine; B: OP2S Engine with Centralised Piston-Bowl; C: OP2S Engine with Piston-Bowl at Edge; D: OP2S Engine with Offset Piston Bowl; E: OP2S Engine with Raised Piston Crown*

The green parts of the piston crowns underneath the cylinder diagrams represent the ‘squish region’ (where gases flow from as the combustion chamber decreases in volume and in the direction of the green arrows) [5]. The approximate location of the spark plug is shown with a red circle. In A, as the piston ascends the mixture is displaced to the left by the flat part of the cylinder head and flat piston crown, into the larger wedge volume where the spark plug is located. In B, the bowls in the two OP2S pistons displace the mixture toward their centre – away from the spark plug (which is connected via a channel in the piston crown to its edge). In C, the offset bowls in the piston crowns displace the mixture toward the spark plug on the left, but they result in the piston crowns being lower on one side than the other. Thus, the ports on the left side of the cylinder will open earlier and close later than the ports on the right side. In D, the bowls are offset so also direct the mixture toward the spark plug. However, they result in a very thin piston wall close to the spark plug that may be susceptible to overheating,

particularly considering the doubled firing frequency over a four-stroke engine. In E, the raised piston crowns direct the mixture out towards the combustion chamber edge where the spark plug is located, but also into a wider ‘ring’ around the combustion chamber, which may increase heat loss to coolant. Also, such raised piston crowns might increase the compression ratio to the extent that pre-ignition becomes more likely. Many other bowl geometries could (in theory) be adopted in SI OP2S pistons, but the examples given highlight that the location of the spark plug at the extremity of the combustion chamber still presents a disadvantage in comparison to a conventional engine.

#### **4.4 Summary Comments and an Opportunity for a Significant Research Contribution**

Fuels such as hydrogen, which is of increasing interest due to its potential as an energy carrier and means to store excess renewable electricity, are very well suited to SI operation. SI combustion is technically simple and highly controllable, but it typically results in lower thermal efficiencies compared to CI. This is largely due to the lower compression ratios often used, but the fundamental thermodynamic advantages that OP2S engines have over conventional engines might be able to mitigate this to a degree.

However, SI in OP2S engines faces challenges, such as the large distance from one side of the combustion chamber to the other – particularly in the light of modern emissions standards. Modern four-stroke SI engines are also far more technically sophisticated than they were even at the turn of the millennium, routinely featuring direct injection, alternative engine cycles, and so on. Examining how well a modern SI OP2S engine could compare, and investigate questions like whether gaseous fuel injection is able to overcome difficulties with mixture formation for example, would benefit from empirical data (such as from a cylinder pressure transducer). But, to get such data requires the correct apparatus including, arguably, an SI OP2S engine – one that benefits from many of the same technological advancements of recent years. Unfortunately, real, working, modern SI OP2S engines appear very rare, and of the limited number that do exist, several risk deviating from the well-proven crank-slider.

Designing, building, and test-firing a *modern* SI OP2S engine that is dedicated to the task of engine research would address this rarity and enable the collection of important data, representing a significant contribution to the field. That is the aim of this research project.

## **5. Engine Design and Construction**

In this chapter, the design and construction of a novel prototype SI-OP2S engine is presented, representing the vast majority of the work undertaken. It begins with reviewing the requirements of the engine identified in chapter 2, and constrains important engine parameters (such as bore and stroke) on which the rest of the engine design is then based. Selected drawings and pictures of real components are used to detail how the engine is intended to work, as well as the rationale behind its design. However, appendices are used to avoid excessive length: Appendix A can be consulted for detailed engineering drawings of many of the components designed, as well as the necessary modifications to some of the commercial parts where machining was required (such as enlarging bored holes etc.). Appendix B contains further details of some of the manufacturing and engine assembly processes.

### **5.1 Starting Point**

Several engine requirements were identified as important, in Chapter 2, and these were:

- The engine must be blower-scavenged to retain decoupled pumping work, and ‘self-sustaining’ such that it does not require external mechanical or electrical power to function beyond the typical 12-volt apparatus such as ignition coil and water pump.
- The oil side of the engine needed to be separate from the combustion side, and the fuel needed to be injected directly into the cylinder of the engine to minimise fuel short-circuiting.
- The engine needed to be of a suitable size and design so as to be reasonably manufacturable and transportable, as well as easy to disassemble and maintain by trained personnel.
- It also needs to be able to feature data acquisition apparatus such as a cylinder pressure sensor, and couple up to a load for testing.

These attributes are all reflected in the final prototype at the end of this chapter.

#### **5.1.1 Basic Engine Parameters**

OP2S engines are relatively unique in requiring the synchronisation of the movement of two pistons in each cylinder, and how this would be approached served as a useful grounding for the rest of the engine design. Historic examples have used various different methods to do this (see section 3.3.2), however the multiple crankshaft approach has proven itself to be very successful, as evidenced by the continued successes of Achatés Power (e.g. [92], [121]). Also, because each piston has a separate crankshaft, in a single cylinder engine each crank-slider mechanism can be similar to that seen in a conventional four-

stroke engine. This is because timing is handled by the linkage between the two crankshafts and not each crankshaft itself, so raising the possibility that ‘off-the-shelf’ crankshafts could be used as a basis for an engine design. In an earlier, unpublished undergraduate project by the author, this was exactly the approach chosen through the use of two crankshafts intended for 50 cm<sup>3</sup> Chinese motorcycle engines [122], [123]. The prototype engine in this earlier project, which was never run or tested, did in retrospect have many shortcomings. It was air cooled but with limited area for airflow, featured very small main inlet/exhaust porting, and used the large, square cylinder block to hold together two engine plates on which the crankshafts were supported. It also featured extensive use of filament 3D printing for the manufacture of parts (including a crude ‘blower’). A photo of this prototype is shown below in Figure 28.

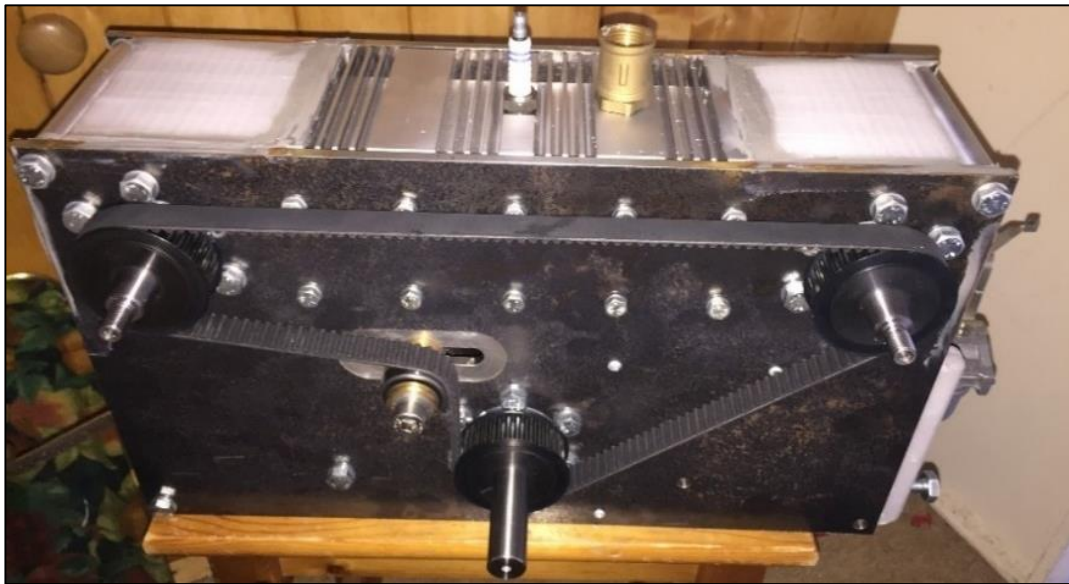


*Figure 28 - Prototype Engine from Undergraduate Project; Engine Width approximately 423 mm*

The brass fitting next to the spark plug was intended as the exhaust port for the engine and was of a size commonly associated with household copper plumbing [122]. Though it never worked, this engine did provide several important takeaways for the new prototype. Key among these was the use of the same type of off-the-shelf crankshafts, since they feature rolling element bearings and are pressed together. Figure 29 shows one of the crankshafts for the new engine. The side of the crankshaft with the woodruff key and timing sprocket is the one used for the timing train of the engine, although the timing sprocket and woodruff key are removed as they are not required. The bearings that support the crankshafts are ball bearings of the 6304 size. By using off-the-shelf components, they avoid the need to produce what are quite complex parts to high tolerances, as well as define the stroke of each piston from which the new design could evolve [123].



*Figure 29 - One of the Crankshafts for the Engine*

It should be noted however that the stroke of the engine, as defined by the throw of the crankshafts, is the greater of two identified, possible values: 41.4 mm, and 41.5 mm. This is because different specifications for the stroke and cubic capacity of the engine for which they were originally intended (TD50Q family) had been found, and these were inconsistent. Also, accurately measuring the throw of the crankshafts by using a lathe for example, would be prohibitively difficult without dismantling (and potentially damaging them). Comprehensive specifications were found via an extensive online database, where the noted 49.6 ccm cubic capacity of the TD50Q correlated closely with the bore and stroke given of 39 mm, and 41.5 mm, respectively [124]. By contrast, a 39 mm bore and 41.4 mm stroke at [125] does not correlate with a 49 cm<sup>3</sup> displacement. Thus, though marginal in difference, 41.5 mm was used for the design basis to avoid potentially catastrophic failures, such as piston crown collision with the spark plug, or piston overrun from the liner that could release the oil control rings. This is because the running zone of a 41.4 mm piston stroke will fit inside that of a 41.5 mm piston stroke, but the same could not be said if the situation were reversed.

Since piston rings for the same motorcycle engine that these crankshafts traditionally suit were also readily available these too were used, and as such, the bore and stroke in millimetres of the engine were defined. The same as in the earlier prototype, these are listed in Table 1:

*Table 1 - Engine Bore and Piston Stroke*

<b>Characteristic Dimension</b>	<b>Dimension Size</b>
Cylinder Bore	39 mm
Piston Stroke	(2x) 41.5 mm

Because the engine has two pistons the combined stroke of both is 83 mm, however the maximum volume between the two piston crowns, as well as the minimum trapped volume, depends on the phasing between the two crankshafts in combination with the cylinder porting and piston geometry. This why the stroke is listed as (2x) 41.5 mm. With the crankshaft phase difference set at 18 CAD, the trapped volume of the new engine is approximately 79 cm<sup>3</sup>, the maximum volume approximately 110 cm<sup>3</sup>, and the minimum volume approximately 13 cm<sup>3</sup> (based on results from 3D CFD simulations; see chapter 6.

### 5.1.2 Engine Synchronisation

In larger, multiple crankshaft OP2S engines, gears are generally favoured for synchronisation (see for example [65]). However, metal gears require lubrication, which would involve enclosing them either inside the main engine cases (potentially making the cases larger and more expensive) or an additional timing case on the back of the engine. A timing belt system on the other hand does not require lubrication, but a rubber timing belt is not capable of transmitting the same loads that steel gears are. This is why a smaller-displacement engine was designed, because it will result in lower mechanical loads that the engine synchronisation system must withstand. Hence, a timing belt system with an 8 mm pitch belt (see [126]) was designed. Figure 30 shows a mock-up of the belt profile to indicate the path of the belt round all three timing belt pulleys. This photo shows the timing pulleys as they were in their originally manufactured, off the shelf condition: they are 8 mm pitch, 48 tooth pulleys (see [127]).

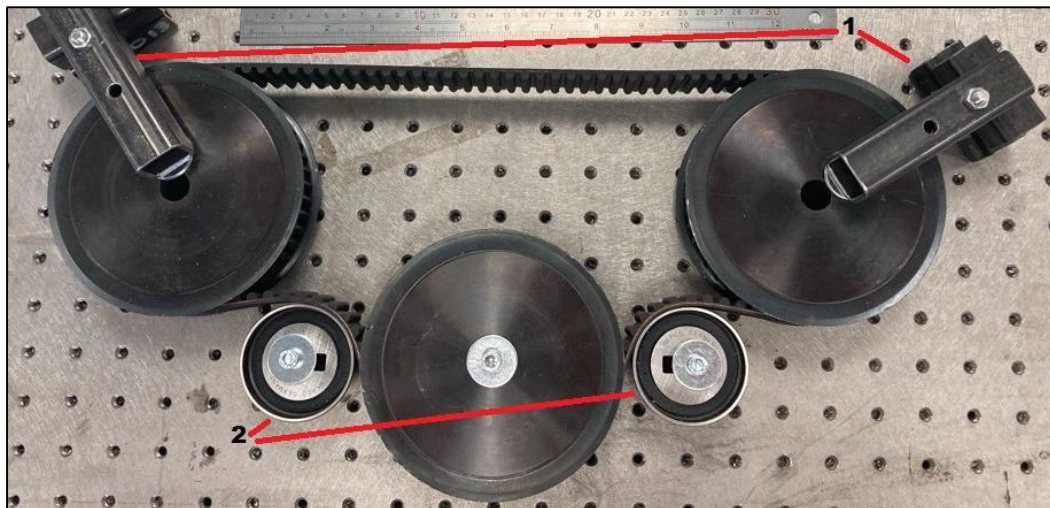


*Figure 30 – Mock-up of the Belt Profile*

Label 1 in Figure 30 indicates the position of two clamps that are holding the crank timing pulleys in place (the output shaft timing pulley is on the bottom). Label 2 identifies the two belt tensioners, which are typical automotive parts; see for example [128]. Two of the pulleys would later be machined to

accommodate RINGFEDER® RfN 7004 locking assemblies, each of which is capable of transmitting in excess of 500 Nm of torque; Table 2 gives important specifications of the size used [129].

*Table 2 - Specifications of RINGFEDER® RfN 7004 Locking Assembly, 19 mm x 47 mm*

Specification	Value
Diameter (Inner x Outer)	19 mm x 47 mm
Overall Length	45 mm
Length Without Screws	39 mm
Ring Width (Clamping Length)	26 mm
Transmissible Torque (at TA)	530 Nm
Axial Load Capability (at TA)	56 kN
Pressure on Hub Surface (at TA)	120 N/mm <sup>2</sup>
Pressure on Shaft Surface (at TA)	298 N/mm <sup>2</sup>
Tightening Torque TA	17 Nm

The engine features a large (211 mm diameter excluding ring gear) flywheel so as to help mitigate any unexpected transient conditions [130]. This is machined from solid steel bar for strength and is sized to fit the ring gear that is of the type used on small industrial diesel engines; see for example [131]. Figure 31 shows a drawing view of the flywheel:

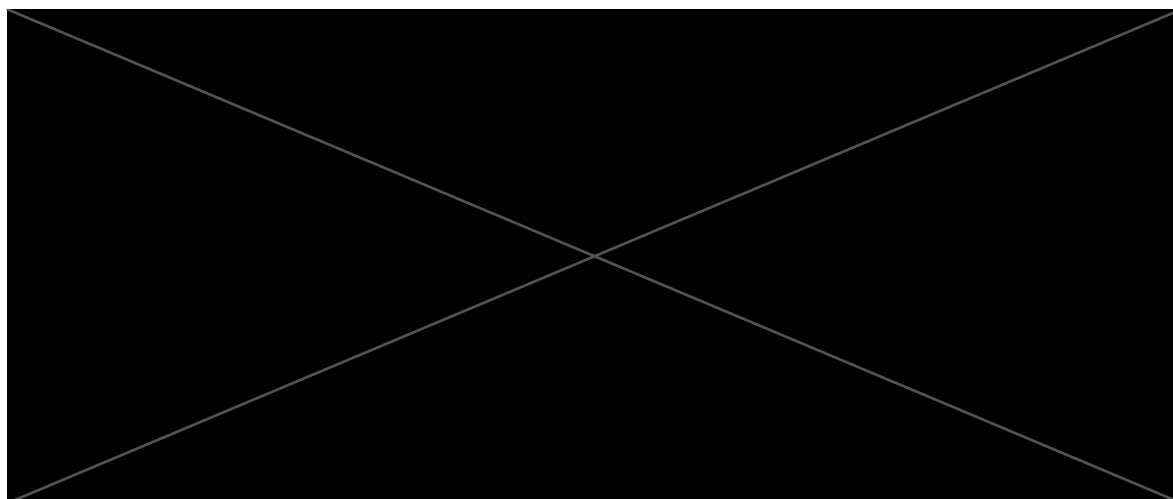


*Figure 31 - Details of the Flywheel Body*

Appendix B contains photographs including part of the machining process of the timing pulley for the flywheel, as well as the assembled flywheel. The 47 mm recess in the flywheel body is for the locking assembly, fastening it to the output shaft. It is noted that by using taper-locking bushes, the timing of the engine can easily be adjusted, and because they are used in combination with a toothed belt, it is not

necessary to dismantle significant amounts of the engine to do so. However, the timing belt is not designed to run in the open: it must be surrounded by a metal shield to contain it in the event of failure (see chapter 7 where this is apparent). Whether or not the use of a timing belt will result in an overall system that is prone to failure could only be known once the engine had been tested, but the literature review supports it in principle: two examples of OP2S engine architectures were identified which succeeded in using a timing belt to link the two crankshafts together [94], [95]. These engines were both of relatively small displacement, though neither as small as this prototype. It should be emphasised however that even if the crankshafts lose timing with respect to one another, the engine is designed such that there is sufficient distance between both piston crowns (as well as other components in the cylinder) to avoid mechanical damage.

## 5.2 Pistons, Cylinder Block and Cylinder Liner

The pistons were made by reusing those from the earlier engine, and the piston rings remained in their original positions that were intended to ensure that the oil rings never cross over the intake/exhaust ports in the liner, whilst allowing a small amount of running zone overlap to the compression ring(s) [122]. They were modified in other ways however, and Figure 32 shows them after modification for the new prototype:



*Figure 32 - Completed Pistons for the New Prototype*

Circlips are used to retain the piston pins (previously the threaded holes in the bottom of the pistons were for grub screws to lock the pins, but these are no longer being used [122]). The chamfered crowns are new and are designed to increase port open time as well as decrease the size of the top ring land. Here also the hollowed-out underside of the pistons can be seen - this is to reduce the reciprocating mass of the pistons even though simplistically, and not accounting for any phase difference between each piston, the reciprocating motion of one piston will largely balance out that of the other piston. However, it is noted that the increased piston mass (over those that the mass-produced crankshafts were

designed to work with originally) will increase the forces in each crank slider. For further information, Heywood provides a thorough explanation of the mechanics of crank slider mechanisms in [5]. A reference drawing for the location of the piston rings is provided in Appendix A. Note that the finished pistons exhibit changes (including the circlip grooves and material removal from the underside) that are not shown in the drawing – these were at the discretion of the machinist.

Another aspect that is shared with the earlier prototype is the use of a horizontal cylinder. The reason for this is to prevent oil pooling on the underside of one of the piston crowns once the engine has stopped. However, the new cylinder block is liquid cooled and differs substantially from the earlier air-cooled design. For example, rather than serving as the core strength of the engine assembly, it is now retained inside two engine cases which form the main structure of the engine. It is made from aluminium bar stock, and the cylinder liner (made of cast iron bar stock) is located inside of it. Figure 33 shows the cylinder block and cylinder liner; intake side is to the left. Due to time constraints, they were outsourced and machined by Kenworth Engineering (see [132]), and are shown before the final machining operations to add the injector, spark plug, and pressure transducer seat were carried out in house at the University of East Anglia (which are discussed in Appendix B). The geometry of the cylinder block accommodates some very minor changes to the central upstand where it meets the round surface, made upon suggestion of Kenworth Engineering to ease the machining process. For detailed engineering drawings of the cylinder block and liner, please see the relevant part of Appendix A.



*Figure 33 - Cylinder Block and Liner*

Figure 34 shows a cutaway of the cylinder liner in position in the cylinder block, as rendered in computer-aided-design software [133], which shows how they fit together:

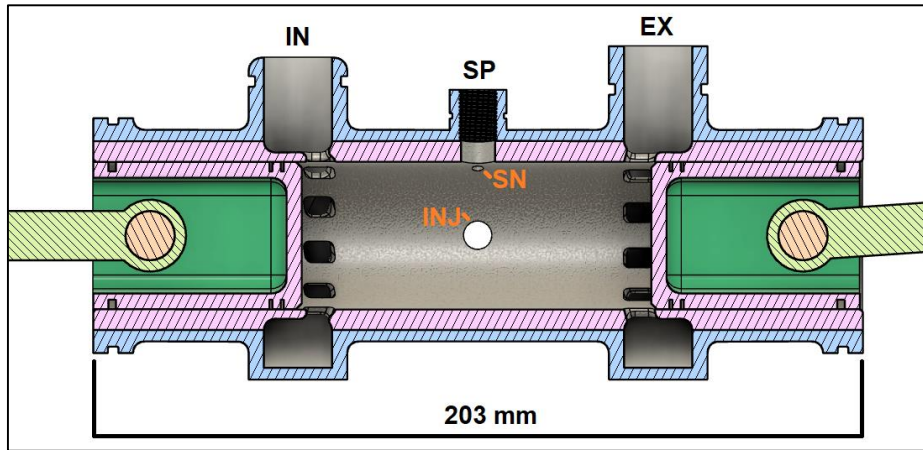


Figure 34 - Cylinder Block and Liner Cutaway with Component Locations; IN = Intake, EX = Exhaust, SP = Spark Plug, SN = Sensor, INJ = Injector

Here, it is prudent to discuss some of the characteristics of the design. Firstly, in Figure 34 the exhaust piston (to the right) is shown leading the intake piston – this represents the 18 CAD difference described above. Of note is the square cross section of the outer edges of the intake and exhaust galleries – like the earlier prototype this design was intended to make it easier to machine in a manual lathe using an internal grooving tool, see for example [134]. The pistons and connecting rods are simplified versions of the real components. The ends of the cylinder block are rounded squares, and these are designed to locate into the matching recesses in the engine cases. The upstands for the intake, exhaust, spark plug and injector(s) are similarly designed, and all are of very high tolerance. Figure 35 shows a drawing view of the cylinder block, in which this can be seen:

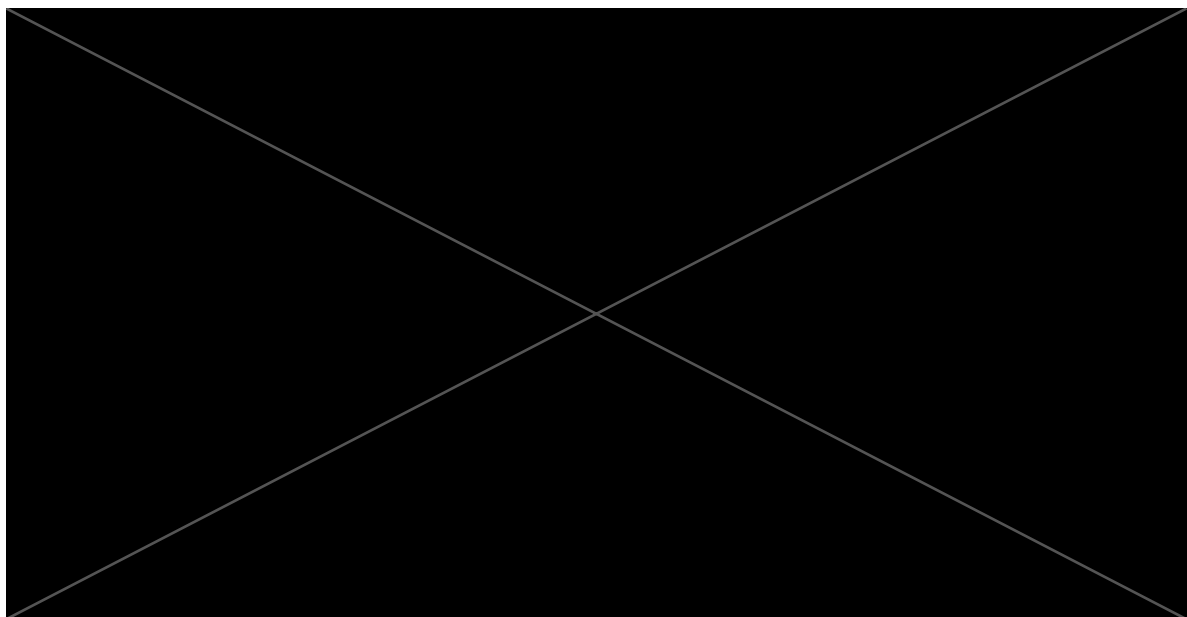


Figure 35 - Cylinder Block Drawing View

Here, it is to be noted that many of the dimensions are referenced from the same datum. The reason for this is explained in Figure 36, which is like a much-simplified version of a ‘worst-case scenario’ tolerance analysis; see for example [135] for further information. The top example in Figure 36 shows how positions A, B and C have their tolerances expressed in a similar way as those for upstands on the cylinder block in Figure 35. Because all are referenced from the same datum, the maximum error at point A, B, or C is  $\pm x$ , as shown. However, the bottom shows how the errors can add up if position B is referenced to position A, and position C to position B. At position C, the maximum error from the datum also includes the errors at B and A – so a total of  $\pm 3x$ . Although the tolerances are tight, if  $x$  is 0.04 mm as it is in the location of the upstands from the datum, this would add up to  $\pm 0.12$  mm, and would risk the cylinder block not fitting at all, or being so loose in the engine cases that the O-rings do not seal.

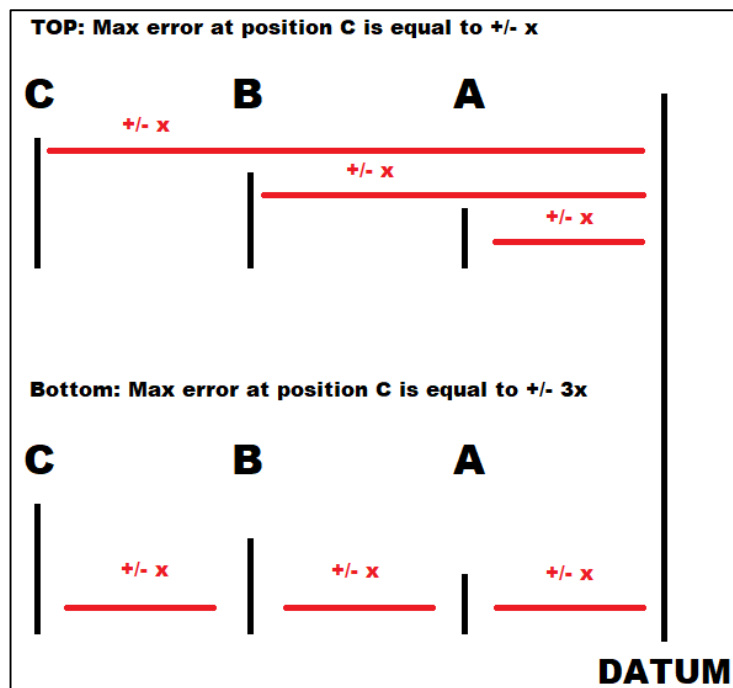


Figure 36 - Simple Example of Worst-Case Scenario Tolerance Stack Up

Figure 37 shows another simplified example of the careful consideration involved in specifying tolerances. It applies in cases such as the corner radii of some of the features on the cylinder block, and the matching recesses into which they fit in the engine cases. The green line represents the maximum tolerance for the recess (the engine case), the blue line is the maximum tolerance position for the insert (the cylinder block), and the black line the nominal position of both. Note that this diagram does not consider the tolerances of the straight edges which are assumed as fixed. The green and blue coloured arrows show the direction in which the tolerance lines move with respect to the nominal line as they increase to the maximum.

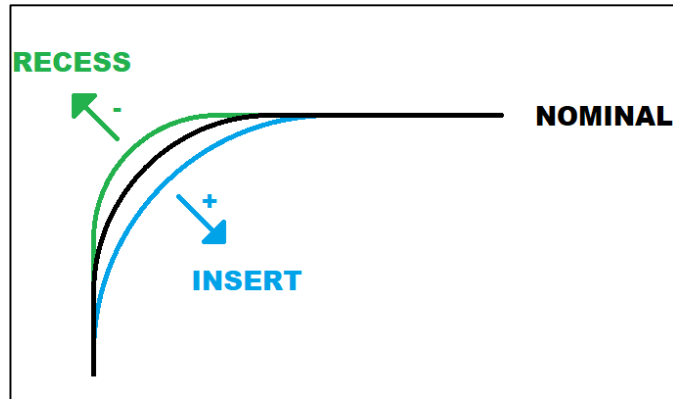


Figure 37 – Simple Example of Corner Radius Tolerances

In other words, an increase in the tolerance of the recess decreases its radius and it moves away, and an increase in the tolerance of the insert increases its radius, and it too moves away. What this means is that with this configuration of tolerance, the insert should not be able to foul on the recess. In practise, as can be reviewed in the engineering drawings in Appendix A, not all of the radii of components had their tolerances expressed in *exactly* this way, but the result was the same nevertheless.

The cylinder liner was designed to be a tight ‘slip fit’ in the cylinder block and be locked in place using retaining compound. The reasons for using a slip fit as opposed to a transition or interference fit are two-fold. Firstly, the cross section of the liner at the intake/exhaust port locations is thinner which is likely to reduce its strength, and the presence of the galleries in the cylinder block have a similar effect on it. A slip fit therefore removes any risks of mechanical damage to either the liner or block that might otherwise occur were the two pressed together. The second reason for using retaining compound was to allow easier ‘clocking’ of the liner once it is inserted, such that the ports are at a suitable angle, before the retaining compound cures. Were they pressed together, they would need to be lined up beforehand and great care taken to ensure they did not rotate out of position during assembly. Clocking the liner in the correct orientation was important to ensure that in line with the centre of the piston pins, there is always cylinder liner material: the piston compression rings are pinned in this same orientation so that they cannot rotate. With this configuration therefore, the gaps in the piston rings do not align with a port hole, preventing mechanical damage (for example if the edge of a ring caught on a porthole). The same was true of the earlier prototype, despite the differences in liner and block design [122].

### 5.2.1 Liner Porting

The intake ports of the new cylinder liner feature a swirl-inducing geometry, which was achieved by way of radially offsetting the central port axis from the cylinder centreline by 10 mm. Figure 38 shows a drawing view for the cylinder liner of the engine:

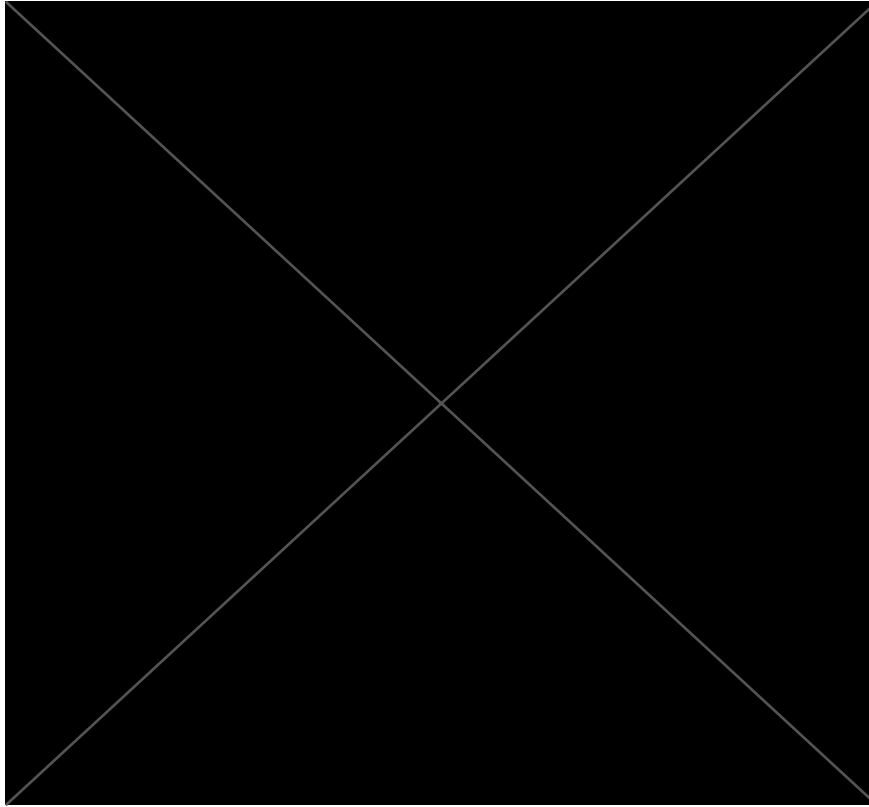


*Figure 38 - Inlet Port Pattern*

The tangent radius of the ports is slightly over half that of the liner itself; the literature suggests this should provide a reasonable scavenging front profile over most conditions [5] (see section 4.2). These ports also point slightly inwards towards the axial centre of the cylinder by 15 degrees, so where they intersect the inner liner surface their shape is stretched between opposite corners. This has the effect of increasing the intake port height such that the actual phase difference (i.e., between EPO and IPO) is approximately 15 CAD, even though the crankshaft phasing is 18 CAD. This can be seen more clearly later in section 6.1.1, but is evidenced by the size of the openings of the main intake and exhaust ports in Figure 33, and the shape of the ports in Figure 34.

In addition, a spiral-like shape is used for the intake gallery by way of the gallery intake being offset. The objective of these features is to aid fuel mixing, as well as to mitigate against the large flame propagation distance from one side of the combustion chamber to the other. Conversely, the exhaust gallery outlet extends the full width of the gallery, and whilst the exhaust liner ports point inwards towards the axial centre of the cylinder by approximately 15 degrees like the intake liner ports, they are not radially offset from the cylinder centreline. They also feature a slightly larger nominal width of 5.5 mm as opposed to 5 mm for the intake ports. The resulting increase in available cross sectional flow area through which (and the resulting volume into which) the exhaust gases initially flow is intended to account for the increased volume of the burned mixture leaving the cylinder over the cooler intake air

entering. The port holes themselves were designed to be 'cut' into the liner by projecting profiles along their main port axes. This is best indicated in the engineering drawings in Appendix A, however Figure 39 details the two profiles that are projected:

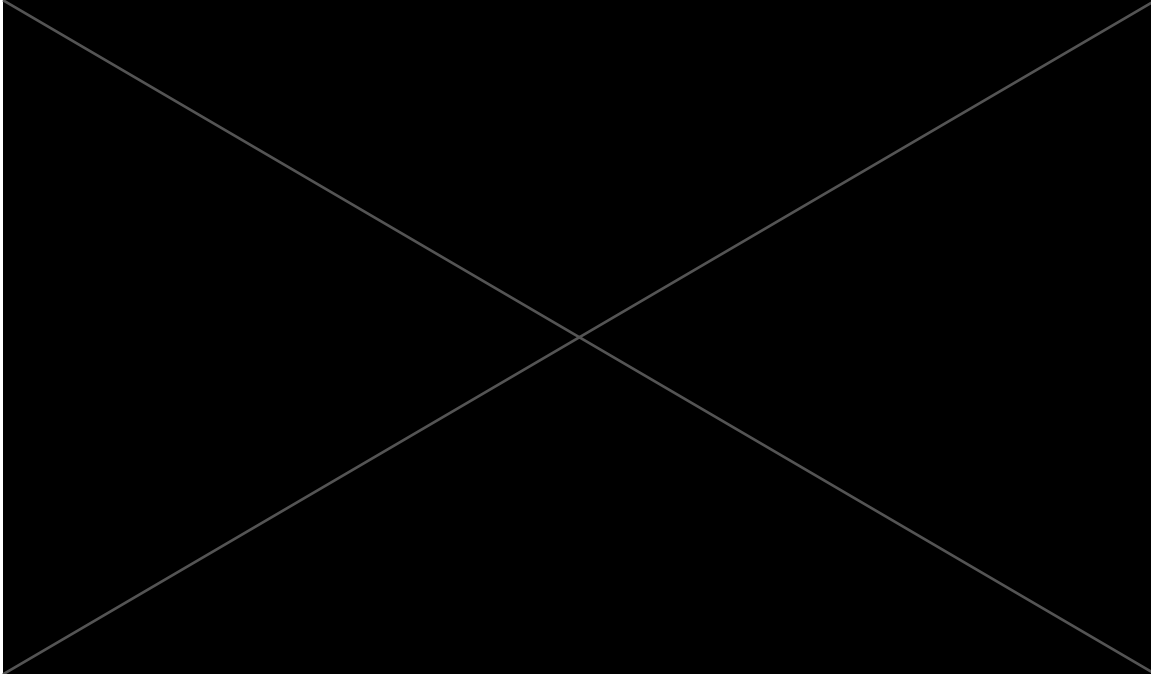


*Figure 39 - Intake and Exhaust Port Profiles, Projected Along Port Central Axes; Dimensions in mm*

The heights of both port profiles that are projected is less than 8 mm. But, because the axes along which these are projected is tilted inwards towards the axial centre of the cylinder by 15 degrees, these profiles cross the inner surface of the liner at an angle. This has the effect that the resulting (nominal) height of the portholes on the inner liner surface is then approximately 8 mm.

### **5.2.2 Injector, Spark Plug and Cylinder Pressure Transducer**

The machining of the seats for the injector, spark plug, and cylinder pressure transducer could be undertaken only once the cylinder liner had been inserted into the cylinder block, so as to ensure the perfect alignment of through-holes, component seats, threads, and so on. Figure 40 shows the kind of fuel injector used in the engine, Bosch type 0-261-500-01A. This injector is a commercially manufactured automotive injector, and features a flow-rate of 1050 cm<sup>3</sup> per minute at a supply pressure of 100 bar [136].

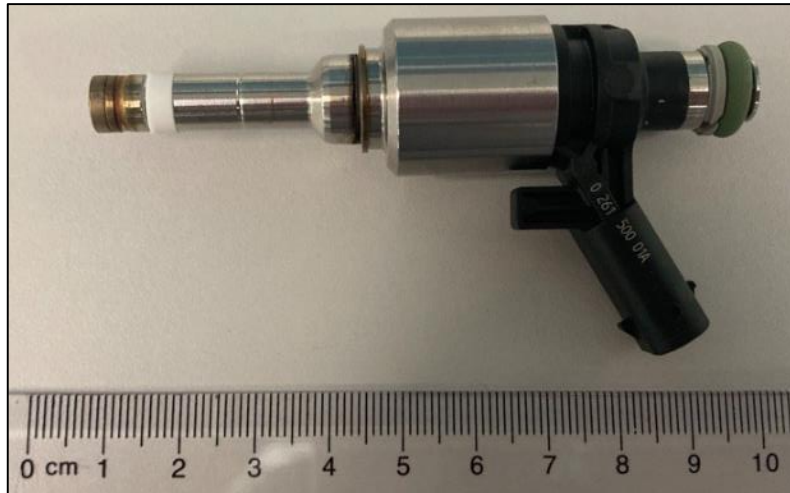


*Figure 40 - Bosch Fuel Injector*

The spray pattern was not able to be obtained, but the injector was chosen due to its availability as well as the fact that it has multiple spray nozzles, a total of 6, which should increase fuel dispersion. The injector is located in the axial centre of the cylinder, i.e. the same region as the spark plug, as is a cylinder pressure transducer. The latter was included to enable the collection of real-time in-cylinder pressure measurements, that could be useful for future research like combustion analysis – recall that the prototype is intended for engine research and not mass production. A Kistler type 6054C-3-2 pressure transducer (see [137]) was chosen – this sensor is very small at only 5mm wide, and is shown next to a 5 pence coin for scale in Figure 41.



*Figure 41 - Kistler 6054 Pressure Transducer*

To site the transducer, the middle ‘upstand’ of the cylinder block was made wider than would be necessary for a spark plug alone. This was easier than including a separate upstand for transducer and still meant that it could point directly towards the radial centre of the cylinder. Figure 42 shows a cross

section located in the middle of the central upstand of the cylinder block and cylinder liner assembly, looking towards the exhaust ports (for the full engineering drawings see Appendix A), detailing the seat for the injector and pressure transducer. Here the liner is shown in position.

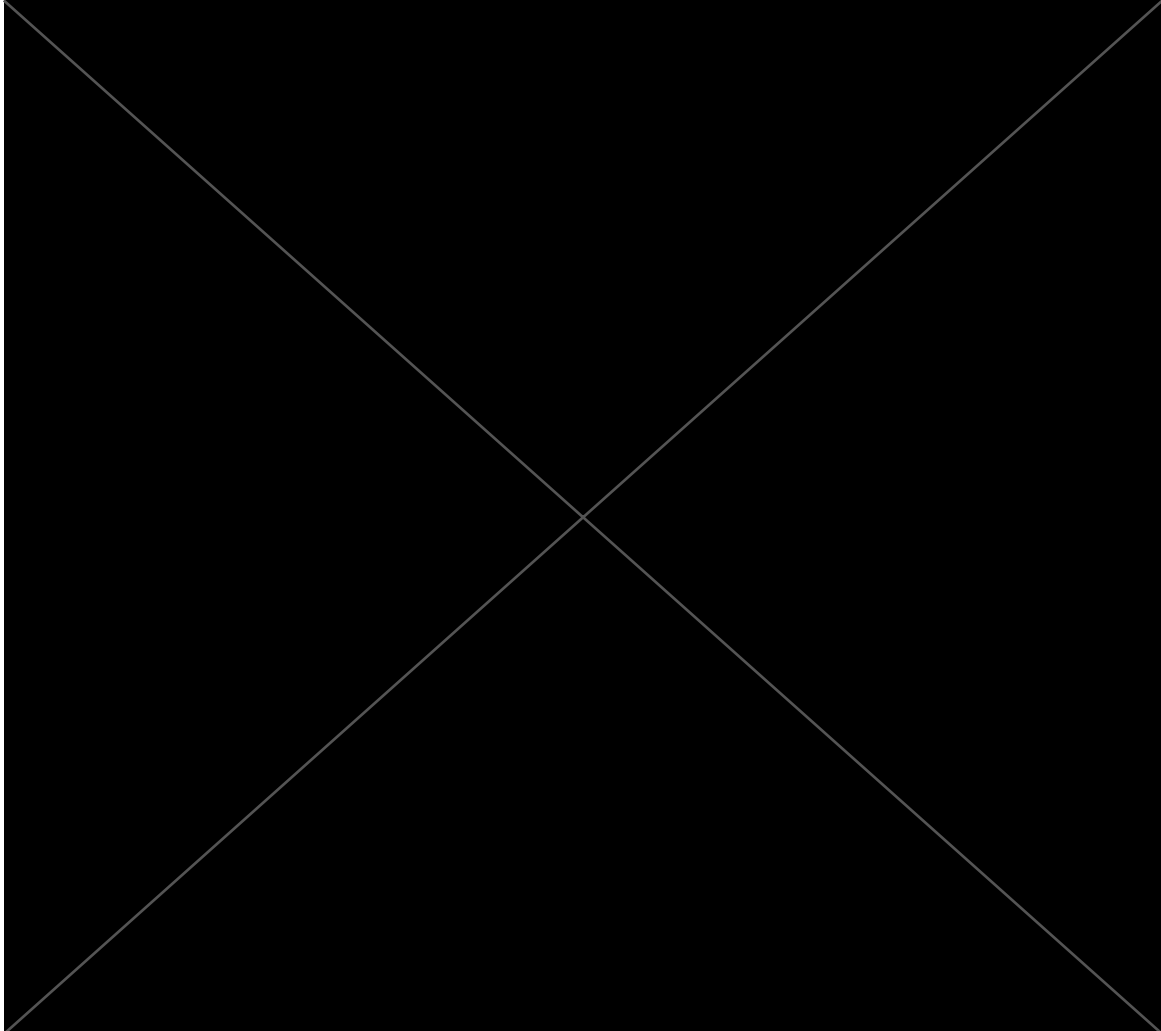


*Figure 42 - Cross Section at Central Upstand of Cylinder Block and Cylinder Liner Assembly;  
Dimensions in degrees and mm*

The injector port is located to the left, the spark plug port is in the central top, and the transducer seat shown at a 25-degree angle to the latter; note the spark plug threads are not shown. The injector seat incorporates a tapered opening, against which the body of the injector seals – its depth is intended to be adjusted so that the nose of the injector is just visible in the cylinder.

The seat for the pressure transducer is designed to meet the requirements specified in Kistler documentation, specifically for the case of a sealing face that is located in a cast-iron material; for convenience, important specifications of the 6054C in general are reproduced in Table 3 [138]:

Table 3 - Kistler 6054C Sensor Specifications

Item	Unit	Value
Measuring range	bar	0...300
Calibrated ranges (23°C, 200°C, 350°C)	bar	0...100, 0...150, 0...200, 0...300
Overload	bar	350
Sensitivity (at 23°C)	pC/bar	-17
Natural frequency (measuring element)	kHz	Approx. 185
Linearity (at 23°C)	%FSO	±0.3
Tightening torque, greased	N·m	1.5
Shock resistance (half sinus 0.2 ms)	g	>= 2 000
Acceleration Sensitivity		
Axial	mbar/g	0.8
Radial	mbar/g	0.2
Sensitivity shift 23°C ... 350°C	%	± 0.75
Sensitivity shift 200 ± 50°C	%	± 0.25
Operating temperature range	°C	-20 ... 350
Temperature, min./max.	°C	-40 ... 400
Thermal shock error (at 1,500 1/min, IMEP = 9 bar)		
Δp (short-term drift)	bar	±0.25
ΔIMEP	%	±1.5
Δpmax	%	±1.0
Insulation resistance (at 23°C)	Ω	≥ 10 <sup>13</sup>
Capacitance sensor	pF	8
Connector, sapphire insulator		M3x0.35
Protection rating, with cable Type 7 (IEC 60529)	IP	65
Weight sensor	g	1.5

Figure 43 shows a view inside the cylinder, where the injector orifice, pressure transducer connecting tube and spark plug thread are visible in the same orientation as they are in Figure 42. Here, the view is from the intake end of the cylinder and a piston has been loosely inserted in the exhaust end, showing the light pattern that is produced by the exhaust ports; the intake ports are visible in the foreground but are slightly blurry.

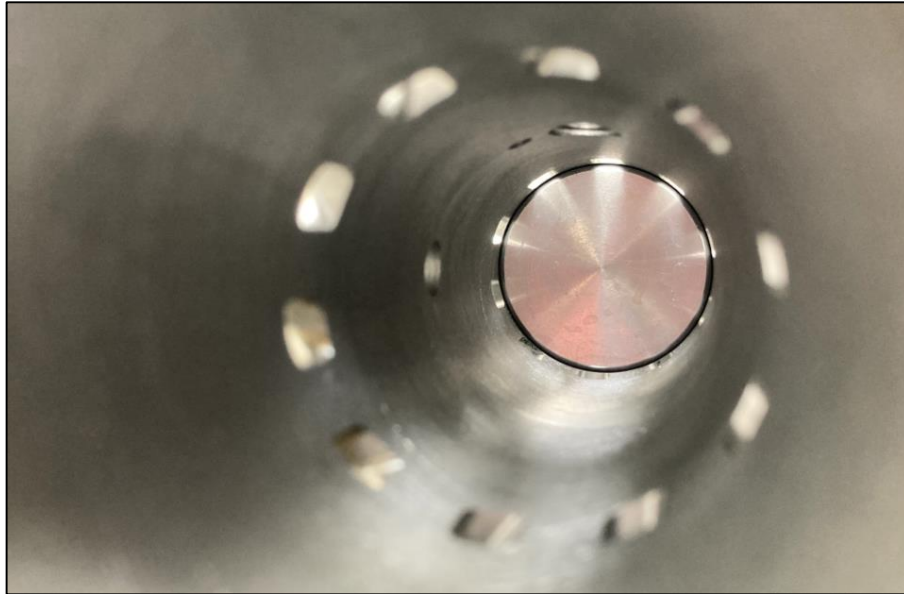


*Figure 43 - View into the Cylinder Liner from the Intake End; Inner Diameter of Liner 39 mm*

Figure 44 shows the pressure transducer loosely installed in the cylinder block, in its central upstand. Note that in this image the engine is largely assembled, and part of the spark plug can be seen towards the top of the image. The pressure transducer was not tightened into position in this case, since a plug was inserted in its place for the purposes of initial engine testing. This is because having the sensor in position whilst not being used would be an unnecessary risk.



*Figure 44 - Pressure Transducer in Position*

### **5.3 Main Engine Cases**

Two large aluminium plates were designed, which make up the front and rear engine cases. They enclose major engine components such as the cylinder block and liner, and have evolved over approximately two years of progressive refinement. Again, due to time constraints these were outsourced to Kenworth

Engineering, and each was machined from a solid billet of aluminium. Together with the cylinder block and liner, they separate three key regions of the engine: air-side, water-side, and oil-side. Figure 45 shows inside the rear engine case, annotated to show these three ‘fluid regions’ of the engine. The boundaries of the water jacket that are formed when the cylinder block is inserted are shown with red lines, the red and white arrows show the location of bearing seats for the engine crankshafts and output shaft, and the black arrows show the direction oil is intended to drain.

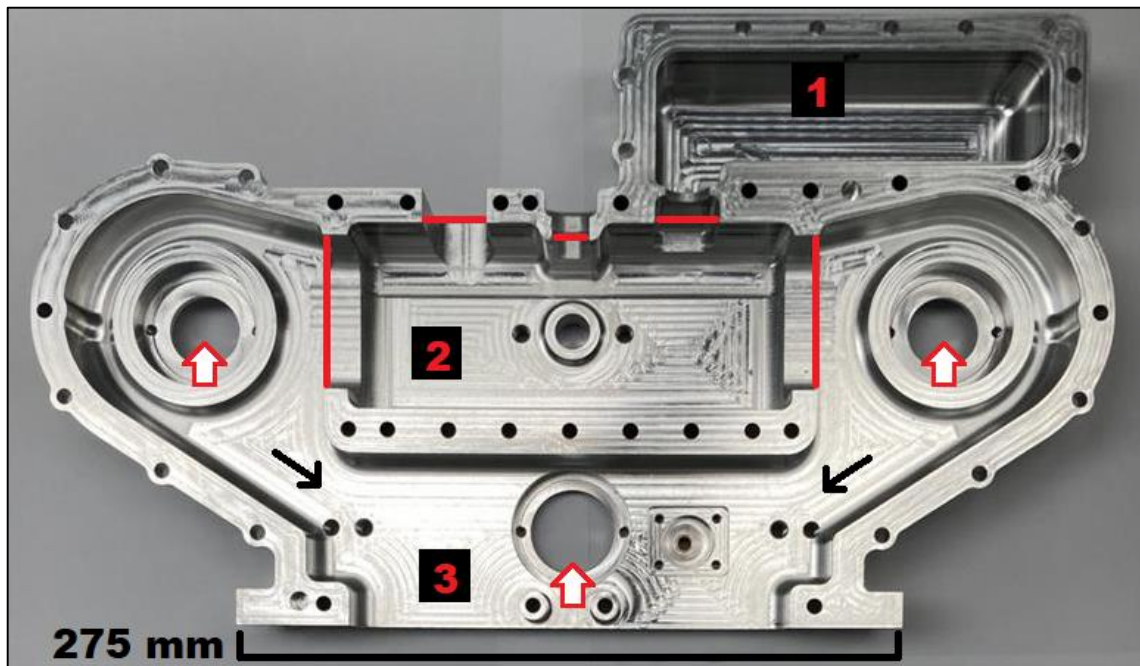


*Figure 45 – Inside Rear Engine Case – 1: Air Reservoir; 2: Cooling Jacket; 3: Oil Side; Black Arrows: Oil Drainage Channels; Red and White Arrows: Bearing Locations*

The oil drainage channels are designed to ensure that excessive quantities of lubricating oil do not build up in the region of the crank slider assemblies, and lead to the bottom of the engine cases, which sit on top of the oil sump. Also, the design of the water jacket (region 2 in Figure 45) is designed to completely surround the cylinder block, save for where the components intersect each other. Heat transfer calculations were not performed at this stage. Instead, the engine cases were designed to ensure that coolant flows from one end of the jacket to the other. Specifically, the coolant enters the lower right of the jacket, and flows toward the upper left of the jacket (i.e. from the intake to exhaust end from the perspective of Figure 45). To illustrate this, Figure 46 shows the front engine case resting on top of the rear engine case, and several features of the front engine case have been labelled with letters, since the engine cases (particularly the front engine case) attach to and support various other parts. These are as follows: A is the inlet to the surge chamber (discussed shortly), to which a duct mounts that receives air from the charge air cooler. B is the discharge/recirculation port of the surge chamber, which connects to the bypass valve (see section 5.6). C, D and E are openings indicating the location of the exhaust

crankshaft, intake crankshaft and output shaft, respectively. F is where the single fuel injector is located, corresponding to the middle of the cylinder block (see section 5.2). G is the coolant water inlet, while H is the opening through which the governor drive shaft takes power to the governor assembly. I is where the oil discharge manifold is located, that (via an oil distribution block) feeds two oil jets which are positioned at K and L. J is the coolant water outlet, originally intended to house a thermostat but in practise one was not fitted (see Appendix B). M is a cross-over passage at the top of the water jacket, to prevent air bubbles around the central upstand of the cylinder block. N is a series of M8 x 1.25 bolt holes where the blower mount is located. O is one of the pistons, for reference.

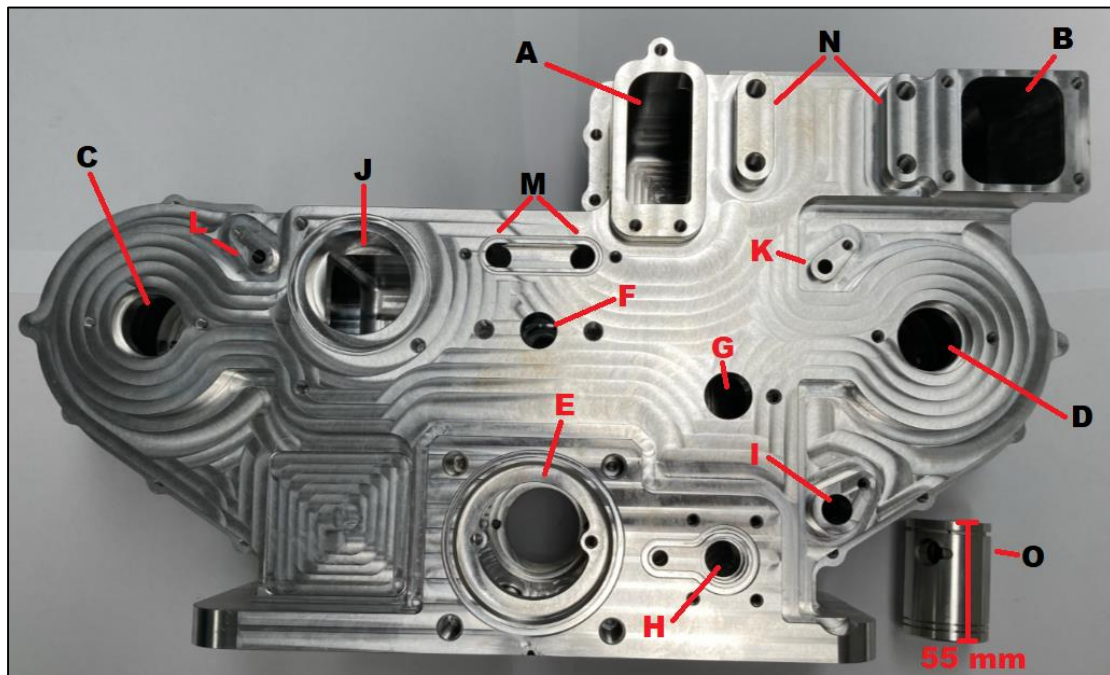


*Figure 46 - Front and Rear Engine Cases with Piston*

Since the engine cases form the majority of the structure of the engine, they have been deliberately over-engineered for the sake of strength. For example, wall thickness and rigidity have been prioritised over the weight and packaging volume of the engine, given that it is intended as a research prototype rather than being optimised for commercial production. They are designed to seal using O-ring cords, and where seals intersect, a small amount of gasket sealant could be added. Like the cylinder block itself, the tolerances for the recesses into which the cylinder block locates are tight, as are those for the larger bearings (crankshaft and output shaft bearings). The two engine cases are bolted together using M6 x 1.0 cap-head screws, which are inserted through the rear engine case, and they feature two 8 mm diameter dowel pins to assist in alignment. Disassembly of the cases is provided for with the inclusion of threaded holes for jackscrews to press against the bearing races. Figure 47 shows a drawing view for the rear engine case (for detailed engineering drawings, please see the relevant part of Appendix A). Visible are the tolerances for the bearing seats:

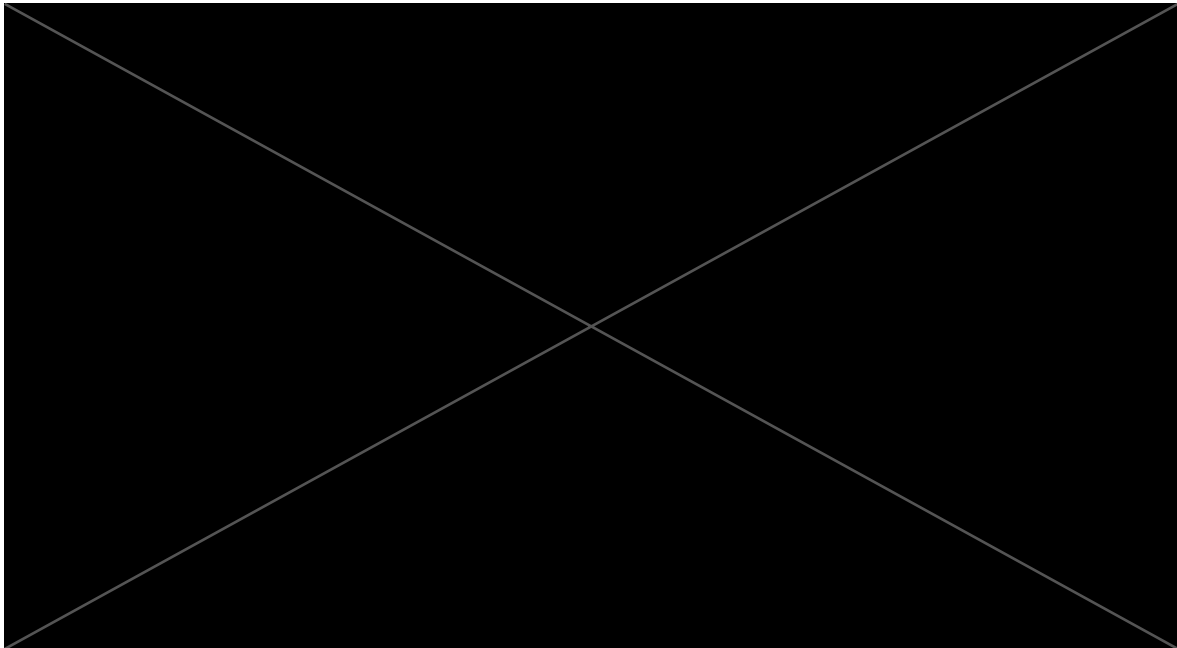


*Figure 47 - Drawing View of Rear Engine Case; Dimensions in mm*

Note that the seats for the crankshaft bearings are located slightly deeper in the case than they need to be; bearing shims are therefore placed behind the crankshaft bearings (between the jack screws and the outer bearing races). This way, the position of the crankshafts (front to back) could be adjusted – for example to extend the length that protrudes through the rear engine case to make installation of the timing gear easier. Also, it meant that the location of the upper most face of the bearing recess, from which its depth is specified, were not explicitly dimensioned in drawing, since the STEP files used for the machining process were sufficiently accurate. However, for the benefit of the reader, in Appendix A an additional dimension has been added to indicate their locations for both front and rear cases, in their respective drawings. The dimensions for the diameter of the three main-shaft bearing seats (the two crankshafts, and output shafts) are 51.98 mm +/- 0.01 mm. This is designed to be a transition fit for the bearings, which all have an external diameter of 52 mm (the crankshafts use bearings from the 6304 family, and the output shaft uses bearings from the 6205 family). The reason for specifying this dimension, especially with a tight tolerance, is due to the need to balance ease of assembly/disassembly, and the risks posed by thermal expansion. That is, the tighter the bearing seats are, the greater the forces required during assembly/disassembly of the engine. This is particularly relevant for the crankshafts, installed through the use of a hydraulic press applying pressure to their ends. Because the crank pin is off centre, when pressing the crankshafts into position a bending load will be applied about the crank pin. Naturally if this load is too great, it could damage the crankshafts. On the other hand, the bearing seat cannot be so loose that, as the engine warms, the bearings damage the casings – this would amount to a catastrophic failure. Aluminium has a greater thermal expansion coefficient than steel [139], and

so the bearing seat may expand more with temperature than the outer race of the bearing. If the assumption is made that a material is uniform then, over small temperature ranges, there exists a relationship between change in temperature and thermal expansion. Specifically [140]:

$$\frac{\Delta L}{L_0} = \alpha * \Delta T \quad \text{Eq. 13}$$

Where  $\Delta L$  is the (fractional) linear change in length of a specimen,  $L_0$  is the original length of the specimen,  $\alpha$  is the thermal expansion coefficient, and  $\Delta T$  is the change in temperature [140]. Rearranging Eq. 13 to find  $\Delta L$ , and using an approximate value for the fractional thermal expansion coefficient of aluminium of  $24 * 10^{-6}$  per  $^{\circ}\text{C}$  (at  $20^{\circ}\text{C}$ ) [139], then the increase in the diameter of the main bearing seats as they increase in temperature from  $20^{\circ}\text{C}$  to  $78^{\circ}\text{C}$  can be calculated as follows:

$$\Delta L = L_0 * \alpha * \Delta T = 51.98 \text{ mm} * (24 * 10^{-6}) * (78^{\circ}\text{C} - 20^{\circ}\text{C}) \approx 0.072 \text{ mm} \quad \text{Eq. 14}$$

Therefore, the bearing seat will expand to a diameter of approximately 52.052 mm – slightly larger than the outside diameter of the bearing itself. Of course, the diameter of the bearing would similarly increase but to a lesser extent due to the differing thermal expansion coefficients. If the assumption is made that the bearing race is steel, with a thermal expansion coefficient of  $13 * 10^{-6}$  per  $^{\circ}\text{C}$  (at  $20^{\circ}\text{C}$ ) [139], and it similarly increases from  $20^{\circ}\text{C}$  to  $78^{\circ}\text{C}$ , then the increase in external diameter of the outer bearing race would be:

$$\Delta L = L_0 * \alpha * \Delta T = 52 \text{ mm} * (13 * 10^{-6}) * (78^{\circ}\text{C} - 20^{\circ}\text{C}) \approx 0.039 \text{ mm} \quad \text{Eq. 15}$$

So, the outside diameter of the bearing would increase to approximately 52.039 mm. Given the tolerances of  $\pm 0.01$  mm, the limits for the expansion of the bearing seat would therefore be approximately 52.062 mm and 52.042 mm, for a ‘cold’ dimension of 51.99 mm and 51.97 mm, respectively. The upper temperature limit of  $78^{\circ}\text{C}$  assumes that the temperature of the engine cases is uniform throughout and is equal to a known thermostat opening temperature [141]. Consequently, at the looser limit of the bearing seat tolerance, the bearing seat would only be approximately 0.023 mm larger than the outside bearing race, and at the tighter end, 0.003 mm larger. These calculations are based on the idea that thermal expansion occurs equally in all directions [140]. Therefore, a hole would increase in diameter by the same amount as a bar of identical material, that is measuring its diameter, would increase in length.

## 5.4 Engine Lubrication

In addition to making up the main structure of the engine, the front and rear engine cases have several internal features to accomplish other important functions, such as forming part of the oil pump. Figure 48 shows the oil pump rotors in a dedicated recess in the rear engine case. These rotors were sourced from a commercially made oil pump for a small motorcycle engine; see for example [142].



Figure 48 - Oil Pump Parts in Recess in Rear Engine Case

As can be seen the bronze bushing is off centre from the axis of the larger rotor. As both rotors rotate in the housing in an anticlockwise direction (from this viewpoint), there exists a gradually expanding volume on the bottom half, and a gradually contracting volume on the top half of the rotors – the red arrow represents the approximate changeover point. With a matching oil pump housing to fit in the ‘rectangular’ pocket, the bottom half therefore draws oil from the sump and the top half pumps it out to a separate oil discharge manifold. The manifold exits the front engine case at position I in Figure 46. Figure 49 shows the matching oil pump housing and some of the associated parts:

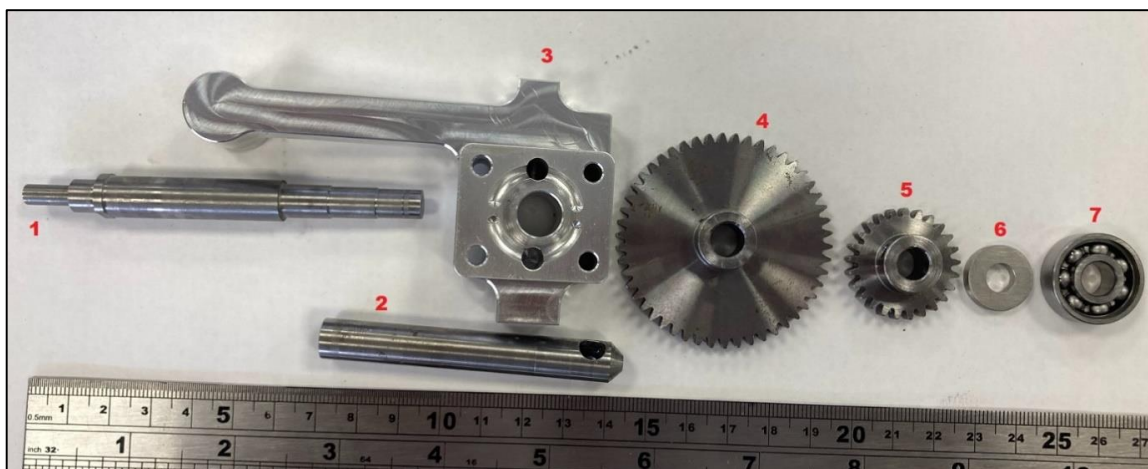
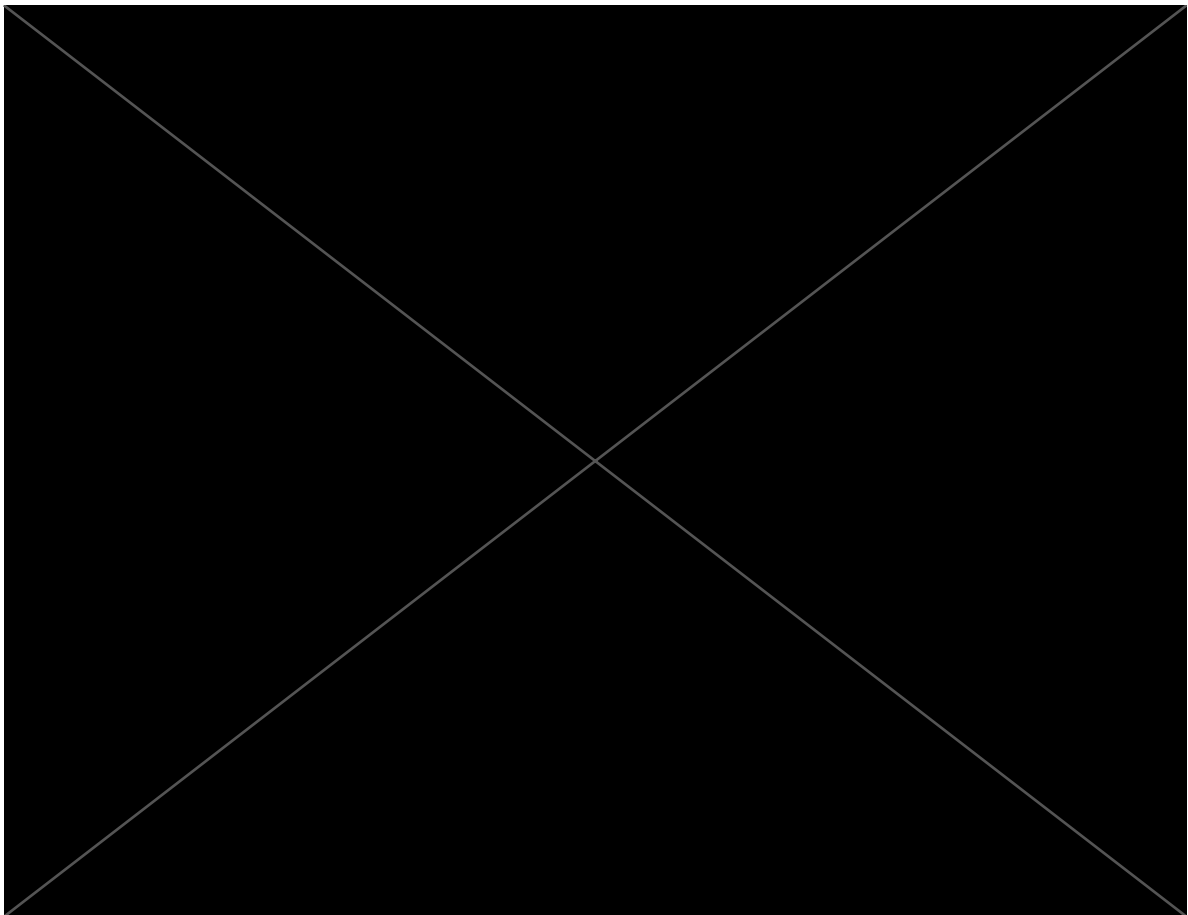


Figure 49 - Oil Pump Housing and Associated Parts

Here, part 1 is the oil pump shaft, part 2 the oil pickup tube and part 3 is the oil pump housing itself. The two crescent shaped recesses in the oil pump housing are each connected to a small port hole. These link the expanding/contracting volumes of the two oil pump rotors in Figure 48. The bottom recess is fed by the oil pickup tube, and the top half discharges into an internal gallery (which extends leftward in Figure 49). The oil pump shaft has a flat that engages with the smaller rotor in Figure 48. It is held captive in the oil pump housing due to this. The 50-tooth module 1 metric spur gear (part 4 in Figure 49), the 25-tooth module 1 metric spur gear (part 5), a 3 mm spacer (part 6) and the bearing (part 7) were thus installed after the shaft was located in the oil pump housing. The bearing is size 627. Figure 50 shows a drawing of the oil pump housing, illustrating how the oil passages are connected together; section B-B has been surrounded with a red box for clarity.



*Figure 50 – Extract of Pump Housing Drawing; Dimensions in mm*

For full engineering drawings please see Appendix A. A pressure relief valve screws into the M6 x 0.75 mm thread (of the type used on some toy steam engines, see for example [143]), and a grubscrew used to seal the vertical access hole via the M6 x 1.0 mm thread. This access hole connects the discharge side of the pump rotor to the top of the housing. Figure 51 shows the oil-pickup tube in position and its close

proximity to the bottom of the oil sump, it is inserted into the 9.8 mm hole at the bottom of the housing in Figure 50. The reason for this was to ensure that the pickup tube could not fall out even if the retaining compound holding it in the pump housing were to fail. The holes through which the oil is drawn are slightly above the bottom because of this to prevent blockage, as well as to reduce the chance of picking up any debris.



*Figure 51 - Oil Pickup Tube Position*

Figure 52 shows the assembled parts from Figure 49 in position in the rear engine case. The red coloured arrow indicates the outlet of the oil pump where it connects to the oil discharge manifold.



*Figure 52 - Oil Pump in the Rear Engine Case*

The 50-tooth gear takes power from the matching gear on the main engine output shaft to drive the oil pump and governor (the latter of which is fed power through the 25-tooth gear on the oil pump shaft). The oil discharge manifold takes the oil outside of the front engine case and, via a copper pipe, to the oil distribution block. The pressure relief valve was installed after the output shaft was pressed into the rear engine case, since it would have prevented the insertion of one of the main bearings. It should be noted that the oil system of the engine is not pressurised in the traditional meaning of the word, since

there are no pressurised bearings. Instead, oil is sent to a distribution block, shown in Figure 53 alongside the crankcase breather (to the right) loosely in position on the front shaft housing. The distribution block former feeds two oil jets that squirt oil to the underside of each piston via copper lines, as well as an oil pressure switch and a dripper that is incorporated into the retaining fastener (not shown).



*Figure 53 - Oil Distribution Block and Crankcase Breather in Position on the Front Shaft Housing*

The dripper provides lubrication to the GDI pump cam and follower. Note also the two threaded holes on the left of Figure 53, which are M5 x 0.8 – these are to allow an adjustment screw or control cable for the governor spring tensioner. Figure 54 shows the two oil feed jets, each of which has a small hole to squirt oil to the underside of each piston. These locate into positions K and L in Figure 46. Like the oil distribution block and discharge manifold, the brass fittings allow the insertion of 4 mm (external) diameter copper pipe. The oil feeds were designed to be outside the engine cases, since space is limited, and it is easier to see if something is going wrong (i.e. an oil leak) before any engine damage occurs.



*Figure 54 - Oil Feed Jets*

An oil filter is not included in the engine design at this stage, however because the oil system is fed through a common copper line from outside the engine cases, it is designed to easily accommodate one if it is found to be necessary.

#### 5.4.1 Oil Sump

Figure 55 shows the oil sump and some of the components that are attached to it. The oil sump forms the base of the engine, to provide a reservoir of lubricating oil for the oil pump to draw from, which is the large volume in the centre of Figure 55. Additionally, it supports the starter motor, which is visible at the top of Figure 55. This is attached to the oil sump by a two-piece aluminium bracket and is of the type used on small industrial diesel engines; see for example [144]. The sump seals against the engine cases using O-Ring cord.

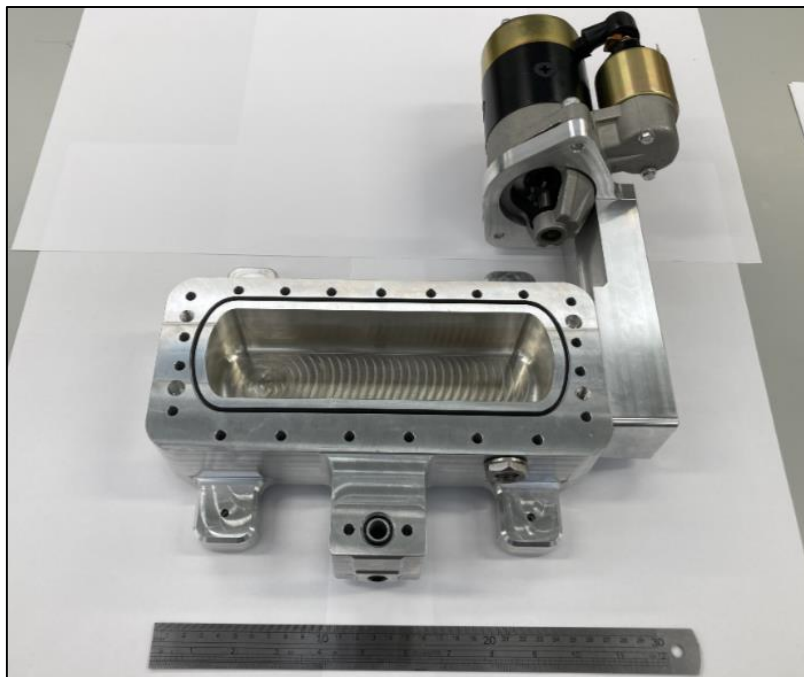


*Figure 55 - The Oil Sump and Associated Components*

At the bottom of Figure 55 is a platform, extending forward of the main sump volume, which bolts up to the underside of the front shaft housing. It receives oil from the front shaft housing, acting as a drain back to the main sump volume, and features a drain hole for the oil reservoir (i.e. for oil changes) that is closed via an M12 x 1.75 bolt. Also, on the front of the main sump volume is a sight glass, since the engine does not use a dipstick, and underneath the sump are four ‘feet’, through which the engine is mounted to its test stand. These feet were designed with clearance holes for fasteners (see Appendix A for detailed engineering drawings), however in practise the threaded holes that were used to retain it on the computer numerical control (‘CNC’) milling machine were left in place. Figure 56 shows an extract

of the drawing for the oil sump when viewed from the back of the engine, where its depth (to allow more space for oil foam) is apparent (for full engineering drawings please see Appendix A). The position of the sight glass (the hole for which is the larger circle in the top left of section A-A) was not dimensioned; this was determined following the completion of other components to ensure adequate line of sight. Detail B is a zoomed in view of the O-Ring groove, sized to standard for a 2 mm wide O-ring cord [145].

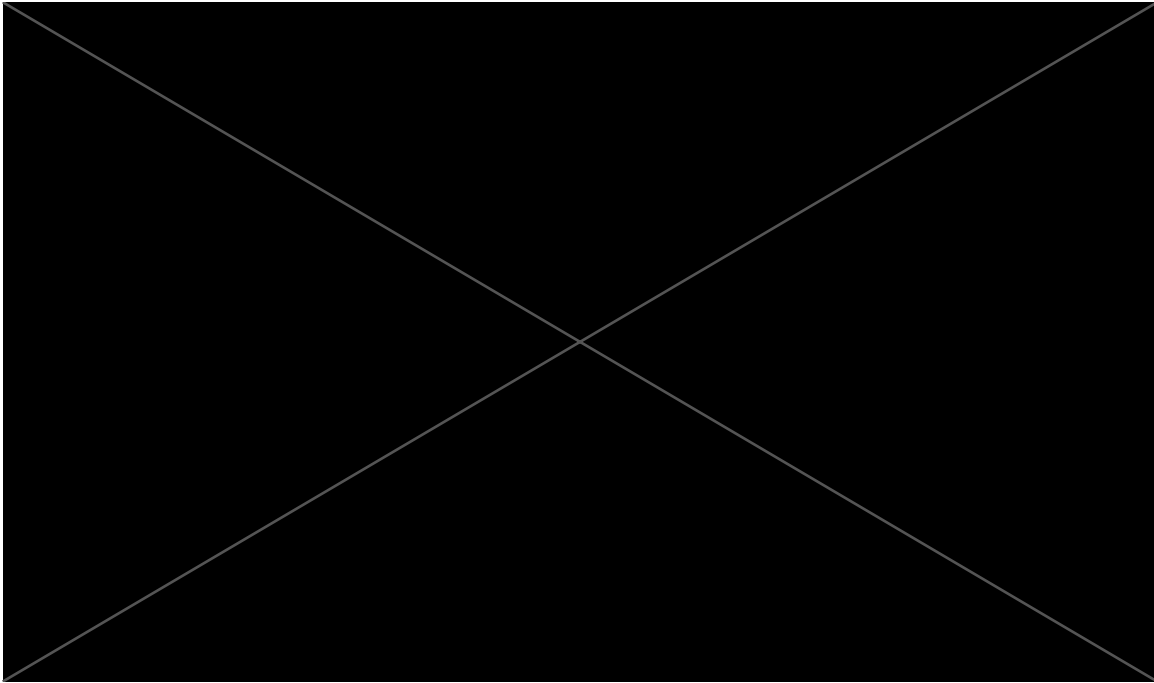


*Figure 56 – Extract of Oil Sump Drawing; Dimensions in mm*

### **5.5 Front Shaft Housing and Output Shaft**

Another structural component of the engine is the front shaft housing, so called because it sits in front of the engine cases. It too serves multiple purposes in addition to supporting the output shaft of the engine. Figure 57 shows several drawing views of the front shaft housing (for detailed engineering drawings, please see Appendix A). Here, details for mounting points for the GDI pump (Hitachi P/N 2503070), oil distribution block, governor spring adjuster, crankcase breather and front support bracket are visible, in addition to its own mounting holes. The crankcase breather fits into the  $\frac{1}{2}$  BSP pipe thread, and is positioned where it is because it is arguably the ‘quietest’ part of the engine, where there is not expected to be a great deal of windage due to it being forward of the GDI pump cam. The large 60 mm recess shown at the top right is for a separate housing that holds the front bearing (6004) and oil seal, and the plunger for the GDI pump runs in a yellow-metal insert, drawings of both the housing and insert can be reviewed in Appendix A.

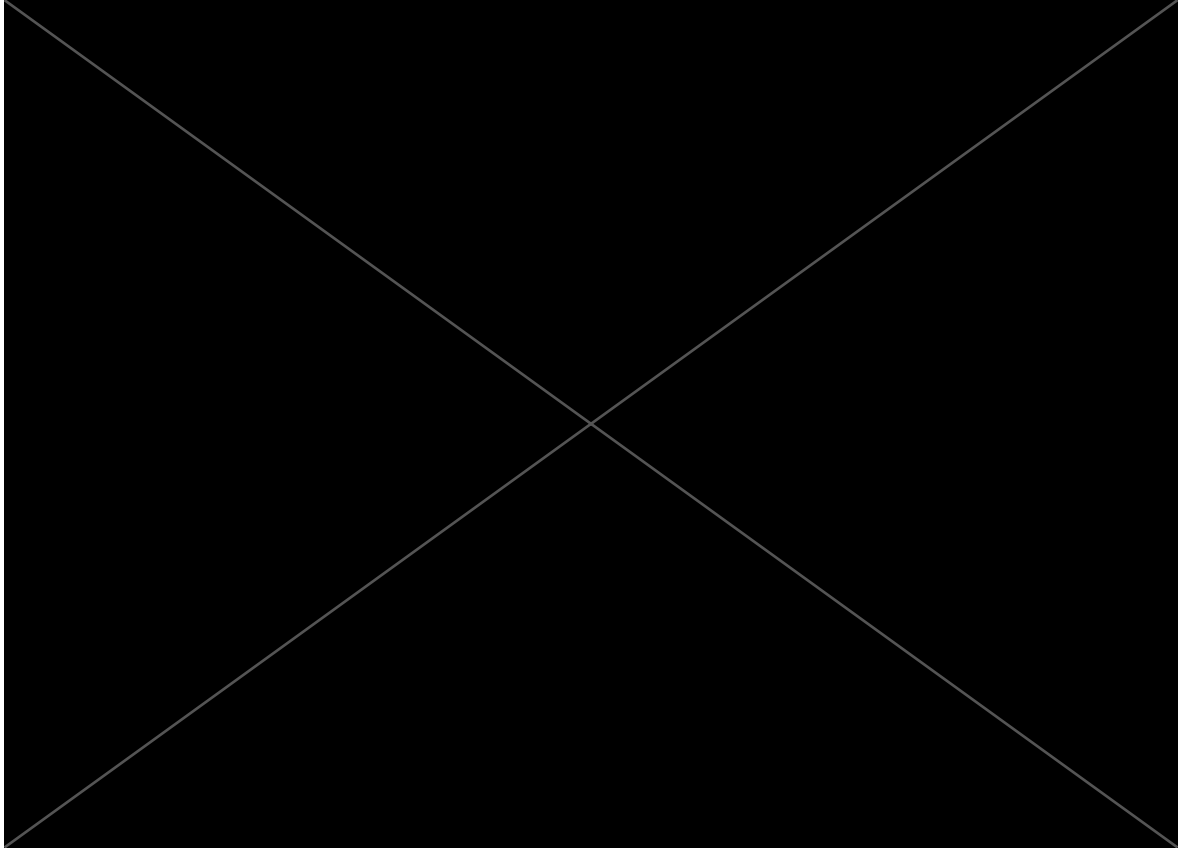


*Figure 57 - Front Shaft Housing Details*

Figure 58 shows the GDI pump plunger that runs in the insert, as well as a steel pad that acts as a spacer, which sits inside the plunger. The purpose of the spacer is to ensure there is a small amount of preload on the (spring loaded) pump piston such that it is always in contact with it regardless of the engines crank position. Were this not the case then the plunger could lift off the pump piston every time the engine rotates, because the piston is driven by a cam on the output shaft. Such a situation could result in serious damage to the pump piston, plunger, or both.



*Figure 58 - GDI Pump Plunger and Steel Pad*

The output shaft was machined from a piece of EN24 steel for strength; A drawing of the output shaft is shown in Figure 59; for full engineering drawings please see Appendix A. It runs the full length (front

to back) of the engine, attaching to the flywheel assembly at the back and the drive pulley for the blower (which also includes a timing wheel) at the front.

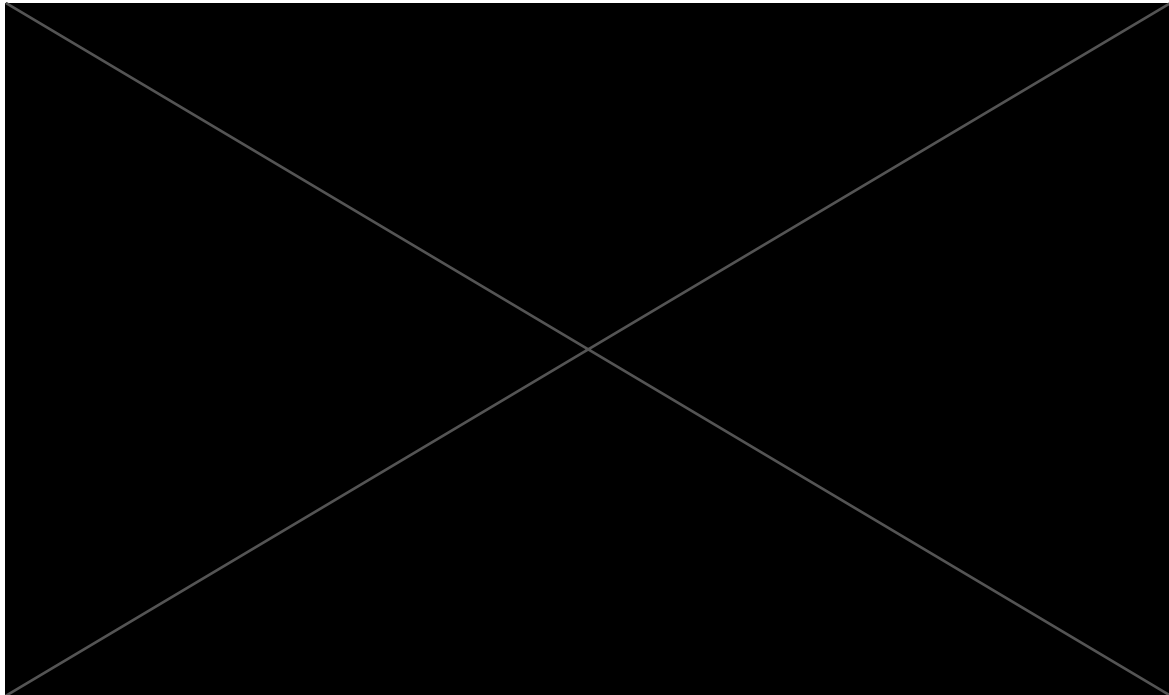


*Figure 59 - Engine Output Shaft Drawing*

It also drives a 50-tooth gear and matching internal gearing inside the engine, as well as the GDI pump cam. The cam is an eccentric, with a lift of approximately 7 mm. An eccentric was chosen due to ease of manufacturability; because it is pressed onto the output shaft, it can be easily replaced if it is found not to work. Because of this, the output shaft alone drives all of the mechanical components of the engine, as well as the ‘crankshaft position’ that the ECU sees. This means the crankshafts are mechanically separated, connected only via the timing mechanism. Therefore, they can be adjusted with respect to one-another, without altering anything else, giving a much greater degree of freedom in adjusting the engine. This is possible because the ECU does not need to ‘know’ there are two crankshafts, since the output shaft is being used for crank position; it can instead be programmed to run a ‘normal’ direct injection two-stroke engine, making configuration simpler.

## **5.6 Scavenging Arrangement**

A Roots-type blower provides scavenging pressure to the engine, in this case a TX02 Supercharger by Ogura (see [146]) as shown in Figure 60; this is driven by the output shaft, via a poly-vee belt situated at the front of the engine.

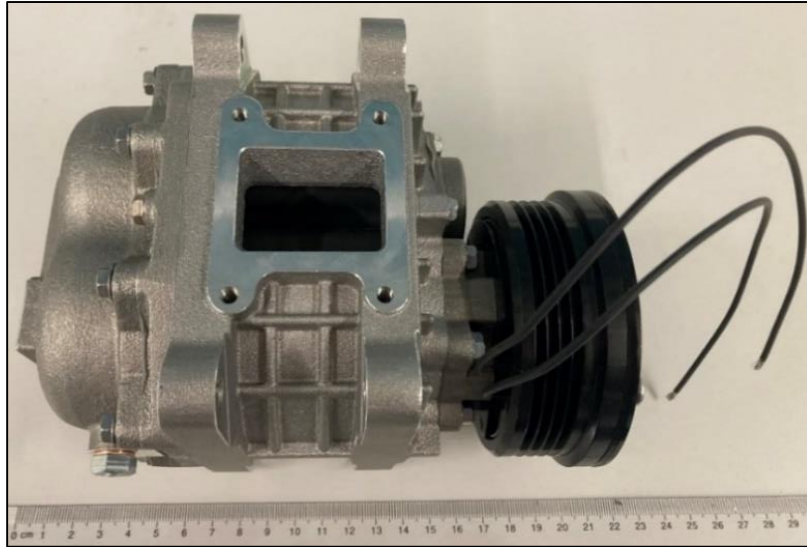


Figure 60 - Ogura TX02 Roots Type Supercharger

Figure 61 shows a performance map for the TX02, reproduced with permission from Ogura [147]:

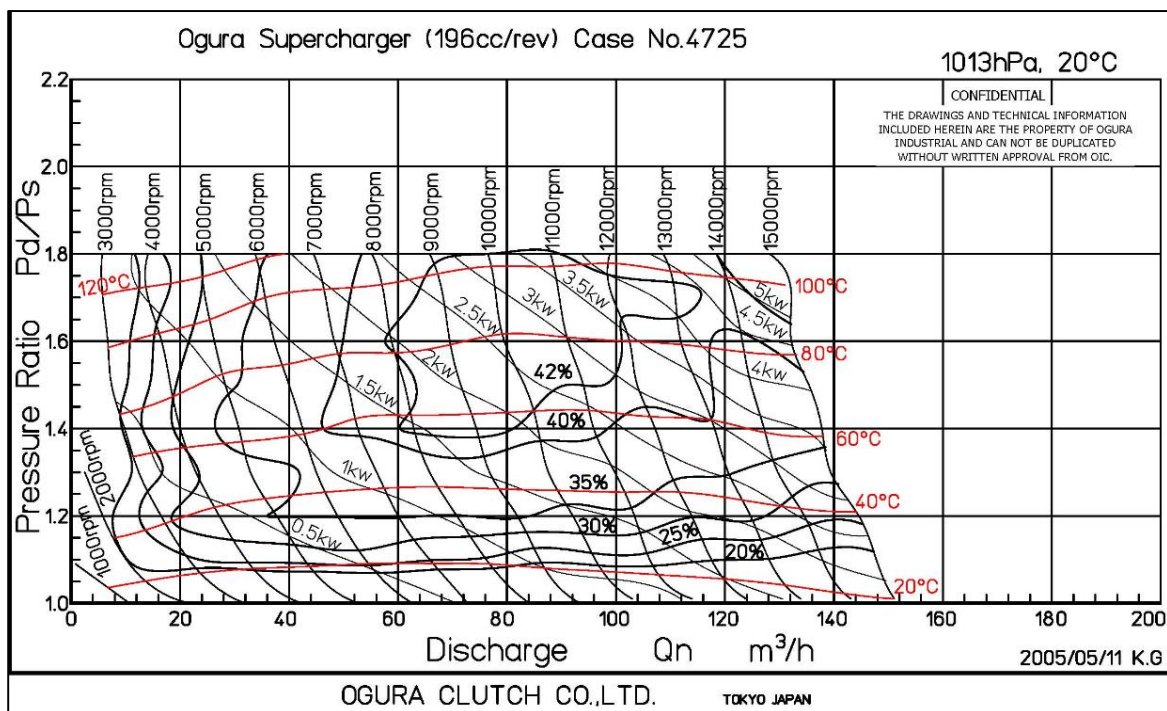


Figure 61 - Performance Map for the TX02 Supercharger [147]

The TX02 (one of the smallest Roots-blowers that were available) is straight-lobed. Since straight-lobed blowers produce pulsating outputs and the prototype uses a single cylinder, a large air storage volume or ‘surge chamber’ was incorporated between the blower discharge and the intake gallery [5]. The principle aims of this chamber, in conjunction with a bypass valve, are to reduce pressure fluctuations as well as to regulate the scavenging pressure. A simplified schematic of how the engine scavenging

system is intended to work is shown in Figure 62; crankshaft phasing is not shown to scale. This is in some respects a more basic version of the arrangement used in an Achates Power GCI engine, except that in this engine the bypass valve is located downstream (and not upstream) of the charge air cooler after the blower, there is no turbocharging and associated cooler, and no EGR or aftertreatment [65]:

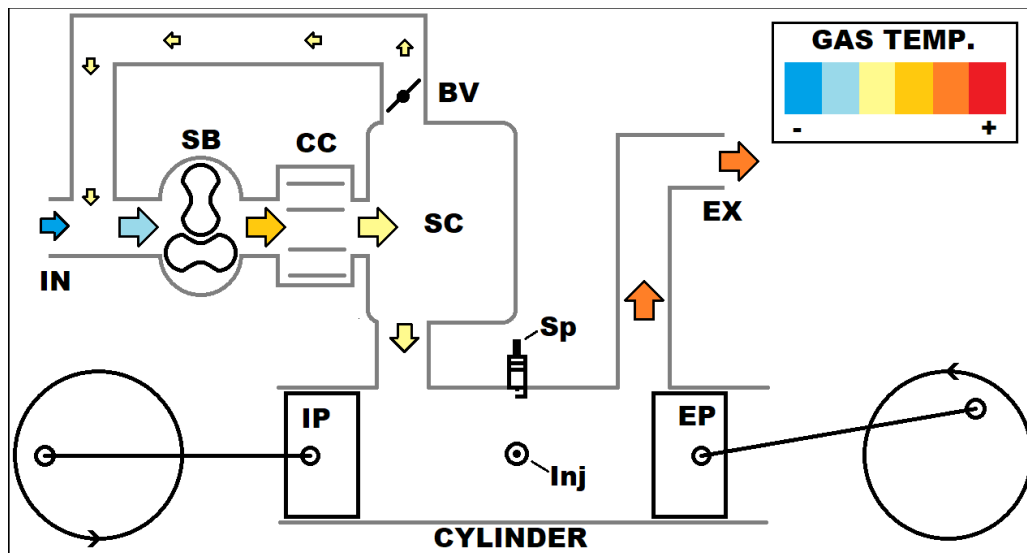
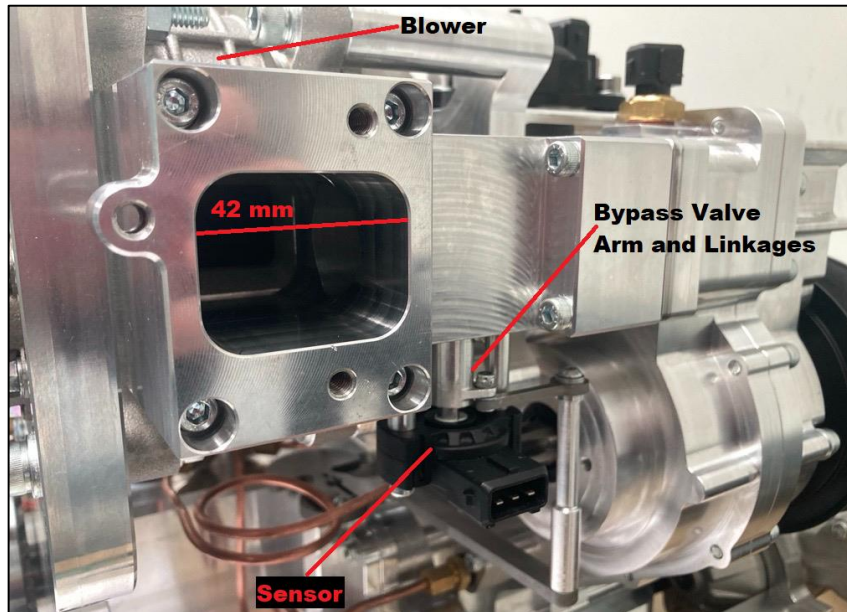


Figure 62 - OP2S Scavenging System

In Figure 62 ‘IN’ is the intake, ‘SB’ is the scavenging blower, ‘CC’ is the charge air cooler, ‘SC’ is the surge chamber, ‘BV’ is the bypass valve, ‘IP’ is the intake piston, ‘Sp’ is the spark plug, ‘Inj’ is the injector, ‘EP’ is the exhaust piston, and ‘EX’ is the exhaust. The coloured arrows are a simplified representation of air flow, sized according to flowrate and coloured according to temperature; both scales are for visual indication only and are not intended to be an accurate representation.

The bypass valve is the sole intended means of controlling the scavenge pressure in this prototype, in a way that could be said to be analogous to the inverse of a throttle plate. Opening the bypass valve will cause pressurised air in the surge chamber to flow back to the intake of the blower. This will displace some of the incoming atmospheric air and therefore reduce the net amount of air pumped into the surge chamber. In so doing, the pressure in the surge chamber will drop, and by controlling the pressure in the surge chamber (i.e., the scavenging pressure), the air flow through the engine can be varied. Therefore, while opening a throttle butterfly in a conventional engine will increase flow to the cylinders, in this engine the bypass butterfly is closed to achieve the same effect. The reason for using a bypass valve and not simply throttling the intake to the blower is because the latter could cause the pressure ratio across the blower to rise unacceptably, risking severe damage. Figure 63 shows the bypass valve assembly in position on the engine. It is attached directly to the intake of the blower, with the opening in the foreground being the location of the air filter; this is approximately 42 mm x 33 mm, to fit the

blower intake; see for further dimensions: [146]. A smaller round opening inside and to the right is where the bypass valve itself is located, and uses the throttle shaft and butterfly from a carburettor for a small industrial engine; see for example [148]. The location of the valve corresponds to where the bypass valve arm is, and the position of the valve is controlled by a mechanical governor and associated linkages; a position sensor is affixed underneath the arm. Appendix B contains Figure 138, and Figure 139, which show views inside the bypass valve when it is open and closed.



*Figure 63 - Bypass Valve Assembly in Position on the Engine*

Figure 64 shows a simplified drawing of the bypass valve housing; the left view is looking into the bypass valve bore from the engine, and section A-A viewed looking into the intake of the blower from the air filter side.

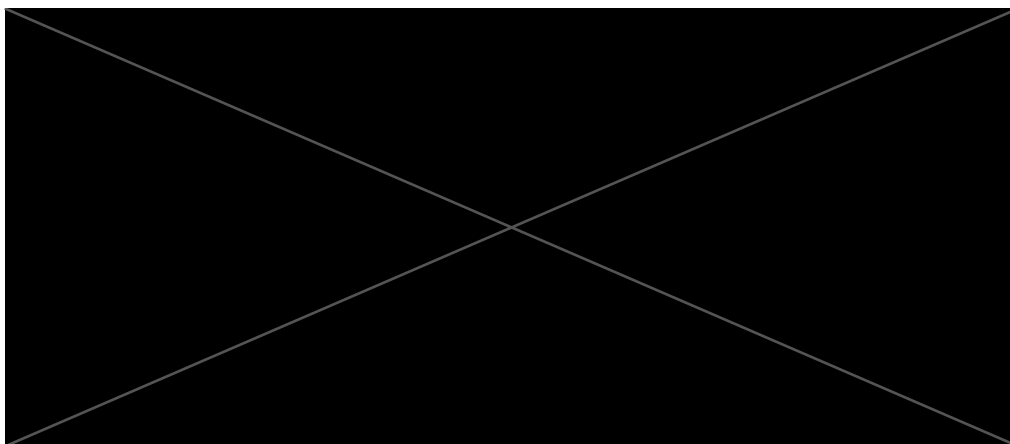


*Figure 64 – Simplified Bypass Valve Housing Drawing; Dimensions in mm*

The bypass valve butterfly is located at the 7 mm journals; for full engineering drawings please see Appendix A.

### 5.6.1 Engine Governor

A mechanical governor controls the bypass valve, acting against a spring. Figure 65 shows the components that make up the governor, aside from the bearings (2 of size 618/8) that its drive shaft sits in.

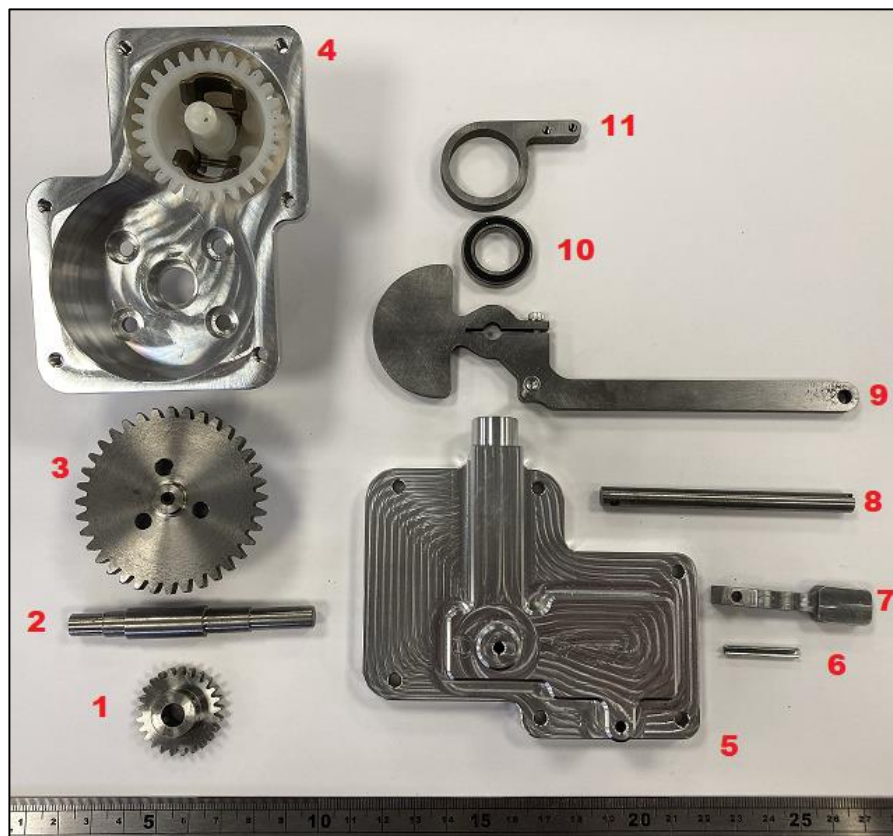


*Figure 65 - Mechanical Governor Components*

These are numbered as follows: 1 is a 25-tooth module 1 metric spur gear, this takes power from the oil pump shaft inside the engine cases to drive the governor; 2 is the governor drive shaft which takes this power outside the engine cases to the governor drive gear (3), located inside the governor housing (4) in which the fly-weight governor itself\* is in position; 5 is the governor housing cover, in which the governor arm (7) is located and attached to the governor arm shaft (8) via a spring pin (6). This shaft is then coupled to the larger governor arm (9) which is connected (via an aluminium upstand that is not shown) to the bypass valve linkage. 9 and 10 are a ball bearing (15 mm inner diameter and 24 mm outer diameter), and the spring tensioner respectively – these are located together on the round journal at the top of the governor housing cover, and a spring connected between the tensioner and large governor

arm. The spring tensioner can be adjusted to vary the force required from the governor to open the bypass valve. Wherever possible in this engine design, components like gears were specified as standardised components which can be readily purchased and then machined to fit (for example bored to suit a particular journal). This includes the governor drive gear – a module 1.5 metric spur gear was chosen based on its reasonably close fit with the plastic governor gear.

\*An off-the-shelf small engine governor was utilised, since these devices are very well proven and inexpensive; see for example [149]. The governor assembly is driven by internal gears inside the engine cases, which take power from the output shaft of the engine to drive both the oil pump and governor.

### 5.7 Exterior Engine Components and Assembly

Presently, it is easier to address other design features of the engine in the context of the general engine assembly, and less in isolation. Figure 66 shows the engine during a ‘test assembly’ after the crank-sliders, cylinder block and output shaft had been assembled (see Appendix B for installation of the crank sliders). Key components are highlighted.

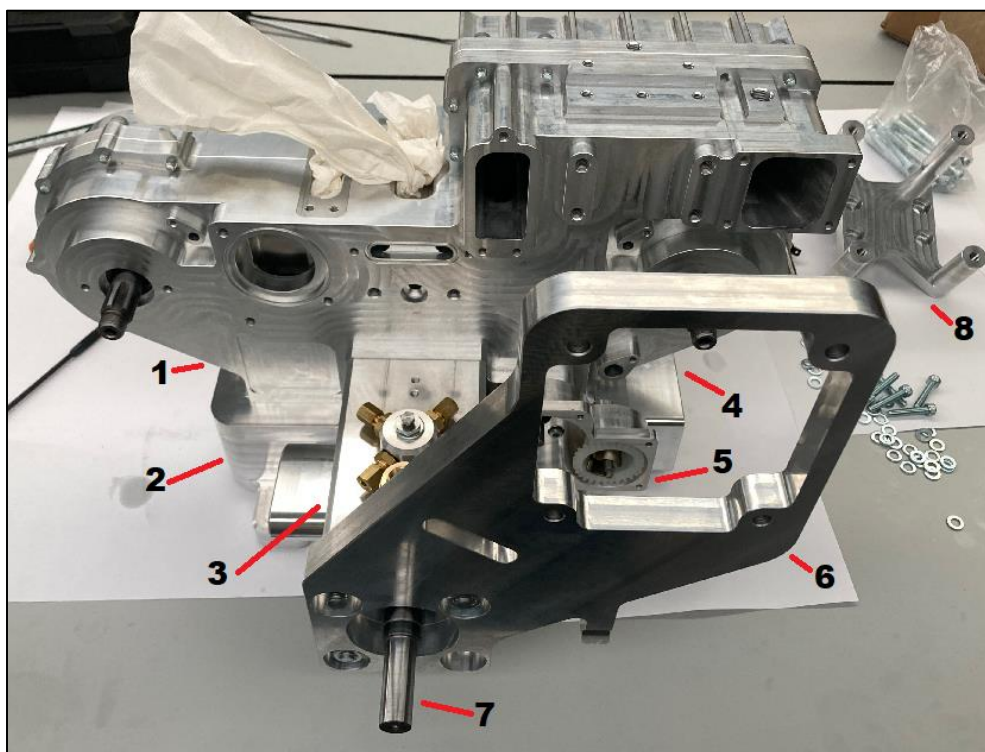


*Figure 66 - The Engine During a Test Assembly*

Label 1 indicates the front and rear engine case assembly, which is bolted to the oil sump (2). The front shaft housing (3) is retained in place on the engine cases using component 6, which is the front support bracket. The front support bracket ‘pulls’ the separate front bearing housing into place in the front shaft

housing, and it works in conjunction with component 8, the blower mount, to hold the blower. The blower mount is shown not fixed to the engine; see Appendix B for details of how it fastens to the front engine case. Component 4 is part of the bracket that supports the starter motor (Figure 55) and component 5 is the governor (Figure 65 and Figure 140). Component 7 is the output shaft. The front and rear engine cases are identified together in Figure 66 because in practise, they are rigidly held together at this point. Figure 67 shows a front view of the engine during further fitting of components.

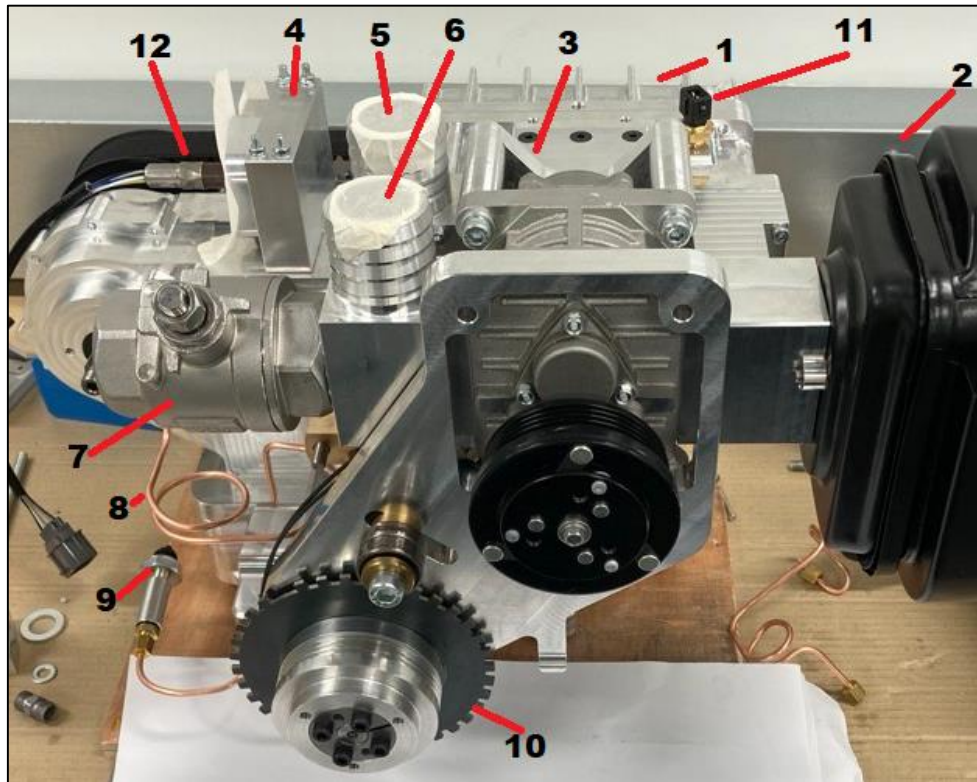


*Figure 67 - Front View of the Engine During Further Assembly*

Item 1 is the front and rear cases of the engine. Item 2 is the air filter, of the type used on small industrial diesel engines, see for example [150], attached to the intake and recirculation duct that was discussed earlier. 3 is the blower mount, with a better view of the three countersunk M6 x 1.0 screws fixing it to the top of the engine. 4 is the exhaust manifold, which bolts up to the external face of the exhaust gallery on the cylinder block – it is not bolted to the engine cases. 5 and 6 are the surge chamber duct and blower duct respectively. These link to a charge air cooler via large diameter hoses, completing the flow path from the discharge side of the blower to the surge chamber. On the underside of the blower duct is an air temperature sensor (not shown) – this is there to monitor the temperature of the blower to make sure it does not overheat. Item 7 is a large (38 mm bore) ball valve – present for the eventuality that the blower approaches temperature limits. By opening the valve and cranking (but not starting) the engine, atmospheric air can be moved through the blower to cool it. 8 is one of the four oil lines on the engine. In this case, it is that which feeds the oil jet for the exhaust piston, and features a coil shape for the

purposes of strain relief. 9 is the oil pressure switch. 10 is 36-1 timing wheel, which is read by a hall-effect sensor that bolts up to the small lug extending downward from the front support bracket. 11 is an air temperature sensor, which reads the temperature of the air in the surge chamber, and 12 is a wideband lambda sensor. Specifications for the lambda sensor are included below in Table 4 [151]:

*Table 4 – NTK Lambda Sensor Specification*

Specification	Value
Pin out:	A: +12V; B: lambda heater; C: lambda GND; D: lambda I; E: lambda V; F: not connected
Operating Tip Temperature	750 °C to 850 °C
Maximum Tip Temperature	950 °C
Maximum Tip Rate of Change	65 °C/second
Heater Voltage	10 V ± 0.5 V
Heater Current	1800 mA
Thread	M18 x 1.5 mm
Seal	22 mm Hex
Weight	80 g
Connector	AS6-10-98PN
Max Tightening Torque	40 Nm

Details of the other sensors fitted to the engine (that are not already discussed) are given in Table 5:

*Table 5 - Details of Engine Sensors*

Sensor	Model	Description
Engine position	Ford Zetec Type [152]	2-pin (non-polarised)
EGT	Generic [153]	2-wire (yellow: positive; red: negative)
MAP	Cosworth Style [154]	3 bar, 3-pin (1: 5V ref.; 2: GND; 3: signal)
Air temperature (x2)	FAE 33160 [155]	Thermistor NTC, 2 pin
Coolant temperature	FAE 33595 [155]	Thermistor NTC, 2 pin
Bypass valve position	Bosch Style [156]	3-pin (1: 5V; 2: signal; 3: GND)
Oil pressure	Lucas SOB807 [157]	Switch, 1 pin, 0.2 – 0.4 bar (non-polarised)
GDI Pressure	Bosch 0261545113	3-pin

Note the MAP sensor is specified as 2 bar boost, hence 3 bar in the above for absolute pressure. The 36-1 timing wheel in Figure 67 is affixed to the back of the front pulley, which is fixed to the front of

the output shaft by a taper-locking coupler (16 mm x 24 mm, see [158]). This pulley was machined largely using a manual lathe, to fit the belt profile of the blower. Figure 68 shows a top view of the engine when it is nearly fully assembled. An exhaust temperature sensor is shown at position 1 and the starter motor at position 2. The scavenge pressure sensor, shown at position 3, is fastened on top of the blower mount and to two bolt holes in the front engine case – this is why the M6 bolts for the former were countersunk. The corresponding hose (not shown) connects to a small hose-barb situated immediately behind the 3-pin connector. A thermostat housing is shown at position 4, though as previously noted a thermostat was not eventually used. This was because of a fitment issue, and it was decided that for the purposes of initial engine testing (i.e. proving the engine works) a thermostat was not necessary and could be added later.

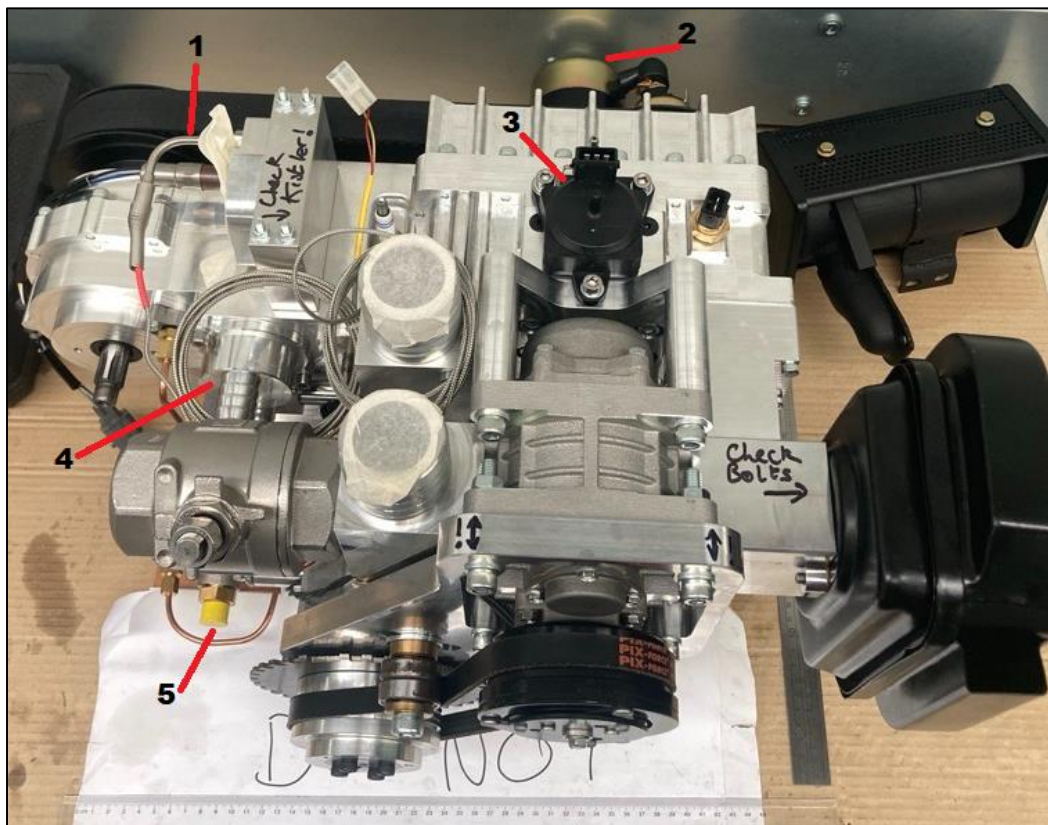
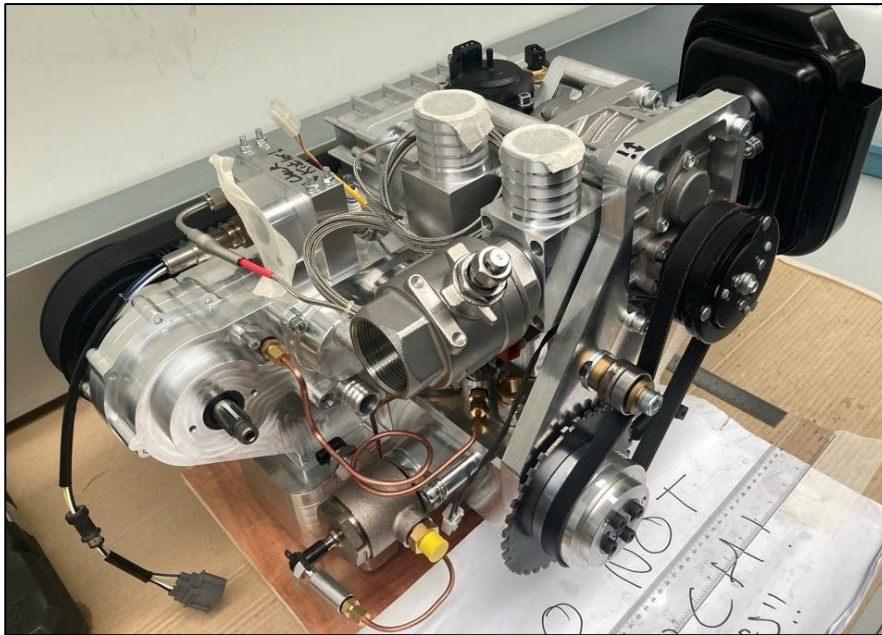


*Figure 68 - Top View of the Engine when Close to Completion*

Also shown in Figure 68 is the location of the GDI pump outlet (5), that is covered by a yellow cap whilst not in use. To this coupling mounts a custom-made high-pressure fuel line, which was one of the last components manufactured due to it needing to navigate around various other engine components. The exhaust silencer can be seen next to engine at the top of Figure 68, and is of the type used on some small industrial diesel engines; see for example [159].

Figure 69 shows a general overview of the engine when close to completion, where the GDI pump is much clearer to see. Also visible is the oil distribution block immediately underneath the large ball

valve, as well as the positive crankcase ventilation ('PCV') valve which is a simply a one-way valve typical of that used in domestic applications; see for example [160].



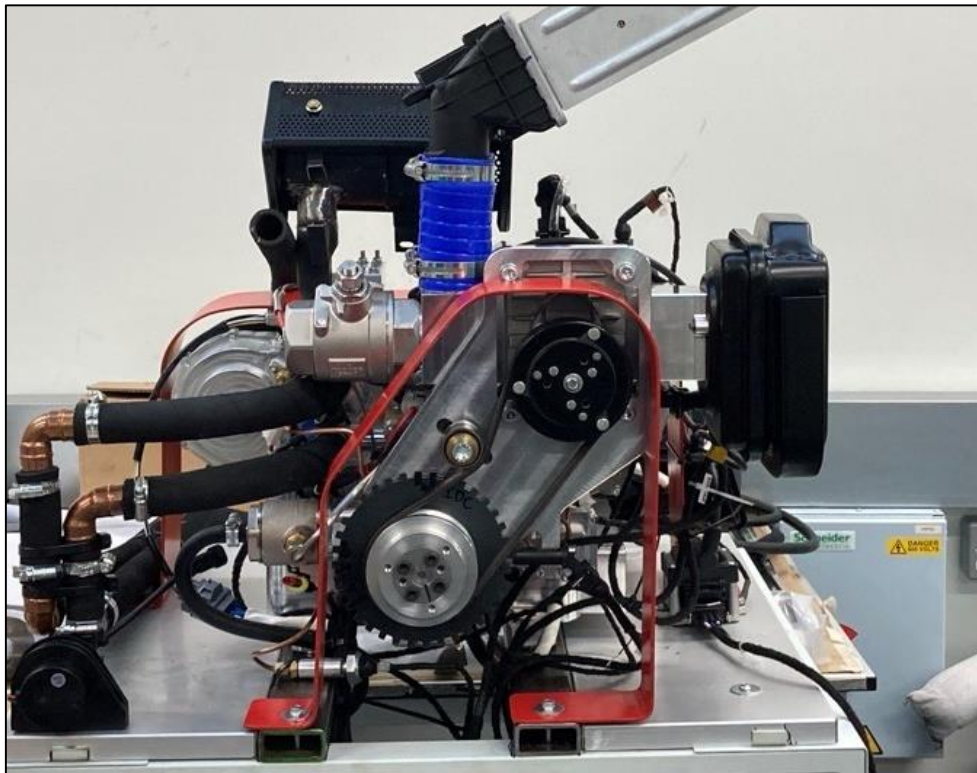
*Figure 69 - General Overview of the Front of the Engine when close to Completion*

Figure 70 shows a rear view of the engine. The exhaust silencer was modified so that the outlet points backwards, as well as better clearing the hoses for the charge air cooler.



*Figure 70 - Rear View of the Engine on a Running Stand*

The engine has been mounted to a running stand in preparation for the first firing (see chapter 7). Notice that the output shaft extends beyond the back of the flywheel – the purpose of this is to allow for a coupling to be added to the engine when required, without having to modify the flywheel – a key requirement of the engine identified earlier. This could be achieved through using the same type of taper lock bush as those used in the timing train, for example. In the background, the top of the (large) charge air cooler can just be seen, this of the automotive type (see [161]). Figure 71 shows the front of the completed engine. Here, the wiring harness, coolant lines, coolant pump, ignition coil and so on have been added to the stand. Two belt guards were also added and are made of 3 mm steel plate; the rear belt guard is partly visible in the background.



*Figure 71 - View of the Completed Engine on the Running Stand.*

## **5.8 Summary Comments on Engine Design**

In this chapter, the design of the engine has been detailed, in accordance with the identified criteria that were noted as important. It is a small engine, making it easier to transport to test facilities, and includes features such as jack screws to facilitate disassembly and maintenance. A built-in oil pump provides lubrication to all major components of the engine, supplied by a large sump at its base, and fuel is injected directly into the cylinder of the engine using an incorporated GDI pump: every mechanical component of the engine is driven by the engine itself including the scavenge blower. It therefore does

not need any external power beyond a typical 12 V automotive-style battery, which is used to drive ancillary components such as a water pump, ignition coil, fuel feed pump, ECU and so on. Provision for a cylinder pressure transducer is also included to facilitate data acquisition, and the output shaft extends beyond the flywheel to enable coupling the engine to a load.

Selected images and drawing views of the engine/engine components have been included, but due to the extent of the work performed two appendices have been used to avoid excessive length. Detailed engineering drawings of many important engine components are included in Appendix A, including of the modifications required to some of the commercial components used. Appendix B includes additional pictures of components, as well details of some of the manufacturing and assembly processes.

## **6. Engine Simulation**

This chapter describes 3D CFD simulations that were performed of the engine. The aim of these simulations was to solve an engineering problem of programming the engine ECU to inject the correct amount of fuel, with no empirical fuelling test data for the prototype. Because the ECU could use a lookup table based on engine speed and scavenge pressure, the approach chosen was to simulate the air-side engine geometry to estimate the amount of air trapped within the cylinder of the engine at an array of different engine speeds and scavenging pressures. The results were then used to populate a ‘fuel table’ similar to that used in the ECU, wherein an estimation of the required fuel at a given engine speed/scavenge pressure condition could be obtained via a simple calculation using the appropriate air/fuel ratio [5]. Following this, the accuracy of the motored simulations was evaluated by performing targeted fuelled engine simulations, and evaluating how closely the in-cylinder equivalence ratio matched what was expected given a specified fuel mass. Mesh dependency for both the motored and fuelled simulations was assessed using the 3000 rpm, 150 kPa scavenge pressure condition.

CONVERGE® CFD was used for the simulations. This software generates the (cartesian) volume mesh at runtime and can control flow between different regions of a flow domain based upon the proximity of user-specified surface mesh geometries [162], [163], [164], [165].

### **6.1 Structural Geometry**

The following geometry was used in all the simulation cases and closely reflects that of the air-side surfaces of the cylinder block and liner assembly detailed in section 5.2, but with the addition of an injector tip and spark plug tip to seal the flow domain. Geometries external to the cylinder block, such as the surge chamber, are not included in the simulation; this is discussed in section 6.2.

#### **6.1.1 Intake and Exhaust Porting**

Figure 72 and Figure 73 show a cross section of the (airside) engine cylinder and porting geometry, as well as end views of the intake and exhaust galleries in CONVERGE Studio®. Like all the surface geometry in the simulation, the surface meshes are composed of triangular elements, but the individual triangle edges have been hidden for the sake of clarity since the triangles themselves are numerous and are very small. In Figure 72 the stretched intake port shape discussed in section 5.2 is easy to see, whereas in Figure 73 it is much clearer that there is a big difference in the widths of the main intake and exhaust ports [163].

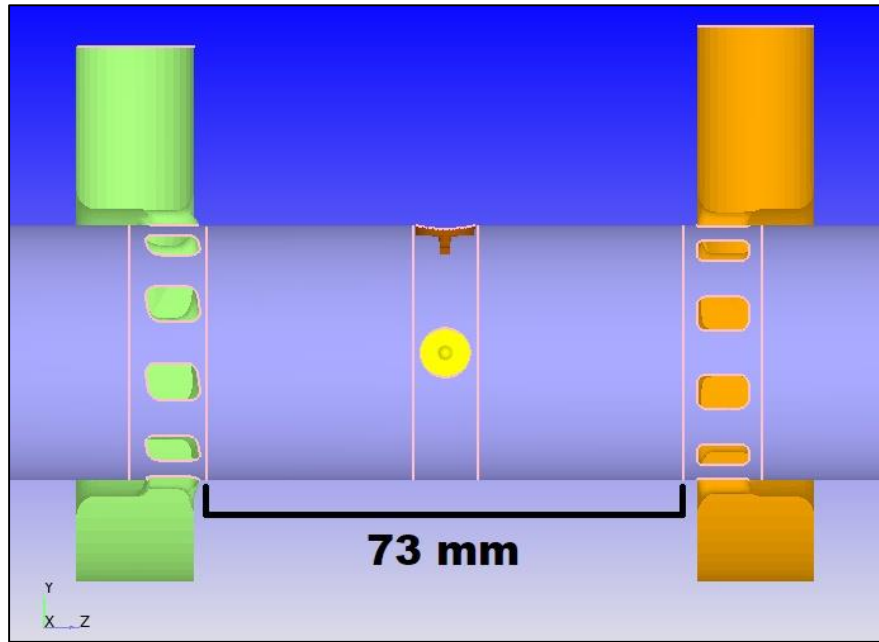


Figure 72 - Cross Section Showing Cylinder (purple), Intake Gallery (green) and Exhaust Gallery (orange)

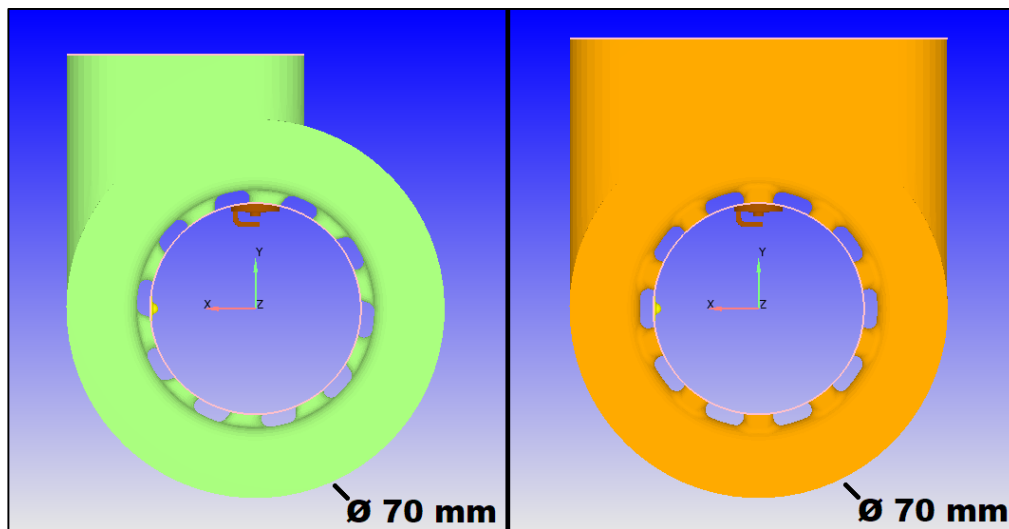
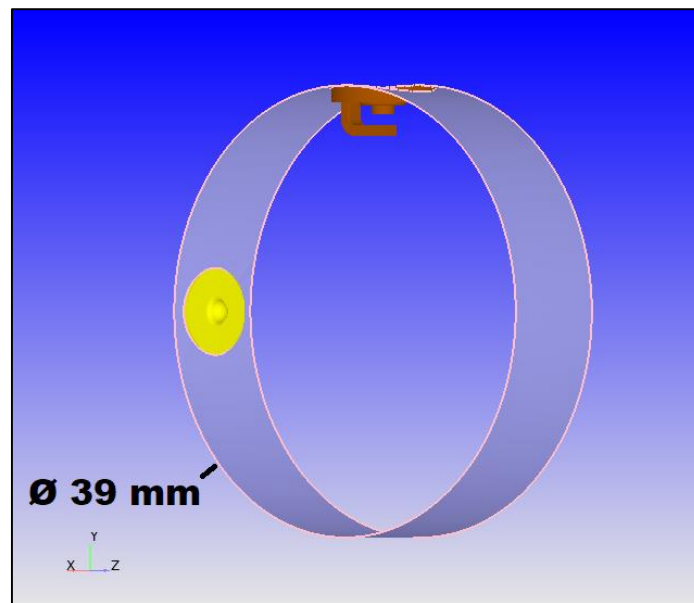


Figure 73 – Left: View of Intake Gallery from Cylinder End; Right: View of Exhaust Gallery from Cylinder End

Recall that the intake is intended to generate swirl, but the exhaust is intended to maximise the volume into which the heated gases can flow at EPO to aid scavenging. This is why the liner exhaust ports are also wider than the intake ports, given the increased volume of heated gases.

### 6.1.2 Injector and Spark Plug

As was described in section 5.2, the spark plug is positioned in the axial centre of the cylinder by necessity, with the tip protruding just past the inner liner surface. It is expected that the maximum gas velocities at the time of ignition will be close to the inner surface of the liner, which may aid early flame propagation. Figure 74 shows an isolated cross-section of the centre of the engine cylinder, indicating the approximate positions of the spark plug and the injector tip, which is also located in the axial centre of the cylinder [163].



*Figure 74 - Isolated View of Central Part of Cylinder (purple), with Injector Tip (yellow) and Spark Plug Tip (brown)*

The injector and spark plug are only approximations of what a real injector tip and spark plug tip look like. This is not unreasonable given the fact that the real shape of both may vary depending on the manufacturer and the particular specification. Additionally, the spark plug tip may be ‘clocked’ in any position when it is tightened in the real engine, and the injector tip position is dependent on where it seats (which could be altered through shims or by other means). As in the real engine (see Figure 43), when viewed from the intake end of the liner, the radial position of the injector is 90 degrees anticlockwise from the spark plug. In this manner, a second diametrically opposed injector could be added later with less risk of spray directly impinging the spark plug electrodes. However, the second injector tip has not been included here to reflect the initial prototype testing strategy that will be employed, where only one injector will be used. It is noted however that the connecting tube for the cylinder pressure transducer has not been included, due to its very small size - for the purposes of identifying the trapped mass of air in the cylinder, such a miniscule volume (in comparison to the rest of the cylinder) would be of essentially no interest.

### 6.1.3 Complete Geometry

Figure 75 shows the complete geometry used for simulation where the pistons, which as noted in section 5.2 feature flat crowns with chamfered edges, are visible [163].

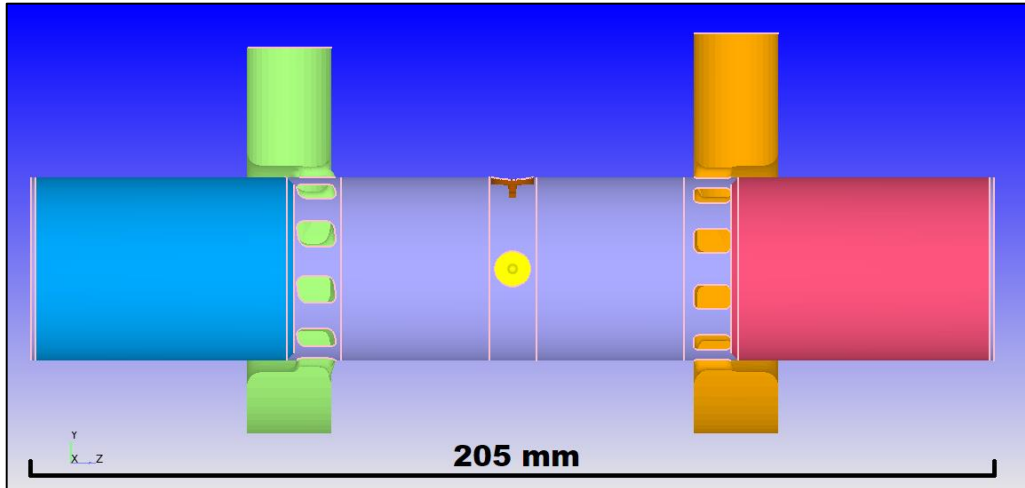


*Figure 75 - Simulation Geometry; Cylinder (Purple, cutaway), Intake Gallery (Green, cutaway), Exhaust Gallery (Orange, cutaway), Intake Piston (Blue), Exhaust Piston (Pink), Injector Tip (Yellow) and Spark Plug Tip (Brown)*

Note that for the purposes of simulation the piston crowns and skirts are separate boundaries, but for ease of viewing they are shown of the same colour in Figure 75. Not visible in the above are the intake, exhaust, cylinder end and piston bottom boundaries [163].

### 6.2 Boundary Conditions

Configuring the simulations required some simplifications of the boundary conditions associated with the geometry above, particularly considering what they were intended to achieve. For example, when the engine is running the pressure in the surge chamber will likely fluctuate over each engine cycle but attempting to model this by including the surge chamber, scavenge blower, bypass valve, and charge cooler (and associated ducting) in the simulation geometry would markedly increase the computational domain. This is only exemplified by the fact that the blower is not timed to the engine – recall that it has an electromagnetic clutch to connect and disconnect it from the drive belt. Therefore, it would not be justifiable to simulate a blower geometry that is timed to the engine when in reality it is not. Accordingly, a less computationally expensive (and more justifiable) approach was required. For the pressure boundary condition at the intake, this was simply to consider what the average pressure in the intake gallery is over one engine cycle, to return a constant value. This is why the simulation intake boundary is located at the top of the intake gallery in Figure 75, since that is the meeting point of the

surge chamber and intake port gallery. This has the effect of reducing the computational domain while assuming that the blower, surge chamber and bypass valve are essentially just a source of scavenging pressure. The pressure boundary condition was therefore configured as a series of fixed scavenging pressures from 110 kPa to 180 kPa in 10 kPa increments, and by similarly defining the engine speeds as a series of 8 values from 1500 rpm to 5000 rpm in 500 rpm increments, an 8 x 8 array of values was generated. The simulation results of this array can then be used to estimate the required fuel for each condition using Eq. 16:

$$m_f = m_a * \frac{1}{\lambda}, \quad \text{Eq. 16}$$

where  $m_f$  is the mass of fuel,  $m_a$  is the trapped air mass, and  $\lambda$  is the air/fuel ratio [5]. A further advantage of this approach is that it closely reflects a speed-density type fuel map – see for example [166].

The minimum rpm value of 1500 rpm reflects the small size of the engine at roughly 79 cm<sup>3</sup> trapped volume, compounded by the blower-scavenged nature. This is because of the performance map of the blower (see section 5.6), where the maximum pressure ratio is effectively limited to 1.1 at 1000 rpm. A higher idle speed will also help ensure the oil pump maintains adequate flow to the oil-jets lubricating the underside of each piston as well as each crankshaft. Hence, speeds lower than 1500 rpm were considered to be for starting only, and the ECU has specific functions for calculating the fuel required for starting; see LifeCAL software for more information [167].

A similar simplification was also required for the intake temperature boundary condition because the blower discharge will be at a higher temperature than ambient [5]. The charge cooler will remove some of this heat, though the bypass valve complicates matters by displacing some of the incoming (cooler) atmospheric air at the blower intake. However, the surge chamber is over 700 cm<sup>3</sup> in volume – significantly larger than the swept volume of the engine – so intake air may reside there for several engine cycles before it reaches the intake gallery and be warmed by the surge chamber surfaces. Since these surfaces are part of the main engine structure, the air temperature was set at a value of 350 K. This is close to a known thermostat opening temperature of 78 °C, and was chosen because the prototype is water-cooled, on the basis that the main engine structure will approach coolant temperature [141].

For the intake species, air is represented as 23.3% oxygen ('O<sub>2</sub>') and 76.7% nitrogen ('N<sub>2</sub>') (CONVERGE recommended values). As there are no combustion events, exhaust backflow is of much less interest in these motored simulations, so the species were rounded to the nearest whole percent at 23% O<sub>2</sub> and 77% N<sub>2</sub>. The exhaust outlet temperature and pressure boundary conditions have been set at 800 K and 101325 Pa respectively; these were estimated with guidance from CONVERGE example case literature, as were the other surface boundary conditions listed in Table 1 [162], [163].

Table 6 - Geometry Boundary Conditions. Note that 'Direction' represents the normal direction of the piston crowns, and 'Phase' the difference between crankshaft position.

Name	Type	Movement	$\Theta$ (Direction)	$\Phi$ (Phase)	Temperature
Cylinder	Wall	Fixed	N/A	N/A	400 K
IntakeCrown	Wall	Translating	0 °	0 °	400 K
IntakeSkirt	Wall	Translating	0 °	0 °	400 K
IntakeBottom	Wall	Translating	0 °	0 °	400 K
ExhaustCrown	Wall	Translating	180 °	-18 °	450 K
ExhaustSkirt	Wall	Translating	180 °	-18 °	450 K
ExhaustBottom	Wall	Translating	180 °	-18 °	450 K
INPortRing	Wall	Fixed	N/A	N/A	350 K
EXPortRing	Wall	Fixed	N/A	N/A	450 K
Sparkplug	Wall	Fixed	N/A	N/A	550 K
Injl	Wall	Fixed	N/A	N/A	400 K
CylinderEnds	Wall	Fixed	N/A	N/A	400 K

It is important to re-emphasise that all of the above estimations, including those guided by CONVERGE and other literature, were made because there are no empirical test data for the engine. The simulations were performed to guide the configuration of the engine ECU, such that empirical data can be gathered. Indeed, as was shown in chapter 5, the prototype has the provision for air temperature sensors for the blower discharge, the main surge chamber, and the exhaust, as well as a pressure sensor attached to the surge chamber, and a cylinder pressure transducer. Once the engine has run, data from these sensors could naturally be used to configure more accurate simulations.

### 6.3 Flow-Control, Initial Conditions, and Simulation Duration

Because CONVERGE can closely mimic the port-sealing events in piston-ported engines, the flow domain was split into three distinct regions: Intake, Cylinder and Exhaust. By correctly configuring the seal geometry (i.e., around the cylinder ports and piston crowns), as the pistons move, the solver controls flow between these regions based on the proximity of the cylinder crowns to the ports. At the start of the simulation at -272 CAD, the intake and exhaust ports are closed and there is no connection between the three regions. At this time, both pistons are moving outwards, and EPO is imminent; -180 CAD represents outer dead centre for the intake piston during the first engine cycle. The initial species, pressure, and temperature conditions in all three regions are summarised in Table 7 [163], [164], [165], [168].

Table 7 - Initial Conditions for Regions at -272 CAD

Region	Pressure	Temperature	Species Mass Percentage
Cylinder Volume	600,000 Pa	1200 K	N <sub>2</sub> 76%, O <sub>2</sub> 11.3%, H <sub>2</sub> O 12.7%
Intake	Case Specified	350 K	N <sub>2</sub> 76.7%, O <sub>2</sub> 23.3%
Exhaust	101,325 Pa	800 K	N <sub>2</sub> 76%, O <sub>2</sub> 11.3%, H <sub>2</sub> O 12.7%

The species in both the cylinder and exhaust regions reflect a burned mixture for hydrogen/air, based upon data from the CONVERGE example case library [163]; the species are N<sub>2</sub>, O<sub>2</sub>, and water ('H<sub>2</sub>O'). By beginning the simulation shortly before EPO and artificially increasing the in-cylinder pressure and temperature, the result is an initial exhaust blowdown at EPO. The purpose of the blowdown was to rapidly establish an in-cylinder motion of gases from an initially stationary in-cylinder flow-field, because in the real engine there will likely be significant in-cylinder motion of the burned mixture before EPO. However, this approach may introduce large velocity gradients at first, so after the initial blowdown each case was run for a total of three complete engine cycles until 900 CAD. This allowed time for any resulting mathematical instabilities (and any other errors), to gradually disperse, whilst balancing the similarly important consideration of not exceeding the available computational memory; [168]. The simple burned mixture also provides a useful method of monitoring the scavenging performance by reviewing the water H<sub>2</sub>O mass concentration in the cylinder between cycles. Although this burned mixture is based on models for hydrogen combustion, H<sub>2</sub>O, O<sub>2</sub> and N<sub>2</sub> are common species to many combustion reactions. Additionally, the precise mixture composition was of less interest than the change in H<sub>2</sub>O mass concentration per cycle [163]. Data files for material properties were sourced from the CONVERGE example case library; these are based upon an enhancement on a skeletal kinetic model by Liu *et al.* for primary reference fuel oxidation [163], [169].

#### 6.4 RANS Equations

CFD simulations are built upon the conservation of mass, momentum, and energy [170]; for a general introduction, see [171] and [172]. Using CONVERGE, in this work a Reynolds-averaged Navier-Stokes ('RANS') method was implemented [162]. In compressible form, the RANS equations, which govern the conservation of both mass and momentum are given by [164]:

$$\frac{\partial \bar{\rho}}{\partial t} + \frac{\partial \bar{\rho} \tilde{u}_j}{\partial x_j} = 0, \quad \text{Eq. 17}$$

and

$$\frac{\partial \bar{\rho} \tilde{u}_i}{\partial t} + \frac{\partial \bar{\rho} \tilde{u}_i \tilde{u}_j}{\partial x_j} = -\frac{\partial \bar{P}}{\partial x_i} + \frac{\partial}{\partial x_j} \left[ \mu \left( \frac{\partial \tilde{u}_i}{\partial x_j} + \frac{\partial \tilde{u}_j}{\partial x_i} \right) - \frac{2}{3} \mu \frac{\partial \tilde{u}_k}{\partial x_k} \delta_{ij} \right] + \frac{\partial}{\partial x_j} (-\bar{\rho} \tilde{u}_i' \tilde{u}_j'), \quad \text{Eq. 18}$$

where  $\rho$  is density,  $u$  is fluid velocity,  $P$  is pressure,  $\mu$  is dynamic viscosity, and  $\delta_{ij}$  is the Kronecker delta. Here, tilde is used to denote properties that have been Favre averaged, which in the case of fluid velocity is defined as [164]:

$$\tilde{u}_i \equiv \frac{\overline{\rho u_i}}{\bar{\rho}}, \quad \text{Eq. 19}$$

where the overbar represents Reynolds averaged values. Favre averaging is a density-weighted average and is useful in situations where there are variations in density, such as an internal combustion engine in which there is compression and expansion of the cylinder volume [5], [173]. The argument of the rightmost term in Eq. 18 represents the effect of turbulence, and involves Reynolds stresses [164]:

$$\tau_{ij} = -\bar{\rho} \tilde{u}_i' \tilde{u}_j'. \quad \text{Eq. 20}$$

To model the Reynolds stresses, a  $k$ - $\varepsilon$  turbulence model was chosen. Like other RANS methods, this models the Reynolds stresses by assuming that the mixing caused by turbulence introduces an effective viscosity  $\mu_t$ , that acts in addition to the dynamic viscosity, defined as [5], [164]:

$$\mu_t = C_\mu \rho \frac{k^2}{\varepsilon}, \quad \text{Eq. 21}$$

where  $C_\mu$  is a model constant,  $k$  is turbulent kinetic energy, and  $\varepsilon$  is the rate of dissipation of turbulent kinetic energy [5], [164]. In these simulations, the Rapid Distortion RNG  $k$ - $\varepsilon$  turbulence model proposed by Han and Reitz was implemented [174]. In this model, the Reynolds stress tensor is written as [164]:

$$\tau_{ij} = -\bar{\rho} \tilde{u}_i' \tilde{u}_j' = 2\mu_t S_{ij} - \frac{2}{3} \delta_{ij} \left( \rho k + \mu_t \frac{\partial \tilde{u}_i}{\partial x_i} \right), \quad \text{Eq. 22}$$

where  $S_{ij}$  is the mean strain rate tensor [164]:

$$S_{ij} = \frac{1}{2} \left( \frac{\partial \tilde{u}_i}{\partial x_j} + \frac{\partial \tilde{u}_j}{\partial x_i} \right), \quad \text{Eq. 23}$$

and both  $k$  and  $\varepsilon$  have their own transport equations, which depend on the particular model employed [164]. In the interest of brevity, the reader is referred to appropriate sources for more detail on the  $k$ - $\varepsilon$  and other RANS/CFD models, including the conservation of energy and other transport equations which are not discussed above [5], [164], [171], [172]. For information on additional conservation laws that

are applicable to internal combustion engine simulation, particular attention is drawn to Internal Combustion Engine Fundamentals, 2<sup>nd</sup> Edition [5], and CONVERGE literature [164].

## 6.5 Volume Mesh and Timestep

In these simulations the volume mesh is generated by the solver at runtime, but the mesh parameters including base grid size, embedded cells and adaptive mesh refinement ('AMR'), need to be appropriately specified. The base grid size, which affects both AMR and embedded cells, was set at a resolution of 3mm x 3mm x 3mm. Fixed embeddings were specified to seed smaller cells of 0.75 mm on both piston crowns, as well as an arbitrarily defined cylindrical region, which encompasses the engine cylinder and the liner ports. The higher resolution in these areas is important for the geometry sealing (i.e., piston porting) processes, and was further guided by an example case in CONVERGE Studio ® [163], [164], [165]. Similarly, AMR (configured using the input file 'amr.in') was enabled based on a velocity gradient of 3 m/s across a cell, with a maximum embedding level of 2 (cell size 0.75 mm) and a maximum cell count of 100,000. Because the fixed embeddings resulted in a cell-count in excess of 100,000 throughout the simulation, AMR would not embed any further [164], [168]. However, by including the 'placeholder amr.in' file, were it found excessive gradients caused poor convergence, AMR could be activated by simply changing these values without having to re-export the entire case set-up. For example, at higher engine speeds and scavenging pressures the velocity gradients might become a problem, where they are not at lower engine speeds and scavenge pressures. The maximum simulation timestep was set at 1E-05 seconds, the minimum timestep 1E-08. For more information on configuring simulations in CONVERGE®, the reader is referred to the appropriate literature [164], [165].

### 6.5.1 Mesh Dependency Analysis

The influence of the volume mesh cell size on the simulation results was assessed, using the trapped mass value (the result of interest). The 3000 rpm 150 kPa case was chosen due to its largely central location in the fuel table, and the size of the volume mesh cells varied. For this purpose, all mesh embeddings were removed and AMR disabled completely, such that the volume mesh cells were consistent throughout the domain. Also, because these simulations were run later on another part of the HPC cluster at UEA due to resource constraints, the 'default' configuration (3 mm and 0.75 mm embeddings, as specified in section 6.5) was rerun to eliminate any effects caused by the difference in computation cores.

For convenience, Table 8 shows the resulting mesh configurations that were evaluated. Note that 'embedding layers' is only applicable to the surface embeddings (i.e. the piston crown boundaries),

where an embedding layer denotes a layer of cells of the specified size embedded upon the identified surfaces, for more information the reader is referred to CONVERGE® literature [164], [165].

Table 8 - Mesh Dependency Simulation Cases

Simulation No.	Bash Mesh	Embeddings	Embedding Level	Embedding Layers
Default	3 mm	Yes	2 (0.75 mm)	2
NE_6mm	6 mm	No	N/A	N/A
NE_3mm	3 mm	No	N/A	N/A
NE_1.5mm	1.5 mm	No	N/A	N/A
NE_0.75mm	0.75 mm	No	N/A	N/A
NE_0.375mm	0.375 mm	No	N/A	N/A

Figure 76 shows the variation in 3<sup>rd</sup> cycle trapped mass as the base mesh size is decreased from 6 mm to 0.375 mm, with no embedding, as well as a line showing the trapped mass value from the rerun 'Default' simulation:

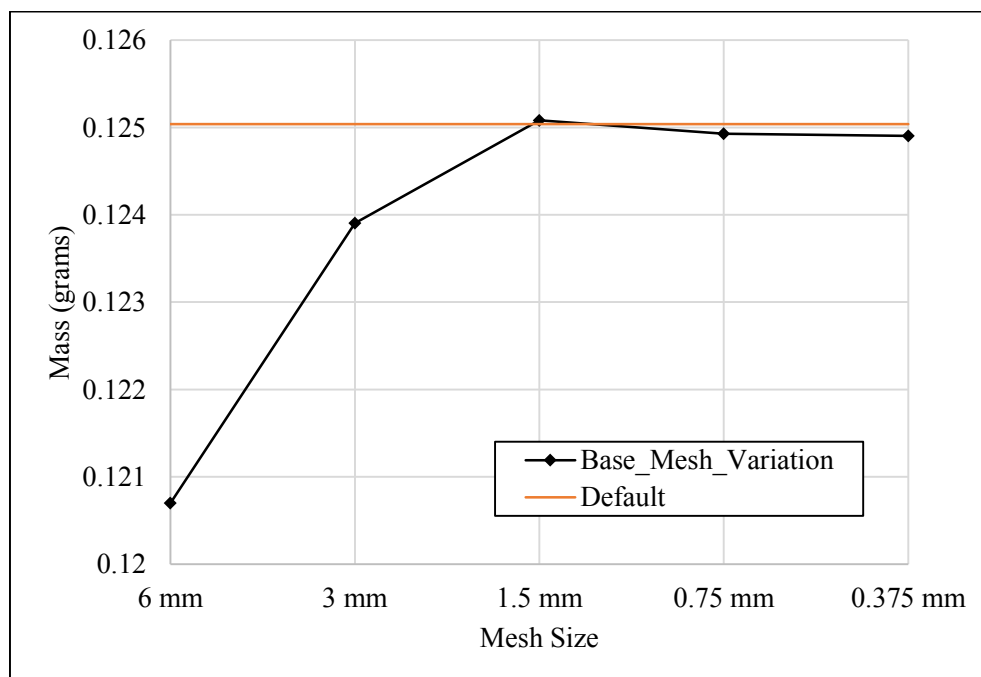


Figure 76 - Trapped Mass Variation with Mesh Size, and Default Configuration

As the mesh size is halved from 6 mm to 3 mm, the trapped mass increases by approximately 2.6 %, however when it is halved again from 3 mm to 1.5 mm, the trapped mass increases by approximately 0.9 %. As it is halved again to 0.75 mm, the difference is less than 0.2 % and from 0.75 mm to 0.375

mm, the difference is much less than 0.1 %. The default value is between that of the 1.5 mm and 0.75 mm value. Figure 77 and Figure 78 show the variation in maximum cell-count and computation time (runtime) respectively, as well as the ‘Default’ value as before. Aside from runtime of the 6 mm case (which is higher than for the 3 mm case) both increase significantly as the base mesh cell size decreases:

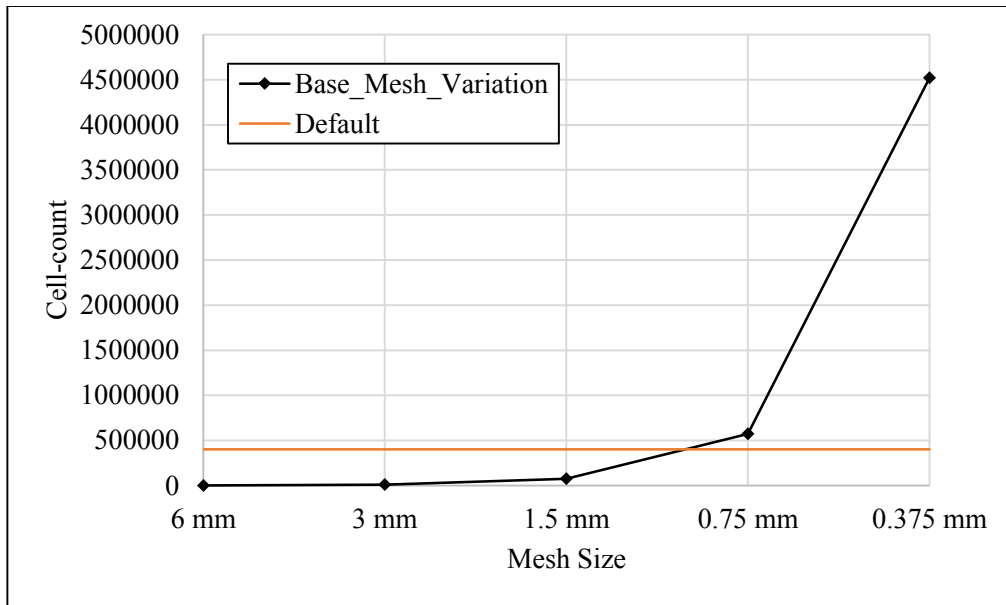


Figure 77 - Cell-Count Variation with Mesh Size, and Default Configuration

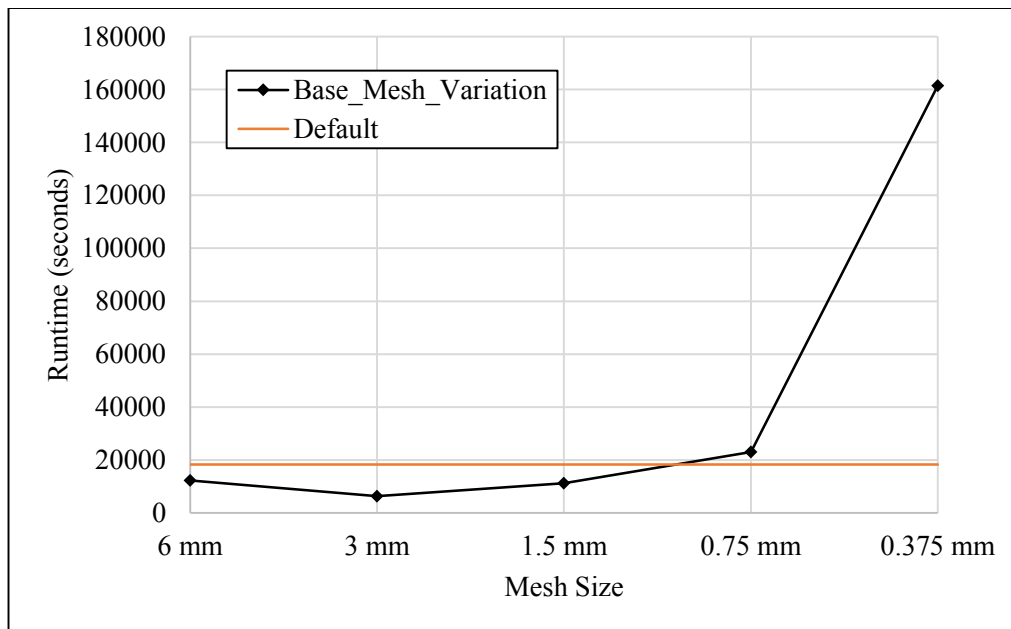


Figure 78 - Runtime Variation with Mesh Size, and Default Configuration

The maximum cell-count increases with decreasing cell size for obvious reasons, from less than 2000 cells at 6 mm to more than 4,500,000 at 0.375 mm. The maximum cell count with a base mesh of 0.75

mm is approximately 573,000, whilst for the default configuration it is roughly 30% lower at approximately 402,000 for a very similar result. The computation time reflects this: a little over 23,000 seconds for the 0.75 mm case and roughly 18,300 for the default case. The difference in cell-count and runtime is much greater when comparing to the 0.375 mm case, yet the results are still mesh independent to well-within 1% of each other. It can therefore be concluded that the default configuration suitably balances resource and time constraints, with the need for accuracy.

### 6.6 Motored Simulation Results

The following results are collated into data series delineated by engine speed for the first, second and third cycles. The trapped mass of all species in the cylinder is shown on a cycle-by-cycle basis in Figure 79 through Figure 81, followed by the remaining percentage of the original in-cylinder species mixture, also on a cycle-by-cycle basis, in Figure 82 through Figure 84. This percentage is in reference to the original trapped mass fraction of H<sub>2</sub>O at the start of each simulation as detailed in Table 7, which was kept constant for all simulations, and assumes a homogenous in-cylinder mixture.

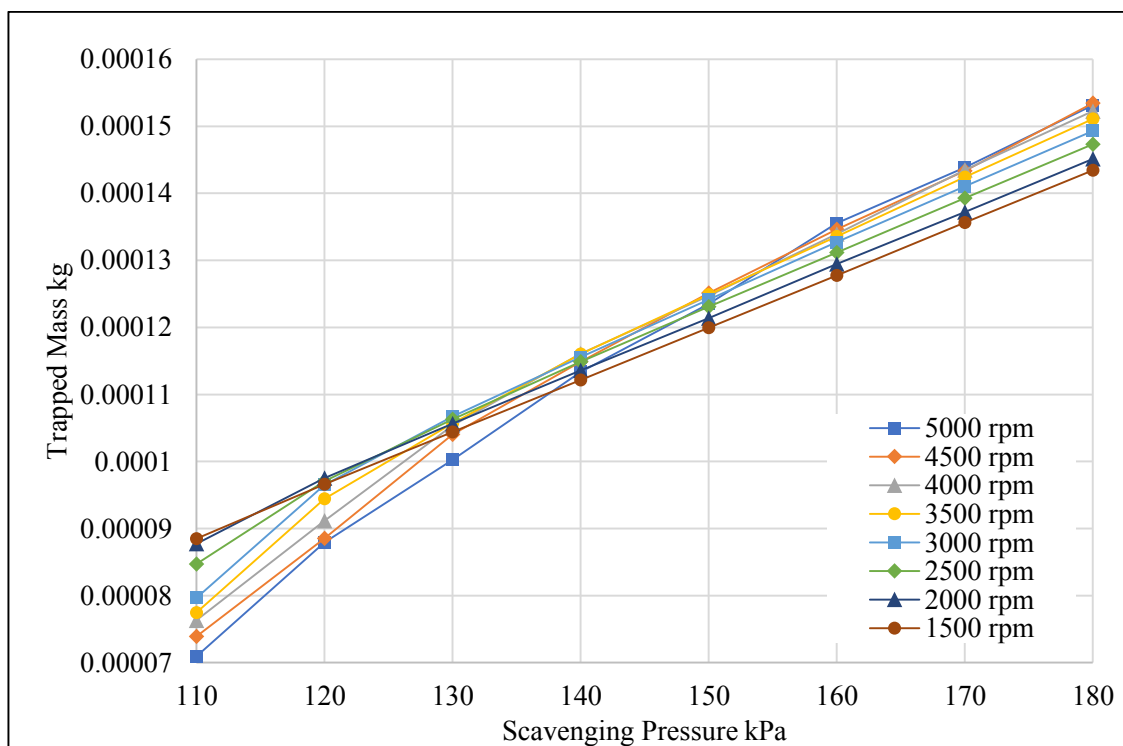


Figure 79 - In Cylinder Trapped Mass of all Species, 1st Engine Cycle

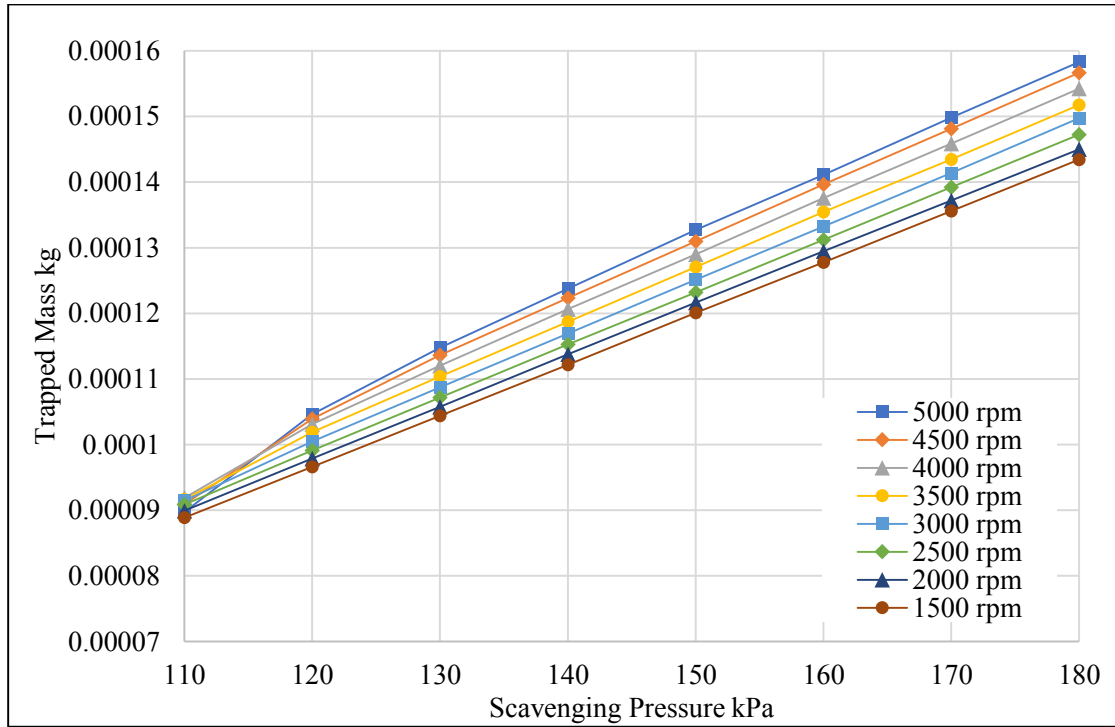


Figure 80 - In Cylinder Trapped Mass of all Species, 2nd Engine Cycle

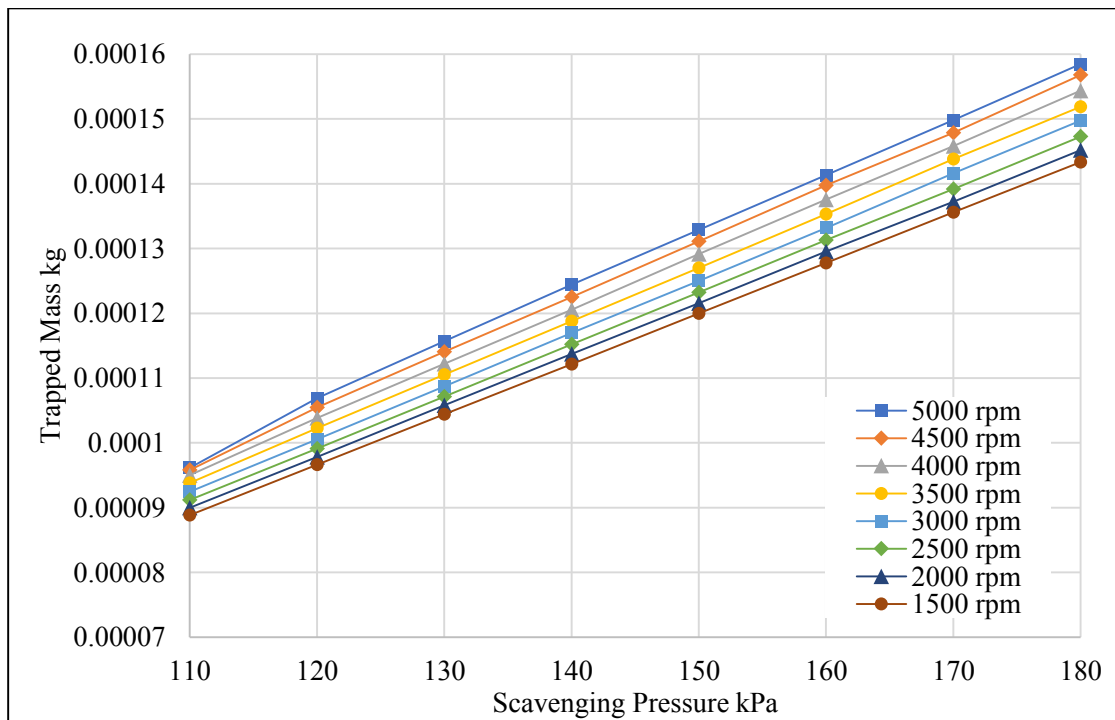


Figure 81 - In Cylinder Trapped Mass of all Species, 3rd Engine Cycle

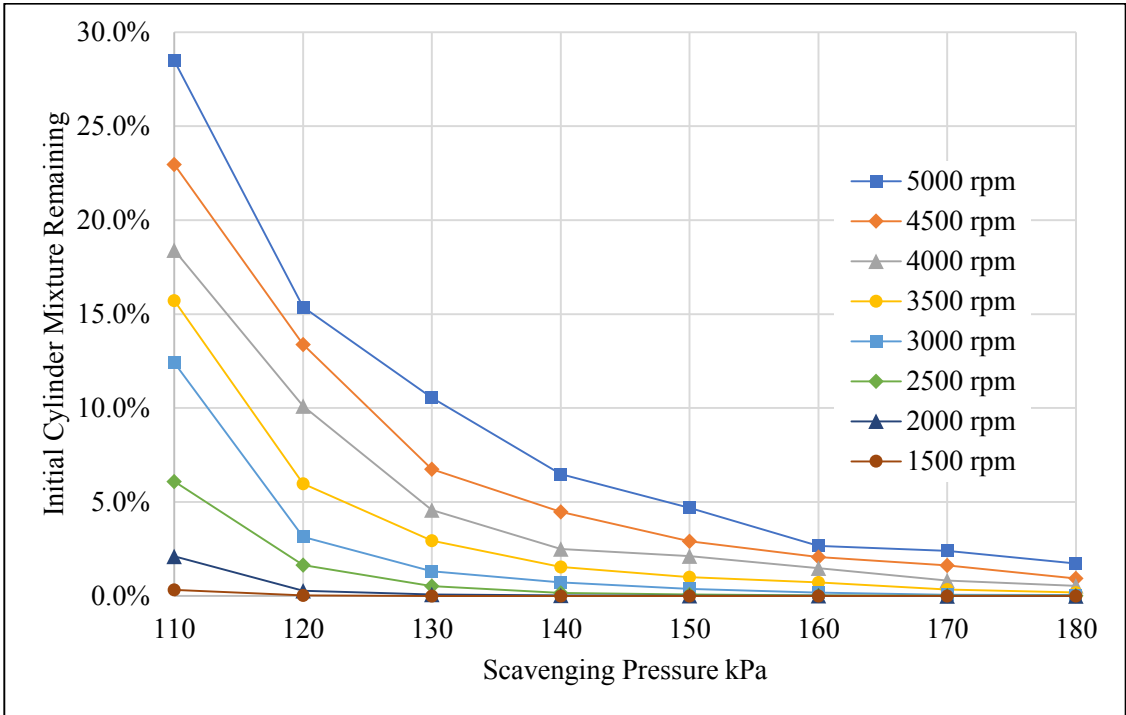


Figure 82 - 1st Cycle Initial Cylinder Mixture Remaining

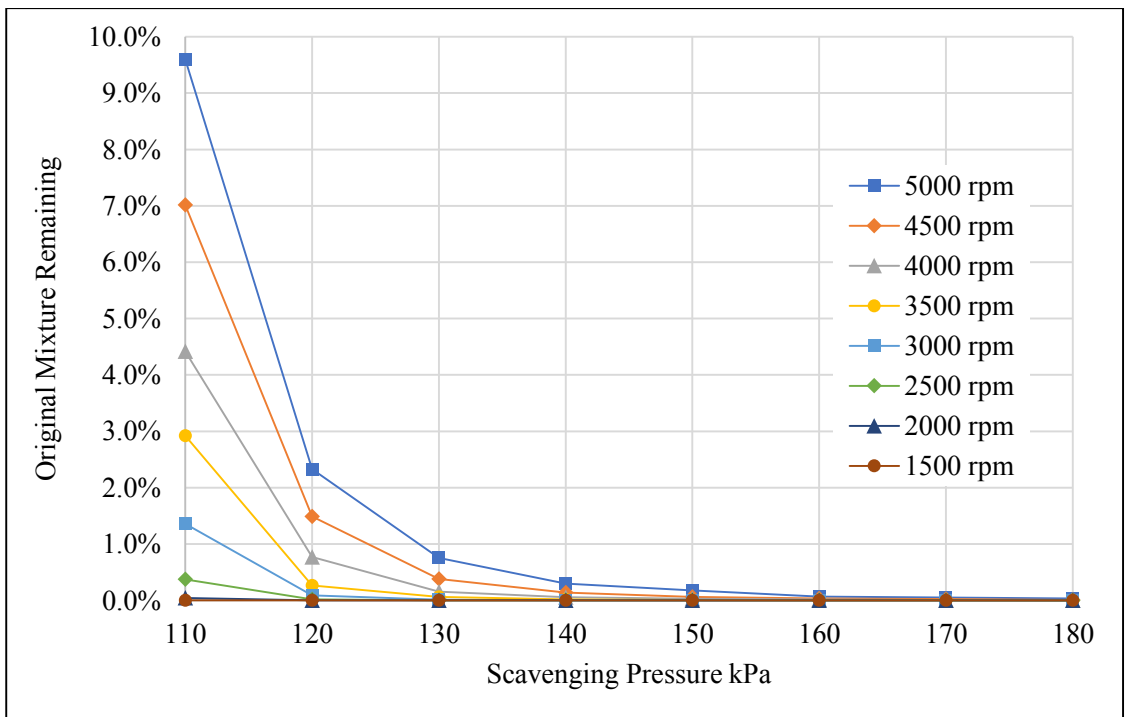


Figure 83 - 2nd Cycle Initial Cylinder Mixture Remaining

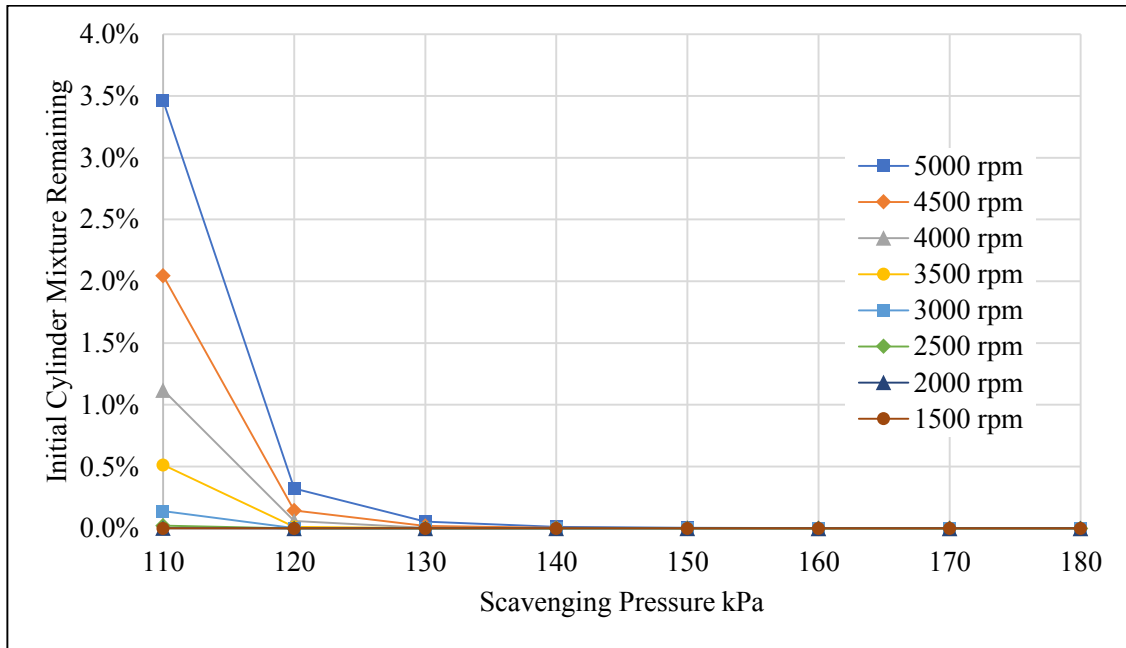


Figure 84 - 3rd Cycle Initial Cylinder Mixture Remaining

The progression of the in-cylinder trapped mass through each cycle highlights some interesting characteristics of the geometry. Beginning with the first cycle (which includes the initial blowdown), the trapped mass decreases as engine speed increases at lower scavenging pressures yet it increases with engine speed at higher scavenging pressures (although there is some crossover of the 4500 rpm and 5000 rpm curves). This might be explained by the fact that port open time decreases with engine speed, and the initial conditions for all the simulations were the same. Lower scavenge pressures take longer to influence in-cylinder motion and overcome any backflow caused by excess in-cylinder pressure at IPO, especially considering the initially stationary in-cylinder flow field. However, at higher engine speeds there is less time for intake backflow to occur after exhaust port closure ('EPC'), and (where the scavenge pressure is high enough) the trapped mass increases. Whilst the influence of the initial conditions cannot be ruled out after only one engine cycle, the remaining original in-cylinder mixtures broadly reflect these phenomena. After the first cycle the higher rpm curves indicate that at the lowest scavenge pressures of 110 kPa and 120 kPa, in the region of 15% - 30% of the original in-cylinder mass is still present after scavenging, but at 130 kPa scavenging pressure and above the scavenging performance appears to increase with more than 90% of the original mass cleared except at 5000 rpm. By the third cycle though, sufficient time has elapsed such that the initial conditions have largely dispersed, and the trapped mass now increases both with scavenge pressure and engine speed. However, for the 5000 rpm curve the drop in trapped mass from 120 kPa to 110 kPa is clearly greater than it is from 130 kPa to 120 kPa. There is also in excess of 1%, 2% and 3% of the original trapped mass present at 4000 rpm, 4500 rpm and 5000 rpm respectively at the 110 kPa data point even after three engine

cycles, yet less than 0.5% after three engine cycles above 120 kPa. Such behaviour is not unexpected, since a high engine speed and low scavenge pressure condition in a fuelled engine would be akin to a throttle being closed in a conventional four-stroke engine. In other words, in the OP2S engine, the scavenging performance is decreased at higher engine speeds and lower scavenge pressures. It should therefore be expected that in these ‘extreme’ conditions, the estimate of the required fuel may be excessive; indeed, this is demonstrated by later fuelled simulations in section 6.7.3.

Given that the motored trapped mass values appeared to have largely stabilised after three cycles (Figure 81), these values were used to generate a 2-dimensional (‘2D’) array. The maximum speed load point of 5000 rpm and 180 kPa scavenge pressure was used as a reference point, and all the other data points then evaluated against it and expressed as a percentage. The resulting array of trapped air masses effectively generates a ‘fuelling table’, which is presented in Table 9 (rounded to the nearest 0.1 %). By modifying Eq. 16, and using an appropriate air fuel ratio, any point in Table 9 can be used to approximate the required fuel with Eq. 24:

$$m_{fuel_x} = \frac{1}{100} * \frac{\%_x}{\lambda} * m_{air_{full}} \quad Eq. 24$$

where  $m_{fuel_x}$  is the mass of fuel required at datapoint ‘x’ (in kilograms (‘kg’)),  $\%_x$  is the air mass ‘percent of full’ indicated at that point in Table 9,  $m_{air_{full}}$  is the full load trapped air mass indicated in Table 9 (in kg), and  $\lambda$  is the desired air/fuel ratio; note that ‘x’ represents a coordinate, described by a speed and a scavenge pressure. As was stated earlier, the advantage of configuring the simulations as a series of fixed engine speeds and scavenging pressures is that the results can be easily delineated in a manner that closely reflects one of the approaches sometimes used in an ECU – recall an example being a popular aftermarket unit where values are similarly expressed as a percentage of full load [166].

Table 9 – Fuel Table: In-Cylinder Air Mass as a Percentage of Full Speed and Load

Trapped Air Mass % Full Load									
Full Load Trapped Air Mass in kg:						0.000158474			
Scavenge Absolute Pressure (Bar)	1.8	90.5	91.6	92.9	94.5	95.8	97.4	98.9	100.0
	1.7	85.6	86.6	87.8	89.4	90.7	92.0	93.3	94.5
	1.6	80.6	81.7	82.8	84.0	85.4	86.8	88.2	89.2
	1.5	75.7	76.7	77.8	78.9	80.2	81.5	82.7	83.8
	1.4	70.8	71.8	72.7	73.8	74.9	76.1	77.3	78.5
	1.3	65.9	66.8	67.6	68.6	69.7	70.8	72.0	73.0
	1.2	61.0	61.7	62.6	63.4	64.5	65.5	66.6	67.5
	1.1	56.1	56.8	57.5	58.3	59.2	60.0	60.5	60.7
		1500	2000	2500	3000	3500	4000	4500	5000
Engine Speed (RPM)									

The intrinsic value of Table 9 therefore is that it will significantly aid programming of the ECU fuel table to enable the physical testing of the prototype engine. Without it, because of the unusual nature of the prototype, the lack of any other data would have required a rather riskier approach of simply turning up the fuel until the engine fires, with an additional lack of any guidance on how fuel demand might vary depending on speed and load. However, it was already identified that at high engine speeds and low scavenge pressures the table may tend to over-estimate the fuelling requirements, particularly since in a fuelled engine there will be an exhaust blowdown event during each cycle. In order to evaluate this risk, a series of 9 fuelled simulations were carried out using methane ('CH<sub>4</sub>') as the fuel species.

## 6.7 Fuelled Simulations

Bearing in mind the computational constraints described in section 6.3, CH<sub>4</sub> was chosen as a fuel because it is the simplest of the alkane fuels and is gaseous [175]. Whilst the engine is designed to run on gasoline, simulating gasoline (using isooctane, say) would involve the additional complexity of modelling the injection and evaporation of fuel parcels, possible wall film effects, and so on. This is much more computationally expensive, and in the case of wall films and moving surfaces can be particularly challenging numerically. It is also unnecessary: the primary objective is to test the fuel table and not to accurately model engine performance. The fuel table is fuel agnostic, so it does not *in this context* matter what specific fuel is used; the primary objective is to understand if the required fuel mass predicted by the fuel table (to generate a desired equivalence ratio) is correct. Setting the air/fuel ratio to stoichiometric ( $\phi = \lambda = 1$ ) in Eq. 9 therefore makes the results easy to compare, too.

The simulation cases run were at 1500 rpm, 3000 rpm and 5000 rpm and at scavenge pressures of 120 kPa, 150 kPa and 180 kPa, to reflect the upper and lower limits of the fuel table. It will be noted that 110 kPa was not modelled; this is because it was already clear from the motored simulations that such a low scavenge pressure is unlikely to provide satisfactory results.

### 6.7.1 Configuration

Apart from the injector nozzle (and associated tube and inlet), the geometries and boundary conditions are exactly the same as those used for the motored simulations, as are the initial conditions in the intake, cylinder and exhaust regions, the settings for the base grid and fixed embeddings, and the data files for the material properties. The injector nozzle geometry was altered to incorporate a simple tube, located in its own region and with an intake boundary (similar, though not identical, to the air intake boundary) located at the end. The temperature of these additional boundaries was set at 400 K, the same temperature as the cylinder wall, and the initial conditions in the injector region were a species concentration of 100% CH<sub>4</sub> at a pressure of 101325 Pa (atmospheric). Figure 85 shows the modified

injector geometry in the centre of the cylinder; though not identical, the diameter and length of the tube were guided by a hydrogen case from the CONVERGE® example case library, and are approximately 2 mm and 3 mm respectively [163]:

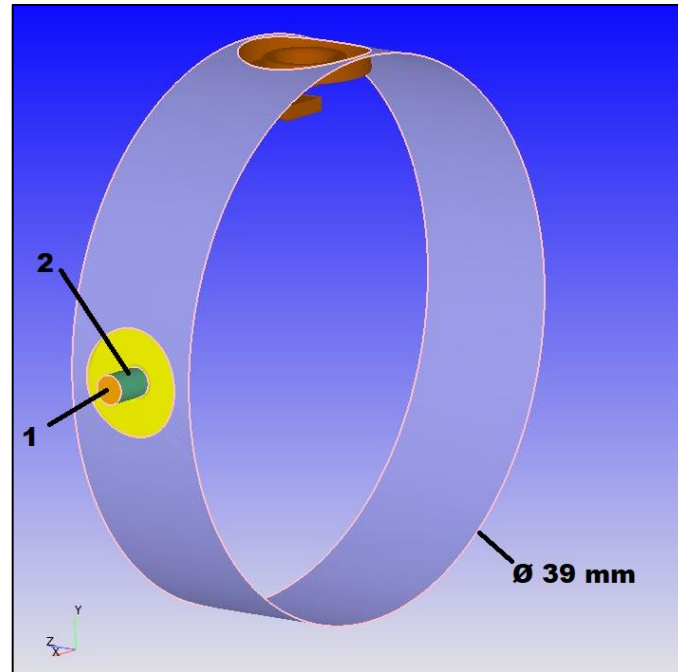


Figure 85 - Isolated View of Central Part of Cylinder (purple), with Injector Tip (yellow) and Spark Plug Tip (brown) and Injector Gas Inlet (1) and Injector Tube (2)

At the injector gas inlet boundary, due to the small diameter of it and the injector tube, the turbulence length scale was reduced by a factor of 10 to 0.3 mm (i.e. below 20% of the hydraulic diameter, as recommended by CONVERGE®). Also, instead of setting a fixed pressure, a mass flow-rate profile was specified, over a duration of 30 CAD. Similar to the same hydrogen example case, the profile incorporates an ‘on ramp’ and ‘off ramp’ each of which lasts for a duration of 1 CAD; the maximum flowrate occurs for (nominally) 28 CAD. The mass flowrate for 3000 rpm, 150 kPa is shown below in Table 10 as an example [163].

Table 10 - Fuel Gas Mass Flow Rate for 3000 rpm 150 kPa Fuelled Simulation

Timing Crank Angle Degrees	Flowrate kg/s
-113	0.000000000
-112.9	0.000435973
-112.8	0.000871947
-112.7	0.001307920

<b>Timing Crank Angle Degrees</b>	<b>Flowrate kg/s</b>
-112.6	0.001743893
-112.5	0.002179866
-112.4	0.002615840
-112.3	0.003051813
-112.2	0.003487786
-112.1	0.003923759
-112	0.004531008
-84	0.004531008
-83.9	0.003923759
-83.8	0.003487786
-83.7	0.003051813
-83.6	0.002615840
-83.5	0.002179866
-83.4	0.001743893
-83.3	0.001307920
-83.2	0.000871947
-83.1	0.000435973
-83	0.000000000
<b>Desired Mass kg</b>	<b>7.266221E-06</b>

The maximum flowrate, in this case 0.004531008 kg/s, incorporates a correction factor to account for the mass injected during the on and off ramps, such that over the whole injection profile the total mass injected should be very close to the ‘Desired Mass’. In practise, it was found that until the simulation time reaches -83.9 CAD the mass flowrate might be remaining at the maximum rate (i.e. it does not follow the gradient of the line if Table 10 were graphed). This additional mass flow may increase the overall mass injected *very* slightly (recall it is only for 0.1 CAD), so in the interest of due diligence, the mass that has flowed from the injector region to the cylinder region is included later in Table 13, where it can be seen that the difference is always less than 1%. This is sufficiently accurate to facilitate the primary objective of these simulations: to test how well the motored simulations predict the required fuel mass, and not to evaluate engine performance, emissions, and so on. Note that the flowrates are all in kg/s and not kg/CAD. Because the injector internals are located in their own region, the flow between this ‘injector’ region and the cylinder region is switched on at -115 CAD to allow the mass flowrate at the injector inlet to flow into the cylinder, and off at -80 CAD. This is shortly before and after the timing

of the mass flow rate profile to allow pressure equalisation before, and more time for any residual fuel gas in the injector tube to enter the cylinder after ‘injection’.

The ignition timing was kept constant for all the simulation cases at -30 CAD, and the SAGE detailed chemistry solver was used for combustion simulation. This was set to run only around the time of combustion to reduce computation time, with CH<sub>4</sub> set as the fuel species and ignition initiated through the addition of two spherical energy sources in the spark plug gap. The use of two heat sources reflects the initial discharge and afterglow of an electrical spark, and together these raise the temperature locally above the specified combustion cut-off temperature of 600 K; Table 11 details the ignition source volumes [168]:

*Table 11 - Ignition Energy Sources*

Source	Size	Location X,Y,Z	Energy	Max Temp.	Timing
S1-1	Ø 0.8 mm	0, 0.01655, 0	0.02 Joules	50,000 K	-30 to -29.5 CAD
S1-2	Ø 0.8 mm	0, 0.01655, 0	0.02 Joules	50,000 K	-30 to -20 CAD
S2-1	Ø 0.8 mm	0, 0.01655, 0	0.02 Joules	50,000 K	-15 to -14.5 CAD
S2-2	Ø 0.8 mm	0, 0.01655, 0	0.02 Joules	50,000 K	-15 to -5 CAD

For reference, coordinate X,Y,Z = 0,0,0 represents the location of the axial and radial centre of the cylinder. Sources S2-1 and S2-2 represent a secondary spark, added for the eventuality that the first spark failed to ignite the mixture.

Settings for AMR were mostly unchanged with the velocity criterion remaining the same throughout at 3m/s across a cell with a maximum embedding level of 2 (cell size 0.75 mm). However, from -31 CAD to 60 CAD an additional embedding criterion was added based on a temperature gradient of 2.5 K across a cell, with a maximum embedding level of 4 (cell size 0.1875 mm); the maximum cell count was increased from 100,000 to 250,000 accordingly (from -35 CAD to 60 CAD). This was to accommodate the smaller length scales associated with the early stages of combustion and reduce any grid-induced diffusive errors [168]. Furthermore, to avoid stability issues the maximum timestep was reduced from 1E-05 seconds to 5E-06 seconds from -31 CAD to 105 CAD inclusive (i.e. the maximum timestep returns to 1E-05 at 106 CAD); the minimum timestep was left intact.

It is prudent at this point to re-emphasise that the *primary* objective of these simulations is not to serve as an evaluation of the performance of the engine geometry and configuration by, for example, generating a realistic in-cylinder PV plot. Rather, it is to solve an engineering problem by generating and testing a fuel table that is of sufficient accuracy so as to guide the setup and physical engine testing

of a novel prototype, for which there are at the time of writing, no empirical results. Therefore, provided they do not cause the simulation to become unstable, things like grid-induced diffusive errors, early or late ignition timing, or the velocity of gases in the injector, are not of great concern. This is because even if they may contribute to an over- or under-estimated maximum-pressure-rise-rate ('MPRR') and peak-firing-pressure ('PFP') in the cylinder, the simulated combustion processes are solely intended to achieve a moving in-cylinder flow field and exhaust blow-down for each engine cycle. This provides the opportunity to evaluate how closely the bulk in-cylinder equivalence ratio reflects what it *should* be if the motored simulations are able to accurately estimate the fuel required, especially considering the discussion associated with Figure 79 through Figure 84 in section 6.6. The following section lists the results from the fuelled cases, as well as an overview of the OP2S engine cycle and the way in which a bulk swirling motion is generated in the cylinder.

### 6.7.2 Mesh Dependency Analysis

As with the motored simulations, a mesh dependency analysis was conducted for the fuelled simulations, using the same point in the fuel table (3000 rpm, 150 kPa scavenge pressure). Again, the 'default' configuration (i.e. with embeddings, AMR...) was rerun to remove any effects of the different CPU configuration caused by running on a different part of the HPC cluster. Likewise, for the comparison simulations, the embeddings and AMR were disabled and the base mesh varied from 1.5 mm to 0.375 mm. This is because the 3 mm case crashed early on, so it and the 6 mm were not considered given that they were clearly too coarse to run stably with the added complexity of gaseous injection and a chemically reacting mixture. Figure 86 shows the variation in equivalence ratio in the cylinder shortly before SOC on the third engine cycle, with respect to the base mesh size, as well as the same value as in the default configuration:

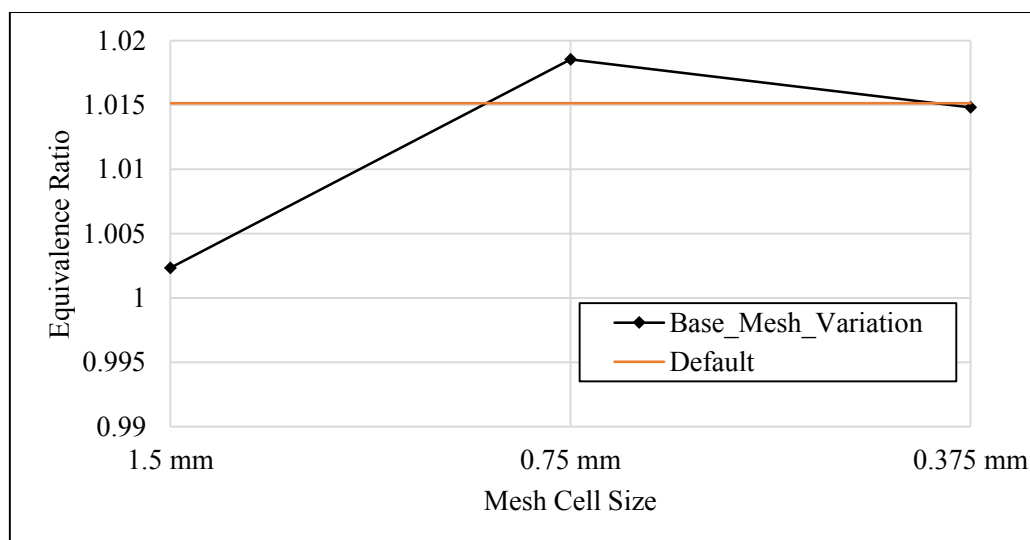


Figure 86 - Equivalence Ratio Variation with Base Mesh Cell Size, and Default Configuration

The change in equivalence ratio between the 1.5 mm and 0.75 mm case is within 2%, and between 0.75 mm and 0.375 mm it is within 0.5%. The value for the default configuration lies between the 0.75 mm and 0.375 mm values. Figure 87 shows the variation in cell count, Figure 88 the variation in runtime with base mesh cell size, as well as the values for the default configuration:

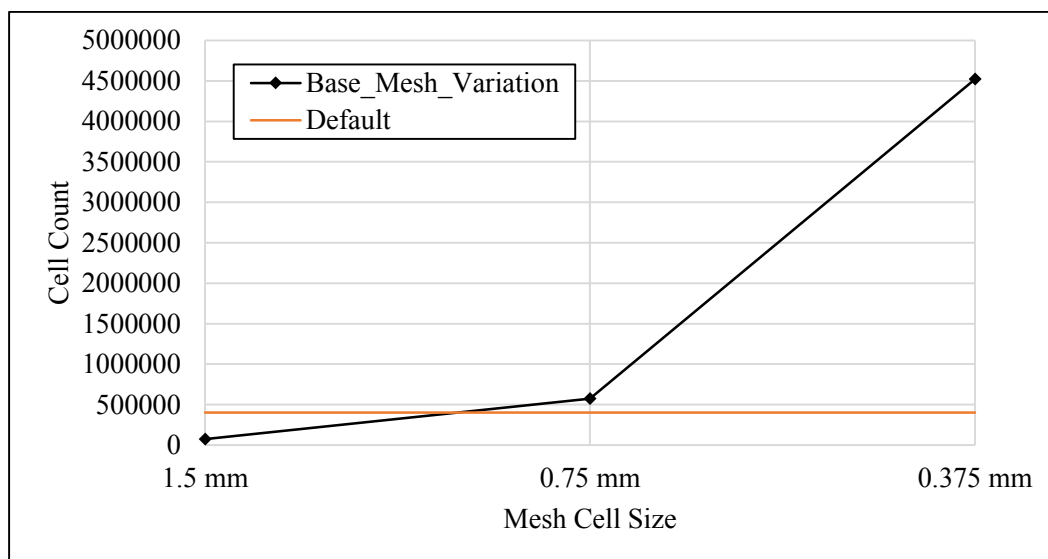


Figure 87 - Cell Count Variation with Base Mesh Cell Size, and Default Configuration

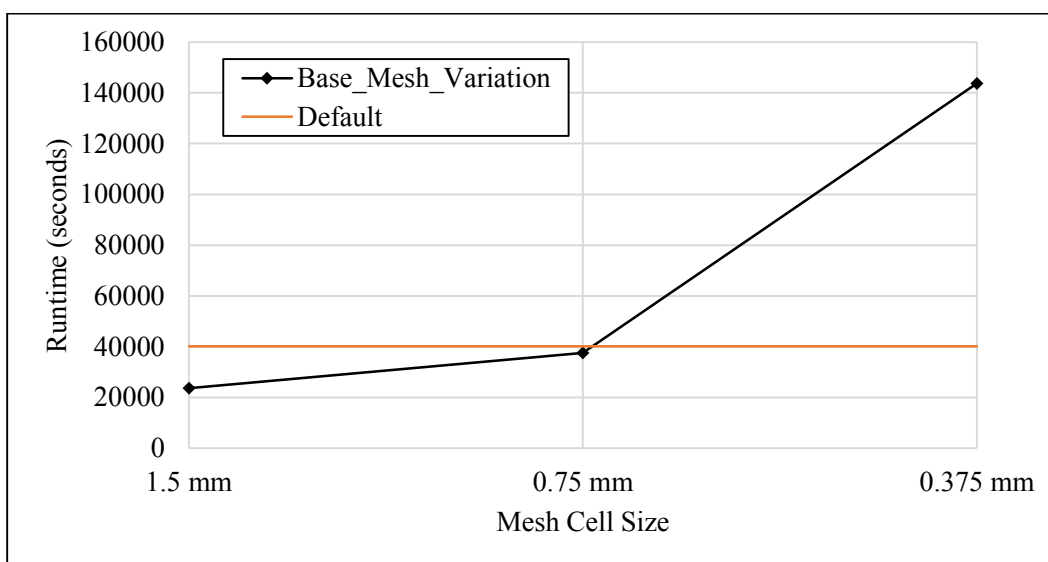


Figure 88 - Runtime Variation with Base Mesh Cell Size, and Default Configuration

Interestingly, the runtime of the default configuration is higher than it is for the 0.75 mm mesh, even though the latter has a higher cell count. One reason for this might be the embedded cells due to AMR around the combustion event, however Figure 89 and Figure 90 show the cylinder pressure vs. crank angle and cylinder pressure vs. volume for the third engine cycle respectively, for the above cases:

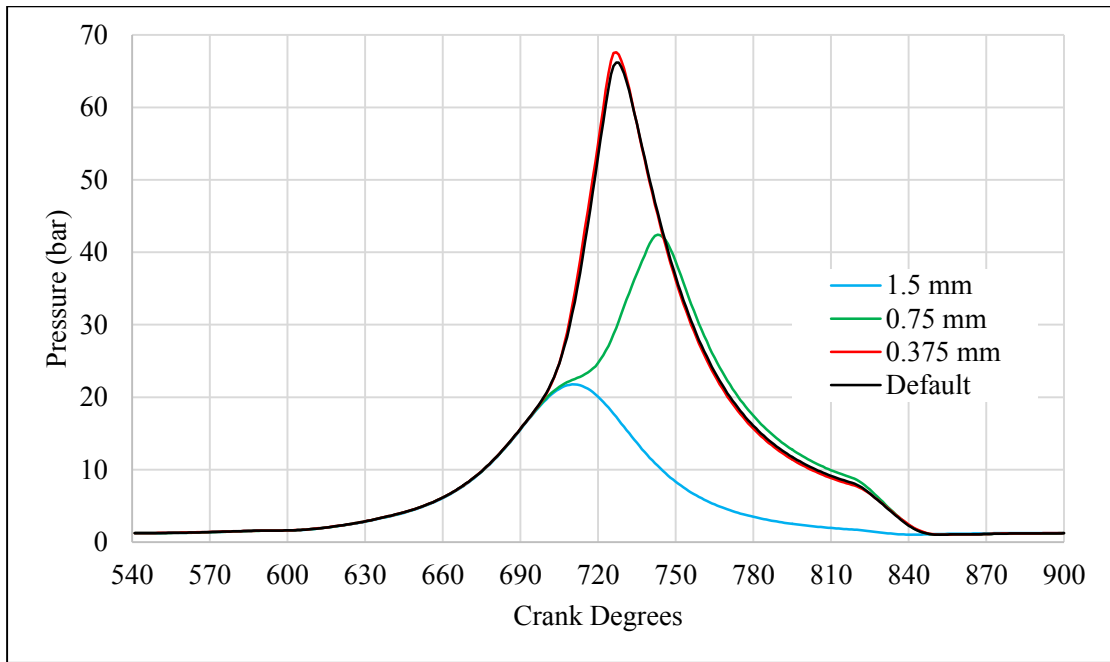


Figure 89 - Cylinder Pressure vs. Crank Angle for 3rd Engine Cycle with Variation in Base Mesh Cell Size, and Default Configuration

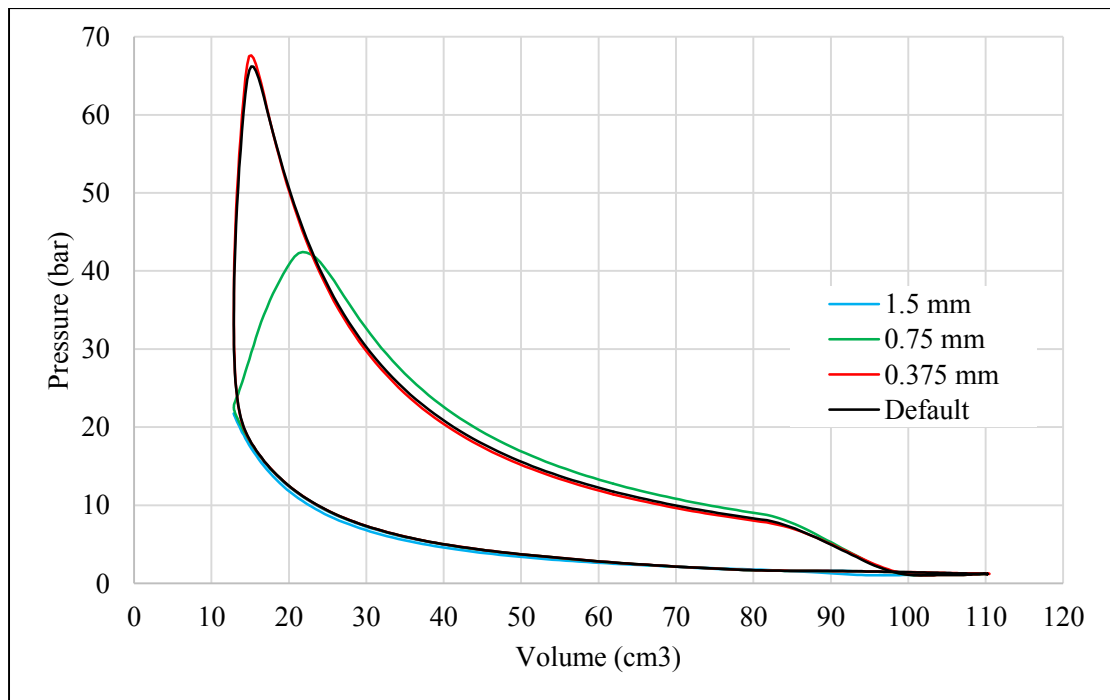


Figure 90 - Cylinder Pressure vs. Volume for 3rd Engine Cycle with Variation in Base Mesh Cell Size, and Default Configuration

The 1.5 mm case does not appear to have any meaningful ignition, whereas the combustion rates (and consequently the pressure rise rate) of the 0.75 mm appear significantly impacted. However, the 0.375

mm case, and the default configuration, appear very similar in their evolution except for the peak cylinder pressure, which is marginally higher and earlier in the 0.375 mm case. Given that the 0.375 mm case resulted in a maximum cell count more than 10 times that of the default configuration, and a runtime more than 3 times greater, it can be concluded that the default configuration is sufficiently independent of the mesh for the purposes of evaluating the equivalence ratio.

### 6.7.3 Fuelled Simulation Results

The air/fuel equivalence ratio is given for the first, second and third cycles in Table 12, followed by the mass of fuel injected per cycle in Table 13, all at -50 CAD before IDC for each cycle. Note that the mass injected per cycle reflects the data for the total mass flow between the injector region and the cylinder region, and not the mass flow through the injector gas inlet boundary. Note also that the required fuel mass for each case was calculated based on its (motored) trapped mass of air, and not from the percentages given in the fuel table; this was to avoid compounding errors. That is, they are calculated in a similar manner as the percentages expressed in the fuel table, but to a higher degree of precision. Given that, as discussed earlier, there is a small error between the calculated mass required and the actual mass that is injected into the cylinder during each cycle (see Table 13), this is why the fuel table percentages have been rounded to the nearest 0.1%.

Table 12 - Equivalence Ratio and Error Per Cycle

Simulation	Phi Target	Phi Actual 1	Phi % Error 1	Phi Actual 2	Phi % Error 2	Phi Actual 3	Phi % Error 3
1500_120	1.000	0.999	-0.103%	1.000	0.037%	0.999	-0.052%
1500_150	1.000	0.998	-0.234%	1.000	-0.042%	0.999	-0.069%
1500_180	1.000	0.997	-0.290%	0.998	-0.209%	0.999	-0.135%
3000_120	1.000	1.060	5.985%	1.071	7.144%	1.082	8.159%
3000_150	1.000	1.004	0.411%	1.011	1.100%	1.016	1.591%
3000_180	1.000	1.002	0.218%	1.008	0.783%	1.008	0.812%
5000_120	1.000	1.300	29.998%	1.352	35.197%	1.433	43.286%
5000_150	1.000	1.094	9.393%	1.154	15.416%	1.171	17.124%
5000_180	1.000	1.042	4.222%	1.094	9.449%	1.100	9.964%

Table 13 - Injected Fuel Mass (kg) and Error Per Cycle

Simulation	Required Fuel Mass	Mass Injected 1	Mass % Error 1	Mass Injected 2	Mass % Error 2	Mass Injected 3	Mass % Error 3
1500_120	5.617E-06	5.630E-06	0.237%	5.638E-06	0.375%	5.638E-06	0.378%
1500_150	6.977E-06	6.991E-06	0.209%	7.003E-06	0.373%	7.003E-06	0.372%
1500_180	8.334E-06	8.351E-06	0.201%	8.364E-06	0.366%	8.365E-06	0.374%
3000_120	5.845E-06	5.860E-06	0.261%	5.869E-06	0.399%	5.869E-06	0.412%
3000_150	7.266E-06	7.283E-06	0.227%	7.295E-06	0.394%	7.294E-06	0.389%
3000_180	8.706E-06	8.725E-06	0.215%	8.740E-06	0.391%	8.739E-06	0.383%
5000_120	6.215E-06	6.232E-06	0.284%	6.240E-06	0.404%	6.243E-06	0.455%
5000_150	7.725E-06	7.744E-06	0.240%	7.767E-06	0.549%	7.764E-06	0.507%
5000_180	9.214E-06	9.234E-06	0.219%	9.252E-06	0.418%	9.254E-06	0.439%

The values in Table 12 are encouraging, except for high engine speed and low scavenge pressure conditions. The cells in both Table 12 and Table 13 are coloured according to the percentage error between the target value, and the actual value: +/- 0% to 5% is dark green, +/- 5% to 10% is light green, +/- 10% to 15% is yellow, +/- 15% to 20% is orange, and greater than +/- 20% is red. As discussed earlier for the motored simulations, a high engine speed but low scavenge pressure condition is akin to the throttle being closed in a conventional four-stroke engine. This was reflected in how well the scavenge pressure was able (or otherwise) to clear the initial in-cylinder conditions. The same characteristics are seen with the fuelled simulations, where there is a significant overestimation of the required fuel for the 5000 rpm 120 kPa case of approximately 30% for the first cycle, 35% for the second cycle, and 43% for the third cycle.

The increasing equivalence ratio in Table 12 despite the relatively consistent injected mass in Table 13 is indicative of the cylinder not being fully flushed. At 5000 rpm and 150 kPa, this behaviour is still visible but to a much lesser extent. However, by 5000 rpm 180 kPa (full speed/load) it has mostly disappeared. Furthermore, the results of the 1500 rpm and 3000 rpm fuelled simulations suggest that the motored simulations were able to predict the trapped mass quite well at low to medium engine speeds, given that only the 3000 rpm 120 kPa case had an equivalence ratio error in the +/- 5% to 10% region, and all the other cases were within +/- 2% error. In all cases the injected mass was well within 1% of the required fuel mass throughout. As was noted in section 5.2 the intake liner ports and gallery are so designed as to encourage a bulk swirling motion in the cylinder (that is, the gases rotate around the cylinder axis -though are not necessarily centred on it). Notwithstanding the effects of fuel injection on charge motion within the cylinder (which can have significant effects, see for example [54]), this motion persists until after SOC. Figure 91, which shows the equivalence ratio in the central axial plane of the cylinder from 618 CAD to 693 CAD evidences this (note the scale has been constrained to slightly lean and slightly rich of stoichiometric):

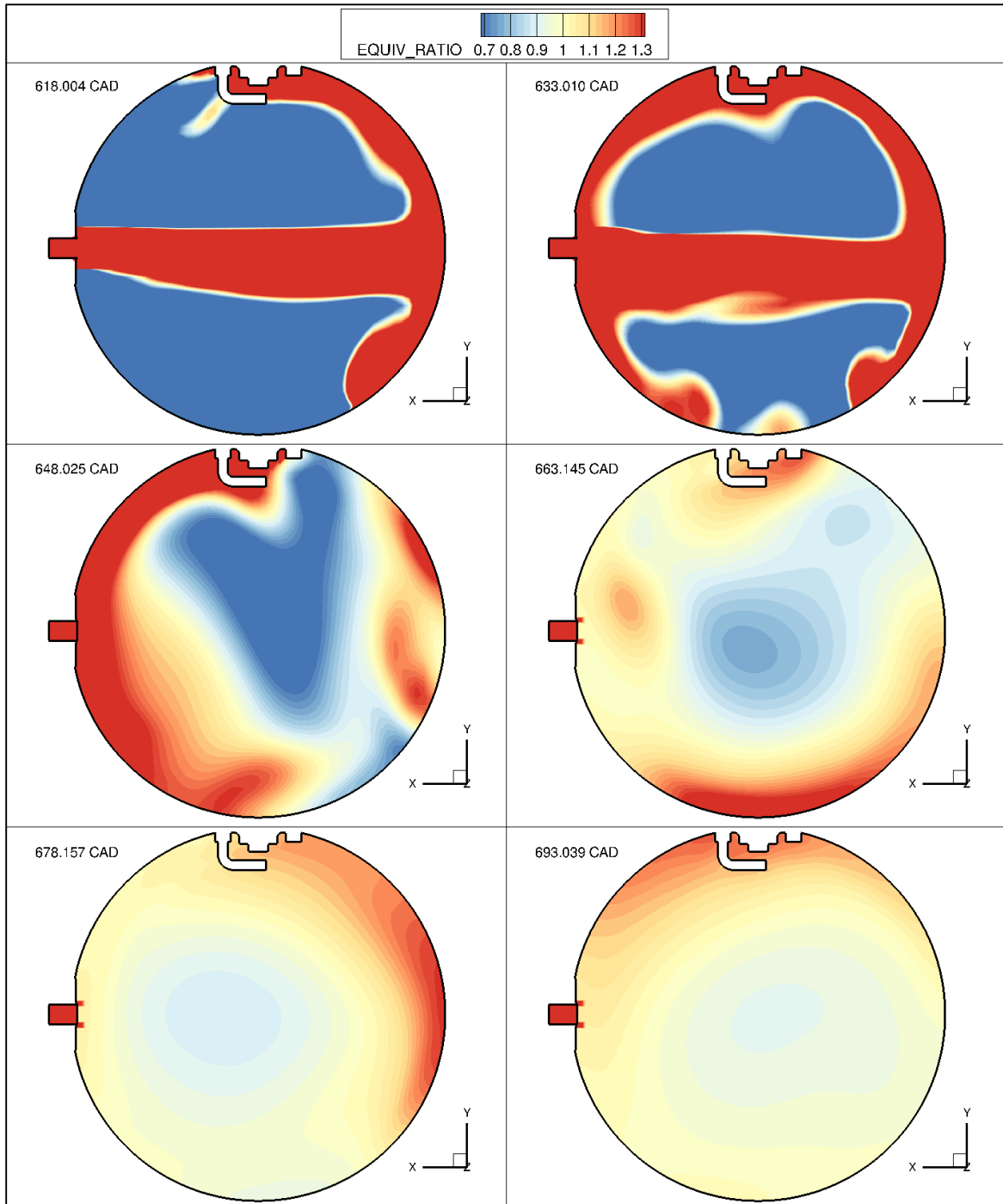


Figure 91 - Equivalence Ratio in the Centre of the Cylinder, 618 CAD to 693 CAD

This was the 3000 rpm, 150 kPa scavenging pressure case. Although the jet of gas impacts the other side of the combustion chamber from the injector, by the time the engine reaches 678 CAD a combustible mixture is forming even though (from this perspective) it is stratified richer toward the extremity. A particularly rich region, rotating anti-clockwise about the central axis of the cylinder, is in the region of the spark plug at 693 CAD, which is shortly after SOC. Figure 92 through Figure 94 show

temperature contours of the central slice of the cylinder, beginning at shortly after SOC for the third cycle. These show (from left to right) slices through the centre of the domain in the Z, X and Y direction:

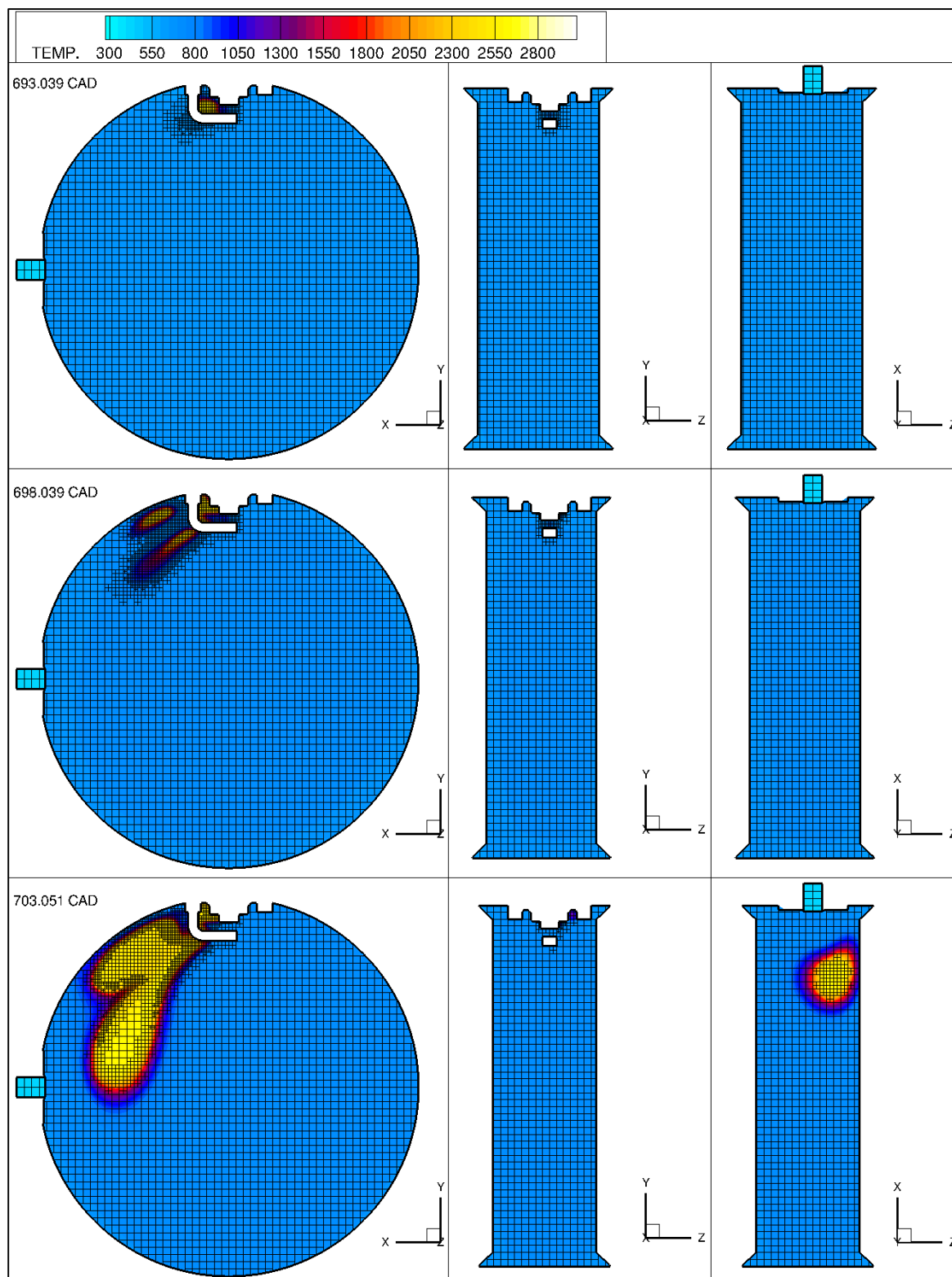


Figure 92 - Temperature Contour Slices at  $Z=0$  (left),  $X=0$  (middle),  $Y=0$  (right) for 3rd Cycle Combustion Event, 693 CAD to 703 CAD

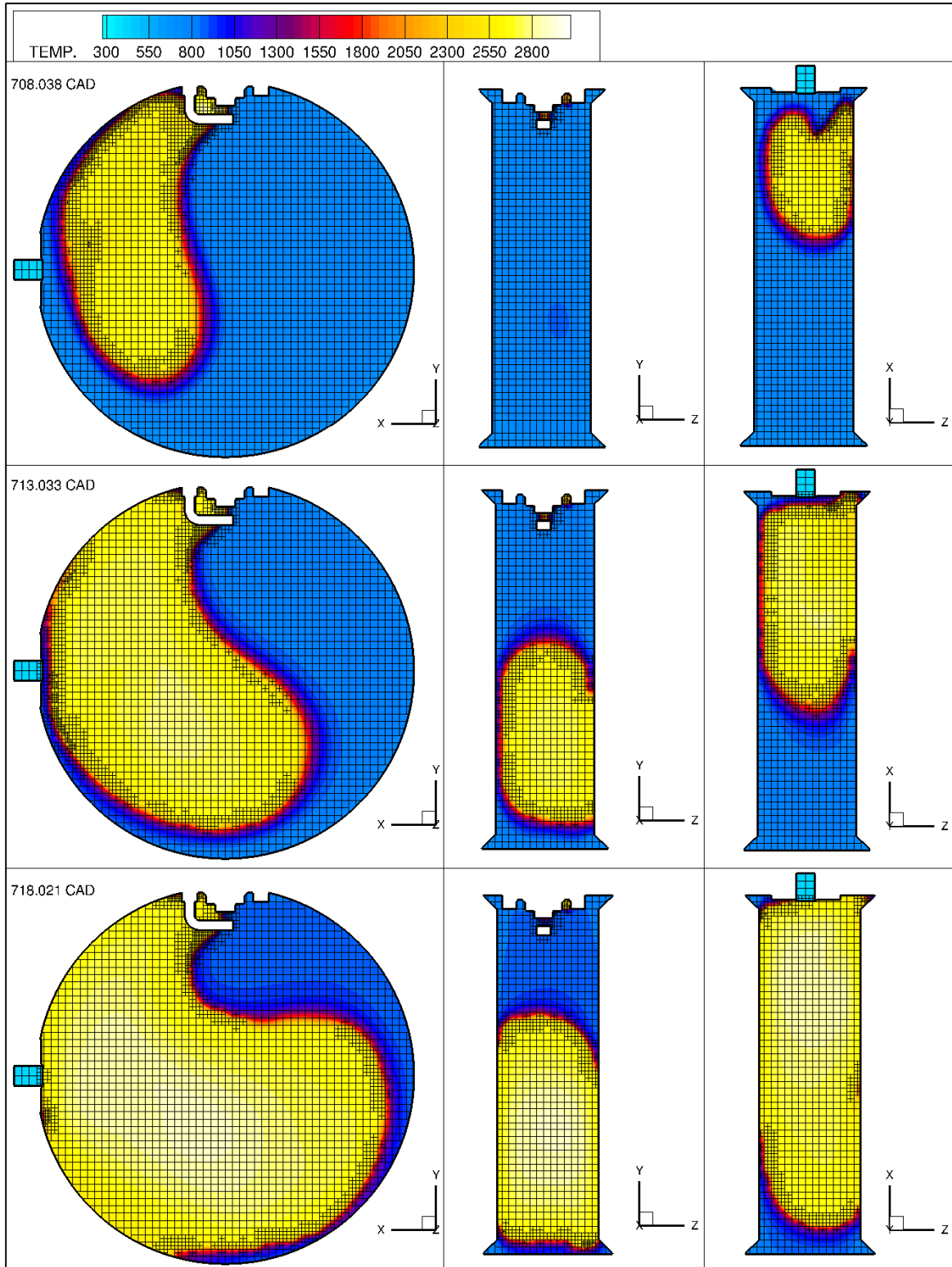


Figure 93 - Temperature Contour Slices at  $Z=0$  (left),  $X=0$  (middle),  $Y=0$  (right) for 3rd Cycle Combustion Event, 708 CAD to 718 CAD

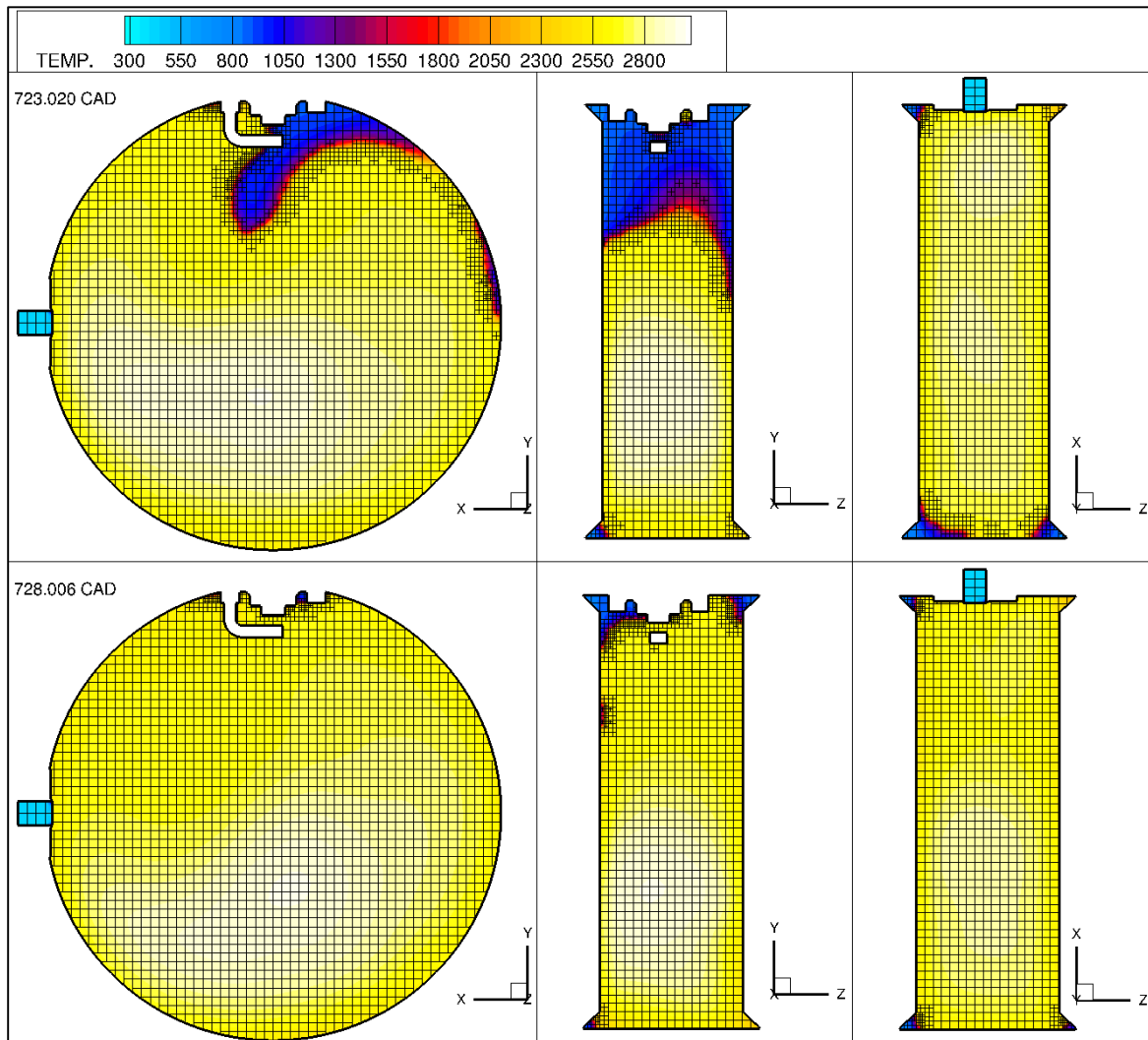


Figure 94 - Temperature Contour Slices at  $Z=0$  (left),  $X=0$  (middle),  $Y=0$  (right) for 3rd Cycle Combustion Event, 723 CAD and 728 CAD

Here, the mesh has been included to highlight the smaller cells that AMR has embedded due to the large temperature gradient between the burned and unburned mixtures; the temperature scales have been configured for good viewability. These clearly illustrate the importance of the rotating motion and the fact that it persists: were it not present and the flame front allowed to progress radially from the spark plug, it could be expected to slow down as it approaches the other side of the cylinder, increasing combustion duration [5]. With it present, the flame instead wraps around the combustion chamber.

The difference between 693, 698 and 703 CAD suggests this includes an influence even on the early flame propagation, since the ‘flame front’ appears to be advancing almost exclusively in the anti-clockwise direction (when viewing the  $Z$ -slice). By 728 CAD the combustion chamber appears fully enflamed from this perspective, however when viewing the slices in the  $X$  and  $Y$  planes it is clear the

volumes in the regions of the chamfered piston crowns are not. Also, the obvious trade-off is the proximity of the flame to the liner, where more heat could be lost to coolant and impact efficiency.

### 6.7.3.1 Cylinder Pressure Graphs

Figure 95 shows a pressure graph for a 3000 rpm, 150 kPa fuelled case, as well as (for the sake of comparison) the third cycle of the 3000 rpm 150 kPa motored simulation case, at a 1 CAD resolution.

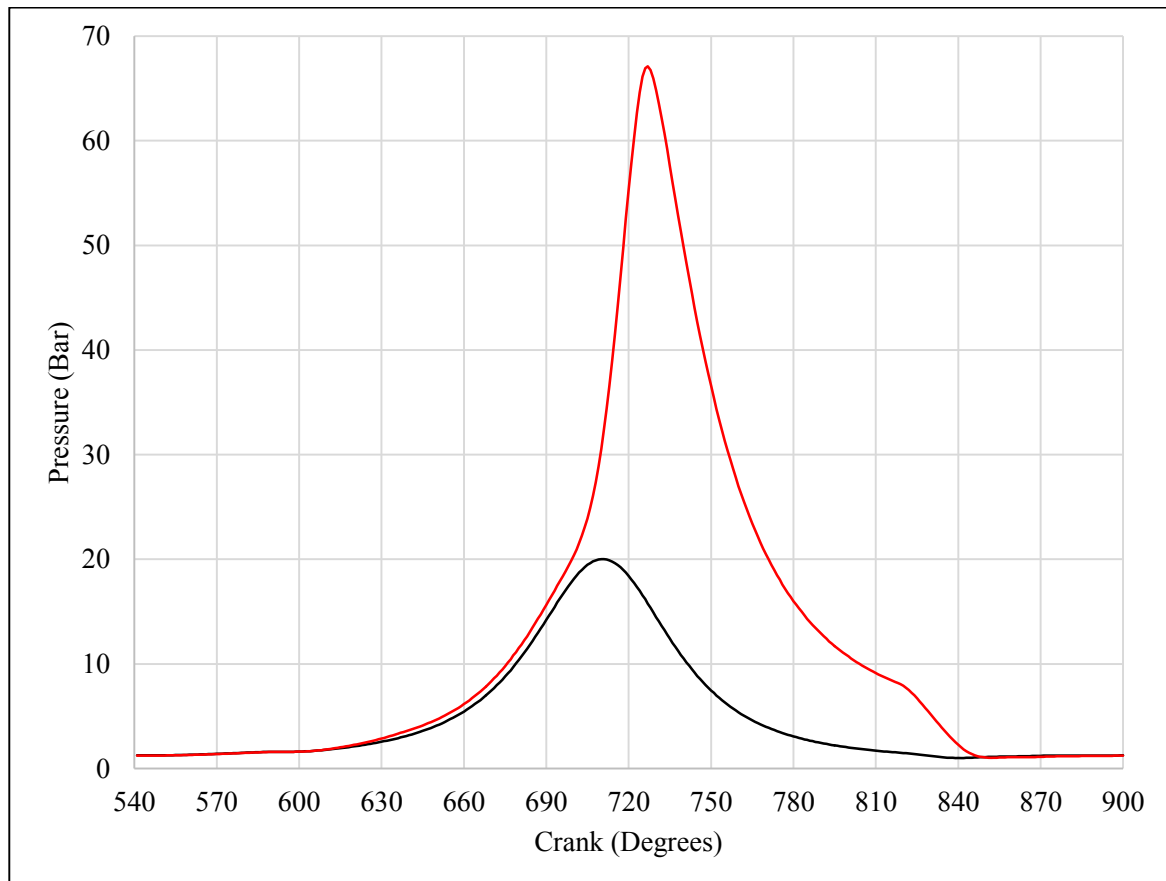


Figure 95 - In-Cylinder Pressure Tracing for Motored Case (Black Line) and Fuelled Case (Red Line)

Whilst the PFP and MPRR should not be viewed as indicative of real-world performance (not least because a pressure tracing like this in a gasoline-fuelled engine would be suggestive of spark knock [5]), the rate and amount of reduction in pressure before EPO (approx. 820 CAD) highlights the increased expansion rate of two pistons over one. A higher stroke to bore ratio typically improves engine efficiency, but it is not always practical to achieve in four-stroke engines due to the corresponding increase in mean piston speed. Yet by splitting the stroke between two pistons the OP2S architecture can achieve a high stroke to bore ratio, without increasing the mean piston speed [19]. Figure 96 shows the same data as a PV graph, the difference between the OP2S cycle and the four-stroke cycle is further

evidenced through the lack of any visible pumping loop. In a four-stroke engine this would appear as an additional smaller loop at lower pressures, and roughly from maximum to minimum volume [5].

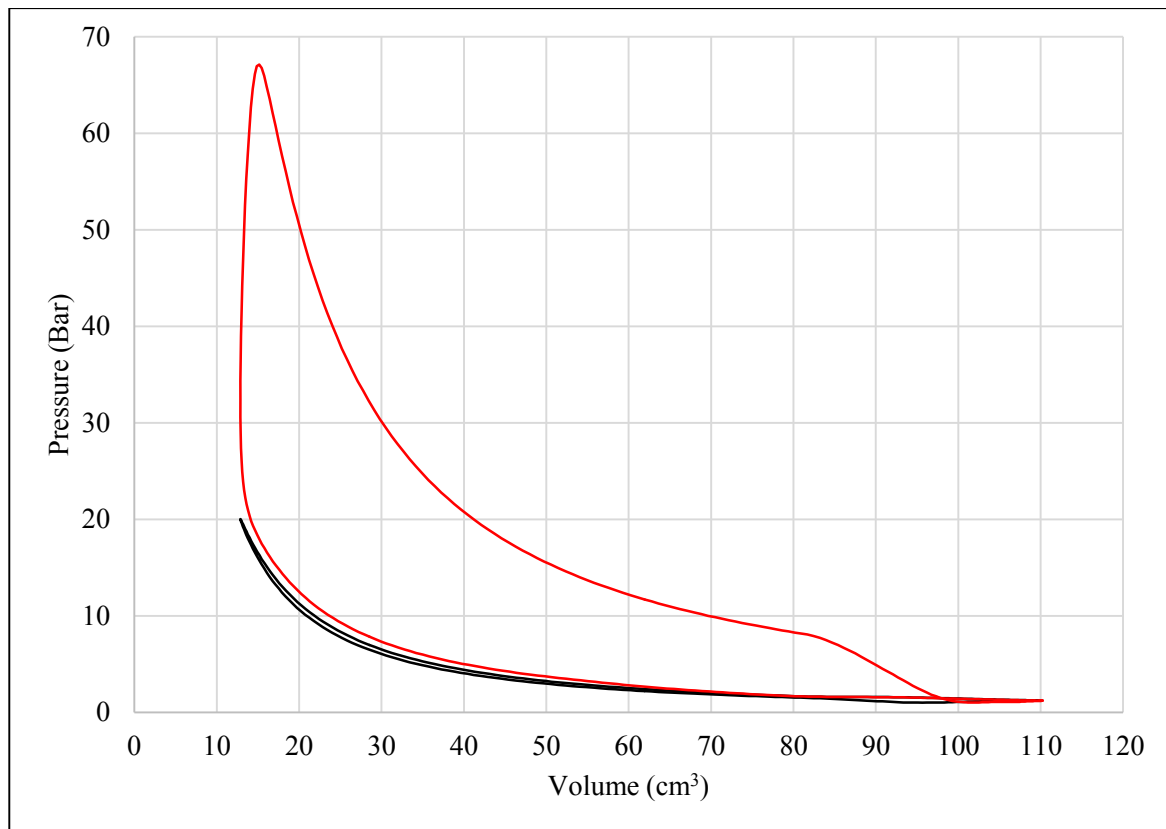


Figure 96 - Pressure Volume Graph for the Motored Case (Black Line) and Fuelled Case (Red Line)

This pumping loss does not appear on the OP2S PV graph because the pumping work is decoupled from piston motion, and in the case of the prototype is driven by an external scavenging blower. As discussed early on, whilst the scavenge pump represents a parasitic load, the decoupling of pumping work from piston motion offers a further degree of control and scope to improve engine efficiency over conventional engines [27], [64]. To illustrate the different loads, Figure 97 through Figure 99 show pressure/volume curves for the third engine cycle (541 to 900 CAD) for the 1500 rpm, 3000 rpm, and 5000 rpm simulation cases at a 1 CAD resolution respectively, at 120 kPa, 150 kPa and 180 kPa scavenge pressure:

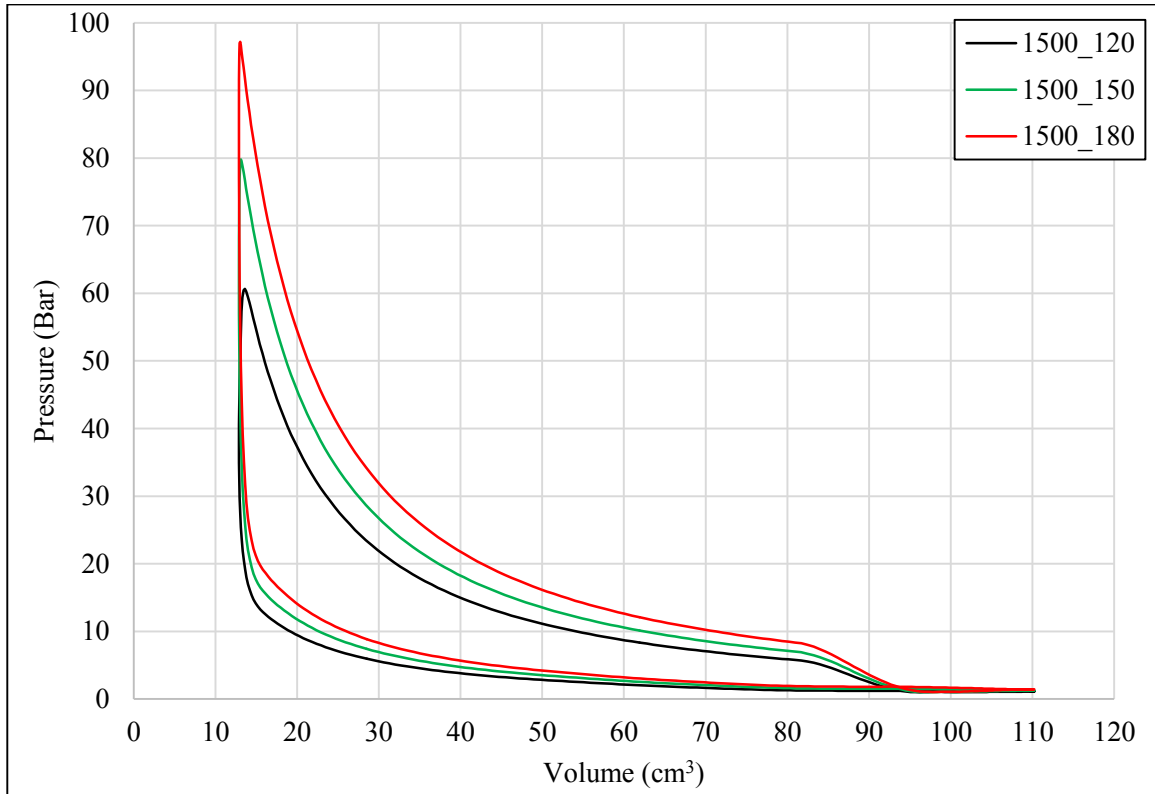


Figure 97 - Cylinder Pressure vs. Volume for 1500 rpm, 120/150/180 kPa Fuelled Cases, 3rd Engine Cycle

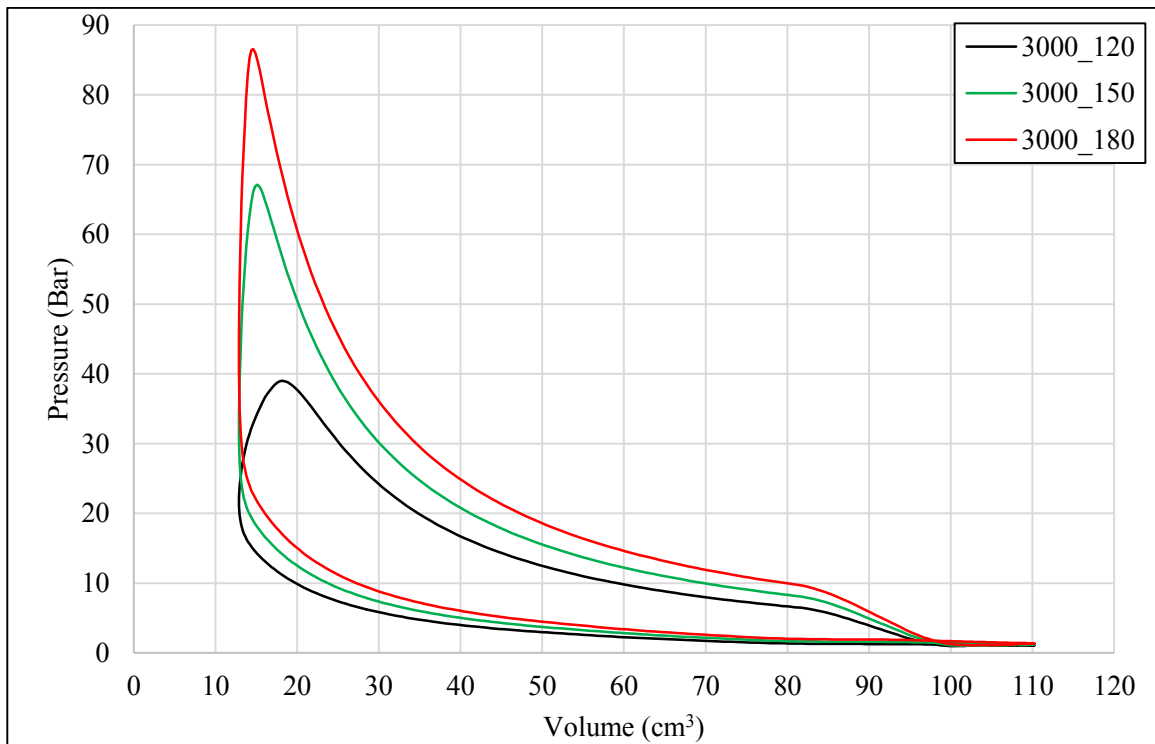


Figure 98 - Cylinder Pressure vs. Volume for 3000 rpm, 120/150/180 kPa Fuelled Cases, 3rd Engine Cycle

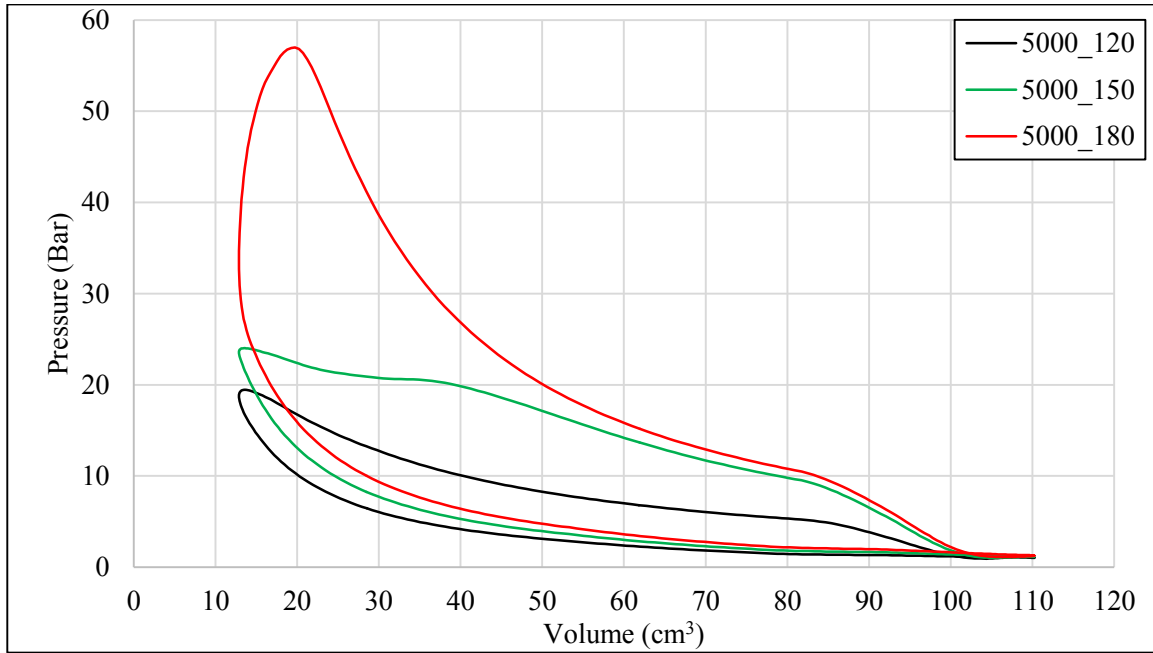


Figure 99 - Cylinder Pressure vs. Volume for 5000 rpm, 120/150/180 kPa Fuelled Cases, 3rd Engine Cycle

Once again, due to the nature of the simulations these graphs should not be confused as being indicative of engine performance, but there are striking differences between those at high scavenge pressure and low speed, and low scavenge pressure and high speed. It is much clearer the negative effect the overestimation of the required fuel has at the 5000 rpm conditions, given the absence of area enclosed within the curves in these cases. Yet in some of the 1500 rpm cases, MPRR is so severe that one would suspect catastrophic spark knock in a real engine [5]. More importantly, the motored simulations provided sufficiently accurate results to be able to configure the fuelled simulations to work first time for the majority of the conditions tested. These will help save significant time when configuring the ECU of the prototype engine, given the absence of any empirical data for the novel design.

### 6.7.3.2 Air Motion During Scavenging

As was evidenced in the literature review, the charge motion within the cylinder of an OP2S engine differs significantly in many respects from that which may traditionally be associated with an SI engine. For example, OP2S engines by necessity tend to employ swirl instead of tumble, even though the latter is generally advantageous in SI combustion (see section 4.3.1). The following figures are therefore used to provide a visual representation of the scavenging motion in the prototype engine at 3000 rpm, 150 kPa scavenging pressure. Figure 100 through Figure 101 show the velocity magnitude during the scavenging process in the central X and Y plane, from shortly after EPO at 463 CAD to shortly before IPC at 603 CAD, and Figure 102 shows the same thing in the Z direction, through the intake ports:

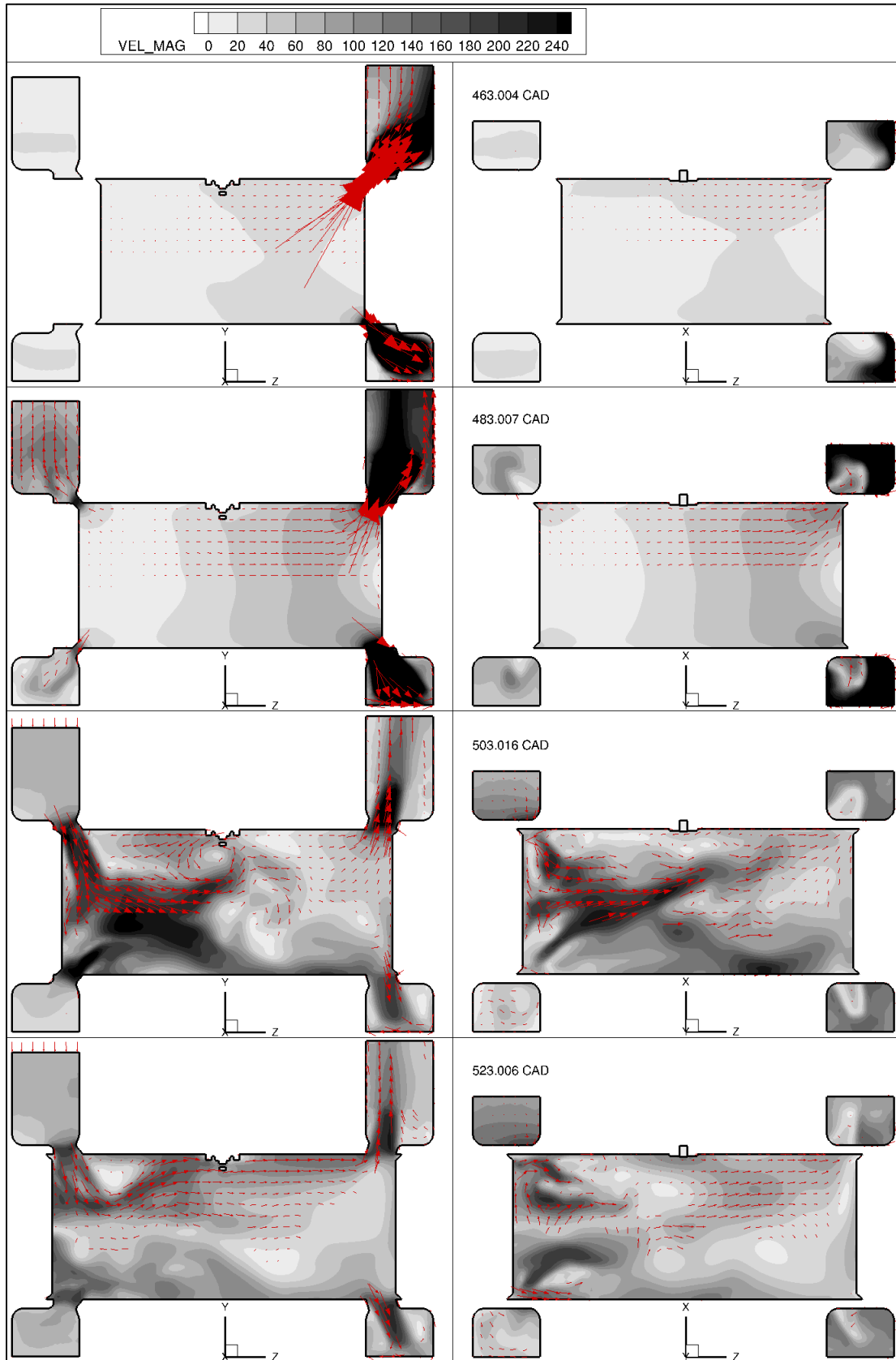


Figure 100 - Velocity Magnitude in the X Plane (Left) and Y Plane (Right) of the Cylinder, 463 CAD to 523 CAD

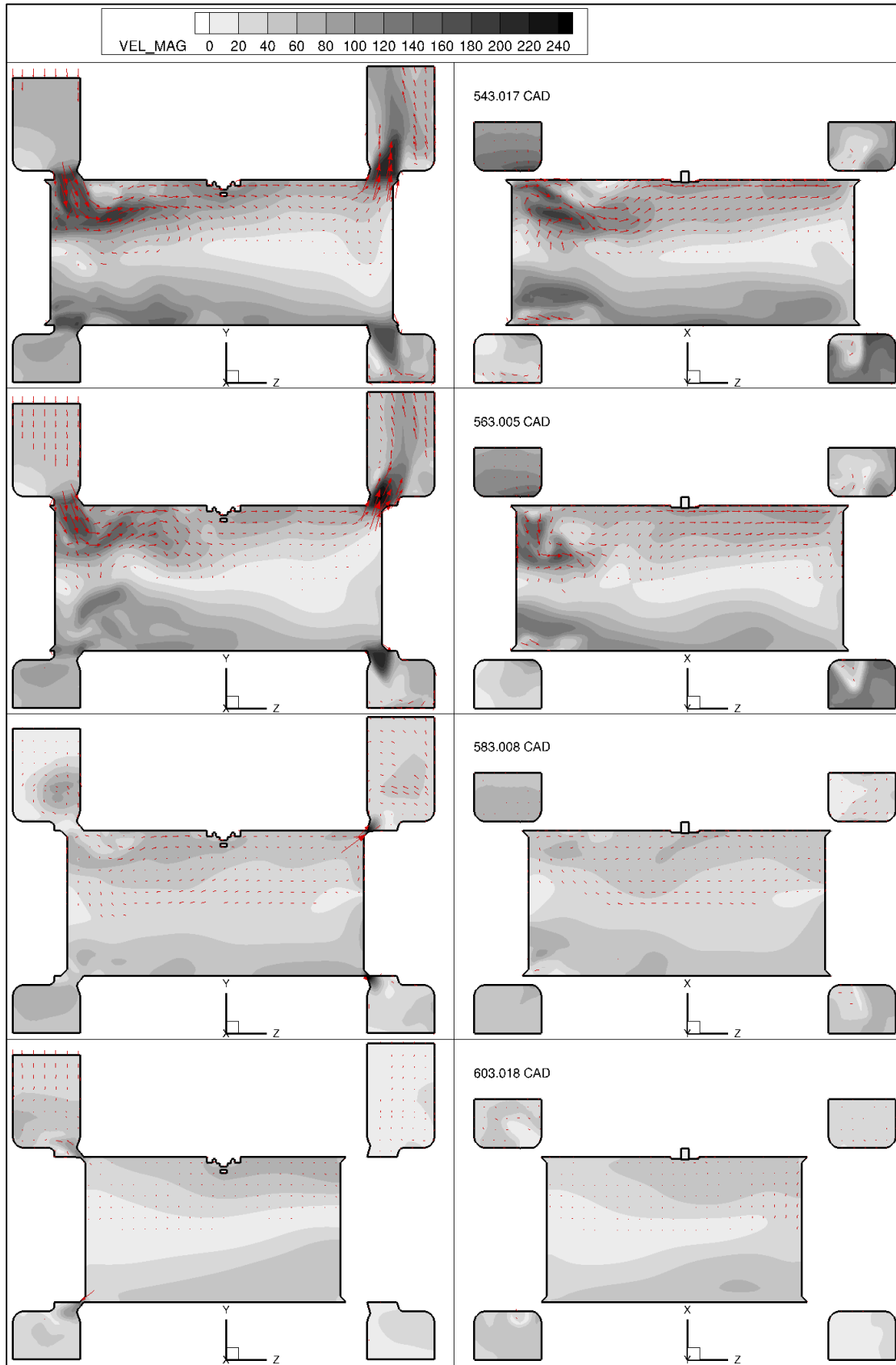


Figure 101 - Velocity Magnitude in the X Plane (Left) and Y Plane (Right) of the Cylinder, 543 CAD to 603 CAD

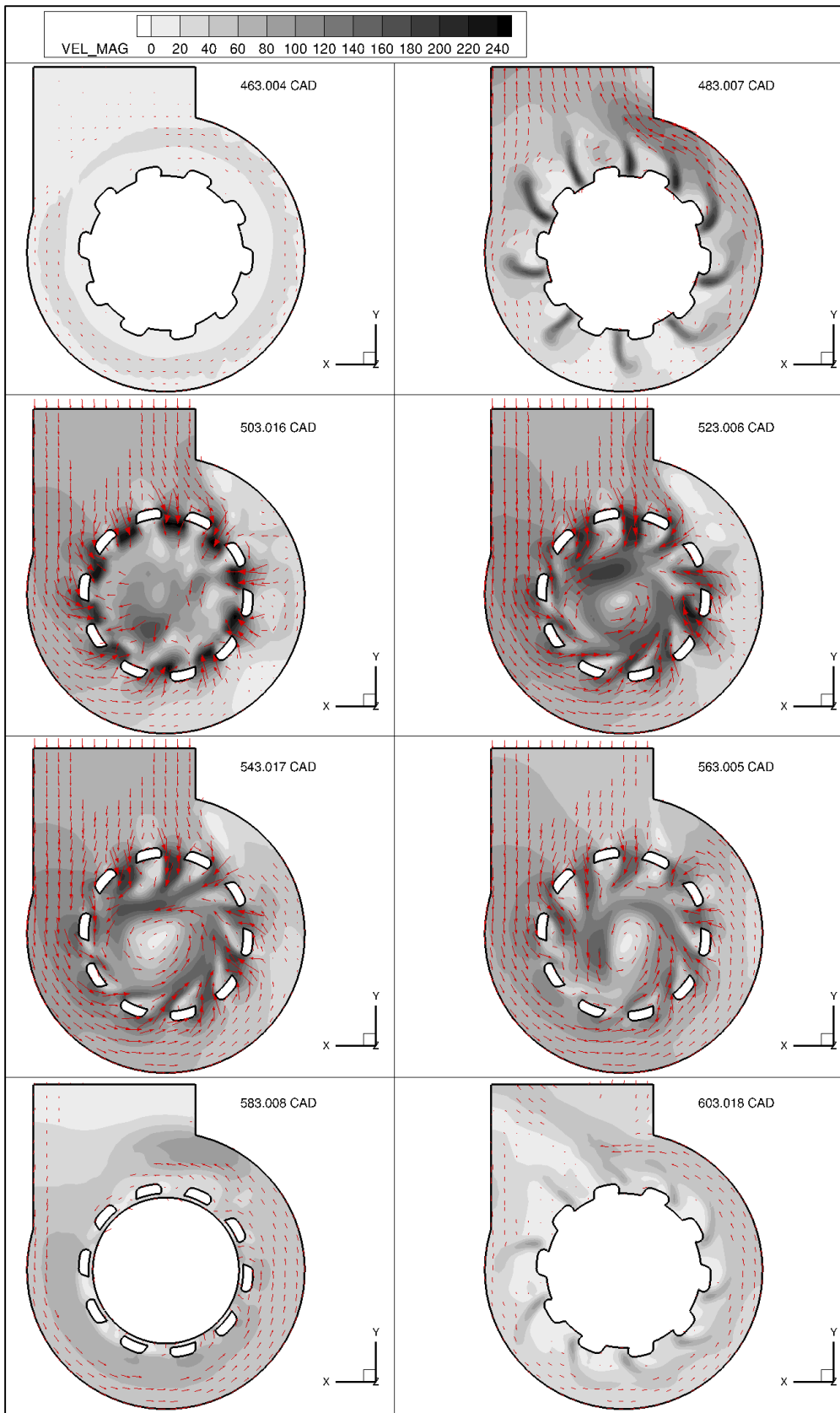


Figure 102 - Velocity Profile Through Intake Ports (Z Slice), 463 to 603 CAD

Note that the contour ranges have been limited to preserve contrast; the three-dimensional ‘head-at-point’ arrows represent velocity vectors and scale with intensity. In the X and Y planes, these suggest generally higher velocities in the quadrant of the cylinder that is closest to the main inlet tube (i.e. the offset entry to the intake gallery) throughout the scavenging process. It is also clear that following the energetic exhaust blowdown event, the cylinder pressure is still sufficient that an initial backflow of gases to the intake occurs after IPO; see 483 CAD for example. This is visible through the intake ports, too. After this, the flow direction reverses such that gases flow through the intake ports into the cylinder. This results in a velocity field of greater magnitude towards the axial centre of cylinder at 503 CAD, for that part of the cylinder that is closer to the intake ports than the exhaust ports. Later, the situation is reversed, with higher velocities occurring further from the axial centre of the cylinder, for example at 523 and 543 CAD. Towards the end of the scavenging process, there is a further back-flow event into the intake – this is the reason why injecting fuel before IPC is risky, since any fuel that makes it into the intake gallery could short-circuit during the next scavenging event.

It is noted that it takes time for the swirling motion to become established during scavenging. This clearly occurs somewhere between 503 CAD and 523 CAD in Figure 102. There are also large velocity gradients between the jets of gases flowing through the ports into the cylinder, and the regions that exist directly downstream of the port bridges in the cylinder. To show the effects of this, Figure 103 shows the turbulent velocity, and Figure 104 the TKE through the intake ports, from 463 to 603 CAD: downstream of the bridges across the intake ports there exist higher turbulent velocities, as well as greater TKE. The TKE propagates along the cylinder during the scavenging process, and this is shown in Figure 105 through Figure 106, which show TKE in the central X and Y planes from 463 to 603 CAD. Note that the scales have been constrained to improve contrast in all cases:

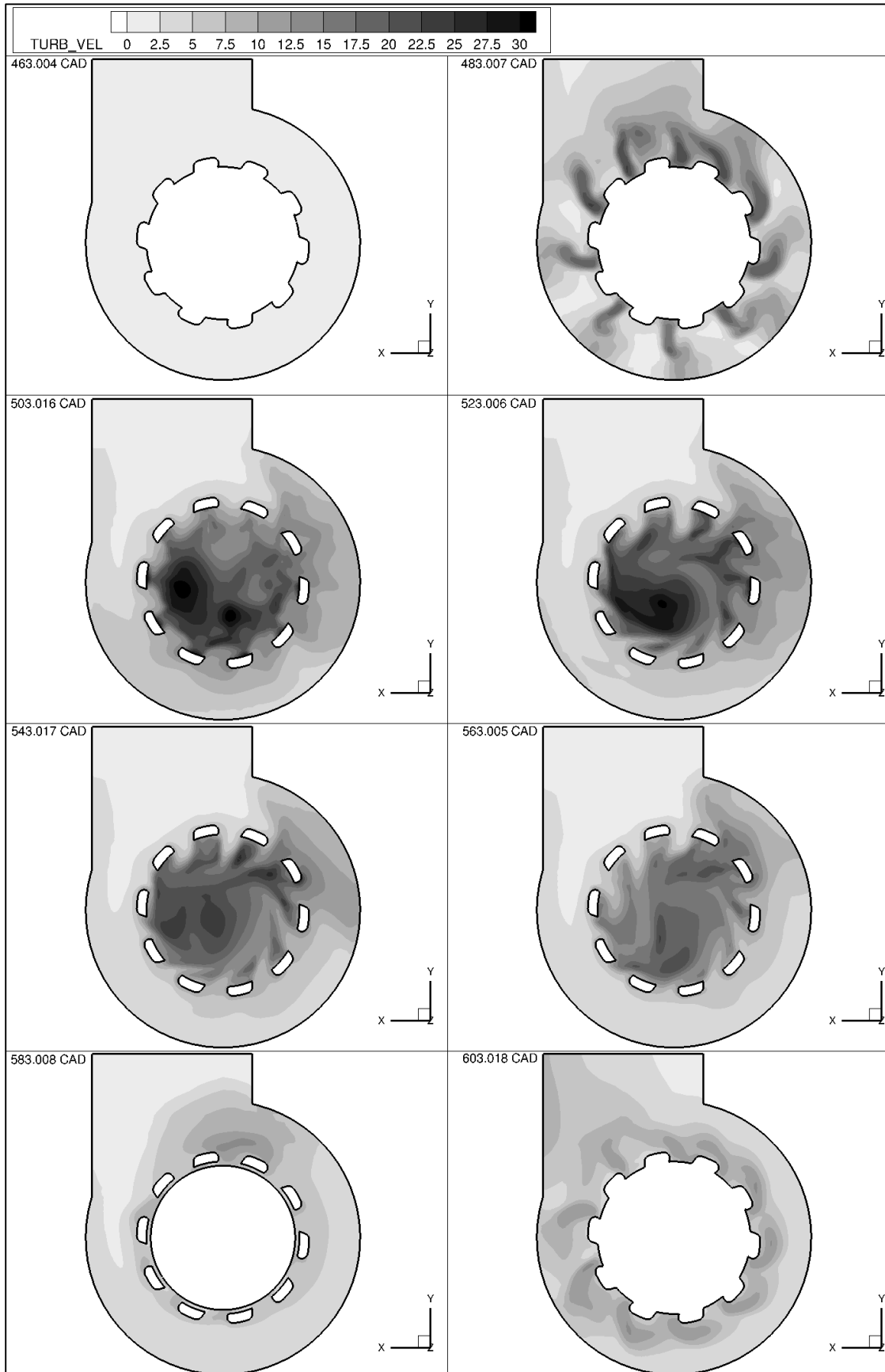


Figure 103 - Turbulent Velocity (m/s) through the Intake Ports, 463 to 603 CAD

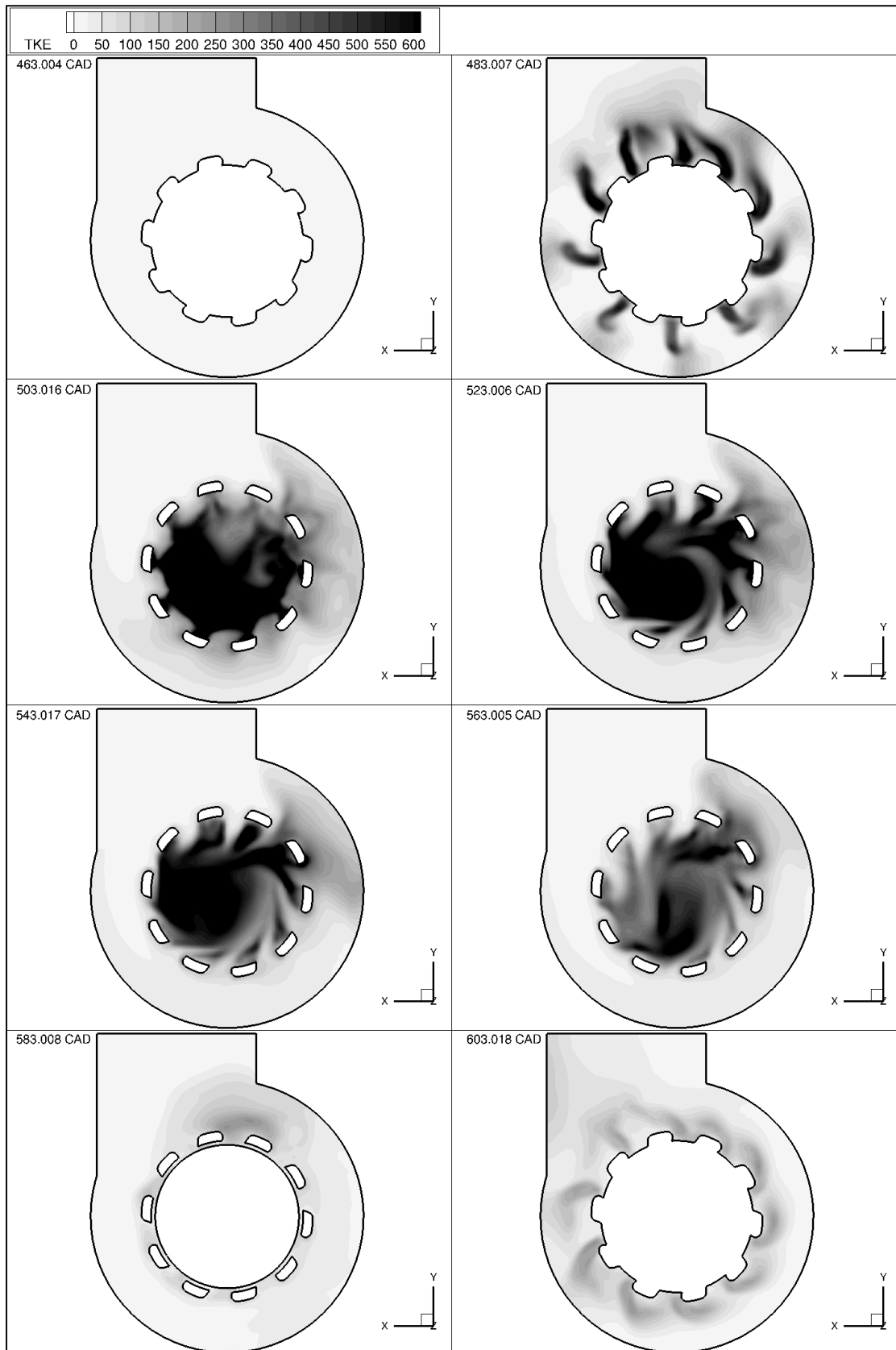


Figure 104 - TKE Through the Intake Ports, 463 to 603 CAD

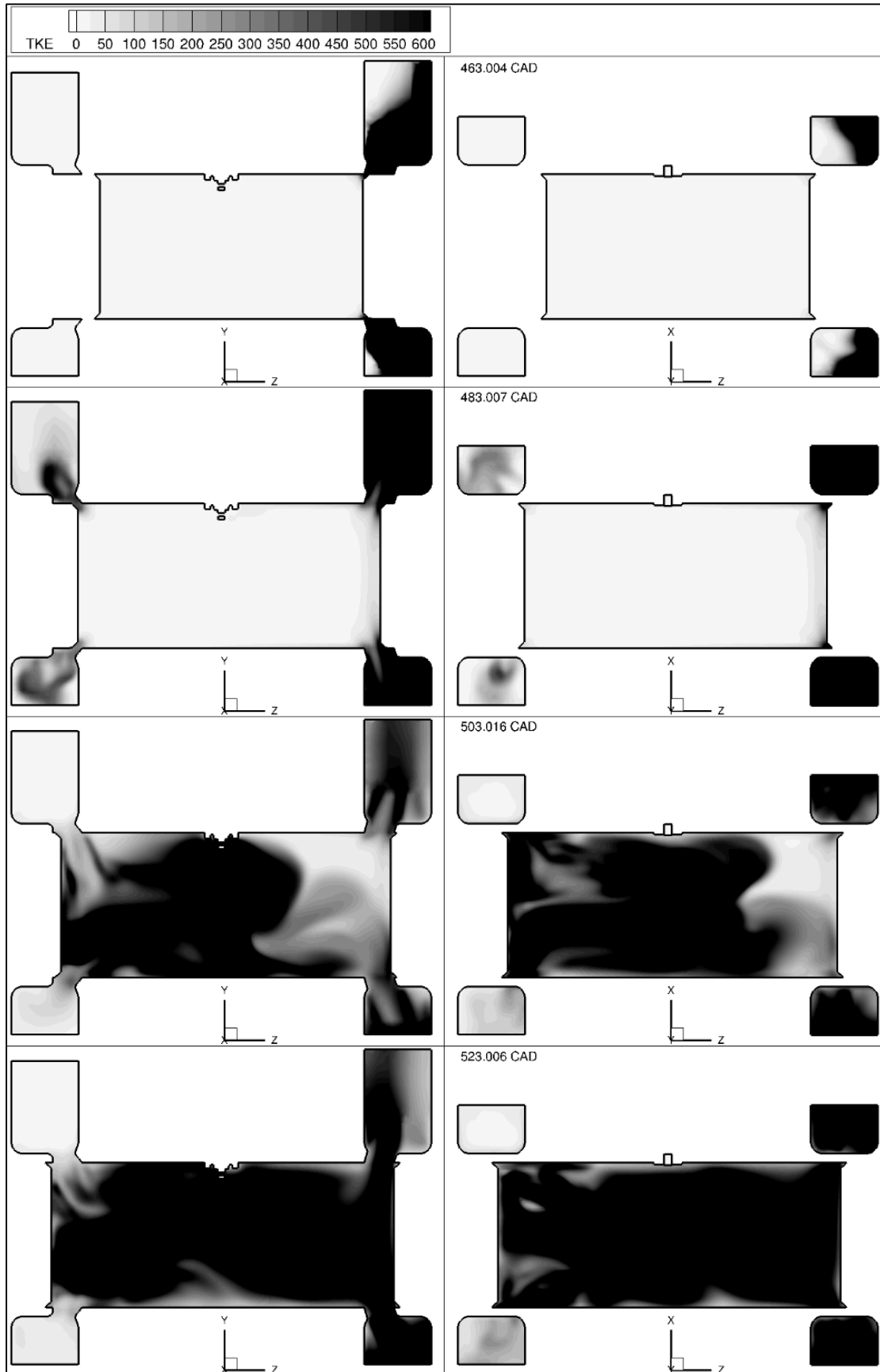


Figure 105 - TKE in the X Plane (Left) and Y Plane (Right) of the Cylinder, 463 CAD to 523 CAD

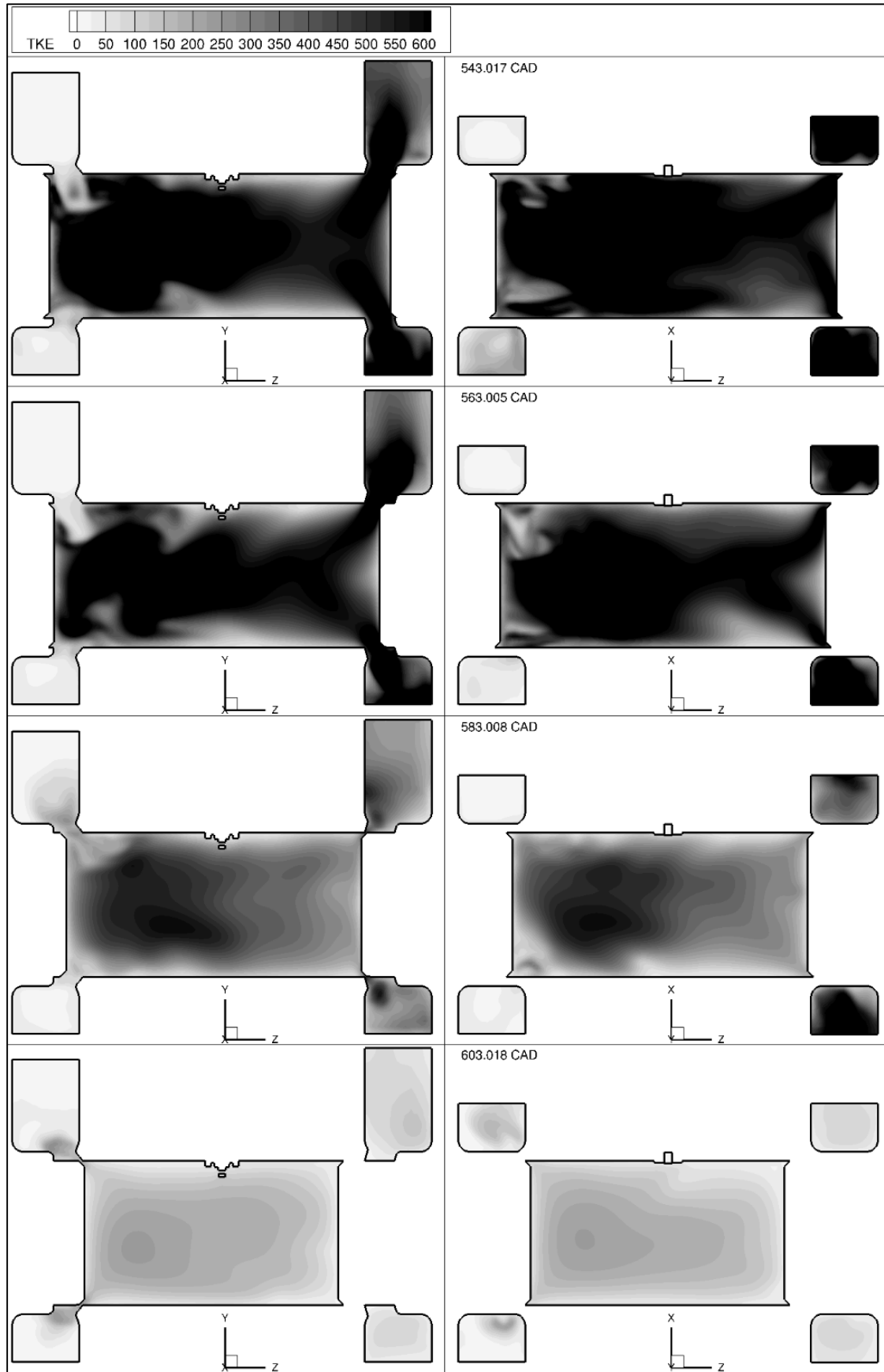


Figure 106 - TKE in the X Plane (Left) and Y Plane (Right) of the Cylinder, 543 CAD to 603 CAD

An interesting point is 503 CAD in Figure 105, where there is a boundary between the more turbulent region, and the less turbulent region towards the exhaust ports. However, the velocity profile in the X plane at 503 CAD (see Figure 100) suggests there are two notable areas of rotation in the region of the spark plug during this time: one counterclockwise, and one clockwise. This might be indicative of vorticity and mixing between the fresh charge and burned fractions, so Figure 107 shows the H<sub>2</sub>O mass fraction in the central X and Y planes of the cylinder, from 483 to 523 CAD:

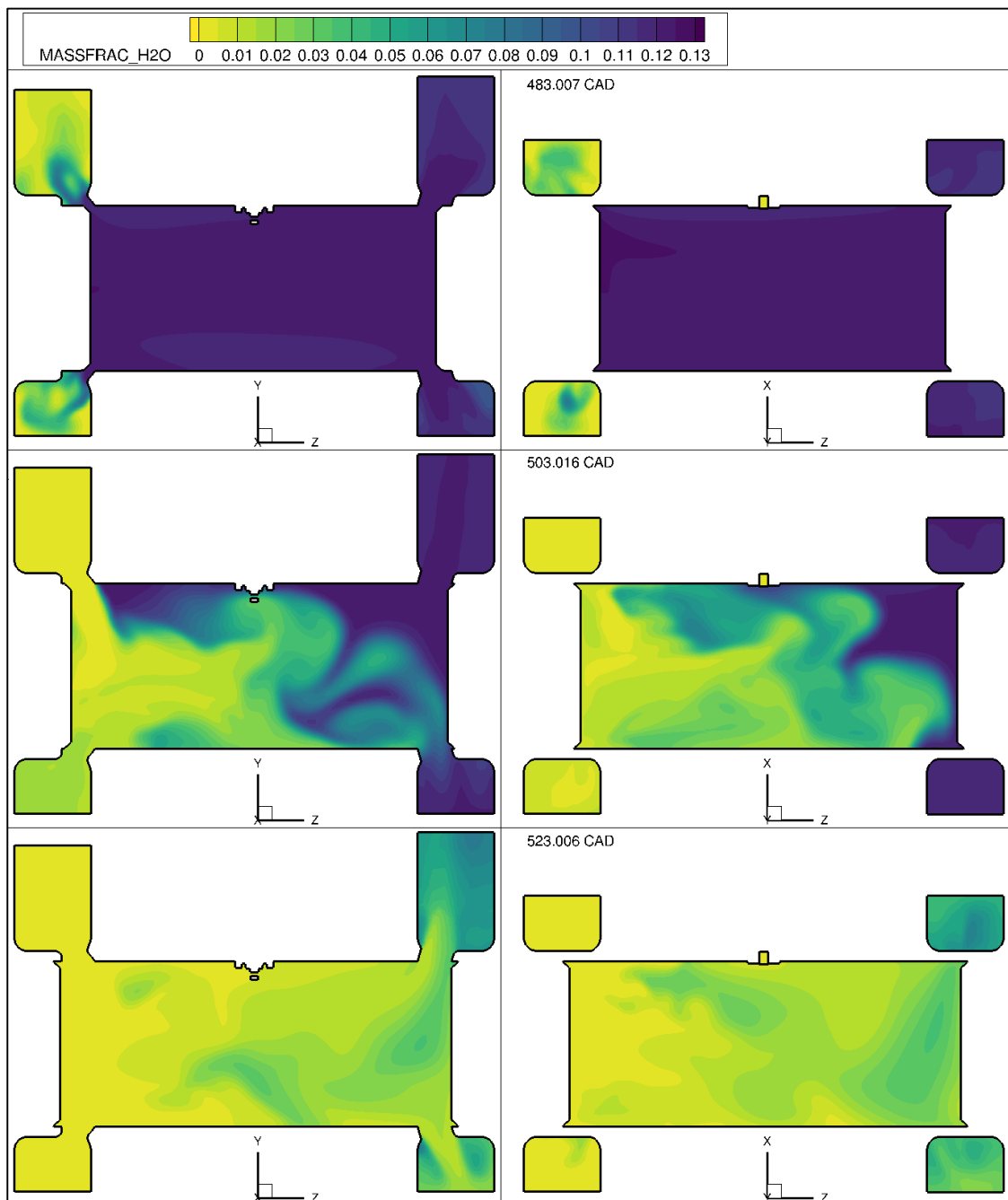


Figure 107 - H<sub>2</sub>O Mass Fraction in the X Plane (Left) and Y Plane (Right), 483 CAD to 523 CAD

From this, and using H<sub>2</sub>O as a visual trace of the burned fraction, it can be deduced that there is indeed mixing of the fresh charge and the burned fractions in the cylinder in these regions, and this will negatively impact the scavenging efficiency of the engine. For example, at 523 CAD in Figure 107, there is still a degree of burned mixture present towards the intake ports. Nevertheless, that mixing occurs is not unexpected, and is in agreement with the literature [5], [30]. It is also not sufficient in this case to prevent adequately scavenging the cylinder, even though a greater delivery ratio is required because of it. Figure 108 shows the H<sub>2</sub>O mass fraction in the central X and Y planes of the cylinder from 583 to 603 CAD. The in-cylinder mixture appears largely uniform, and a small amount of burned fraction has mixed with the fresh charge - on the order of a few percent (recalling that these contours represent H<sub>2</sub>O, which is only part of the burned mixture):



Figure 108 - H<sub>2</sub>O Mass Fraction in the X Plane (Left) and Y Plane (Right), 583 CAD to 603 CAD

## 6.8 Summary Comments on Engine Simulation Work

In this chapter, an engineering problem – the lack of empirical data with which to program the engine ECU - has been mitigated through the use of CFD simulations. The approach used was to model the engine cylinder geometry over an array of (motored) scavenge pressure and engine speed conditions,

and the trapped mass in the cylinder used to generate a fuel table. To test the accuracy of the motored simulations, a selection of scavenge pressure and rpm conditions were chosen, and their calculated trapped masses used to predict the required fuel to configure fuelled simulations. Methane was chosen as the fuel, due to the comparative ease of modelling since no spray/wall film/evaporation effects needed to be considered. It was found that generally, the motored trapped mass (in conjunction with the appropriate air/fuel ratio) could be used to predict the required fuel with sufficient accuracy to enable a combustible mixture under most conditions. The exception was those at higher engine speeds and lower scavenge pressures, where the residual fractions still in the cylinder due to imperfect scavenging had a negative effect, and consequently the required fuel was over-estimated – by more than 40% in one instance.

## 7. Test Firing the Engine

In this chapter, the work undertaken to design and build the engine, as well as simulate the cylinder geometry, was combined to enable the first firing of the engine. The ECU and main power wiring that support the engine operation are detailed, as well as the control pendant used to start and stop it. Example pin assignments to the ECU are given for reference. Preparation of the engine before taking it for testing, including assembly of the ECU, wiring harness and engine onto a suitable stand, is discussed. An overview of how the engine was timed as well as an important ‘dry cranking’ process (used to confirm the function of essential engine components like the oil system), are noted. Following these sections, a record of the first successful run of the engine is presented. This was not intended to be a robust testing regime; rather it is the first evidence of the fact that the engine and combustion system are able to function. Important observations of the engine behaviour that were gained in the process are discussed, alongside future steps towards the next stages of engine testing.

### 7.1 Engine Control Unit, Wiring Harness

The prototype engine features direct injection: direct injectors require more complex driving circuitry than port injectors, typically featuring a high current pulse to open the injector quickly, followed by a lower current used to hold the injector open [5], and not all aftermarket ECUs are able to do this. The LifeRacing F88GDi4 V2 ECU is however capable of driving direct injectors and was used as a starting point for the wiring harness [176]. Selected specifications of the ECU are included in Table 14 (for full specifications please see [177]).

Table 14 - Life Racing ECU Specifications

Specification	Value
Maximum dimension including connector	183 mm x 125 mm x 36 mm
Mass	520 g
Maximum operating temperature	85 °C
Connector	88-pin Bosch Type
Ignition coil outputs	4 (TTL or IGBT)
General PWM/port injector outputs	10
Inductive load/general PWM outputs	2
Direct injector outputs	4
Power supply	6 V – 32 V (with reverse polarity protection)

An example of a pinout configuration is given in Table 15, showing how sensors/components can be attached to the ECU. Note that this is only an example and should be viewed with caution. The column entitled ‘LifeCAL Flag’ refers to the software LifeCAL: this is used to program the ECU, and is available at [167]. The reader is also advised that ‘flags’ for certain components, such as the GDI pump, require special configuration in this software in order to work correctly.

*Table 15 - Example ECU Pin Configuration*

<b>Component</b>	<b>ECU Pin</b>	<b>LifeCAL Flag</b>
GDI pressure (pin 2)	15 (INPUT #05)	Direct Injection Pressure 1A
Bypass valve (pin 2)	14 (INPUT #07)	Throttle Position 1A
MAP sensor (pin 1)	11 (INPUT #10)	Manifold Absolute Pressure 1A
Surge chamber temp.	8 (INPUT #16)	Air Charge Temperature 1A
Blower discharge temp.	16 (INPUT #03)	Air Charge Temperature 1B
Coolant temp.	10 (INPUT #12)	Engine Coolant Temperature 1
EGT 1	40 (THERMO - #01)	N/A
EGT 2	70 (THERMO + #01)	Exhaust Gas Temperature 1
Crank sensor	9 (INPUT #14)	Crank Position A
Coil signal (pin 2)	2 (IGNITION #08)	Cylinder 01 Primary Ignition
Injector +ve	27 (GDI + #01)	N/A
Injector -ve	54 (GDI - #01)	Cylinder 01 Primary Injector
Injection Pump +ve	58 (GDI PUMP +)	Ignition #12
Injection Pump -ve	32 (GDI PUMP -)	Ignition #12
Relay 1 (radiator fan)	30 (FUEL #14)	Fan5
Relay 2 (blower drive)	31 (FUEL #13)	Fan2
Relay 3 (start solenoid)	N/C Manual Button	N/A
Relay 4 (fuel lift pump)	34 (FUEL #09)	Fuel Pump 1
Relay 5 (ign. coil 12 V)	6 (FUEL #10)	Engine Enabled Output
Relay 6 (charge air fan)	49 (FUEL #08)	Fan4
Relay 7 (coolant pump)	22 (FUEL #07)	Fan1
Lambda V	18 (LAMBDA V #01)	N/A
Lambda Ground	77 (LAMBDA GROUND)	N/A
Lambda I	76 (LAMBDA I #01)	N/A
Lambda Heater (10 V)	20 (FUEL #15)	Lambda Heater 1

The ECU was attached to a large enclosure, which serves as the central meeting point of the wiring harness. It contains the relays, fuses, and various connections between components in an environment

where they are better protected from physical damage or exposure to the elements. It provides strain relief for all of the wires, which connect through glands on the sides, and similarly reduces the risk of damage to the ECU interface since both it, and its matching connector, are attached to the enclosure. Initially, the enclosure also served as the point of control for the engine, with a key-switch, start button, emergency stop button and an oil pressure warning light. The emergency stop button was connected to an input on the ECU. However, a detailed risk assessment (necessary before engine testing could commence) established that the controls for the engine must be suitably remote, such that operators could remain at a safe distance from the engine during testing. It also established that the emergency stop must cut-off all power to the engine as well as the supply of fuel, independent of the ECU. Therefore, the enclosure was modified extensively, and the engine controls removed from it, although a large manual isolator switch on the side of the box remained, as did a voltmeter on the top.

### 7.1.1 Revised Wiring System

The revised wiring system includes a remote pendant, shown in Figure 109. All the engine controls (apart from speed, which is controlled by the preset governor spring) are operated from this pendant, including power to the running stand. The toggle switch (A) sends a signal to the ECU (engine enable), and the red light (B) is an oil light connected directly to the oil pressure switch i.e. not via the ECU. The start button (C - top left) is connected directly to the starter solenoid: this means the ECU can be disconnected and the engine cranked without it, for example to confirm adequate oil pressure. The main power for the stand is routed through a large relay, which connects the positive 12 V of the battery through to the manual isolator on the wiring enclosure. To operate the relay solenoid, power is taken from the main 12 V input to the relay, through both the emergency stop button (D) and key switch (E) at the pendant: if power is turned off at the pendant, power is lost to the stand. Additionally, a solenoid valve was incorporated in the fuel line feeding the fuel lift pump, such that the valve shuts off fuel to the engine if it is without power. Note that the valve has a manual over-ride for the purpose of fuel draining.

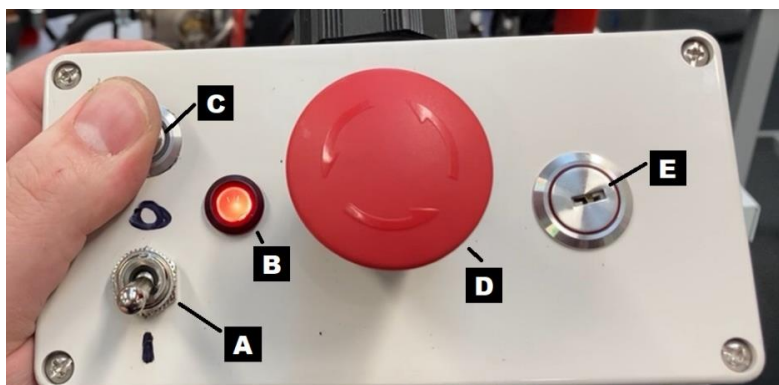


*Figure 109 - The Handheld Control Pendant*

A simple schematic of the main power circuit is included below in Figure 110. The thicker black lines indicate the main power wires, whereas the thinner wires indicate those which connect to the pendant and solenoid.

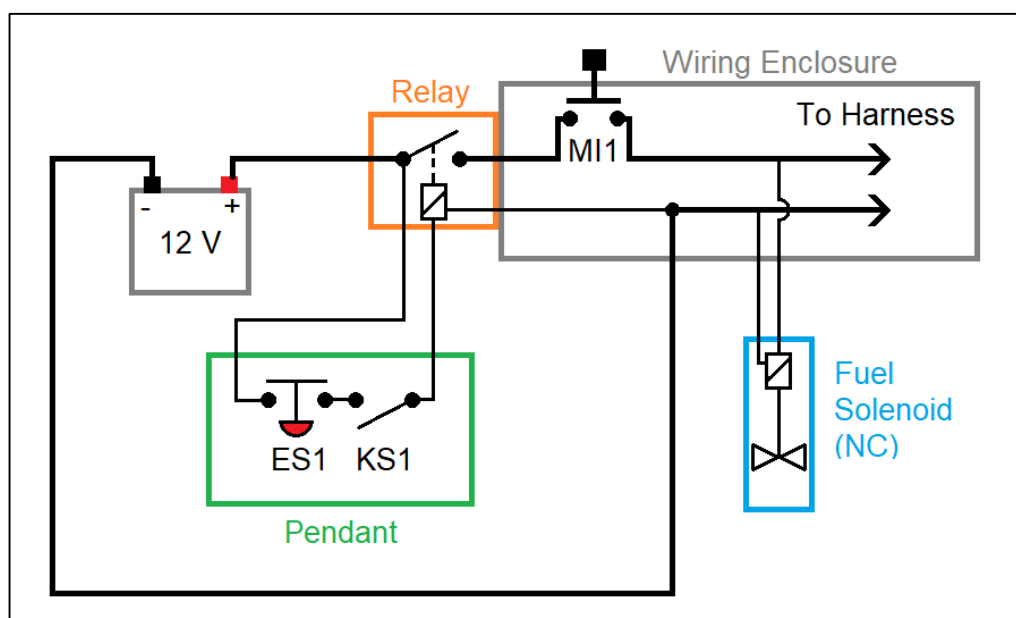


Figure 110 - Main Power Circuit: *ES1 = Emergency Stop Switch; KS1 = Key Switch; MI1 = Manual Isolator; NC = Normally Closed*

The large arrows and ‘To Harness’ indicate the point at which the power connects to the rest of the wiring harness, including the ECU and power to the starter motor. Figure 111 shows a view inside of the wiring box when it had been modified to include the remote-control pendant. Whilst it is complex, the layout is quite deliberate. On the left-hand side of the lower case is a wiring gland (larger than it was previously because conduit was added). This brings in the positive line from the power relay, via the isolator switch on the front of the lower case, as well as the ‘ground’ terminal. The ground terminal is fastened to the back of the enclosure where fly-leads to the various components join to it. The back of the isolator switch has been covered with some rubber-bonded cork sheet, whose purpose is to prevent wires rubbing on the terminals on the back which could then short out.



*Figure 111 - Inside the Wiring Box*

Just visible on the left-hand side of the back of the lower case is another cable gland. This takes 12-volt power to the engine, connecting at the starter motor and its mount. The signal to the starter motor has a dedicated relay in the lower case which is hidden behind the front-most wall. The wiring to the ECU connector exits through another cable gland on the back of the lower case, on the right-hand side (obscured by the internal wiring). The upper case features an array of fuses on the left – these are typical automotive-style blade fuses, and the 12-volt positive from the battery is distributed to various components (including the starter signal relay) via these fuses. Note however that the power supply to the ECU is not fused. Out of view, on the inside of the top of the case, are all of the other relays which control various functions like the water pump, fuel-lift pump, power to the ignition coil etc., and many of these are controlled by the ECU. Additionally, also out of view are two cable glands on the back of the upper case, which take control, power and signal wires to the various components on the engine.

### **7.1.2 Running Stand**

The engine and wiring harness are supported by a portable running stand. The completed stand is shown below in Figure 112. This was made by modifying a steel-framed trolley, salvaged and donated by one of the technicians at UEA. Bearing in mind the small size of the engine and the need to be able to transport it to suitable facilities, it has several desirable features. These include caster wheels (which were renewed) that support two welded tubular steel frames making up the front and back. These are connected by steel profiles - two of which form diagonals, making the assembly quite rigid, and two aluminium covers were fastened to connecting rails on the top. The engine is fastened to two mild steel tubes, which are bolted to the top of the front and rear frames of the stand, allowing the fasteners for the engine to be inserted from underneath into the threaded holes in the engine sump.

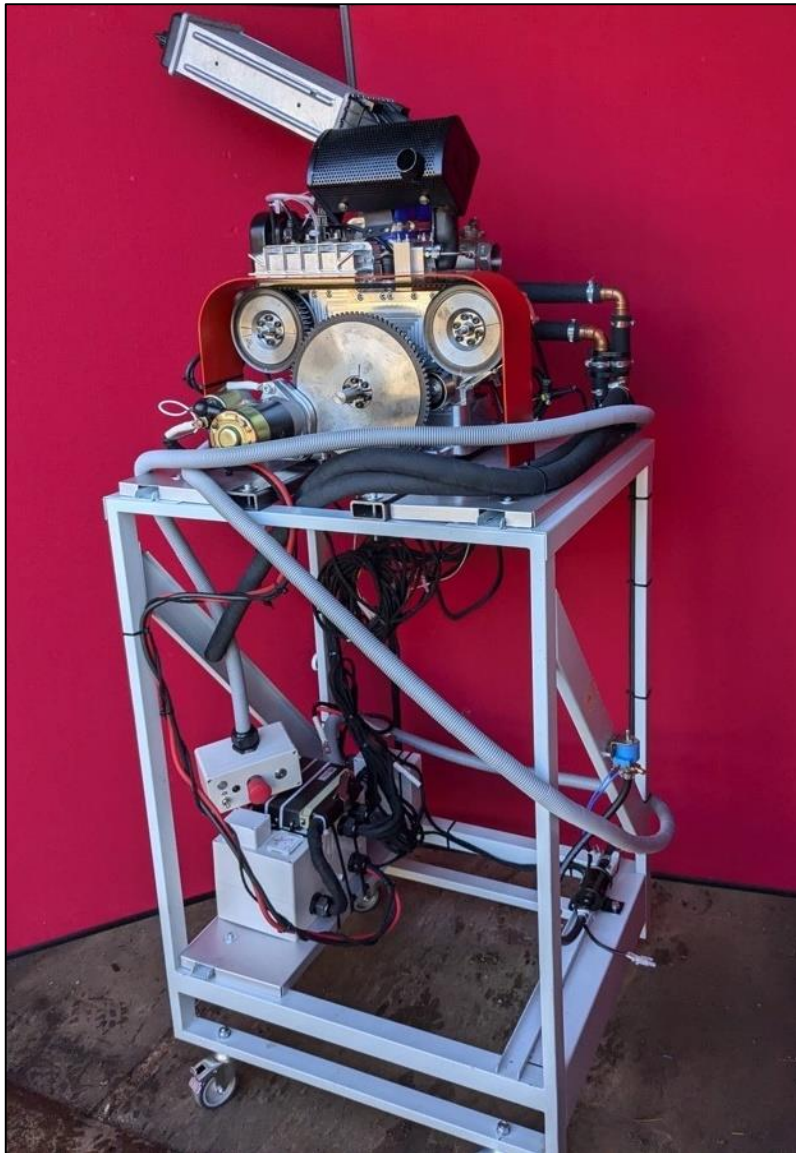


*Figure 112 - Completed Test Stand with Engine ready for Testing*

On the bottom of the stand, the wiring enclosure was fastened to another aluminium cover connected to one of the lower steel profiles. Figure 113 shows the layout on the bottom of the engine test stand, showing the wiring enclosure (1), and the location of the main cutoff relay inside a smaller box at position 2. The grey conduit extending from this box connects to the remote-control pendant. Position 3 indicates the location of the fuel cutoff solenoid (largely hidden by the running stand, but this is visible on the right of Figure 112). Components have been attached using cable-ties where possible, including the wiring box, to reduce the number of drilled holes that could weaken the stand.

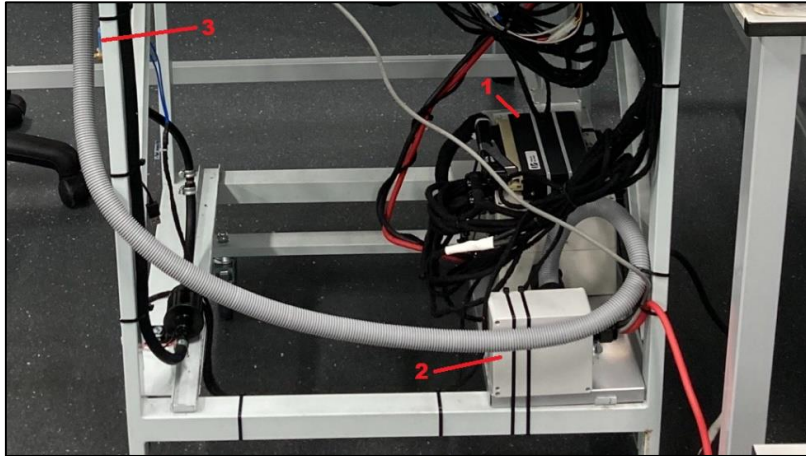


*Figure 113 - Test Stand Wiring*

## **7.2 Timing the Engine and Programming the ECU**

Figure 114 shows part of the process by which the engine can be timed. The slot for the woodruff key on each crankshaft roughly aligns with the crankpin, so was used as an approximate reference for IDC for each piston. Using an angle gauge as in Figure 114, a set of timing marks were drawn on the intake crankshaft pulley: one to be aligned with the woodruff key-slot, the other 18 degrees anticlockwise (ahead) of it.



*Figure 114 - Adding Timing Marks to the Crankshaft Pulleys*

On the other pulley a single timing mark was added, to be aligned with the key-slot on the exhaust crankshaft. The pulleys were placed onto the respective shafts on the back of the engine. Taking advantage of the RINGFEDER® locking assemblies, a straight edge was placed along the back of the engine and used to align the single timing mark of the exhaust crankshaft (facing towards the centre of the engine) with the 'ahead' mark on the intake crankshaft (also facing the centre of the engine). Then, the key-slots in both crankshafts were aligned with their respective marks, and the locking assemblies were tightened with the timing belt in place, setting the timing of the exhaust piston ahead of the intake

piston by approximately 18 CAD. In a similar manner, the GDI pump cam was timed by removing the GDI pump and feeling for the low point on the cam. It was configured such that injection occurred during the window of time that the cam was rising and actuating the GDI pump. The timing wheel, on the front of the engine, was set using the taper-lock bush in the centre of the front pulley, to which it is attached. Note that it was expected that these methods bring with them a limit to accuracy, but for the purposes of a first firing of the engine they were expected to be sufficient. For the purposes of future engine research, greater accuracy would naturally be required - for example by using timing wheels keyed to the crankshafts.

### 7.2.1 ECU Parameters and Fuelling Configuration

Table 16 shows the basic ECU parameters that were used for the first firing of the engine. As noted above, the values for timing should be viewed with the expectation that there is some degree of inaccuracy, likely on the order of a few CAD.

*Table 16 - ECU Parameter Configuration for Engine Testing*

ECU Parameter	Value
Base Ignition Angle 1	15 CAD before IDC
Primary Fuel Injection Start Angle 1	220 CAD after IDC
Direct Injection Pressure Limit	35 Bar

The GDI pressure limit was kept deliberately low because of the reduced fuel flowrates that were expected to be required for such a small engine. Also, the ignition timing of the engine was retarded versus the timing that was used in simulations (see section 6.7) as a precaution, especially given the steep slope of the low-speed PV curves in Figure 97. Notwithstanding the different fuel and the cautionary evaluation of the graphs themselves, this was to reduce the chance of engine damage. The injector timing was configured using the fuel table generated in chapter 6. This was achieved by way of setting the maximum injection time at 30 ms for the full speed/load condition, and all other points determined by multiplying this value by the respective percentage in the fuel table. This produced the injection timings shown in Table 17. These values were calculated using the rounded percentages in the fuel table in chapter 6. The ECU allows a global multiplier to be applied: for example, if a global multiplier of 0.1 were defined, the maximum injection duration would be 3 ms, the value at 3000 rpm and 150 kPa would be circa. 2.367 ms, and so on. It is noted that whilst the simulated gaseous injection profiles needed to account for the change in CAD per ms with rpm, the real injection timings do not. This is because they are already in terms of ms and not in terms CAD, so there is no need for a conversion.

Table 17 - Injection Base Timing for ECU

Base Fuel Injection Duration in Milliseconds									
Max fuel is:							30	Milliseconds	
Scavenge Absolute Pressure (Bar)	1.8	27.15	27.48	27.87	28.35	28.74	29.22	29.67	30
	1.7	25.68	25.98	26.34	26.82	27.21	27.6	27.99	28.35
	1.6	24.18	24.51	24.84	25.2	25.62	26.04	26.46	26.76
	1.5	22.71	23.01	23.34	23.67	24.06	24.45	24.81	25.14
	1.4	21.24	21.54	21.81	22.14	22.47	22.83	23.19	23.55
	1.3	19.77	20.04	20.28	20.58	20.91	21.24	21.6	21.9
	1.2	18.3	18.51	18.78	19.02	19.35	19.65	19.98	20.25
	1.1	16.83	17.04	17.25	17.49	17.76	18	18.15	18.21
		1500	2000	2500	3000	3500	4000	4500	5000
RPM									

### 7.2.2 Dry Cranking

Dry cranking of the engine was performed to enable troubleshooting in a low-risk manner. For this process, the sump was filled with lubricating oil, but the engine was not fuelled so it could not start. The water pump and fuel-lift pump were disconnected to avoid damage from running dry. The starter motor was then used to turn the engine over, and minor modifications made to the ECU configuration to ensure various sensors were communicating as required (for example the engine position sensor). Figure 115 and Figure 116 show front and rear views respectively of the engine rotating:

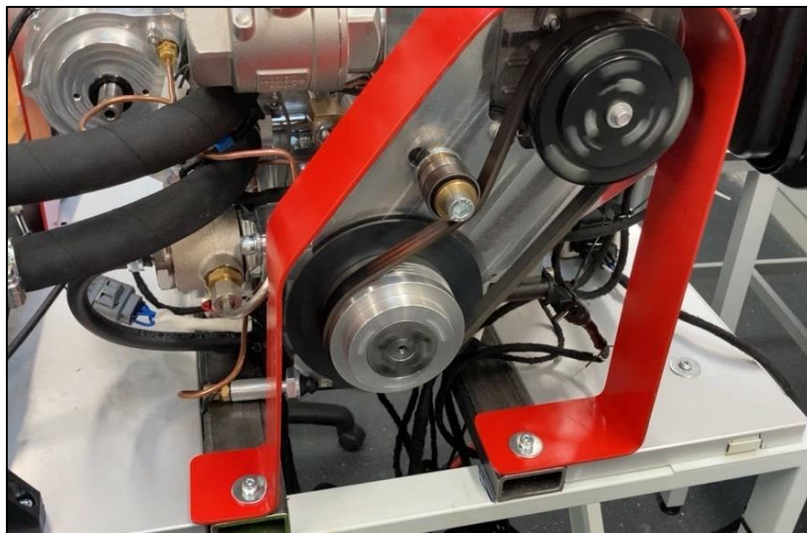
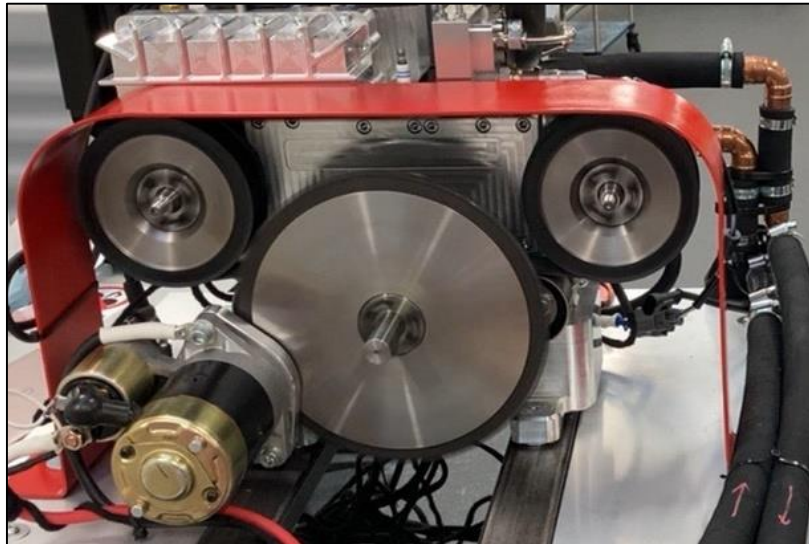


Figure 115 – Front View of Engine Turning during Dry-Cranking

These confirm several important requirements. Firstly, the starter motor engaged with and drove the engine correctly, and subsequently disengaged when power was removed. Secondly, in Figure 115 the

front poly-vee belt can be seen running, and the clutch on the blower-drive has engaged as it should do. This is important, since it confirms that the ECU has synchronised with the engine rotation: the engine position sensor is working, and the ECU has activated the relay that powers the clutch to the blower. Thirdly, in Figure 116 both the intake and exhaust crankshaft can be seen to rotate, alongside the flywheel. This means that the timing system is working, and the belt is not adversely fouling on any of the other components or running off any of the pulleys/tensioners.



*Figure 116 - Rear View of Engine Turning during Dry-Cranking*

Additionally, dry-cranking identified some minor oil leaks around several of the oil pipe glands, which were subsequently rectified. More importantly, the engine oil warning light went out when the engine was turning, confirming that the oil pump is working satisfactorily, as shown in Figure 117:

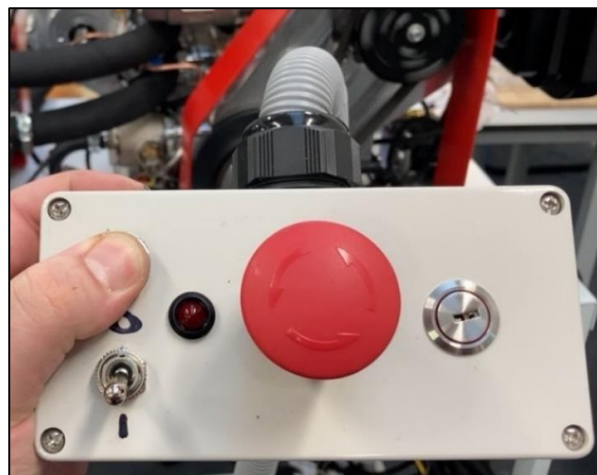


*Figure 117 - Oil Light off Indicating Oil Pump Function*

Once the engine had stopped turning, the oil light re-lit (flashed) indicating the pressure switch was working normally (i.e. it was not a loss of connection between the switch and indicator light, for example). The engine was therefore ready to be taken for initial testing.

### **7.3 First Firing of the Engine**

The same risk assessment that resulted in the modifications to the control system of the engine also precluded the possibility of initial testing the engine at UEA, due to a lack of appropriate facilities. Therefore, for the first firing of the engine, it and its supporting equipment were transported to Expansion Engines Limited in Great Ellingham, Norfolk, in October 2024. A significant factor in choosing Expansion Engines Limited was its comparatively remote location, since fewer people in the local vicinity meant there was less risk of harm in the event of catastrophic mechanical failure.

#### **7.3.1 Scope and Results**

The first firing of the engine is not the same thing as a robust engine testing regime, rather it is a pre-requisite to allow future testing. The objective of the first firing therefore is to determine if the engine and its combustion system works at all, and to do so using a conventional, widely available pump gasoline (BP Ultimate). Recall that an SI OP2S engine faces challenges, such as lack of tumble, large flame propagation distance from the spark plug, and the need for direct injection. The latter in particular presents its own challenges such as spray wall impingement, reduced time for fuel dispersion, evaporation and mixing - all of which are magnified by the small 39 mm cylinder diameter of the engine. Additionally, errors in programming the ECU, or the mechanical or electrical failure of components, and other similar eventualities could also have prevented the engine starting. There were therefore many things that could have caused the engine not to meet its first design goal. However, following preparations which included bleeding the fuel system of the engine, an attempt was made at starting it, and after an initial period of cranking, the engine fired, and then started. At this stage, it did not run for very long before it stopped: it is suspected that this was due to an over-fuelling condition that, in part, may have been caused by an incorrectly configured lambda sensor (an error made when programming the ECU prior to testing). However, even after re-configuring the lambda sensor, the issue persisted. This led to questions as to whether the engine was actually over-fuelling, or whether another issue was causing the problem. To test this, the ECU was re-configured by using a zero global multiplier to the fuel injection, such that the fuel injection was effectively turned off. The engine re-started – suggesting that it was indeed receiving too much fuel. Figure 118, Figure 119 and Figure 120 capture some of the first cycles of the engine, showing the discharge from the exhaust. The process of fuelling 100% and fuelling 0% (as well as in between) - was repeated several times, with the same result, and consequently the engine never ran long enough to warrant filling the cooling system.



*Figure 118 - First Engine Start Video Still 1*



*Figure 119 - First Engine Start Video Still 2*



*Figure 120 - First Engine Start Video Still 3*

Nevertheless, following the first runs of the engine a physical investigation was performed, and it was identified that the high-pressure injector line was leaking where it attaches to the injector header. The suspected cause of this was a mis-matched taper and ball seal combining with a slightly misaligned pipe, as it had not initially appeared to be leaking. The high-pressure fuel line was removed and adjusted for a slightly better fit. Shortly after this, the engine ran for longer and audibly picked up speed. However even from the first runs, as the engine fired some undesirable behaviour was observed from the timing system. The timing belt, despite being tightened, developed a vertical oscillating motion, on some occasions actually hitting the belt guard above. Figure 121 and Figure 122 show one of the runs where this behaviour was observed.

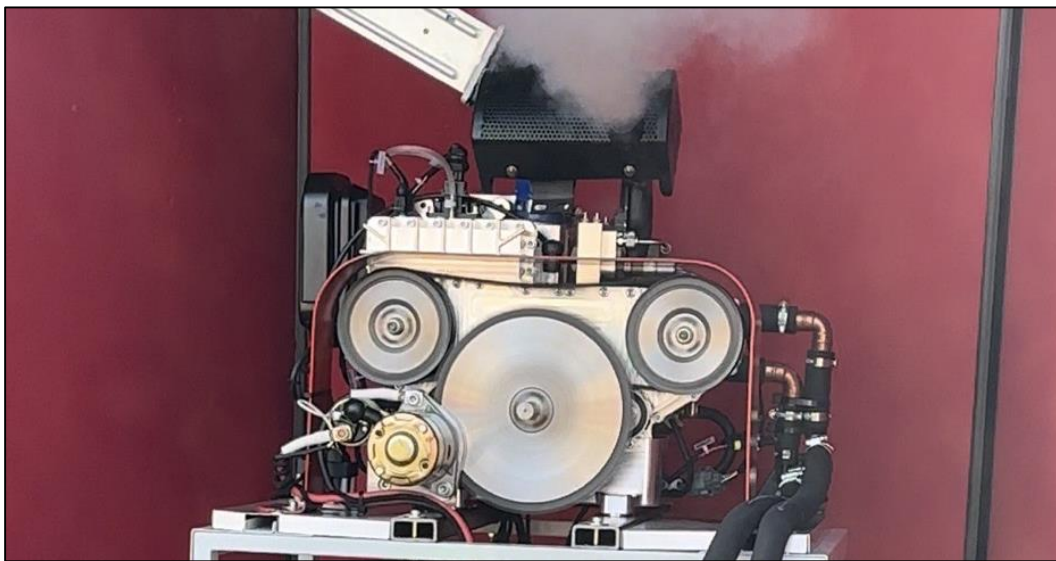


*Figure 121 - Engine Run Video Still Belt Motion 1*

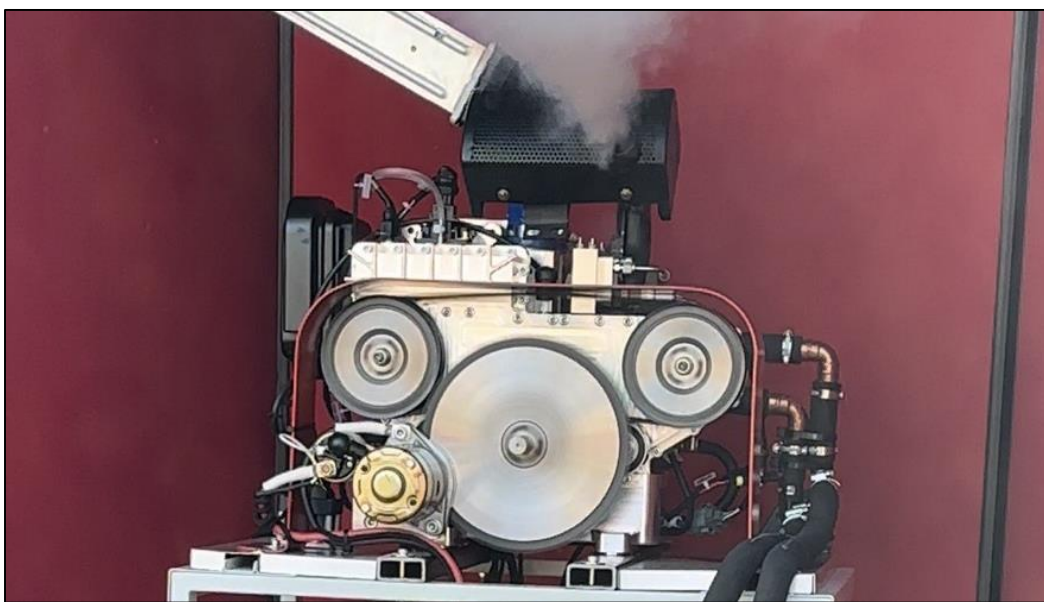


*Figure 122 - Engine Run Video Still Belt Motion 2*

This behaviour was absent from the dry-cranking process, but could actually be heard at times over the sound of the engine when it was running: this is evidence of the importance of the belt guards since such violent ‘flapping’ of the belt might have caused it to fail. One theory behind this behaviour is that it is caused by the differences in crankshaft timing. Recall the exhaust crankshaft leads the intake crankshaft and that the engine, when viewed from behind, rotates in an anticlockwise direction. Therefore, because the exhaust crankshaft passes IDC first, the increased cylinder pressure due to combustion may be causing it to temporarily ‘overtake’ the intake piston (with respect to its intended timing), so slackening the belt on the top of the engine given its direction of rotation. Then, as the intake piston passes IDC, it may then ‘catch-up’ to the exhaust piston, restoring the belt tension. Whatever the cause, this behaviour could be resolved by adding an additional belt tensioner on the top of the belt run.

### 7.3.2 Final Comments on Testing

The primary intention of the first firing of the engine was to prove that it worked, and as evidenced by Figure 118 through Figure 122, this was certainly the case. It is therefore one of very few working modern, direct injection SI OP2S engines, and is able to drive itself without the need for any other source of mechanical or electrical power beyond a typical 12 V battery. It also evidences the value of the CFD simulations conducted, since these guided the setup of the ECU, and confirms that whilst SI OP2S engines do face challenges, the high-swirl combustion system is able to work sufficiently well. It therefore meets the identified requirements in chapter 2, but clearly a number of important takeaways have been gained, and these serve to inform future work requirements.

Firstly, the engine over-fuelled significantly. This may be due to an error in configuring the ECU, but needs to be resolved before the engine could be used in further engine research. Secondly, the timing system of the engine works, but requires remedial modification to prevent the belt oscillating violently, since this could lead to failure. Thirdly, the engine needs to demonstrate stable, smooth running under a load, over an extended period (to confirm durability), and the cylinder pressure transducer utilised to gain an understanding of how *well* the combustion system is able to work. These three areas should therefore form the foundation of any further use of the engine.

## 8. Conclusions and Further Work

Opposed-piston two-stroke engines possess inherent thermodynamic advantages over conventional four-stroke engines. Historically, spark- and compression-ignition engines were developed, with examples of the latter often being amongst the most efficient engines in their class at the time and by far the most common of the two combustion systems. Different mechanical arrangements were explored to overcome the technical challenges of linking the motion of the two pistons together, for example extended connecting rods in combination with additional crank throws, folded crankshafts, and multiple crankshafts. Unfortunately, despite their notable successes opposed-piston two-stroke engines fell out of favour in the latter half of the 20th century, much like other piston-ported two-stroke engines. One of the main reasons was likely ever more stringent emissions standards that were easier to achieve with four-stroke engines at the time.

But with growing concerns around climate change in particular, the internal combustion engine is coming under ever increasing pressure to improve. This has led to re-evaluations of the opposed-piston two-stroke architecture and its thermodynamic advantages, with new compression ignition examples recording impressive results. However, given the urgency of the need to reduce greenhouse gas emissions, it is surprising that research into spark-ignition opposed-piston engines appears less prevalent, particularly in regards to real working engines. This is even though certain low-carbon fuels, like bio-methane or bio-ethanol for example, are much easier to use in a spark-ignited engine. Spark-ignition does typically bring with it a penalty to brake thermal efficiency due to reduced compression ratios, but by using an opposed-piston two-stroke architecture and leveraging its thermal advantages, it might be possible to partially compensate for this. If so, a spark ignition opposed-piston engine may then present a way to exploit fuels like bio-methane or bio-ethanol more efficiently in a spark-ignition context. In so doing, it could offer another option towards reducing emissions.

### 8.1 Significant Research Contribution

To evaluate the possible opportunities of SI in modern OP2S engines empirically, the appropriate apparatus is required – including a suitable (SI OP2S) engine that benefits from modern engine technology like GDI. But of the very limited number of contemporary examples that were identified, several introduced additional risks by veering from the well-proven crank-slider arrangement, for example by using cam-plates or a free-piston design. Whilst significant and impressive undertakings themselves, it is clear that an SI OP2S engine dedicated to the task of engine research would present a significant contribution by facilitating future empirical data acquisition. This is particularly relevant given the fact that the OP2S architecture does present challenges to SI combustion, such as a lack of

tumble and a large flame-propagation distance from the spark plug to the other side of the combustion chamber.

The aim of this research project therefore was to design, build, simulate and proof-test a suitable research engine. The result is a new and novel, working SI OP2S engine, that does not require any external power to run beyond a typical 12 V battery. It is also quite compact: the maximum dimension of each engine case is less than 450 mm, and its swept cylinder volume is less than 120 cm<sup>3</sup>. Despite this, it still features de-coupled (from piston motion) scavenging using a positive-displacement blower, a separate, sump-type oil system, ECU-controlled direct fuel injection, and two crank-slider assemblies. Furthermore, it incorporates a capability to provide cylinder-pressure data, since it features a seat for a cylinder pressure transducer, and can couple up to a load. In using a simple to adjust timing mechanism – in which both intake and exhaust crankshafts can be adjusted independent of anything else - it is also deliberately designed to be as fuel agnostic and flexible as possible, whilst being very much over-built.

Before test-firing the engine, detailed CFD simulations were run to aid the programming of the ECU that controls it, based on evaluating the trapped mass of air in the cylinder under various motored-engine conditions. This provided a fuel-agnostic table, delineated by engine speed and scavenge pressure, from which the real injection timing could be estimated, but it also served as a useful grounding for the expected behaviour of the engine. In particular, by using fuelled simulations where the required fuel was estimated based on the results from selected motored conditions, it was found that the scavenging performance of the engine is likely to decrease at higher speeds and lower scavenging pressures. This resulted in a fuelled simulation at 5000 rpm and 120 kPa scavenge pressure in which the required fuel had been overestimated by more than 40 %, based on an in-cylinder equivalence ratio that was in excess of 1.4 when the target was stoichiometric. At 5000 rpm and 150 kPa the overestimation was closer to 20 %, and the 3000 rpm/120 kPa and 5000 rpm/180 kPa cases were both closer to 10%. Conversely, at 1500 rpm and 120/150/180 kPa, and 3000 rpm and 150/180 kPa, results indicated that the motored results were able to predict the required fuel within 2%. Furthermore, evaluating a roughly central condition of 3000 rpm and 150 kPa, it was found that the swirl inducing geometry of the air-side surfaces of the engine appeared to have the desired effect in encouraging a bulk swirling motion in the cylinder. This should aid fuel mixing and flame propagation, helping to mitigate against the large flame propagation distance from one side of the combustion chamber to the other.

Following the design, construction and simulation of the engine, supporting equipment was also commissioned. This included a running stand that features a stand-alone wiring system and remote-control pendant, and requires only a fuel tank, 12-volt battery and coolant hopper to enable the engine to work. Using this test stand, the engine was taken for a first test run on petrol, at Expansion Engines Limited in Great Ellingham, Norfolk. This provided a highly significant result: the engine started and

ran repeatedly, despite being a previously unproven. It is therefore among very few known contemporary examples of the SI-OP2S engine architecture, particularly those using engine-driven blower-scavenging and ECU-controlled direct fuel injection. In doing this, it proved that the custom-designed swirl-based combustion system was able to work sufficiently well, even though it was suspected that fuel dispersion and mixing would prove challenging due to the lack of tumble in an OP2S design. However, challenges were encountered, including a persistent over-fuelling issue which requires further investigation, and the need for remedial modifications to the timing system to prevent possible timing-belt failure. Several important avenues for future work have therefore been identified, in order for the prototype to reach its full potential.

## **8.2 Future Works**

The first objective of any future undertakings involving the prototype should be to achieve stable, extended duration, and loaded running. This should include using more accurate means to time the engine than were necessary for the purposes of ‘proof of concept’ running, as well as taking advantage of its capability to use a cylinder pressure transducer. By using the cylinder pressure transducer, a much greater understanding of how well the combustion system performs will be possible. This might include, for example, determining how effectively the swirling regime contributes to a reliable combustion process, by evaluating the pressure rise rate(s) following SOC, and the variation between engine cycles.

Running the engine over an extended period and under load will also allow the benchmarking of the engine against conventional four-stroke engines, such as by measuring its thermal efficiency under different conditions. A further benefit of such operation is it will help to fully seat the piston rings and allow other engine components to wear in. This might offer an opportunity to conduct analyses on the engine oil – for example to establish how much wear material is present, or whether it has significantly degraded due to overheating.

Once these focus areas have been suitably addressed, the prototype could offer the opportunity to explore various other aspects of OP2S engine research, for example the combustion of alternative, spark-ignition suitable fuels, such as hydrogen or ethanol. It is notable in this regard that by replacing the cylinder liner and/or cylinder block – which are a subassembly that fit into the engine cases – it might be possible to investigate different porting arrangements in addition. It is therefore clearly demonstrated that this research project has made a significant contribution in delivering a novel prototype research engine, that could be a useful aid to future engine research in the quest to reduce climate-changing greenhouse-gas emissions.

## References:

- [1] P. K. Senecal and F. Leach, 'Diversity in transportation: Why a mix of propulsion technologies is the way forward for the future fleet', *Results in Engineering*, vol. 4, p. 100060, Dec. 2019, doi: 10.1016/j.rineng.2019.100060.
- [2] G. Kalghatgi, 'Is it the end of combustion and engine combustion research? Should it be?', *Transportation Engineering*, vol. 10, p. 100142, Dec. 2022, doi: 10.1016/j.treng.2022.100142.
- [3] G. Kalghatgi, A. K. Agarwal, F. Leach, and K. Senecal, *Engines and Fuels for Future Transport*. Singapore, SINGAPORE: Springer Singapore Pte. Limited, 2021. [Online]. Available: <http://ebookcentral.proquest.com/lib/uea/detail.action?docID=6826338>
- [4] 'The role of agricultural machinery in decarbonising agriculture', European Agricultural Machinery Association Website. Accessed: Aug. 02, 2024. [Online]. Available: [https://www.cema-agri.org/images/publications/position-papers/CEMA\\_decarbonising\\_agriculture\\_27-04-22.pdf](https://www.cema-agri.org/images/publications/position-papers/CEMA_decarbonising_agriculture_27-04-22.pdf)
- [5] J. Heywood, *Internal Combustion Engine Fundamentals 2E*. McGraw Hill LLC, 2018.
- [6] 'BP Statistical Review of World Energy 2022', 2022. Accessed: Apr. 20, 2023. [Online]. Available: <https://www.bp.com/content/dam/bp/business-sites/en/global/corporate/pdfs/energy-economics/statistical-review/bp-stats-review-2022-full-report.pdf>
- [7] M. Kampa and E. Castanas, 'Human health effects of air pollution', *Environmental Pollution*, vol. 151, no. 2, pp. 362–367, 2008, doi: 10.1016/j.envpol.2007.06.012.
- [8] G. Conway, A. Joshi, F. Leach, A. García, and P. K. Senecal, 'A review of current and future powertrain technologies and trends in 2020', *Transportation Engineering*, vol. 5, p. 100080, 2021, doi: <https://doi.org/10.1016/j.treng.2021.100080>.
- [9] 'Boosting the European car sector', European Commission Website. Accessed: Mar. 06, 2025. [Online]. Available: [https://commission.europa.eu/topics/business-and-industry/boosting-european-car-sector\\_en](https://commission.europa.eu/topics/business-and-industry/boosting-european-car-sector_en)
- [10] T. Burton, S. Powers, C. Burns, G. Conway, F. Leach, and K. Senecal, 'A Data-Driven Greenhouse Gas Emission Rate Analysis for Vehicle Comparisons', *SAE International Journal of Electrified Vehicles*, vol. 12, no. 1, pp. 14-12-01–0006, Apr. 2022, doi: 10.4271/14-12-01-0006.
- [11] 'Press Release: Pollution From Tyre Wear 1,000 Times Worse Than Exhaust Emissions', 2020, *Emissions Analytics Website*. [Online]. Available: <https://www.emissionsanalytics.com/news/pollution-tyre-wear-worse-exhaust-emissions>
- [12] 'Motoring: Zero emissions claims', Advertising Standards Authority Website. Accessed: Aug. 07, 2024. [Online]. Available: <https://www.asa.org.uk/advice-online/motoring-zero-emissions-claims.html>

- [13] N. Duarte Souza Alvarenga Santos, V. Rückert Roso, A. C. Teixeira Malaquias, and J. G. Coelho Baêta, ‘Internal combustion engines and biofuels: Examining why this robust combination should not be ignored for future sustainable transportation’, *Renewable and Sustainable Energy Reviews*, vol. 148, p. 111292, Sep. 2021, doi: 10.1016/j.rser.2021.111292.
- [14] ‘HYBRIT; a collaboration between SSAB, LKAB and Vattenfall’. [Online]. Available: <https://group.vattenfall.com/what-we-do/roadmap-to-fossil-freedom/industry-decarbonisation/hybrit>
- [15] A. A. Alabbadi, O. A. Obaid, and A. A. AlZahrani, ‘A comparative economic study of nuclear hydrogen production, storage, and transportation’, *Int J Hydrogen Energy*, vol. 54, pp. 849–863, 2024, doi: <https://doi.org/10.1016/j.ijhydene.2023.08.225>.
- [16] ‘The Future of Hydrogen’. [Online]. Available: <https://www.iea.org/reports/the-future-of-hydrogen>
- [17] D. Helm, ‘Net Zero Realism’, Professor Sir Dieter Helm Website. Accessed: Aug. 07, 2024. [Online]. Available: <https://dieterhelm.co.uk/natural-capital-environment/net-zero-realism/>
- [18] D. Helm, ‘Climate realism – time for a re-set’, Professor Sir Dieter Helm Website. Accessed: Mar. 06, 2025. [Online]. Available: <https://dieterhelm.co.uk/energy-climate/climate-realism-time-for-a-re-set/>
- [19] G. Regner, A. Salvi, L. Fromm, and F. Redon, ‘The opposed-piston engine: The next step in vehicle efficiency’, *VDI Berichte*, vol. 2016, no. 2289, pp. 101–129, 2016.
- [20] G. Regner *et al.*, ‘The achates power opposed-piston two-stroke engine: Performance and emissions results in a medium-duty application’, *SAE Int J Engines*, vol. 4, no. 3, pp. 2726–2735, 2011, doi: 10.4271/2011-01-2221.
- [21] G. Regner, R. Herold, M. Wahl, J. Lemke, F. Redon, and E. Dion, ‘The Renaissance of the Opposed-Piston Two-Stroke Diesel Engine for Commercial Applications’, in *13. Tagung “DER ARBEITSPROZESS DES VERBRENNUNGSMOTORS”*, Graz, Sep. 2011. Accessed: Mar. 02, 2025. [Online]. Available: [https://achatespower.com/wp-content/uploads/2019/12/renaissance\\_of\\_the\\_opposed\\_pistons1.pdf](https://achatespower.com/wp-content/uploads/2019/12/renaissance_of_the_opposed_pistons1.pdf)
- [22] S. Naik, F. Redon, G. Regner, and J. Koszewnik, ‘Opposed-piston 2-stroke multi-cylinder engine dynamometer demonstration’, *SAE Technical Papers*, 2015, doi: 10.4271/2015-26-0038.
- [23] D. Woodyard, *Pounder’s marine diesel engines and gas turbines*, 9th ed. NV. Butterworth-Heinemann, 2009.
- [24] M. Huo, D. Sapkal, and E. El-Hannouny, ‘Hydrogen Opposed-Piston Engine with Direct Injection, Compression Ignition Combustion’, Achates Power. Accessed: Nov. 24, 2023. [Online]. Available: <https://achatespower.com/wp-content/uploads/2023/11/Hydrogen-Opposed-Piston-Engine-with-Direct-Injection-Compression-Ignition-Combustion.pdf>

- [25] Z. Stępień, ‘A comprehensive overview of hydrogen-fueled internal combustion engines: Achievements and future challenges’, *Energies (Basel)*, vol. 14, no. 20, 2021, doi: 10.3390/en14206504.
- [26] ‘Heavy-Duty Diesel Demonstration Program Review’, Achates Power. Accessed: Feb. 27, 2023. [Online]. Available: <https://achatespower.com/wp-content/uploads/2022/06/Achates-Power-HD-Demo-Technical-Review-May-4-2022.pdf>
- [27] R. E. Herold, M. H. Wahl, G. Regner, J. U. Lemke, and D. E. Foster, ‘Thermodynamic benefits of opposed-piston two-stroke engines’, *SAE Technical Papers*, 2011, doi: 10.4271/2011-01-2216.
- [28] R. Van Basshuysen and F. Schaefer, *Internal Combustion Engine Handbook*, vol. 2nd edition. Warrendale, Pa: SAE International, 2016. Accessed: May 03, 2025. [Online]. Available: <https://research.ebsco.com/c/7fhaq6/search/details/lfo2wajvfv?db=nlebk>
- [29] V. Smil, *Prime movers of globalization : the history and impact of diesel engines and gas turbines*. Cambridge, Mass.: MIT Press, 2010. [Online]. Available: <http://site.ebrary.com/id/10453049>
- [30] E. Sher, ‘Scavenging the two-stroke engine’, *Prog Energy Combust Sci*, vol. 16, no. 2, pp. 95–124, 1990, doi: 10.1016/0360-1285(90)90045-5.
- [31] T. Tredgold, *The Steam Engine: Comprising an Account of its Invention and Progressive Improvement*. Cambridge University Press, 2014. doi: DOI: 10.1017/CBO9781107279940.
- [32] W. L. Withuhn, *American Steam Locomotives: Design and Development, 1880–1960*. in *Railroads Past and Present*. Bloomington, Indiana: Indiana University Press, 2019. [Online]. Available: <https://books.google.co.uk/books?id=6guIDwAAQBAJ>
- [33] ‘End of an Era: China’s Last Steam Railroad Closes’, *Railfan & Railroad Magazine Website*. Accessed: Jun. 20, 2024. [Online]. Available: <https://railfan.com/end-of-an-era-chinas-last-steam-railroad-closes/>
- [34] C. Heather, ‘The Beeching Axe’. Accessed: Jun. 20, 2024. [Online]. Available: <https://blog.nationalarchives.gov.uk/the-beeching-axe/>
- [35] ‘North Norfolk Railways’, *North Norfolk Railway Website*. Accessed: Jun. 20, 2024. [Online]. Available: <https://www.nnrailway.co.uk/>
- [36] A. Burton, *Steam Traction on the Road: From Trevithick to Sentinel: 150 Years of Design & Development*. Pen & Sword Books, 2018. [Online]. Available: <https://books.google.co.uk/books?id=rLPNDwAAQBAJ>
- [37] E. F. C. Somerscales, ‘STEAM AND INTERNAL COMBUSTION ENGINES’, in *An Encyclopedia of the History of Technology*, I. McNeil, Ed., 2002, ch. 5. doi: 10.4324/9780203192115.
- [38] ‘THE BRAYTON READY MOTOR OR HYDROCARBON ENGINE’, *Sci Am*, vol. 34, no. 20, p. 303, 1876, [Online]. Available: <http://www.jstor.org.uea.idm.oclc.org/stable/26051100>

- [39] C. Meyer, 'The farm debut of the gasoline engine', *Agric Hist*, vol. 87, no. 3, pp. 287–313, 2013, doi: 10.3098/ah.2013.87.3.287.
- [40] D. W. Edgington, *The Lister D Story 1926-1964*. 2004.
- [41] M. E. Toepel 1870-, *Automotive magneto ignition : its principle and application with special reference to aviation engines*. New York: Spon, 1918. [Online]. Available: <http://books.google.com/books?id=4g1KAAAIAAJ>
- [42] G. G. Lutz, 'Stuart, Herbert Akroyd (1864 - 1927)', 1990. Accessed: Jun. 17, 2024. [Online]. Available: <https://adb.anu.edu.au/biography/stuart-herbert-akroyd-8705/text15235>
- [43] D. A. Wrangham, *The theory and practice of heat engines*. Cambridge [England]: University Press, 1960.
- [44] 'Petters', Grace's Guide to British Industrial History. Accessed: Aug. 01, 2024. [Online]. Available: <https://www.gracesguide.co.uk/Petters>
- [45] G. P. Blair, *The Basic Design of Two-Stroke Engines*. SAE International, 1990. [Online]. Available: <https://books.google.co.uk/books?id=IXJ0EAAAQBAJ>
- [46] 'Marshall, Sons and Co: Tractors', Grace's Guide to British Industrial History. Accessed: Aug. 02, 2024. [Online]. Available: [https://www.gracesguide.co.uk/Marshall,\\_Sons\\_and\\_Co:\\_Tractors](https://www.gracesguide.co.uk/Marshall,_Sons_and_Co:_Tractors)
- [47] R. Alexander, 'History of Detroit Diesel Engines', Hoffmeier Trucking Company Website. Accessed: Jun. 20, 2024. [Online]. Available: <https://www.hoffmeier.com/history-of-detroit-diesel-engines/>
- [48] R. W. East, 'A Tale of a Two-Stroke - The Foden FD Engine', The Foden Society Website. Accessed: Jun. 20, 2024. [Online]. Available: <https://www.thefodensociety.org.uk/the-foden-engine/>
- [49] S. Banerjee, C. Naber, M. Willcox, C. E. A. Finney, and D. K. Edwards, 'High-Performance Computing and Analysis-Led Development of High Efficiency Dilute Opposed Piston Gasoline Engine', *J Eng Gas Turbine Power*, vol. 140, no. 10, Jun. 2018, doi: 10.1115/1.4039845.
- [50] F. Leach, G. Kalghatgi, R. Stone, and P. Miles, 'The scope for improving the efficiency and environmental impact of internal combustion engines', *Transportation Engineering*, vol. 1, p. 100005, 2020, doi: <https://doi.org/10.1016/j.treng.2020.100005>.
- [51] J. Zhao, 'Research and application of over-expansion cycle (Atkinson and Miller) engines – A review', *Appl Energy*, vol. 185, pp. 300–319, 2017, doi: <https://doi.org/10.1016/j.apenergy.2016.10.063>.
- [52] J. ATKINSON, 'GAS ENGINE', US336505A, 1886 Accessed: Aug. 07, 2024. [Online]. Available: <https://patents.google.com/patent/US336505A/en>
- [53] X. Lu, F. Zhang, Y. Liu, and S. Wang, 'Analysis on influences of scavenging ports width to scavenging process based on opposed piston two stroke diesel engine', *Energy Procedia*, vol. 158, pp. 5838–5843, 2019, doi: 10.1016/j.egypro.2019.01.543.

- [54] W. Wang, Y. Liang, Z. Zuo, B. Jia, and W. Wang, 'Effect of swirl-spray impact on the comprehensive performance of uniflow-scavenging opposed-piston engines', *Appl Therm Eng*, vol. 239, 2024, doi: 10.1016/j.applthermaleng.2023.122176.
- [55] R. Byers, *Flying Man : Hugo Junkers and the Dream of Aviation*, vol. First edit, no. number twenty. Texas A&M University Press, 2016. Accessed: May 05, 2025. [Online]. Available: <https://research.ebsco.com/c/7fhaq6/search/details/6lo2prcdhf?db=nlebk>
- [56] J. P. Pirault and M. L. S. Flint, *Opposed Piston Engines: Evolution, Use, and Future Applications*. SAE International, 2009. [Online]. Available: <https://books.google.co.uk/books?id=jXJ0EAAAQBAJ>
- [57] 'Napier Culverin ', Napier - Power Heritage Trust. Accessed: Feb. 21, 2025. [Online]. Available: <https://npht.org/about-napier/products/aero-engines/piston/culverin/>
- [58] D. Napier and Sons, 'Deltic CT18-42K engine: Napier', Photographic print; archived online at the Institution of Mechanical Engineers Archive. Accessed: Feb. 20, 2025. [Online]. Available: <https://archives.imeche.org/archive/engines/d-napier-son/deltic-napier/588223-deltic-ct18-42k-engine-napier?>
- [59] M. Erskine, 'Rootes TS3 - Two-stroke, Opposed piston, Diesel Engine.' [Online]. Available: <http://www.commer.co.nz/history>
- [60] *Workshop Manual for the Rootes Diesel Engine. Publication No. 715*. Edwards the Printers Ltd., Coventry. Archived online by M. Erskine at Rootes TS3 Engine Services, Favona, Auckland, New Zealand: <https://www.commer.co.nz/Technical>. Accessed: Feb. 20, 2025. [Online]. Available: <https://drive.google.com/file/d/1jgEv2yYyarAOPzS0oM-1UjXGu6AWWpw5/view>
- [61] 'A Horizontally Opposed Two-Stroke Engine.', *The Motor Cycle (on Internet Archive)*, London, Aug. 06, 1914. Accessed: Apr. 21, 2023. [Online]. Available: [https://archive.org/details/motorcycle132lond\\_/page/n285/mode/1up?view=theater](https://archive.org/details/motorcycle132lond_/page/n285/mode/1up?view=theater)
- [62] W. Pearce, 'Napier Deltic Opposed-Piston Diesel Engine', Old Machine Press. Accessed: Feb. 29, 2024. [Online]. Available: <https://oldmachinepress.com/2019/09/05/napier-deltic-opposed-piston-diesel-engine/>
- [63] G. Regner, D. Johnson, J. Koszewnik, E. Dion, F. Redon, and L. Fromm, 'Modernizing the opposed piston, two stroke engine for clean, efficient transportation', *SAE Technical Papers*, vol. 5, 2013, doi: 10.4271/2013-26-0114.
- [64] S. Naik *et al.*, 'Practical applications of opposed-piston engine technology to reduce fuel consumption and emissions', *SAE Technical Papers*, vol. 12, 2013, doi: 10.4271/2013-01-2754.
- [65] A. Salvi, R. Hanson, R. Zermeno, G. Regner, M. Sellnau, and F. Redon, 'Initial results on a new light-duty 2.7L opposed-piston gasoline compression ignition multi-cylinder engine', *ASME 2018 Internal Combustion Engine Division Fall Technical Conference, ICEF 2018*, vol. 1, 2018, doi: 10.1115/ICEF2018-9610.

- [66] D. Chown *et al.*, ‘Achieving Ultra-Low Oil Consumption in Opposed Piston Two-Stroke Engines’, *SAE Technical Papers*, vol. 2019-Janua, no. January, 2019, doi: 10.4271/2019-01-0068.
- [67] D. Akal, U. Akyol, and K. Uzuneanu, ‘A review of new technologies in valve systems of internal combustion engines and their effects’, *IOP Conf Ser Mater Sci Eng*, vol. 595, no. 1, 2019, doi: 10.1088/1757-899X/595/1/012034.
- [68] F. Duronio, A. De Vita, L. Allocca, and M. Anatone, ‘Gasoline direct injection engines – A review of latest technologies and trends. Part 1: Spray breakup process’, *Fuel*, vol. 265, Apr. 2020, doi: 10.1016/J.FUEL.2019.116948.
- [69] F. Duronio, A. De Vita, A. Montanaro, and C. Villante, ‘Gasoline direct injection engines – A review of latest technologies and trends. Part 2’, *Fuel*, vol. 265, 2020, doi: 10.1016/j.fuel.2019.116947.
- [70] L. Fromm, ‘Hydrogen Opposed Piston Engines’, Achates Power. Accessed: Jan. 25, 2023. [Online]. Available: <https://achatespower.com/wp-content/uploads/2021/05/Hydrogen-Opposed-Piston-Engines.pdf>
- [71] Y. H. Teoh *et al.*, ‘A review on production and implementation of hydrogen as a green fuel in internal combustion engines’, *Fuel*, vol. 333, 2023, doi: 10.1016/j.fuel.2022.126525.
- [72] ‘Bosch at Agritechnica 2023’. Accessed: Jul. 16, 2024. [Online]. Available: <https://www.bosch-press.de/pressportal/de/en/bosch-at-agritechnica-2023-260160.html>
- [73] C. Lhuillier, P. Brequigny, F. Contino, and C. Mounaïm-Rousselle, ‘Experimental study on ammonia/hydrogen/air combustion in spark ignition engine conditions’, *Fuel*, vol. 269, p. 117448, 2020, doi: <https://doi.org/10.1016/j.fuel.2020.117448>.
- [74] M. Comotti and S. Frigo, ‘Hydrogen generation system for ammonia-hydrogen fuelled internal combustion engines’, *Int J Hydrogen Energy*, vol. 40, no. 33, pp. 10673–10686, 2015, doi: 10.1016/j.ijhydene.2015.06.080.
- [75] ‘CNG Fuels’, CNG Fuels Website. Accessed: Aug. 06, 2024. [Online]. Available: <https://www.cngfuels.com/>
- [76] P. Richards, ‘Automotive Fuels Reference Book’, 2014, *SAE International*. [Online]. Available: <https://search.ebscohost.com/login.aspx?direct=true&db=nlebk&AN=1805016&site=eds-live&scope=site>
- [77] M. Yao, Z. Zheng, and H. Liu, ‘Progress and recent trends in homogeneous charge compression ignition (HCCI) engines’, *Prog Energy Combust Sci*, vol. 35, no. 5, pp. 398–437, 2009, doi: 10.1016/j.pecs.2009.05.001.
- [78] R. D. Reitz and G. Duraisamy, ‘Review of high efficiency and clean reactivity controlled compression ignition (RCCI) combustion in internal combustion engines’, *Prog Energy Combust Sci*, vol. 46, pp. 12–71, 2015, doi: 10.1016/j.pecs.2014.05.003.

- [79] V. Manente, B. Johansson, P. Tunestal, and W. J. Cannella, 'Influence of inlet pressure, EGR, combustion phasing, speed and pilot ratio on high load gasoline partially premixed combustion', *SAE Technical Papers*, 2010, doi: 10.4271/2010-01-1471.
- [80] J. E. Dec and Y. Yang, 'Boosted hcci for high power without engine knock and with ultra-low nox emissions - using conventional gasoline', *SAE Int J Engines*, vol. 3, no. 1, pp. 750–767, 2010, doi: 10.4271/2010-01-1086.
- [81] Y. Feng, T. Chen, K. Xu, X. Wang, H. Xie, and H. Zhao, 'The comparison between traditional spark ignition and micro flame ignition in gasoline high dilution combustion', *Proceedings of the Institution of Mechanical Engineers, Part D: Journal of Automobile Engineering*, vol. 235, no. 8, pp. 2242–2252, 2021, doi: 10.1177/0954407020983164.
- [82] Z. Wang, X. He, J.-X. Wang, S. Shuai, F. Xu, and D. Yang, 'Combustion visualization and experimental study on spark induced compression ignition (SICI) in gasoline HCCI engines', *Energy Convers Manag*, vol. 51, no. 5, pp. 908–917, 2010, doi: 10.1016/j.enconman.2009.11.029.
- [83] A. F. El-Sayed, *Aircraft Propulsion and Gas Turbine Engines*, vol. Second edi. CRC Press, 2017. Accessed: May 03, 2025. [Online]. Available: <https://research.ebsco.com/c/7fhaq6/search/details/dqb7zqrpar?db=nlebk>
- [84] Y. Ju, K. Maruta, and C. P. Cadou, *Microscale Combustion and Power Generation*. Momentum Press, 2015. Accessed: May 03, 2025. [Online]. Available: <https://research.ebsco.com/c/7fhaq6/search/details/rcmdnpjvkb?db=nlebk>
- [85] 'Motore Wankel Fichtel & Sachs KM 48'. [Online]. Available: <http://www.museomotori.unipa.it/scheda.php?id=29&lang=en>
- [86] 'Liquid Piston', Liquid Piston Website. Accessed: Aug. 07, 2024. [Online]. Available: <https://www.liquidpiston.com/>
- [87] A. Shkolnik *et al.*, 'COMPACT, LIGHTWEIGHT, HIGH EFFICIENCY ROTARY ENGINE FOR GENERATOR, APU, AND RANGE-EXTENDED ELECTRIC VEHICLES', Aug. 2018, *Novi, Michigan*. Accessed: Apr. 27, 2025. [Online]. Available: [https://cdn.prod.website-files.com/5f6086e9bbbabd41a20f2984/5f9acc0f3f8f455bebc45f3\\_94%20Shkolnik%2C%20Alexander\\_final%20paper.pdf](https://cdn.prod.website-files.com/5f6086e9bbbabd41a20f2984/5f9acc0f3f8f455bebc45f3_94%20Shkolnik%2C%20Alexander_final%20paper.pdf)
- [88] M. Borghi, E. Mattarelli, J. Muscoloni, C. A. Rinaldini, T. Savioli, and B. Zardin, 'Design and experimental development of a compact and efficient range extender engine', *Appl Energy*, vol. 202, pp. 507–526, 2017, doi: 10.1016/j.apenergy.2017.05.126.
- [89] P. Duret, 'Direct Injection 2 Stroke Web Page'. Accessed: Jan. 24, 2023. [Online]. Available: <https://di2-stroke-engine-di2s.com/>
- [90] S. S. Rathore, S. Mishra, M. K. Paswan, and Sanjay, 'A Review on Design and Development of Free Piston Linear Generators in Hybrid Vehicles', *IOP Conf Ser Mater Sci Eng*, vol. 691, no. 1, 2019, doi: 10.1088/1757-899X/691/1/012053.

- [91] ‘US Army awards Cummins \$87M contract to deliver the opposed-piston Advanced Combat Engine’, Green Car Congress. Accessed: Feb. 27, 2023. [Online]. Available: <https://www.greencarcongress.com/2021/08/20210803-ace.html>
- [92] ‘Opposed-Piston Heavy-Duty Diesel Engine Performance and Emissions Summary’, Achates Power Website. Accessed: Dec. 15, 2023. [Online]. Available: <https://achatespower.com/wp-content/uploads/2023/11/Heavy-Duty-Diesel-Engine-Performance-and-Emissions-Summary.pdf>
- [93] ‘Hydrogen Opposed Piston Engine Working Group’. Accessed: Jan. 21, 2023. [Online]. Available: <https://www.h-ope-wg.com/>
- [94] ‘U.S. Army Phase II SBIR – Stryker – Opposed Piston APU’, Baker Engineering Website. Accessed: Aug. 07, 2024. [Online]. Available: <https://bakerengineering.com/case-study/us-army-phase-ii-sbir-stryker-opposed-piston-apu/>
- [95] F. Ma *et al.*, ‘Experimental investigation of combustion characteristics on opposed piston two-stroke gasoline direct injection engine’, *Energies (Basel)*, vol. 14, no. 8, 2021, doi: 10.3390/en14082105.
- [96] ‘What ever happened to this revolutionary engine?’, Dynacam Website. Accessed: Aug. 07, 2024. [Online]. Available: <https://dynacam-engine.com/>
- [97] ‘Continuous Variable-Displacement Type Compressors’, Toyota Industries Corporation Website. Accessed: Aug. 07, 2024. [Online]. Available: <https://www.toyota-industries.com/products/automobile/compressor/variable/index.html>
- [98] ‘Devize Motors Website’, Devize Motors Website. Accessed: Jul. 30, 2024. [Online]. Available: <https://devizemotors.com/>
- [99] ‘INNEngine Website’. Accessed: Jul. 30, 2024. [Online]. Available: <https://innengine.com/>
- [100] ‘Our Technology - INNEngine’, INNEngine website. Accessed: Apr. 20, 2023. [Online]. Available: <https://innengine.com/our-technology/>
- [101] ‘Concept - INNEngine’, INNEngine Website. Accessed: Aug. 07, 2024. [Online]. Available: <https://innengine.com/concept/>
- [102] M. Pattakos, E. Pattakos, P. Pattakou, and E. Pattakos, ‘Connecting rod valve’, US9303637B2, 2014 Accessed: May 05, 2025. [Online]. Available: <https://patents.google.com/patent/US9303637B2/en?q=US9303637B2>
- [103] M. Pattakos, E. Pattakos, P. Pattakou, and E. Pattakos, ‘Reciprocating piston engine’, WO2012020384A4, 2010 Accessed: May 05, 2025. [Online]. Available: <https://patents.google.com/patent/WO2012020384A4/en?q=WO2012020384A4>
- [104] ‘Pattakon Website’. Accessed: Jul. 30, 2024. [Online]. Available: <https://www.pattakon.com/>
- [105] W. Yang, X.-R. Li, Y. Kang, H. Zuo, and F.-S. Liu, ‘Evaluating the scavenging process by the scavenging curve of an opposed-piston, two-stroke (OP2S) diesel engine’, *Appl Therm Eng*, vol. 147, pp. 336–346, Jan. 2019, doi: 10.1016/j.applthermaleng.2018.10.095.

- [106] J. Gao, G. Tian, P. Jenner, M. Burgess, and S. Emhardt, ‘Preliminary explorations of the performance of a novel small scale opposed rotary piston engine’, *Energy*, vol. 190, p. 116402, 2020, doi: <https://doi.org/10.1016/j.energy.2019.116402>.
- [107] T. Tulwin and P. Karpiński, ‘Analysis of the fuel spray diversity in the opposed-piston engine’, *J Phys Conf Ser*, vol. 1101, no. 1, 2018, doi: 10.1088/1742-6596/1101/1/012045.
- [108] E. Mattarelli, S. Caprioli, T. Savioli, A. Volza, C. M. Di Gaetano Iftene, and C. A. Rinaldini, ‘Virtual Development of a Single-Cylinder Hydrogen Opposed Piston Engine’, *Energies (Basel)*, vol. 17, no. 21, 2024, doi: 10.3390/en17215262.
- [109] E. Sher, *Handbook of air pollution from internal combustion engines : pollutant formation and control*. Boston: Academic Press, 1998. [Online]. Available: <http://site.ebrary.com/id/10251223>
- [110] A. Jante, ‘Scavenging and other problems of two-stroke cycle spark-ignition engines’, *SAE Technical Papers*, 1968, doi: 10.4271/680468.
- [111] G. P. Blair, ‘Studying scavenge flow in a two-stroke cycle engine’, *SAE Technical Papers*, 1975, doi: 10.4271/750752.
- [112] G. P. Blair and R. G. Kenny, ‘Further developments in scavenging analysis for two-cycle engines’, *SAE Technical Papers*, 1980, doi: 10.4271/800038.
- [113] J. G. Smyth, R. G. Kenny, and G. P. Blair, ‘Steady flow analysis of the scavenging process in a loop scavenged two-stroke cycle engine - A theoretical and experimental study’, *SAE Technical Papers*, 1988, doi: 10.4271/881267.
- [114] S. Ishihara, Y. Murakami, and K. Ishikawa, ‘Improvement of pitot tube set for obtaining scavenging pictures of two-stroke cycle engines’, *SAE Technical Papers*, 1988, doi: 10.4271/880171.
- [115] H. Sammons, ‘A Single-Cycle Test Apparatus for Studying “Loop Scavenging” in a Two-Stroke Engine’, *Proceedings of the Institution of Mechanical Engineers*, vol. 161, no. 1, pp. 233–249, Jun. 1949, doi: 10.1243/PIME\_PROC\_1949\_161\_024\_02.
- [116] K. HORI, ‘A Method of Measuring Scavenging Efficiency and its Application’, *Bulletin of JSME*, vol. 5, no. 18, pp. 327–334, 1962, doi: 10.1299/jsme1958.5.327.
- [117] P. H. Schweitzer and F. DeLuca, ‘The tracer gas method of determining the charging efficiency of two-stroke-cycle diesel engines’, 1942, *N.A.C.A Technical Note 838*; Archived online on *NASA Technical Reports Server*. Accessed: May 03, 2025. [Online]. Available: <https://ntrs.nasa.gov/api/citations/19930081598/downloads/19930081598.pdf>
- [118] R. S. Benson, ‘A new gas dynamic model for the gas exchange process in two stroke loop and cross scavenged engines’, *Int J Mech Sci*, vol. 19, no. 12, pp. 693–711, 1977, doi: 10.1016/0020-7403(77)90056-X.
- [119] R. Venugopal, N. Abani, and R. Mackenzie, ‘Effects of injection pattern design on piston thermal management in an opposed-piston two-stroke engine’, *SAE Technical Papers*, vol. 9, 2013, doi: 10.4271/2013-01-2423.

- [120] F. Ma, J. Xu, W. Yang, F. Li, Y. Li, and J. Zhang, ‘Asymmetric spray characteristics of opposed-piston two-stroke gasoline direct injection engine’, *International Journal of Engine Research*, vol. 24, no. 6, pp. 2552–2567, 2023, doi: 10.1177/14680874221136465.
- [121] M. Sellnau *et al.*, ‘Fuel injection system for opposed-piston gasoline compression-ignited (OP-GCI) engines’, *SAE Technical Papers*, vol. 2019-April, no. April, 2019, doi: 10.4271/2019-01-0287.
- [122] S. F. Furze, ‘Investigation of Fuel Efficiency in a Spark Ignition Opposed Piston Engine for Portable Power Applications’, 2018.
- [123] ‘Crankshaft for TD50Q’, Chinese Motorcycle Parts Online. Accessed: Nov. 24, 2023. [Online]. Available: <https://www.chinesemotorcyclepartsonline.co.uk/part/CRS028>
- [124] ‘Lexmoto Hunter 50 2021’, Bikez.com Motorcycle Encyclopaedia. Accessed: Jan. 26, 2025. [Online]. Available: [https://bikez.com/motorcycles/lexmoto\\_hunter\\_50\\_2021.php](https://bikez.com/motorcycles/lexmoto_hunter_50_2021.php)
- [125] ‘TD50Q-2’, Llexeter Ltd. Dealer Network Website. Accessed: Apr. 27, 2025. [Online]. Available: <https://dealers.lexmoto.com/TD50Q-2.php>
- [126] ‘Contitech 1120 8M 30 Timing Belt, 140 Teeth, 1120mm Length, 30mm Width’, RS Components Website. Accessed: Oct. 26, 2024. [Online]. Available: <https://uk.rs-online.com/web/p/timing-belts/4750844>
- [127] ‘RS PRO Timing Belt Pulley, Steel 30mm Belt Width x 8mm Pitch, 48 Tooth’, RS Components Website. Accessed: Oct. 26, 2024. [Online]. Available: <https://uk.rs-online.com/web/p/belt-pulleys/0183619>
- [128] ‘MAPCO 23362 Tensioner Pulley, timing belt’, MAPCO Website. Accessed: Oct. 26, 2024. [Online]. Available: <https://www.mapco.com/en/carparts/25859/>
- [129] ‘Locking Assemblies RfN 7004’, RINGFEDER® website. Accessed: Apr. 21, 2025. [Online]. Available: <https://www.ringfeder.com/products/locking-assemblies/rfn-7004/>
- [130] A. G. Atkins and M. P. Escudier, *A dictionary of mechanical engineering*, Second edition. in Oxford quick reference. Oxford: Oxford University Press, 2019. Accessed: May 03, 2025. [Online]. Available: <https://research.ebsco.com/c/7fhaq6/search/details/arxy5brrij?db=nlebk&db=nlbk>
- [131] ‘Gear Ring fits Yanmar L48AE Series Engines - Replaces OEM No. 14262 21600’, L&S Engineers Website. Accessed: Oct. 26, 2024. [Online]. Available: <https://www.lseniengineers.co.uk/gear-ring-fits-yanmar-l48-engine-replaces-yanmar-no-114262-21600.html>
- [132] ‘Kenworth Engineering’, Kenworth Engineering Website. Accessed: Sep. 04, 2024. [Online]. Available: <https://kenworthengineering.co.uk/>
- [133] ‘Autodesk Fusion®’, *Autodesk Incorporated*. Accessed: May 03, 2025. [Online]. Available: <https://www.autodesk.com/products/fusion-360/overview>

- [134] ‘Internal Grooving’, Sandvik Coromant. Accessed: Nov. 24, 2023. [Online]. Available: <https://www.sandvik.coromant.com/en-gb/knowledge/parting-and-grooving/internal-grooving>
- [135] ‘What are Worst Case, RSS and Monte Carlo calculation methods and when to use them in tolerance analysis?’, Enventive Engineering Website. Accessed: Oct. 26, 2024. [Online]. Available: <https://enventive.com/tolerance-analysis-resources/worst-case-rss-and-monte-carlo-simulation-calculations-for-tolerance-analysis/>
- [136] ‘1050cc/min HDEV5.1 Direct Injector’, Bosch Motorsport Australia Website. Accessed: Apr. 16, 2025. [Online]. Available: <https://www.bosch-motorsport-shop.com.au/1050cc-min-hdev5.1-direct-injector-026150001A>
- [137] ‘Cylinder pressure sensors, M5x0.5, new generation / 6054C’, Kistler Group Website. Accessed: Sep. 04, 2024. [Online]. Available: <https://www.kistler.com/GB/en/cp/cylinder-pressure-sensors-6054c/P0000401>
- [138] ‘Compact M5 cylinder pressure sensor’, Kistler Group Datasheet. Accessed: Sep. 04, 2024. [Online]. Available: [https://kistler.cdn.celum.cloud/SAPCommerce\\_Download\\_original/003-458e.pdf](https://kistler.cdn.celum.cloud/SAPCommerce_Download_original/003-458e.pdf)
- [139] R. Nave, ‘Thermal Expansion Coefficients at 20 C’, Hyperphysics Website. Accessed: Apr. 18, 2025. [Online]. Available: <http://hyperphysics.phy-astr.gsu.edu/hbase/Tables/thexp.html#c1>
- [140] R. Nave, ‘Thermal Expansion’, Hyperphysics Website. Accessed: Apr. 18, 2025. [Online]. Available: <http://hyperphysics.phy-astr.gsu.edu/hbase/thermo/thexp.html#c3>
- [141] ‘Gates OE Type Coolant Thermostat (TH64978G1)’, OPIE OILS Website. Accessed: Apr. 21, 2023. [Online]. Available: <https://www.opieoils.co.uk/p-240628-gates-oe-type-coolant-thermostat-th64978g1.aspx>
- [142] ‘Oil Pump - Chinese GY6 50cc’, PedpartsWebsite. Accessed: Oct. 20, 2024. [Online]. Available: <https://www.pedparts.co.uk/product/3422/oil-pump--chinese-gy6-50cc>
- [143] ‘Wileco 01513 Nickel M6 Fine 0.75 saftey Valve Fits 1990 on’, Forest Classics Website. Accessed: Oct. 20, 2024. [Online]. Available: <https://www.forest-classics.co.uk/wileco/wileco-spares/wileco-01513-nickel-m6-fine-0-75-saftey-valve-fits-1990-on>
- [144] ‘12V Starter Motor for Yanmar L48, L70, L100 Engines - Replaces OEM No. 114399-77010’, L&S Engineers Website. Accessed: Oct. 26, 2024. [Online]. Available: <https://www.lsenineers.co.uk/12v-starter-motor-for-yanmar-l48-l70-l100-engines-replaces-oem-no-114399-77010.html>
- [145] ‘METRIC O-RING GROOVE DESIGN’, Seal & Design Inc. Website. Accessed: Oct. 26, 2024. [Online]. Available: <https://www.sealanddesign.com/technical/o-ring-groove-design/o-ring-groove-design-metric/>
- [146] ‘Roots blower (supercharger) by size’, Ogura Clutch Co. Ltd. Accessed: Jan. 24, 2023. [Online]. Available: <https://www.oguraclutch.co.jp/product/ogura-super-charger-by-size/>

- [147] ‘TX02 Supercharger Map’, 2005, *Ogura Industrial Corp. / Ogura Clutch Co., Ltd. Japan; Reproduced with Permission. Also available online.* Accessed: Apr. 04, 2025. [Online]. Available: [https://ogura-clutch.com/downloads/marketbrochures/Ogura-BlowerSupercharger\\_2018.pdf](https://ogura-clutch.com/downloads/marketbrochures/Ogura-BlowerSupercharger_2018.pdf)
- [148] ‘Carburettor (Non Genuine) Fits Honda GX390 - Replaces 16100-ZF6-W31’, L&S Engineers Website. Accessed: Oct. 20, 2024. [Online]. Available: <https://www.lseniengineers.co.uk/honda-gx390-carburettor-non-genuine.html>
- [149] ‘Governor Assembly Fits Honda GX110 GX120 GX140 GX160 - 16510-ZE1-000’, L&S Engineers Website. Accessed: Oct. 20, 2024. [Online]. Available: <https://www.lseniengineers.co.uk/governor-assembly-for-honda-gx110-gx120-gx140-gx160.html>
- [150] ‘Air Filter Assembly for Yanmar L100, 186F, L75, L90, L75AE, L90AE, L100AE Engines - 714650-12560’, L&S Engineers Website. Accessed: Oct. 26, 2024. [Online]. Available: <https://www.lseniengineers.co.uk/air-filter-assembly-for-yanmar-l75-l90-l100.html>
- [151] ‘NTK Lambda Sensor Datasheet’, Life Racing Website. Accessed: Apr. 22, 2025. [Online]. Available: [https://www.liferacing.com/uploads/files/Datasheets/NTK\\_Lambda\\_Sensor\\_Datasheet\\_V1.0.pdf](https://www.liferacing.com/uploads/files/Datasheets/NTK_Lambda_Sensor_Datasheet_V1.0.pdf)
- [152] ‘Ford Zetec Crank Sensor Datasheet’, Motorsport Electronics Website. Accessed: Apr. 27, 2025. [Online]. Available: <https://motorsport-electronics.co.uk/wp-content/uploads/2022/11/Ford-crank-sensor-Datasheet.pdf>
- [153] ‘Exhaust Gas Temperature Sensor Datasheet’, Motorsport Electronics Website. Accessed: May 02, 2025. [Online]. Available: <https://motorsport-electronics.co.uk/wp-content/uploads/2022/11/EGT-Datasheet.pdf>
- [154] ‘Universal Manifold Pressure Sensor Datasheet’, Motorsport Electronics Website. Accessed: Apr. 27, 2025. [Online]. Available: <https://motorsport-electronics.co.uk/wp-content/uploads/2022/11/MAP-sensor-Datasheet.pdf>
- [155] ‘FAE Catalogue: Engine Management CGM4 - 1111813’, FAE Website. Accessed: May 02, 2025. [Online]. Available: [https://www.fae.es/wp-content/uploads/2024/09/1111813\\_cat.\\_FAE\\_CGM4\\_Engine-Management\\_Gestion-Motor\\_02.pdf](https://www.fae.es/wp-content/uploads/2024/09/1111813_cat._FAE_CGM4_Engine-Management_Gestion-Motor_02.pdf)
- [156] ‘Universal Throttle Position Sensor Datasheet’, Motorsport Electronics Website. Accessed: Apr. 27, 2025. [Online]. Available: <https://motorsport-electronics.co.uk/wp-content/uploads/2022/11/TPS-Datasheet-1.pdf>
- [157] ‘Lucas SOB807 Oil Pressure Switch’, Parts in Motion Website. Accessed: Apr. 22, 2025. [Online]. Available: <https://www.partsinmotion.co.uk/lucasoilpressureswitchsob807-detail>

- [158] ‘TOLLOCK Locking Bush TLK110 16 X 24 mm, 16mm Shaft Diameter’, RS Components. Accessed: Apr. 27, 2025. [Online]. Available: <https://uk.rs-online.com/web/p/locking-bushes/1065536?searchId=74232556-f3c4-4100-99f5-5a223f2f6e00&gb=s>
- [159] ‘Exhaust Assembly for Yanmar L40/L48 Series Engines - Replaces 114250-13521’, L&S Engineers Website. Accessed: Oct. 26, 2024. [Online]. Available: <https://www.lseniengineers.co.uk/exhaust-assembly-for-yanmar-l40-l48.html>
- [160] ‘RS PRO Brass Single Check Valve, BSP 1/2in, 16 bar’, RS Components Website. Accessed: Oct. 26, 2024. [Online]. Available: <https://uk.rs-online.com/web/p/check-valves/2422836>
- [161] ‘Abakus 0380180004 Intercooler’, ML Performance Website. Accessed: Oct. 26, 2024. [Online]. Available: <https://www.mlperformance.co.uk/products/abakus-038-018-0004-intercooler>
- [162] K. J. Richards, P. K. Senecal, and E. Pomraning, ‘CONVERGE 3.0’, 2021, *Convergent Science, Madison, Wisconsin*.
- [163] K. J. Richards, P. K. Senecal, and E. Pomraning, ‘CONVERGE Studio 3.0’, 2021, *Convergent Science, Madison, Wisconsin*.
- [164] K. J. Richards, P. K. Senecal, and E. Pomraning, *CONVERGE 3.0 Manual*. Madison, Wisconsin: Convergent Science, 2021.
- [165] K. J. Richards, P. K. Senecal, and E. Pomraning, *CONVERGE Studio 3.0 Manual*. Madison, Wisconsin: Convergent Science, 2022.
- [166] ‘Fuel (VE) Table’, Speeduino Manual. Accessed: May 19, 2023. [Online]. Available: [https://wiki.speeduino.com/en/configuration/VE\\_table](https://wiki.speeduino.com/en/configuration/VE_table)
- [167] ‘LifeRacing Downloads Page’, LifeRacing Website. Accessed: Apr. 23, 2025. [Online]. Available: <https://www.liferacing.com/downloads/>
- [168] ‘Premixed Combustion Modelling’, 2020, *Convergent Science*. Accessed: Jun. 07, 2023. [Online]. Available: <https://hub.convergecfcd.com/login>
- [169] Y.-D. Liu, M. Jia, M.-Z. Xie, and B. Pang, ‘Enhancement on a skeletal kinetic model for primary reference fuel oxidation by using a semidecoupling methodology’, *Energy and Fuels*, vol. 26, no. 12, pp. 7069–7083, 2012, doi: 10.1021/ef301242b.
- [170] J. Blazek, *Computational Fluid Dynamics: Principles and Applications*, vol. 2nd ed. Amsterdam: Elsevier Science, 2005.
- [171] S. Jayanti, *Computational Fluid Dynamics for Engineers and Scientists*. Dordrecht: Springer Netherlands, 2018. doi: 10.1007/978-94-024-1217-8.
- [172] J. Tu, G.-H. Yeoh, and C. Liu, *Computational Fluid Dynamics - A Practical Approach (3rd Edition)*. Elsevier, 2018. [Online]. Available: <https://app.knovel.com/hotlink/toc/id:kpCFDAPA19/computational-fluid-dynamics/computational-fluid-dynamics>
- [173] T. Atkins and M. Escudier, ‘Favre averaging’, 2013, *Oxford University Press*. doi: 10.1093/acref/9780199587438.013.2107.

- [174] Z. HAN and R. D. REITZ, 'Turbulence Modeling of Internal Combustion Engines Using RNG  $\kappa$ - $\epsilon$  Models', *Combustion Science and Technology*, vol. 106, no. 4–6, pp. 267–295, Jan. 1995, doi: 10.1080/00102209508907782.
- [175] R. Nave, 'Alkanes', Hyperphysics. Accessed: Mar. 22, 2024. [Online]. Available: <http://hyperphysics.phy-astr.gsu.edu/hbase/Organic/alkane.html>
- [176] 'F88GDI4 V2', Life Racing Website. Accessed: Oct. 27, 2024. [Online]. Available: <https://www.liferacing.com/products/ecus/f88/f88gdi4/>
- [177] 'F88GDi4 V2 Datasheet', LifeRacing website. Accessed: Apr. 23, 2025. [Online]. Available: <https://www.liferacing.com/uploads/files/Datasheets/F88GDi4%20V2%20Datasheet%20v.1.1.pdf>
- [178] S. F. Furze, S. Barraclough, D. Liu, and S. Melendi-Espina, 'Model based mapping of a novel prototype spark ignition opposed-piston engine', *Energy Convers Manag*, vol. 309, 2024, doi: 10.1016/j.enconman.2024.118434.

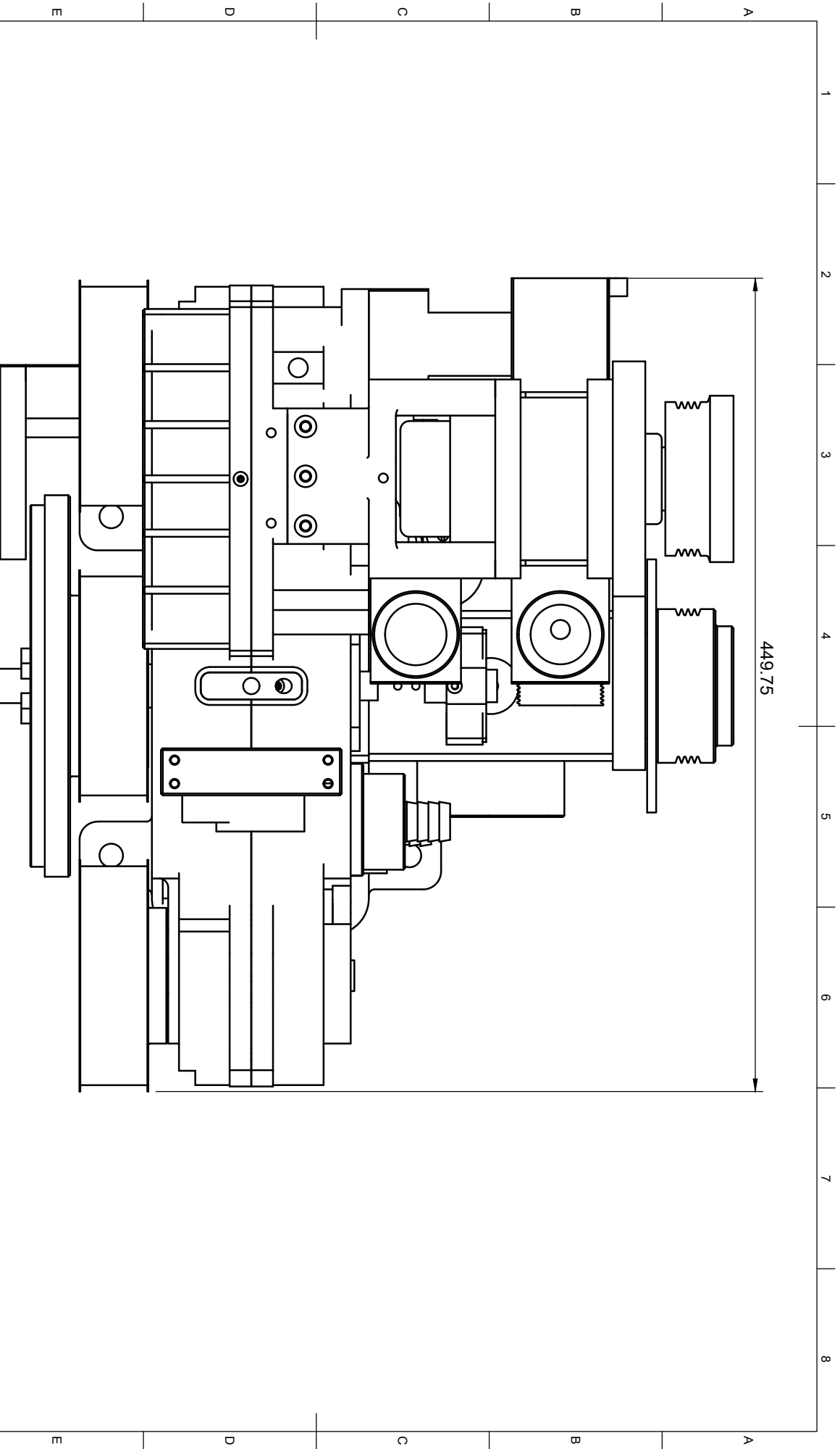
## Bibliography:

Included below are some useful sources that the reader may wish to review. Although not cited in the text, they have proven useful to the author.

- a) Engineering ToolBox (2001) [online] Available at: <https://www.engineeringtoolbox.com> [Accessed 02/05/2025]. A helpful website with lots of information on subjects relating to engineering.
- b) Trelleborg ISO Fits & Tolerances [online]. Available at: <https://www.trelleborg.com/en/seals/resources/design-support-and-engineering-tools/iso-fits-and-limits> [Accessed 02/05/2025]. A website with a QR code link to an app that is useful in determining tolerances for shafts and seats.
- c) R. A. Granger, "Fluid Mechanics," 1995, *Dover Publications*. [Online]. Available: <http://app.knovel.com/hotlink/toc/id:kpFM000001/fluid-mechanics> [Accessed: May 03, 2025]. A useful publication on the subject of fluid mechanics.
- d) Thomas, B. (1993) *The Industrial Revolution and the Atlantic economy : selected essays*. London: Routledge. Available at: <http://www.crcnetbase.com/isbn/9780203161210> (Accessed: May 2, 2025). An interesting read on the subject of industrial history.
- e) A. R. Rogowski and C. L. Bouchard, "Scavenging a piston-ported two-stroke cylinder," Nov. 1938, *N.A.C.A. Technical Note 674*; archived online on *Nasa Technical Reports Server*. [Online]. Available: <https://ntrs.nasa.gov/api/citations/19930081490/downloads/19930081490.pdf> [Accessed: May 03, 2025]. A study from 1938 that explored various configurations of port arrangement using a specially constructed engine.

## **Appendix A: Engineering Drawings**

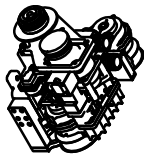
A selection of engineering drawings for many of the manufactured/modified components of the engine. Please note that they do not include 'ad-hoc' changes made upon suggestion of machinists (for example, making a thread depth shallower or deeper), or any minor alterations that were subsequently required to fit pre-manufactured parts. They are provided 'as-is', in good faith, and incorporate corrections where any errors have been identified prior to the submission of the final version of this thesis. All engineering drawings may be subject to revision without notice.

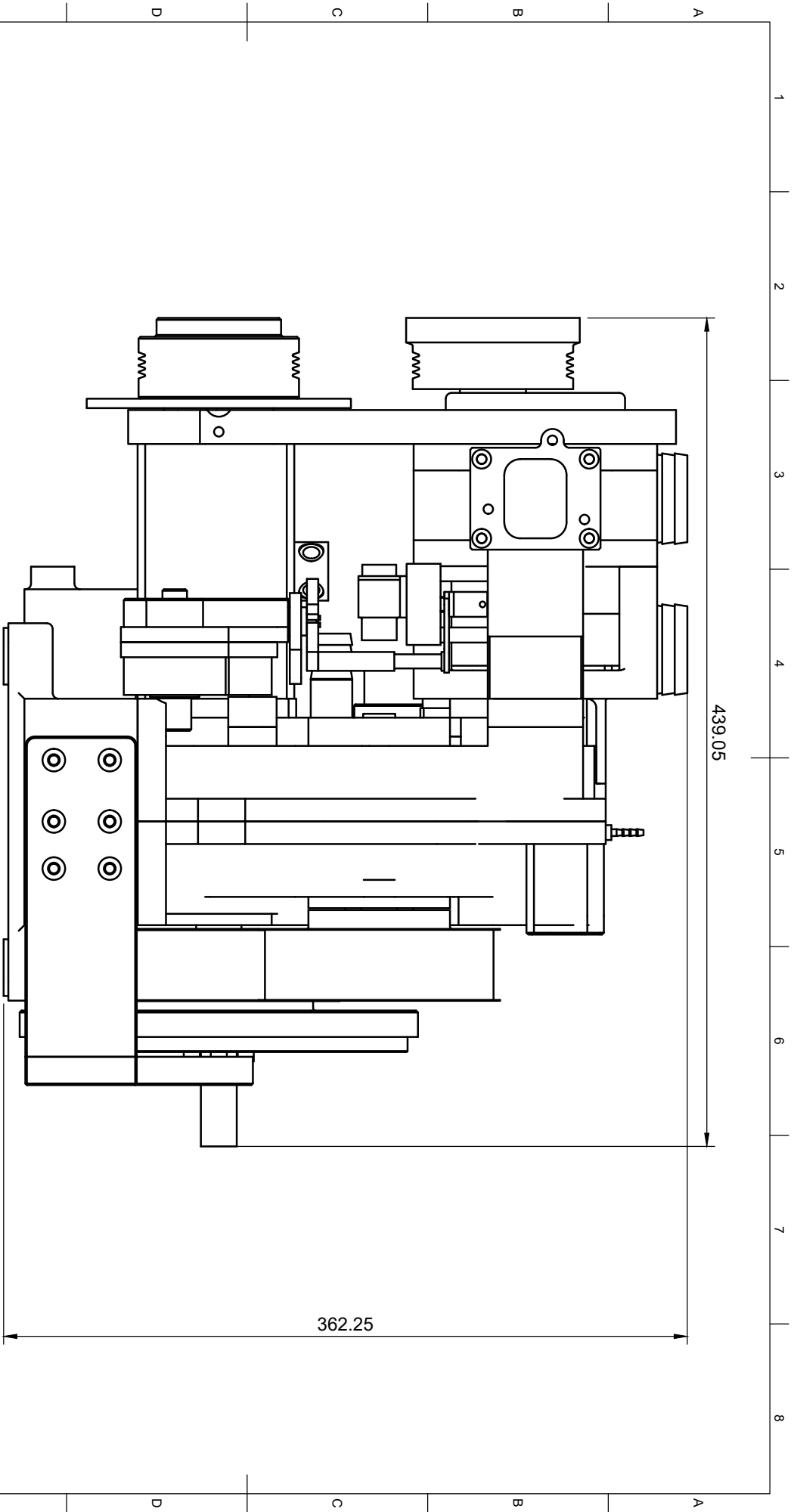


449.75

Note: all dimensions for indication only. Overviews of engine do not include ancillaries such as GDI pump, air filter, exhaust silencer, starter motor etc.

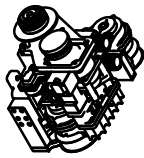
Dept:	Technical reference General Tolerances $\pm 0.1 \text{ mm}$	Created by <b>Samuel Frederick Furze</b>	Approved by
		Document type	Document status
		Title <b>Main Engine Overview</b>	DWG No. <b>OV1</b>
		Rev.	Date of issue
			Sheet <b>1/5</b>

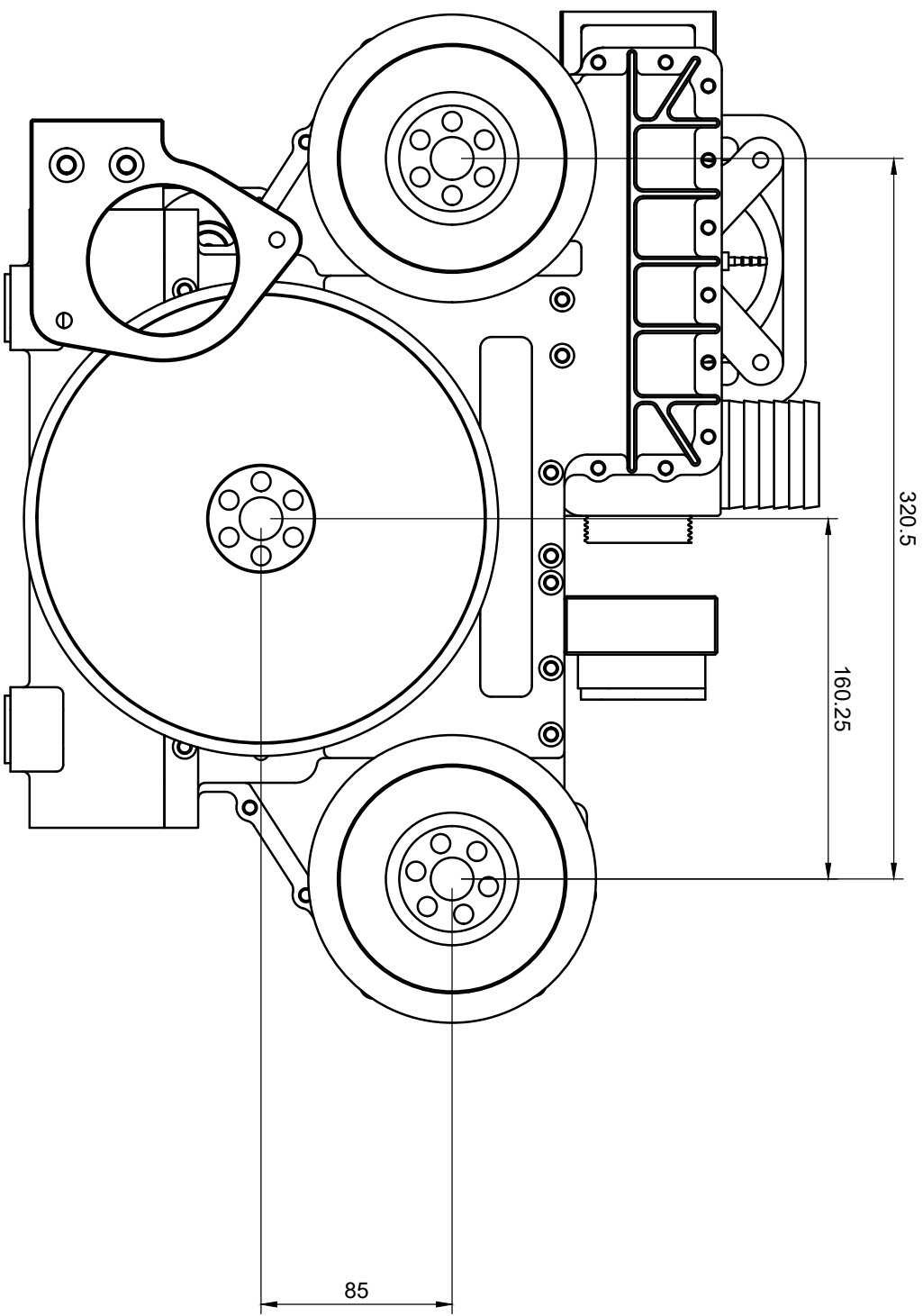




Note: all dimensions for indication only. Overviews of engine do not include ancillaries such as GDI pump, air filter, exhaust silencer, starter motor etc.

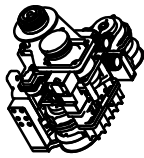
Dept.	Technical reference General Tolerances $\pm 0.1 \text{ mm}$	Created by <b>Samuel Frederick Furze</b>	Approved by
		Document type <b>Main Engine Overview</b>	Document status <b>Thesis</b>
		Title <b>Main Engine Overview</b>	DWG No. <b>OV1</b>
		Rev.	Date of issue
			Sheet <b>2/5</b>

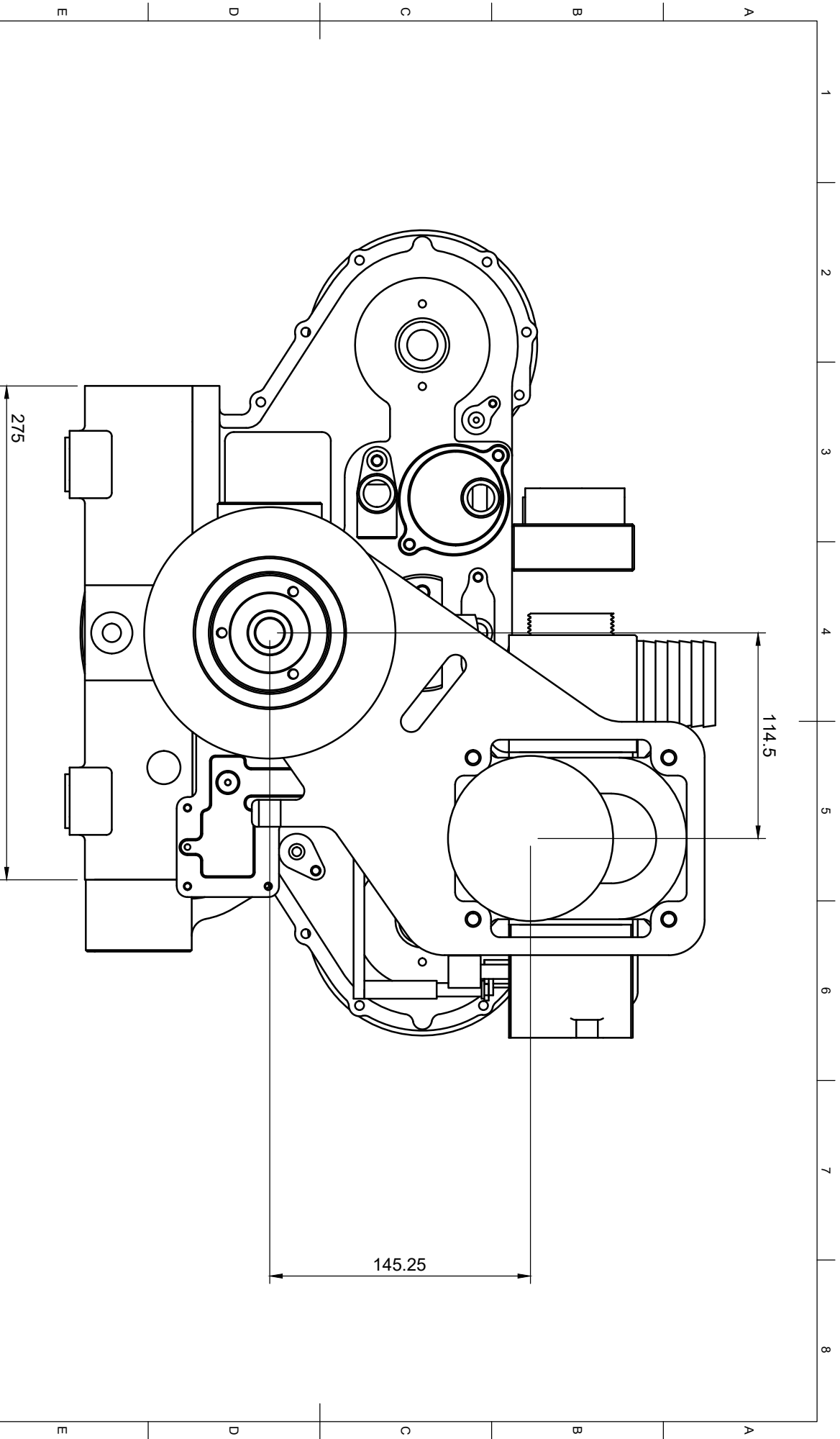




Note: all dimensions for indication only. Overviews of engine do not include ancillaries such as GDI pump, air filter, exhaust silencer, starter motor etc.

Dept.	Technical reference General Tolerance $\pm 0.1 \text{ mm}$	Created by <b>Samuel Frederick Furze</b>	Approved by
		Document type	Document status
		Title	DWG No.
		<b>Main Engine Overview</b>	<b>OV1</b>
		Rev.	Date of issue
			<b>3/5</b>
			Sheet

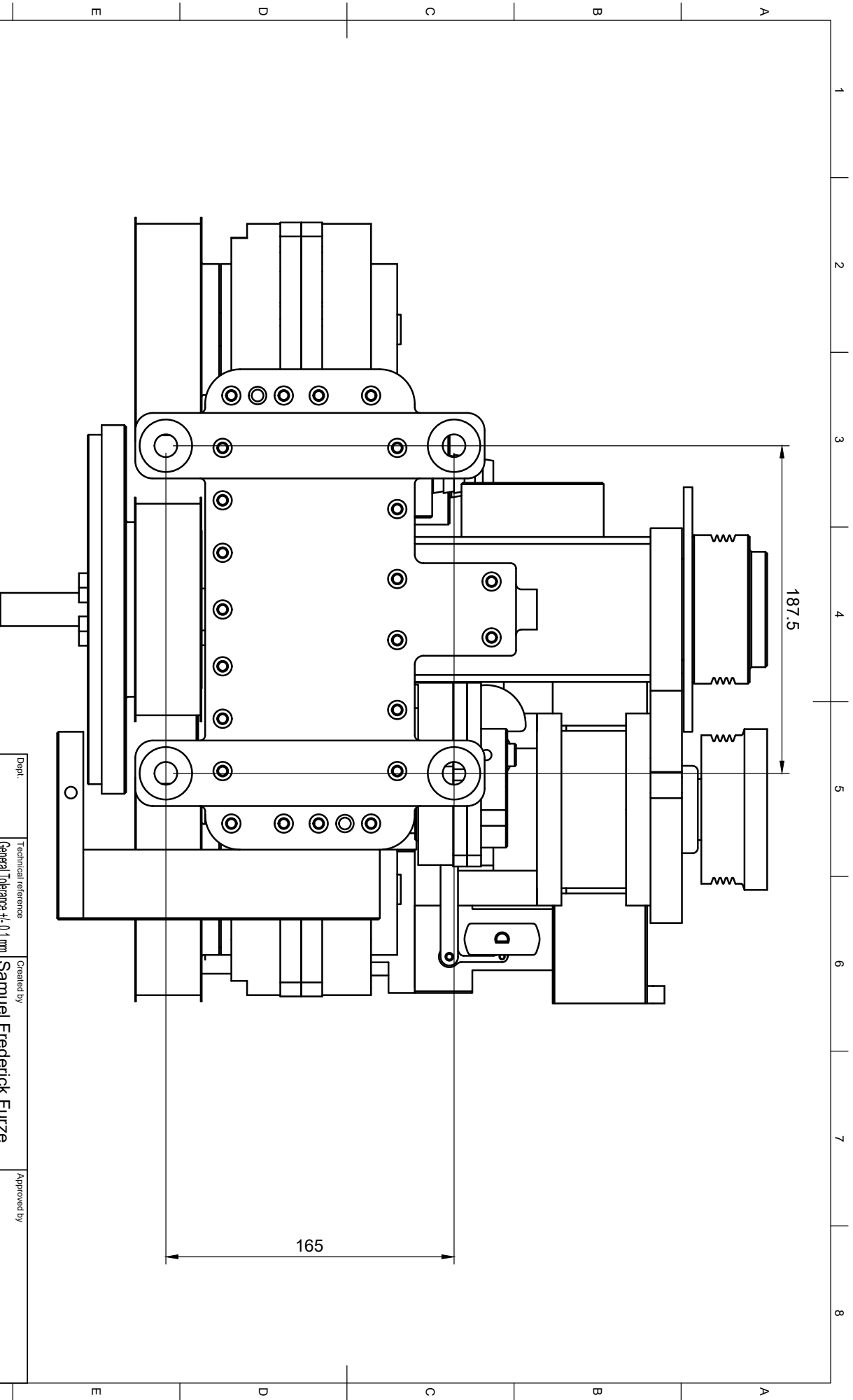




Note: all dimensions for indication only. Overviews of engine do not include ancillaries such as GDI pump, air filter, exhaust silencer, starter motor etc.

Dept.	Technical reference General Tolerance $\pm 0.1 \text{ mm}$	Created by <b>Samuel Frederick Furze</b>	Approved by
		Document type <b>Thesis</b>	Document status
		Title <b>Main Engine Overview</b>	DWG No. <b>OV1</b>
		Rev.	Date of issue
			<b>4/5</b>
			Sheet
			<b>4/5</b>

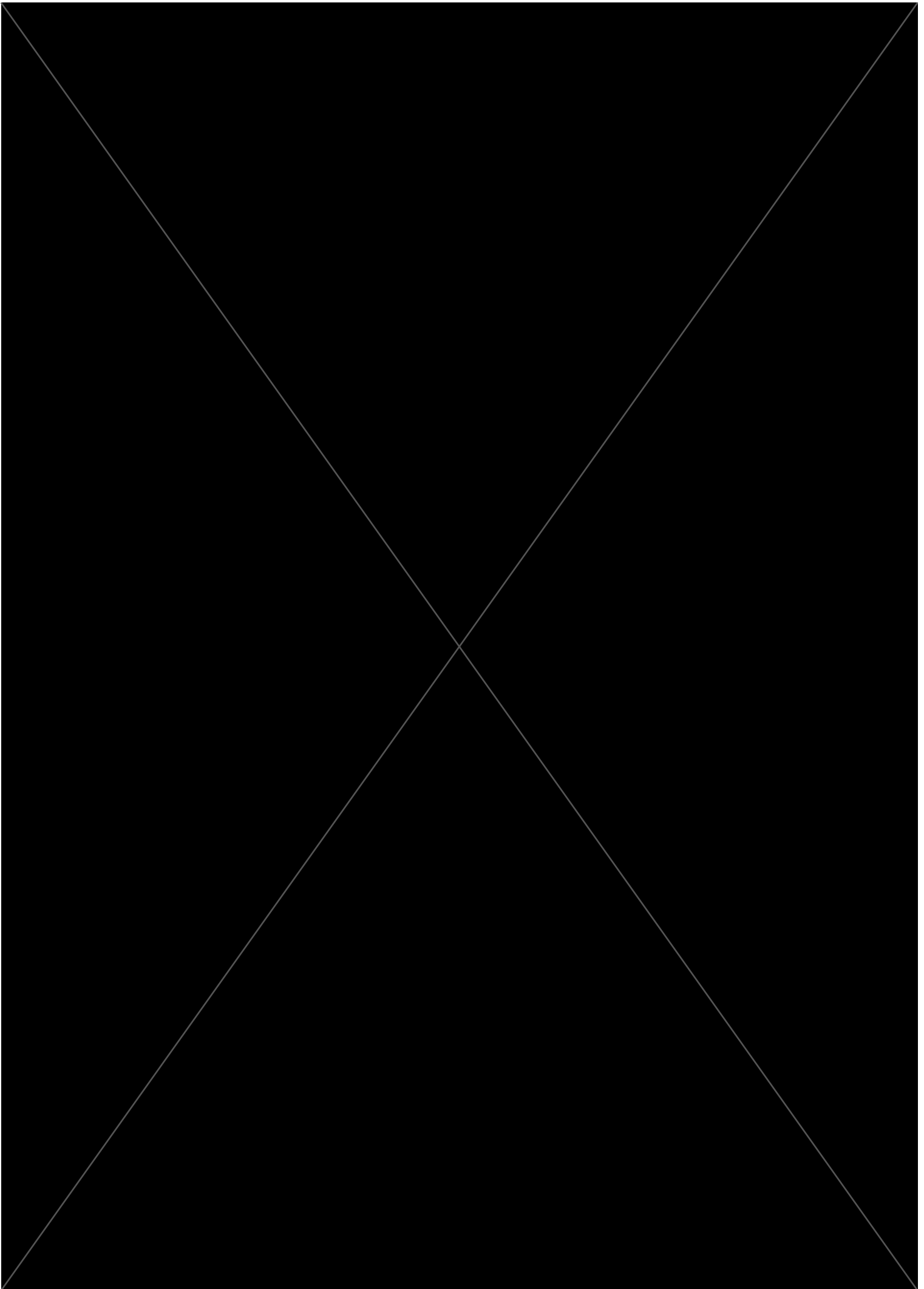


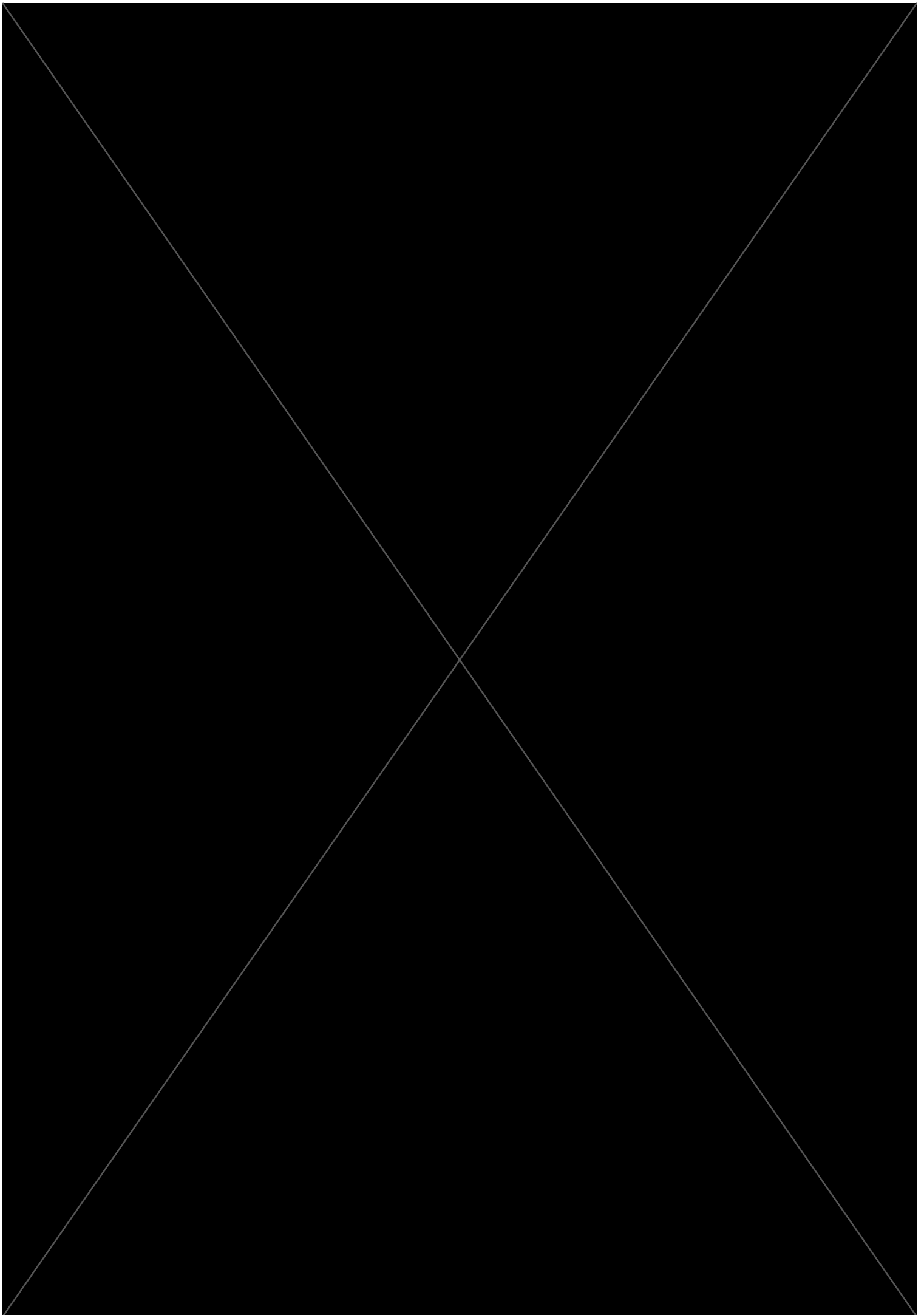


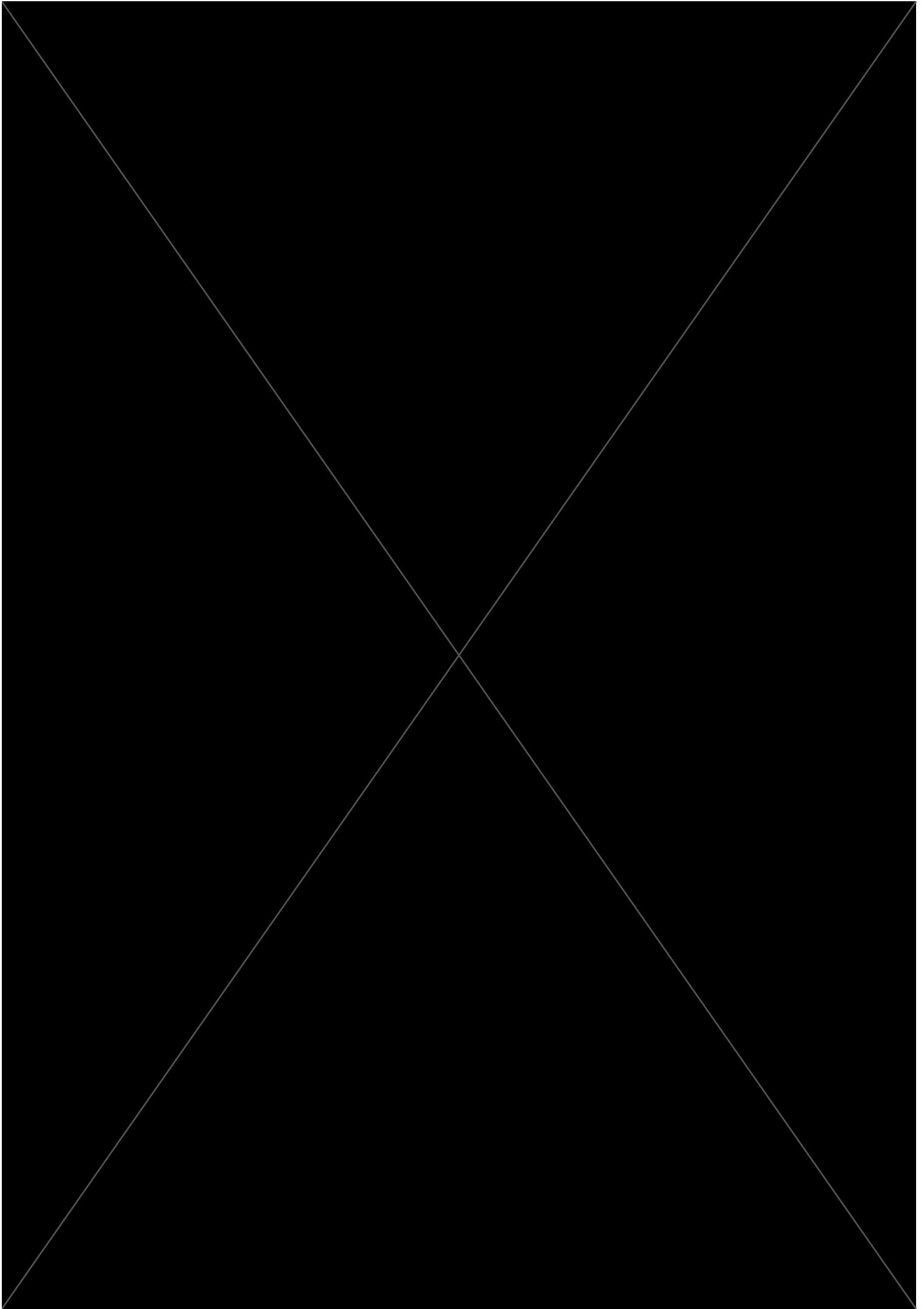
Note: all dimensions for indication only. Overviews of engine do not include ancillaries such as GDI pump, air filter, exhaust silencer, starter motor etc.

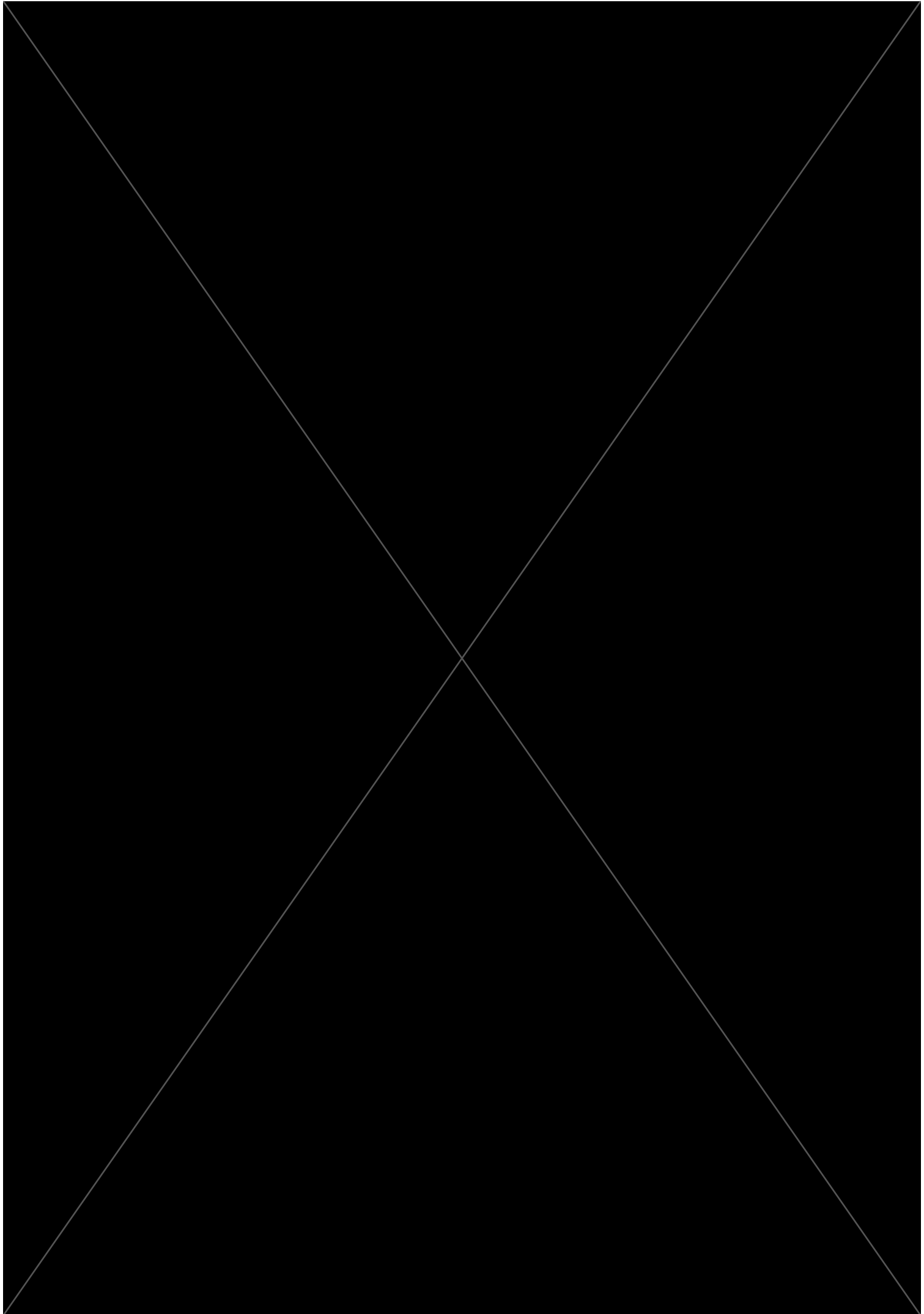
Dept.	Technical reference General Tolerances $\pm 0.1 \text{ mm}$	Created by <b>Samuel Frederick Furze</b>	Approved by
		Document type <b>Thesis</b>	Document status
		Title <b>Main Engine Overview</b>	DWG No. <b>OV1</b>
		Rev.	Date of issue
			<b>5/5</b>
			Sheet
			<b>5/5</b>

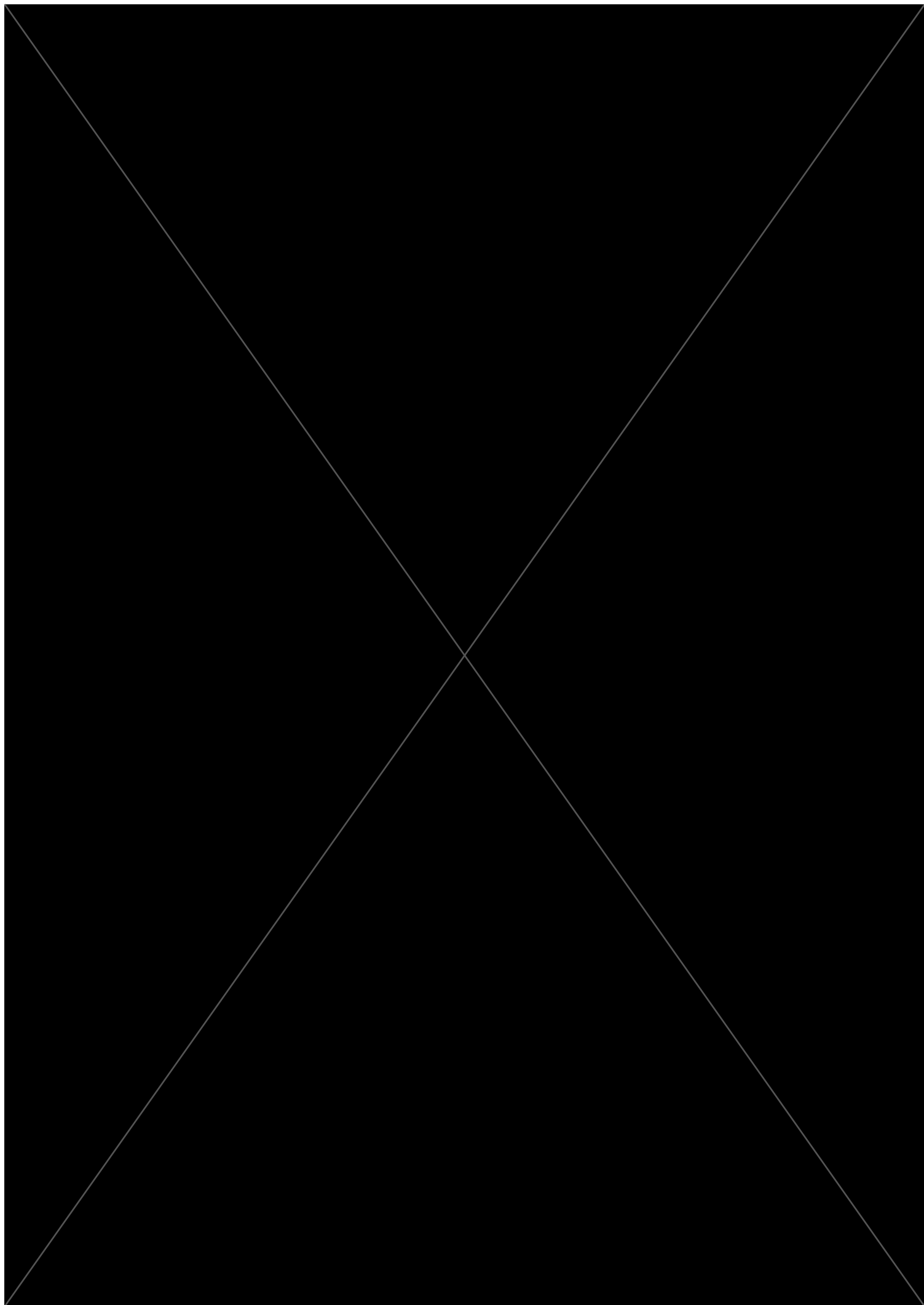


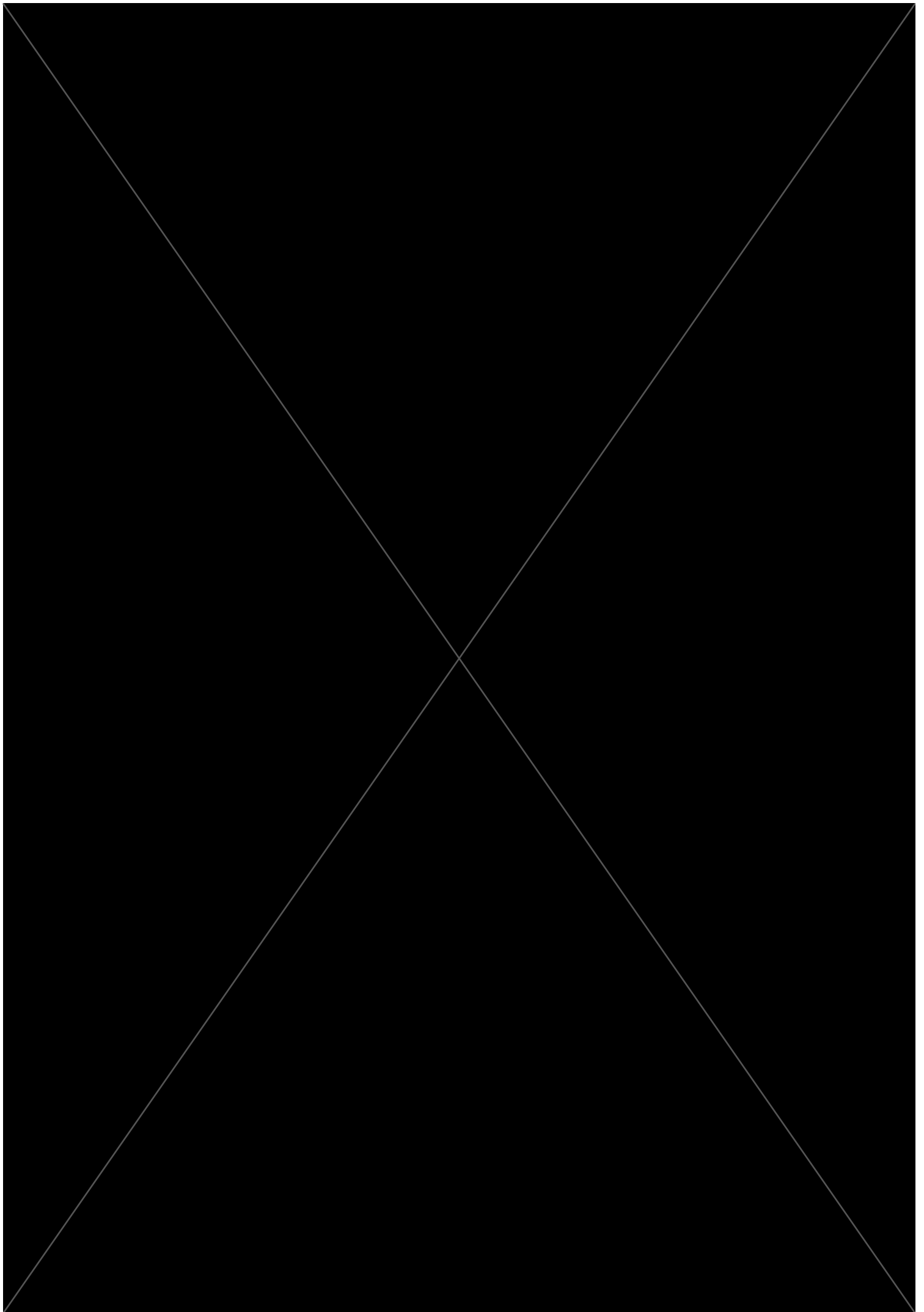


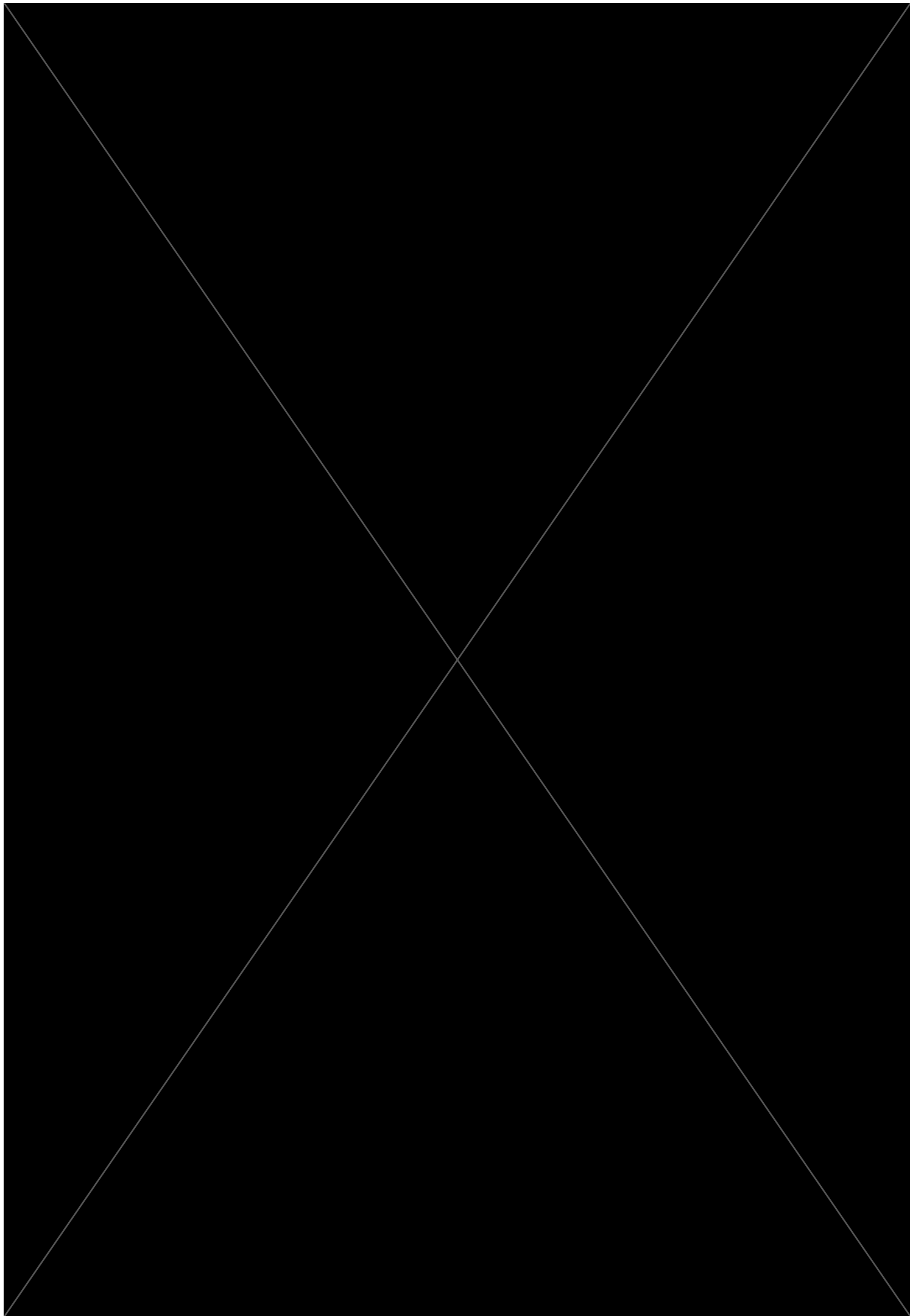


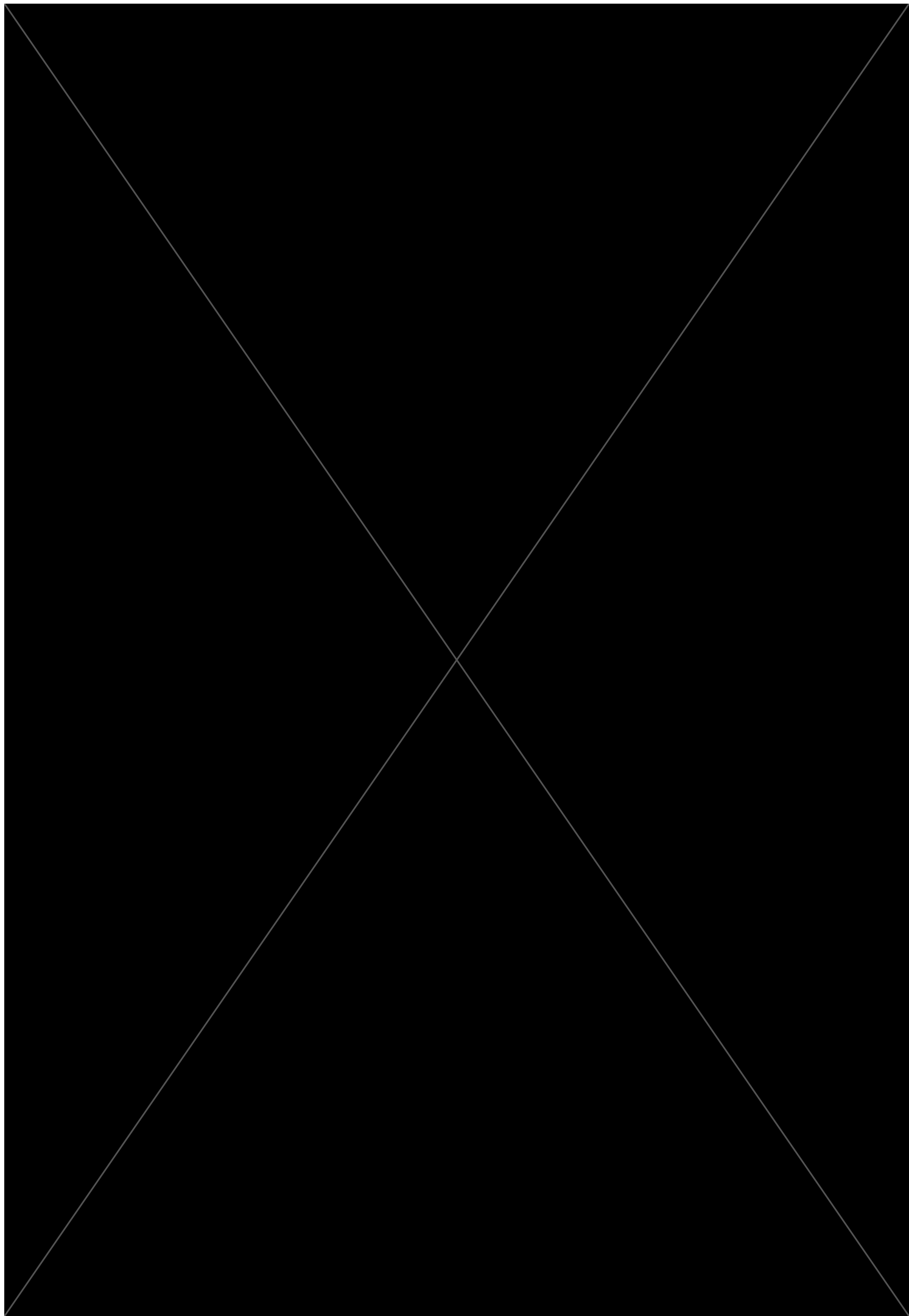


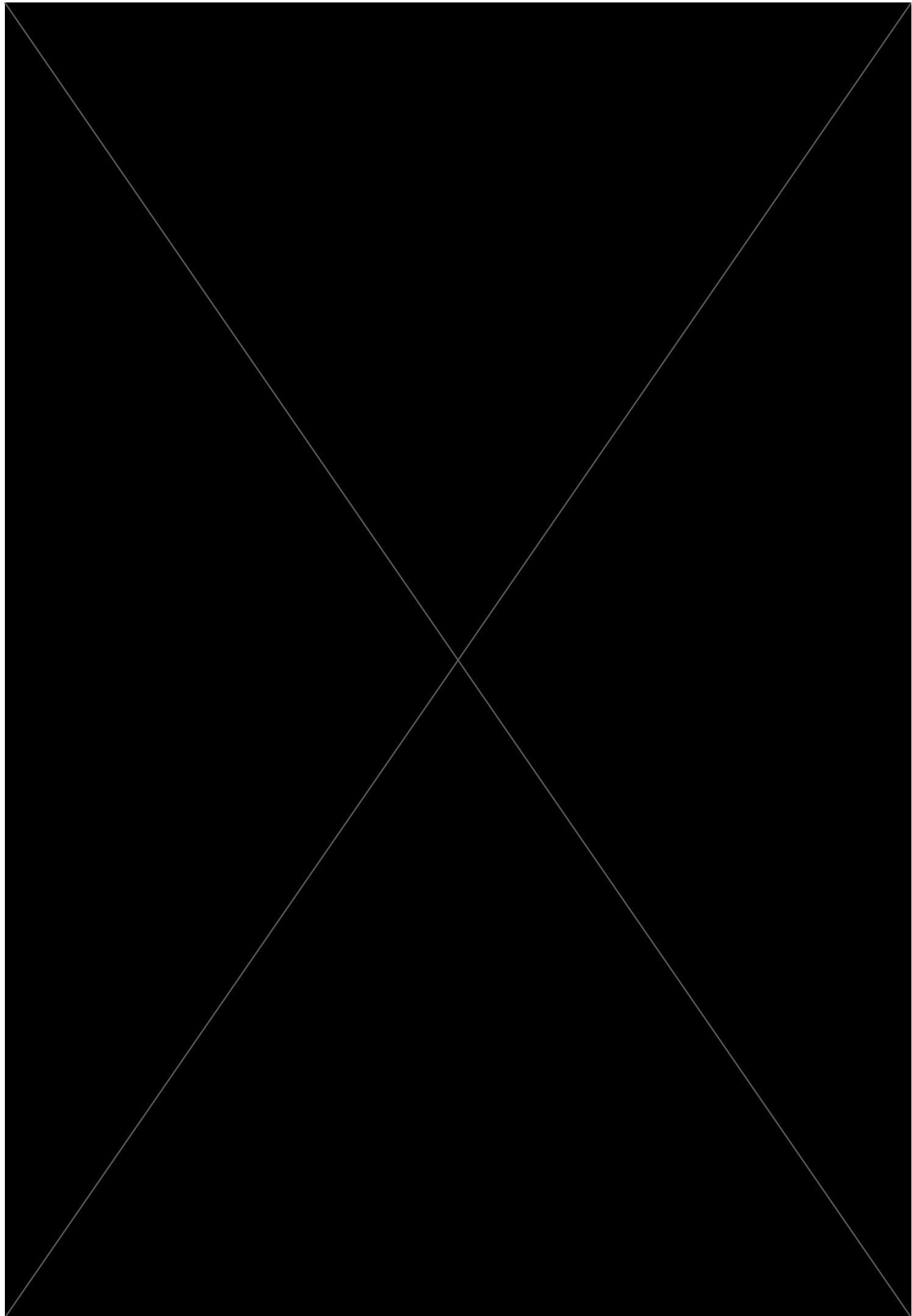


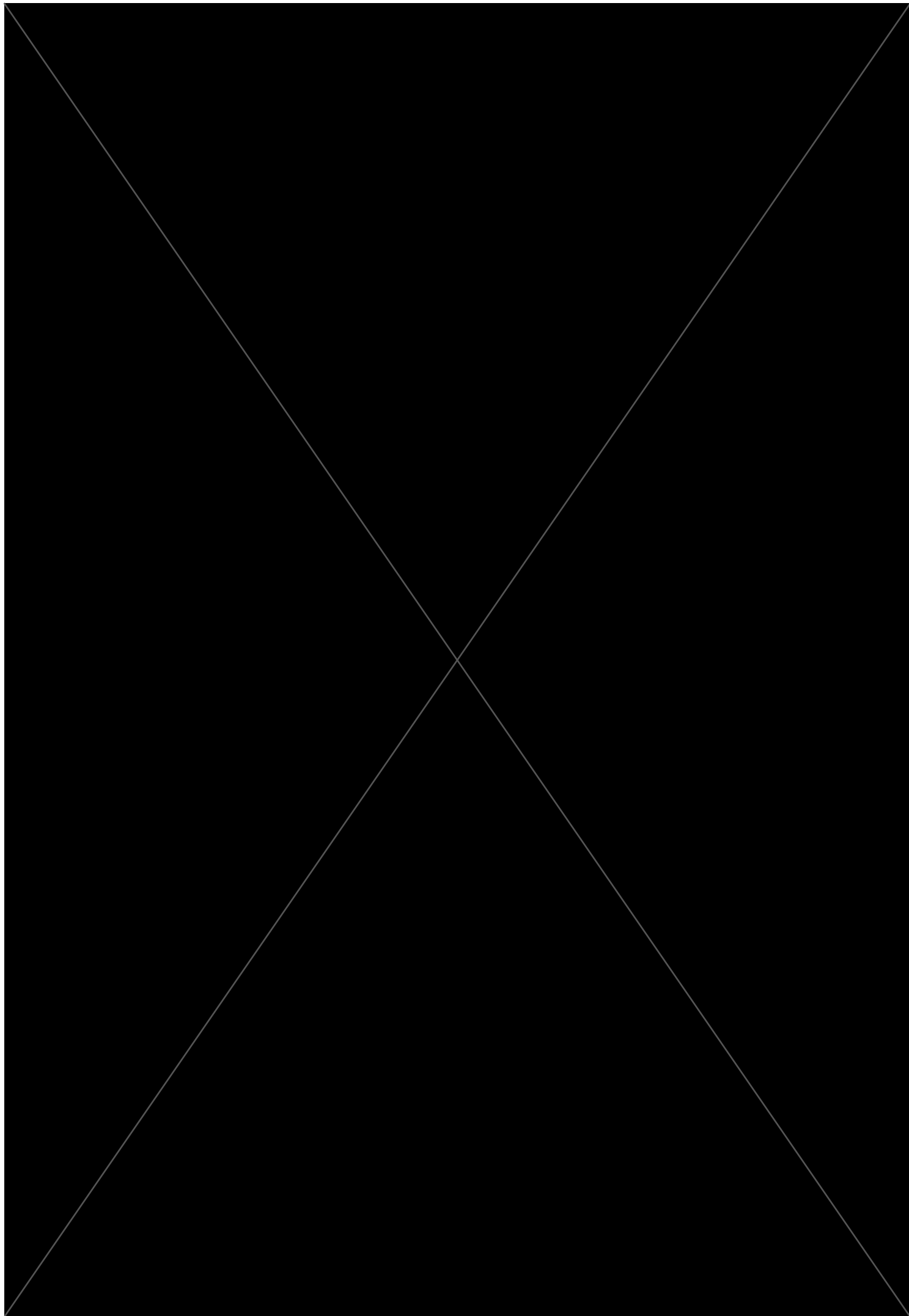


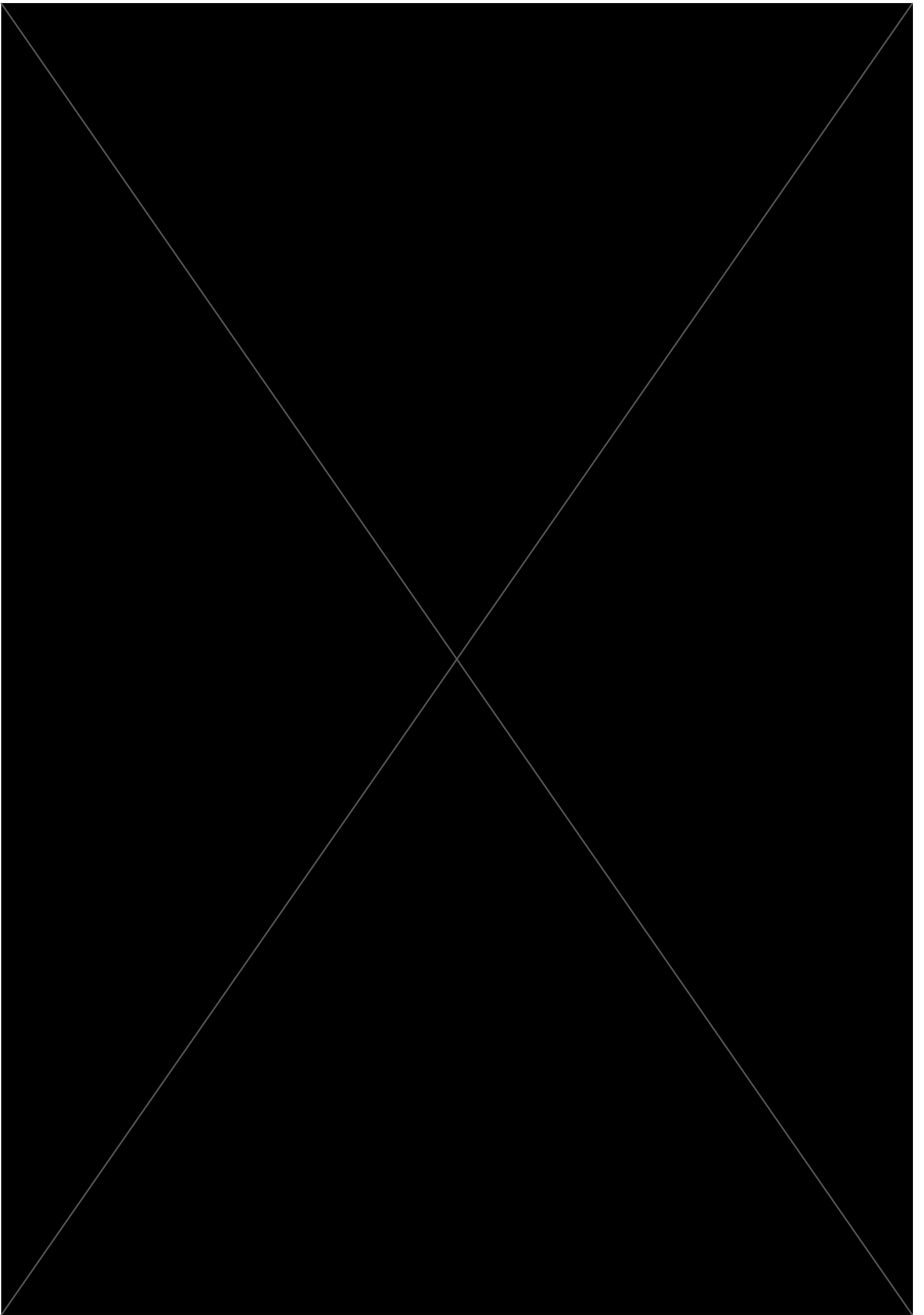


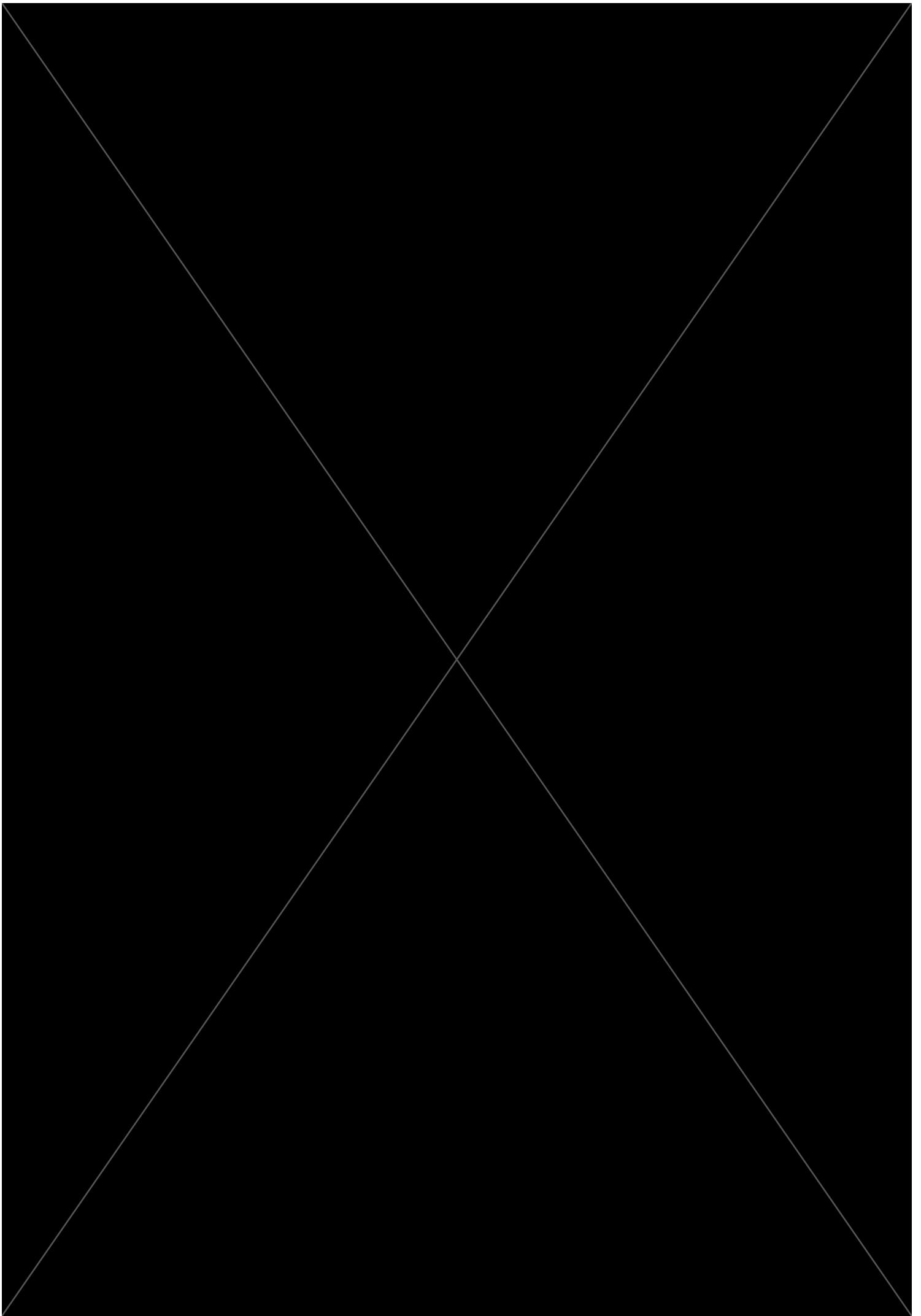


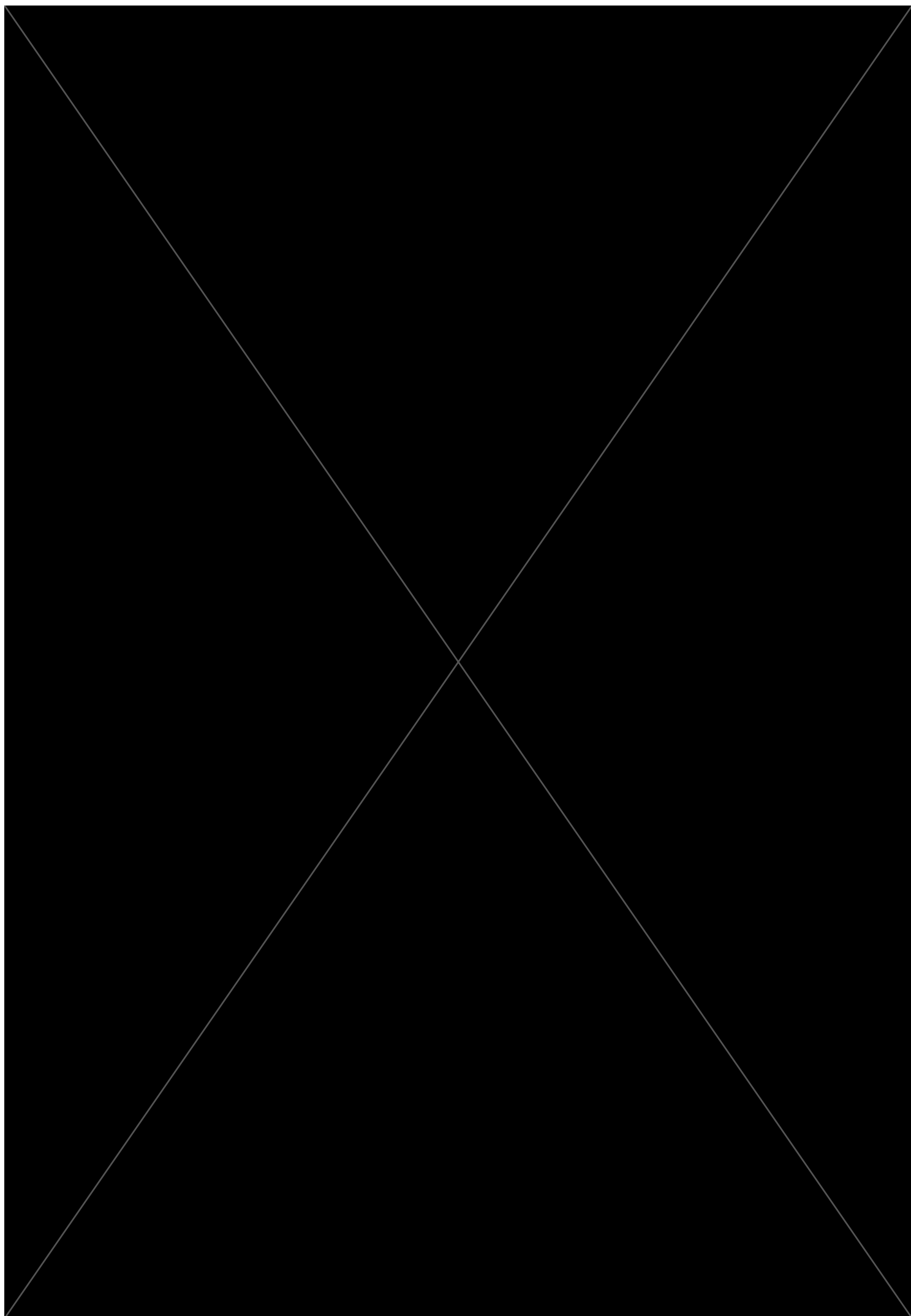


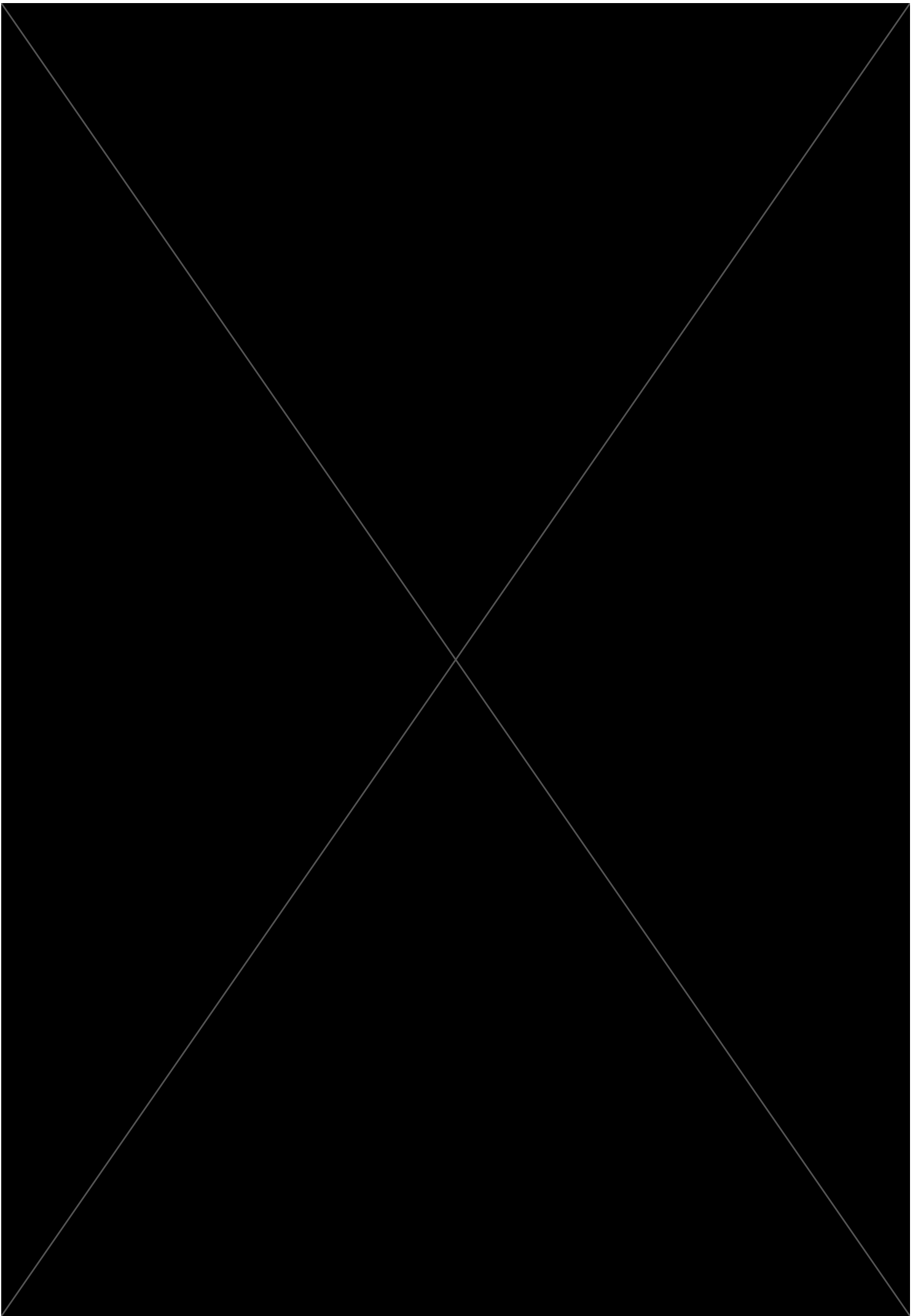


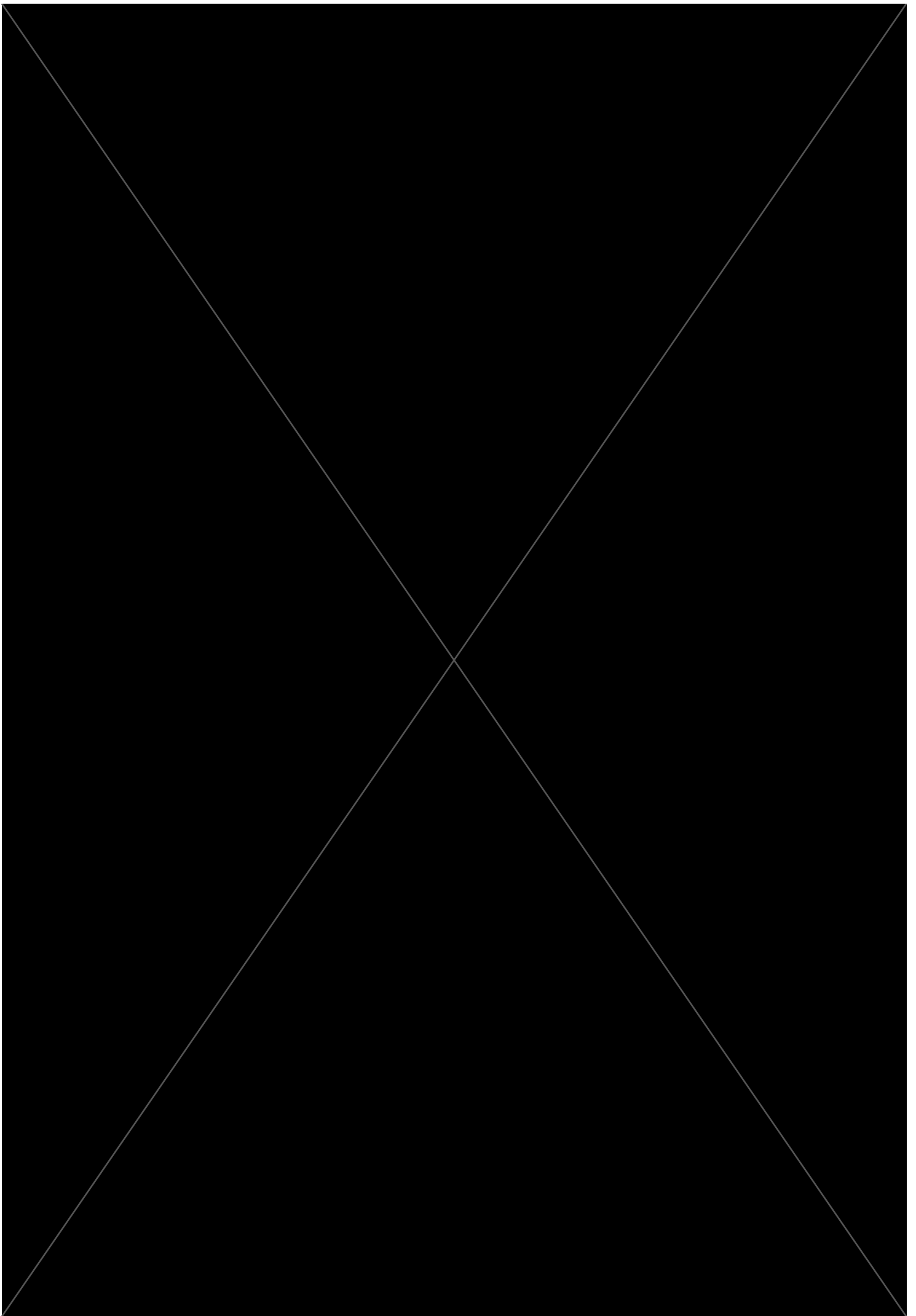


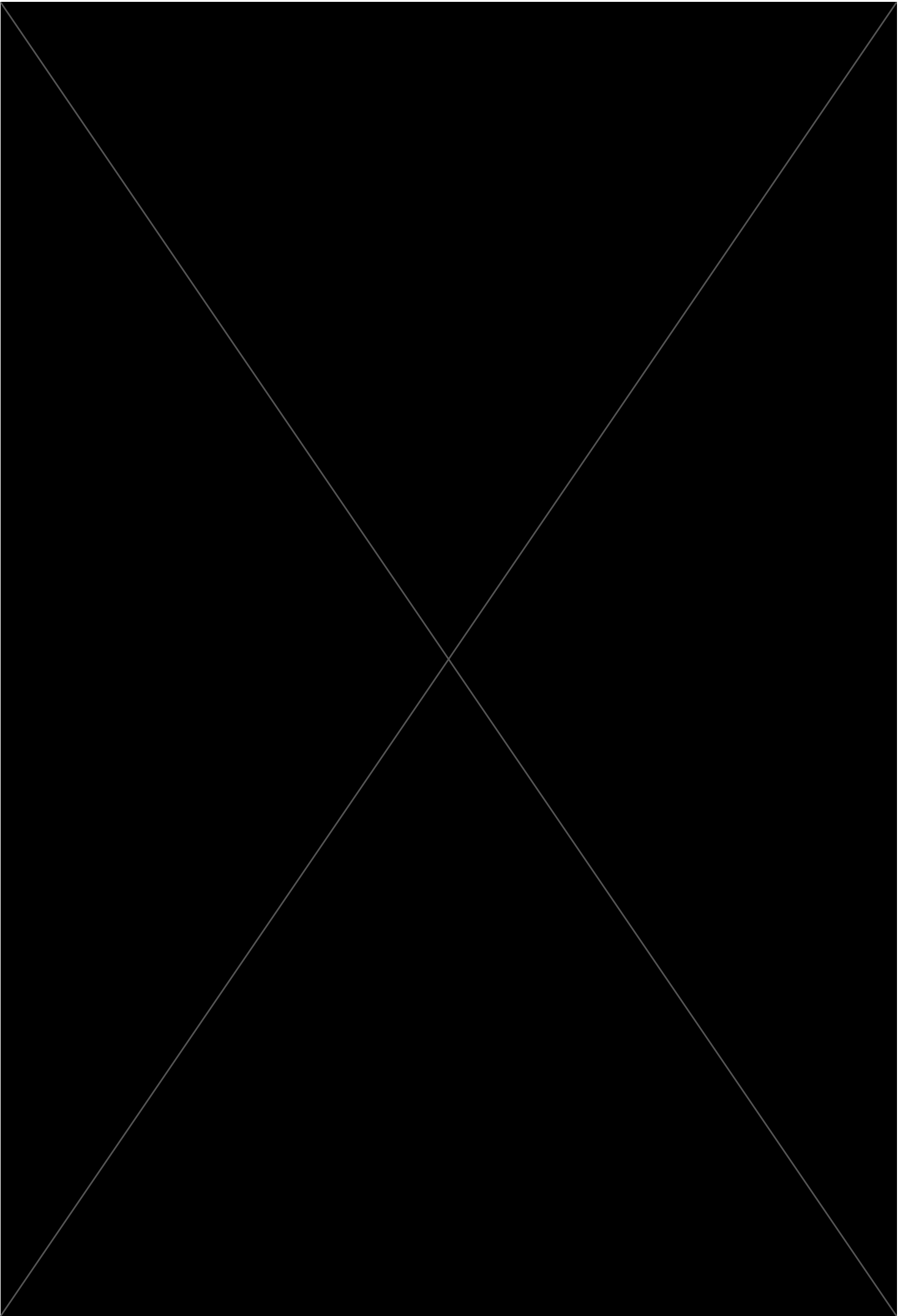


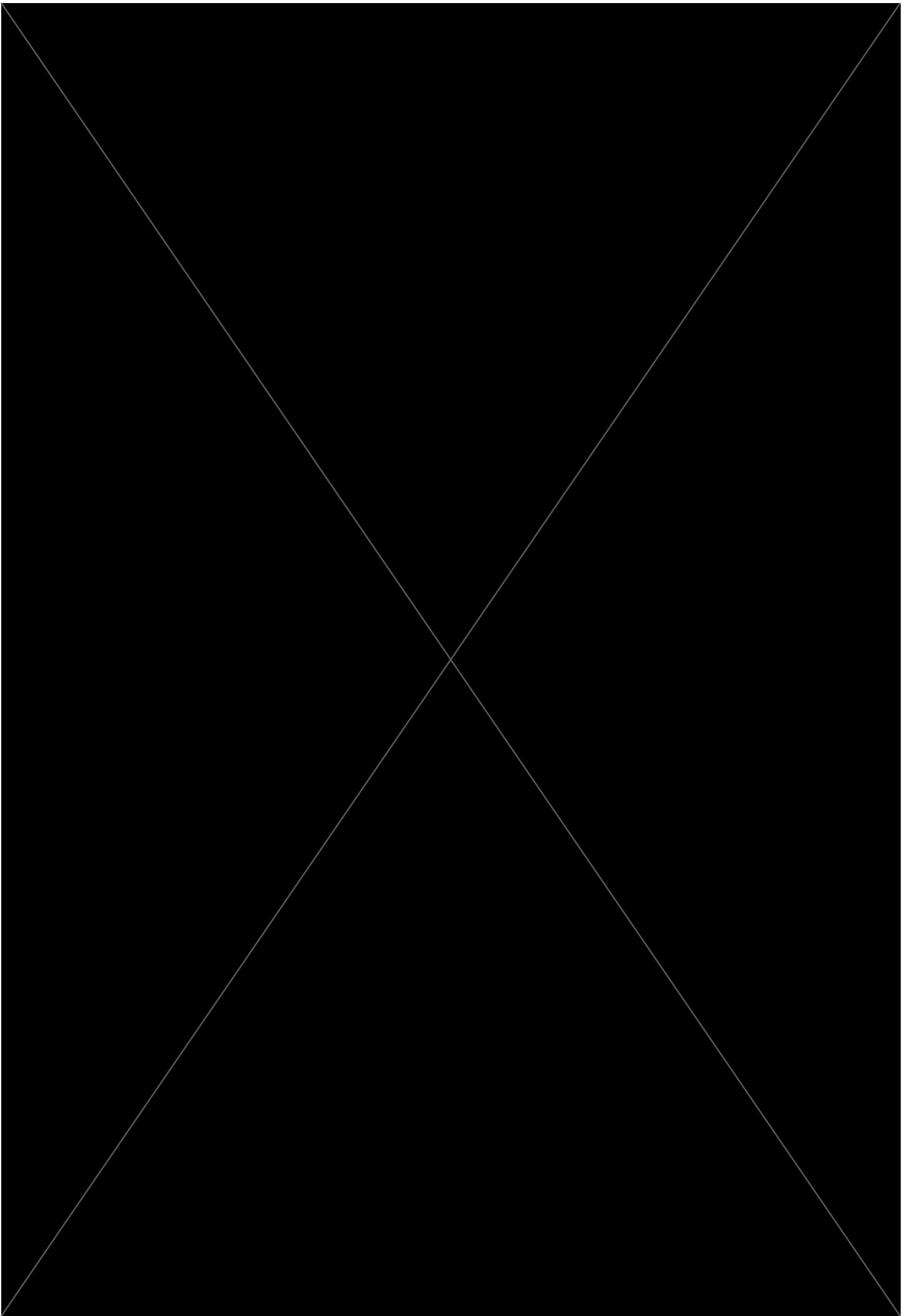


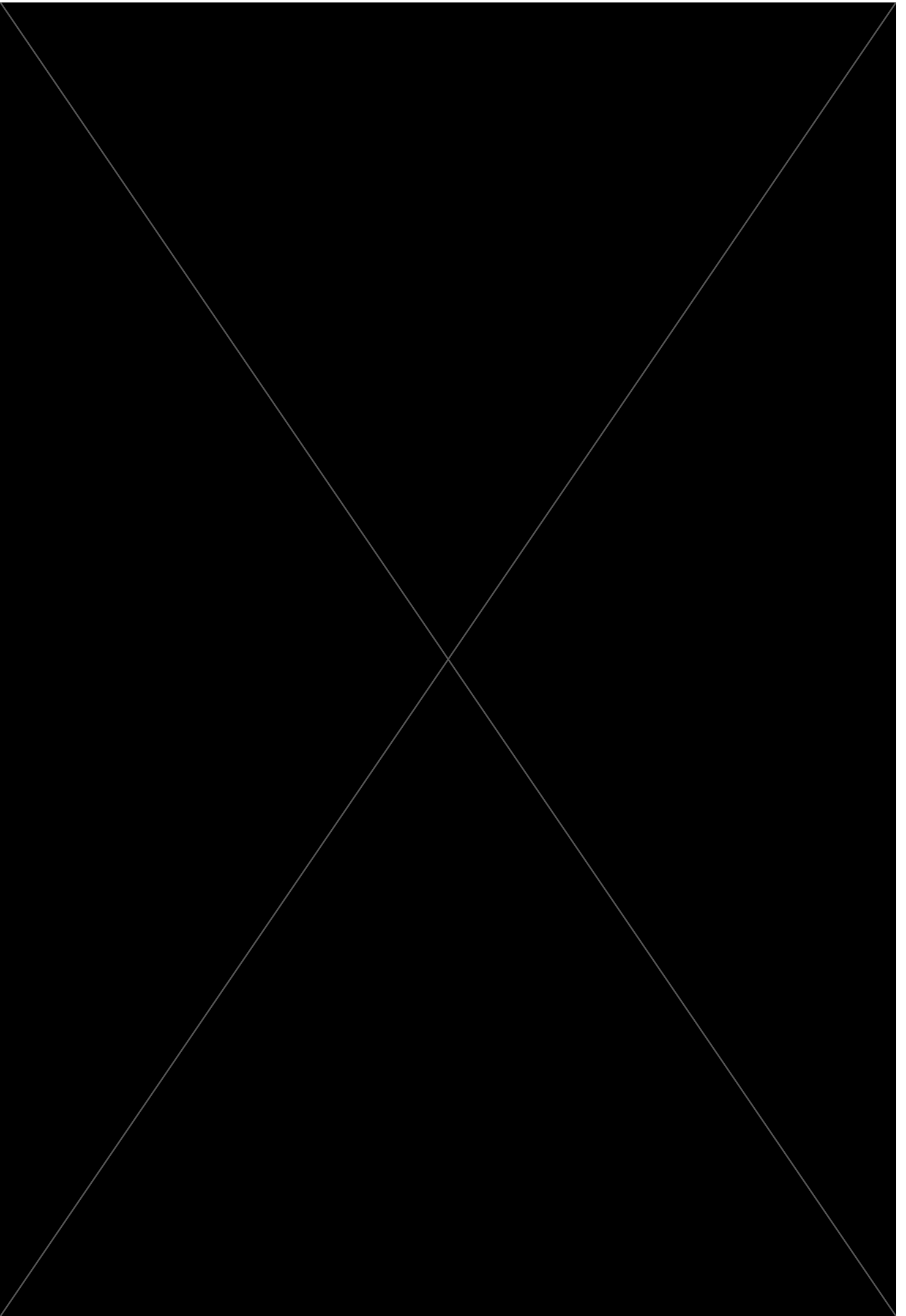


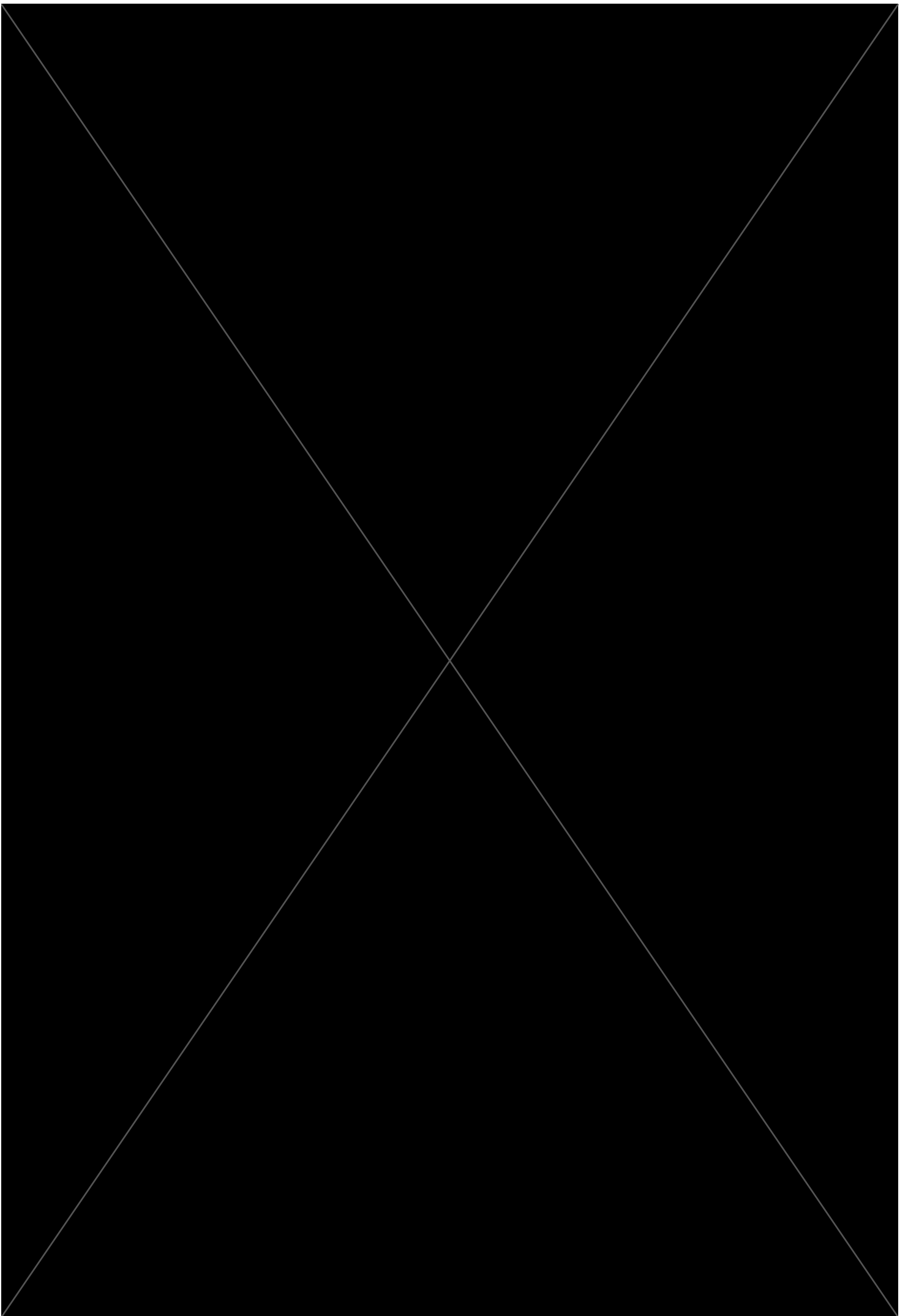


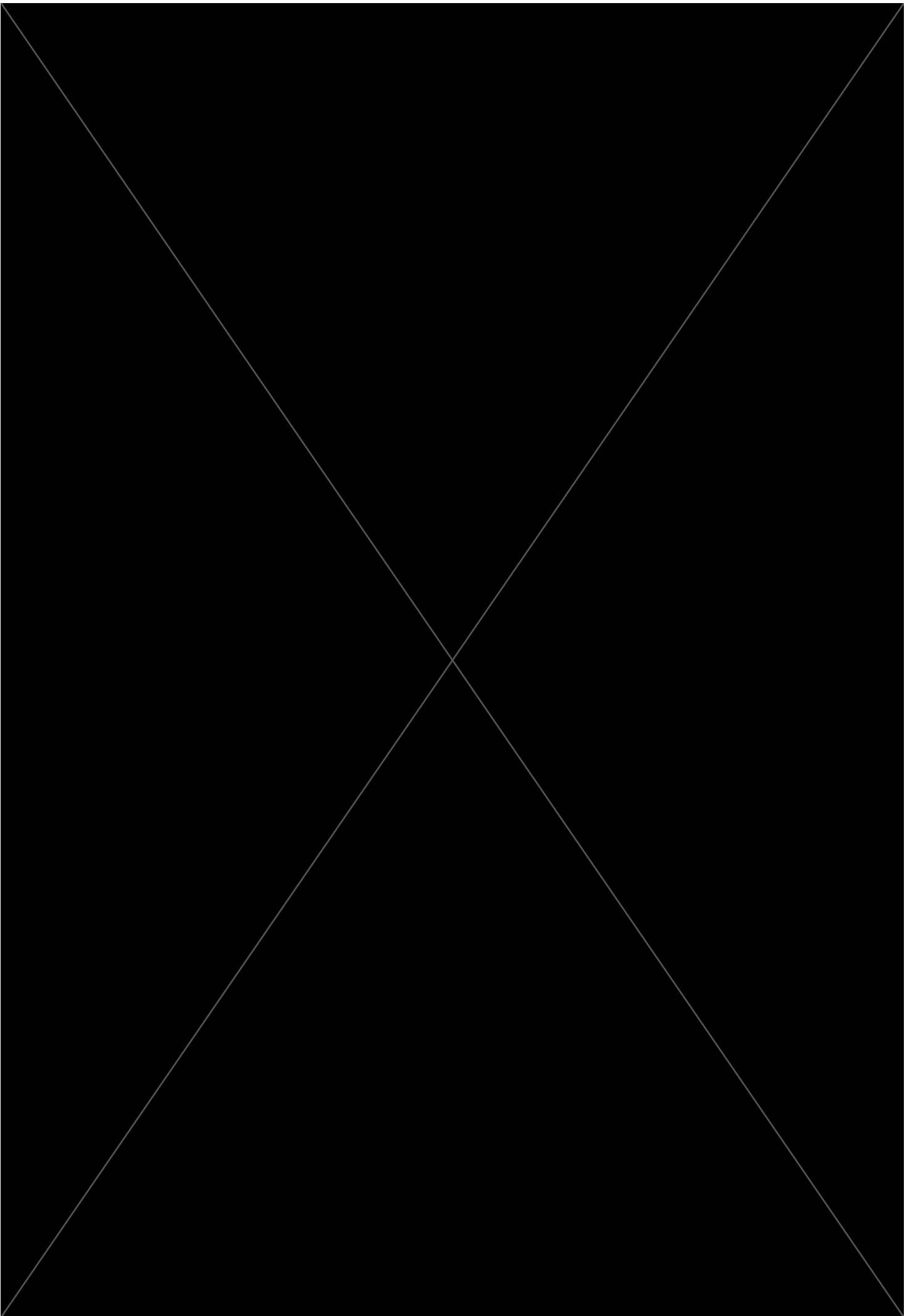


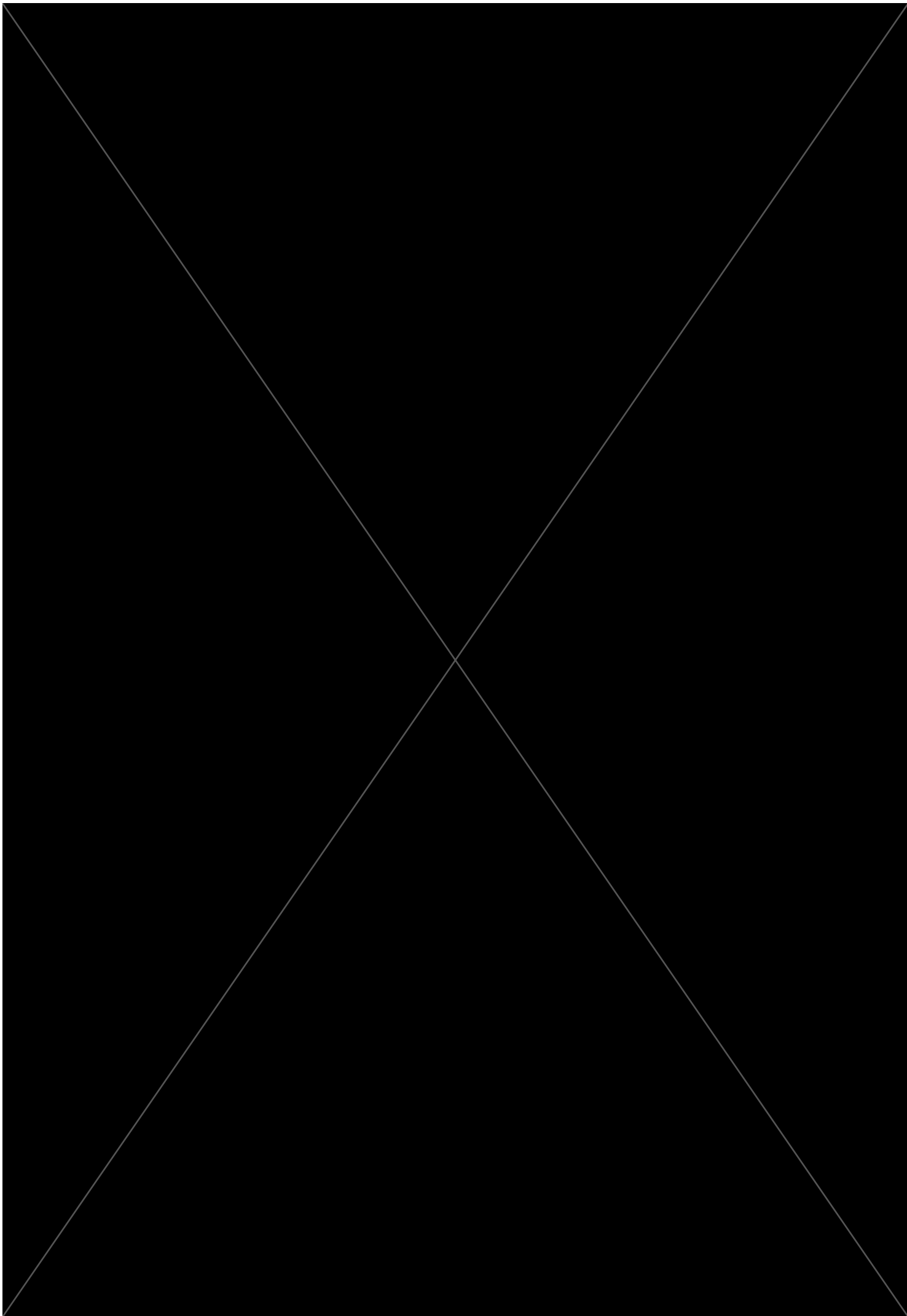


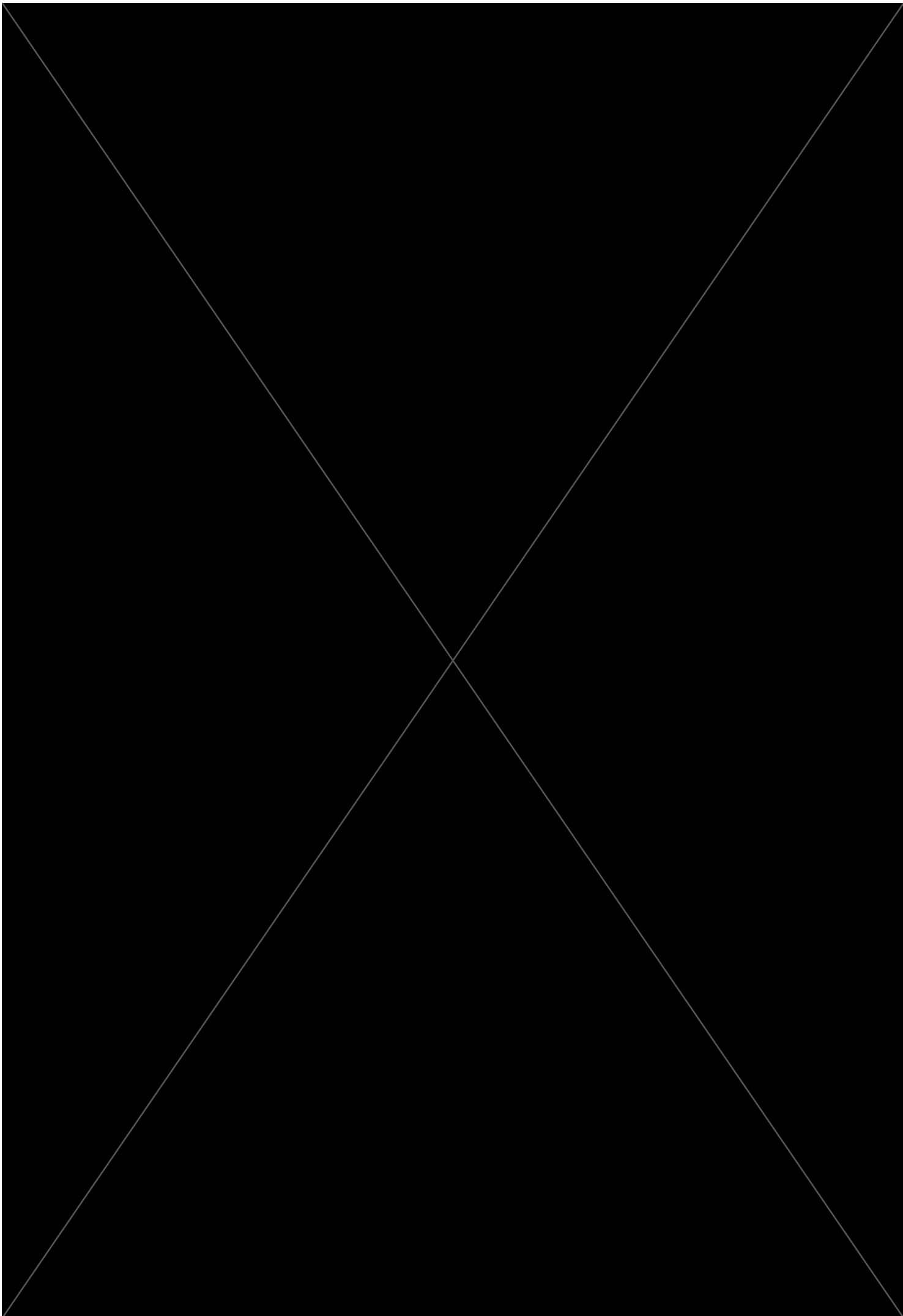


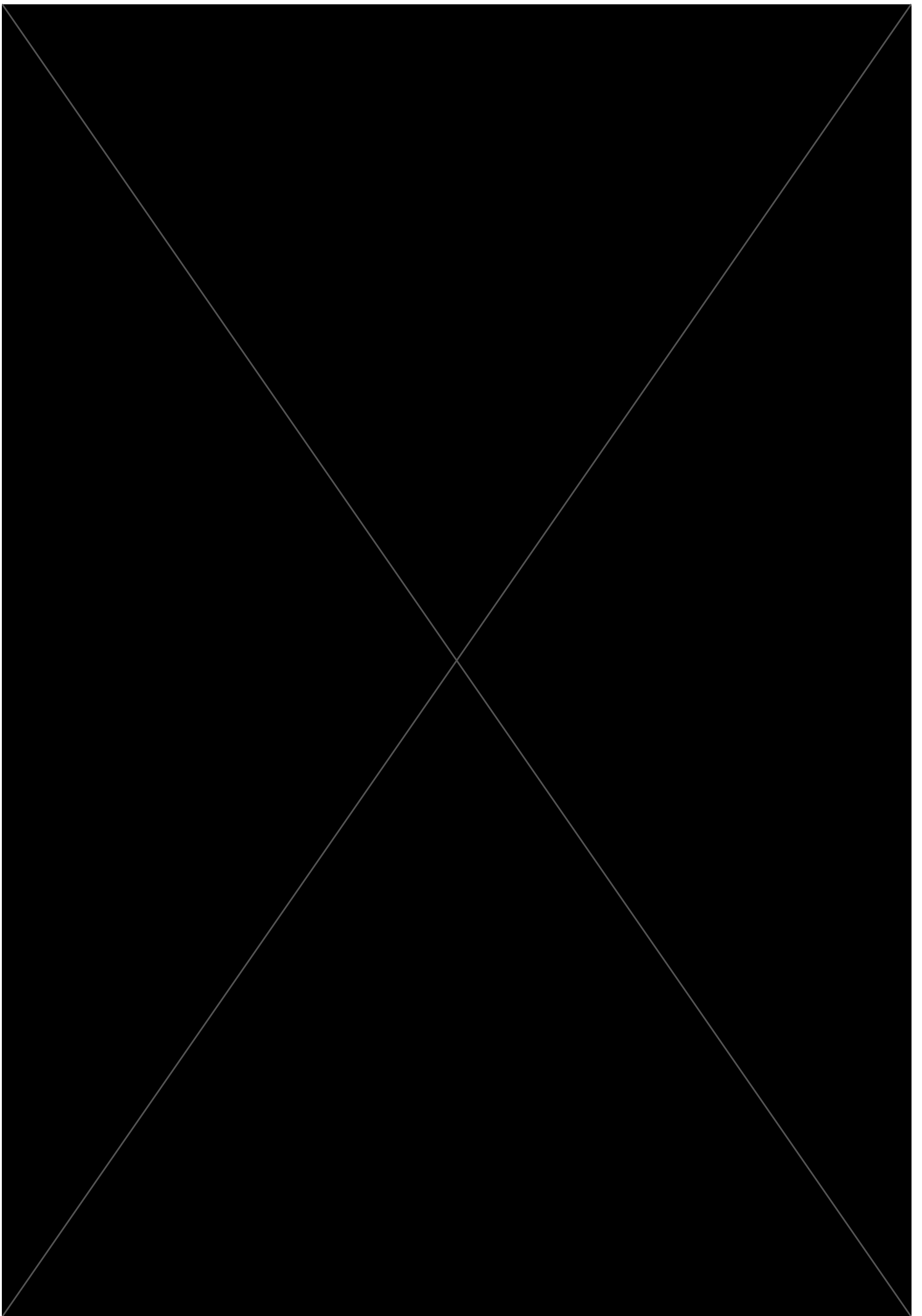


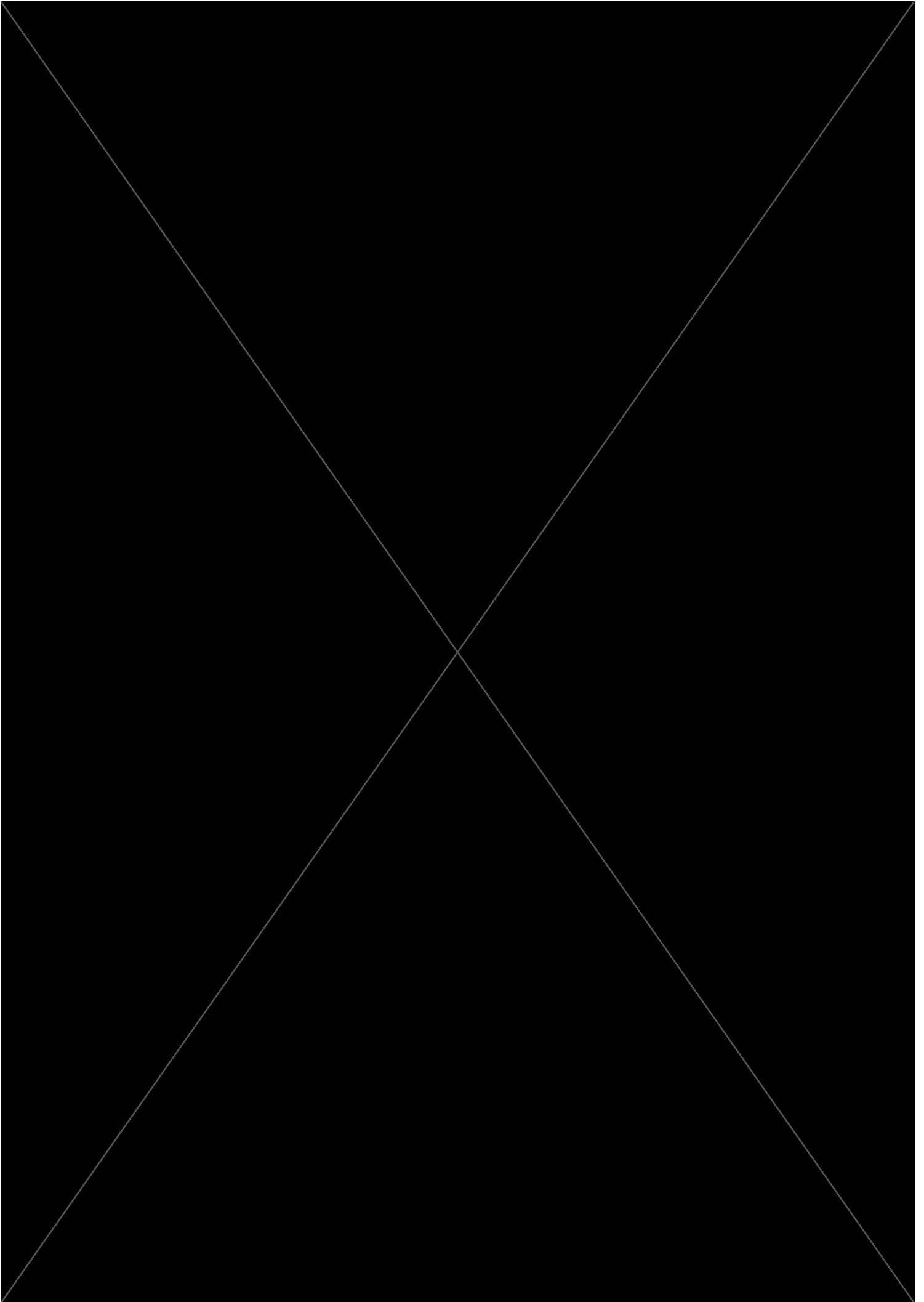


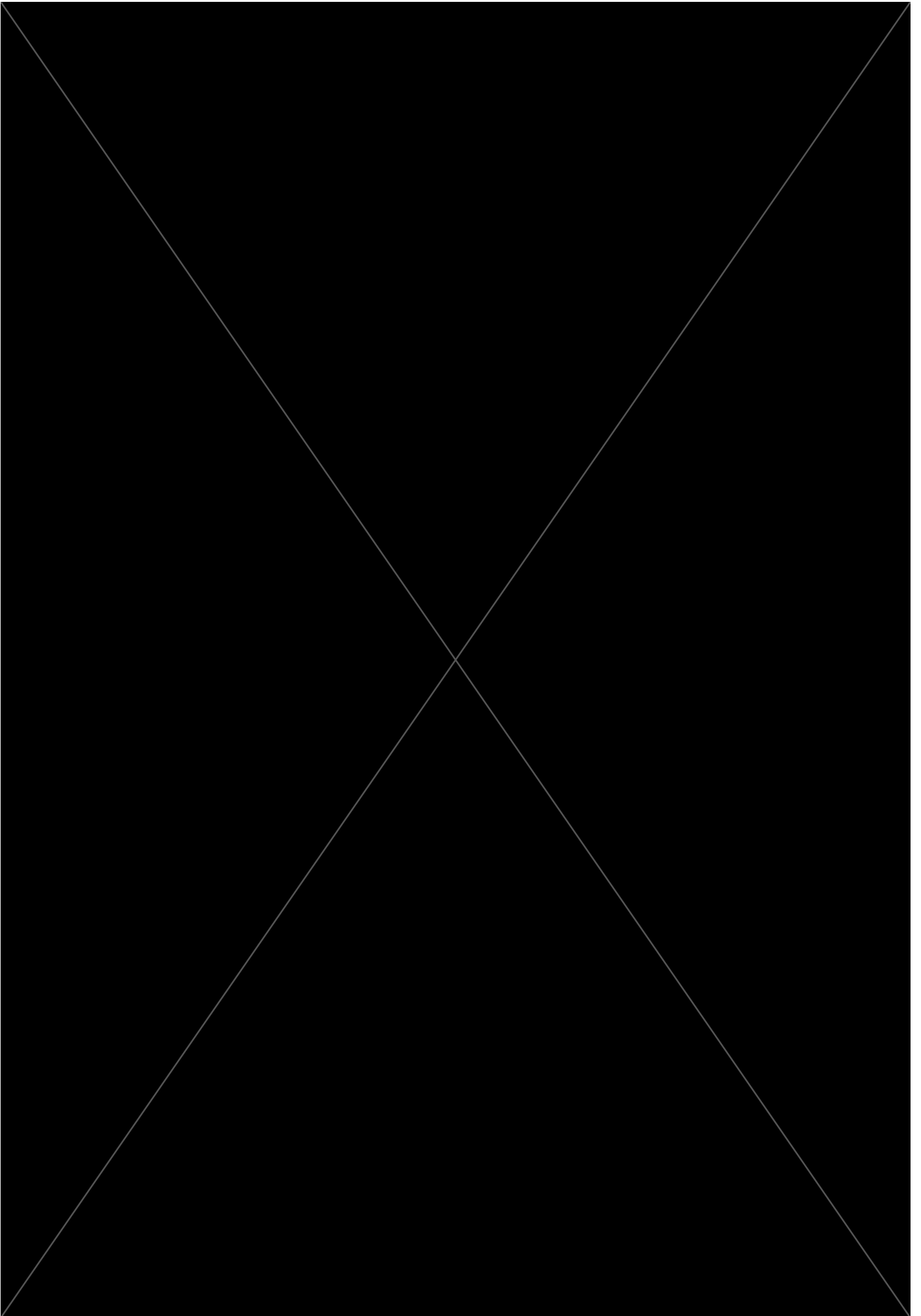


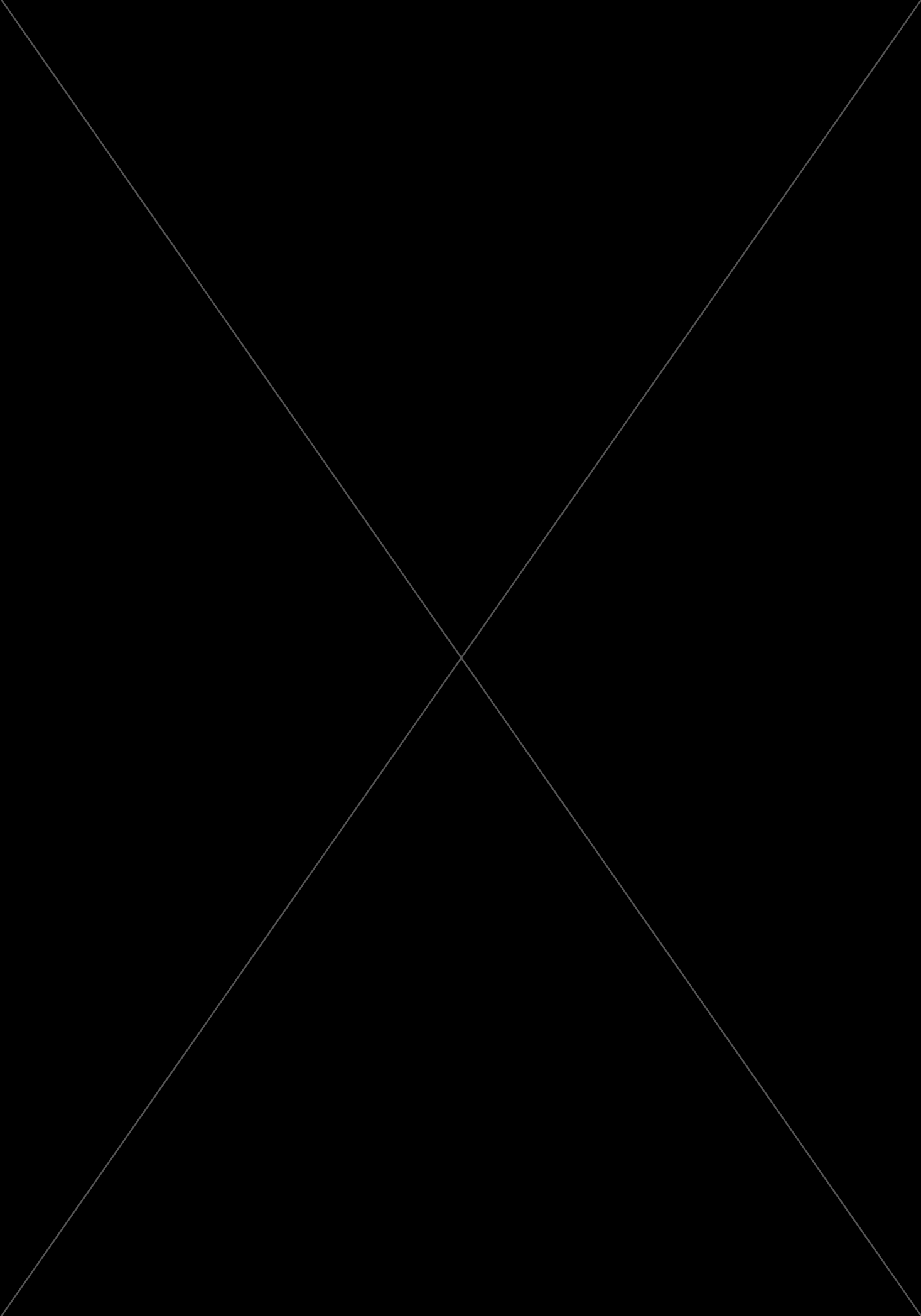


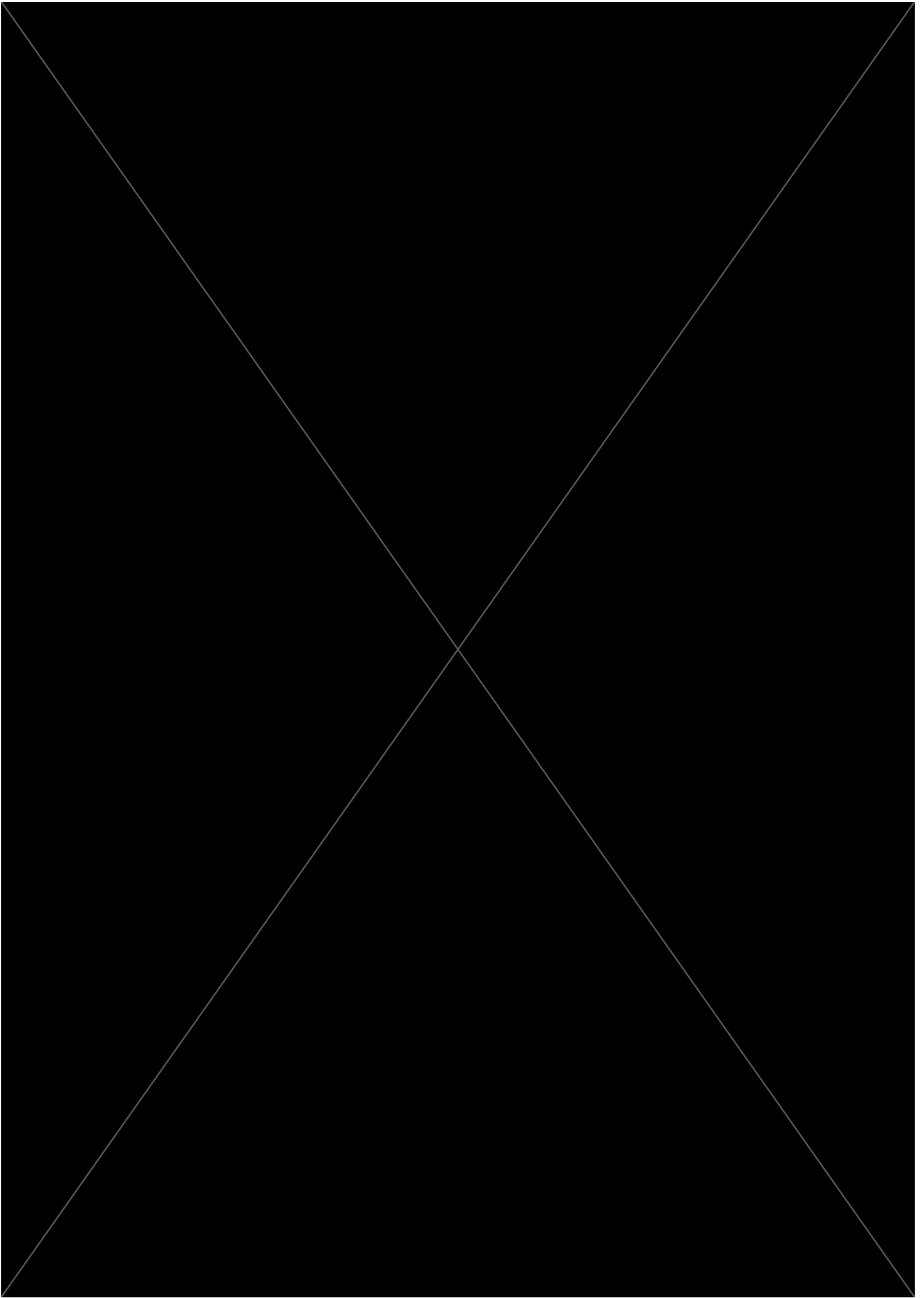


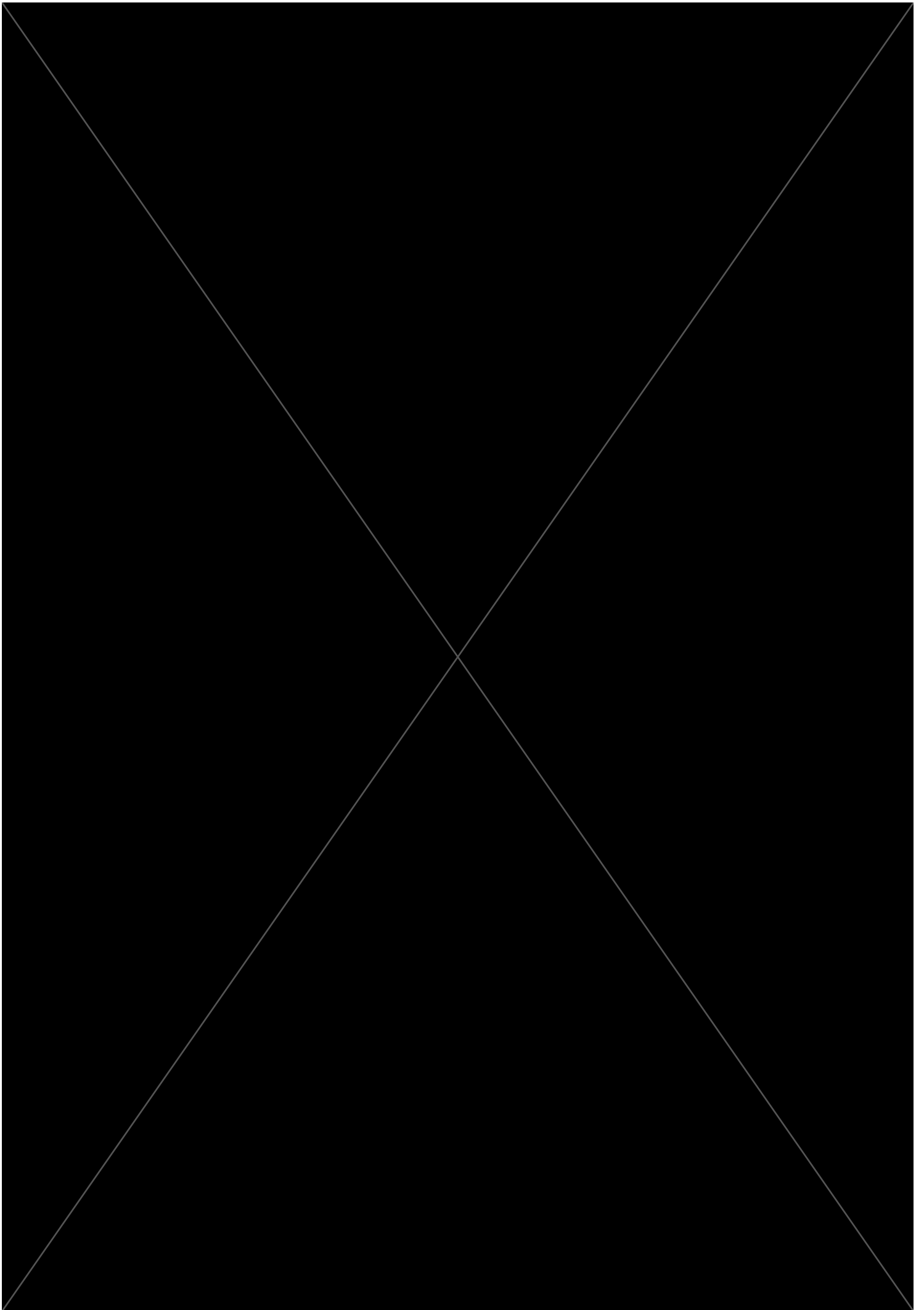


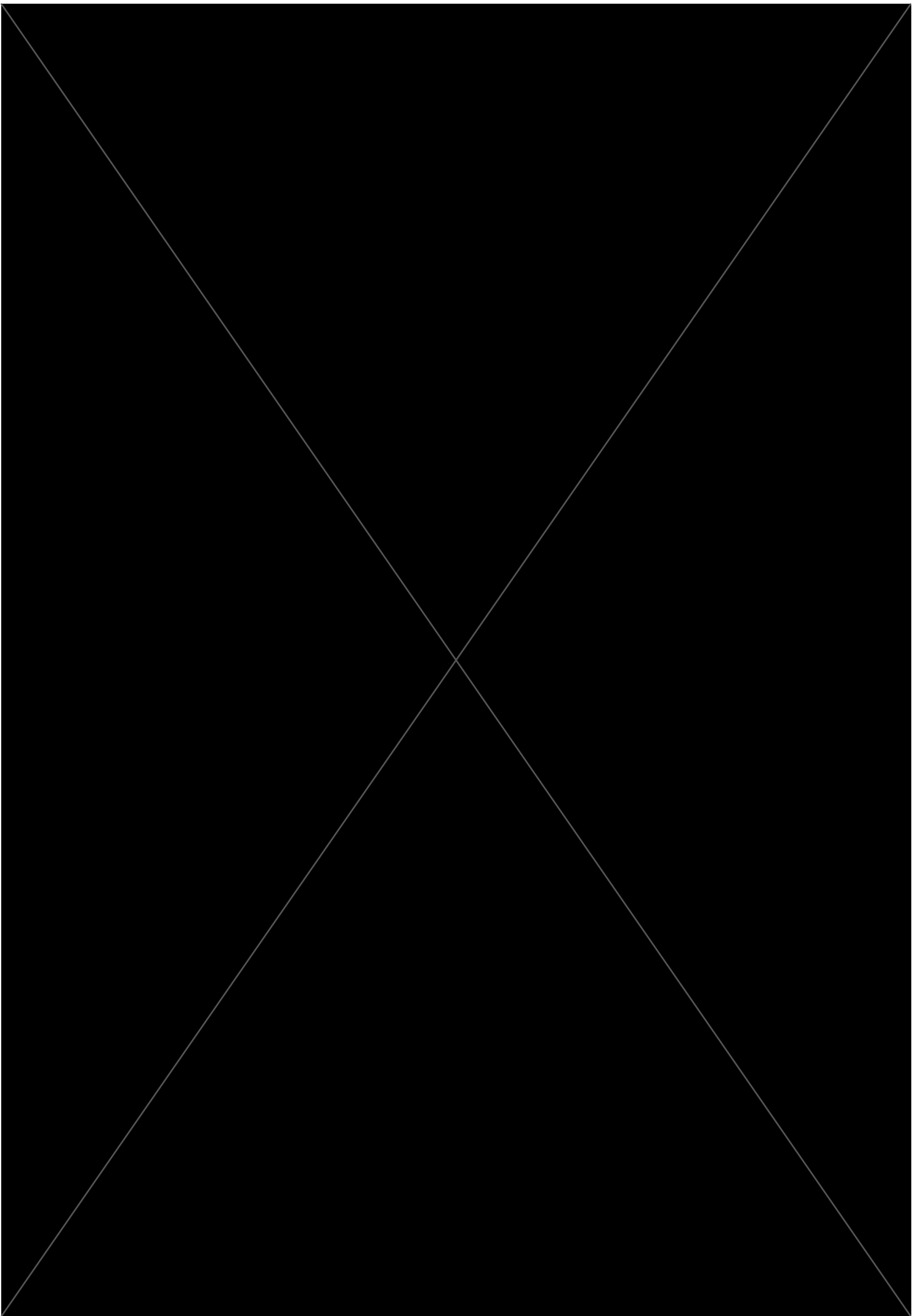


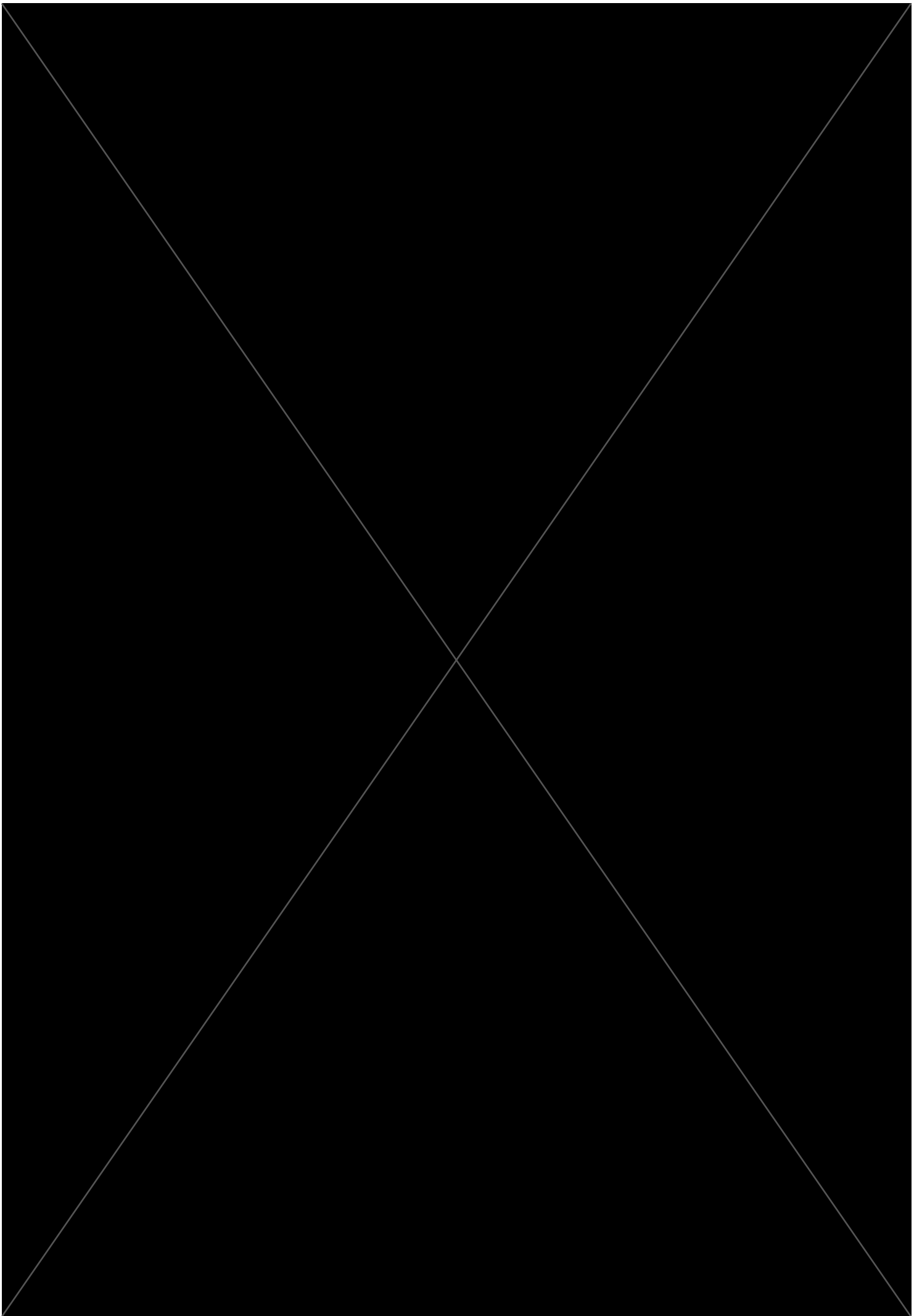


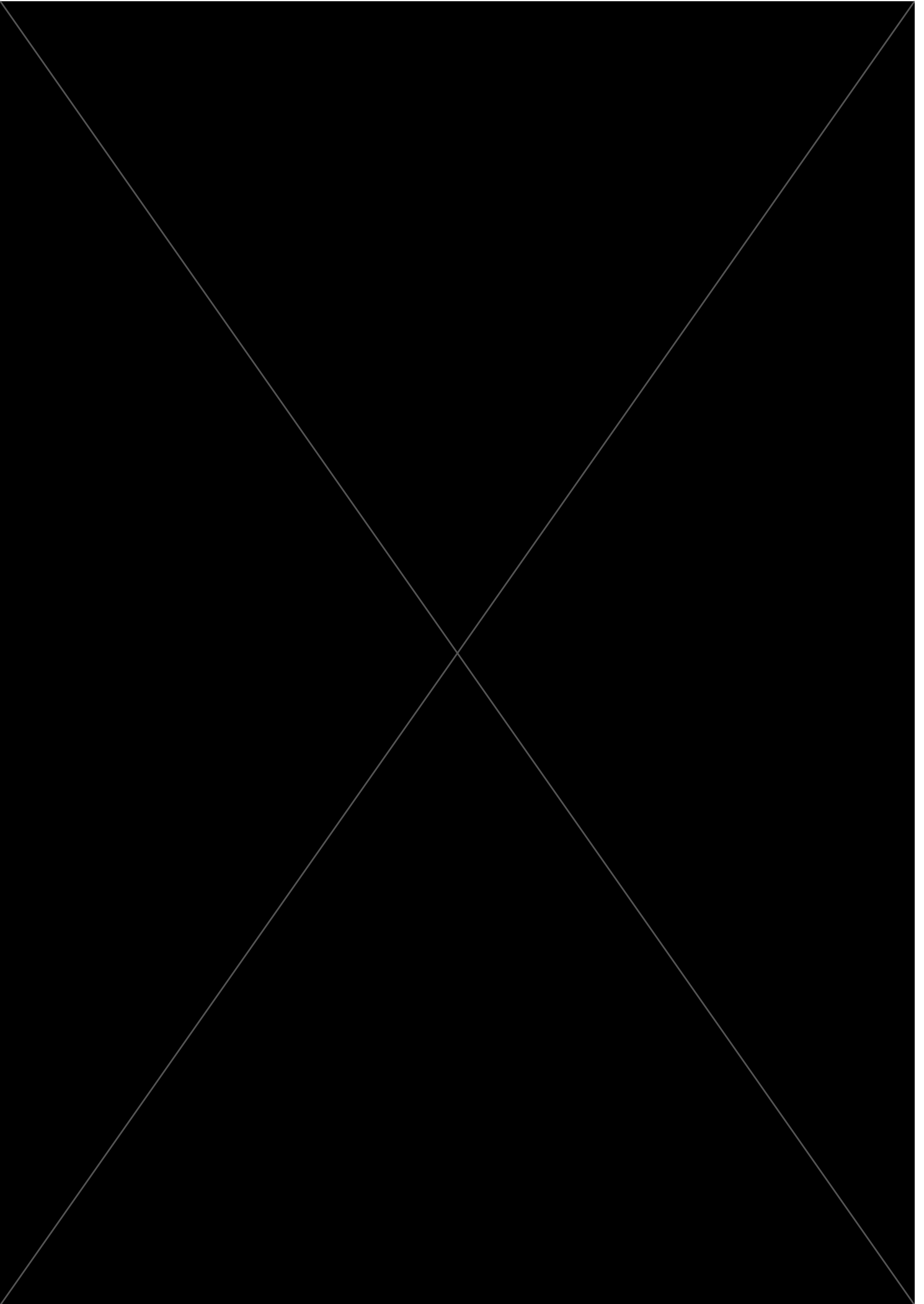


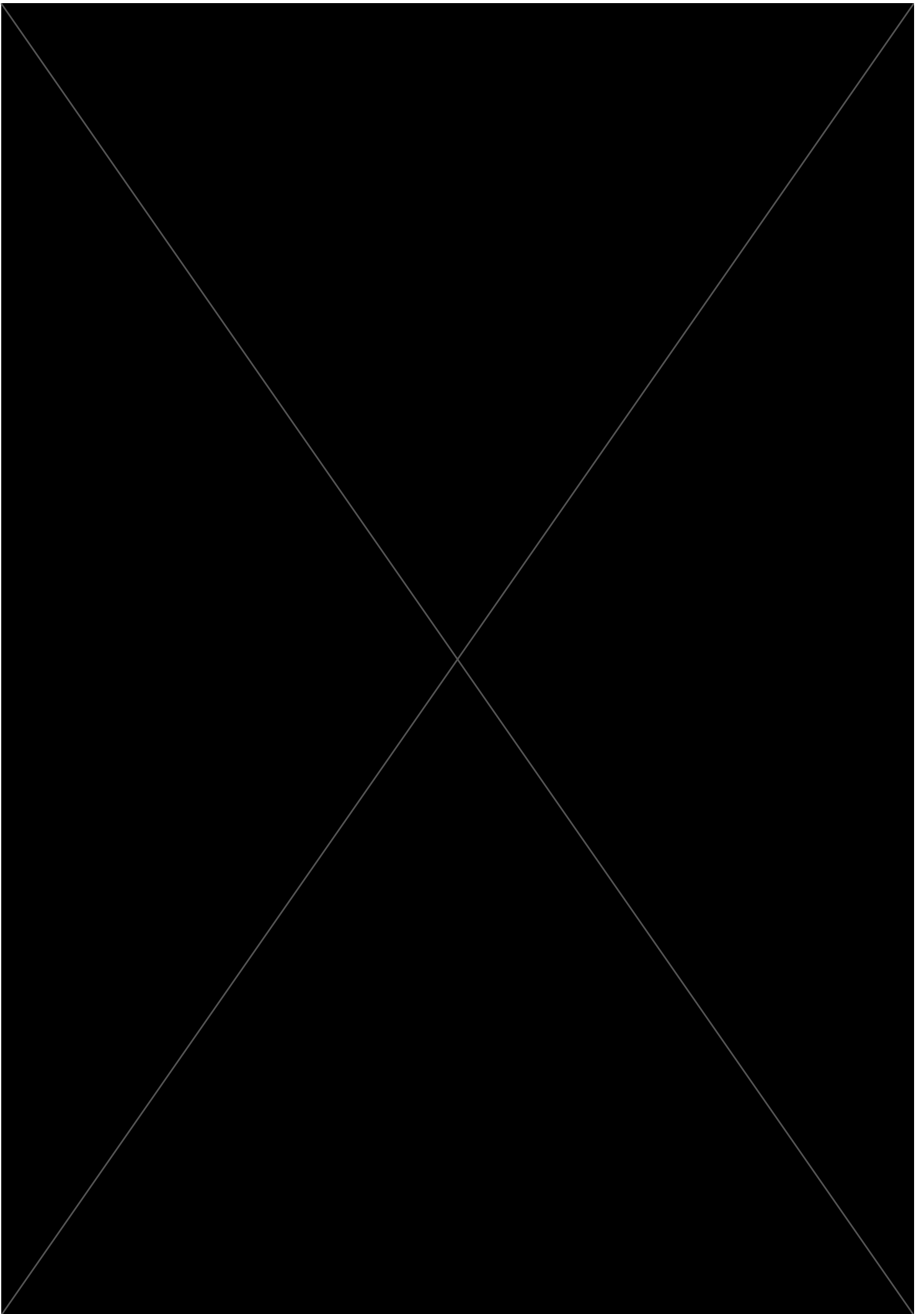


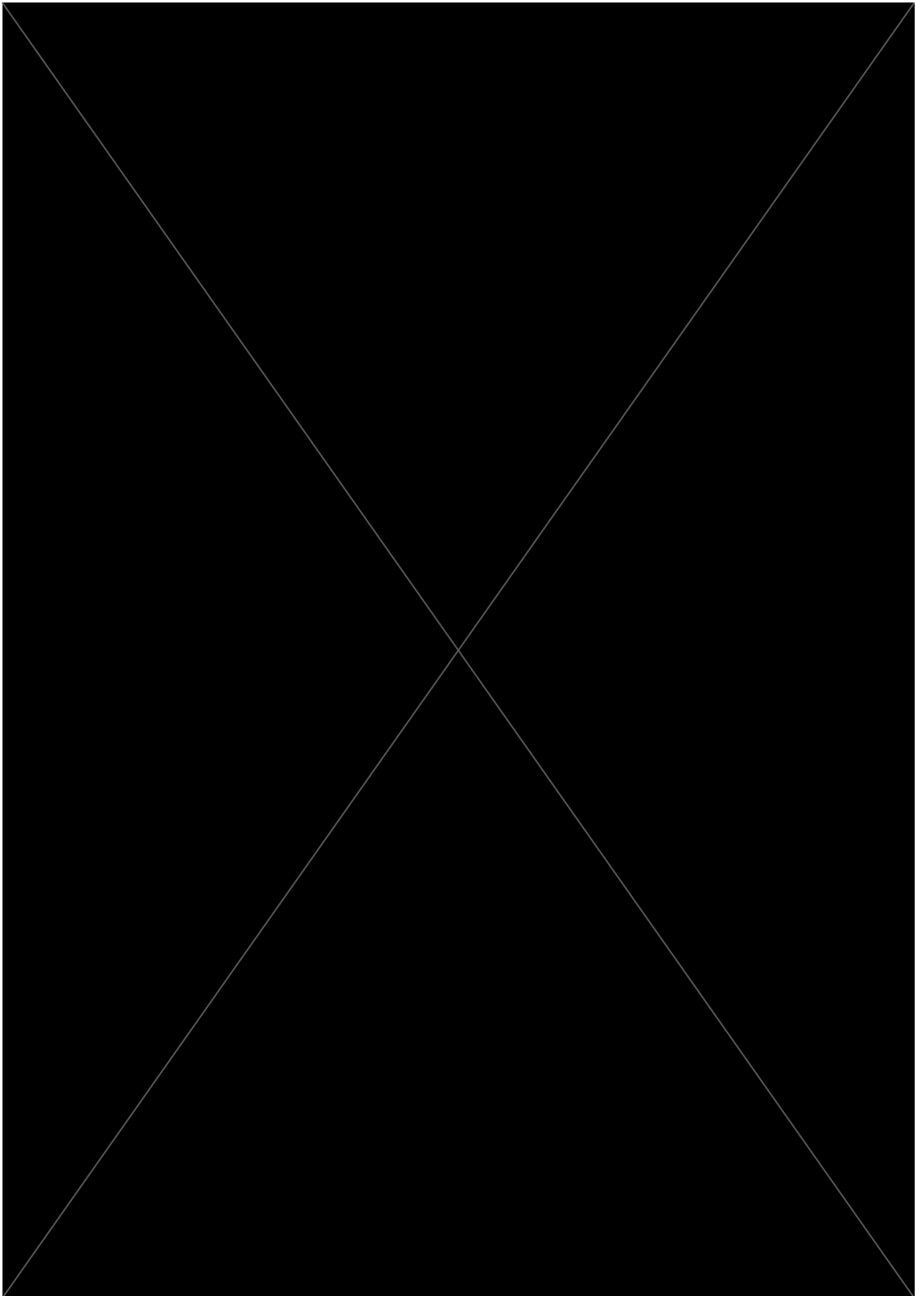


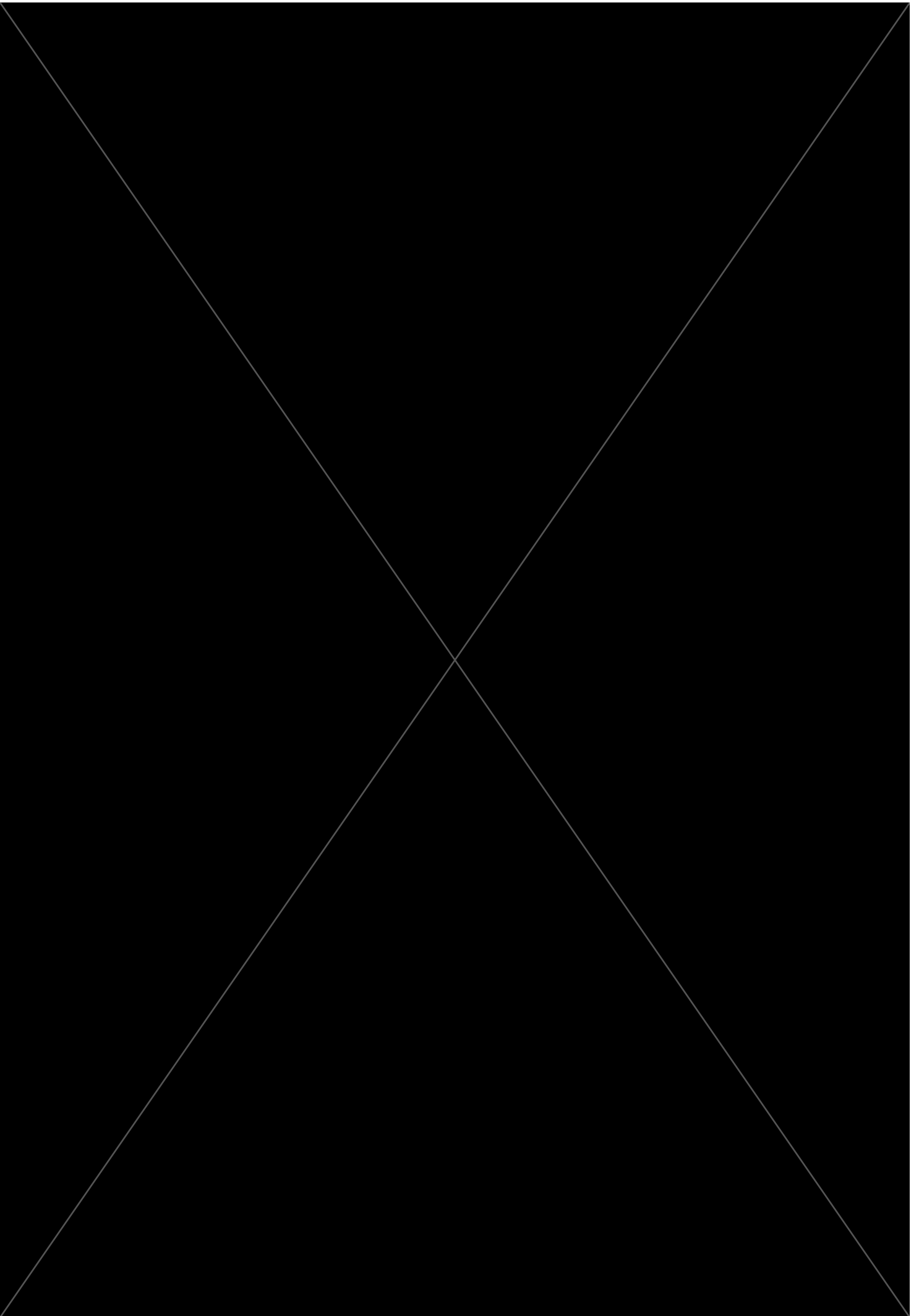


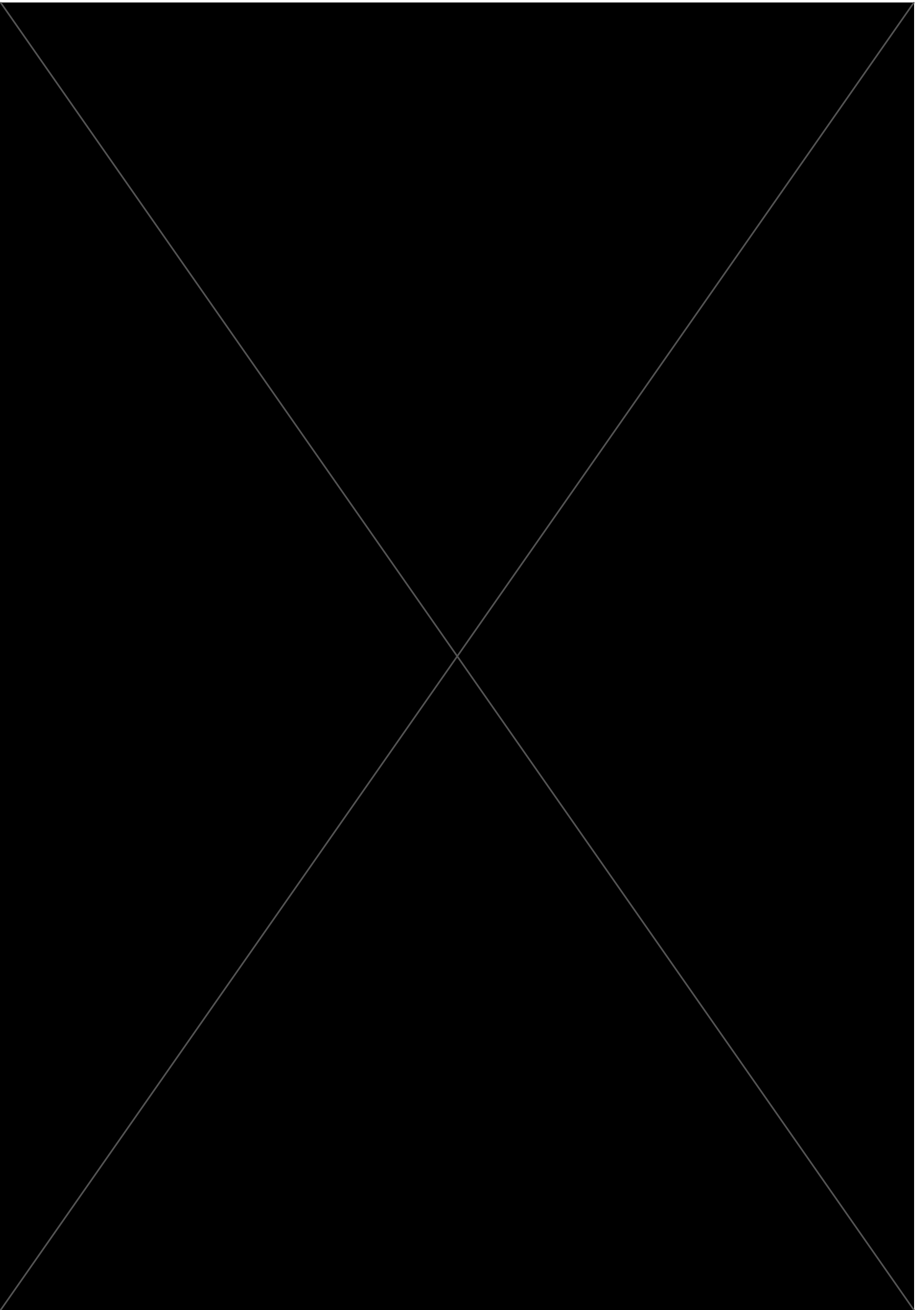


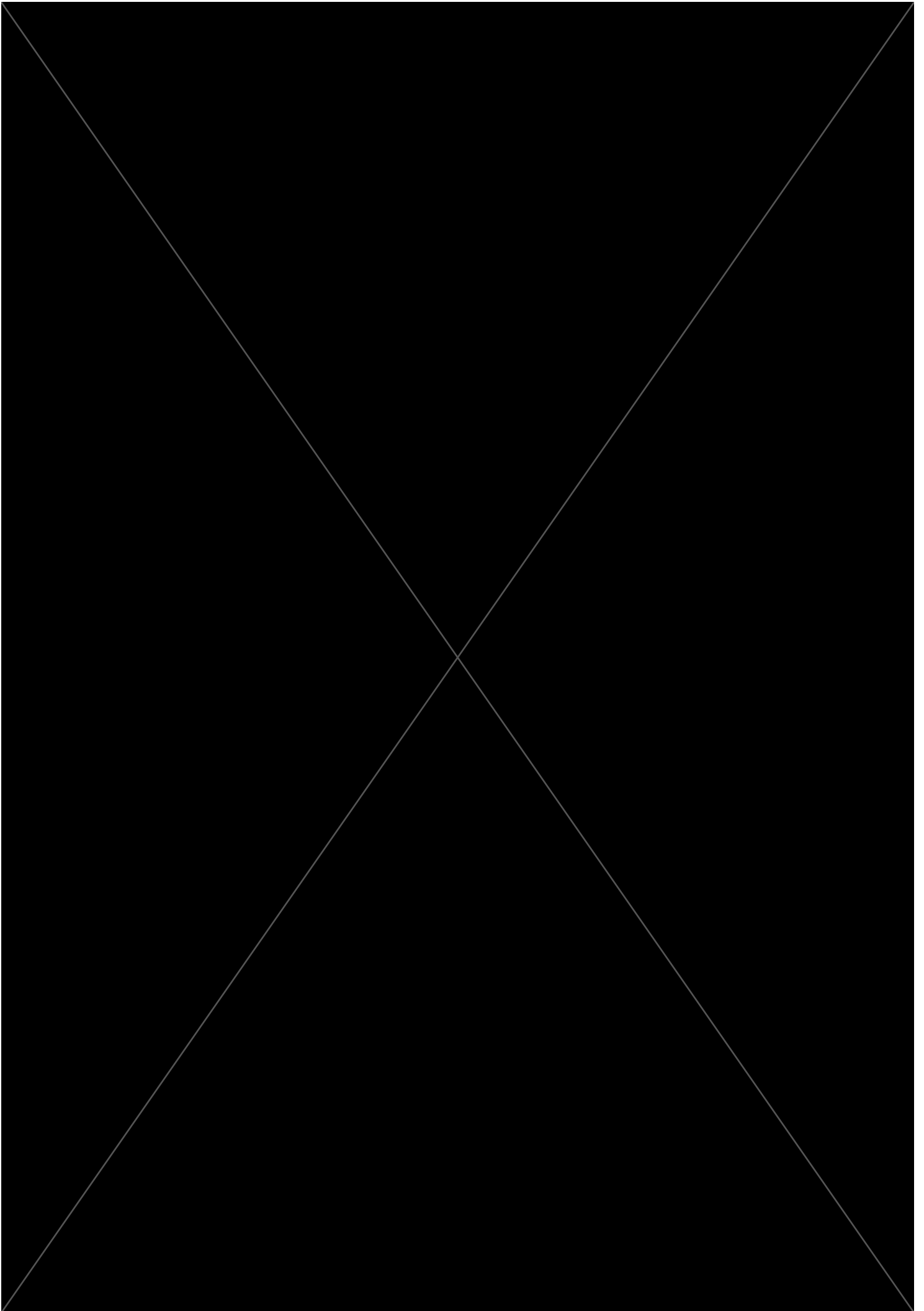


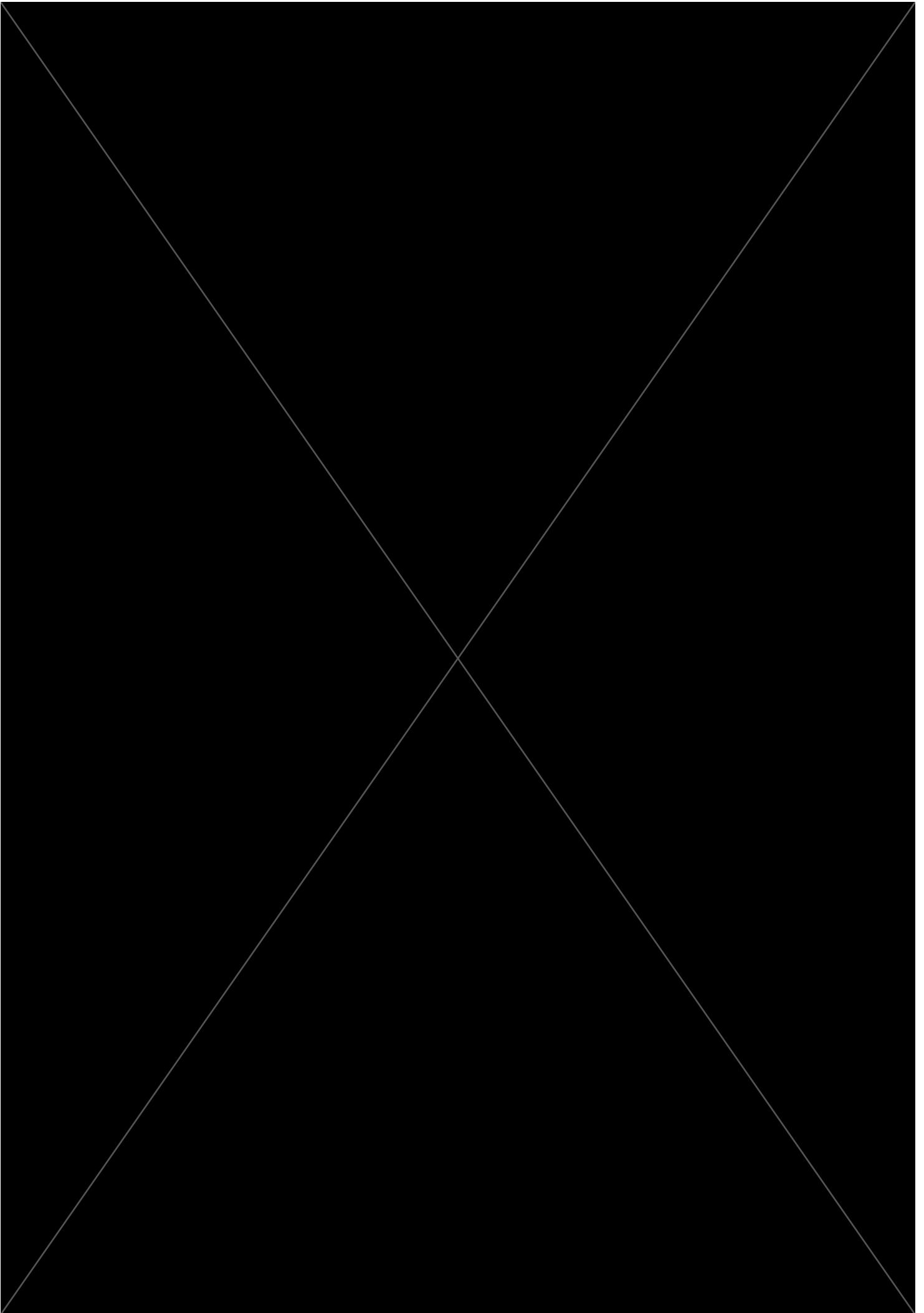


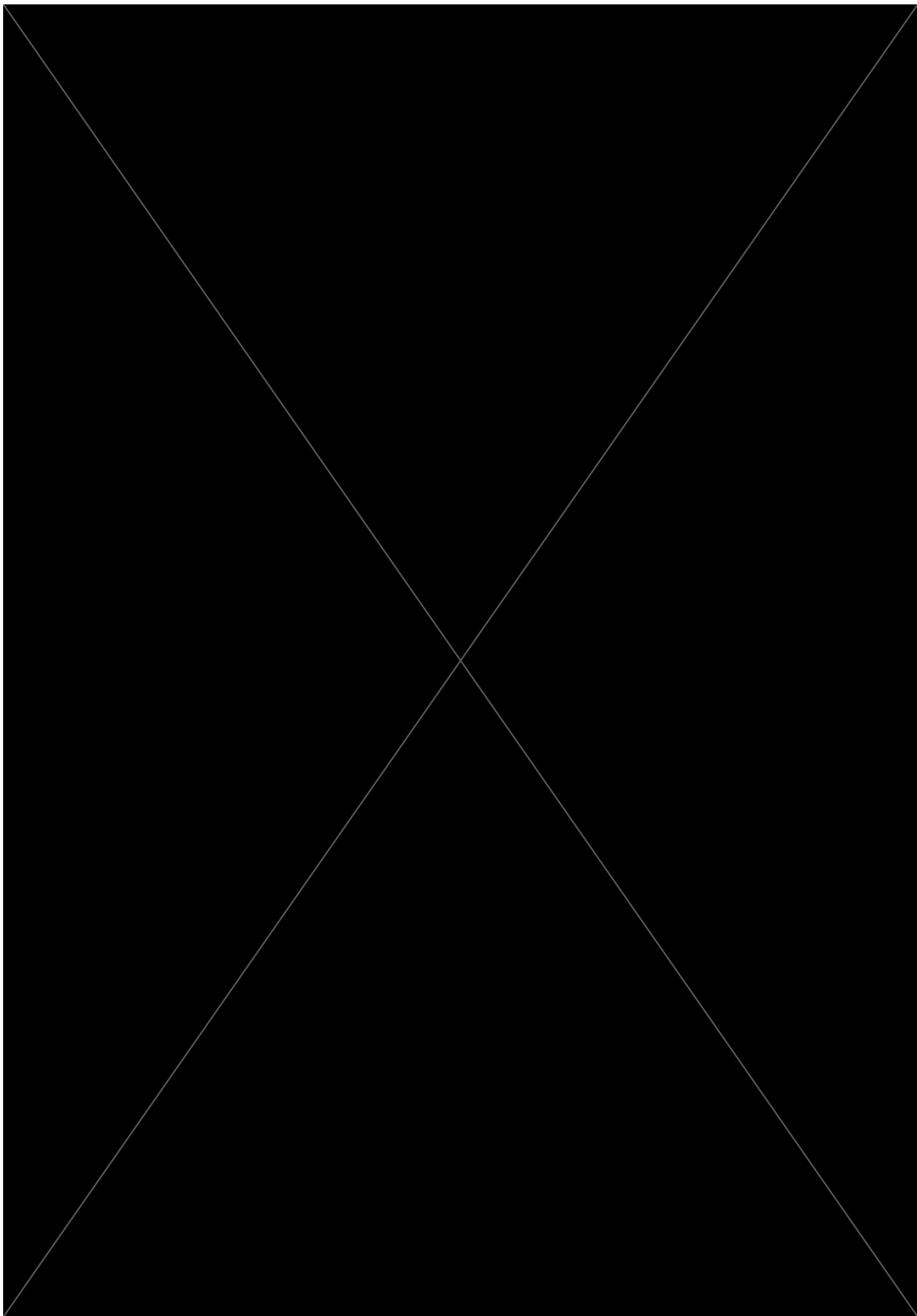


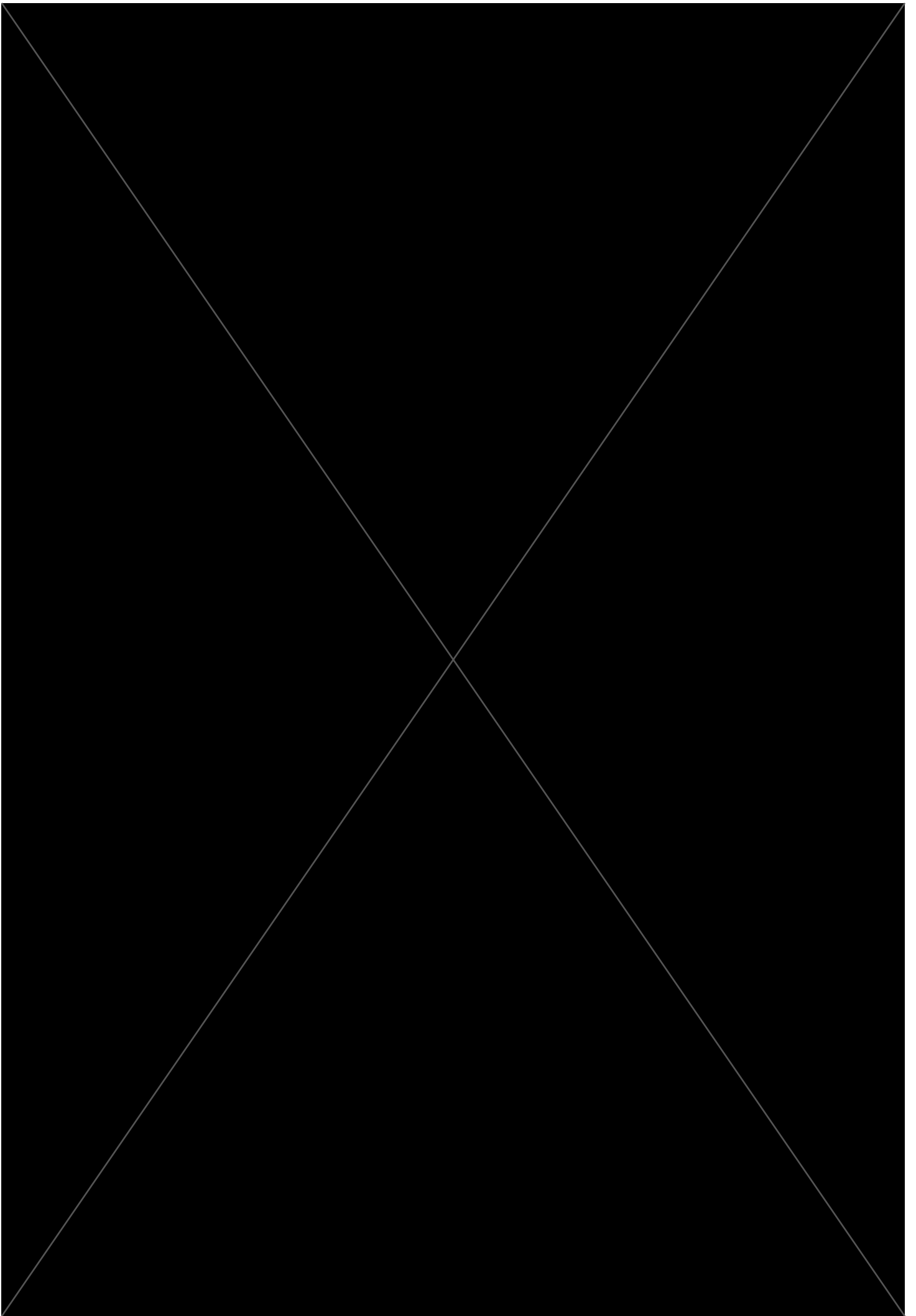


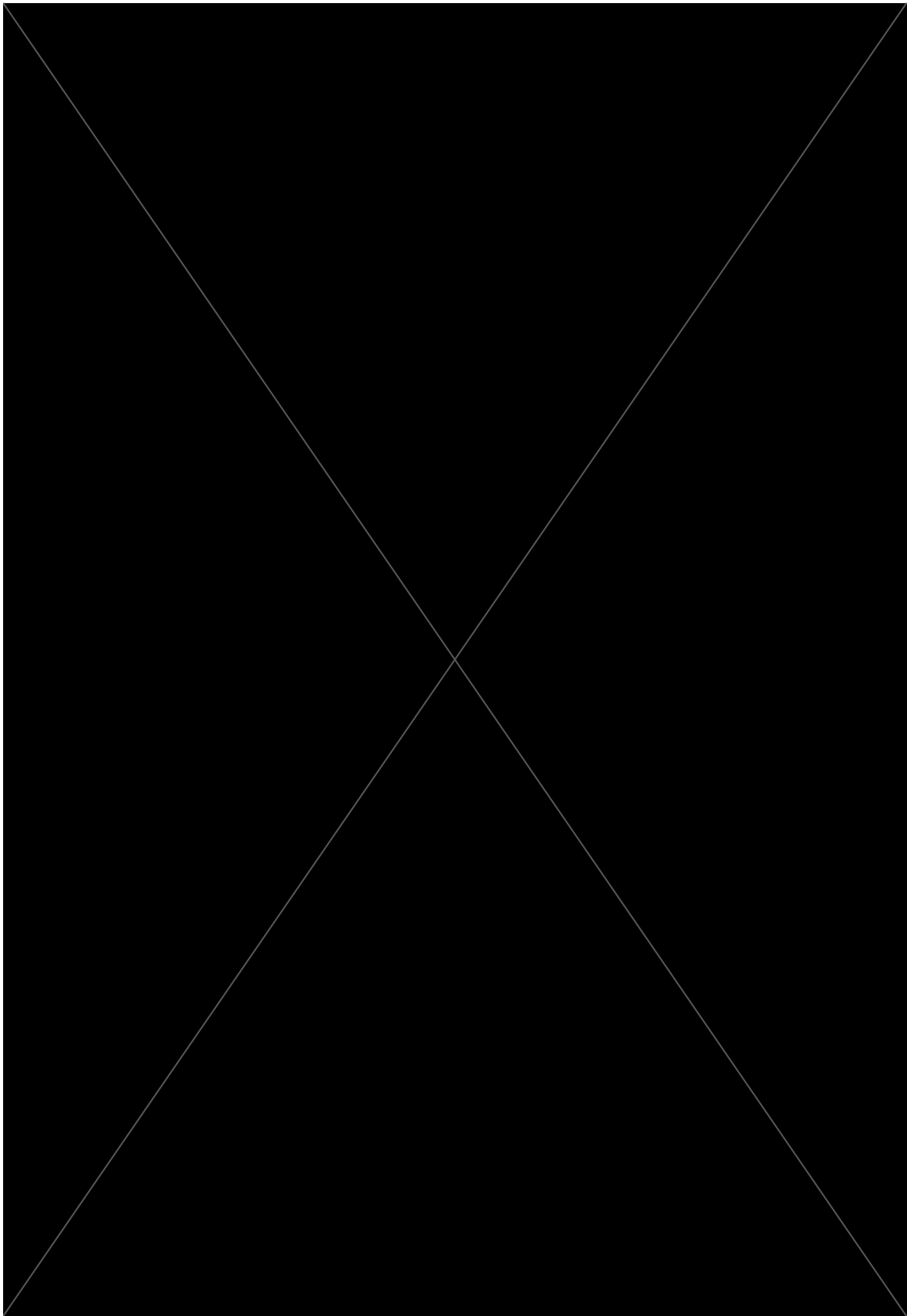


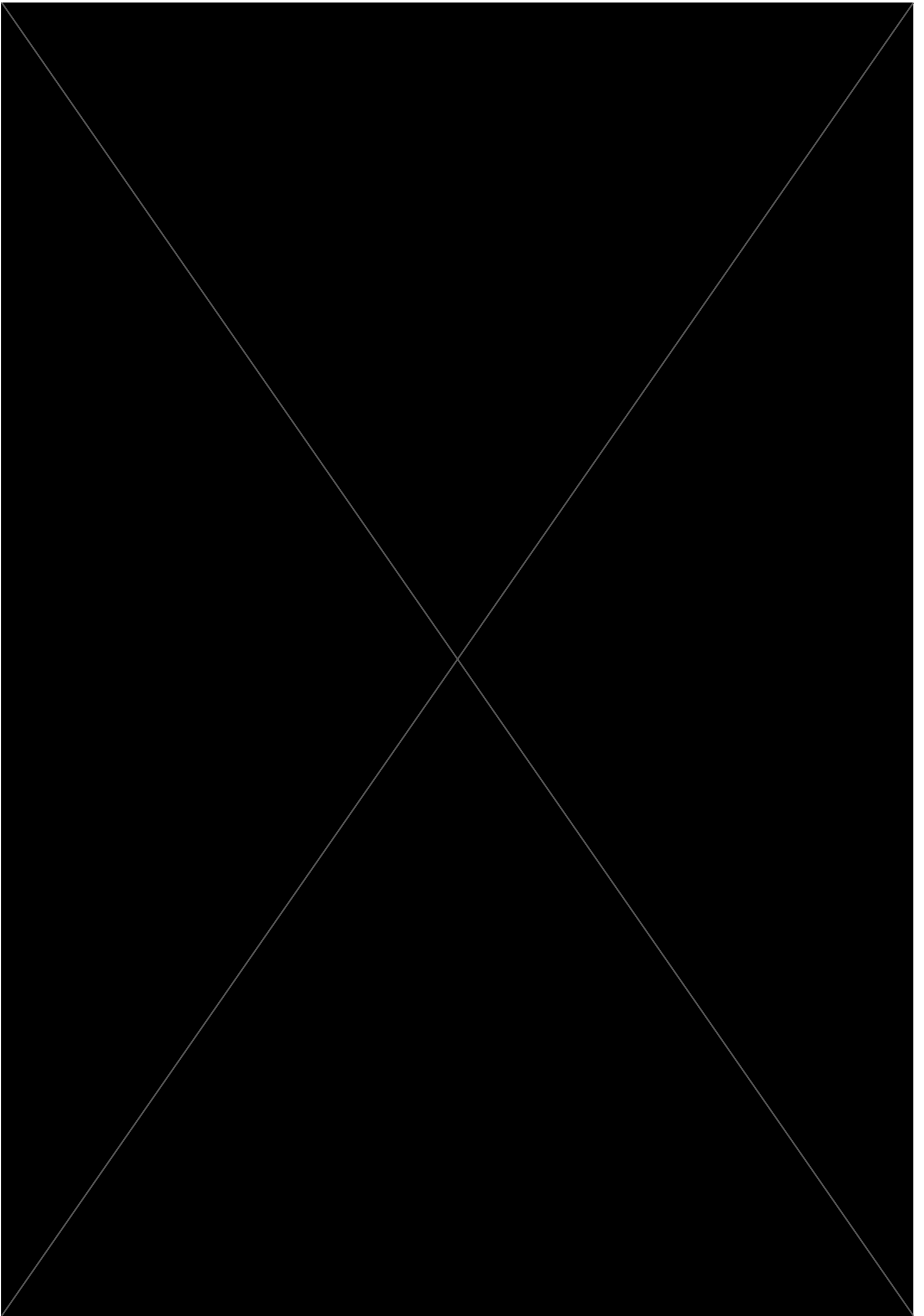


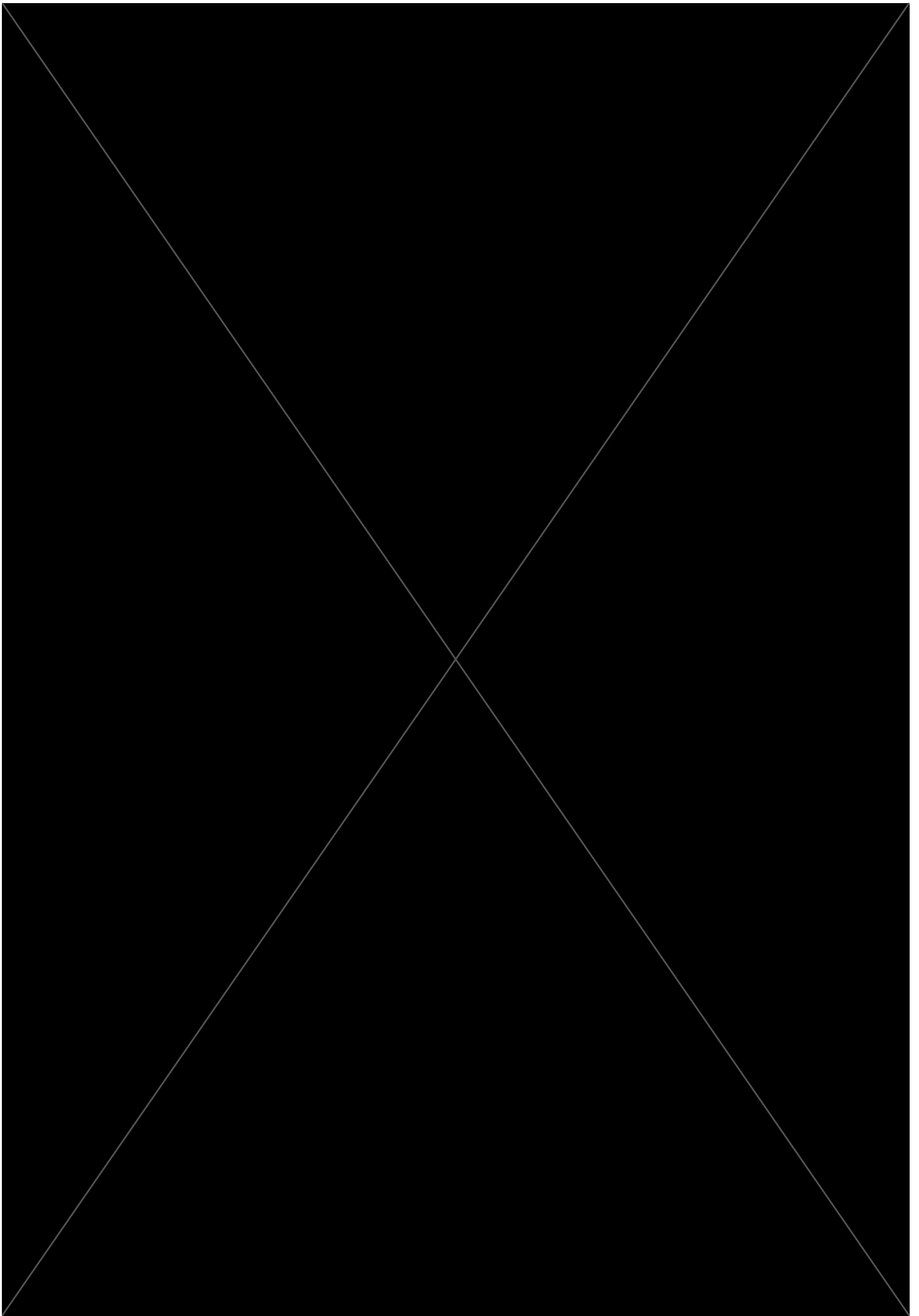


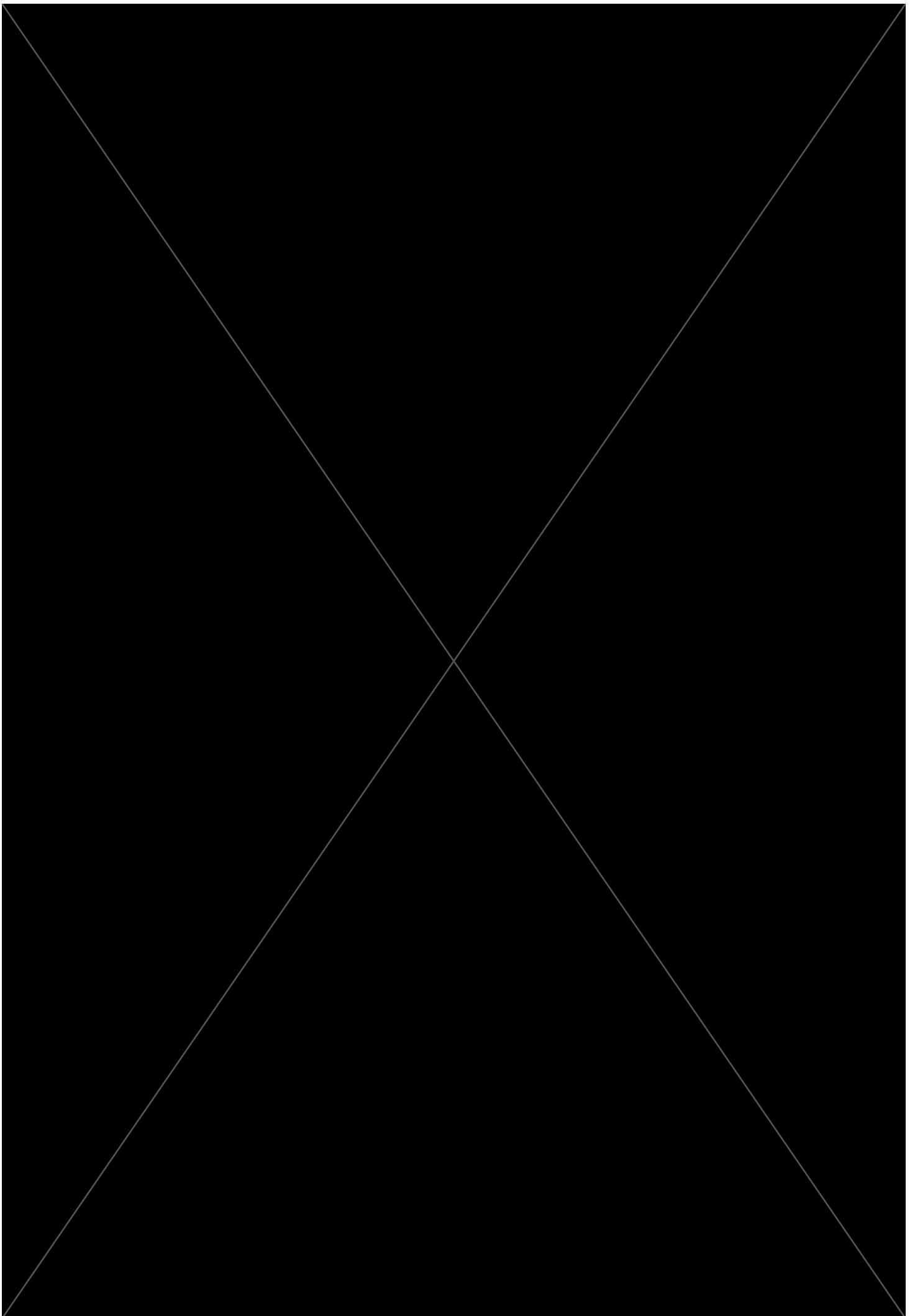


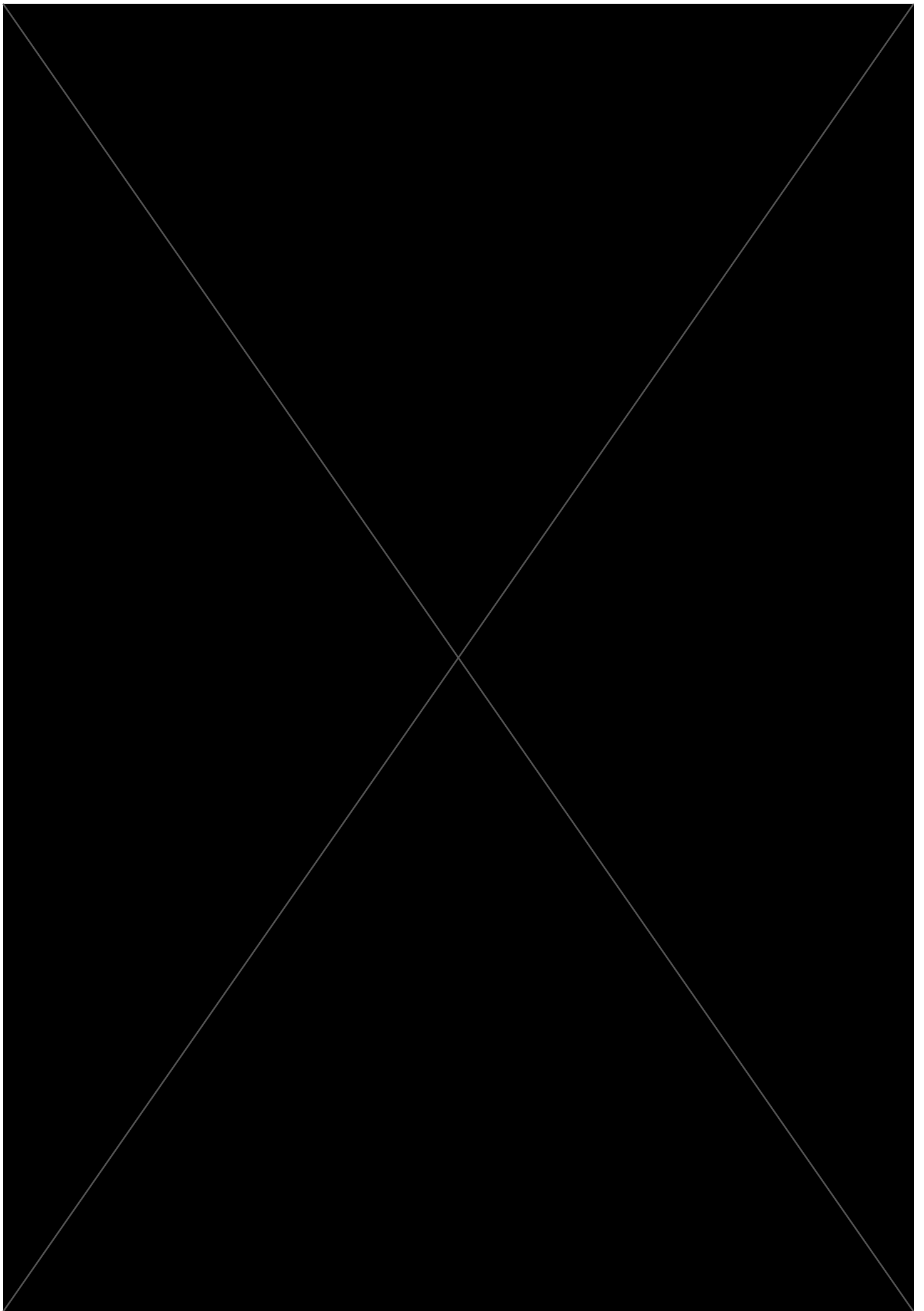


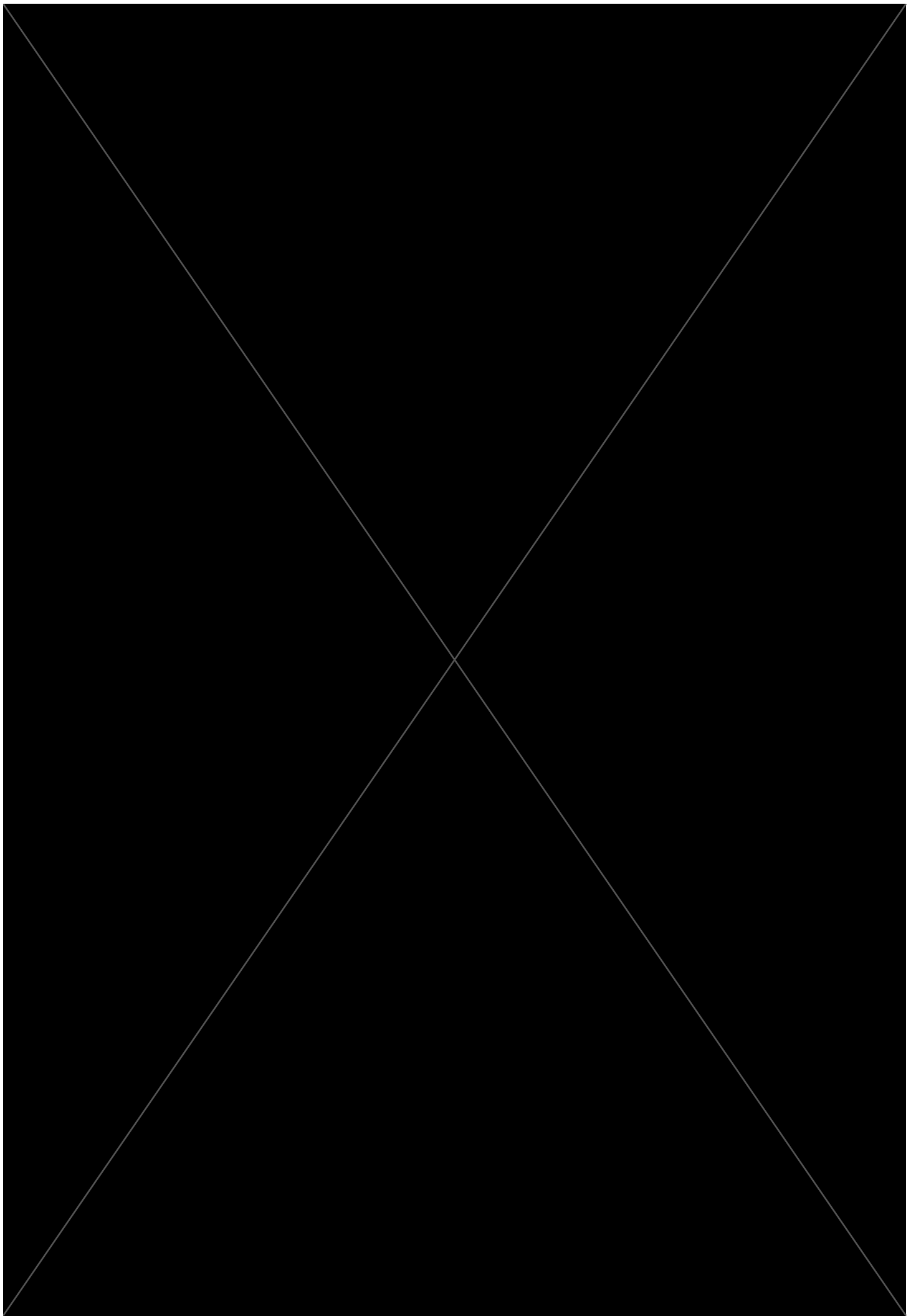


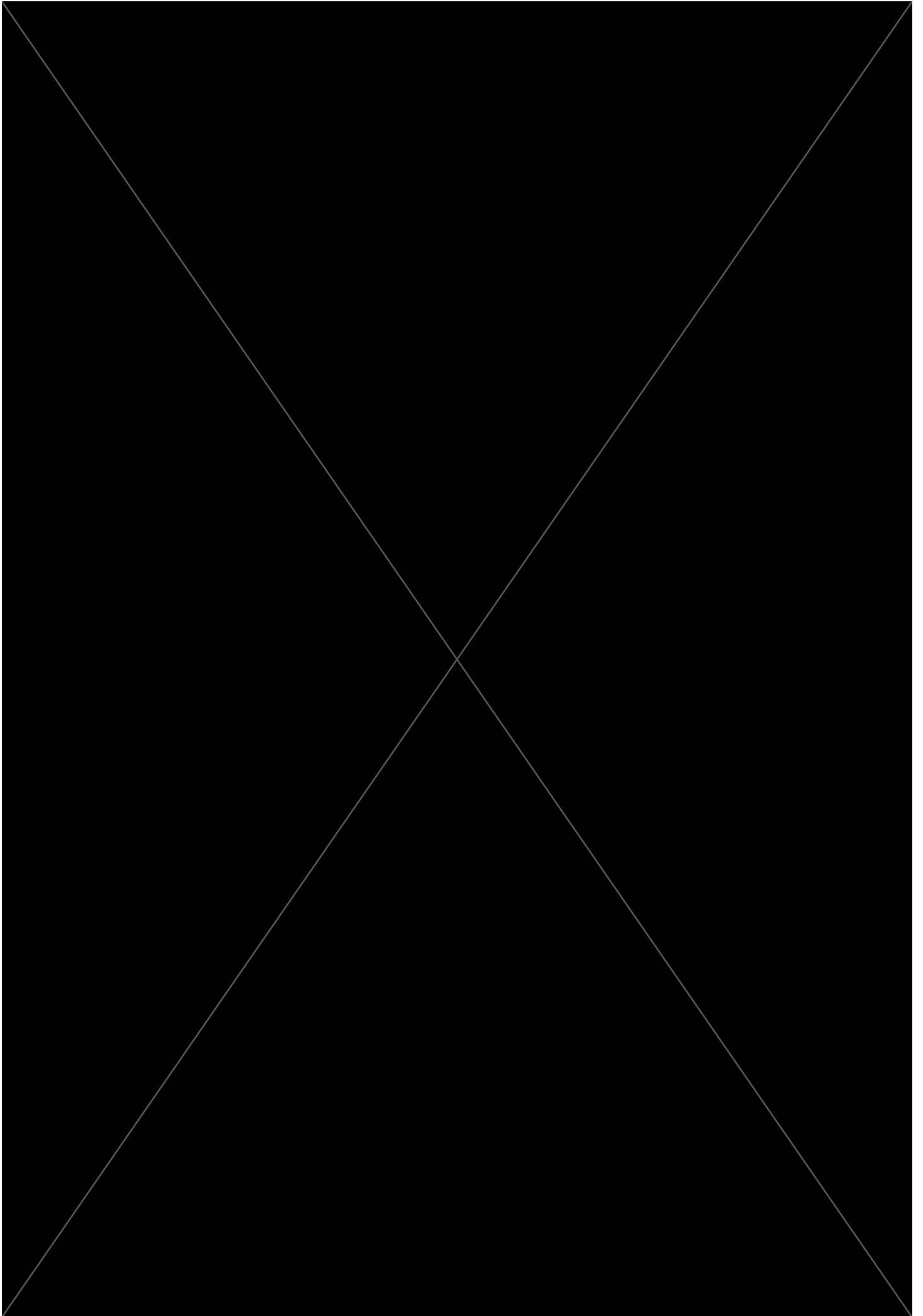


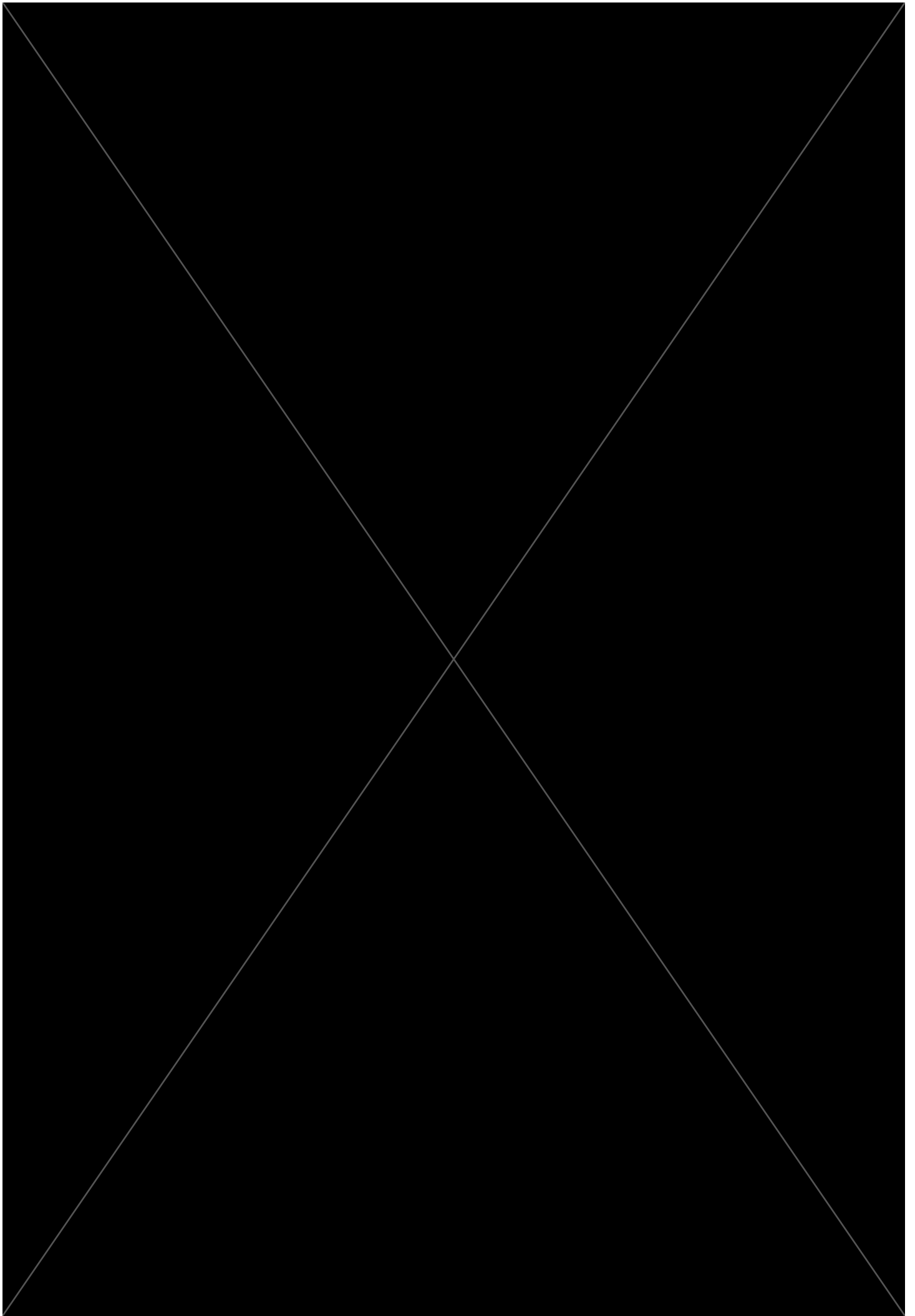


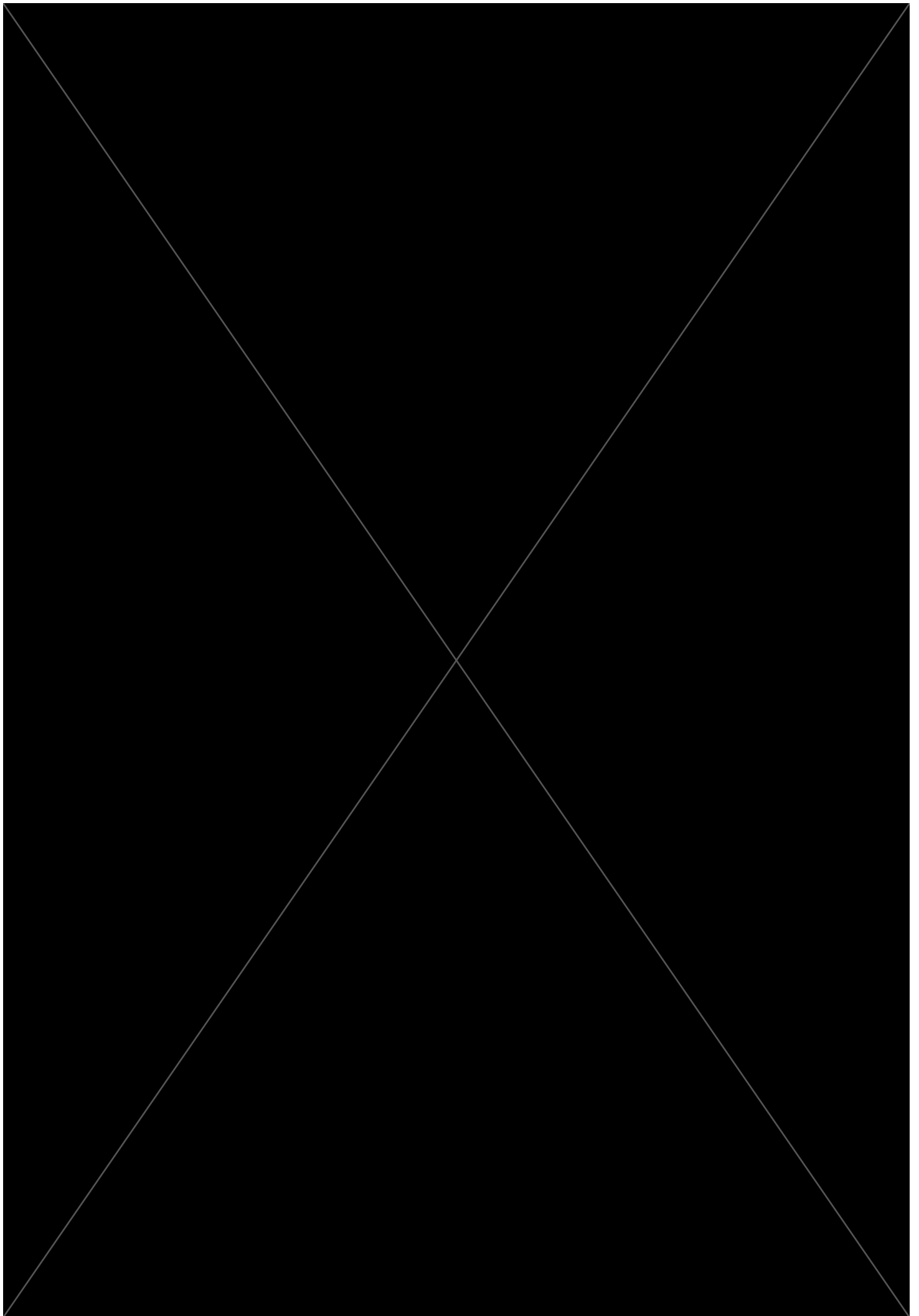


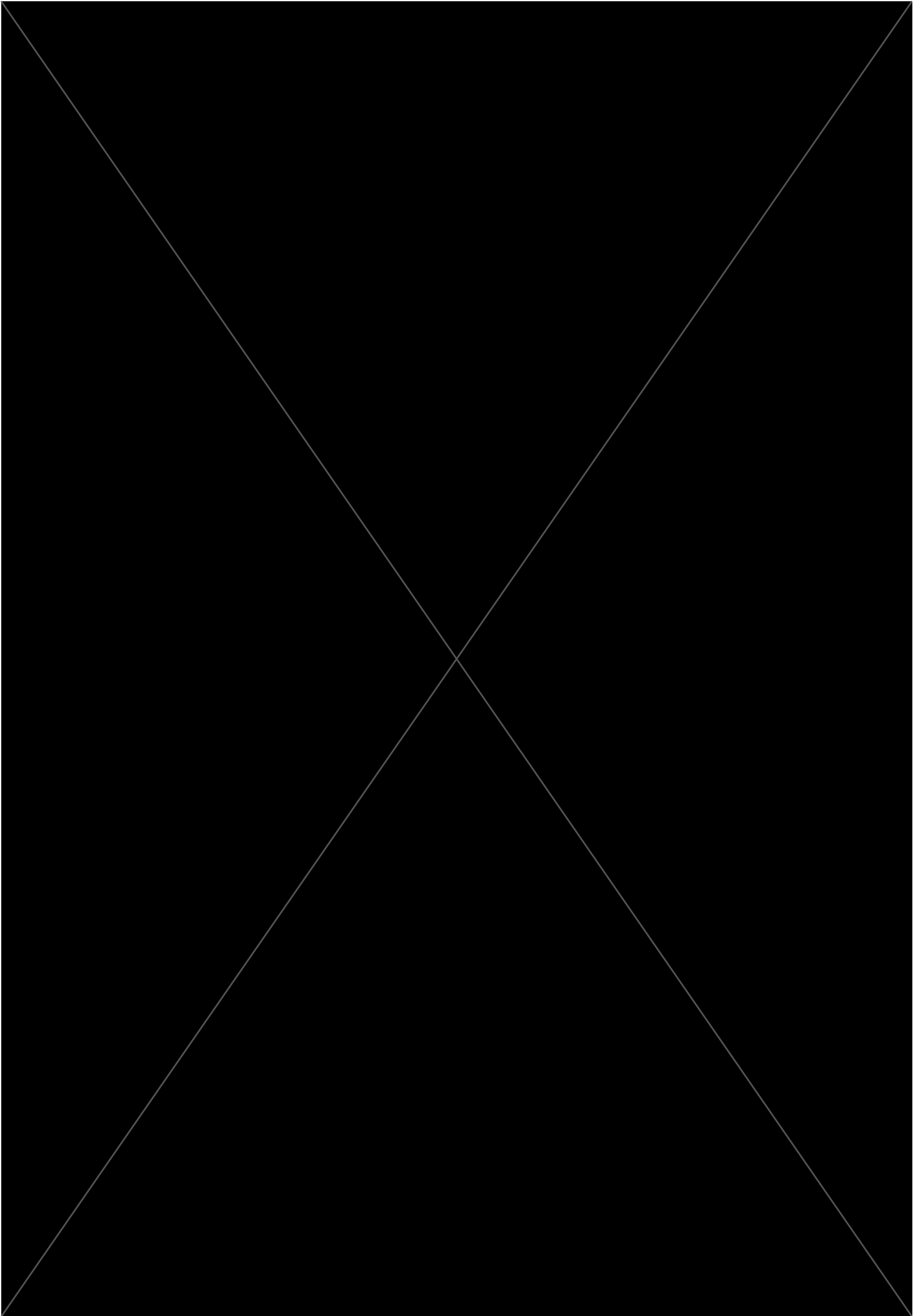


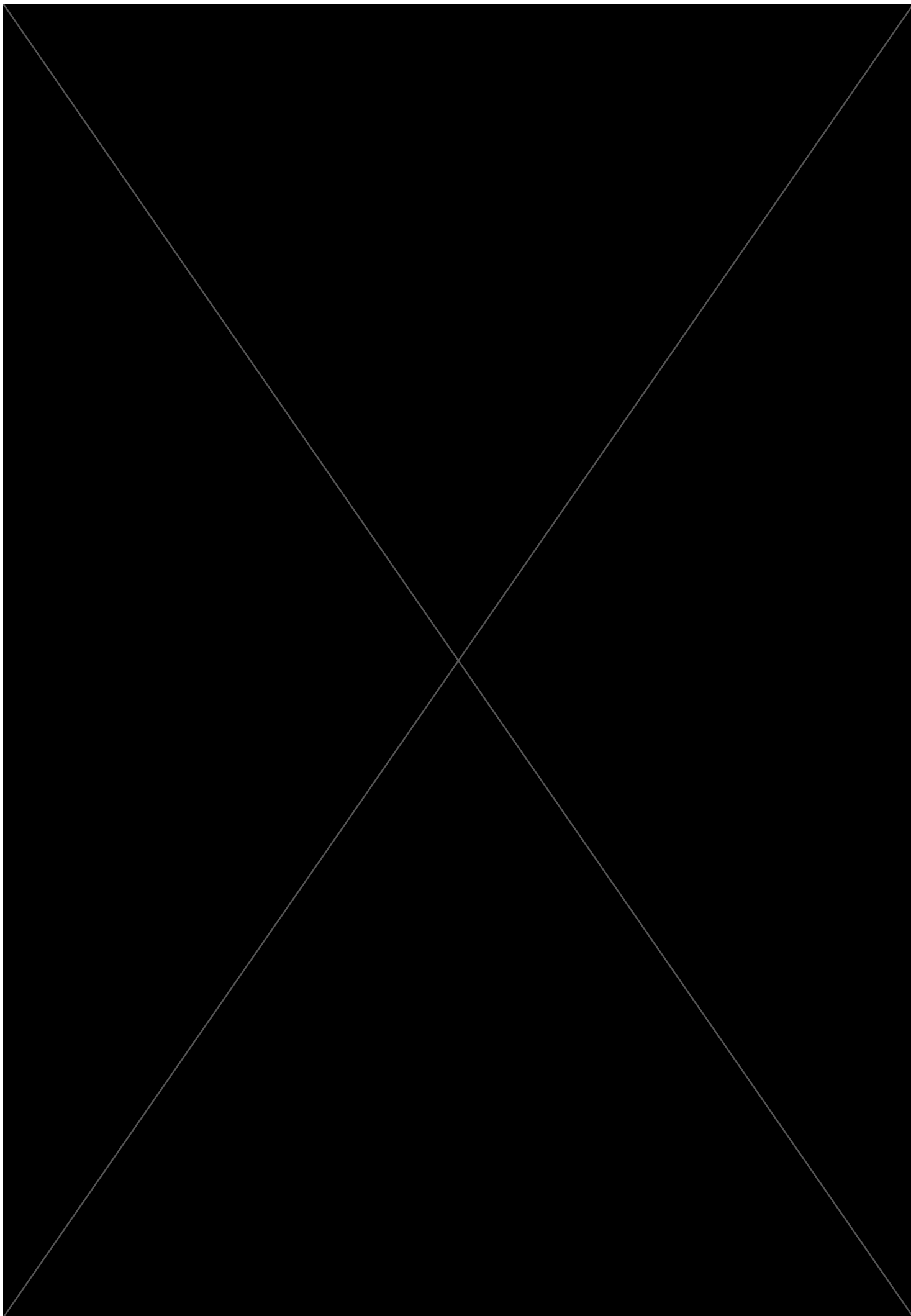


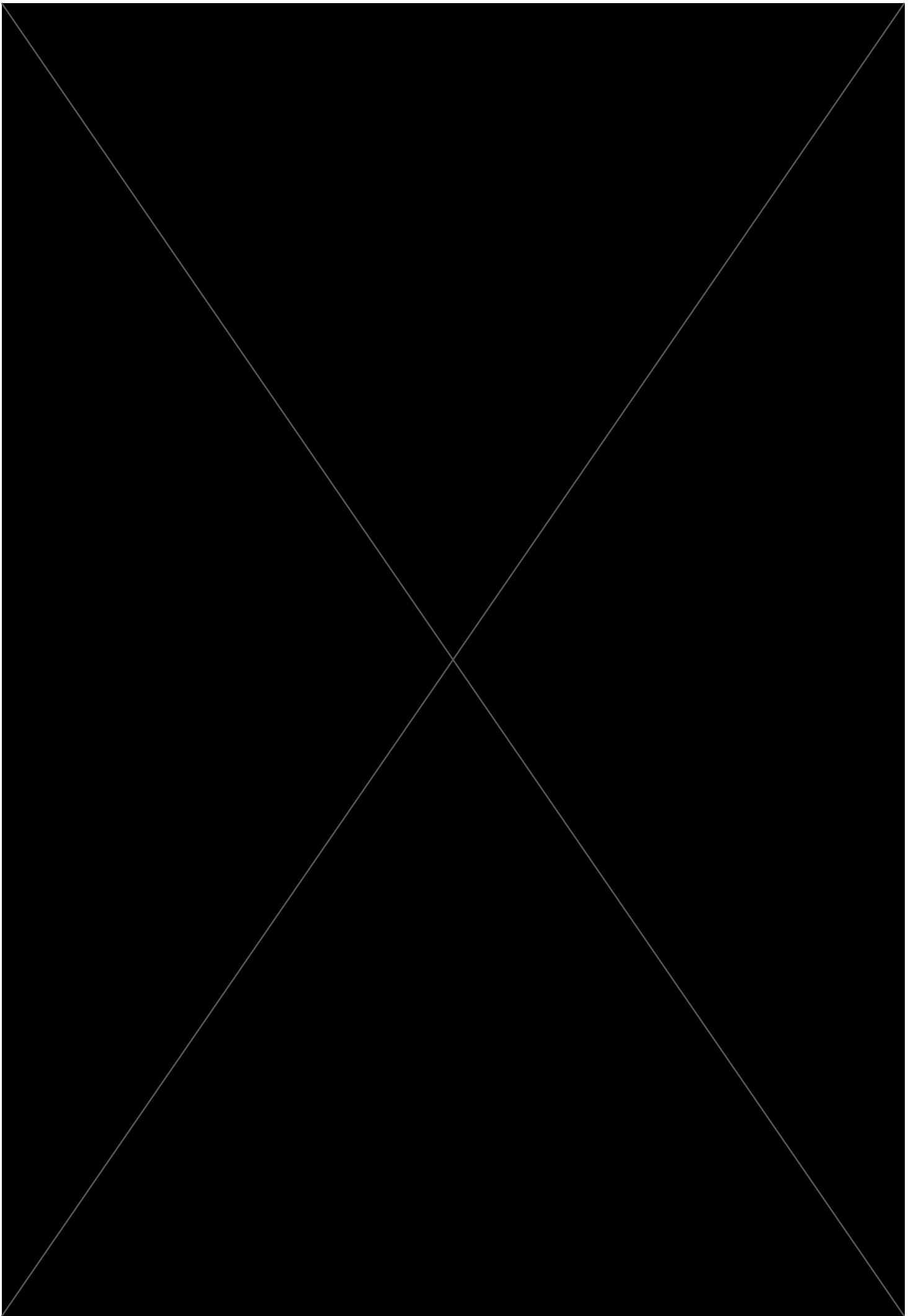


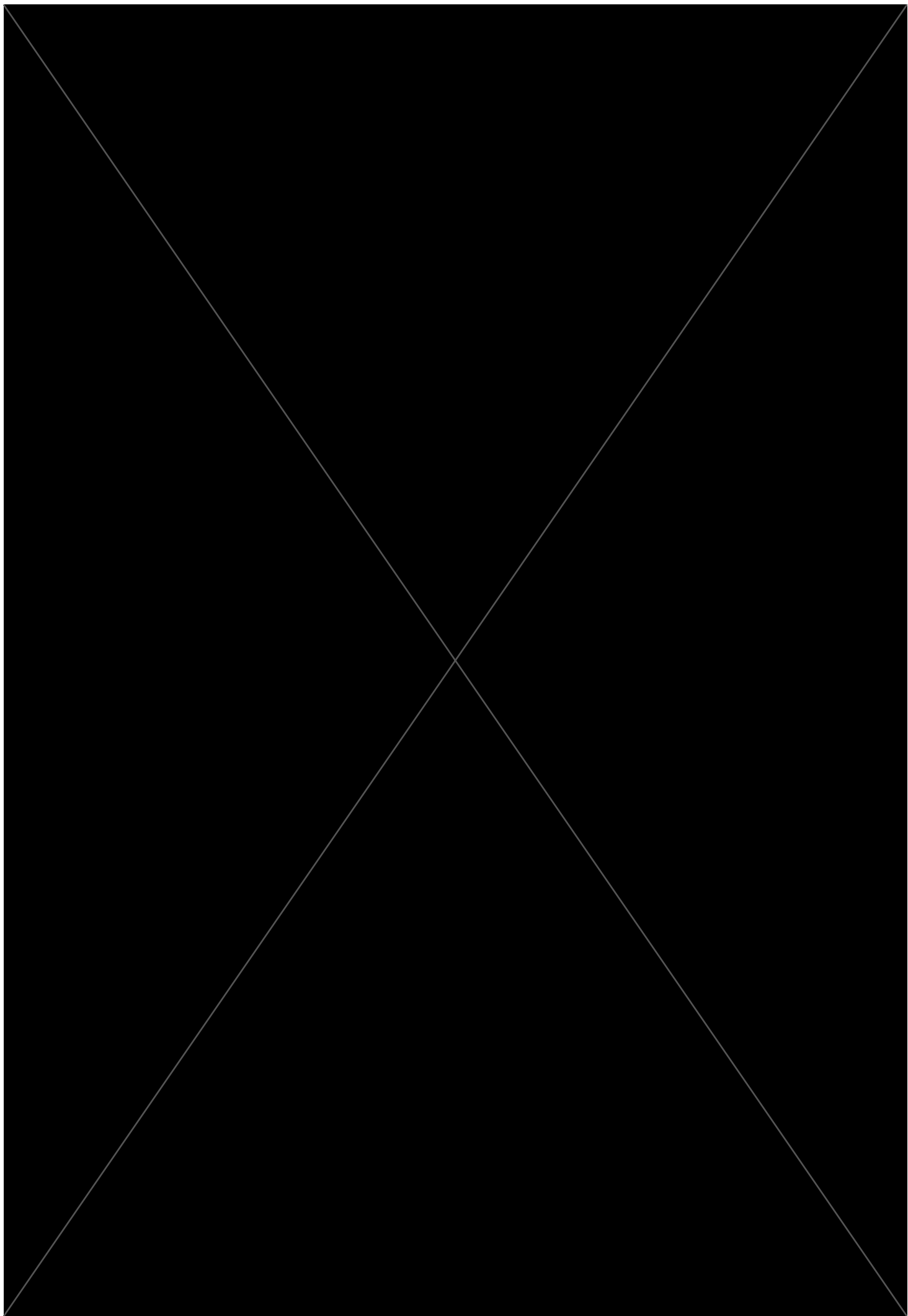


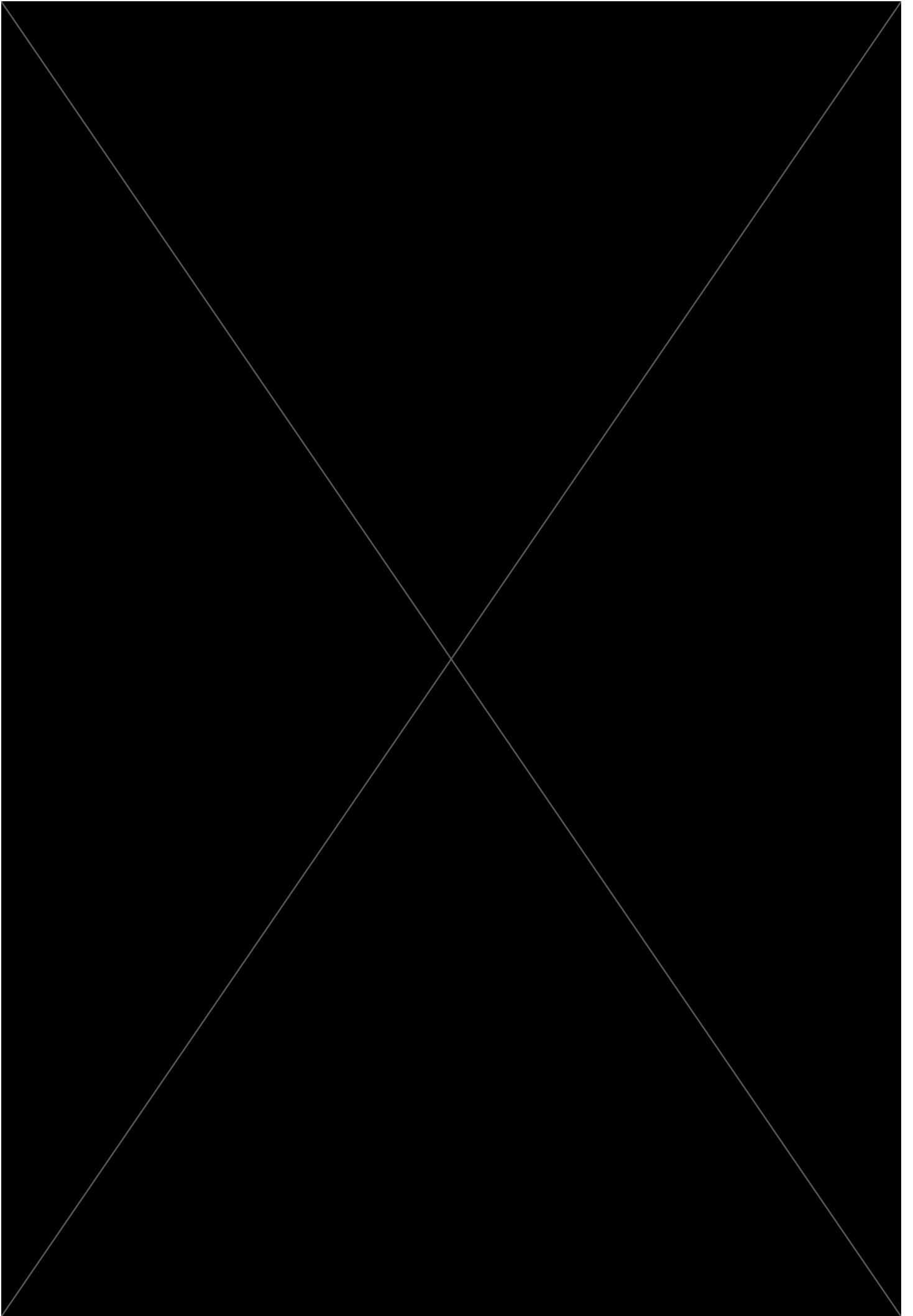


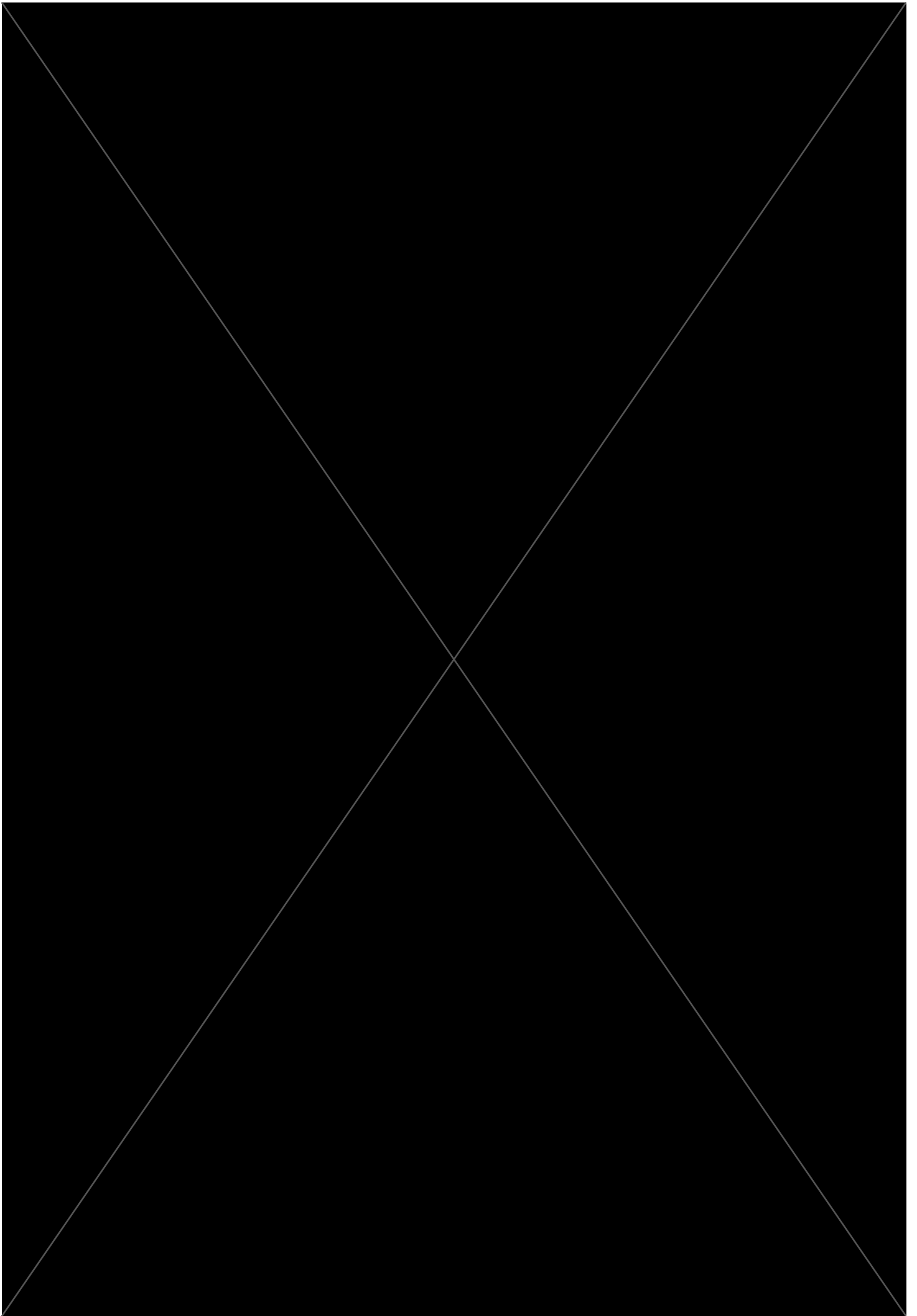


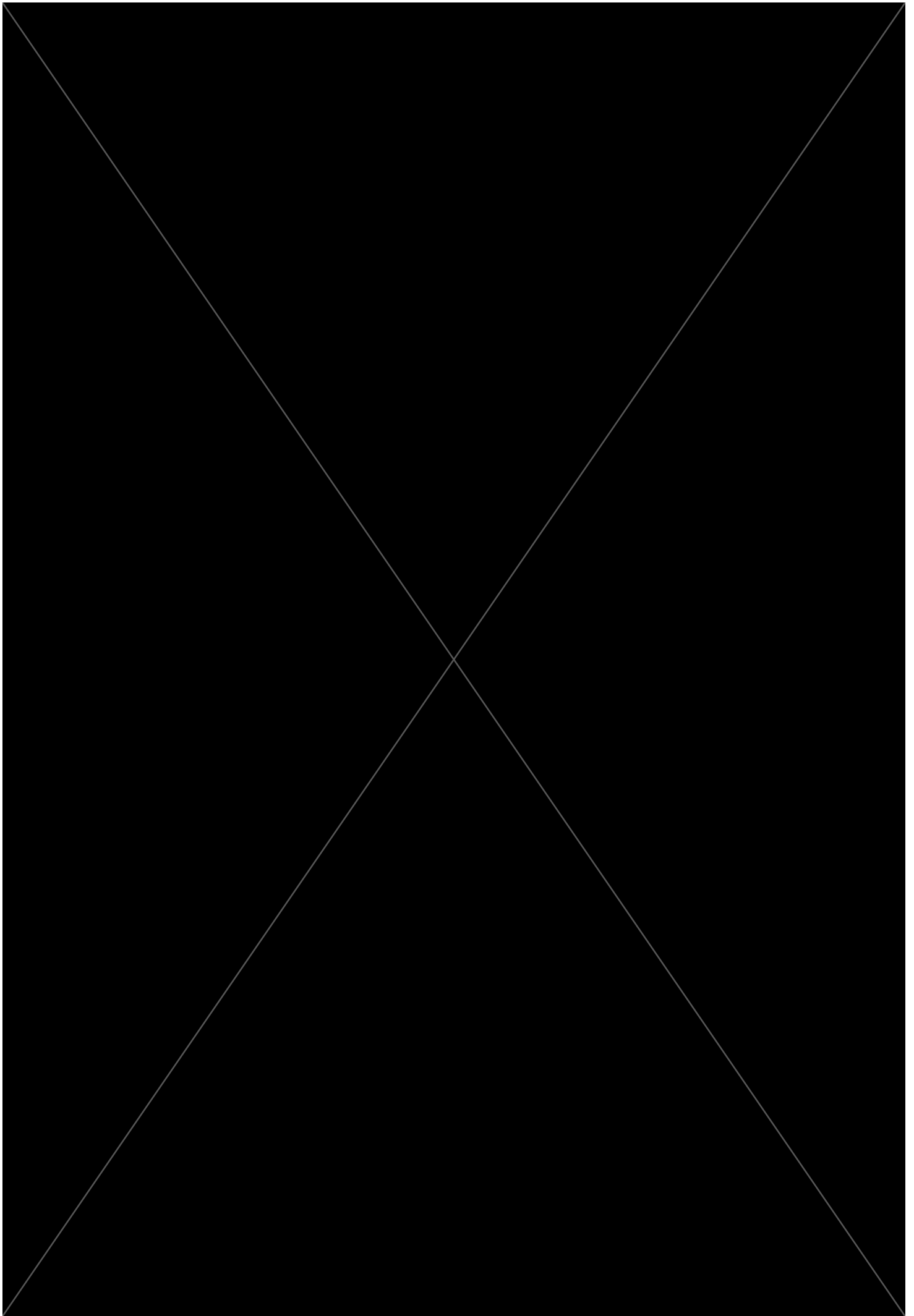


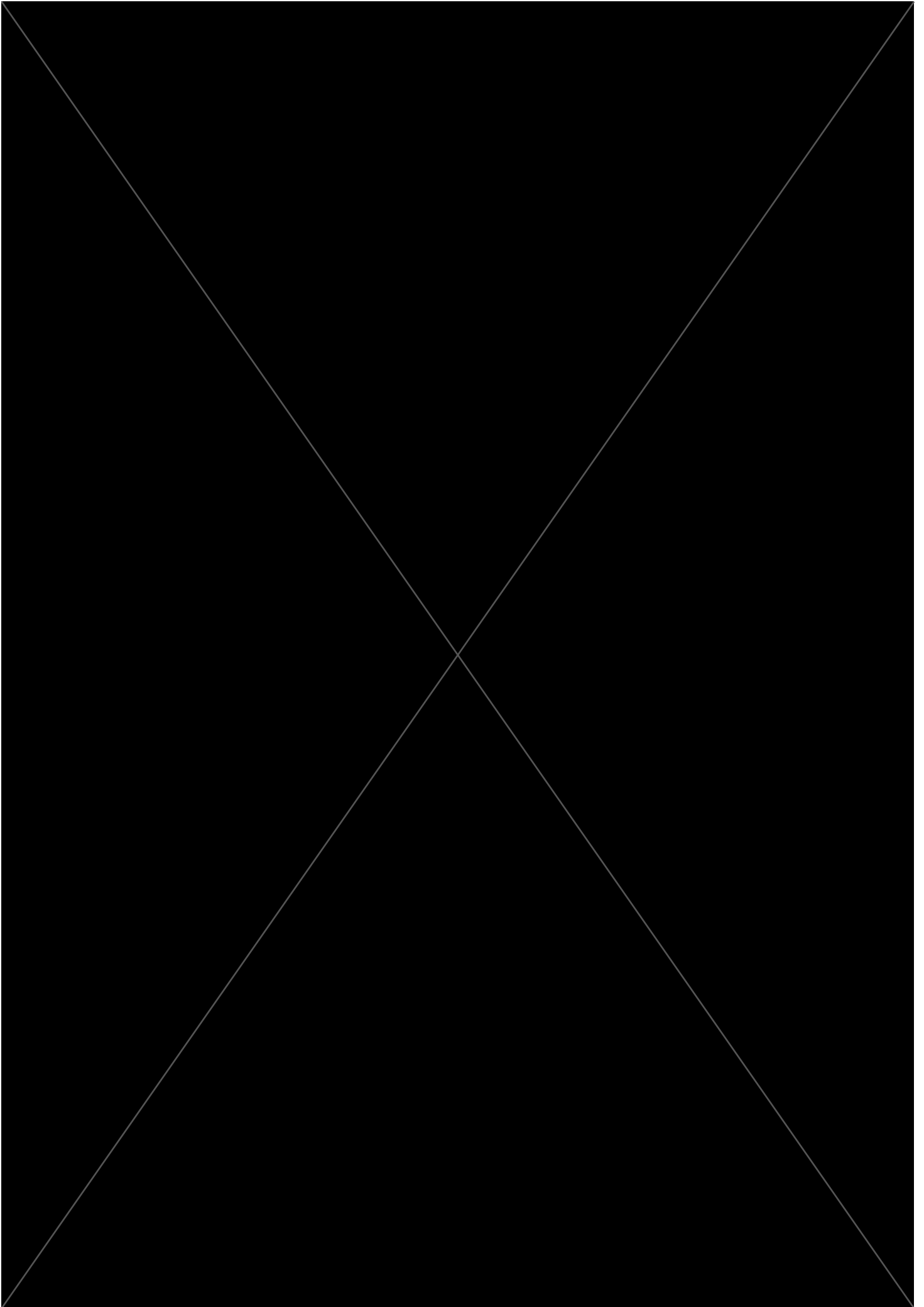


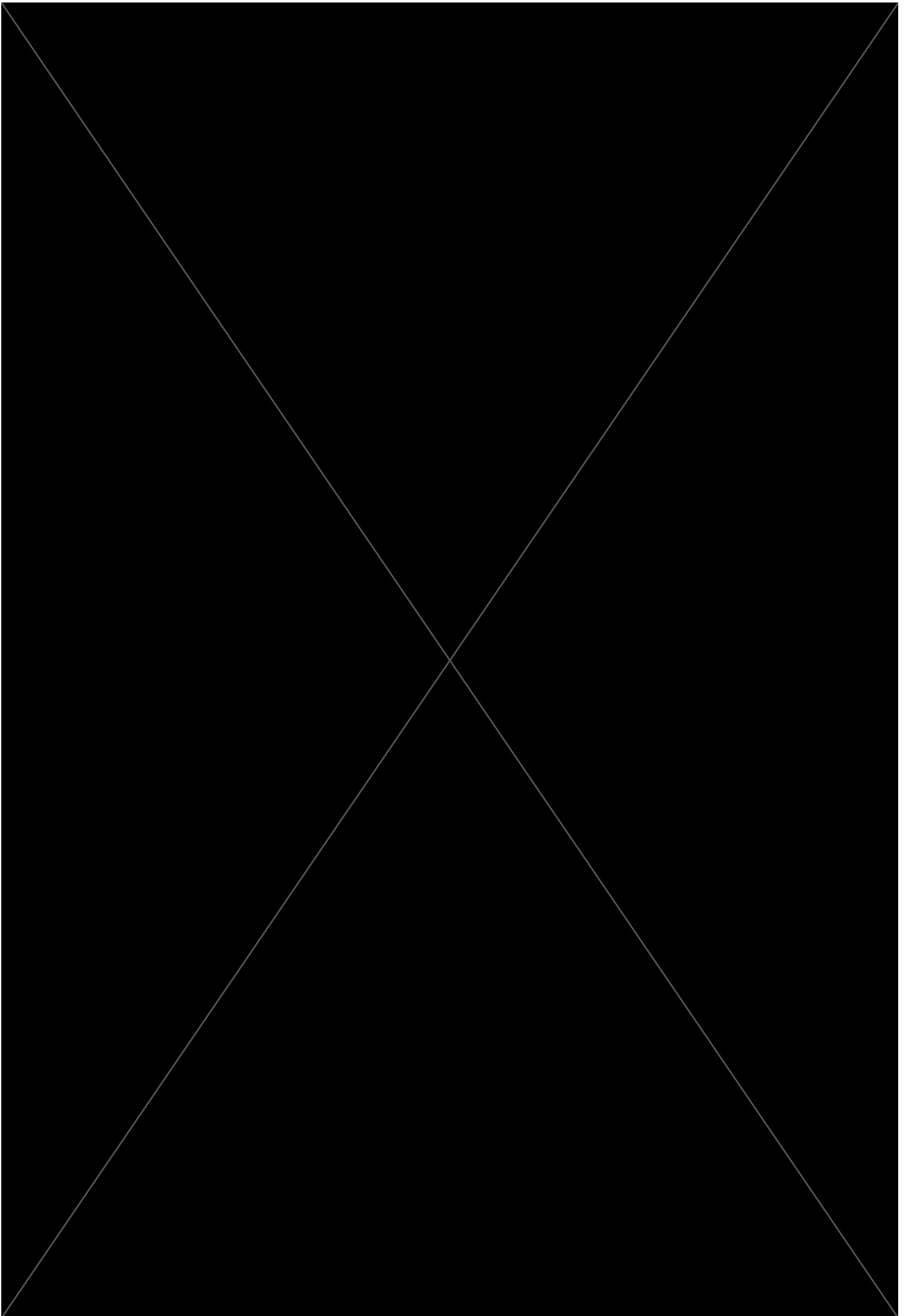


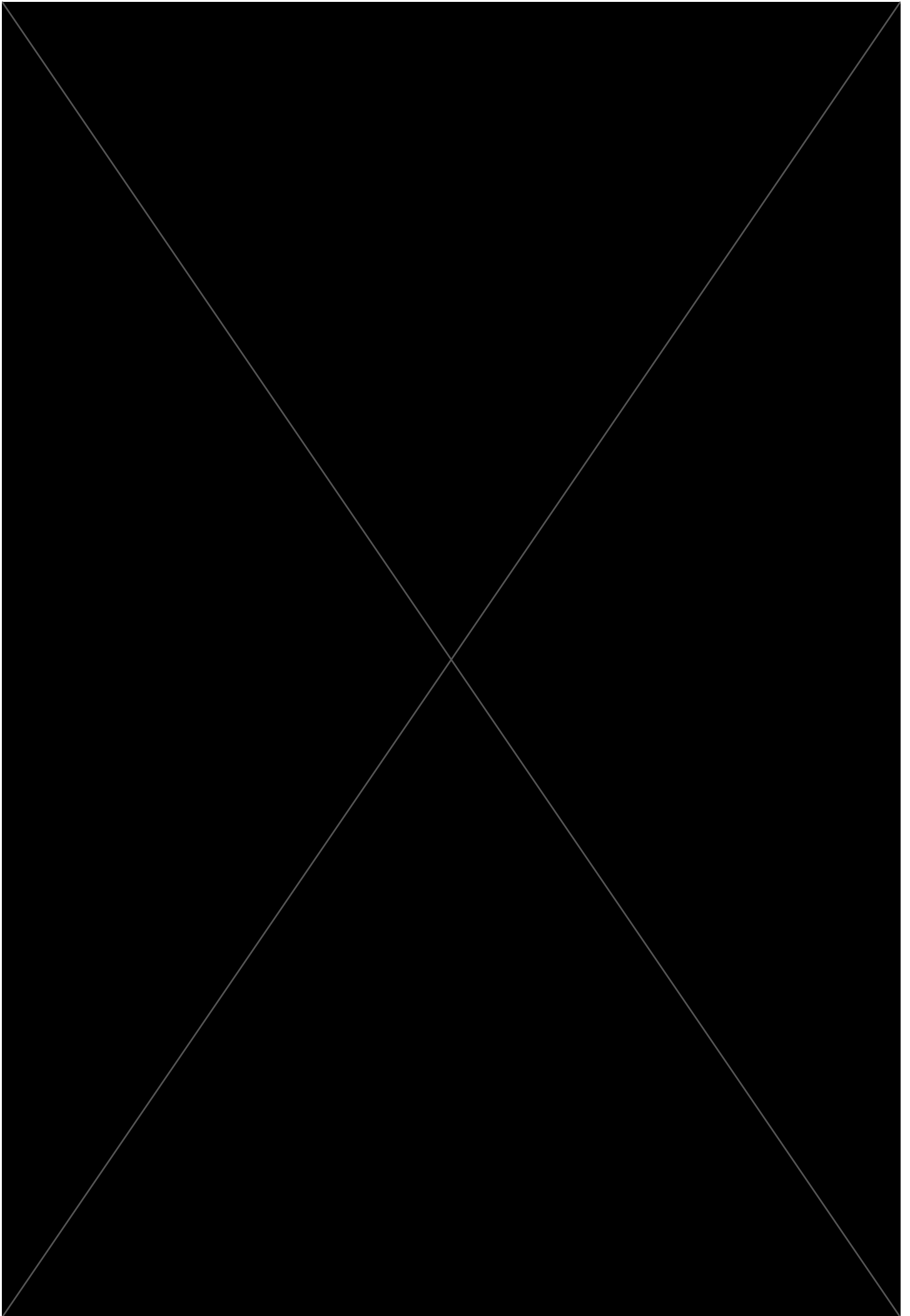


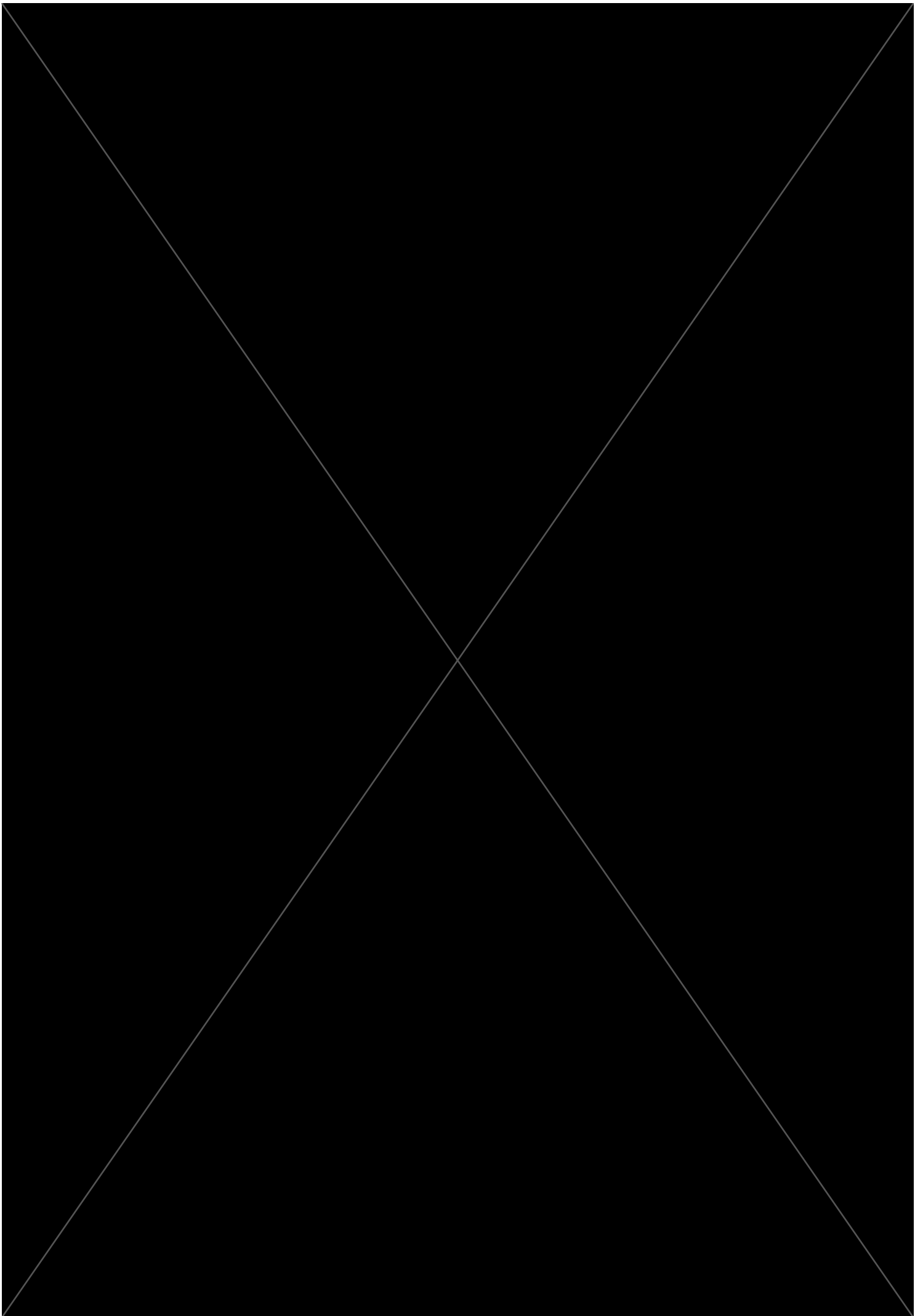


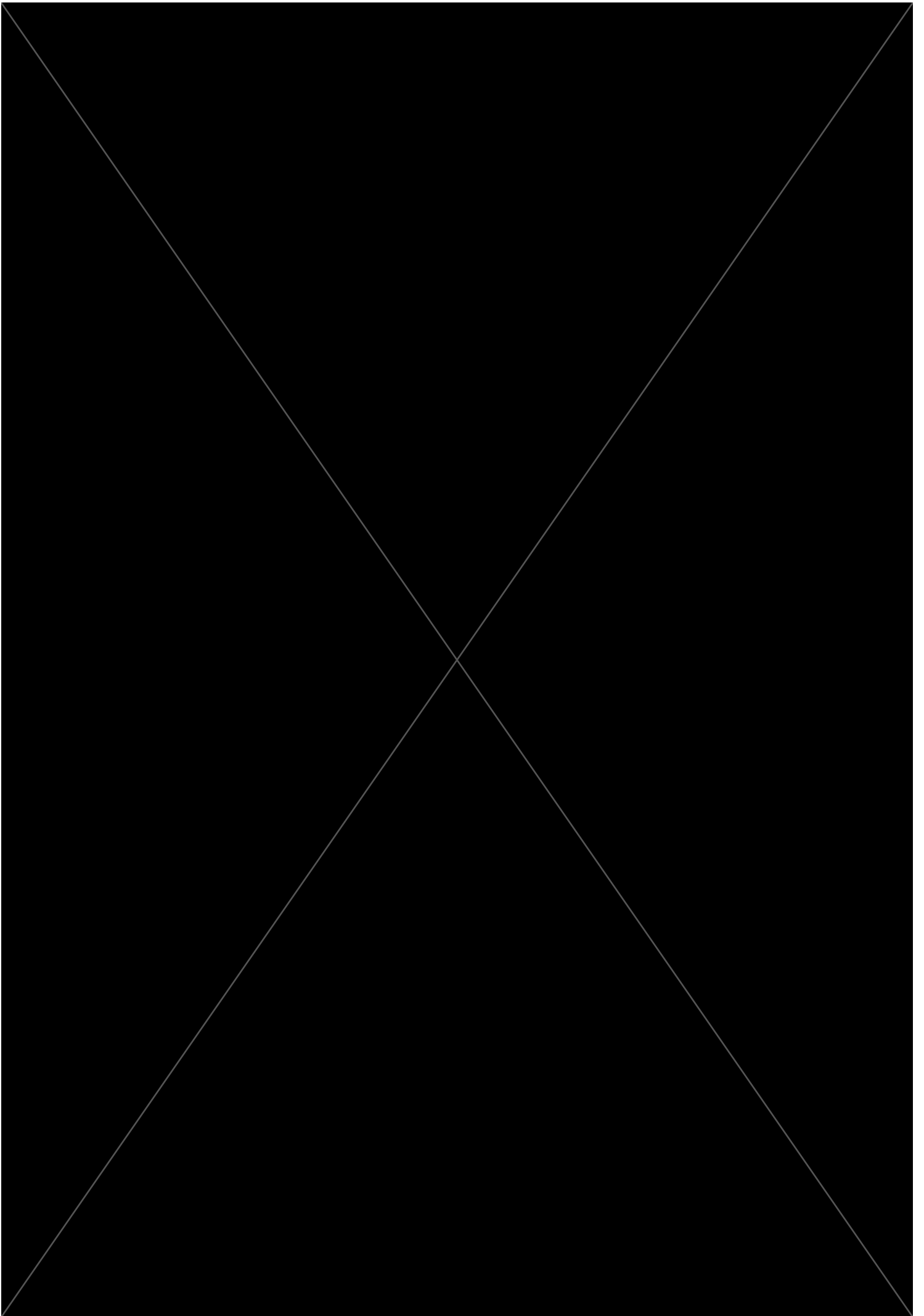


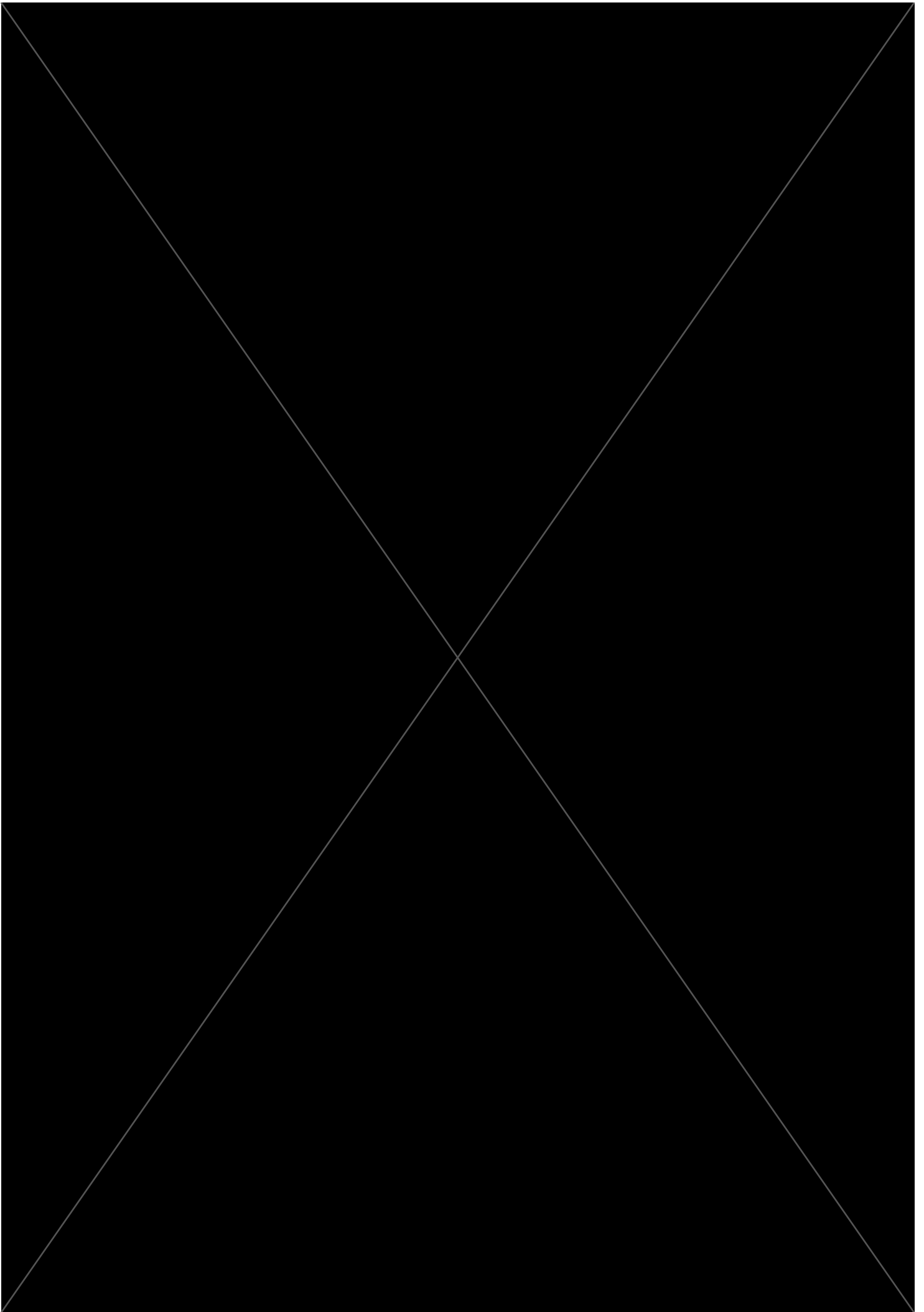


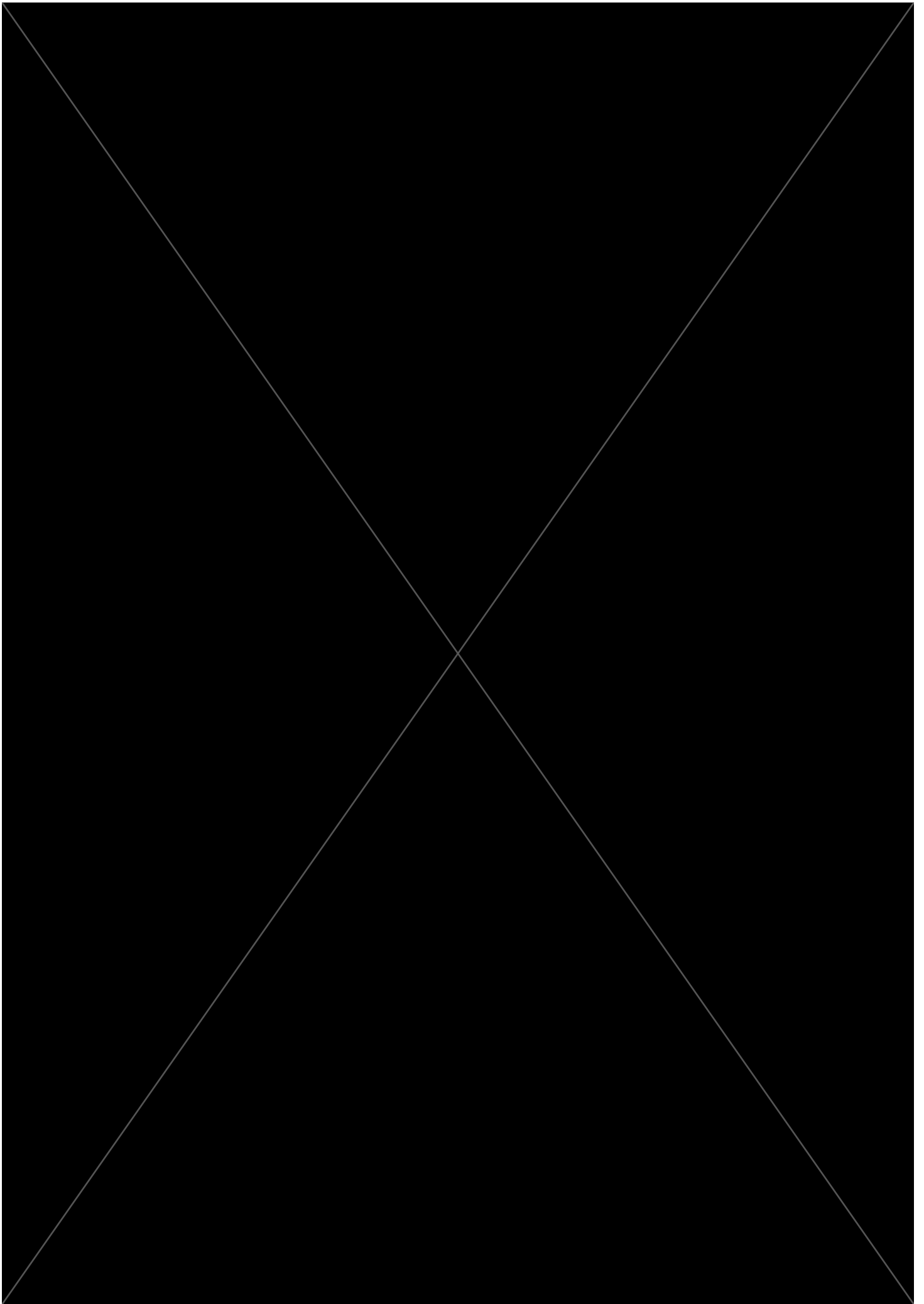


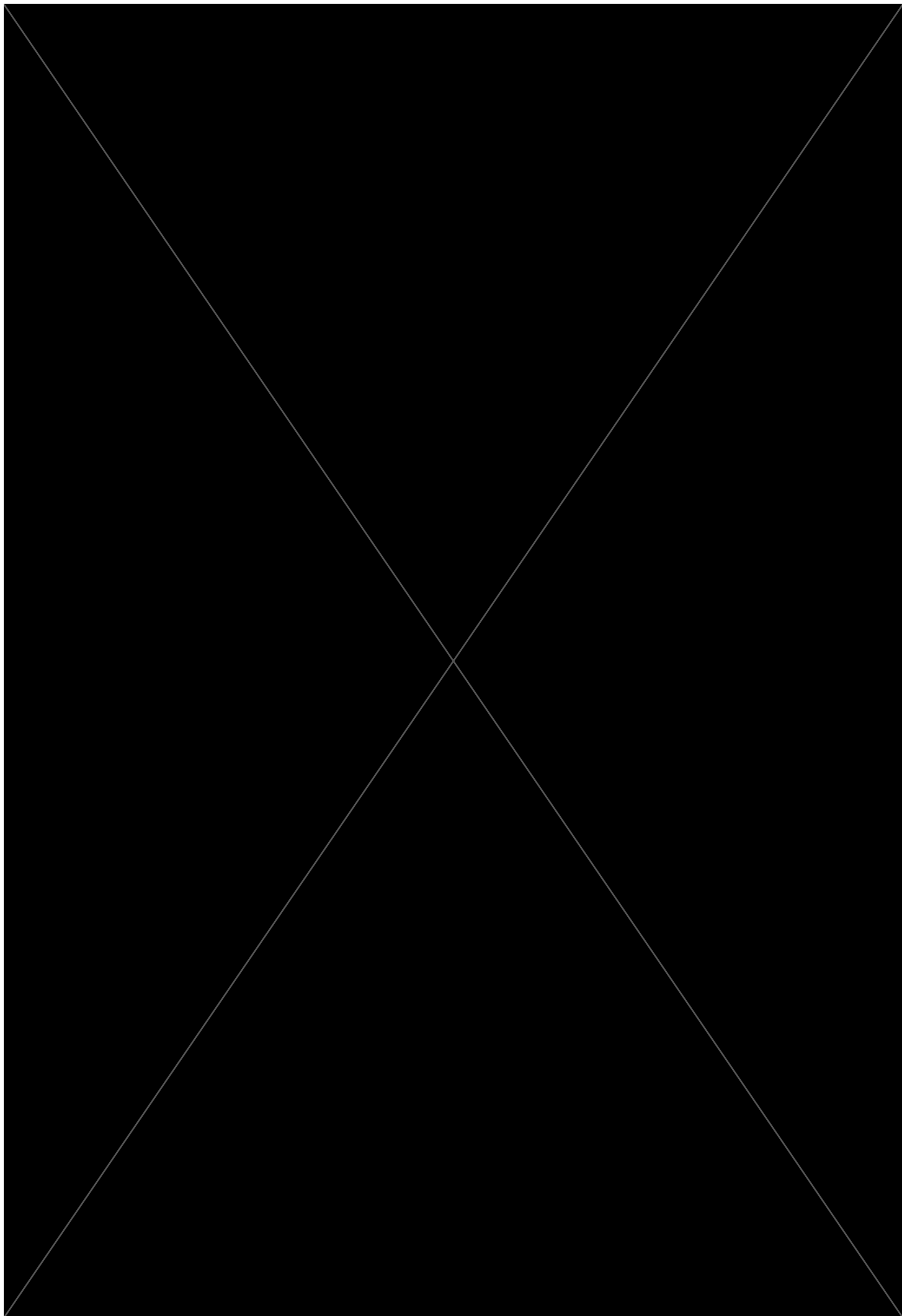












## **Appendix B: Additional Engine/Component Photographs, Machining and Assembly Processes**

This appendix includes various aspects of manufacturing and assembling the engine, as well as additional photographs that were too large and/or numerous to include in chapter 5.

### **i. Machining the Seats for the Injector, Spark Plug and Cylinder Pressure Transducer**

Figure 123 shows the location of the fuel injector in the cylinder block and liner assembly. The seat was cut using a manual milling machine, and two machine vices for work-holding. Similarly, the spark plug can be seen in position in Figure 124, with its seat also having been machined.

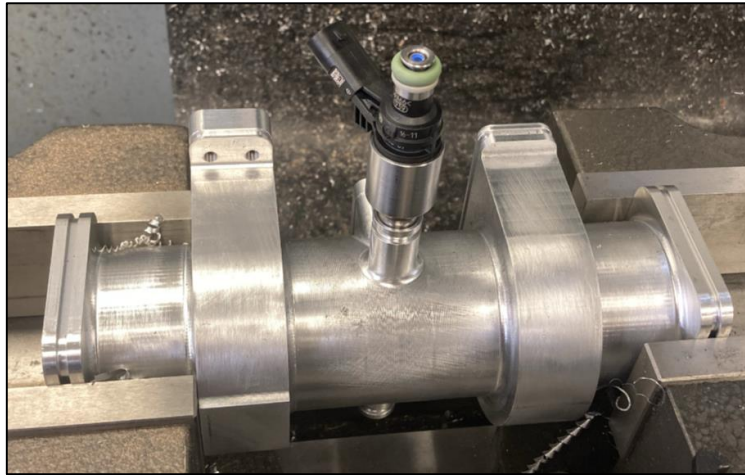


*Figure 123 - Fuel Injector Located in its Seat after that has just been Machined; Overall Cylinder Block Length 203 mm*

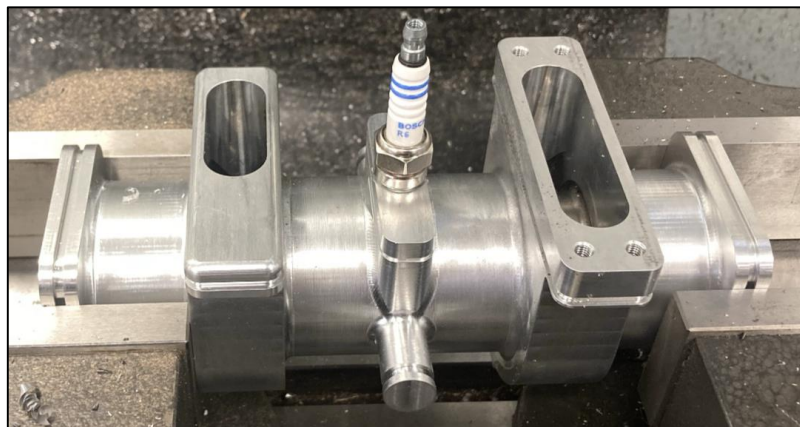


*Figure 124 - Spark Plug in Position in the Middle of the Intake and Exhaust Galleries; Overall Cylinder Block Length 203 mm*

The injector and spark plug seats were relatively simple to add, but the seat for a cylinder pressure transducer required a more complex setup and a very high degree of precision in the machining of the seat itself. Figure 125 shows (partly) how the seat for the pressure transducer was machined. Notice that the milling head is tilted back at an angle of 25 degrees, and the two drill blanks used to locate the central axis of the seat as per the dimensions given in the engineering drawings. Once machining had begun on this seat, the part was not moved until this process was complete as this could endanger its accuracy, which needed to be very high for the pressure transducer to seal and function correctly.

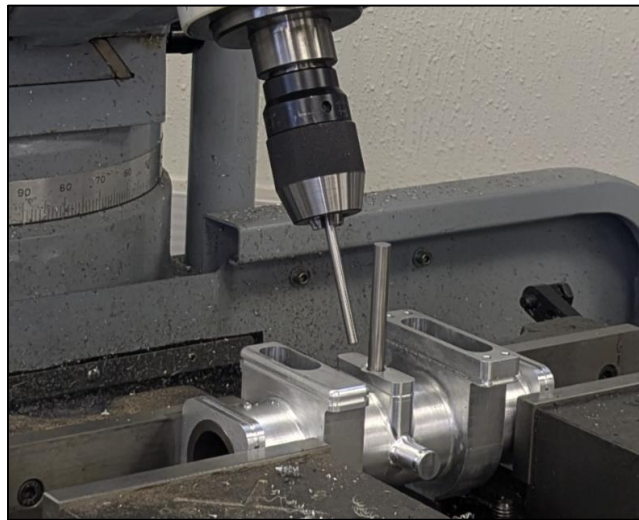


*Figure 125 - Positioning of the Milling Machine Quill to Machine the Pressure Sensor Seat*

Figure 126 shows the cylinder block and liner assembly completed, and ready for installation into the front and rear engine cases, once the seals have been added. Notice that a small additional counterbore exists for the spark plug – this was to ensure that the electrodes protrude an appropriate amount into the cylinder when the spark plug sealing ring is added.



*Figure 126 - Completed Cylinder Block and Liner Assembly, With Spark Plug, Injector and Pressure Transducer Seats, Ready for Installation; Overall Length of Cylinder Block 203 mm*

**ii. Further Pictures of the Front and Rear Engine Cases**

Figure 127 and Figure 128 respectively show interior and exterior views of the front and rear engine cases with a scale. The 275 mm scale is in reference to the base of each engine case where it attaches to the oil sump; note that the rear engine case has a bronze bush pressed into place for one end of the oil pump shaft.

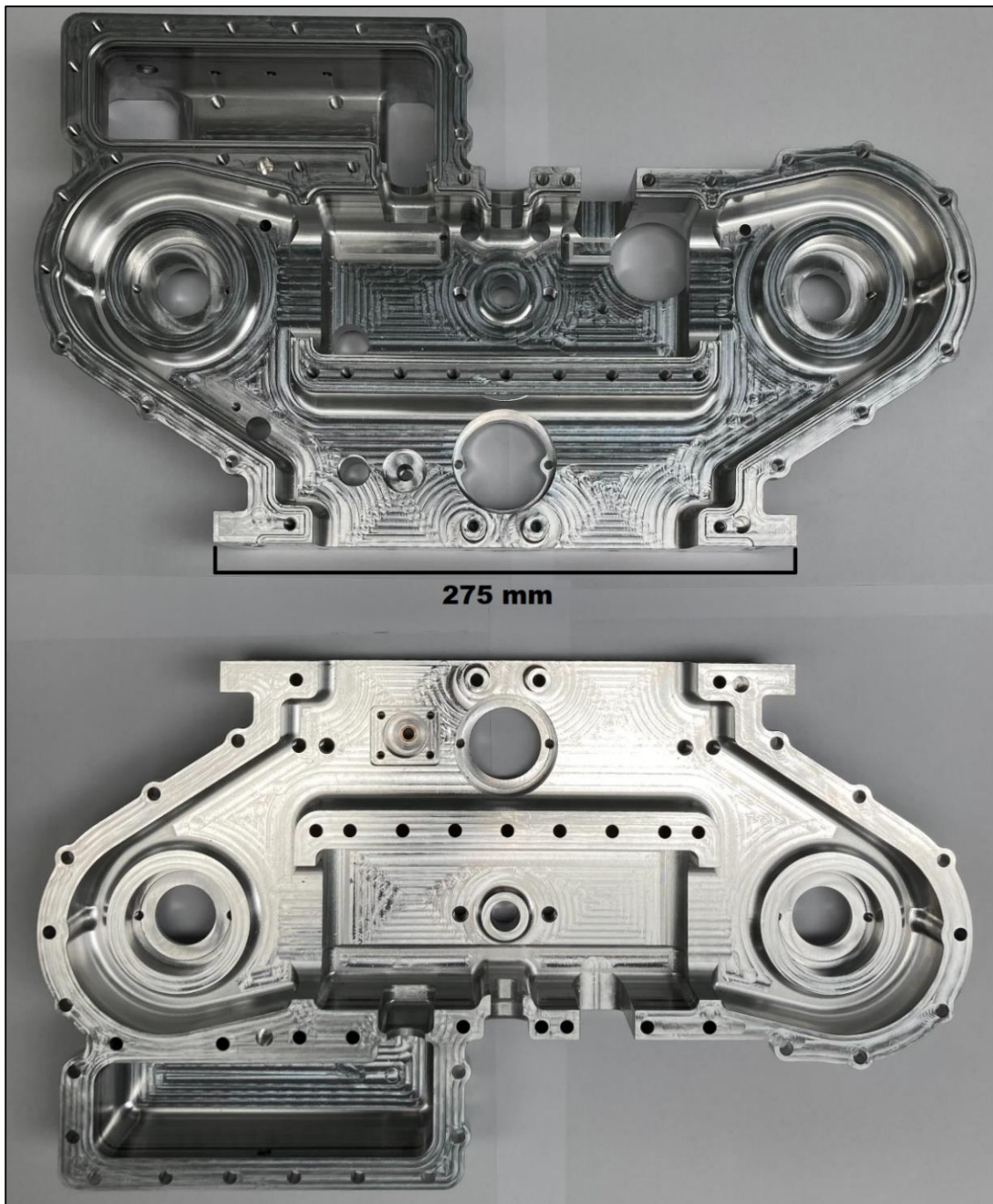


*Figure 127 - Front (top) and Rear (bottom) Engine Cases - Interior View*

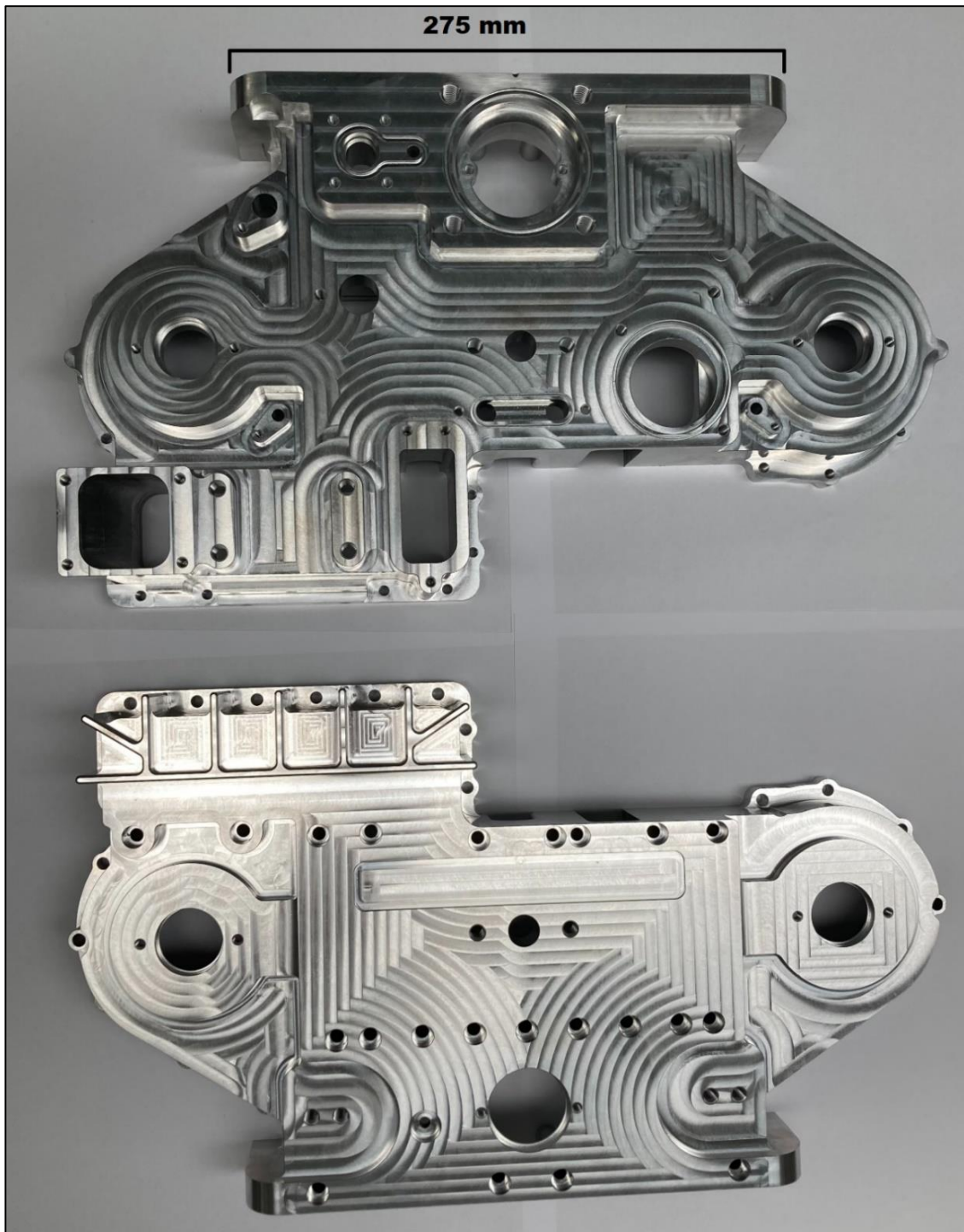


*Figure 128 - Front (top) and Rear (bottom) Engine Cases - Exterior View*

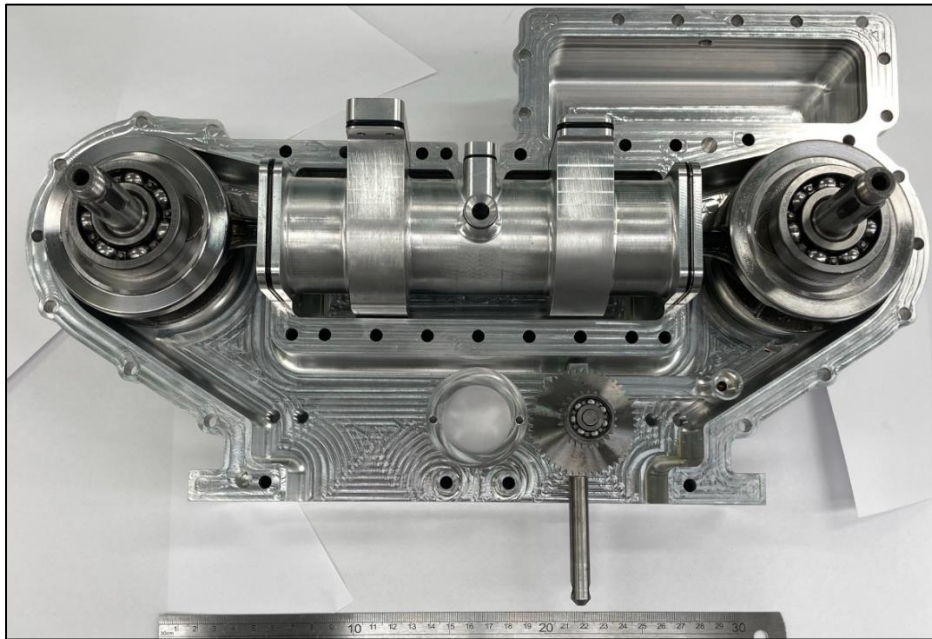
**iii. Installing the Cylinder Block, Crank-Sliders, and Output Shaft**

Figure 129 shows the crank slider mechanisms and the cylinder block and liner assembly, before these were inserted into the engine.



*Figure 129 - Crank Slider Mechanisms and Cylinder Block and Liner Before Assembly*

The rubber O-rings (which seal off the oil side, water side and air side of the engine) have been installed on the block; in this orientation, the view would be of the back of the engine, which is where the timing apparatus, flywheel and starter motor are located.



*Figure 130 - Inserting the Cylinder Block and Crank Sliders into the Rear Engine Case*

Figure 130 shows the cylinder block and liner, and both crank sliders, partially assembled to the rear engine case, as well as the relative position of the oil pump. A hydraulic press for the bearings, and a soft mallet for the cylinder block, aided installation. Once the output shaft had been installed in the rear engine case and the oil pressure relief valve fastened to the oil pump, the entire 'assembly' in Figure 130 was sat loosely on the oil sump for convenience, and the front engine case bolted up to it gradually. The output shaft was similarly inserted using a hydraulic press. Figure 131 shows the output shaft and

associated components assembled prior to installation, except for the front bearing. The back of the engine would be on the right-hand side of the picture when the shaft is installed.



*Figure 131 - Output Shaft Assembly*

Figure 132 shows the rear engine case ‘assembly’ sat as above before the front engine case was installed.

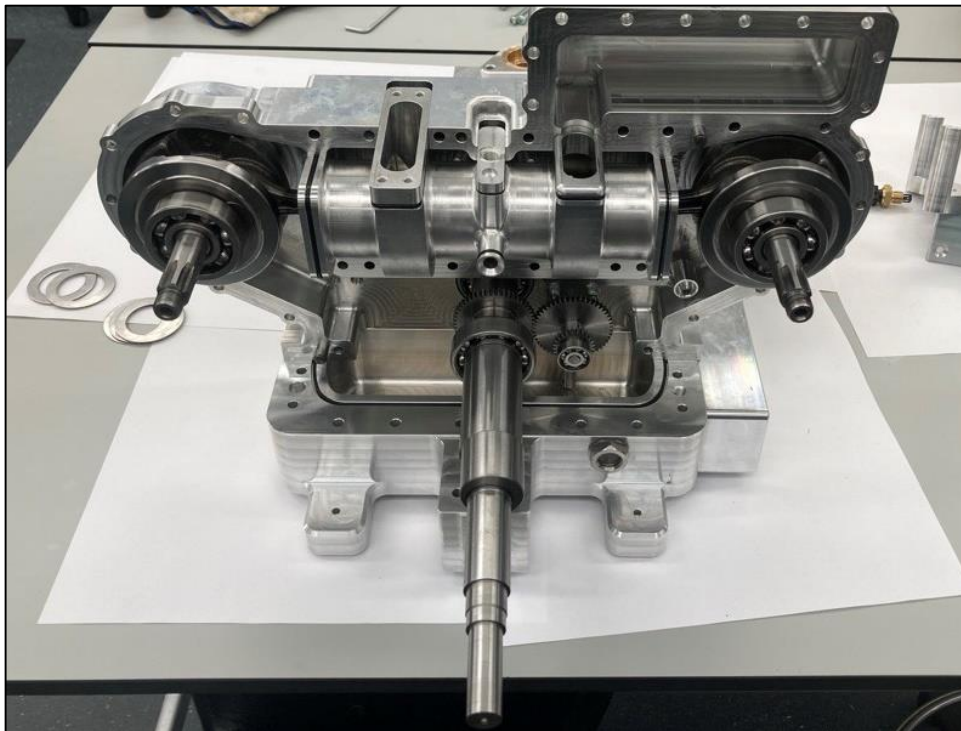


*Figure 132 - Rear Engine Case on top of the Oil Sump*

The process of installation was tenuous because of the tolerances involved combining with the need to make sure everything (including the shafts) was aligned correctly. The cases were not pressed together, instead the fastening bolts were used to gradually pull the two cases together and fully seat the crank sliders, the output shaft, the oil pump shaft (front of), and the cylinder block in position. The small 1 mm thick O-ring on the spark plug upstand unfortunately became ‘pinched’ on the edges of the engine cases. It had to be carefully trimmed back to allow the plates to pull up; a smaller diameter O-ring which

would be in greater tension when installed might avoid this issue. Note some of the crankshaft bearing spacer shims that are visible on the left of Figure 132.

**iv. Machining the Flywheel Pulley and Test Fitting the Timing Gear**

Figure 133 shows the flywheel pulley during machining by the machinist S. Barraclough on a manual lathe, and Figure 134 shows it having been shrink fitted on the back of the flywheel.



*Figure 133 - Flywheel Pulley during Machining*



*Figure 134 - The Flywheel Assembly*

Figure 135 shows the rear of the engine during a test fit of the timing apparatus of the engine. Item 1 is the exhaust crankshaft pulley, 2 is the flywheel assembly (flywheel, ring gear and output shaft pulley), 3 is the intake crankshaft pulley, and 4 is the spark plug, for reference. The flywheel assembly required some fettling to fit onto the shaft, hence why its RINGFEDER® locking assembly is not present, whereas as those for the intake and exhaust crankshaft pulleys are. One of these locking assemblies is shown in isolation in Figure 136.

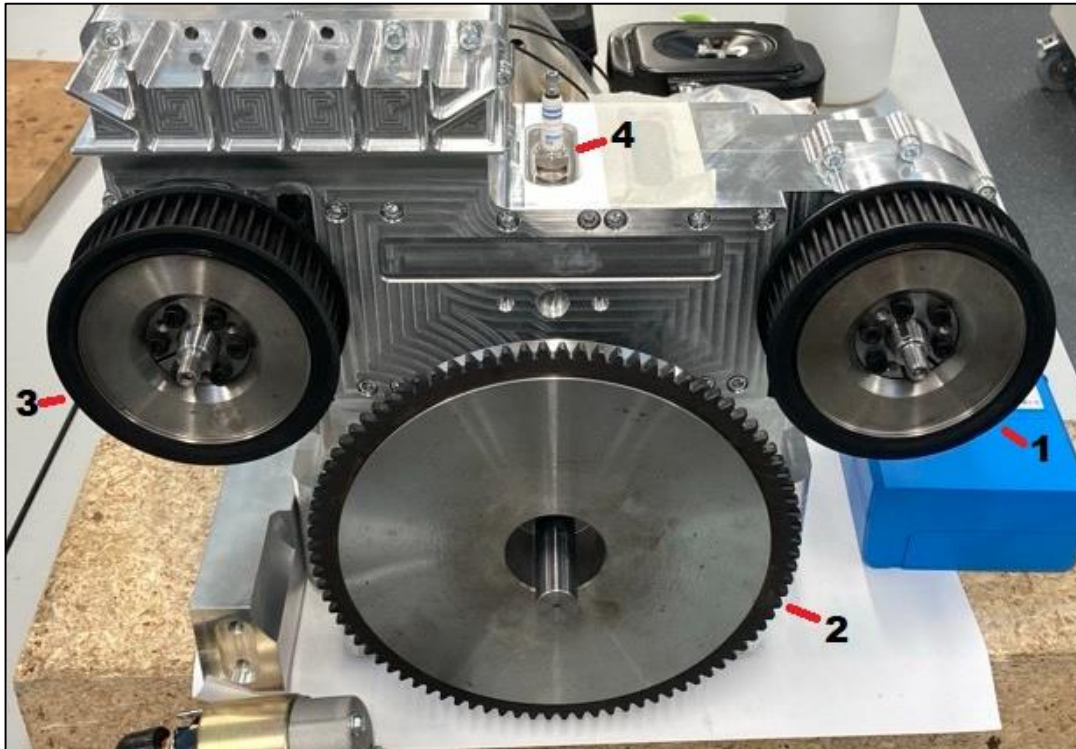


*Figure 135 - Rear of the Engine During a Test Fit of the Timing Apparatus*

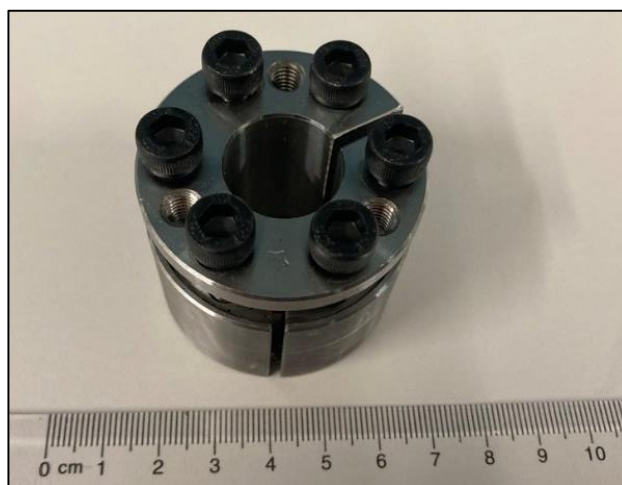


*Figure 136 – RINGFEDER® Locking Assembly*

**v. Supporting the Blower**

Figure 137 shows the blower (1) being checked for fit on the engine. Some of the M6 and M8 fixings for the blower mount (2) are indicated by 3 and 4 respectively, and 5 highlights the position of an adjustment slot for a belt tensioner. The blower has an electric clutch located directly in front of the poly-vee pulley, which requires 12V to provide drive, but is driven by the output shaft of the engine.

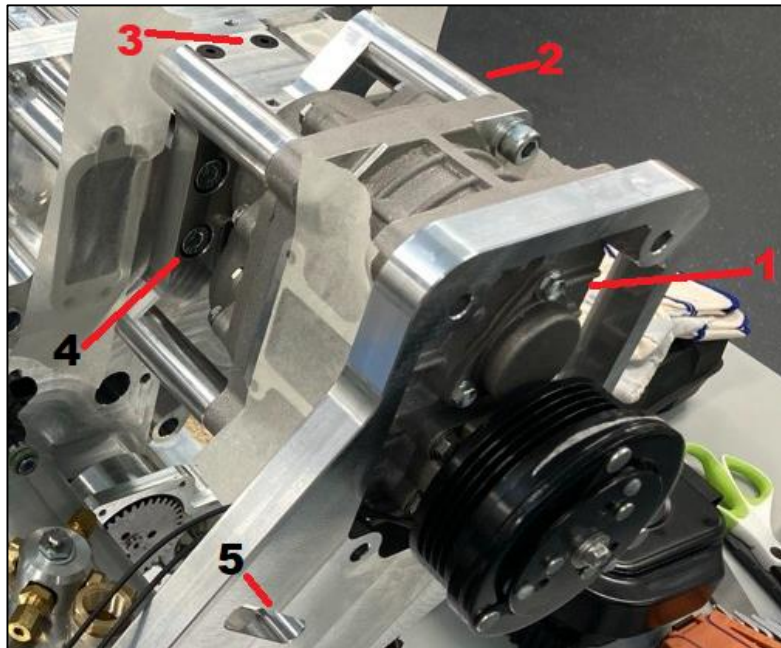


*Figure 137 - Detail of Blower Mounting*

In this case, an earlier test fit had proved valuable since a modelling error meant that the front support bracket fouled on part of the blower. Fortunately, it was possible to remove a small part of the casting from the blower in such a way that its integrity was not compromised, and it then fitted neatly as above.

**vi. View Inside the Bypass Valve**

Figure 138 and Figure 139 show the bypass valve in approximately the fully open and closed positions respectively; the diameter of the bore is approximately 27 mm. Recall that in this engine, a closed bypass valve should result in an increase in scavenge pressure; an open bypass valve should result in a decrease in scavenge pressure. The actuator under the valve body has a drive flat that engages with the position sensor.

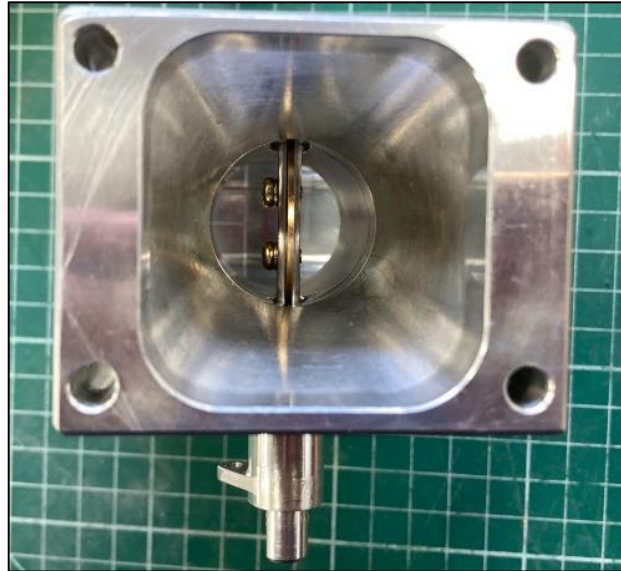


*Figure 138 - Bypass Valve Open; Bore Diameter Approximately 27 mm*

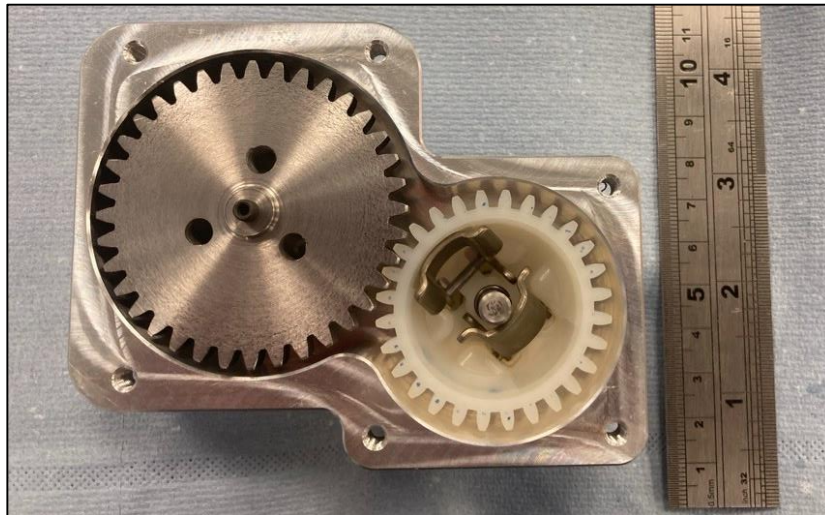


*Figure 139 - Bypass Valve Closed; Bore Diameter Approximately 27 mm*

Unfortunately, during the final assembly of the engine, the bypass valve shaft seized. It is not clear why this occurred, but an unidentified burr on the valve shaft was suspected. It was possible to recover the bypass valve housing however, and fit a new bypass valve shaft. The new shaft was polished to a slightly looser fit, thoroughly deburred, and assembled into the housing with plenty of lubricating oil. Some of this oil can be seen in Figure 138 as a faint ring around the inside of the valve bore, which reflects the closed position of the butterfly in Figure 139.

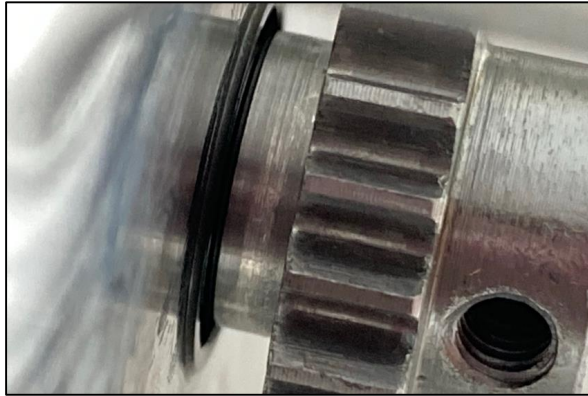
## vii. Inside the Governor Housing

Figure 140 shows a view of the governor drive gear loosely resting in the governor housing (approximately central to its respective recess), and the fly-weight governor in position on its shaft in the housing. After installing the governor on the engine and before the cover was added later, the drive gear was locked onto the governor drive shaft by means of retaining compound; the small grub screw in the centre is intended to aid removal in future if necessary – it is not present in the assembled governor. Because the drive shaft takes drive from inside the engine case, the governor drive gear could not be pressed into position prior to installation. This is because the fasteners that hold the housing on the front engine case are located behind this gear. Notwithstanding the fact the drive gear is only resting in the housing loosely in Figure 140, extra clearance has been provided between it and the fly-weight governor itself. The reason for this is to allow for the fact that the latter rotates freely on a shaft with a degree of clearance and may also tend to deform (i.e. expand) at higher engine speeds.



*Figure 140 - Governor Drive Gear and Fly-Weight Governor*

Figure 141 shows the governor shaft installed into the front engine case, with its 25-tooth drive gear (component 1 in Figure 65) on the right, and the bearing pressed into the housing. It was later found that an additional spacer was needed between the bearing and the gear – the interference fit of the bearing alone was not enough to stop it moving during installation into the housing. The (roughly 3 mm) spacer solved this problem and is visible immediately behind the gear teeth in Figure 141. The interference fit of the gear was supplemented with retaining compound as an extra precaution.



*Figure 141 - The Governor Shaft and its Drive Gear in Position*

Note that the threaded hole visible is one of two that were provided with grubscrews since the gear is a standard part bored to fit the shaft. However, such a fixing mechanism was deemed entirely insufficient for such an important component so was not used in favour of a press fit, and this is true of all the gears inside the engine cases.

**viii. Yellow Metal Insert for the GDI Pump Plunger**

The insert for the GDI pump plunger is positioned such that the semi-circular groove (in which an alignment pin runs) was on the bottom – the threaded holes for jackscrews proving their worth. This was to allow lubricating oil to pool in the groove before draining. Figure 142 shows the insert installed in the front shaft housing, in position on the engine.

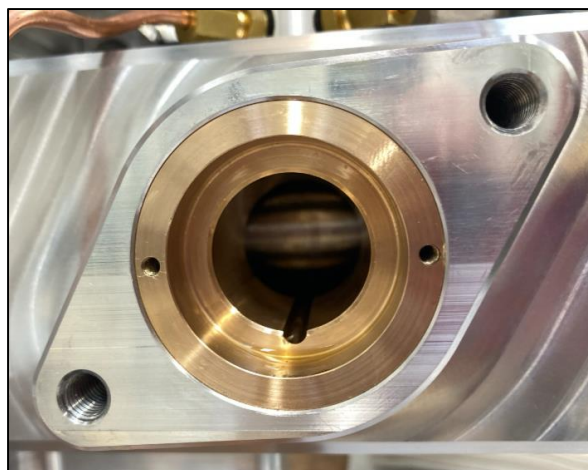


*Figure 142 - Yellow Metal Insert for GDI Pump Plunger*

#### ix. Modifying the Thermostat Housing

Figure 143 shows the coolant outlet hose attached to the thermostat housing. A thermostat was not used since it was found that it would foul on the cylinder block in the assembled engine; this could be remedied with an additional spacer between the thermostat and front engine case. However, for initial proof testing, the housing was modified to hold the coolant temperature sensor, which is immediately below the outlet hose.

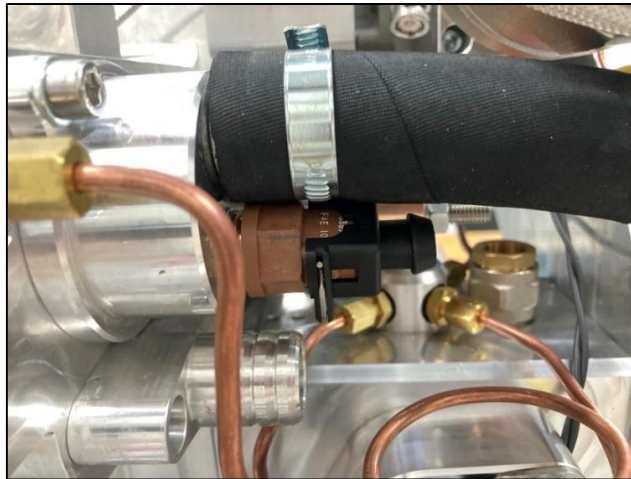


*Figure 143 - The Coolant Outlet Hose and Temperature Sensor*

As is quite clear in Figure 143, space was tight but there was just enough room for the connector to the sensor (a spare connector was used as a test fit). Originally this was to be sited in the cover of the crossover passage in the cooling jacket (see position M in Figure 46), however due to space constraints this was not possible. The oil distribution can also be seen from a slightly different angle, as can the coolant inlet hose barb that is immediately below the thermostat housing. This hose barb is connected to the coolant inlet of the engine cooling jacket by means of a 15 mm pipe that runs across the front of the engine to the other side (see position G in Figure 46)

### Appendix C: Published Paper

'Model based mapping of a novel prototype spark ignition opposed-piston engine'. Please note that only the first page is included herein; for the full version see (reference number [178]):

DOI: 10.1016/j.enconman.2024.118434

Please note that an administrative error was made in Figure 12 and in Equation (9) of this paper. Calculated values of fuelling requirements were not affected. These should be as follows:

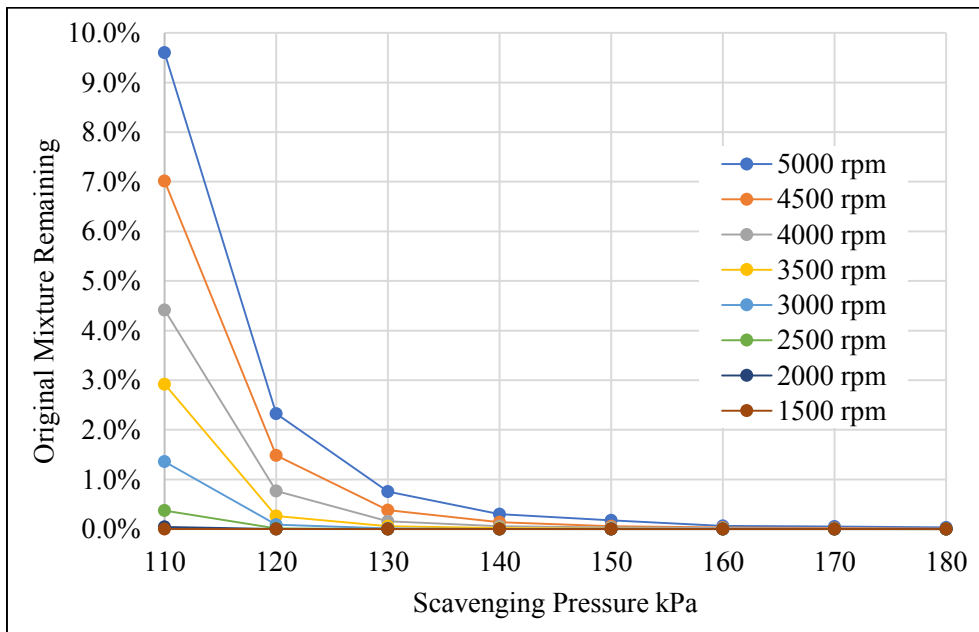
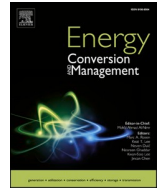


Fig. 12. 2<sup>nd</sup> Cycle Initial Cylinder Mixture Remaining

And:

$$m_{fuel_x} = \frac{1}{100} * \frac{\%_{O_2}}{\lambda} * m_{air_{full}} \quad (9)$$



## Research Paper

# Model based mapping of a novel prototype spark ignition opposed-piston engine

S.F. Furze<sup>\*</sup>, S. Barraclough, D. Liu, S. Melendi-Espina

School of Engineering, University of East Anglia, Norwich Research Park, NR4 7TJ Norwich, United Kingdom

## ARTICLE INFO

## Keywords:

Internal combustion engine  
Opposed piston two stroke  
Spark ignition  
Externally scavenged  
Alternative fuels

## ABSTRACT

Blower-scavenged opposed-piston two-stroke engines possess inherent thermodynamic advantages over four stroke engines. Increasingly well demonstrated in compression ignition form, they are less so in spark ignition form, where there is clearly room for further investigation. Using CONVERGE® CFD, in this work therefore the fuelling requirements of a novel and under-construction small-displacement, two-stroke, spark-ignition, blower-scavenged opposed-piston engine prototype were estimated using three-dimensional computational fluid dynamics simulations. Trapped air mass values generated from motored simulations were used to populate a fuel-agnostic table of speed/scavenge pressure conditions, which will significantly aid the configuration of the engine ECU. This table was tested using targeted fuelled simulations, based on bulk in-cylinder equivalence ratio. Results indicate it was able to predict the required fuel within  $\pm 2\%$  at 1500 rpm, 120/150/180 kPa and 3000 rpm, 150/180 kPa, within  $\pm 10\%$  at 3000 rpm, 120 kPa and 5000 rpm, 180 kPa, and within  $\pm 20\%$  at 5000 rpm, 150 kPa. It performed less well at 5000 rpm, 120 kPa where it overestimated the required fuel by over 43%, although this was to be expected given the reduced scavenging performance at high speed, low scavenge pressure conditions. The swirl-imparting geometry also appeared to aid in flame front propagation.

## 1. Introduction

In 2021, fossil fuels provided more than 82 % of global primary energy consumption [1,2]. Reducing GHG emissions is a particularly prominent issue in the present time, though it is clearly one that faces many very significant hurdles. Indeed, in a particularly critical review, Kalghatgi raises serious questions as to whether it is even feasible to achieve 'Net Zero' decarbonisation targets in the timeframes and to the extents often stated [1]. Moreover, reducing emissions from the transportation sector is one of the most challenging, owing to its reliance on energy-dense hydrocarbon fuels, which are very difficult to replace, especially in cases such as long-haul road-freight transport [1,3]. Whilst electrification using BEVs is commonly the most discussed decarbonisation strategy, it is not often well-suited to all use-cases, such as those described above. Furthermore, there is growing concern over its

sustainability and environmental impact, not only in terms of GHG emissions, but also in terms of resource intensity, end of life material disposal, human toxicity potential and ensuring the additional electricity generation comes from low-carbon sources [1,4]. A more pragmatic assessment is that a diverse approach to decarbonisation of these sectors is far more likely to be successful in reducing emissions overall, than a prescribed 'one-size-fits-all' scenario. This includes electrification but also other strategies, like alternative fuels and improvements in internal combustion engine technology [4–6]. Such a pragmatic view is particularly pertinent given the findings of a recent study by Burton *et al.* which considered a method of determining the GHG emissions rates of different powertrains by more accurately representing the U.S. electricity grid, instead of relying on average grid emission rates. It was concluded that BEVs do not lead to uniform reductions in emissions rates in comparison to HEVs, and in many scenarios have higher emissions

**Abbreviations:** AMR, Adaptive Mesh Refinement; BEV, Battery Electric Vehicle; BTE, Brake Thermal Efficiency; CAD, Crank Angle Degrees; CI, Compression Ignition; ECU, Engine Control Unit; EPC, Exhaust Port Close; EPO, Exhaust Port Open; GCI, Gasoline Compression Ignition; GHG, Greenhouse Gases; HCCI, Homogenised Charge Compression Ignition; HEV, Hybrid Electric Vehicle; HRR, Heat Release Rate; ICE, Internal Combustion Engine; IDC, Inner Dead Centre; IMEP, Indicated Mean Effective Pressure; IPC, Intake Port Close; IPO, Intake Port Open; LES, Large Eddy Simulation; MAP, Manifold Absolute Pressure; MPRR, Maximum Pressure Rise Rate; ODC, Outer Dead Centre; OP2S, Opposed Piston Two Stroke; PCCI, Premixed Charge Compression Ignition; PFP, Peak Firing Pressure; RANS, Reynolds Averaged Navier-Stokes; RNG, Renormalisation Group; SCR, Selective Catalytic Reduction; SI, Spark Ignition.

<sup>\*</sup> Corresponding author.

E-mail address: [s.furze@uea.ac.uk](mailto:s.furze@uea.ac.uk) (S.F. Furze).

<https://doi.org/10.1016/j.enconman.2024.118434>

Received 8 February 2024; Received in revised form 28 March 2024; Accepted 13 April 2024

Available online 22 April 2024

0196-8904/© 2024 The Authors. Published by Elsevier Ltd. This is an open access article under the CC BY license (<http://creativecommons.org/licenses/by/4.0/>).